

# **Self-Starting Interior Permanent Magnet Motor Drive for Electric Submersible Pumps**

**by**

**© Sheikh Fazle Rabbi, B. Eng., M. Eng.**

A thesis submitted in partial fulfillment of the requirements for the degree of

**Doctor of Philosophy**

**Department of Electrical and Computer Engineering  
Faculty of Engineering and Applied Science  
Memorial University of Newfoundland**

**October 2017**

**St. John's**

**Newfoundland**

**Canada**

## **Abstract**

The interior permanent magnet (IPM) motor drive has evolved as the most energy efficient technology for modern motion control applications. Electric submersible pumps (ESPs) are electric motor driven fluid recovery systems. ESPs are widely used for producing oil and gas from deep downhole reservoirs. Standard ESPs are driven by classical squirrel cage induction motors (IMs) due to its self-starting capability from a balanced 3-phase ac excitation, ruggedness, simplicity, low cost and wide scale availability. Although there has been a tremendous growth in the design and development of highly efficient and reliable IPM motors for traction drive systems, application of the IPM motor technology in ESPs is still in its infancy due to challenges associated with the design and control of IPM motors. In this thesis, a new self-starting, efficient and reliable IPM motor drive technology is proposed for ESP systems to extend their efficiency, longevity and performance.

This thesis investigates two different types of self-starting interior permanent magnet (IPM) motors: cage-equipped IPM motors known as line-start IPM motors and a new type of hybrid self-starting motors called hysteresis IPM motors. The limited synchronization capability of line-start IPM motors for high inertial loads is explained in this thesis. To overcome the starting and synchronization problems associated with line-start IPM motors, a new type of hybrid hysteresis IPM motor is proposed in this thesis. Equivalent circuit modeling and finite element analysis of hysteresis IPM motors are carried out in this thesis. A prototype 2.5 kW hysteresis IPM motor is constructed and experimentally tested in the laboratory. In order to limit the inrush current during starting, a stable soft

starter has been designed, simulated and implemented for variable speed operations of the motor. The simulation and experimental results are presented and analyzed in this thesis.

Self-starting IPM motors suffer from hunting induced torsional oscillations. Electric submersible pumps are vulnerable against sustained hunting and can experience premature failures. In this thesis, a novel stator current signature based diagnostic system for detection of torsional oscillations in IPM motor drives is proposed. The diagnostic system is non-intrusive, fast and suitable for remote condition monitoring of an ESP drive system.

Finally, a position sensorless control technique is developed for an IPM motor drive operated from an offshore power supply. The proposed technique can reliably start and stabilize an IPM motor using a back-emf estimation based sensorless controller. The efficacy of the developed sensorless control technique is investigated for a prototype 3-phase, 6-pole, 480V, 10-HP submersible IPM motor drive.

In summary, this thesis carried out modeling, analysis and control of different types of self-starting IPM motors to assess their viability for ESP drive systems. Different designs of self-starting IPM motors are presented in this thesis. In future, a fully scalable self-starting IPM motor drive will be designed and manufactured that can meet the industrial demands for high power, highly reliable and super-efficient ESP systems.

## **Acknowledgement**

I would like to express my sincere gratitude to my supervisor Dr. Md Azizur Rahman for introducing me to the IPM motor technology and providing me an opportunity to carry out an independent curiosity-based research. I would like to sincerely thank the School of Graduate Studies and Dr. Rahman for their financial supports. I am also thankful to my supervisory committee members Dr. Glyn George and Dr. Stephen Butt for providing valuable suggestions and comments during the preparation of this thesis. I would like to thank Dr. Michael Hinchey for his scholarly suggestions. In addition, I would like to acknowledge Mr. Greg O'Leary and Mr. Glenn St. Croix for helping me with their technical expertise throughout the entire program.

I am also indebted to my parents Sheikh Salim and Nilufa Yesmin, my sister Rifat Sharmin, my aunt Alta Rahman, my friends Nahidul Khan, Babara Pye, Wayne and Priscilla Edwards, Maxwell Little, Justin Royce as well as my other friends and family members for their relentless encouragements and supports to keep me sane during the herculean graduate program. Finally, I would like to thank my fellow graduate students for their useful assistance and support.

## Table of Contents

Abstract .....	ii
Acknowledgement .....	iv
List of Tables .....	x
List of Figures .....	xi
List of Symbols .....	xxii
List of Abbreviations .....	xxix
Chapter 1 .....	1
1.1 Thesis Objectives .....	5
1.2 Scope of Work .....	8
1.3 Publications .....	10
1.4 Thesis Organization .....	14
Chapter 2 .....	17
2.1 Introduction .....	17
2.2 Average Torque Analysis .....	23
2.3 Critical Criteria for Successful Synchronization of Line-Start IPM motors .....	31
2.4 Analytical Results for Line-Start IPM Motors .....	41
2.5 Simulation Results .....	45
2.6 Experimental Results .....	51
2.7 Conclusions .....	59

References.....	59
Chapter 3.....	64
3.1 Introduction.....	64
3.2 Hysteresis Interior Permanent Magnet Motor .....	65
3.3 Equivalent Circuit Modeling of a Hysteresis IPM Motor.....	68
3.3.1 Modeling of Hysteresis Phenomenon .....	69
3.3.2 Modeling of Permanent Magnet Excitation .....	77
3.3.3 Magnetic Equivalent Circuits of a Hysteresis IPM Motor.....	80
3.3.4 Electrical Equivalent Circuits of a Hysteresis IPM Motor .....	82
3.4 Analytical Results .....	88
3.5 Finite Element Analysis.....	94
3.6 Experimental Results .....	104
3.7 Conclusions.....	106
Appendix.....	107
References.....	115
Chapter 4.....	119
4.1 Introduction.....	119
4.2 Radial Flux Hysteresis IPM Motor .....	121
4.3 Design of a Radial Flux Hysteresis IPM Motor .....	124
4.4 Performance Analysis .....	133
4.5 Conclusions.....	146
References.....	148

Chapter 5.....	150
5.1 Introduction.....	150
5.2 Mechanical Dynamics of an Electric Submersible Pump System.....	160
5.3 Bond Graph Modeling of ESP-Dynamics .....	168
5.4 Simulation Results .....	174
5.5 Experimental Results .....	184
5.6 Conclusion .....	189
References.....	189
Chapter 6.....	191
6.1 Introduction.....	191
6.2 Design of a Soft-Starter for a Hysteresis IPM Motor Drive.....	191
6.3 Simulation Results .....	198
6.4 Experimental Results .....	207
6.5 Conclusion .....	215
References.....	215
Chapter 7.....	217
7.1 Introduction.....	217
7.2 Hunting in IPM Motor Drives.....	221
7.3 Stator Current Signature for Detection of Hunting.....	224
7.4 Detection of Hunting using Short-Time Fourier Transform.....	227
7.5 Diagnosis of Hunting Using Wavelet Packet Decomposition (WPD) .....	235
7.5.1 Wavelet Packet Decomposition (WPD).....	236

7.5.2 Diagnosis of Hunting Using WPD.....	239
7.5.3 Feature Extraction .....	241
7.6 Simulation Results .....	242
7.7 Experimental Results .....	250
7.8 Conclusions.....	258
Appendix.....	259
References.....	260
Chapter 8.....	266
8.1 Introduction.....	266
8.2 Real Time Diagnosis of Hunting .....	269
8.2.1 Signal Conditioning .....	270
8.2.2 Detection of Hunting Phenomenon.....	272
8.2.3 Identification of the Severity of Hunting .....	275
8.2.4 Decision .....	277
8.3 Simulation Results .....	279
8.4 Experimental Results .....	289
8.4.1 Operated from the Line Supply.....	290
8.4.2 Operation from a $V/f$ Controlled Inverter.....	294
8.4.3 Effects of Source Impedance .....	297
8.5 Conclusion .....	301
Appendix.....	302
References.....	305

Chapter 9.....	307
9.1 Introduction.....	307
9.2 Submersible IPM Motor Drive .....	310
9.3 Sensorless Control of IPM-ESP Drives .....	316
9.3.1 Estimation of the Rotor Position Using Motor Back-Emfs .....	319
9.3.2 Sensorless $V/f$ Controller for Starting an IPM-ESP Drive .....	325
9.3.3 Sensorless Vector Controller for IPM-ESP Drives .....	327
9.4 Simulation Results .....	331
9.5 Conclusion .....	342
Appendix.....	342
References.....	344
Chapter 10.....	348
10.1 Research Conclusions .....	348
10.2 Major Contributions.....	351
10.3 Future Works .....	353

## List of Tables

Table 2.1. 1-HP line-start IPM motor. ....	51
Table 3.1. Comparison between hysteresis and squirrel-cage self-start IPM motors. ....	68
Table 3.2. Design parameters of the hysteresis IPM motor. ....	96
Table 4.1. Design Parameters of Self-Starting IPM Motors. ....	147
Table 7.1. 'db6' filter coefficients. ....	259
Table 7.2. Parameters of the line-start IPM motor. ....	260
Table 8.1. Performance of the proposed technique for different levels of hunting in the 5- kW line-start IPM motor drive. ....	302
Table 8.2. Performance of the proposed technique for different levels of hunting in the 1- HP line-start IPM motor drive. ....	302
Table 8.3. 'db6' wavelet decomposition and reconstruction filter coefficients. ....	303
Table 8.4. Parameters of the 5kW and 1-HP line-start IPM (LSIPM) motors. ....	304
Table 9.1. Relative comparison between different types of submersible motors. ....	311
Table 9.2. Specification of the 10-HP submersible IPM motor. ....	315
Table 9.3. Comparison between a Franklin submersible motor and the IPM motor. ....	316

## List of Figures

Figure 1.1. Offshore power system for ESP drives. ....	3
Figure 2.1. Equivalent circuits: (a) $q$ -axis and (b) $d$ -axis.....	24
Figure 2.2. Average asynchronous torques of a line-start IPM motor.....	32
Figure 2.3. Instantaneous torque vs. speed curves of a line-start IPM motor.....	33
Figure 2.4. Slip vs. load angle trajectory of a line start IPM motor.....	34
Figure 2.5. Synchronous torque vs. load angle for an IPM motor.....	36
Figure 2.6. Pole slips of an IPM motor during the start of the synchronization. ....	37
Figure 2.7. A sinusoidal approximation of the last pole slip. ....	37
Figure 2.8. Flowchart for determining the critical criteria of a cage equipped IPM motor. .....	40
Figure 2.9. Critical inertia vs. percentage rated load for constant and dynamic loads. ....	42
Figure 2.10. Critical slip vs. percentage rated load for constant and dynamic loads.....	42
Figure 2.11. Apparent kinetic energy vs. inertia for different load torques.....	43
Figure 2.12. Approximate last pole slip based during synchronization.....	44
Figure 2.13. Simulated run-up responses: (a) Constant load torque and (b) Dynamic load torque. ....	46
Figure 2.14. Run-up trajectories in the $s$ - $\delta$ plane (a) slip vs. load-angle and (b) torque vs. speed. ....	49
Figure 2.15. Analytical vs. simulated critical inertia of the motor for a constant load.....	50
Figure 2.16. Analytical vs. simulated critical inertia of the motor for a dynamic load. ....	50
Figure 2.17. A prototype squirrel-cage IPM Motor: (a) rotor and (b) cross section.....	52

Figure 2.18. Experimental run-up responses. ....	54
Figure 2.19. Experimental slip vs. load-angle trajectories.....	55
Figure 2.20. Experimental phase-A current waveform at 75% of the rated load. ....	56
Figure 2.21. Experimental phase-A current waveform at rated load. ....	57
Figure 2.22. Experimental responses of the motor for step changes in the load torque: (a) speed and (b) current.....	58
Figure 3.1. Rotor of a prototype hysteresis interior permanent magnet motor. ....	66
Figure 3.2. Cross-section of a hysteresis interior permanent magnet motor.....	66
Figure 3.3. Average asynchronous torques of a hysteresis-start IPM motor. ....	67
Figure 3.4. Hysteresis loops of a soft-magnetic material [25].....	71
Figure 3.5. Parallelogram modeling of the hysteresis loops of a soft-magnetic material. .	71
Figure 3.6. Rectangular modeling of the hysteresis loops of a soft-magnetic material ....	72
Figure 3.7. Major hysteresis loop of 36% Cobalt-Steel alloys. ....	74
Figure 3.8. Elliptical approximation of hysteresis loops. ....	75
Figure 3.9. Elliptical modeling of the hysteresis loop for 36% Cobalt-Steel alloys.....	77
Figure 3.10. Demagnetization curves of an Nd-B-Fe magnet. ....	78
Figure 3.11. Modeling of the permanent magnet a source of mmf.....	78
Figure 3.12. Equivalent mmf of a permanent magnet.....	79
Figure 3.13. Magnetic equivalent circuits of a hysteresis IPM motor: (a) $d$ -axis and (b) $q$ -axis. ....	81
Figure 3.14. Electrical equivalent circuits: (a) $d$ -axis and (b) $q$ -axis.....	87
Figure 3.15. Run-up responses of a hysteresis IPM motor. ....	89

Figure 3.16. Electromagnetic torque responses of a hysteresis IPM motor.....	90
Figure 3.17. Traces of the peak line current of a hysteresis IPM motor.....	91
Figure 3.18. Hysteresis lag angle of a hysteresis IPM motor. ....	92
Figure 3.19. Equivalent rotor resistance of a hysteresis IPM motor.....	93
Figure 3.20. Equivalent hysteresis inductance of a hysteresis IPM motor. ....	93
Figure 3.21. An Ansys Maxwell 2D finite element model of a hysteresis IPM motor.....	95
Figure 3.22. A quarter Ansys Maxwell 2D FE model. ....	97
Figure 3.23. Magnetic flux density distribution in the motor. ....	98
Figure 3.24. Magnetic flux lines inside the motor. ....	99
Figure 3.25. (a) Air-gap flux density due to the magnets and (b) air-gap back-emf. ....	100
Figure 3.26. Analytical and FEA run-up responses of the motor. ....	101
Figure 3.27. Analytical and FEA torque responses of the motor.....	102
Figure 3.28. Analytical and FEA current responses of the motor.....	103
Figure 3.29. Rotor core losses of the motor.....	104
Figure 3.30. Experimental vs analytical run-up response of the motor. ....	105
Figure 3.31. Experimental vs analytical line current of the motor. ....	106
Figure 3.32. Closed magnetic path inside a hysteresis motor.....	108
Figure 4.1. Flux distribution for: (a) CF-hysteresis and (b) RF- hysteresis IPM motors.	122
Figure 4.2. Comparisons between CF and RF hysteresis IPM motors: (a) torque vs. speed and (b) torque vs. current. ....	124
Figure 4.3. Self-start IPM motor: (a) Cage rotor and (b) radial flux hysteresis rotor.....	126
Figure 4.4. Starting torque vs. ring thickness for a radial flux hysteresis motor. ....	127

Figure 4.5. Steady-state torque vs. ring thickness for a radial flux hysteresis IPM motor. .....	128
Figure 4.6. Output torque vs. magnet width. ....	129
Figure 4.7. Efficiency vs. magnet width for variable magnet thickness. ....	130
Figure 4.8. Output torque vs. $\omega$ . ....	131
Figure 4.9. Design B of the RF-hysteresis IPM motor. ....	131
Figure 4.10. (a) Design A and (b) Design B of the RF-hysteresis IPM motor. ....	133
Figure 4.11. Run-up responses of the Design A radial flux hysteresis IPM motor. ....	134
Figure 4.12. Developed torque of the Design A radial flux hysteresis IPM motor. ....	135
Figure 4.13. Phase current of the Design A radial flux hysteresis IPM motor. ....	136
Figure 4.14. Torque vs. speed trajectory at rated load of the Design A motor. ....	137
Figure 4.15. Run-up responses of the Design B type: (a) RF-hysteresis IPM and (b) CF- Hysteresis IPM motors. ....	139
Figure 4.16. Run-up torque responses of the Design B type: (a) RF-hysteresis IPM and (b) CF-Hysteresis IPM motors. ....	141
Figure 4.17. Run-up current responses of the Design B type: (a) RF-hysteresis IPM and (b) CF-hysteresis IPM motors. ....	142
Figure 4.18. Air-gap flux density of a RF-hysteresis IPM motor. ....	143
Figure 4.19. Air-gap flux density of a CF-hysteresis IPM motor. ....	143
Figure 4.20. Performance analysis of the Design B RF-Hysteresis IPM motor: (a) efficiency and (b) power factor. ....	145

Figure 4.21. Run-up responses of a cage-IPM motor and a RF-hysteresis IPM motor for high inertial loads.....	146
Figure 5.1. An offshore oil and gas production well using electric submersible pumps [1]. .....	150
Figure 5.2. Inflow performance relationship (IPR) curves [2]. .....	151
Figure 5.3. IPR vs. tubing intake pressure for a: (a) stable well and (b) dead well [2]. ..	153
Figure 5.4. Major types of artificial lift systems [3]. .....	154
Figure 5.5. Pressure vs. flow rates of a well for different artificial lift techniques [3]....	154
Figure 5.6. Comparative analysis between popular lift techniques in terms of well depth and production rate [3]......	156
Figure 5.7. Production Rate vs. Well Life. ....	158
Figure 5.8. A hysteresis IPM motor equipped ESP. ....	161
Figure 5.9. Cross sectional view of a multi-stage ESP. ....	161
Figure 5.10. Rotor of a submersible hysteresis IPM motor. ....	162
Figure 5.11. Characteristics curves of a variable speed ESP. ....	163
Figure 5.12. A lumped element model of the 4-stage ESP system. ....	167
Figure 5.13. Word Bond Graph Model of an ESP System. ....	168
Figure 5.14. Electromagnetic Coupling between electrical and mechanical system. ....	169
Figure 5.15. A 2-level interconnection between $\{a, b, c\}$ and $\{d, q\}$ bond graph models. .....	170
Figure 5.16. I-field relations and casualties for the rotor and the stator in the $d-q$ axis ..	171
Figure 5.17. Gyrator structure for torque and induced voltages. ....	171

Figure 5.18. A bond graph model of a hysteresis IPM motor.....	172
Figure 5.19. A bond graph torsional model of a shaft-segment.....	173
Figure 5.20. A bond graph torsional model of an impeller.....	174
Figure 5.21. Speed responses of the motor for different shaft-lengths. ....	175
Figure 5.22. Torque responses of the motor for different shaft-lengths. ....	177
Figure 5.23. The speed response of the motor for different shaft-diameters.....	178
Figure 5.24. Torque responses of the motor for different shaft-diameters. ....	179
Figure 5.25. Speed responses of the ESP impellers.....	180
Figure 5.26. The shaft torque response of the ESP.....	181
Figure 5.27. Comparative performances between IM-ESP and hysteresis IPM-ESP drives: (a) impeller load factor (b) shaft torque (c) shaft speed and (d) input line current.....	184
Figure 5.28. Experimental test set-up. ....	185
Figure 5.29. Experimental run-up responses: (a) 60 Hz and (b) 50 Hz. ....	187
Figure 5.30. Experimental torque responses: (a) 60 Hz and (b) 50 Hz.....	188
Figure 5.31. Experimental line current of the motor at 60 Hz.....	188
Figure 6.1. Block diagram of a typical open loop $V/f$ controller. ....	192
Figure 6.2. Block diagram of a $V/f$ controller for a hysteresis IPM motor drive.....	194
Figure 6.3. Phasor diagram for a hysteresis IPM motor. ....	195
Figure 6.4. Simulated run-up responses of the motor for 10 Hz-90Hz frequencies .....	199
Figure 6.5. Simulated torque of the motor for 60Hz frequency.....	201
Figure 6.6. Simulated line current of the motor for 60Hz frequency.....	202

Figure 6.7. Responses of the motor for step change in load: (a) torque, (b) hysteresis lag angle, (c) flux density vector and (d) line current.....	205
Figure 6.8. Responses of the $V/f$ controller for a step change in load: (a) command voltage and (b) magnitude of the current vector.....	207
Figure 6.9. Block diagram of the experimental setup.....	208
Figure 6.10. The prototype hysteresis IPM motor.....	208
Figure 6.11. Experimental run-up responses for 10Hz-90Hz command frequencies.....	209
Figure 6.12. Experimental line current for 60Hz.....	210
Figure 6.13. Experimental response of the motor for step load change at 60Hz: (a) torque, (b) line current and (c) command voltage.....	212
Figure 6.14. Experimental vs. simulated responses of the motor for a step load change at 50Hz: (a) torque, (b) line current and (c) command voltage.....	214
Figure 7.1. Synchronous torque vs. load angle of an IPM motor.....	222
Figure 7.2. Oscillations in load angle during hunting.....	223
Figure 7.3. Limit cycles in an IPM motor.....	224
Figure 7.4. Simplified magnetic equivalent circuit of an IPM motor.....	226
Figure 7.5. Bessel functions of the first kind for different orders.....	229
Figure 7.6. Current response at normal operation: (a) phase-A current and (b) PSD of the current signal.....	232
Figure 7.7. Responses during hunting condition: (a) rotor speed, (b) phase-A current (c) PSD of the current signal and (d) PSD of the rotor speed oscillations.....	235
Figure 7.8. Magnitudes of the frequency responses of 'db6' wavelet filters.....	239

Figure 7.9. Wavelet packet decomposition tree of the current signal.....	240
Figure 7.10. Finite element model of the 1-HP LSIPM motor. ....	243
Figure 7.11. Responses of the motor during hunting at 60 Hz supply frequency: (a) torque, (b) speed and (c) current. ....	245
Figure 7.12. Spectrogram for 60Hz using: (a) STFT and (b) WPD.....	246
Figure 7.13. Feature coefficients at 60Hz command frequency. ....	248
Figure 7.14. Spectrogram for 50Hz using: (a) STFT and (b) WPD.....	249
Figure 7.15. Feature coefficients at 50Hz command frequency. ....	250
Figure 7.16. Responses of the motor during hunting at 60 Hz: (a) speed and (b) current. ....	252
Figure 7.17. Spectrogram of the current using: (a) STFT and (b) WPD. ....	253
Figure 7.18. Hunting at 60Hz: (a) Coefficients of node 32 and (b) feature coefficients. ....	255
Figure 7.19. Hunting at 50 Hz: (a) speed, (b) current and (c) feature coefficients. ....	256
Figure 7.20. Hunting at 90 Hz: (a) speed, (b) current and (c) feature coefficients. ....	258
Figure 8.1. Block diagram of the hunting diagnostic process.....	270
Figure 8.2. Frequency responses of the applied notch filter: (a) magnitude and (b) phase. ....	271
Figure 8.3. A 3-level wavelet packet tree of the current signal. ....	275
Figure 8.4. Wavelet reconstruction of the level 3 nodes.....	276
Figure 8.5. Flowchart of the hunting diagnosis algorithm.....	278
Figure 8.6. Finite element models of line-start IPM motors: (a) 5-kW and (b) 1-HP. ....	279

Figure 8.7. Responses of the motor: (a) rotor speed, (b) stator phase current and (c) Fourier spectrum of the motor current during hunting. ....	281
Figure 8.8. Response of the hunting diagnostic algorithm: (a) magnitude of the feature coefficient, (b) modulating current signal and (c) degree of stator current modulation. .	283
Figure 8.9. Responses for the 1HP motor drive: (a) rotor speed, (b) phase current, (c) modulating current signal and (d) magnitude of the feature coefficient $F_{a3, 1}$ . ....	285
Figure 8.10. Responses for the 1HP motor drive: (a) magnitude of the feature coefficient $F_{d3, 1}$ (b) magnitude of the feature coefficient $F_{a3, 2}$ , (c) magnitude of the feature coefficient $F_{d3, 2}$ and (d) degree of stator current modulation. ....	286
Figure 8.11. Responses during practically stable hunting: (a) rotor speed (b) modulating current signal, (c) magnitude of the feature coefficients and (d) degree of stator current modulation. ....	289
Figure 8.12. Block diagram for the real time diagnosis of hunting. ....	290
Figure 8.13. Responses of the diagnostic technique for detecting hunting at 60Hz: (a) rotor speed, (b) motor phase current, (c) modulating current signal and (d) magnitude of the feature coefficient of node $a_{(3,1)}$ . ....	292
Figure 8.14. Responses of the diagnostic technique for detecting hunting at 60Hz: .....	293
Figure 8.15. Responses of the diagnostic technique for detecting hunting at 50Hz: (a) rotor speed, (b) motor phase current, (c) modulating current signal and (d) magnitude of the feature coefficient of node $a_{(3,1)}$ . ....	295
Figure 8.16. Responses of the diagnostic technique for detecting hunting at 50Hz: (a) $F_{d(3, 1)}$ , (b) $F_{a(3, 2)}$ , (c) $F_{d(3, 2)}$ and (d) relative degree of modulation. ....	296

Figure 8.17. Effects of source impedance on the: (a) rotor speed, (b) phase voltage and (c) phase current. ....	299
Figure 8.18. Performance of the sub-synchronous hunting detection algorithm: (a) modulating current (b) $F_{a(3,1)}$ , (c) $F_{d(3,1)}$ , (d) $F_{a(3,2)}$ , (e) $F_{d(3,2)}$ and (f) $\chi$ . ....	300
Figure 9.1. Submersible IPM motor: (a) assembly and (b) rotor cross section. ....	313
Figure 9.2. Performance of the submersible IPM motor: (a) efficiency and (b) power factor. ....	314
Figure 9.3. Flowchart of the sensorless controller for IPM-ESP drives. ....	318
Figure 9.4. Block diagram of the back-emf estimation algorithm. ....	323
Figure 9.5. Sensorless $V/f$ control algorithm for starting the IPM-ESP drive. ....	326
Figure 9.6. Sensorless vector control technique for the IPM-ESP drive. ....	328
Figure 9.7. The simplified $d$ -axis current controller. ....	328
Figure 9.8. The simplified speed and $q$ -axis current controllers. ....	330
Figure 9.9. The MTPA trajectory for an IPM motor. ....	330
Figure 9.10. Variation of the ESP load torque with command frequency: (a) supply frequency, (b) speed and (c) ESP load torque. ....	332
Figure 9.11. Actual vs estimated run-up responses of the IPM motor. ....	333
Figure 9.12. Actual vs estimated rotor position of the motor at low speed. ....	334
Figure 9.13. Actual vs estimated position of the rotor at a high speed. ....	335
Figure 9.14. Trajectory of the position error for: (a) low speed operation and (b) high speed operation. ....	336
Figure 9.15. Actual vs. estimated currents: (a) $d$ -axis and (b) $q$ -axis. ....	337

Figure 9.16. Responses of the motor: (a) torque and (b) line current. ....338

Figure 9.17. Performance of the controller for a step change in the command frequency.  
.....339

Figure 9.18. Performance of the sensorless controller for a step change in the load: (a)  
load torque, (b) speed and (c) electromagnetic torque.....340

Figure 9.19. Performance of the sensorless controller for a step change in the load: (a)  
actual vs. estimated rotor position and (b) actual vs. estimated speed of the rotor.....341

## List of Symbols

$V_{qs}$ and $V_{ds}$	$q$ - $d$ axes stator voltages
$V'_{qr}$ and $V'_{dr}$	$q$ - $d$ axes rotor voltages, referred to stator side
$i_{qs}$ and $i_{ds}$	$q$ - $d$ axes stator currents
$i'_{qr}$ and $i'_{dr}$	$q$ - $d$ axes rotor currents, referred to the stator side
$L_{qs}$ and $L_{ds}$	$q$ - $d$ axes stator synchronous inductances
$L'_{qr}$ and $L'_{dr}$	$q$ - $d$ axis rotor self-inductances, referred to the stator side
$L_m$	Magnetizing inductance of a motor
$L_{mq}$ and $L_{md}$	$q$ and $d$ axes stator magnetizing inductances
$\theta_r$	Rotor position angle
$\omega_{rm}$	Mechanical speed of the rotor
$\omega_{re}$	Rotor electrical angular speed
$\omega_b$	Base electrical angular speed
$P$	Number of poles
$p$	Number of pole pairs
$i'_m$	Current due to permanent magnet excitation
$\lambda'_m$	Equivalent permanent magnet flux
$\lambda'_{mh}$	The peak flux linkage due to the permanent magnet excitation and hysteresis effect
$\lambda_{qs}, \lambda_{ds}$	$q$ - $d$ axes flux linkages of the stator
$\lambda'_{qr}, \lambda'_{dr}$	$q$ - $d$ axes flux linkages of the rotor, referred to the stator

$T_c$	Cage torque
$T_b$	Magnet brake torque
$i_{qm}$	$q$ -axis current due to permanent magnet excitation
$i_{dm}$	$d$ -axis current due to permanent magnet excitation
$T_e$	Developed electromagnetic torque
$F$	Frictional constant
$H$	Pump head
$Q$	Pump flow rate
$T_{bmax}$	Maximum brake torque
$s$	Slip of the motor
$s_{cr}$	Critical slip of the motor
$s_{Tbmax}$	Slip of the motor at the maximum brake torque
$T_e(\delta)$	Pulsating synchronizing torque
$\delta$	Electrical load angle
$\delta'_s$	Unstable electrical load angle
$\delta_{max}$	Maximum electrical load angle
$\varphi$	Phase shift of the current
$T_L$	Load torque
$J$	Inertia constant of the total system
$J_{cr}$	Critical inertia
$K_p$	Proportional gain
$T_s$	Synchronous Torque

$T_{mag}$	Magnet alignment torque
$T_{rel}$	Reluctance torque
$K_i$	Integral gain
$E_0$	Excitation voltage
$X_{ds}$ and $X_{qs}$	$d$ - $q$ axes stator reactances
$r_s$	Stator resistance per phase
$r'_{r'q}$ and $r'_{r'd}$	$q$ - $d$ axes rotor cage resistances, referred to the stator side
$X'_{lr}$	Rotor leakage reactance, referred to the stator side
$T_{damp}$	Damping torque
$L_{rc}$	Recoil inductances of permanent magnet
$I_m$	Equivalent peak current due to permanent magnet excitation
$\zeta$	Ratio of the quadrature axis stator reactance to the direct axis one
$V$	Supply voltage / phase rms
$T_{p1}, T_{p2}, T_{p3}$ and $T_{p4}$	Components of pulsating synchronizing torque
$T_{av}$	Average asynchronous torque
$T_a$	Net accelerating torque
$T_L$	Load torque
$V_{th}, r_{th}$ and $X_{th}$	Thevenin equivalent voltage, resistance and reactance
$I_2$	Cage current
$T_{f+w+c}$	Friction, windage and core loss of an IPM motor
$\rho$	Fluid density

$\eta$	Pump efficiency
$K_{scr}$	Apparent kinetic language
$K_p$	Pull-in energy
$B$	Magnetic flux density
$B_m$	Maximum magnetic flux density
$B_{rm}$	The effective residual flux density of a permanent magnet
$H$	Magnetic field intensity
$\mu$	Magnetic permeability
$\mu_0$	Magnetic permeability of the air
$\mu_{rm}$	Recoil permeability of the magnet
$\varphi_0$	Initial phase shift of the current
$r_r$	The average of the inner and the outer radius of the rotor
$r_g$	The average radius of the air-gap
$t_r$	Thickness of the rotor hysteresis ring
$l$	Axial length of the rotor hysteresis ring
$l_g$	The radial length of the air-gap
$\mathcal{F}_m$	Magnet mmf
$\mathcal{F}_{md}$ and $\mathcal{F}_{mq}$	$d$ - $q$ axes magnet mmfs
$\mathcal{F}_{ad}$ and $\mathcal{F}_{aq}$	$d$ - $q$ axes armature mmfs
$l_m$	The radial length of the magnet
$\gamma$	The angular width of the magnet in radian

$V_h$	Volume of the hysteresis ring
$K_{sw}$	The winding factor of the stator
$N_{sw}$	The number of stator series turns per phase
$r_s$ or $R_s$	Stator phase resistance
$r_r'$ or $R_r$	Equivalent rotor resistance, referred to the stator
$R_h$	Equivalent hysteresis resistance
$R_e$	Equivalent eddy current resistance
$k_{fq}$ and $k_{fd}$	$d$ - $q$ axes armature reaction form factors
$\alpha$	The ratio of the width of the pole shoe to the pole pitch
$I_m$	Equivalent peak current due to permanent magnet excitation, referred to the stator.
$\mathcal{R}_{ad}$ and $\mathcal{R}_{aq}$	$d$ - $q$ axes reluctances of the stator back iron
$\mathcal{R}_{gd}$ and $\mathcal{R}_{gq}$	$d$ - $q$ axes reluctances of the air-gap
$\mathcal{R}_{ald}$ and $\mathcal{R}_{alq}$	$d$ - $q$ axes leakage reluctances of the stator
$\mathcal{R}_{rld}$ and $\mathcal{R}_{rlq}$	$d$ - $q$ axes leakage reluctances of the rotor
$\mathcal{R}_{hd}$ and $\mathcal{R}_{hq}$	$d$ - $q$ axes reluctances of the rotor hysteresis ring
$L_{md}$ and $L_{mq}$	$d$ - $q$ axes magnetizing inductances of a motor
$B_{aq}$ and $B_{ad}$	$d$ - $q$ axes armature flux densities
$T_{hys}$	Torque generated due to hysteresis phenomenon in the rotor
$N_s$	Synchronous speed of a motor
$g$	The gravitational acceleration

$J_1 \dots J_4$	The inertias of impellers 1...4, respectively
$D_m$	The viscous damping coefficient of the motor
$D_1 \dots D_4$	The viscous damping coefficients of impellers 1...4, respectively
$K_{l1} \dots K_{l4}$	The load torque coefficients of impellers 1...4, respectively
$C_{m1}$	The compliance of the shaft between motor and impeller 1
$C_{12}, C_{23}$ and $C_{34}$	The compliances of the shafts between the impellers 1...4
$D_{12}, D_{23}$ and $D_{34}$	The viscous damping coefficients between impeller shafts 1...4
$\theta_m$	The angular position of the motor
$\theta_1 \dots \theta_4$	The angular positions of the impellers 1...4, respectively
$\tau$	Transmitted torque in a bond graph
$\xi$	Damping ration in a second order low pass filter
$J_m$	Bessel function of the first kind of $m^{\text{th}}$ order
$\phi(t)$	Normalized scaling function
$\psi(t)$	Mother wavelet function
$\mathcal{L}^2(\mathbb{R})$	A Lebesgue space
$g[k]$ and $h[k]$	Wavelet low pass and high pass filter coefficients
$F_{i,j}$	Feature coefficient of node $(i, j)$ in the wavelet packet tree
$I_{i,j} [k]$	The magnitude of the co-efficient $k$ at node $(i, j)$
$\sigma^2_{i,j}, \mu_{i,j}$	The variance and the mean of the coefficients at node $(i, j)$
$f_n$	Natural frequency of a second order notch filter
$a_1^I$ and $d_1^I$	The first level approximate and detail coefficients of the current

	samples using WPD
$a_2^l$ and $d_2^l$	The second level approximate and detail coefficients of the current samples $a_1^l$ using WPD
$a_{3,1}^l, d_{3,1}^l, a_{3,2}^l, d_{3,2}^l$	The third level approximate and detail coefficients of the current samples $a_2^l$ and $d_2^l$ .
$\chi$	Severity of hunting
$g^R[k]$ and $h^R[k]$	Wavelet low pass and high pass reconstruction filter coefficients
$\theta_{re}^{est}$	Estimated rotor position
$\theta_{com}$	Phase compensation angle

## List of Abbreviations

AC	Alternating Current
CF	Circumferential Flux
DC	Direct Current
<i>d-q</i>	Direct and Quadrature
EMF	Electromotive force
ESP	Electric Submersible Pump
ESPCP	Electric Submersible Progressive Cavity Pump
FE	Finite Element
FT	Fourier Transform
GY	Gyrator
HEM	Hauser Energetic model
IM	Induction Motor
IPM	Interior Permanent Magnet
IPR	Inflow Performance Relationship
JAM	Jiles-Atherton model
MCSA	Motor Current Signature Analysis
MGY	Modulated Gyrator
MMF	Magnetomotive Force
MTF	Modulated Transformer
MTPA	Maximum Torque Per Ampere
NPV	Net Present Value

PLL	Phase Locked Loop
PM	Permanent Magnet
PMM	Permanent Magnet Motor
PSD	Power Spectral Density
RF	Radial Flux
SMO	Sliding Mode Observer
STFT	Short-time Fourier Transform
TF	Transformer
THD	Total Harmonics Distortion
VSD	Variable Speed Drive
WPD	Wavelet Packet Decomposition
WPT	Wavelet Packet Tree
WT	Wavelet Transform

# Chapter 1

## Introduction and Thesis Organization

Electric submersible pumps (ESPs) are widely used as downhole artificial lift devices in both land based and offshore oil and gas production units for improved oil recovery. An ESP is a motor/pump configuration comprised of multi-stage impellers driven by electric ac motors. ESPs are particularly suitable for low flow/low pressure oil reservoirs as they increase the fluid pressure gradually by each pump stage in order to achieve high recovery factors. Each stage of the centrifugal pump consists of an impeller driven by the motor and a diffuser which directs the flow to the next stage of the pump. Since the inception of ESPs, polyphase squirrel-cage rotor induction motor drives have been used for ESPs in offshore oil and gas. Induction motors are used in ESPs because of their ruggedness, simplicity, relatively good efficiency, low cost and wide scale availability. However, induction motors have some inherent limitations. An induction motor is an asynchronous motor and always runs in a lagging power factor with a slip. It cannot develop any torque at the constant synchronous speed and always runs with a slip power loss in the rotor. The speed of the induction motor always varies with changing loading conditions and these motors do not operate efficiently at all speeds. It is not always possible for an inverter drive to run an induction motor at the command speed as well as at the best efficiency point. The cost and the complexity of the control equipment for induction motor drives are high.

Submersible motors have unique constructional features. The uniqueness lies in their long stator and narrow construction. It is also extremely difficult and unreliable to build an induction motor that has an extremely long rotor with a small outer diameter capable of meeting the power requirement of an ESP. Thus, a multi-rotor induction motor is used for electric submersible pumps. The multi-rotor assembly suffers from frequent failure and shaft breakdowns due to extreme mechanical stress. Induction motor driven ESPs suffer from relatively higher failure rates and longer downtime than other lift techniques in downhole harsh environments. For a harsh offshore environment, the total cost to replace or repair an ESP unit is very high. Thus, any improvements in ESP reliability and performance can be significant for the offshore oil and gas industries, and the requirements for reducing power consumption and efficient energy usage have become major issues, especially during the time when oil price is low.

Figure 1.1 displays a typical power system for oil and gas recovery from downhole reservoirs using ESPs. Gas turbines and diesel generators are normally the main sources of power generation for offshore and isolated land based oil and gas production units. Variable speed drives (VSDs) including filters and step-up transformers are situated on the platform. Power is supplied to downhole ESPs through long cables that run down the well. Standard ESP cables are rated as 3kV (L-L) and 5kV (L-L). The depth of the well can vary from a few hundred feet to several thousands of feet under the surface. For offshore applications, the cable length can be extremely long. Thus, a step-up transformer is needed at the load side, if the voltage boost capability is not available in the VSD. The load side filters are usually passive, designed to reduce the higher harmonics induced by the VSD. The percentage of low frequency harmonics also goes up as the length of the

cable increases. Thus, special load side filters are also deployed to remove both low and high frequency harmonics for improving the power quality of the supply voltage to ESPs.

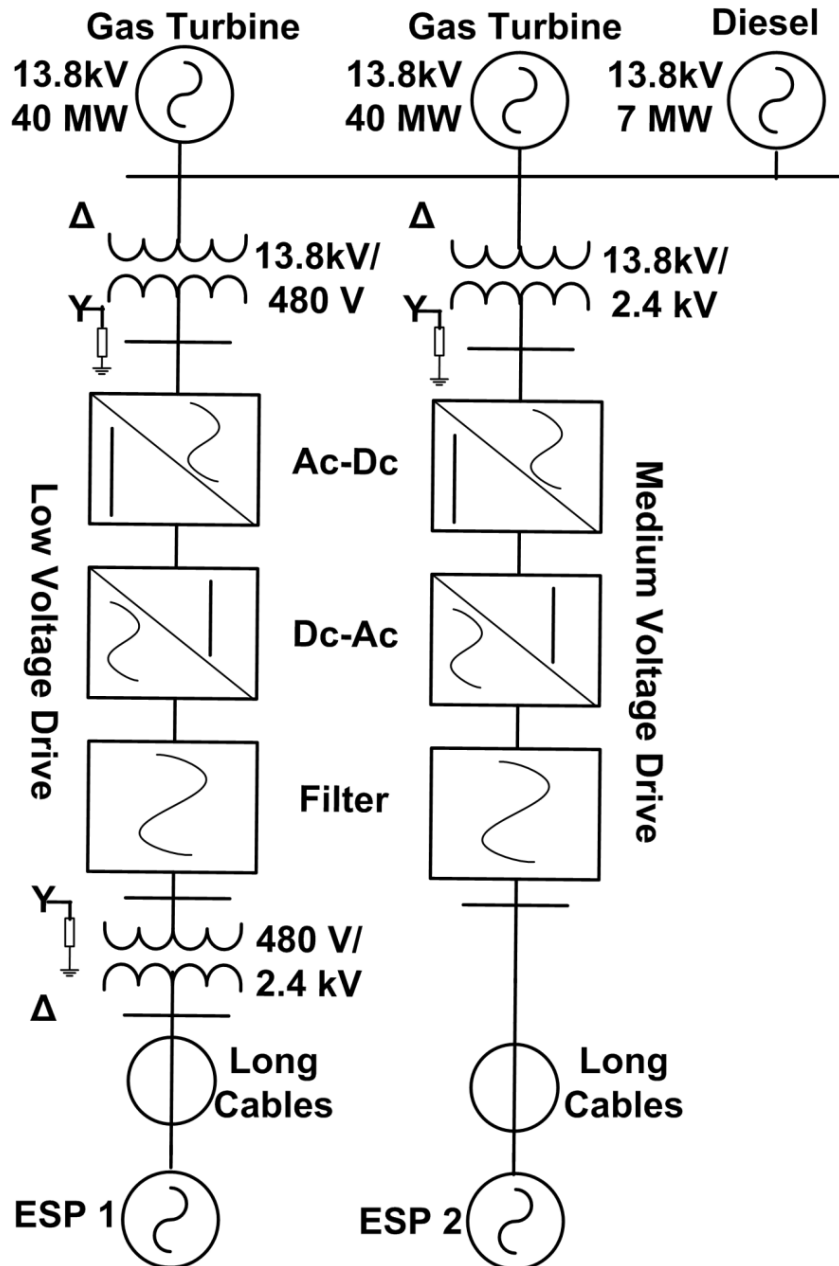


Figure 1.1. Offshore power system for ESP drives.

Self-starting IPM motors are the class of synchronous motors that have an inherent capability of producing starting torque from the rotating magnetic field in the airgap created by a balanced 3-phase fixed frequency ac excitation in the stator. Due to the rotor excitation provided by permanent magnets, these motors do not require any external dc excitation in the rotor. These motors are highly efficient and belong to the class of NEMA premium/super premium motors. Self-starting IPM motors can provide the damping torque during any change in the load condition or supply voltage. Thus, self-starting IPM motors are suitable for drive applications that cannot have any position sensors such as resolvers/encoders. In the case of submersible drives in deep-water downhole environments, it is not possible to take instantaneous readings from the position sensors confidently as the motor is thousands of feet under the sea. Relying on the signal received from a long distance reduces the reliability of the ESP, and can cause possible ESP failures. Thus, a self-starting IPM motor is a suitable candidate for ESP drive systems.

## 1.1 Thesis Objectives

The overall objective of this thesis is to investigate the performance of self-starting interior permanent magnet motors for ESP drive applications. It can be divided into the following objectives.

- a) The primary objective of this thesis to investigate the application of self-starting interior permanent magnet (IPM) motors for fluid pumping applications. A standard line-start IPM motor can self-start from a fixed-frequency balanced ac supply with the aid of the starting torque produced by the cage windings without any rotor position sensing. However, it has limited synchronization capability due to the absence of the cage torque at synchronous speed. In a conventional line-start IPM motor, the motor typically acts as a class D type induction motor. Although the cage torque is high during start to accelerate the rotor, it becomes lower during the synchronization process as the slip becomes small, and the cage torque eventually becomes zero at the point of synchronization. As a result, it is essential to investigate the synchronization capability of a cage rotor IPM motor for different starting load torques. The initial objective of this thesis is to carry out an analysis of the synchronization capability of cage equipped IPM motors for fluid pumping type of loads.
- b) A hybrid hysteresis interior permanent magnet motor drive combines the features of hysteresis motors and permanent magnet motors. This type of motors can be a potential replacement of the induction motors for ESP drives. The second

objective of this thesis is to develop an equivalent circuit model to analyze the dynamic performance of a self-starting hysteresis IPM motor for ESP loads.

- c) Design of a self-starting IPM motor for high inertial loads is a major objective of this thesis. The motor is expected to have smooth starting and high synchronization capabilities. The motor must possess inherent damping capability against sudden changes to operating conditions. The motor should also be highly efficient and reliable.
- d) An ESP drive suffers from significant torsional vibration during starting due to high inrush torque and current. The third objective of this thesis is to develop a combined electrical and mechanical model of a hysteresis IPM motor driven ESP system. The developed model will be used to investigate the torsional dynamics of the ESP system during starting. The effects of pump shaft diameters and shaft lengths on the torsional vibration of the ESP system will be investigated in this thesis.
- e) A major objective of this thesis is to develop a sensorless soft-starter for hysteresis IPM motor drives that does not require knowledge of the rotor position. The soft-starter has to start and synchronize a hysteresis IPM motor drive for various loading conditions. It has to be able to compensate for the voltage drop in the line resistance and also needs to adjust the command voltage dynamically with the changing load conditions.
- f) Hunting induced torsional vibration is an inherent phenomenon in IPM motor drives. In ESPs, torsional vibrations are often induced in the drive system due to transients in the long cable or time varying transients in the well caused by the

presence of gas or solids. Detection of torsional oscillations is traditionally carried out using vibration/speed sensors. Vibration sensors are slow and provide noisy readings. Speed sensors are not available in a sensorless ESP drive. An important objective of this thesis is to detect and diagnose in real time the hunting phenomenon in self-starting IPM motor drives, using only the stator current signals of the motor. A fast, non-intrusive and remote torsional vibration detection system will be extremely useful for health monitoring of an ESP drive system.

- g) Although a sensorless soft-starter can operate an IPM motor drive for ESP systems, it is not highly efficient and provides poor dynamic response. The final objective of this thesis is to develop a sensorless control strategy for IPM motor drives that encompasses both high dynamic response and high efficiency. The sensorless control technique has to be able to successfully start an IPM motor drive and run it at the operating frequency without any rotor hunting. It should be robust and easy to implement.

## 1.2 Scope of Work

The objectives of this thesis are achieved by carrying out the following steps.

Step I: The starting and synchronization capabilities of cage-equipped line-start IPM motors are carried out using analytical, simulation and experimental investigations for a prototype 1-HP 3-phase 4-pole line-start IPM motor. Analytical results are obtained using Maple software. Simulations are carried out using Matlab/Simulink software. Experimental investigations are performed for a prototype 1-HP IPM motor drive using a dSPACE ds1104 data acquisition system. An AC dynamometer is used to emulate the pump load.

Step II: Analytical equivalent circuit models of a hysteresis IPM motor drive are developed using elliptical modeling of the hysteresis phenomenon. The equivalent circuit models are solved using Matlab/Simulink software. The analytical results are verified using finite element simulations and experimental investigations for a 2.5-kW 3-phase 4-pole hysteresis IPM motor drive. Ansys Maxwell software is used for the finite element analysis. A Mawdsley generalized machine setup is used for laboratory testing of the prototype motor.

Step III: A high efficiency self-starting radial flux hysteresis IPM motor is designed using a parametric optimization technique. The starting and synchronization capabilities of this motor are investigated using Ansys Maxwell. A relative comparison among radial flux hysteresis IPM, circumferential flux hysteresis IPM and line-start IPM motors is carried out using finite element simulation and experimental investigation.

Step IV: Analysis of the mechanical dynamics of a hysteresis IPM motor driven ESP system is carried out using bond graph. Standard bond graph software 20sim is used to solve the state equations of the system. Experimental investigations are carried out by extending the shaft of the prototype hysteresis IPM motor. A dc generator is connected with the motor as a loading machine. A torque transducer is used to observe the torsional oscillation in the system.

Step V: The developed soft-starter for a hysteresis IPM motor drive is simulated using Matlab/Simulink software. The real time implementation of the soft-starter is carried out using a digital signal processing board dS1104. A 3-phase full bridge IGBT inverter coupled with the ds1104 controller board is used as the variable speed drive. The Mawdsley generalized machine set up is used to emulate the ESP system.

Step VI: A hunting diagnostic algorithm is developed using advanced signal processing techniques. The developed algorithm is simulated using Matlab/Simulink software. Real time diagnosis of hunting for a laboratory motor-dyno system is performed using a digital signal processing board and a variable speed drive system.

Step VII: Finally, the sensorless controller for an IPM motor driven ESP system is developed using a back-emf estimation algorithm. The performance of the developed controller is observed for a 10-HP 3-phase 6-pole ESP drive system.

### 1.3 Publications

The research works presented in this thesis have been published in various transactions and peer reviewed conference proceedings. I have been the principal author of all the publications. I formulated the problems, developed solutions, performed simulations, carried out experimental implementations and prepared the manuscripts. The co-authors have contributed by providing assistance during implementation of the solutions as well as constructive comments and feedbacks during refinement of the manuscripts. The list of papers associated with each chapter of this thesis is provided below.

#### Chapter 2:

1. S. F. Rabbi and M. A. Rahman, “Critical Criteria for Successful Synchronization of Line-Start IPM Motors,” *IEEE Journal of Emerging and Selected Topics in Power Electronics*, Vol. 2, No. 2, pp. 348-358, April 2014.
2. S. F. Rabbi and M. A. Rahman, “Determination of the Synchronization Criteria of Line Start IPM Motors,” *Proceedings of the IEEE International Electric Machines and Drives Conference (IEMDC)*, Chicago, USA, May 12-15, 2013, pp. 1218-1224.
3. S. F. Rabbi and M. A. Rahman “Analysis of Starting and Synchronization Process for Line Start IPM Motors”, *Proceedings of the IEEE International Conference on Electrical and Computer Engineering (ICECE)*, Dhaka, Bangladesh, December 20-22, 2012, pp. 311-314.

### Chapter 3:

1. S. F. Rabbi and M. A. Rahman, “Equivalent Circuit Modeling of a Hysteresis Interior Permanent Magnet Motor for Electric Submersible Pumps”, *IEEE Transactions on Magnetics*, Vol. 52, No. 7, pp. 1-4, July 2016.
2. S. F. Rabbi and M. A. Rahman, “Modeling and Transient Performance Analysis of a Hysteresis IPM Motor”, *Proceedings of the IEEE International Conference on Electrical and Computer Engineering (ICECE)*, Dhaka, Bangladesh, December 20-22, 2014, pp. 607-610.
3. S. F. Rabbi and M. A. Rahman, “Equivalent Circuit Modeling of an Interior Permanent Magnet Hysteresis Motor”, *Proceedings of the IEEE Canadian Conference on Electrical and Computer Engineering (CCECE 2014)*, Toronto, Canada, May 4-7, 2014, pp.1-5.
4. S. F. Rabbi and M. A. Rahman, “Transient Analysis of a Line Start Hysteresis Interior Permanent Magnet Motor”, *Proceedings of the IEEE Energy Conversion Congress and Exposition (ECCE)*, Pittsburgh, USA, Sep. 14-18, 2014, pp. 4866 – 4873.
5. S. F. Rabbi and M. A. Rahman, “Analytical Modeling of a Hysteresis Interior Permanent Magnet Motor”, *Proceedings of the IEEE International Conference on Electrical Machine (ICEM)*, Berlin, Germany, Sep. 2-5, 2014, pp. 2612-2617.

#### **Chapter 4:**

1. S. F. Rabbi, P. Zhou and M. A. Rahman, “Design and Performance Analysis of a Self-Start Radial Flux Hysteresis Interior Permanent Magnet Motor”, *IEEE Transactions on Magnetics*, (in press).
2. S. F. Rabbi and M. A. Rahman, “Analysis of a Radial Flux Hysteresis IPM motor”, *Proceedings of the IEEE Canadian Conference on Electrical and Computer Engineering (CCECE)*, Halifax, NS, Canada, May 3-6, 2015, pp.7-12.

#### **Chapter 5:**

1. S. F. Rabbi, M. M. Sarker, D. G. Rideout, S. D. Butt and M. A. Rahman, “Analysis of a Hysteresis IPM motor Drive for Electric Submersible Pumps in Harsh Atlantic Offshore Environments”, *Proceedings of the ASME 34th International Conference on Ocean, Offshore and Arctic Engineering (OMAE)*, St. John’s, NL, Canada, May 31-June 5, 2015.
2. S. F. Rabbi, M. A. Rahman, M. M. Sarker and S. D. Butt, “Modeling and Performance Evaluation of a Hysteresis IPM Motor Drive for Electric Submersible Pumps”, *Proceedings of the IEEE Energy Conversion Congress and Exposition (ECCE)*, Montreal, QC, Canada, September 20-24, 2016, pp. 4105 – 4112.

## **Chapter 6:**

1. S. F. Rabbi, M. P. Halloran, T. LeDrew, A. Matchem and M. A. Rahman, “Modeling and V/F Control of a Hysteresis Interior Permanent Magnet Motor”, *IEEE Transactions on Industry Applications*, Vol. 52, No. 2, pp. 1891-1901, March 2016.
2. S. F. Rabbi, P. Brown, N. Drover, C. Kennedy and M. A. Rahman, “Modeling and Control of a Hysteresis IPM Motor Drive for Electric Submersible Pumps”, *Proceedings of the IEEE International Electric Machines and Drives Conference (IEMDC)*, Coeur d'Alene, ID, USA, May 10-13, 2015, pp.742-748.
3. S. F. Rabbi, M. A. Rahman and S. D. Butt, “Modeling and Operation of an Interior Permanent Magnet Motor Drive for Electric Submersible Pumps”, *Proceedings of the IEEE/MTS Oceans'14*, St. John's, NL, Canada, Sep. 14-19, 2014, pp.1-5.

## **Chapter 7:**

1. S. F. Rabbi and M. A. Rahman, “Determination of the Existence of Limit Cycles in Line-Start IPM Motors Using Motor Current Signature Analysis”, *IEEE Transactions on Energy Conversion*, to be published.
2. S. F. Rabbi and M. A. Rahman, “Detection of Torsional Oscillations in Line-Start IPM Motor Drives Using Motor Current Signature Analysis”, *Proceedings of the IEEE International Conference on Electrical and Computer Engineering (ICECE)*, Dhaka, Bangladesh, December 20-22, 2016, pp. 98-101.

3. S. F. Rabbi, M. L. Little and M. A. Rahman, “A Novel Technique for Detection and Analysis of Hunting in Line-Start IPM Motors Using Stator Current Signature”, *Proceedings of the IEEE Industry Applications Society Annual Meeting*, Portland, OR, USA, October 2-6, 2016, pp. 1-8.

#### **Chapter 8:**

1. S. F. Rabbi, M. L. Little, S. A. Saleh and M. A. Rahman, “A Novel Technique Using Multi-Resolution Wavelet Packet Decomposition for Real Time Diagnosis of Hunting in Line Start IPM Motor Drives”, *IEEE Transactions on Industry Applications*, Vol. 53. No.3, pp. 3005-3019, May 2017.

#### **Chapter 9:**

1. S. F. Rabbi, M. Constantine and M. A. Rahman, “A Novel Sensorless IPM Motor Drive for Electric Submersible Pumps’, *Proceedings of the IEEE International Electric Machines and Drives Conference (IEMDC)*, Miami, FL, USA, May 21-24, 2017, pp. 1-8.

### **1.4 Thesis Organization**

This thesis is comprised of ten chapters. Chapter one presents the background, objectives and technical scopes of work of the thesis.

Chapter two carries out an analysis of the synchronization process for self-starting interior permanent magnet (IPM) motors. This chapter presents a technique for determining the critical inertia and critical slip of a cage-rotor self-starting IPM motor for

various load torques. The proposed technique is validated with simulation and experimental investigations for a 1-HP IPM motor.

Chapter three deals with the modeling of a circumferential flux hysteresis interior permanent magnet motor to investigate its dynamic behaviors. This chapter presents the magnetic as well as electric equivalent circuits of the motor. Analytical, finite element and experimental test responses for a 2.5-kW circumferential flux hysteresis IPM motor are provided and analyzed in this chapter.

Chapter four introduces a new type of self-starting IPM motor called radial flux hysteresis IPM motor. The design of a 1-HP radial flux hysteresis IPM motor is presented in this chapter. The performance of the proposed design is investigated using finite element simulations. The proposed motor has better self-starting and synchronization capabilities than circumferential flux hysteresis and cage-rotor IPM motors.

An analysis of the torsional dynamics of a hysteresis IPM motor driven electric submersible pump (ESP) system is provided in chapter 5. The existence of severe torsional oscillations during on-line starting of an ESP system is presented in this chapter. The effects of pump shaft geometry on torsional vibration of the electromechanical assembly are depicted in this chapter.

Chapter six is concerned with the development of an autonomous soft-starting controller for a hysteresis IPM motor drive. This chapter presents the design and experimental implementation of a stable sensorless  $V/f$  controller for a hysteresis IPM motor drive. The proposed controller is simulated and experimentally tested for a 3-phase 4-pole 208V 2.5-kW hysteresis IPM motor drive.

Chapter seven presents an analysis of the hunting phenomenon in IPM motor drives. Hunting in an IPM motor influences the electrical supply and introduces modulation in the stator currents, making it nonstationary with time-varying statistical properties. In this chapter, signal processing techniques such as short-time Fourier transform and wavelet packet decomposition are applied for frequency domain analysis of the nonstationary stator current signals for detection of hunting in IPM motor drives. Finite element simulations of a prototype 1-HP 3-phase 4-pole 208V line-start IPM motor are carried out for various loading conditions to validate the proposed stator current signature of hunting. An offline technique for detection of the hunting phenomenon in a laboratory 1-HP line-start IPM motor drive is provided in this thesis.

An algorithm for online diagnosis of hunting in self-start IPM motor drives is provided in chapter 8. The proposed algorithm can successfully detect the onset of hunting in real time. It can also identify the severity of hunting in the drive system. The developed algorithm is simulated for 1-HP and 5-kW line-start IPM motor drives. Experimental validation of the hunting diagnostic technique is carried out for a 1-HP line-start IPM motor drive system.

A novel sensorless controller for submersible IPM motor drives is provided in chapter 9. The sensorless controller can successfully stabilize a submersible IPM motor drive at low speeds. It is also able to operate the ESP system efficiently at variable speeds. The performance of the proposed controller is investigated for a 3-phase 6-pole 480V 10-HP ESP drive system. The performances of the controller are depicted in this chapter.

Conclusions of this thesis work are provided in chapter ten. Future works for this thesis are summarized at the end of this chapter.

## Chapter 2

### Synchronization of Self-Starting Interior Permanent Magnet Motors

#### 2.1 Introduction

Permanent magnet ac motors are synchronous motors from the operational point of view. Thus, permanent magnet synchronous ac motors are generally called PM motors. PM motors can be classified in different ways. Depending on the position of the magnets on the rotor, PM motors can be broadly classified into three categories: (a) interior type PM (IPM) synchronous motors, where the permanent magnets are buried inside the rotor core; (b) surface mounted type, where the permanent magnets are mounted on the surface of the rotor; and (c) inset type, where the permanent magnets are fully or partially inset into the rotor surface [1]-[5]. Depending on the orientation of permanent magnets in the rotor, an IPM motor can be classified into three types: (a) radially oriented type, (b) circumferential type and (c) axial type [1]-[5]. The stator of an IPM machine is equipped with 3-phase distributed or concentrated windings which produces a near sinusoidal magneto-motive force distribution in the air gap. In some cases, the stator is skewed to minimize the cogging torque generated due to the interaction of the rotor magnets with the stator teeth and slots. The rotor of an IPM motor has mechanical reliability equal to that of an induction motor and eliminates excitation losses found in induction and conventional synchronous motors. IPM motors also provide the highest inherent electrical efficiency along with the potential for a life cycle cost (initial cost plus the operating cost) equal to or lower than that of induction motors in similar applications. As the permanent

magnets are inserted inside the rotor in an IPM motor, it provides a smooth rotor surface and a reduced air gap, offering more torque and power density than other PM motors. The IPM motor also provides mechanical robustness and good dynamic performances. The use of IPM motors saves up to 50 percent of the energy for split type inverter-fed air conditioners [1]. The IPM motor technology is the current standard motor drive for hybrid electric vehicles and plug-in hybrid electric vehicles [1]-[4].

Interior permanent magnet motors can be classified into two types based on their operational point of view: (1) self-starting IPM motors and (2) variable speed IPM motors. Design of variable speed IPM motors is characteristically different than self-starting IPM motors. Self-starting IPM motors are capable of producing starting torque from a fixed frequency balanced ac supply. These types of IPM motors have squirrel cage windings or starting windings in the rotor. The cage or damper windings produce the starting cage torque for the motor from a fixed frequency balanced AC supply, works as a shield to protect the permanent magnets against demagnetization during sudden increases in the stator currents, and acts as a damper to the rotor oscillations during sudden load changes to make sure that the motor always stays in synchronism.

Variable speed IPM motors are generally built with high energy density rare earth permanent magnet materials like sintered Nd-B-Fe magnets (>35 MGOe) that can withstand a high reverse magnetic field. These motors have no starting windings in the rotor and cannot self-start from a fixed frequency AC supply. These motors are inverter-fed and operated using a precision rotor position feedback controller. Thus, the squirrel cage in the rotor is not required in a variable speed IPM motor.

Design of self-starting interior permanent magnet motors have been a topic of interest among the researchers since the introduction of permanent magnet machines by Merrill in 1955 [6]. Douglas, Cahill and Adkins also introduced self-start type IPM motors in 1962 [7]-[8]. These motors used low grade ferrite magnets such as Alnico. Consequently, these motors have lower air-gap flux density, power factor and pull-out torque than an induction motor of similar frame size. Due to low energy density magnets, the power and torque density of their self-starting IPM motors were significantly lower than equivalent induction motors. However, Miller predicted that the availability of high energy density magnets will make self-start type permanent magnet motors a feasible alternative solution to induction motors [6].

Designs of high field self-starting IPM motors were first proposed by Binns et. al [9]-[12]. They proposed different designs of self-starting IPM motors using ceramic or metallic magnets in order to increase the efficiency and air-gap flux density. Binns et. al. also introduced designs that utilize the reluctance torque component of interior permanent magnet motors [9]. Binns and Jabbar introduced the design of a 40-kW self-starting IPM motor using the rare earth permanent magnet material Samarium Cobalt (Sm-Co) [12]. They recorded a power factor of more than 0.95 for the motor at 50Hz supply frequency. Honsinger and Miller proposed radial flux and circumferential flux types of magnet orientations inside the rotor for IPM motors using Ferrite and Samarium Cobalt magnets [13]-[15].

Rahman designed and built the first 45-kW high efficiency (>95%) high power factor (>0.98) self-starting IPM motor using high energy density Neodymium Boron Iron (Nd-B-Fe) magnets [1], [16]-[20]. It opened a new era of high power high efficiency

permanent magnet machines utilizing rare earth magnetic materials. Chalmers first introduced the flux focusing V-shape magnet orientation for a self-starting IPM motor in order to increase the air gap flux density and the reluctance torque [21]. Kurihara and Rahman proposed a self-starting IPM motor for high inertia loads using a partial V shaped magnet orientation [22]. Since then, due to the advancement in high-energy density sintered Neodymium-Boron-Iron magnets, there has been a tremendous growth in the development of permanent magnet machines [23].

The synchronization capability of a synchronous motor depends significantly on the inertia and the load torque. Also, the design and the field excitation play an important role in the synchronization process of the motor. In the case of an IPM motor, the magnet brake torque and the value of the energy product of permanent magnets (PM) have major effects on the synchronization capability [24]-[25]. Line starting and synchronization of induction-synchronous motors for various load types have been topics of interest in recent times [24]-[41]. An early analysis of the asynchronous operation of permanent magnet motors is provided by Honsinger [28]. He developed a  $d-q$  axis equivalent circuit model for IPM motors considering the effects of magnetic saliency in the motor. He also presented the effects of magnet brake torque on the starting of an IPM motor. However, he did not provide any analysis for determining the synchronization capability of an IPM motor for different load torques and load inertias. A relatively simple algebraic criterion for determining the pull-in capability of synchronous reluctance motors was presented by Lawrenson and Mathur [29]. They separated the total developed electromagnetic torque into asynchronous and synchronous torque components. They have determined the critical period where the reluctance motor jumps from an asynchronous state to the

synchronization process. They have provided an approximation of the slip during the critical period. An algebraic algorithm has been developed in their paper for determining the criterion for successful synchronization of reluctance motors by balancing the energy required for the successful pull-in to synchronization and the energy developed by the motor, using the motor's slip vs. load angle trajectories.

Miller proposed an energy based method similar to that of Lawrenson and Mathur to determine the synchronization criterion of self-starting permanent magnet motors [24]. In his paper, a curve fitting approach is used to estimate the average asynchronous torque of a permanent magnet motor as a quadratic function of the slip. However, Miller has not provided any exact mathematical formulations for the magnet brake torque, the maximum brake torque, the average cage torque and the average pulsating torque. There is no detailed analysis to determine the critical slip and the critical inertia of an IPM motor for different types of loads in his paper. There are no experimental run-up responses in that paper.

An exhaustive but complicated analytical approach for determining the synchronization capability of a self-starting permanent magnet motor was presented by Osheiba and Rahman [27]. Their method is computationally overburdened to be included in the design procedure of line start IPM motors. They also did not consider any dynamic loading conditions. There are no experimental run-up responses in their paper.

Isfahani and Zadeh have studied the capability of start-up and synchronization of IPM motors for fluid pumping loads as well as constant loads [25]-[26]. They have provided dynamic  $d-q$  axes simulation results and finite element analysis results for two different designs of an IPM motor. They have considered the starting period and the

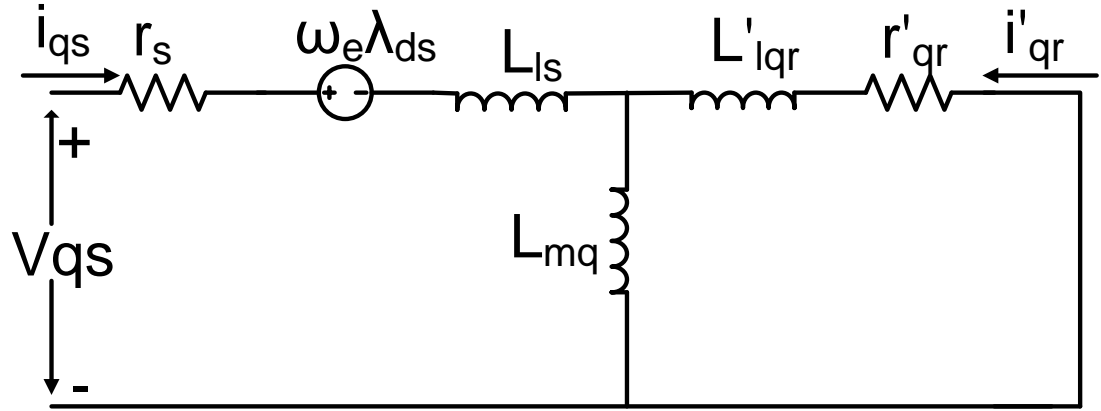
synchronization stage together as a start-up stage. They have developed a criterion for determining the successful start-up of IPM motors based on the maximum brake torque and the starting cage torque. They have concluded that the motor will eventually go to synchronization if it satisfies the start-up criteria. However, an IPM motor may end up in limit-cycles even if it has a successful run-up torque. They did not provide any insights on the states of the motor such as load angle, slip, developed torque, etc. when it jumps from the asynchronous speed to the synchronization process. Isfahani et. al. have investigated the synchronization capability of IPM motors for different load inertias based on a linear assumption about the slip coefficient [26]. But their assumption about the slip coefficient is limited to a specific interior permanent magnet motor and may not be suitable for dynamic and cyclic loads. They have not provided any theoretical or analytical validation behind their assumptions. They have not provided any detailed explanation about the synchronization process and also, there is no in-depth explanation about how the critical slip and pull-in energy of the motor change with the changing of the load torque and inertia. There are no experimental results in their paper. Thus, there exists a need to develop a simplified appropriate analytical method to determine the critical criteria for successful synchronization of self-starting IPM motors for different types of loads including dynamic loads.

This chapter presents an approximate analysis of the synchronization process for determining the critical slip and the critical inertia of cage-equipped self-starting IPM motors. A synchronization criterion has been established to distinguish between successful and unsuccessful synchronizations in IPM motors. An improved simplified mathematical formulation has been developed to determine the critical slip and the critical

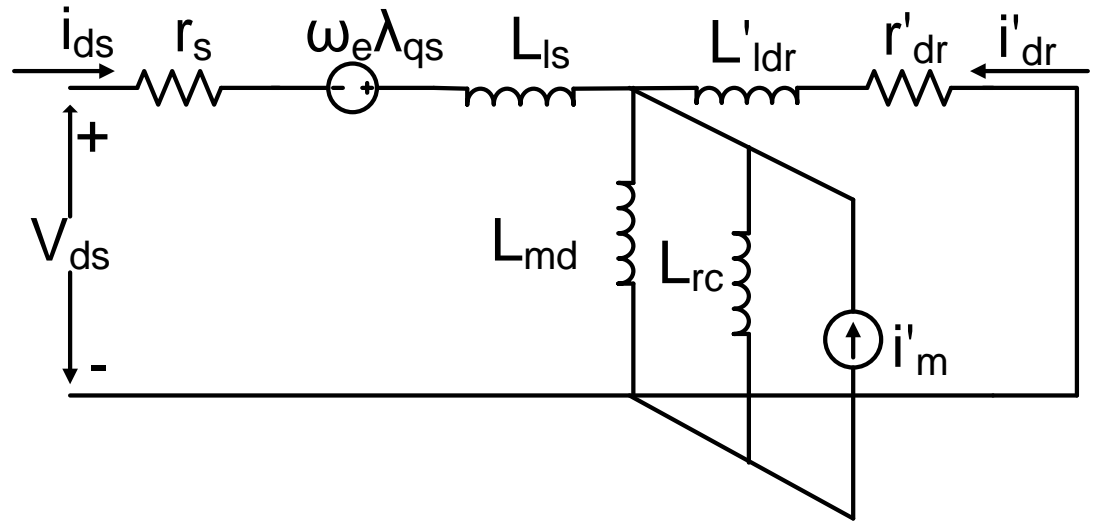
inertia of IPM motors by balancing the energy required for a successful synchronization and the energy developed by the motor. The developed method is suitable for both steady state and dynamic loads. Analytical results are presented and explained in this chapter. A  $d-q$  axis equivalent circuit model including the rotor resistance and reactance is presented in this chapter. Simulations have been carried out using the equivalent circuit solutions to obtain the transient responses of a 1-HP, 3-phase, 4-pole squirrel-cage equipped IPM motor for both constant and fluid pumping type loads. Experimental testing of the same IPM motor has been also performed for different load torques. Both simulation and experimental asynchronous run-up responses of the motor are presented in this chapter. The oscillatory nature of the rotor and the effect of the brake torque during starting of an IPM motor are depicted and explained in this chapter.

## **2.2 Average Torque Analysis**

A self-starting interior permanent magnet (IPM) motor with cage windings is generally called line-start IPM motor. A line-start IPM motor equipped with cage windings, when connected to a fixed frequency 3-phase balanced ac supply, starts asynchronously like an induction motor and runs up toward synchronous speed through the process of run-up towards synchronization [24]-[25]. The run-up torque for a line-start IPM motor has two components: a steady state time averaged component and a pulsating component superimposed on the average torque. The average torque is responsible for driving the motor towards the synchronous speed while the pulsating torque produces noise and vibration during starting. The average torque is comprised of two torques namely the magnet brake torque and the starting torque.



(a)



(b)

Figure 2.1. Equivalent circuits: (a)  $q$ -axis and (b)  $d$ -axis.

The  $q$ - $d$  axis dynamic model of a 3-phase line-start IPM motor is developed with respect to the rotor reference frame and depicted in Figures 2.1a and 2.1b. The set of stator voltage equations in  $q$ - $d$  axes are [28]:

$$V_{qs} = \frac{d\lambda_{qs}}{dt} + r_s i_{qs} + p\omega_{rm}\lambda_{ds} \quad (2.1)$$

$$V_{ds} = \frac{d\lambda_{ds}}{dt} + r_s i_{ds} - p\omega_{rm}\lambda_{qs} \quad (2.2)$$

$$V'_{qr} = \frac{d\lambda'_{qr}}{dt} + r'_{qr}i'_{qr} = 0 \quad (2.3)$$

$$V'_{dr} = \frac{d\lambda'_{dr}}{dt} + r'_{dr}i'_{dr} = 0 \quad (2.4)$$

where  $r_s$  is the phase resistance of the motor,  $V_{qs}, V_{ds}, V'_{qr}$  and  $V'_{dr}$  are  $q$ - $d$  axes stator and rotor voltages.  $\lambda_{qs}, \lambda_{ds}$  and  $\lambda'_{qr}, \lambda'_{dr}$  are  $q$ - $d$  axes flux linkages of the stator and the rotor, respectively. The  $q$ - $d$  axes rotor and stator currents are expressed as  $i'_{qr}, i'_{dr}$  and  $i_{qs}, i_{ds}$ , respectively. The  $q$ - $d$  axes rotor resistances are represented by  $r'_{qr}$  and  $r'_{dr}$ .  $\omega_{rm}$  is the mechanical speed of the rotor. The stator and rotor flux linkage equations are given below [28],

$$\lambda_{qs} = L_{qs}i_{qs} + L_{mq}i'_{qr} \quad (2.5)$$

$$\lambda_{ds} = L_{ds}i_{ds} + L_{md}i'_{dr} + \lambda'_m \quad (2.6)$$

$$\lambda'_{qr} = L'_{qr}i'_{qr} + L_{mq}i_{qs} \quad (2.7)$$

$$\lambda'_{dr} = L'_{dr}i'_{dr} + L_{md}i_{ds} + \lambda'_m \quad (2.8)$$

where  $L_{qs}, L_{ds}$  are stator  $q$ - $d$  axes synchronous inductances. The  $q$ - $d$  axes magnetizing inductances are presented by  $L_{mq}$  and  $L_{md}$ .  $L'_{qr}$  and  $L'_{dr}$  denote rotor self-inductances, referred to the stator side.  $\lambda'_m$  models the permanent magnet flux. The electromagnetic torque, starting torque due to currents flowing in the rotor and brake torque are expressed in the following equations [28]:

Electromagnetic torque,

$$T_e = \frac{3}{2}p(\lambda_{ds}i_{qs} - \lambda_{qs}i_{ds}) \quad (2.9)$$

Starting torque,

$$T_{start} = \frac{3}{2}p(\lambda'_{dr}i'_{qr} - \lambda'_{qr}i'_{dr}) \quad (2.10)$$

Brake torque,

$$T_b = \frac{3}{2}p(\lambda'_m i_{qm} + i_{dm} i_{qm} (L_{ds} - L_{qs})) \quad (2.11)$$

where  $i_{qm}$  and  $i_{dm}$  are  $q$ - $d$  axes currents due to the magnets.

Average torque analysis has been performed based on the assumption that the motor operates under steady state at each slip point. The values of the time derivative components are assumed to be zero and the motor speed is set to a function of motor slip as,

$$p\omega_{rm} = (1 - s)\omega_e \quad (2.12)$$

where  $\omega_e = 2\pi f$  is the electrical synchronous speed of the motor and  $f$  is the supply frequency.

The rotor currents,  $i'_{qr}$  and  $i'_{dr}$  are not considered for finding the magnet brake torque and are set to zero.  $i_{qs}$  and  $i_{ds}$  are replaced by the currents due to the magnets, namely  $i_{qm}$  and  $i_{dm}$ . Due to the fixed magnet excitation, the  $q$ - $d$  axes stator voltages and the time derivatives of the  $q$ - $d$  axes stator flux linkages are set to zero. The expression for the brake torque becomes [41],

$$T_b = -\frac{3p}{2\omega_e} \left[ \frac{r_s^2 + (1-s)^2 X_{qs}^2}{r_s^2 + (1-s)^2 X_{ds} X_{qs}} \right] \left[ \frac{r_s E_0^2 (1-s)}{r_s^2 + (1-s)^2 X_{ds} X_{qs}} \right] \quad (2.13)$$

where  $X_{ds}$  and  $X_{qs}$  are the  $d$  and  $q$  axes reactances and  $E_0$  is the motor back-emf. The maximum brake torque occurs at a certain slip  $s_{Tbmax}$ . The slip at the maximum brake

torque is calculated by differentiating (2.13) with respect to the slip and is given below [41],

$$s_{Tbmax} = 1 - \frac{r_s}{\omega_e \sqrt{L_{ds} L_{qs}}} \quad (2.14)$$

The maximum brake torque is calculated by substituting the value of  $s_{Tbmax}$  into (2.13) and is expressed in the following equation [41],

$$T_{bmax} = -\frac{3p}{2\omega_e} \left[ \frac{r_s^2 \left( 1 + \frac{L_{qs}}{L_{ds}} \right)}{2r_s^2} \right] \left[ \frac{E_0^2 r_s^2}{2r_s^2 \omega_e \sqrt{L_{ds} L_{qs}}} \right] \quad (2.15)$$

It is evident from (2.14) and (2.15) that the brake torque is maximum at high slip and depends largely on the saliency ratio ( $L_{qs}/L_{ds}$ ) of the motor and back-emf  $E_0$ . That's why, a high saliency permanent magnet motor with large back-emf results in greater brake torque.

In squirrel cage equipped IPM motors, the starting torque is produced due to the induced current flowing in the cage and accounts for the successful starting and synchronization of line start IPM motors. The cage current  $I_2$  can be expressed in terms of voltage and impedances as shown in the following equation [41]:

$$|I_2| = \frac{V_{th}}{\sqrt{\left( r_{th} + \frac{r'_r}{s} \right)^2 + (X_{th} + X'_{lr})^2}} \quad (2.16)$$

where  $V_{th}$ ,  $r_{th}$  and  $X_{th}$  are Thevenin equivalent voltage, resistance and reactance, respectively.  $r'_r$  and  $X'_{lr}$  are the rotor resistance and leakage inductance, referred to the stator side. The equation for cage torque  $T_c$  is given below [41]:

$$T_c = 3 \frac{1}{\omega_{rm}} |I_2|^2 \frac{r'_r}{s} \quad (2.17)$$

or

$$T_c = \frac{3}{\omega_{rm}} \frac{V_{th}^2 \left(\frac{r_r'}{s}\right)}{\left(r_{th} + \frac{r_r'}{s}\right)^2 + (X_{th} + X'_{lr})^2} \quad (2.18)$$

For balanced steady state conditions, the electrical angular velocity of the rotor is assumed constant and equal to  $\omega_e$ . The electrical angular velocity of the rotor reference frame becomes the angular velocity of the synchronously rotating reference frame. In this mode of operation, the rotor windings do not experience a change of flux linkage; hence current is not flowing in the short-circuit cage windings. The term  $p\omega_{rm}$  in (2.1)-(2.4) is replaced by  $\omega_e$  and the time rate of change of all flux linkages is neglected. As a result, the steady state versions of the voltage and flux linkage equations can be written as,

$$V_{qs} = r_s i_{qs} + \omega_e \lambda_{ds} \quad (2.19)$$

$$V_{ds} = r_s i_{ds} - \omega_e \lambda_{qs} \quad (2.20)$$

$$\lambda_{qs} = L_{qs} i_{qs} \quad (2.21)$$

$$\lambda_{ds} = L_{ds} i_{ds} + \lambda'_m \quad (2.22)$$

The  $d$  and  $q$  axes voltages  $V_{qs}$  and  $V_{ds}$  can be replaced by,

$$V_{qs} = V \cos \delta \quad (2.23)$$

$$V_{ds} = -V \sin \delta \quad (2.24)$$

where  $V$  is the supply peak voltage and  $\delta$  is the load angle between  $V$  and no load back-emf  $E_0$ . Now, using (2.23) and (2.24), the stator voltage equations (2.19)-(2.20) can be rewritten as

$$V \cos \delta = r_s i_{qs} + X_{ds} i_{ds} + E_0 \quad (2.25)$$

$$V\sin\delta = -r_s i_{ds} + X_{qs} i_{qs} \quad (2.26)$$

The  $q$ - $d$  axes stator currents,  $i_{qs}$  and  $i_{ds}$  are calculated using (2.25)-(2.26),

$$i_{qs} = \frac{V(r_s \cos \delta + X_{ds} \sin \delta) - E_0 r_s}{r_s^2 + X_{ds} X_{qs}} \quad (2.27)$$

$$i_{ds} = \frac{V(X_{qs} \cos \delta - r_s \sin \delta) - E_0 X_{qs}}{r_s^2 + X_{ds} X_{qs}} \quad (2.28)$$

The expression for electromagnetic torque  $T_e$  is calculated using (2.9) and (2.21)-(2.28), and can be written as,

$$T_e = \frac{3p}{2\omega_s (r_s^2 + X_{ds} X_{qs})^2} \left[ (X_{ds} - X_{qs}) \left\{ \frac{V^2}{2} (X_{qs} r_s (1 + \cos 2\delta) + X_{qs} X_{ds} \sin 2\delta - r_s^2 \sin 2\delta - r_s X_{ds} (1 - \cos 2\delta)) \right. \right. \\ \left. \left. - E_0 V r_s X_{qs} \cos \delta + E_0 V r_s^2 \sin \delta - E_0 V X_{qs} r_s \cos \delta - E_0 V X_{qs} X_{ds} \sin \delta \right. \right. \\ \left. \left. + E_0^2 r_s X_{qs} \right\} + E_0 V r_s \cos \delta (r_s^2 + X_{ds} X_{qs}) + E_0 V X_{ds} \sin \delta (r_s^2 + X_{ds} X_{qs}) \right. \\ \left. - E_0^2 r_s (r_s^2 + X_{ds} X_{qs}) \right] \quad (2.29)$$

The electromagnetic torque in (2.29) can be represented as,

$$T_e = T_{e0} + T_e(\delta) \quad (2.30)$$

where  $T_{e0}$  is the constant or average component and  $T_e(\delta)$  is the periodic component superimposed on the constant component. The periodic component is the cause for torque pulsation and is called the synchronizing pulsating torque. It can be expressed as [26],

$$T_e(\delta) = T_{p1}\sin\delta + T_{p2}\sin2\delta + T_{p3}\cos\delta + T_{p4}\cos2\delta \quad (2.31)$$

Now considering the coefficients of  $\sin\delta$ ,  $\sin2\delta$ ,  $\cos\delta$  and  $\cos2\delta$  between (2.29) and (2.31),  $T_{p1-4}$  are given by,

$$T_{p1} = \frac{3pE_0V}{2\omega_e(r_s^2 + X_{ds}X_{qs})^2} [(X_{ds} - X_{qs})(r_s^2 - X_{ds}X_{qs}) + (r_s^2 + X_{ds}X_{qs})X_{ds}] \quad (2.32)$$

$$T_{p2} = \frac{3pV^2}{4\omega_e(r_s^2 + X_{ds}X_{qs})^2} (X_{ds} - X_{qs})(X_{qs}X_{ds} - r_s^2) \quad (2.33)$$

$$T_{p3} = \frac{3pE_0Vr_s}{2\omega_e(r_s^2 + X_{ds}X_{qs})^2} [(r_s^2 + X_{ds}X_{qs}) - 2X_{qs}(X_{ds} - X_{qs})] \quad (2.34)$$

$$T_{p4} = \frac{3pV^2r_s}{4\omega_e(r_s^2 + X_{ds}X_{qs})^2} (X_{ds} - X_{qs})(X_{ds} + X_{qs}) \quad (2.35)$$

When the motor reaches synchronism, it runs under a steady synchronous torque. The synchronous torque  $T_s$  is obtained by neglecting the stator resistance and replacing  $T_e = T_s$  into (2.31), and is expressed in the following equation,

$$\begin{aligned} T_s &= T_{mag} + T_{rel} \\ &= \frac{3pE_0V}{2\omega_e X_{ds}} \sin\delta + \frac{3pV^2(X_{ds} - X_{qs})}{4\omega_e X_{ds} X_{qs}} \sin2\delta \end{aligned} \quad (2.36)$$

During the period of synchronization, the pulsating torque plays the role of the synchronizing torque and becomes the synchronous torque when the rotor is in synchronism. The synchronous torque for an IPM motor is the summation of the magnet alignment torque  $T_{mag}$  and the reluctance torque  $T_{rel}$ .

### **2.3 Critical Criteria for Successful Synchronization of Line-Start IPM motors**

Figure 2.2 shows average asynchronous torque vs. speed curves of a line-start IPM motor. The magnet brake torque becomes maximum at high slip when the motor starts from stand-still. It results in a dip in the resultant average asynchronous torque curve. If the brake torque is excessive, the resultant torque intersects with the load torque and runs at a very low speed, and then eventually fails to synchronize. After passing the torque dip, the motor runs towards the synchronous speed and the resultant torque reaches the peak value due to the maximum cage torque and also due to the low brake torque at a certain speed. The resultant average asynchronous torque intersects with the load curve at a speed slightly below the synchronous speed as indicated by point 'C'. The synchronization point is indicated by point 'D'. The jump from point 'C' to point 'D' is a dynamic process and it is better illustrated in the instantaneous torque curve as shown in Figure 2.3. This dynamic process is called the "pull-in" process.

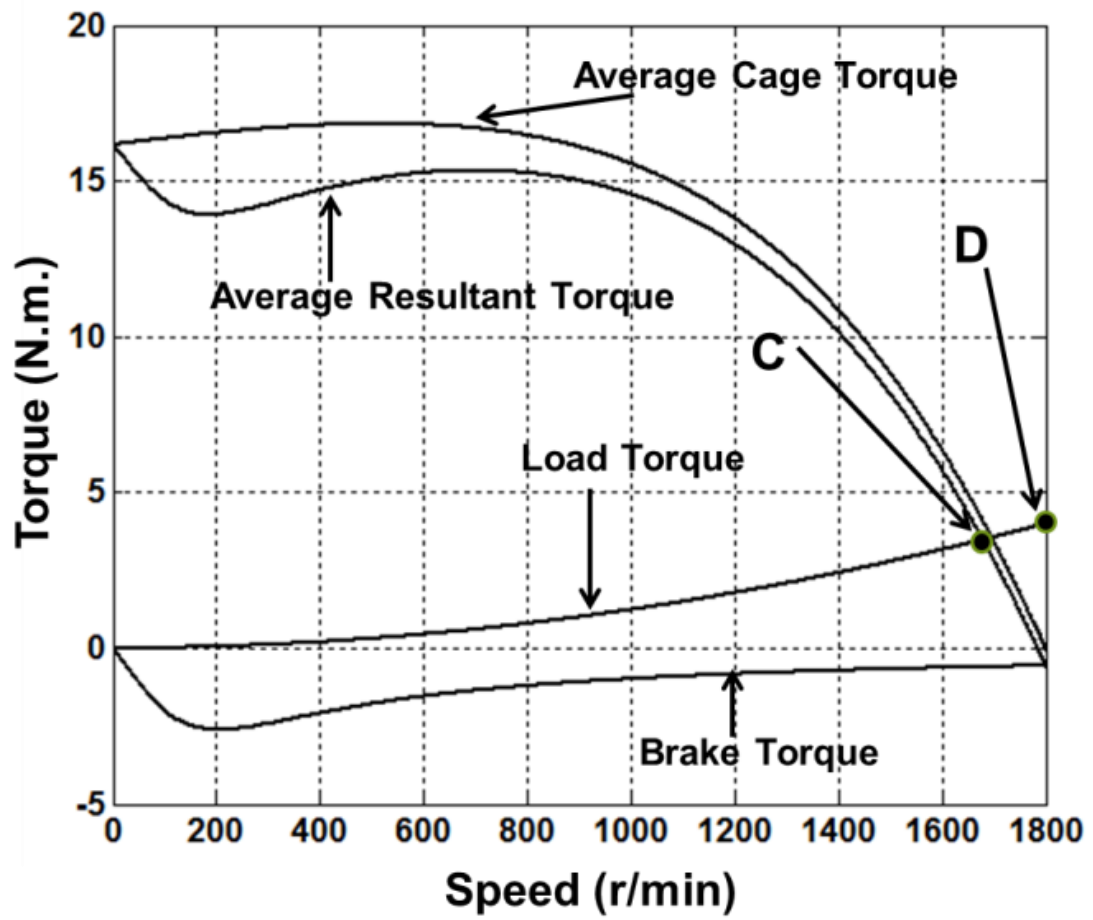


Figure 2.2. Average asynchronous torques of a line-start IPM motor.

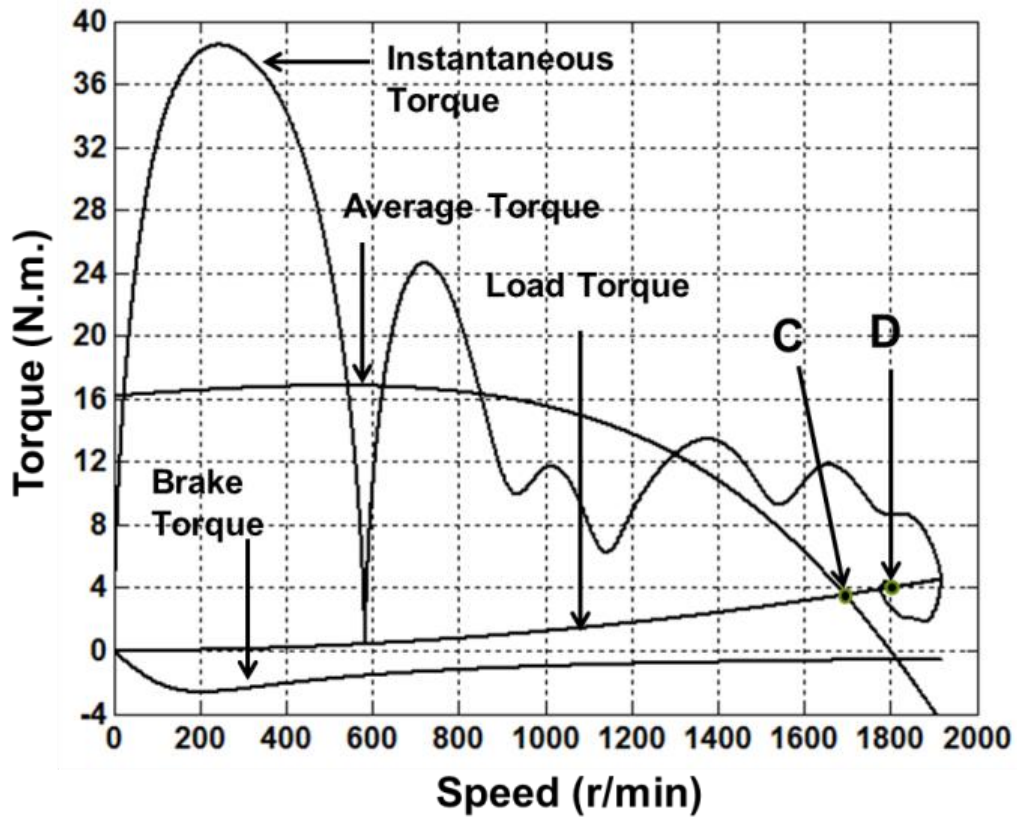


Figure 2.3. Instantaneous torque vs. speed curves of a line-start IPM motor.

Figure 2.4 illustrates the run-up trajectory of an IPM motor in the  $s$ - $\delta$  plane based on the following equation of motion [24]:

$$T_a = -\frac{1}{p}J\omega_s^2s \frac{ds}{d\delta} = T_s(\delta) + T_{av}(s) - T_L(s) \quad (2.37)$$

where  $T_a$  is the net accelerating torque,  $T_{av}$  is the average asynchronous torque which is the summation of the starting torque and the magnet brake torque,  $T_L$  is the load torque that can be constant or a function of the slip and  $\omega_s$  is the synchronous speed of the motor. Fluid pumping loads such as centrifugal pumps have been considered as a dynamic load in this analysis. In a centrifugal pump, the volume of the fluid delivered by the pump

against a constant pressure head is proportional to the power of the motor. The mechanical output power of a centrifugal pump is given below [31],

$$P = \rho H Q g \frac{1}{\eta} \quad (2.38)$$

where  $H$  is the head,  $Q$  is the flow rate,  $\rho$  is the density of the fluid and  $\eta$  is the efficiency of the pump. Head  $H$  varies as the square of the rotating speed and flow rate  $Q$  changes with the rotating speed. The output mechanical power is proportional to the cube of the rotating speed. Thus, the required torque for the pump is proportional to the square of the motor speed. The load torque for such types of loads can be expressed as a function of the slip and is given by,

$$T_L(s) = T_L(1 - s)^2 \quad (2.39)$$

where  $T_L$  is the peak load torque.

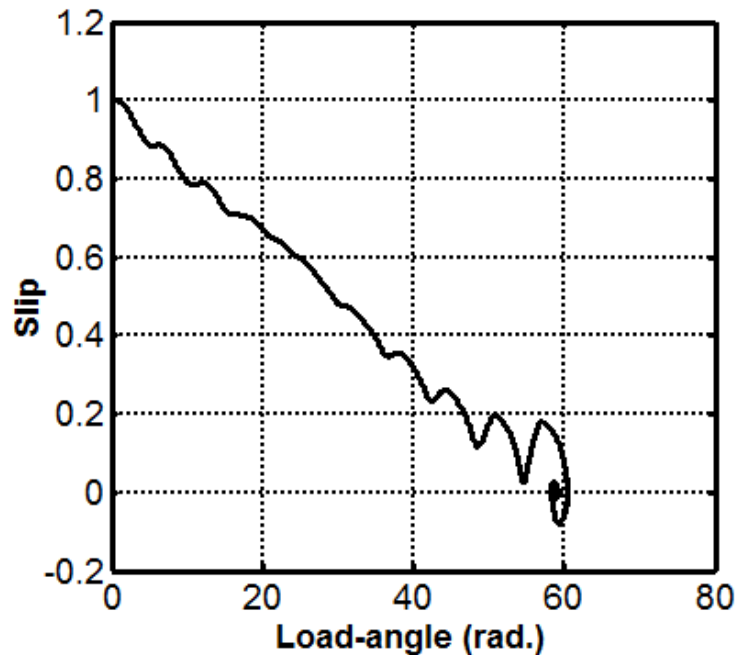


Figure 2.4. Slip vs. load angle trajectory of a line start IPM motor.

The inertia plays an important role in the starting of an IPM motor. The maximum inertia that a motor can carry during starting is high when the torque exerted by the load is small. For fluid pumping loads, the inertia of the system is generally high whereas the load torque is significantly low during start-up. Thus, an IPM motor can start with a large inertial fluid pumping load if the load torque is small.

The motor load-angle increases continuously after a successful start-up and slip  $s$  goes down as the motor accelerates. The average asynchronous torque starts to decrease after becoming maximum and the synchronization process attempts to start when the average asynchronous torque  $T_{av}$  reaches almost zero. At this point, the total acceleration depends largely on the synchronizing torque  $T_s$ .

Figure 2.5 shows the synchronous torque of an IPM motor. The maximum or pull out torque occurs at load angle  $\delta_{max}$  which is between  $45^0$  and  $90^0$  mechanical angle. Load angle  $\delta'_s$  is the unstable load point where the motor reaches synchronous speed for the first time. The net motoring torque and the load torque are balanced at this angle. Due to the inertia and damping factors,  $\delta_s$  is the steady state electrical load angle. When the net acceleration torque  $T_a$  becomes zero for the first time, the pull-in process starts.

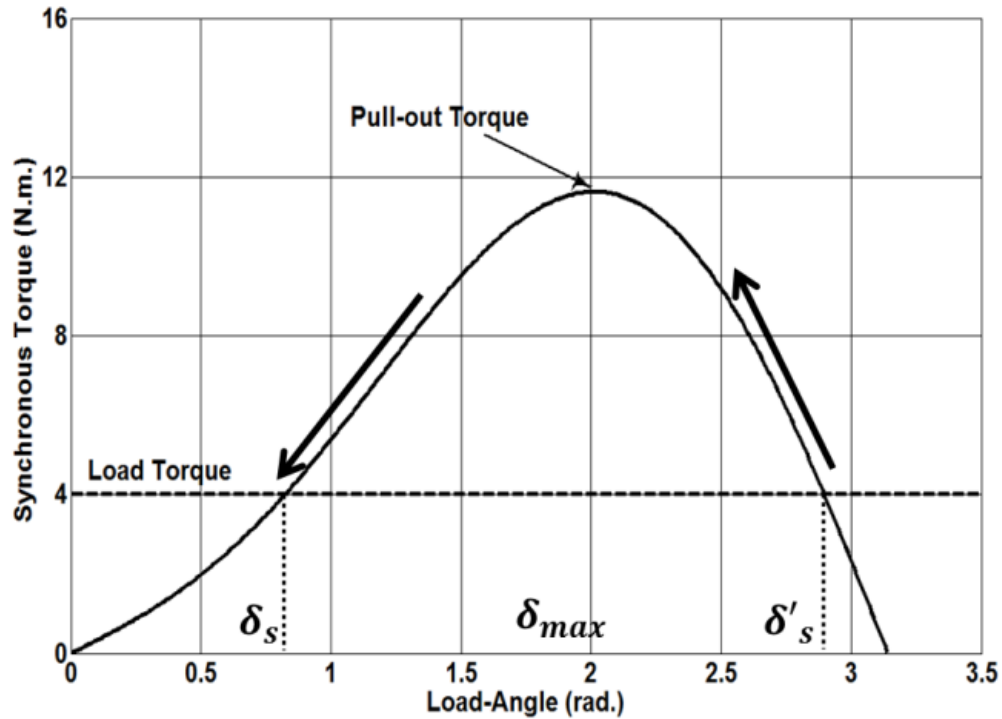


Figure 2.5. Synchronous torque vs. load angle for an IPM motor.

The approximate trajectory of pole slips of the motor during the start of the pull-in process is depicted in Figure 2.6. Successful pull-in occurs during the last pole slip from point ‘R’ to point ‘S’, spanning almost  $2\pi$  electrical radians. The load angle at point ‘S’ is  $\delta'_s$ . Slip at point ‘R’ is neither exactly zero nor less than zero, and therefore synchronization never happened at point ‘R’. The maximum slip during the final jump from ‘R’ to ‘S’ is called the critical slip  $s_{cr}$ . The approximate sinusoidal curve of the last pole slip (from ‘R’ to ‘S’) is depicted in Figure 2.7. The sinusoidal curve in Figure 2.7 can be formulated using the following equation:

$$s = s_{cr} \sin\left(\frac{\delta}{2} + \varphi\right) \quad (2.40)$$

where  $\varphi$  is the phase shift.

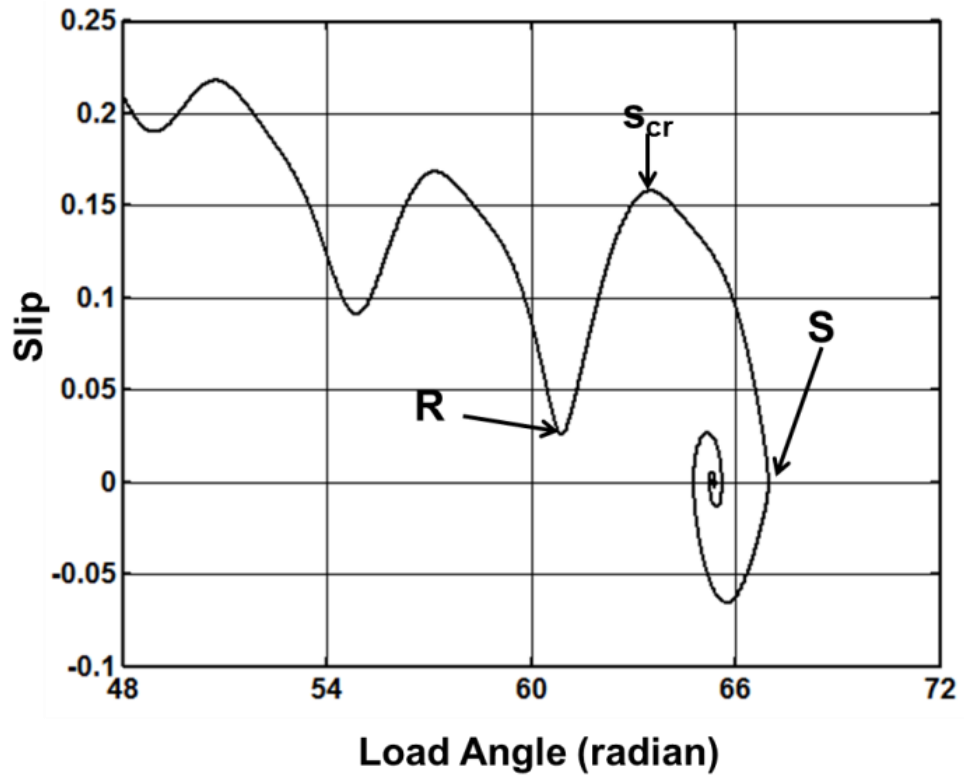


Figure 2.6. Pole slips of an IPM motor during the start of the synchronization.

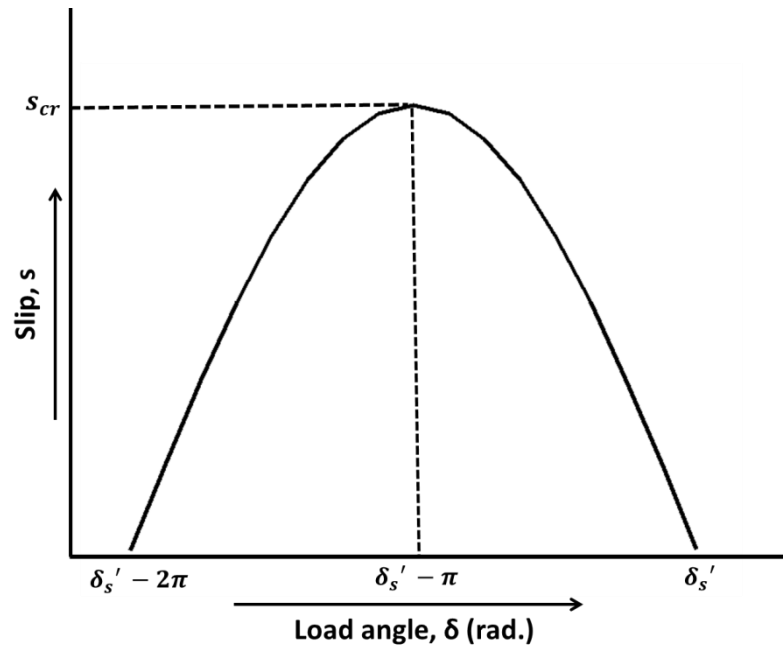


Figure 2.7. A sinusoidal approximation of the last pole slip.

For  $\delta = \delta'_s - \pi$ , (2.40) can be expressed as,

$$s_{cr} \sin\left(\frac{\delta'_s - \pi}{2} + \varphi\right) = s_{cr} \quad (2.41)$$

or

$$\frac{\delta'_s - \pi}{2} + \varphi = \frac{\pi}{2} \quad \xrightarrow{\text{yields}} \quad \varphi = \pi - \frac{\delta'_s}{2} \quad (2.42)$$

Using (2.41)-(2.42), the trajectory of the last pole slip is given by,

$$s = s_{cr} \sin\frac{1}{2}(\delta'_s - \delta) \quad (2.43)$$

At slip  $s = s_{cr}$ , the total accelerating torque is momentarily zero and the torque angle  $\delta_{cr}$  is  $\delta'_s - \pi$ . Using the above constraint, the critical slip for a line start IPM motor can be calculated from the following equation,

$$T_s(\delta'_s - \pi) + T_{av}(s_{cr}) - T_L(s_{cr}) = 0 \quad (2.44)$$

where  $T_L(s_{cr})$  is the load torque at the critical slip.

The required kinetic energy to pull the motor into synchronism from the critical slip  $s_{cr}$  to slip  $s=0$  is called the pull-in energy [8]. For a motor with inertia  $J$ , the apparent kinetic energy at slip  $s_{cr}$  is calculated as,

$$K_{s_{cr}} = \int_{s_{cr}}^0 \left(-\frac{1}{p} J \omega_s^2 s\right) ds = \frac{1}{2p} J s_{cr}^2 \omega_s^2 \quad (2.45)$$

This required pull-in energy is obtained by integrating the right hand side of (2.37) as follows,

$$K_p = \int_{\delta'_s - \pi}^{\delta'_s} (T_s(\delta) + T_{av}(s) - T_L(s)) d\delta \quad (2.46)$$

The integration of the synchronous torque gives the following result,

$$\int_{\delta'_s - \pi}^{\delta'_s} T_s(\delta) d\delta = -\frac{3pE_0V}{\omega_s X_{ds}} \cos(\delta'_s) \quad (2.47)$$

The total average asynchronous torque is transformed into a function of torque angle by using (2.43). The pull-in energy for a line-start IPM motor is expressed as,

$$K_p = -\frac{3pE_0V}{\omega_s X_{ds}} \cos(\delta'_s) + \int_{\delta'_s - \pi}^{\delta'_s} \left[ T_{av} \left( s_{cr} \sin \frac{1}{2} (\delta'_s - \delta) \right) - T_L \left( s_{cr} \sin \frac{1}{2} (\delta'_s - \delta) \right) \right] d\delta \quad (2.48)$$

For successful synchronization of a line start IPM motor, the following condition must be satisfied,

$$K_p \geq K_{s_{cr}} \quad (2.49)$$

Equation (2.49) is the critical criterion for successful synchronization of a line start IPM motor. A line start IPM motor is able to synchronize for a certain load when the pull-in energy  $K_p$  is larger than the apparent kinetic energy of the rotor. The motor snaps into synchronism following some oscillations around the synchronous speed. When  $K_p$  is less than  $K_{s_{cr}}$ , the motor fails to provide the required pull-in energy for synchronization and goes into limit cycles. The critical condition for successful synchronization is the point where  $K_p$  is equal to  $K_{s_{cr}}$ . The inertia at that point is called the critical inertia of the motor  $J_{cr}$  and the slip is the motor's critical slip  $s_{cr}$ . The pull-in energy at that point is expressed as follows by using (2.45),

$$K_{s_{cr}} = \frac{1}{2p} J_{cr} s_{cr}^2 \omega_s^2 = K_p \quad (2.50)$$

The critical inertia of a load  $J_{cr}$  that a motor can successfully synchronize against a certain load torque can be calculated using (2.50) and is expressed below,

$$J_{cr} = \frac{2pK_p}{s_{cr}^2\omega_s^2} \quad (2.51)$$

Figure 2.8 presents the flow chart for determining the pull-in criteria of a line-start IPM motor. The algorithm can be used to determine whether the designed IPM motor can synchronize certain loads. This algorithm can be included in the design procedure of line-start IPM motors to determine the synchronizing capability of a particular designed IPM motor, and the design can be modified accordingly.

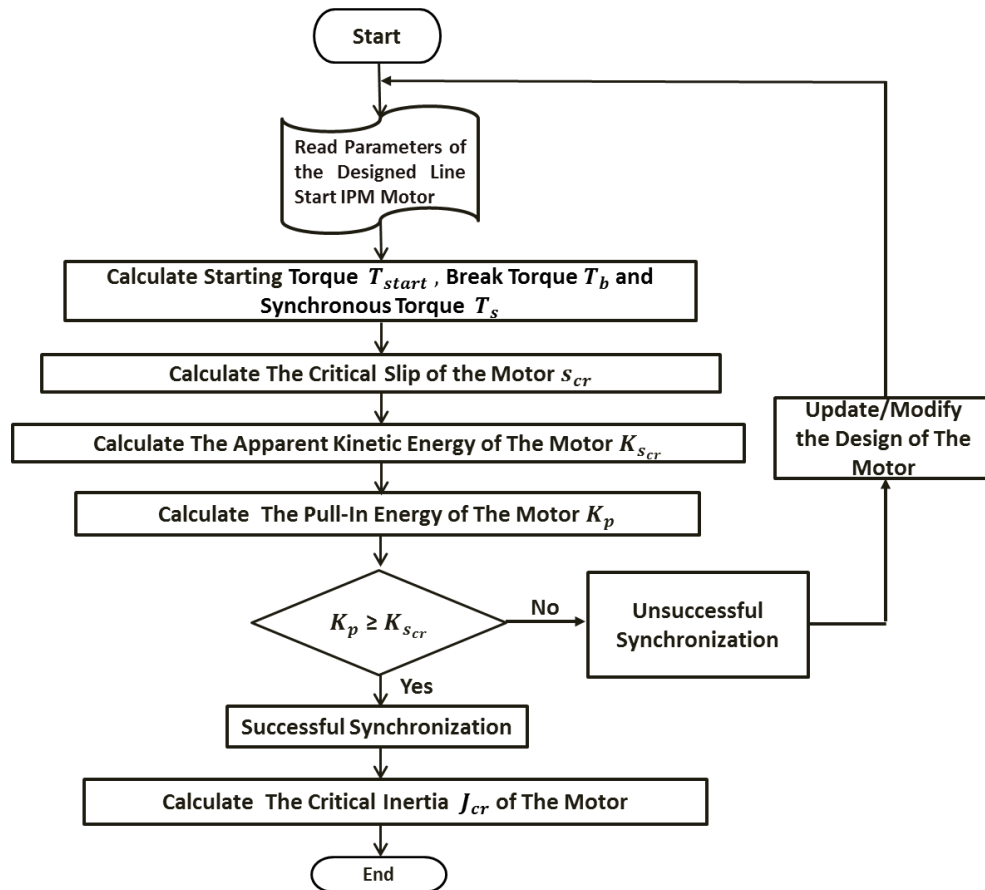


Figure 2.8. Flowchart for determining the critical criteria of a cage equipped IPM motor.

## 2.4 Analytical Results for Line-Start IPM Motors

Analytical results are obtained by solving the equations for determining the critical criteria of a line-start IPM motor using Maple software. Figure 2.9 demonstrates the critical inertia vs. load torque of a 1-HP 208V 4-pole line-start IPM motor for both constant and dynamic loads. Critical inertia of the motor goes down as the load approaches close to the motor rated torque. The maximum inertia is high when the load torque is small. The motor can synchronize large inertial load when the load torque is small. As the load torque crosses 40 percent of the rated torque, the critical inertia falls down drastically following a nonlinear curve and becomes significantly low when the load approaches the rated torque of the motor.

Critical slips for different load torques are shown in Figure 2.10. The critical slip becomes significantly high when the load torque is larger than the rated load. As a result, the pull-in energy falls down and the critical inertia becomes small for the motor. It can be observed from Figures 2.9 and 2.10 that the motor can synchronize larger inertia when the load is dynamic because the critical slip for a dynamic load is smaller than that of a constant load.

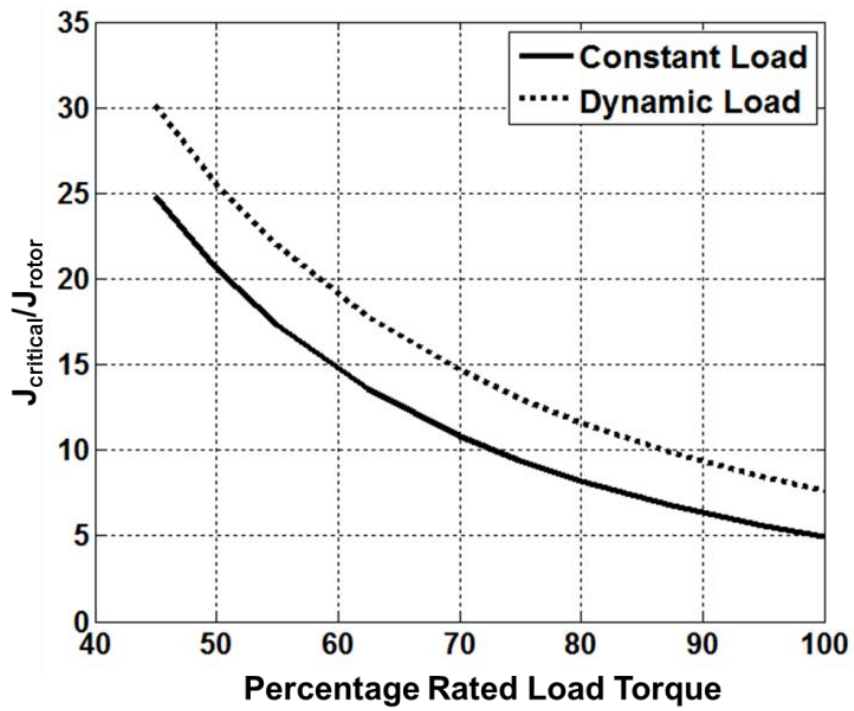


Figure 2.9. Critical inertia vs. percentage rated load for constant and dynamic loads.

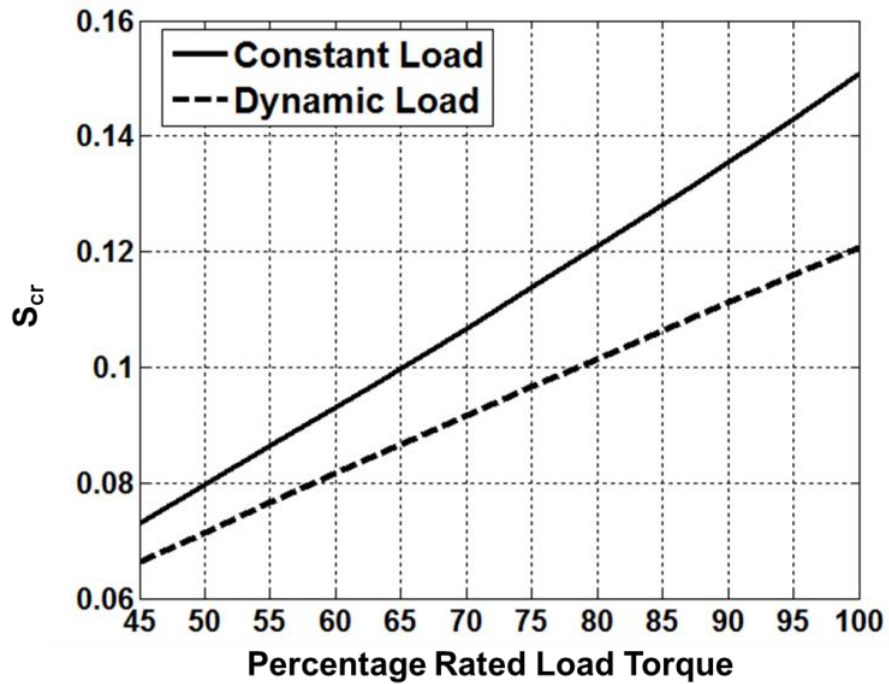


Figure 2.10. Critical slip vs. percentage rated load for constant and dynamic loads.

Figure 2.11 shows the apparent kinetic energy and the pull-in energy of the motor for different inertial loads. The apparent kinetic energy is less than the pull-in energy of the motor when the total inertia is smaller than the critical inertia of the motor. As the load inertia approaches closer to the critical value, the apparent energy becomes almost equal to the pull-in energy. The motor cannot produce the required pull-in energy to overcome the apparent kinetic energy when the total inertia crosses the critical inertia. As a result, the motor fails to synchronize and goes into periodic oscillations called limit cycle.

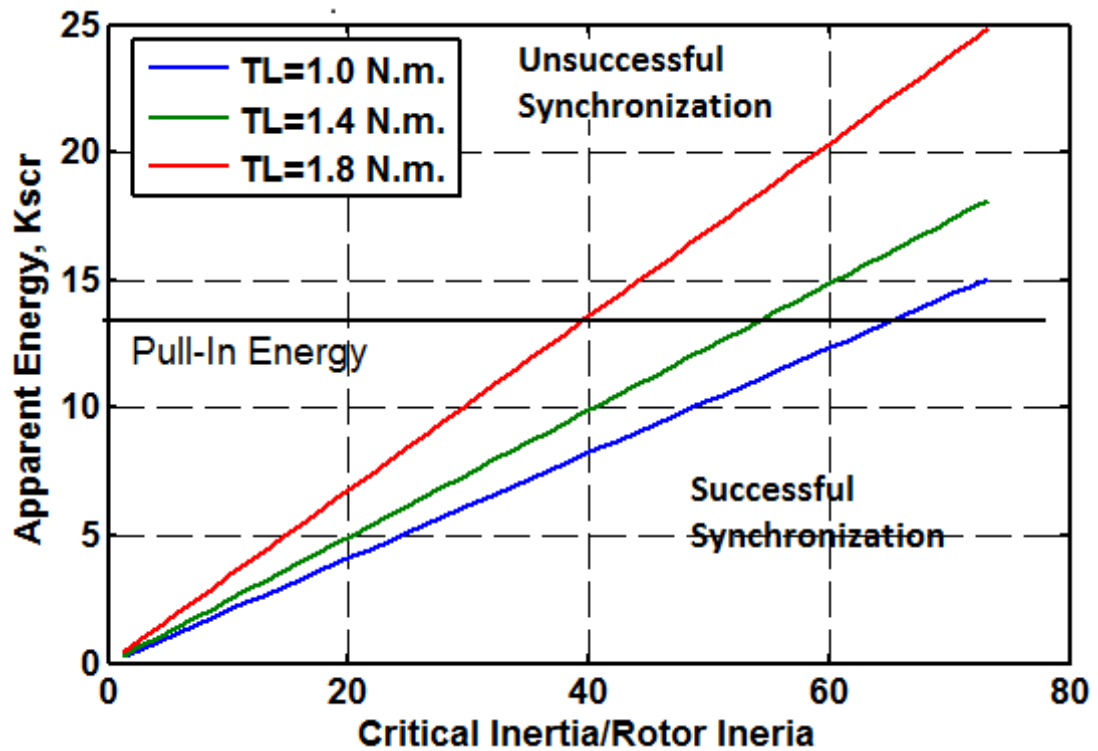


Figure 2.11. Apparent kinetic energy vs. inertia for different load torques.

The approximate sinusoidal curves of the last pole slip for different load torques are plotted in Figure 2.12. The load angle  $\delta$  is varied from  $\delta'_s - 2\pi$  to  $\delta'_s$ . The slip of the motor becomes the critical slip  $s_{cr}$  at the load angle  $\delta'_s - \pi$ . The critical slip gradually becomes higher with the increasing load torque. Accordingly, the stored kinetic energy in the motor goes up, requiring the motor to provide higher pull-in energy to synchronize.

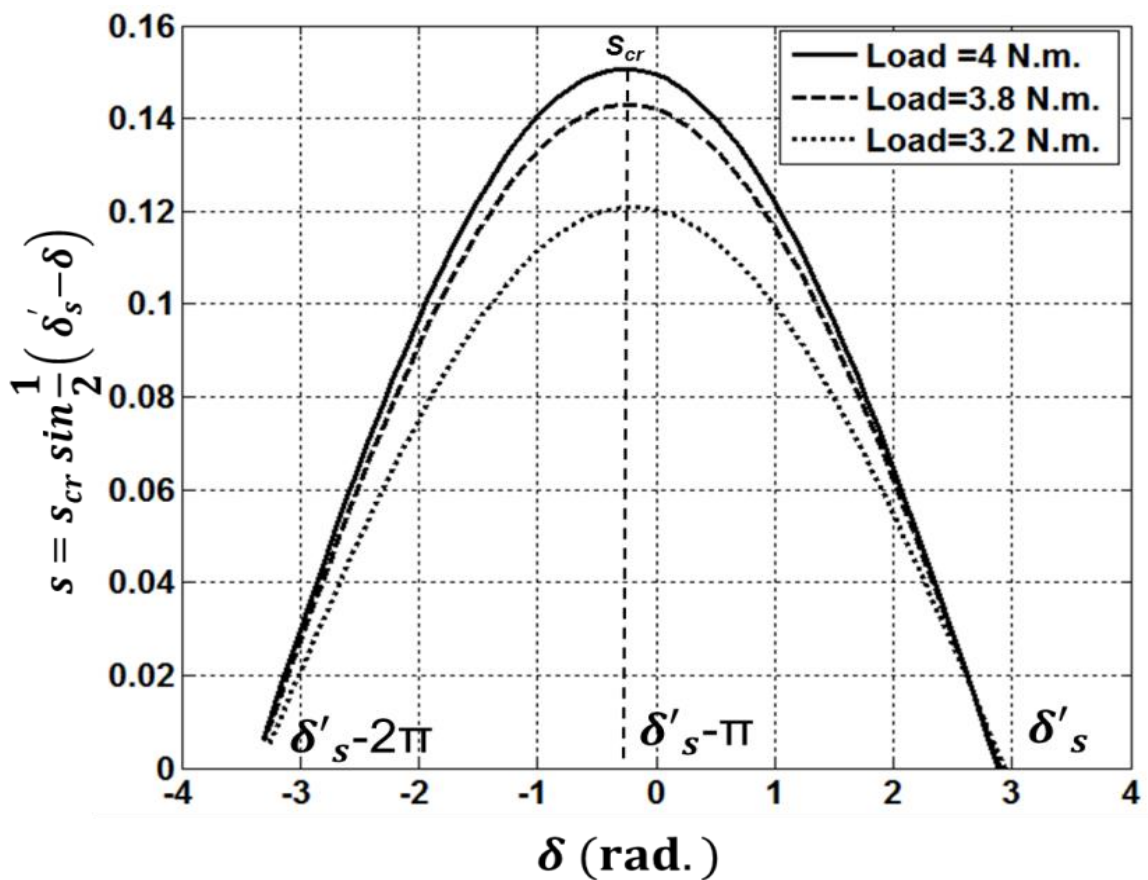
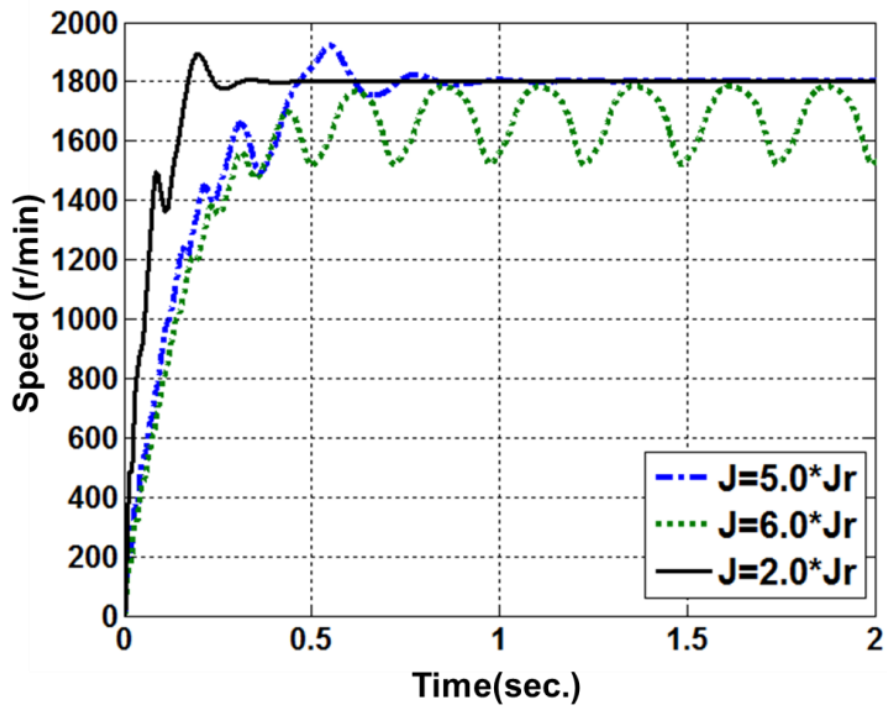


Figure 2.12. Approximate last pole slip based during synchronization.

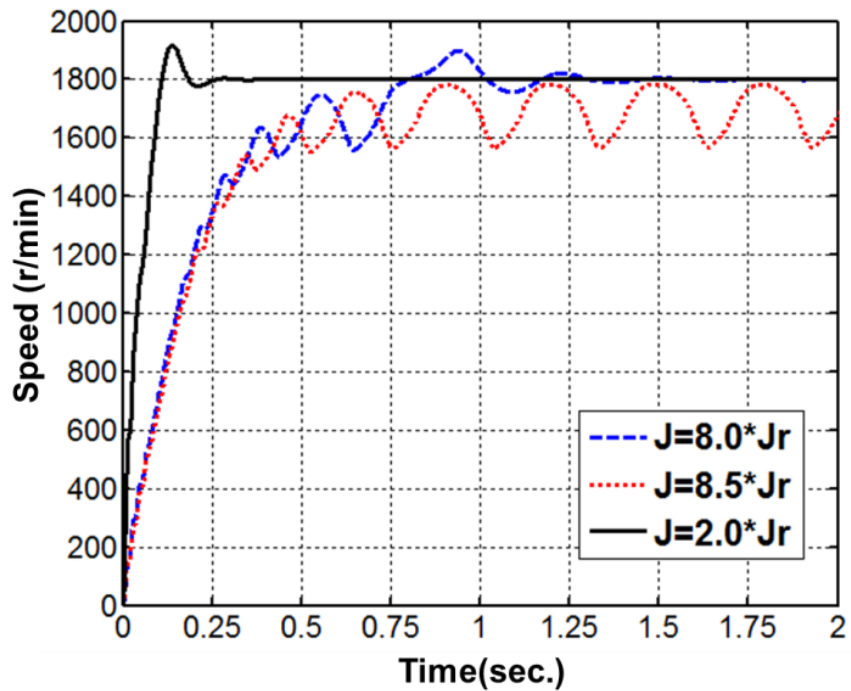
## 2.5 Simulation Results

The simulated run-up responses of a four-pole 1-HP three phase 208V line-start IPM motor for both static and dynamic loads are shown in Figs. 2.13(a)-2.13(b), respectively. The motor is run by a three-phase Y-connected 208V 60-Hz balanced ac supply. The motor synchronizes with ease when the inertia is two times its rotor inertia. The motor is successfully able to synchronize for  $J = 5J_r$  and  $J = 2J_r$ , as the slip becomes less than zero at the super-synchronous speed. The motor goes through more speed overshoots and undershoots gradually with the increasing combined inertia of the system, and eventually stabilizes due to the available system damping. The inertia of the third load is six times higher than the rotor inertia, making the total inertia higher than the motor critical inertia. Consequently, the rotor fails to synchronize because it cannot provide the required pull-in energy to stabilize itself. As a result, the motor experiences periodic rotor oscillations.

Figure 2.14a illustrates slip vs. load angle trajectories of the motor. The slip became negative before synchronization for the first and the second load. Thus, the motor is able to synchronize. The motor experiences more pole slips when the total inertia becomes higher than the rotor inertia. The final jump before synchronization follows a spiral path and the rotor snaps into synchronism with the field during this period. In the case of loads with inertia higher than the critical one, the motor fails to synchronize and goes into successive oscillations with a constant period.



(a)

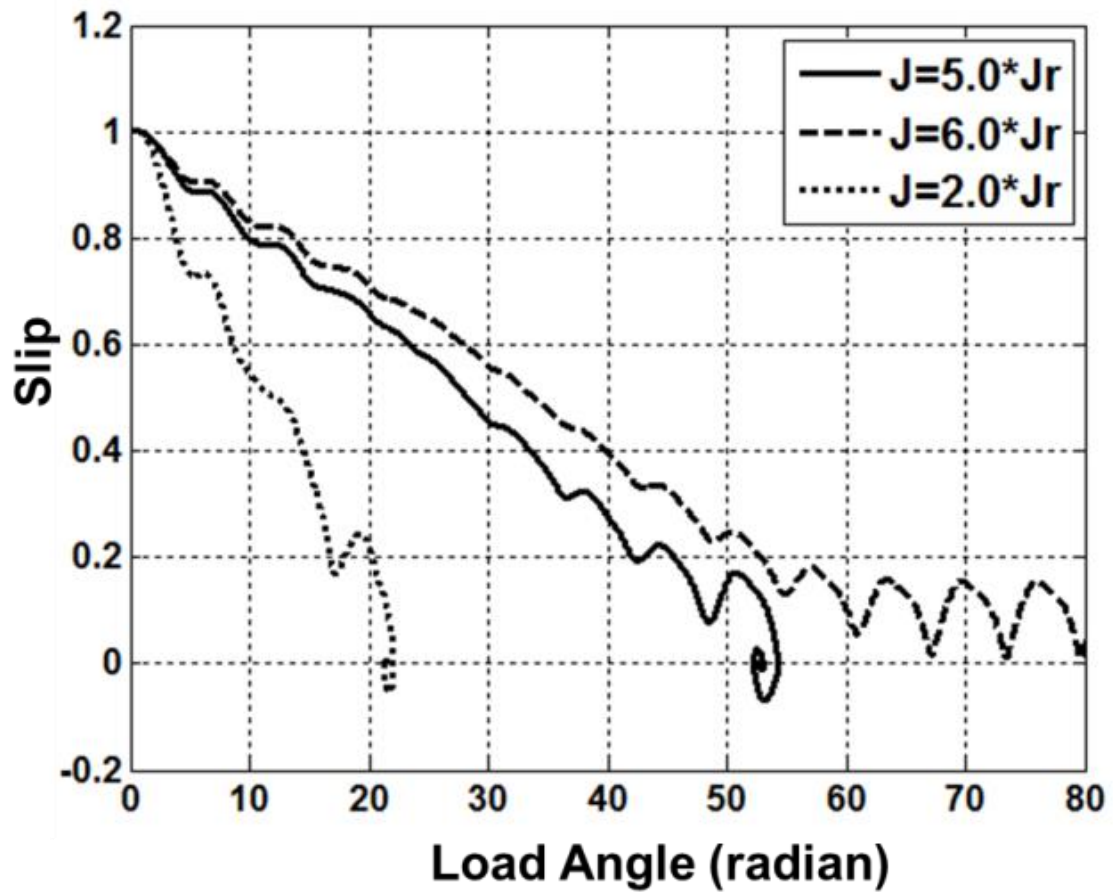


(b)

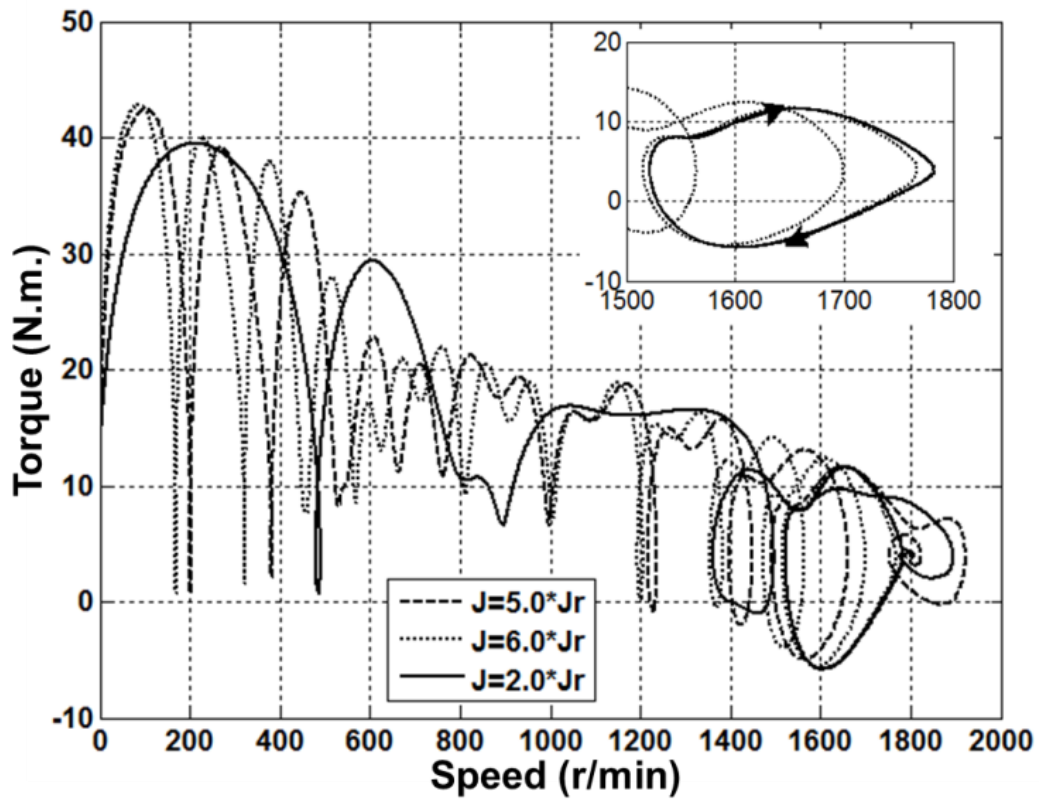
Figure 2.13. Simulated run-up responses: (a) Constant load torque and (b) Dynamic load torque.

In Figure 2.14b, torques vs. speed trajectories for both low and high inertia loads are presented. Because of the interaction between permanent magnet flux and the conduction cage currents, the motor suffers from a large number of torque reversals, and even in the case of low inertial loads, few torque reversals take place. Before reaching the synchronization, there is a series of slow pole-slips which appears in Figure 2.14b as almost elliptical for high inertia loads. The large rotor and stator currents associated with the persistent pole-slipping would cause rapid overheating in the stator windings. The magnet brake torque reaches its peak value at the start-up period, and tries to stop the motor from running. The developed cage torque produces a high accelerating torque to overcome the brake torque and drives the motor towards the synchronous speed. The IPM motor behaves like a class D induction motor at that point. The pulsating synchronizing torque exists throughout the start-up as superimposed on the cage torque. Thus, the motor experiences some speed undershoots and overshoots during the start-up period before reaching close to the synchronous speed. This phenomenon is shown in Figures 2.13-2.14 as speed reversals, pole slips and torque reversals. When the motor reaches close to the synchronous speed, the cage torque and the magnet brake torque become small and, the IPM motor behaves like a hysteresis motor and suffers from oscillatory “hunting” phenomena because of the pulsating synchronous torque. The motor eventually snaps into synchronism following the proposed critical criteria. The motor needs to provide less pull-in energy to overcome the apparent kinetic energy for synchronization in the case of dynamic loads which allows the IPM motor to synchronize a larger inertial load at the rated torque. This phenomenon is depicted in Figure 2.13b for inertia  $J > 6J_{rotor}$ . The final synchronization follows a spiral that originates at the

synchronous speed. At that moment, the motoring torque and the load torque becomes equal and the motor snaps to synchronism following a spiral path. In the case of a load with higher inertia than the critical inertia, the motor goes into limit cycle, and the zoomed in limit cycle is shown at the topmost portion of Figure 2.14b.



(a)



(b)

Figure 2.14. Run-up trajectories in the  $s$ - $\delta$  plane (a) slip vs. load-angle and (b) torque vs. speed.

Figures 2.15 and 2.16 present the analytical and simulated critical inertia of a 4-pole 1-HP 208V squirrel-cage IPM motor for constant load torques and dynamic loads, respectively. There is a close agreement between the proposed analytical results and simulation results. The analysis is carried out based on steady state average torques whereas the simulation is conducted using the dynamic model of line-start IPM motors. That's why, there is a slight difference between the analytical and simulation results.

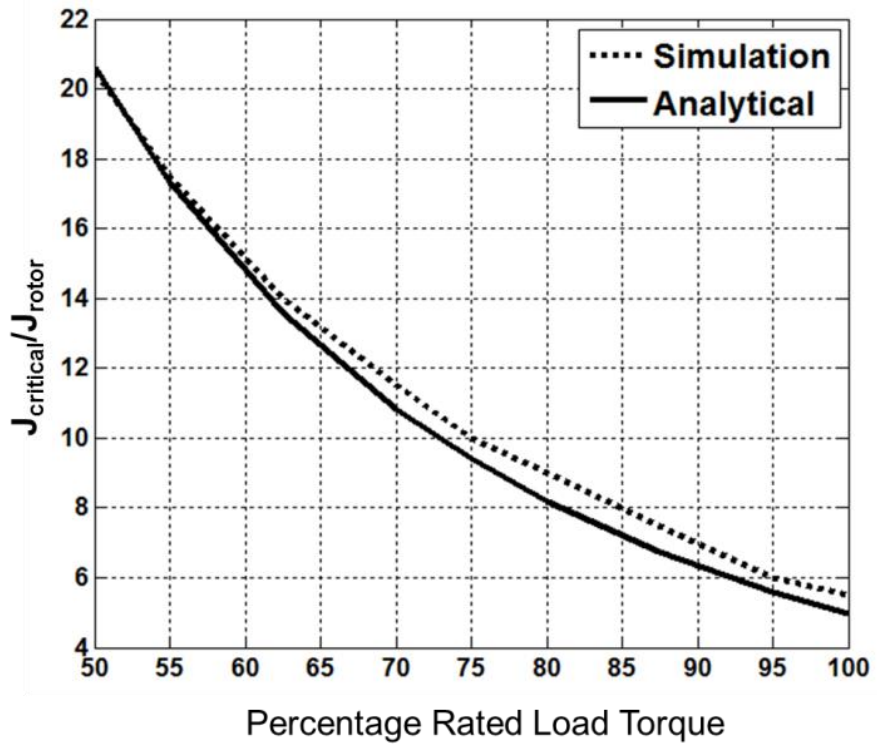


Figure 2.15. Analytical vs. simulated critical inertia of the motor for a constant load.

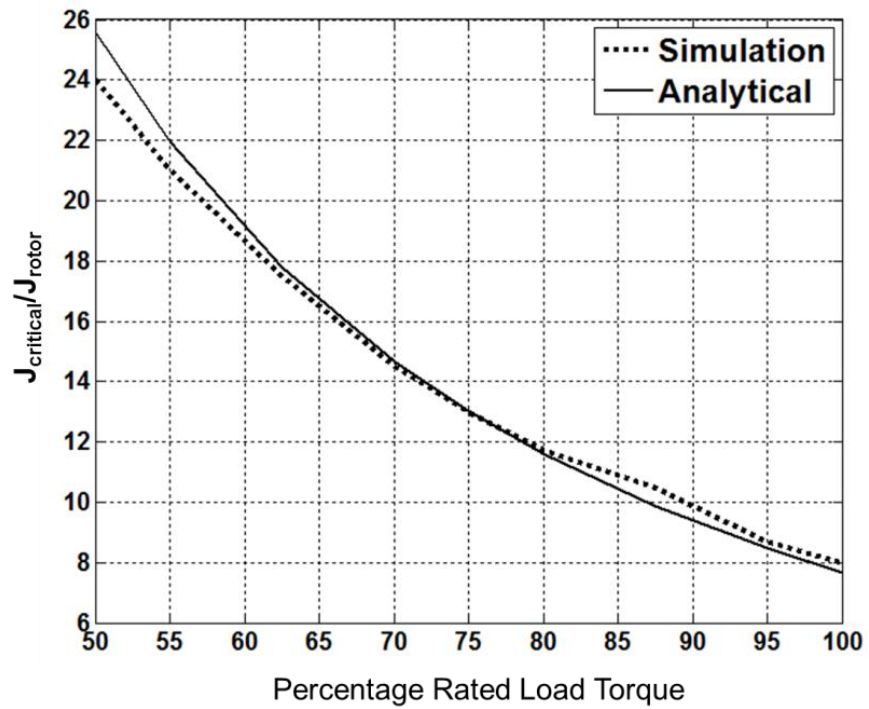


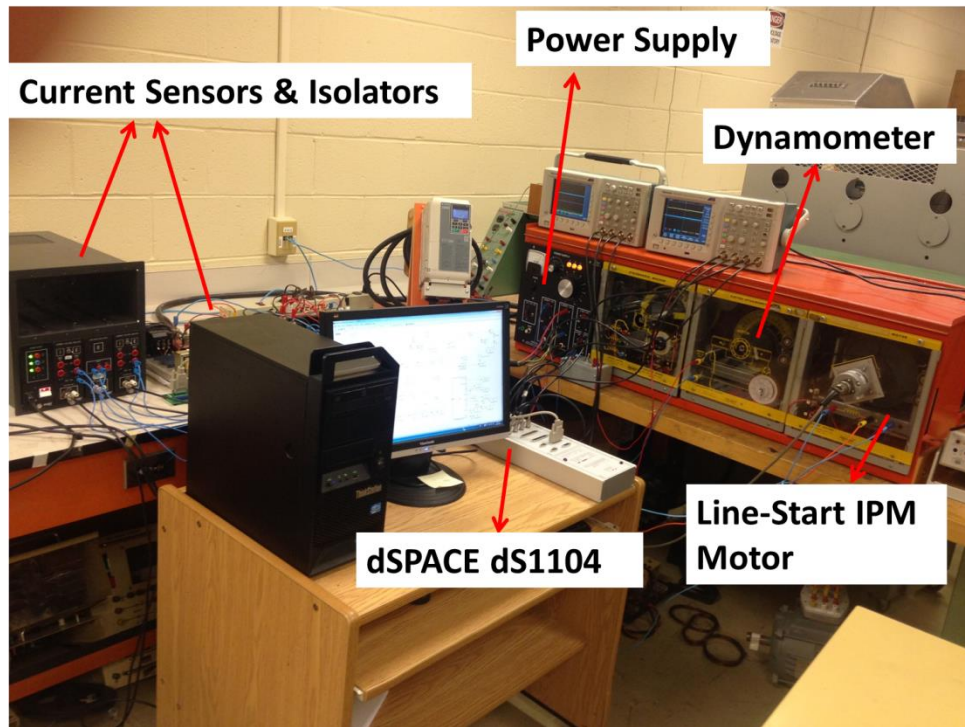
Figure 2.16. Analytical vs. simulated critical inertia of the motor for a dynamic load.

## 2.6 Experimental Results

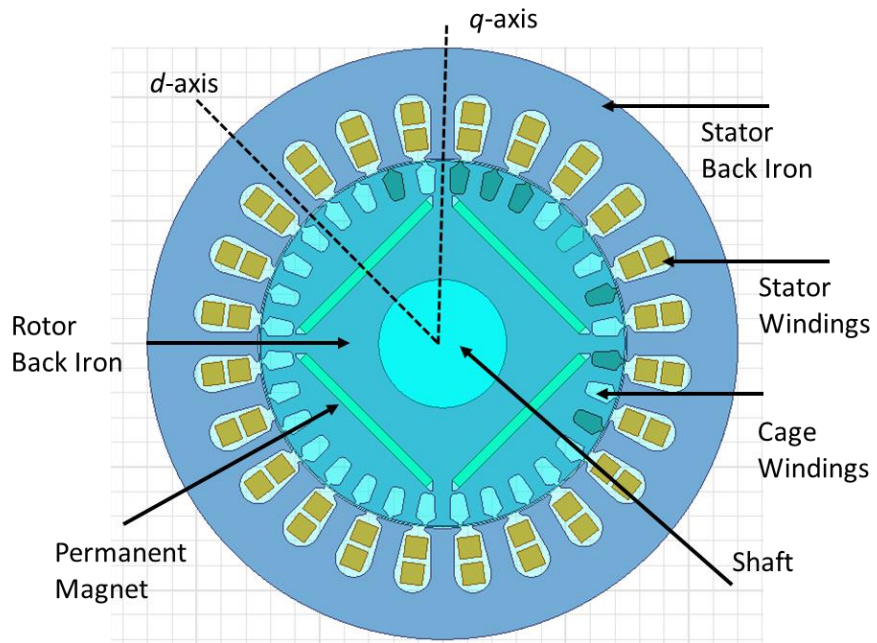
A laboratory 1-HP, 208V, 4-pole line-start IPM motor has been used for experimental evaluation of the motor's asynchronous start-up and pull-in capabilities. The picture of the experimental set-up and the cross section of the motor is shown in Figures 2.17a and 2.17b, respectively. The motor parameters are listed in Table 2.1. The motor is run directly from a Y-connected 3-phase, 208V balanced fixed frequency 60 Hz ac line supply.

Table 2.1. 1-HP line-start IPM motor.

Symbol	Name	Value
$N_p$	number of phases	3
$p$	number of pole pairs	2
$I_{rated}$	rated line current	3 A
$f_{rated}$	rated frequency	60 Hz
$P_{rated}$	rated power	1 hp
$T_{rated}$	rated torque	4 N. m
$V_{rated}$	rated voltage (L-L)	208 V
$L_{qs}$	$q$ -axis inductance	0.07957 H
$L_{ds}$	$d$ -axis inductance	0.04244 H
$r_s$	stator resistance/phase	1.93 $\Omega$
$J$	rotor inertia	0.003 Kg. m <sup>2</sup>
$D_m$	rotor damping constant	0.0008 (N. m)/rad./sec.
$\lambda_m$	magnet flux linkage	0.314 volts/rad./sec.



(a)



(b)

Figure 2.17. A prototype squirrel-cage IPM Motor: (a) rotor and (b) cross section.

The run-up responses of the motor for various load torques are shown in Figure 2.18. The load torque is varied from 0% to 100% of the rated load. The total inertia is kept constant at three times the rotor inertia. In all these cases, the motor is started from the standstill position. The motor is able to start and synchronize for loads up to 75% of its rated load torque from the fixed frequency ac source. The critical inertia of the motor for successful synchronization becomes significantly lower at the rated torque. The motor fails to even start with a constant rated load torque, because the rotor could not overcome the magnet brake torque at the low speed. In the cases of successful synchronization, the motor has suffered from a large number of pole slips and speed reversals during the incipient period because of the effects of the pulsating torque and the magnet brake torque. The effects of the pulsating torque and the magnet brake torque in an IPM motor during starting are more evident in the experimental results than the simulation results, because simulations have been carried out based on an idealized machine with no variations of the machine parameters. The brake torque remains high at low speeds and the motor goes through more speed reversals during the low speed period between 200 and 600 rpm with starting at around 200 rpm when the brake torque becomes more severe as shown in Figure 2.18. After a successful start-up by overcoming the brake torque, the motor accelerates quickly using the cage torque, reaching toward the synchronous speed within 0.2s. When the motor reaches close to the synchronous speed, the number of pole-slips decreases and the motor eventually gets synchronized with little speed overshoots and undershoots because of the hysteresis phenomena [1]. As the load torque increases, the magnitude of speed-overshoots during synchronization period becomes smaller because of the damping of the overall system.

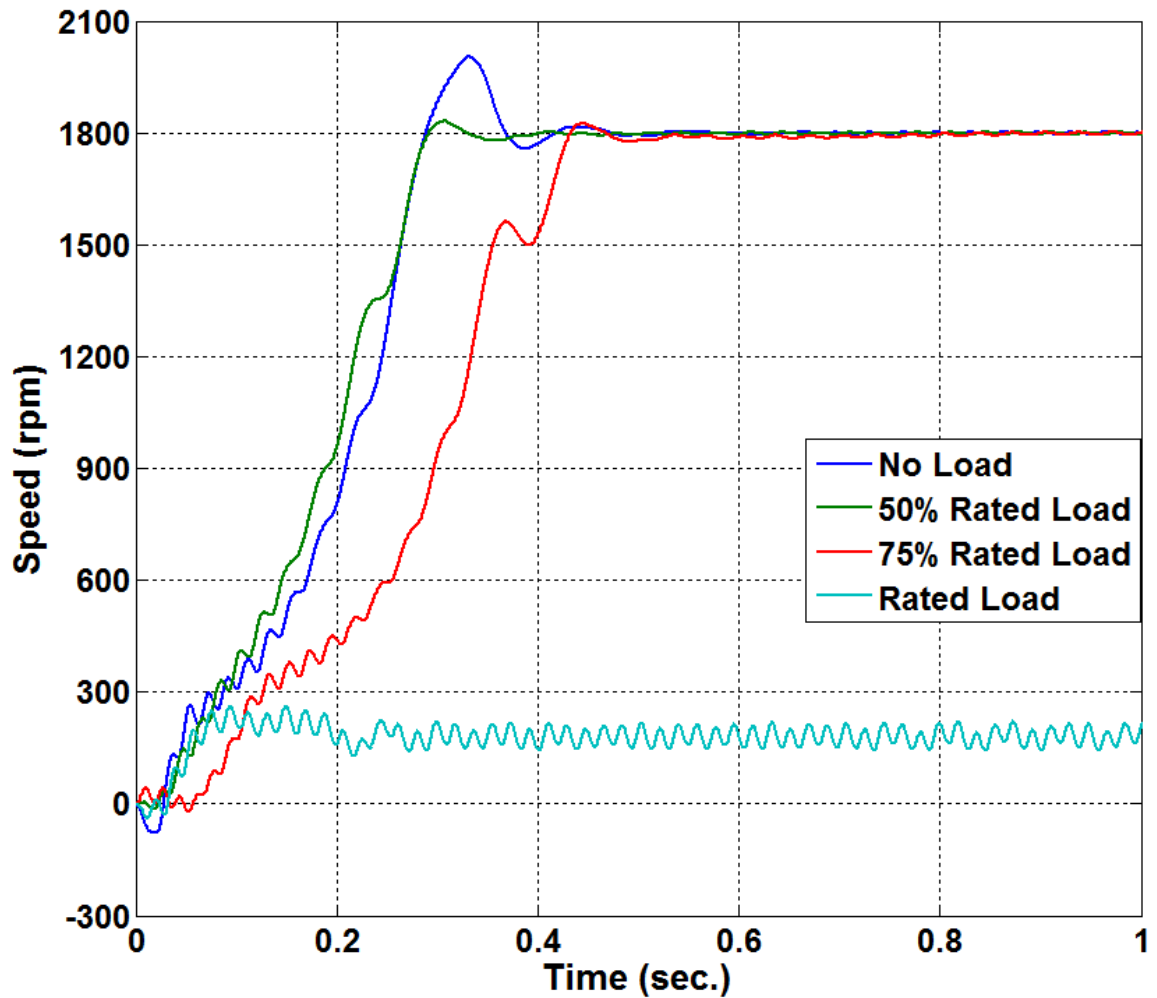


Figure 2.18. Experimental run-up responses.

Figure 2.19 shows the slip vs. torque angle trajectories for 50%, 75% and 100% of the rated load torque. The number of pole slips is higher during the start, resulting in significant vibration of the rotor and high heat dissipation. The frequency of pole slips becomes progressively lower as the motor reaches close to the synchronous speed. The critical slip of the motor for 75% of the rated torque is zoomed in the figure. If the critical

slip is too high, the motor cannot attain the synchronism as depicted in Figure 2.18 for the rated load torque. During the last pole slip before reaching the synchronous speed, the slip becomes negative, achieving successful synchronization of the motor. In order to achieve synchronism, the last pole slip has to become zero or negative. When the inertia becomes higher than the critical inertia, slip never becomes negative or zero. Thus, synchronization never happens in that case.

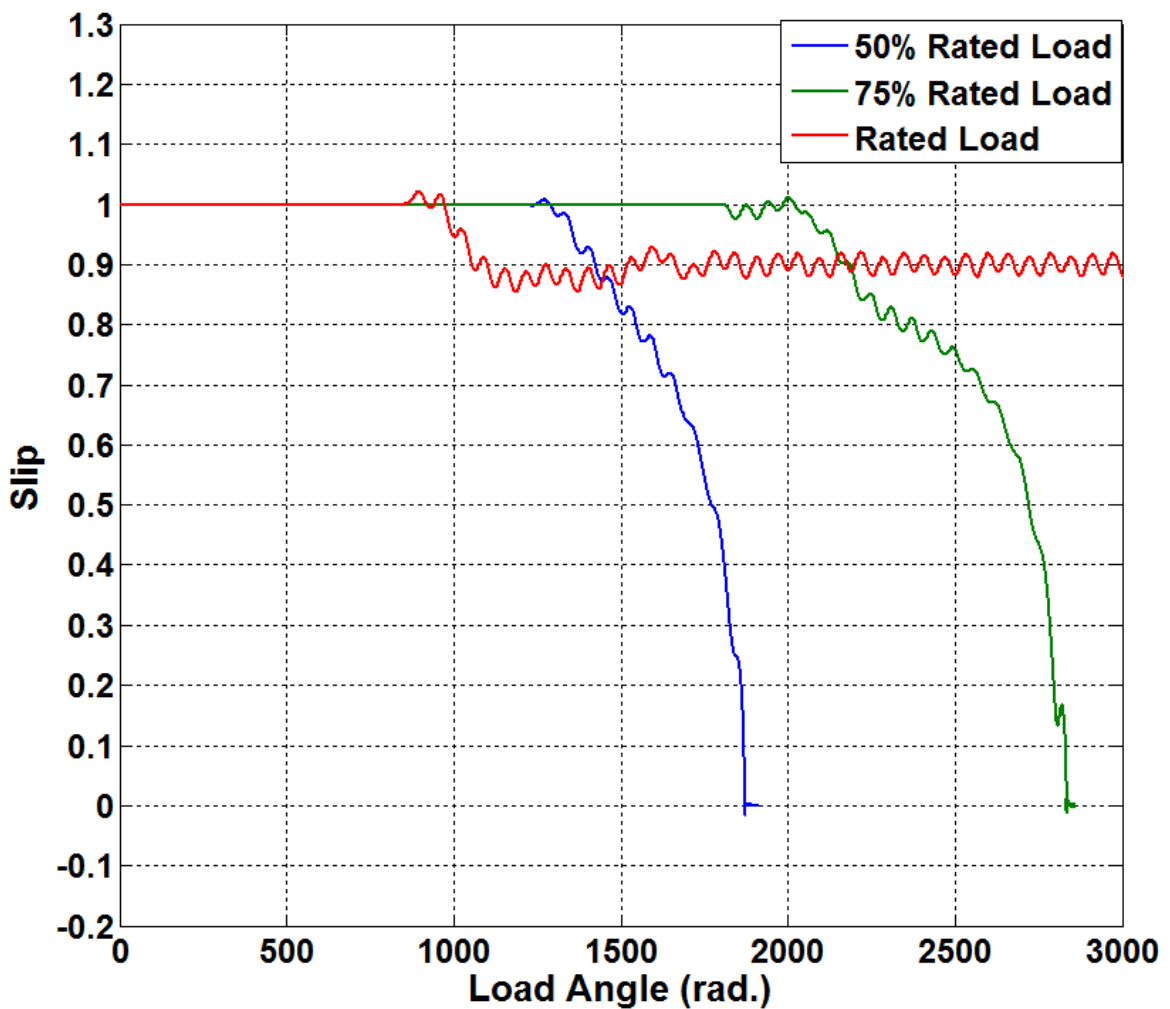


Figure 2.19. Experimental slip vs. load-angle trajectories.

The phase-A currents for different loads are shown in Figures 2.20 and 2.21. The current is significantly higher during the transient period, and the motor tries to reach the synchronous speed during this period. When it approaches the synchronous speed, the current reaches to a steady state value. If the motor fails to synchronize, the stator currents do not reach to a steady state value and remains high as shown in Figure 2.21. This causes over heating of the motor.

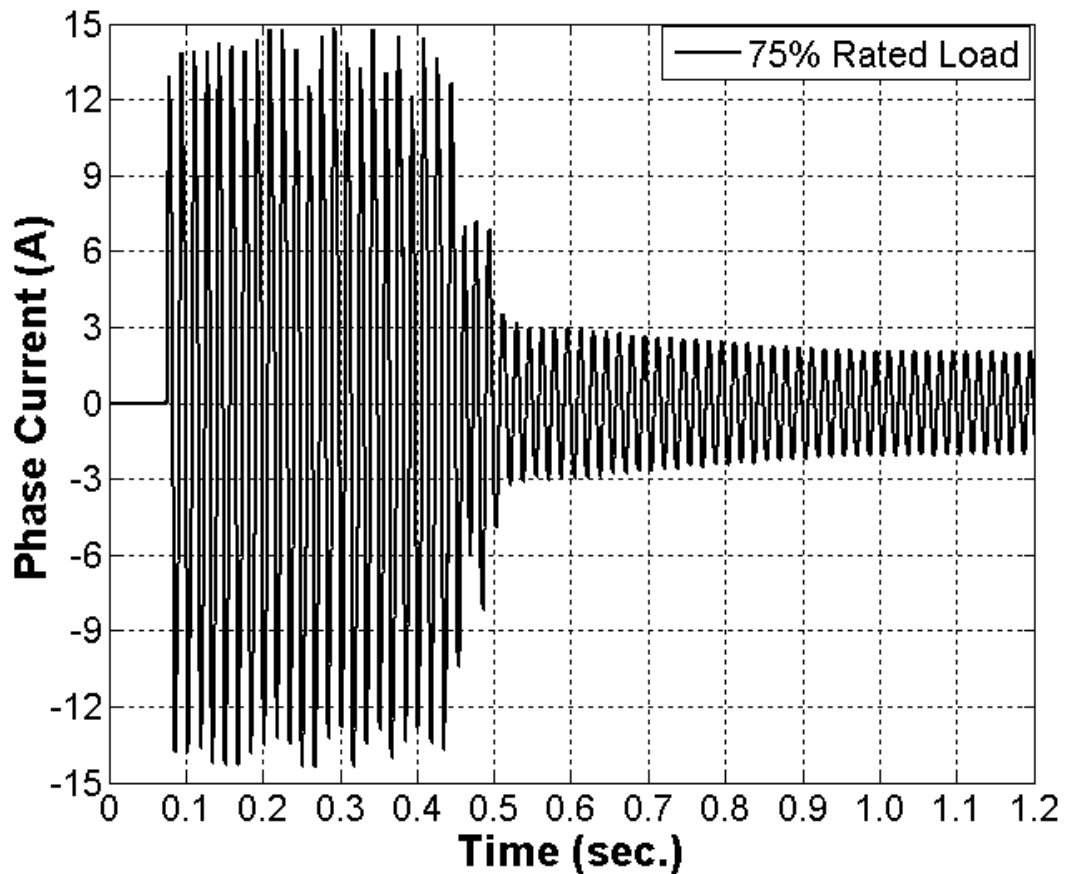


Figure 2.20. Experimental phase-A current waveform at 75% of the rated load.

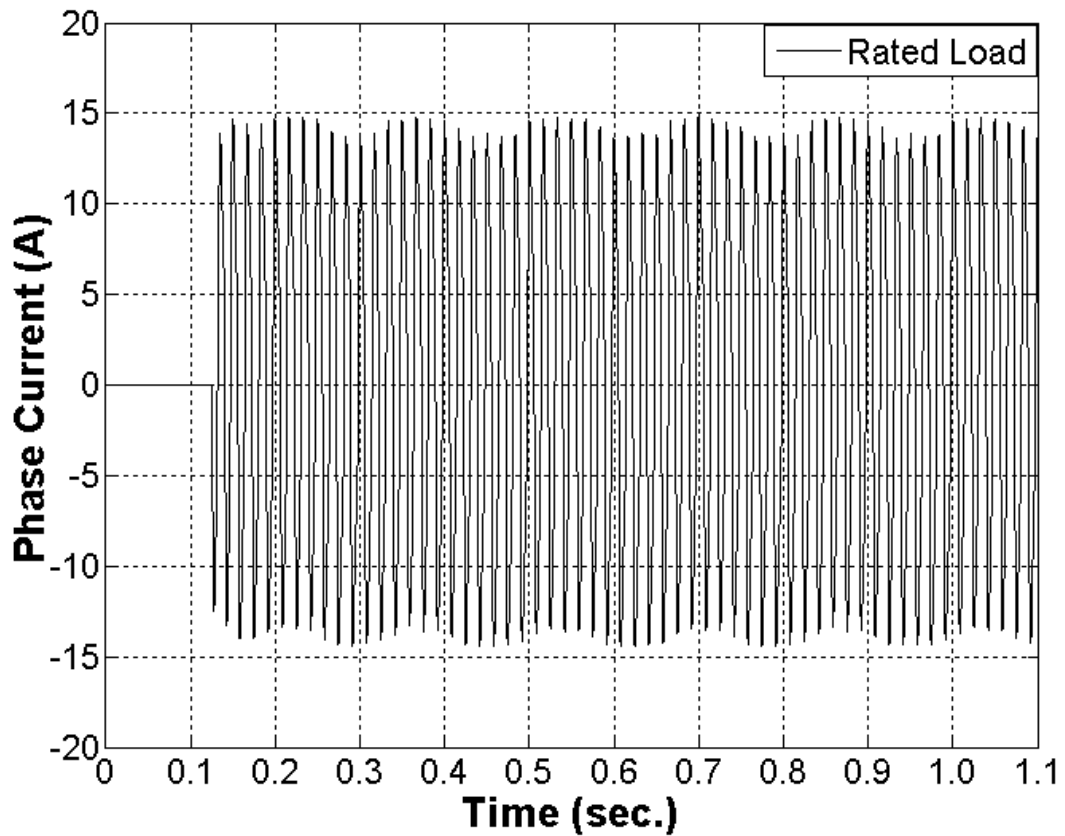
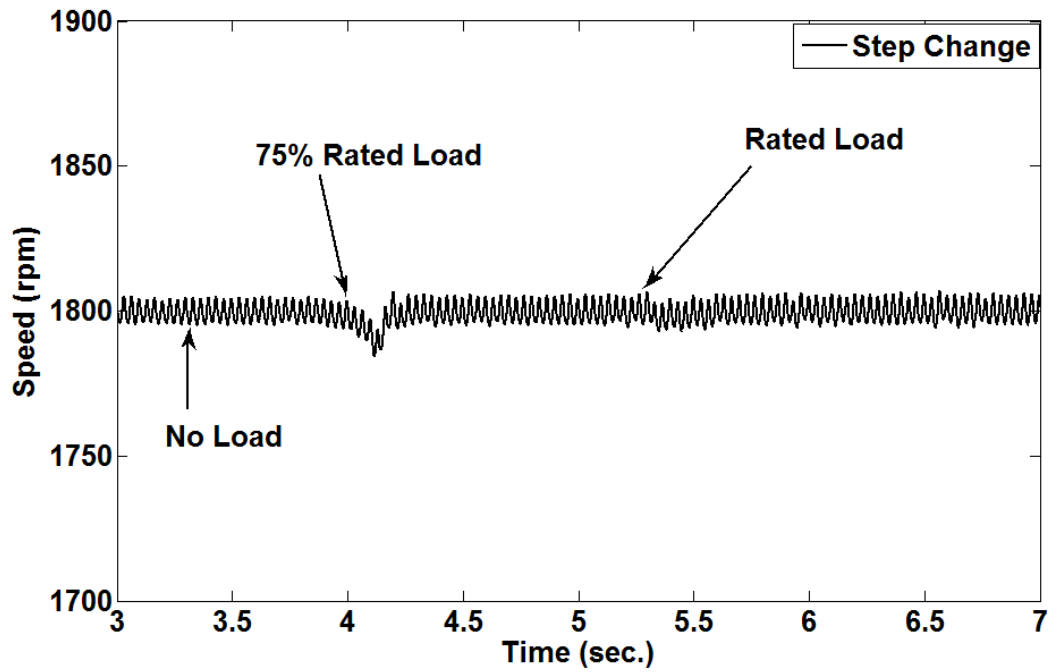
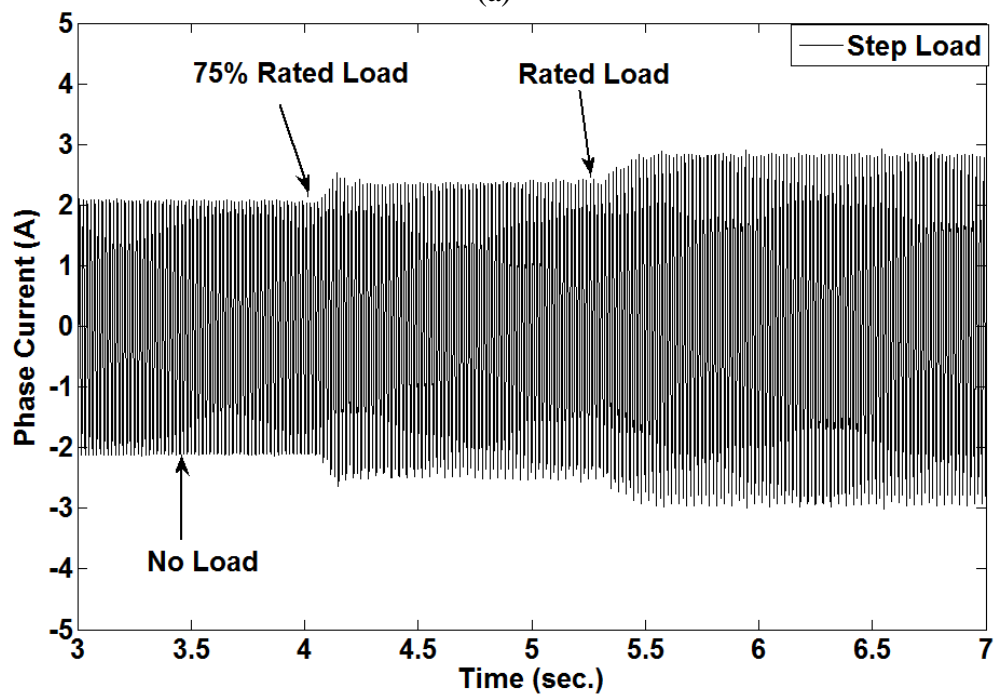


Figure 2.21. Experimental phase-A current waveform at rated load.

The synchronization ability of a line-start IPM motor is greatly enhanced at steady state. Figures 2.22a-2.22b demonstrate speed and current responses of the motor for step changes in the load torque. The motor is initially operating at the synchronous speed under no load condition. The load torque is gradually changed from 75% of the rated torque to full rated load. The motor is able to remain synchronized for both cases. The cage works as a stabilizer for the rotor to keep the motor synchronized with minimum speed oscillations. The sustained speed oscillation depicted in Figure 2.22a is due to the mechanical torsional vibration associated with the setup.



(a)



(b)

Figure 2.22. Experimental responses of the motor for step changes in the load torque: (a) speed and (b) current.

## 2.7 Conclusions

This chapter presents an improved analytical method to examine the synchronization capability of line-start IPM motors including the impacts of the average asynchronous and synchronous torques. An approximate analytical method has been developed to determine the critical inertia and critical slip for successful synchronization of an IPM motor for both constant and dynamic loads. Simulations are carried out to validate the proposed analytical method for a 1-HP line-start IPM motor. Limited experimental results suggest that the proposed method can be applied to determine the critical criteria of successful synchronization for self-starting IPM motors. Based on analytical, simulation and experimental results, it is evident that the synchronization capability of squirrel-cage equipped line-start IPM motors is limited by the load torque and load inertia.

In the next chapter, a new type of self-starting hybrid IPM motor combining hysteresis and permanent magnet materials in the rotor is presented.

## References

1. M. A. Rahman, "History of interior permanent magnet motors," *IEEE Industry Applications Magazine*, vol.19, no. 1, pp. 10-15, Jan. 2013.
2. M. A. Rahman, "*Permanent-Magnet Synchronous Machines*", McGraw-Hill Yearbook of Science and Technology 2011, ISBN 978-007-176371-4, pp. 242-244.
3. M. A. Rahman, "*Permanent Magnet Machines*", The Industrial Electronics Handbook, Second Edition, Publishers: George Kenney, Taylor and Francis, ISBN 978-143-9802-892, Volume 2 , Chapter 5, March 04, 2011, pp.5.1-5.10.

4. M. A. Rahman and Ping Zhou, “Interior Permanent Magnet Motors, *Modern Electric Drives*”, (Book Chapter) NATO Advanced Studies Series, Section III.4, Kluwer Academic Publications, 2000, pp. 115-140.
5. R. T. Ugale, B. N. Chaudhari and A. Pramanik, “Overview of research evolution in the field of line start permanent magnet synchronous motors”, *IET Electric Power Applications*, vol. 8, no. 4, pp. 141-154, 2014.
6. F. W. Merrill, “Permanent magnet excited synchronous motors”, *Transactions of the American Institute of Electrical Engineers. Part III: Power Apparatus and Systems*, vol. 73, no. 2, pp. 1754-1760, January 1954.
7. J. F. H. Douglas, “Characteristics of induction motors with permanent-magnet excitation”, *Transactions of the American Institute of Electrical Engineers. Part III: Power Apparatus and Systems*, vol. 78, no. 3, pp. 221-225, April 1959.
8. D. P. M. Cahill and B. Adkins, “The permanent magnet synchronous motor”, *Proceedings of the IEE - Part A: Power Engineering*, vol. 109, no. 48, pp. 483 - 491, December 1962.
9. K. J. Binns, M. A. Jabbar and W. R. Barnard, “Hybrid permanent magnet synchronous motors”, *Proceedings of the Institution of Electrical Engineers*, vol. 125, no. 3, pp. 203-208, March 1978.
10. K. J. Binns and M. A. Jabbar, “High field permanent magnet synchronous motor”, *Proceedings of the International Conference on Electrical Machines*, Athens, Greece, Part 1, September 15-17, 1980, pp. 304-311
11. K. J. Binns and M. A. Jabbar, “High field self-starting permanent magnet synchronous motor”, *Proceedings of the Institution of Electrical Engineers*, vol. 128, no. 3, pp. 157-160, May 1981.
12. K. J. Binns and T. M. Wong, “Analysis and performance of high field permanent magnet synchronous machine”, *Proceedings of the Institution of Electrical Engineers*, vol. 131, no. 6, pp. 252-258, November 1984.
13. V. B. Honsinger, “Performance of polyphase permanent magnet machines”, *IEEE Transactions on Power Apparatus and Systems*, vol. 99, no. 4, pp. 1510 – 1518, July 1980.

14. V. B. Honsinger, "The fields and parameters of interior type ac permanent magnet machines", *IEEE Transactions on Power Apparatus and Systems*, vol. PAS-101, no.4, pp. 867-876, April 1982.
15. T. J. E. Miller, T. W. Neumann, and E. Richter, "A permanent-magnet excited high-efficiency synchronous motor with line-start capability", *Proceedings of the IEEE IAS Annual Meeting*, Mexico City, 3-7 October 1983, pp.455-461.
16. M. A. Rahman, "Permanent magnet synchronous motor, A review of the design art", *Proceedings of the International Conference on Electrical Machines*, Athens, Greece, Part 1, September 15-17, 1980, pp. 312–319.
17. M. A. Rahman, NSERC-PRAI-CGE Project on IPM. New York: MUN, 1982.
18. M. A. Rahman and T.A. Little, "Dynamic Performance Analysis of Permanent Magnet Synchronous Motor," *IEEE Transactions on Power Apparatus and Systems*, vol. PAS-103, No. 6, pp. 1277-1282, June 1984.
19. M. A. Rahman and G.R. Slemon, "The Promising Applications of Neodymium Boron Iron Magnets in Electrical Machines", *IEEE Transactions on Magnetics*, Vol. MAG-21, No. 5, pp. 1712-1716, September 1985.
20. M. A. Rahman and A.M. Osheiba, "Performance of a large line start permanent magnet synchronous motor", *IEEE Transactions on Energy Conversion*, vol. 5, no.1, pp. 211-217, March 1990.
21. B. J. Chalmers, S. A. Hamed and G. D. Baines, "Parameters and performance of a high-field permanent magnet synchronous motor for variable-frequency operation", *IEE Proceedings B - Electric Power Applications*, vol. 132, no. 3, pp. 117-124, May 1985.
22. K. Kurihara and M. A. Rahman, "High-efficiency line-start interior permanent-magnet synchronous motors," *IEEE Transactions on Industry Applications*, vol. 40, No. 3, pp. 789-796, May/June 2004.
23. M. J. Melfi, S. Evon and R. Mcelveen, "Induction versus permanent magnet motors", *IEEE Industry Applications Magazine*, vol. 15, no. 6, pp. 28-35, November 2009.

24. T. J. E. Miller, "Synchronization of line start permanent magnet ac motors," *IEEE Transaction on Power Apparatus and Systems*, vol. PAS-103, no. 7, pp. 1822-1828, July 1984.
25. A. H. Isfahani and S. Vaez-Zadeh, "Effects of magnetizing inductance on start-up and synchronization of line-start permanent-magnet synchronous motors," *IEEE Transactions on Magnetics*, vol. 47, No. 4, pp. 823-829, April 2011.
26. A. H. Isfahani, S. Vaez-Zadeh and M. A. Rahman, "Evaluation of synchronization capability in line start permanent magnet synchronous motors," in *Proc. of the Intl. Electric Machine and Drives Conference*, Niagara Falls, May 15-18, 2011, pp. 1346-1350.
27. M. A. Rahman, A. Osheiba and T. Radwan, "Synchronization process of line-start permanent magnet synchronous motor," *Electric Machines and Power Systems, Taylor and Francis Ltd*, vol. 25, pp. 577-592, July 1997.
28. V. B. Honsinger, "Permanent magnet machines: asynchronous operation," *IEEE Transactions on Power Apparatus and Systems*, vol. PAS-99, No. 4, pp.1503 - 1509, July 1980.
29. P. J. Lawrenson and R. M. Mathur, "Pull-in criterion for reluctance motors", *Proceedings IEE*, vol. 120, no. 9, pp. 982-986, Sept. 1973.
30. A. D. Alaibad, M. Mirsalim and N. F. Ershad, "Line-start permanent magnet motors: significant improvements in starting torque, synchronization and steady-state performance", *IEEE Transactions on Magnetics*, vol.46, no.12, pp.4066-4072, December 2010.
31. T. Ding, N. Takorabet, F.M. Sargos, and X. Wang, "Design and analysis of different line-start PM synchronous motors for oil-pump applications", *IEEE Transactions on Magnetics*, vol. 45, No. 3, pp. 1816–1819, March 2009.
32. Q. F. Lu and Y. Y. Ye, "Design and analysis of large capacity line start permanent-magnet motor," *IEEE Transactions on Magnetics*, vol. 44, no. 11, pp. 4417–4430, November 2008.

33. G. R. Slemon, "Analytical models for saturated synchronous machines", *IEEE Transactions on Power Apparatus and Systems*, vol. PAS-90, No.2, pp. 409-417, March/April 1971.
34. G. R. Slemon and X. Liu, "Modeling and design optimization of permanent magnet motors", *Electric Machine and Power Systems*, vol.20, no.2, pp.71-92, March/April 1992.
35. A. Consoli and A. Abela, "Transient performance of permanent magnet ac motor drives", *IEEE Transactions on Industry Applications*, Vol.-22, No.1, pp. 32-41, January 1986
36. M. A. Rahman and T.A. Little, "Dynamic Performance Analysis of Permanent Magnet Synchronous Motor," *IEEE Transactions on Power Apparatus and Systems*, vol. PAS-103, no. 6, pp. 1277-1282, June 1984.
37. P. J. Lawrenson and L. A. Agu, "Theory and performance of Polyphase reluctance machines", *Proceedings of the Institution of Electrical Engineers*, vol. 3, No. 8, pp. 1435-1445, August 1964.
38. W. Fei, P. Luk, J. Ma, J. X. Shen, and G. Yang, "A high-performance line-start permanent magnet synchronous motor amended from a small industrial three-phase induction motor," *IEEE Transactions on Magnetics*, vol. 45, no.10, pp. 4724-4727, October 2009.
39. P.J. Lawrenson and J. M. Stephenson, "Average asynchronous torque of synchronous machines, with particular reference to reluctance machines", *Proceedings of the Institution of Electrical Engineers*, vol.116, no. 6, pp. 1049 - 1051, June 1969.
40. M. A. Rahman, A. M. Osheiba, K. Kurihara, M. A. Jabbar, H. W. Ping, K. Wang and H. M. Zubayer, "Advances on Single Phase Line Start High Efficiency Interior Permanent Magnet Motors", *IEEE Transactions on Industrial Electronics*, vol. 59, No.3, pp. 1333-1345, March 2012.
41. S. F. Rabbi, "Analysis of asynchronous start-up and synchronization of line start interior permanent magnet motors", Master's Thesis, MUN, St. John's, NL, Canada, June 2012.

## Chapter 3

### Hysteresis Interior Permanent Magnet Motor

#### 3.1 Introduction

A hysteresis interior permanent magnet motor combines the advantages of both hysteresis and interior permanent magnet motors. It belongs to the class of self-starting permanent magnet motors. It was invented by Rahman in the early 1990s [1]-[4]. Since then, various designs of hysteresis permanent magnet motors with different hysteresis materials have been introduced in the literature [5]-[9]. This chapter presents modeling and analysis of a hysteresis interior permanent magnet (IPM) motor. A novel approach to develop the electrical and magnetic equivalent circuit models of a hysteresis IPM motor using elliptical approximation of hysteresis loops for transient analysis of the motor is provided in this chapter. Approximate magnetic equivalent circuits are developed considering the magnetic saliency of the motor. Dual electrical equivalent circuits in  $d$ - $q$  axes are derived from the magnetic circuits. Both electrical and magnetic equivalent circuits are illustrated and explained in this chapter. Analytical simulations using the developed electrical equivalent circuits and finite element analysis are carried out to obtain the transient responses of a 3-phase, 4-pole, 208V, 2.5-kW laboratory prototype hysteresis IPM motor. Simulation results as well as experimental test results of the prototype motor are presented and analyzed in this chapter.

### **3.2 Hysteresis Interior Permanent Magnet Motor**

A hysteresis interior permanent magnet (IPM) motor is a self-starting solid rotor hybrid synchronous motor. It is a hysteresis-start permanent magnet motor. Its rotor has a cylindrical ring made of composite material such as Cobalt-steel alloys, special Al-Ni-Co, Vicalloy, P6, D2 steel, etc. with high degree of hysteresis energy per unit volume [1]-[9]. The rare earth magnetic materials such as Nd-B-Fe magnets are buried inside the hysteresis ring. The ring is supported by a sleeve made of non-magnetic materials. The non-magnetic sleeve guides the flux to flow circumferentially inside the rotor ring in order to maximize the effective area of the hysteresis material, achieving a high hysteresis torque [3]. Figure 3.1 illustrates the rotor of a prototype hysteresis IPM motor. The hysteresis ring is made of 36% Cobalt-Steel alloy. The cross section of the hysteresis IPM motor depicting the position and orientation of permanent magnets is shown in Figure 3.2. The inclusion of permanent magnets creates rotor saliency without changing the length of the physical airgap. It also provides an additional permanent source of excitation in the rotor. A hysteresis motor does not have any points of synchronization and suffers from hunting while seeking a point of equilibrium. The embedded permanent magnets provide definite points of synchronization for the motor, and thus reduce the hunting associated with classical hysteresis motors.

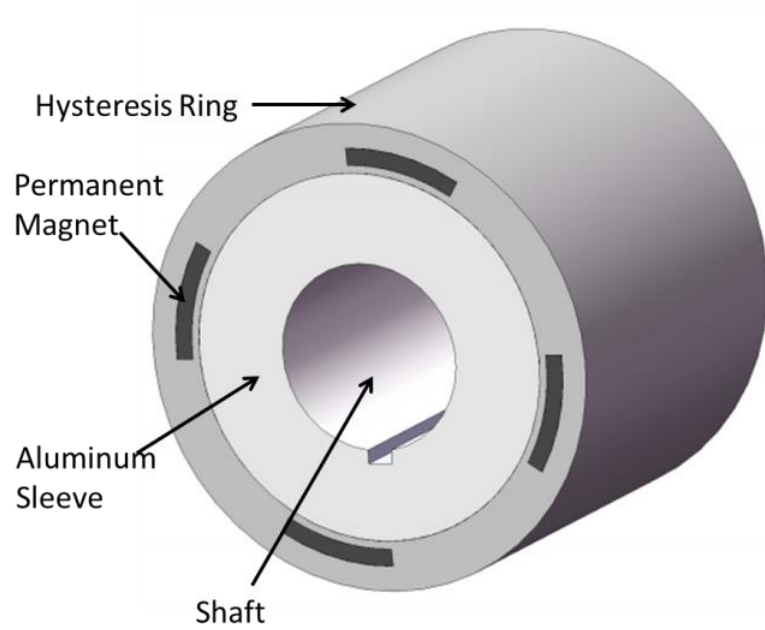


Figure 3.1. Rotor of a prototype hysteresis interior permanent magnet motor.

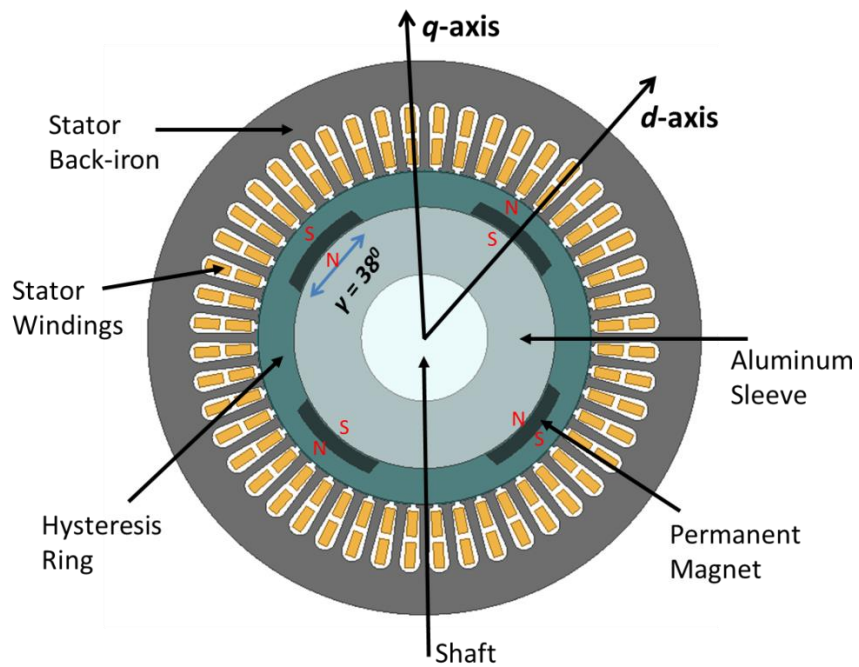


Figure 3.2. Cross-section of a hysteresis interior permanent magnet motor.

Figure 3.3 presents average asynchronous torque vs. speed curves of a hysteresis IPM motor. The induced magnetization of the hysteresis material inside the rotor ring always lags behind the time varying magnetic field. This time lag produces a torque, called hysteresis torque. The induced eddy currents in the solid ring generate some additional starting torque called the eddy current torque. The combination of the hysteresis torque and the eddy current torque results in a high starting torque during on-line starting of a hysteresis IPM motor from a balanced 3-phase AC supply which helps overcoming the magnet brake torque [1]. The eddy current torque becomes zero when the motor synchronizes but the hysteresis ring becomes temporarily magnetized.

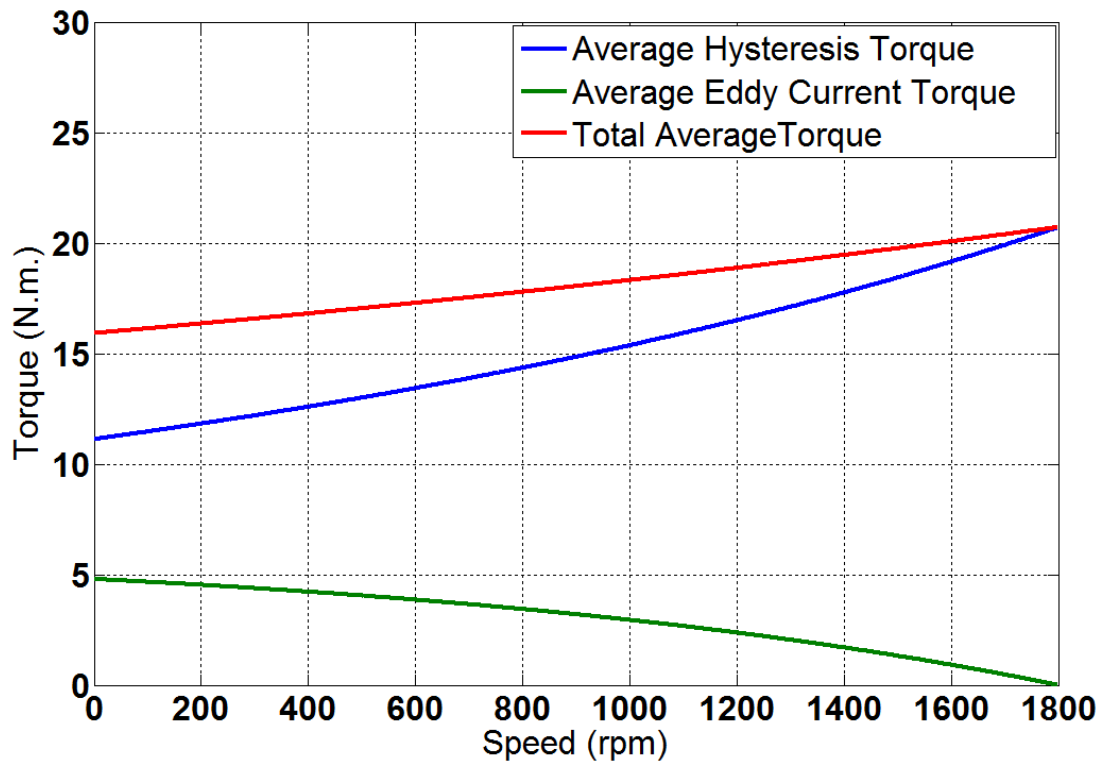


Figure 3.3. Average asynchronous torques of a hysteresis-start IPM motor.

A comparison between squirrel-cage IPM motor and hysteresis IPM motor is provided in table 3.1.

Table 3.1. Comparison between hysteresis and squirrel-cage self-start IPM motors.

<b>Hysteresis IPM Motor</b>	<b>Squirrel-Cage IPM Motor</b>
Smooth self-starting and good synchronization capabilities	Poor self-starting and limited synchronization capabilities
High starting torque	Moderate starting torque
Moderate starting current	High starting current
Predominantly PM motor when synchronized	PM motor when synchronized
Moderate Power Factor	High Power Factor
High Efficiency	High Efficiency
High Reliability	Good Reliability
Provides High Damping Torque	Provides Moderate Damping Torque
Requires Less Rare-Earth Magnets	Requires More Rare-Earth Magnets
High Torque Density	Moderate Torque Density

### **3.3 Equivalent Circuit Modeling of a Hysteresis IPM Motor**

A hysteresis interior permanent magnet motor is hybrid in nature containing dual sources of excitation in the rotor. The first source is the temporarily magnetized hysteresis ring and the second one is the permanent magnet excitation. Both of these sources together provide the necessary excitation for synchronous operation of the rotor. Thus, the equivalent magnetic circuits of the motor can be modelled using the superposition principle considering the contribution of each individual excitation. The electric

equivalent circuits of the motor are obtained from the magnetic circuits using the duality theorem. In order to calculate parameters of the equivalent electrical circuits, at first, the motor is considered as a pure circumferential flux hysteresis motor. The magnetizing inductance and the equivalent rotor hysteresis inductance and resistance are calculated by applying the first principles. After that, the motor is considered as a pure IPM motor and the equivalent magnet current source is obtained. The addition of permanent magnets inside the hysteresis ring creates magnetic armature saliency in a hysteresis motor. The coefficients of armature saliency are calculated to determine the  $d$ - $q$  axes equivalent magnetizing inductances. The following sections describe the detailed process for modeling a hybrid hysteresis IPM motor.

### **3.3.1 Modeling of Hysteresis Phenomenon**

Magnetic hysteresis refers to the dependency of a material's magnetization on the past states of the material, as well as its current state. In the analysis of hysteresis motors, modeling of hysteresis loops has been an issue of interest among the researchers [6]-[25]. One way to model the hysteresis behavior is to use the classical Presaich type model to develop a numerical simulation of the hysteresis motor [10]. However, development of electrical equivalent circuits for hysteresis and hybrid hysteresis IPM motors using the Presaich model is complicated and computationally intensive [25].

The Jiles-Atherton model (JAM) and the Hauser Energetic model (HEM) are popular techniques for modeling static and dynamic magnetic hysteresis for both isotropic and anisotropic magnetic materials [11]-[15]. The JAM and HEM are phenomenological hysteresis models with connection to the physical parameters of magnetic materials [11]-

[15]. Both JAM and HEM use functions to represent the anhysteretic magnetization process, and balance the energy during the magnetization process to reach thermodynamic equilibrium. These models are relatively accurate to calculate the major and minor hysteresis loops of a magnetic material, and computationally simpler than the Presaich model. Both JAM and HEM can be used to calculate the hysteresis loss of a hysteresis IPM motor with good accuracy. However, JAM has five parameters to model the hysteresis, and HEM uses even more parameters than the JAM [11]-[15]. Determination of these parameters requires curve-fitting algorithms or statistical/numerical optimization methods [11]-[15]. Furthermore, JAM uses a hyperbolic tangent to model the anhysteretic function and uses a nonlinear differential equation to determine the magnetization. HEM uses a transcendental equation to determine the parameter which is needed to define the knee of the magnetization curve. It requires either numerical analysis or analytical approximations to determine the approximate solution of a transcendental equation. Thus, determination of the equivalent circuit parameters of a hysteresis IPM motor using JAM/HEM is complicated.

The shape of a magnetic material's hysteresis loop can be curve-fitted by using different geometric shapes such as parallelograms, rectangles or ellipses [16]-[25]. These approximate  $B$ - $H$  loop area matching models are computationally less intensive than the Presaich model, the JAM and the EM. The hysteresis loop of a soft-magnetic material, and its parallelogram and rectangular approximation of hysteresis loops are illustrated in Figures 3.4, 3.5 and 3.6, respectively.

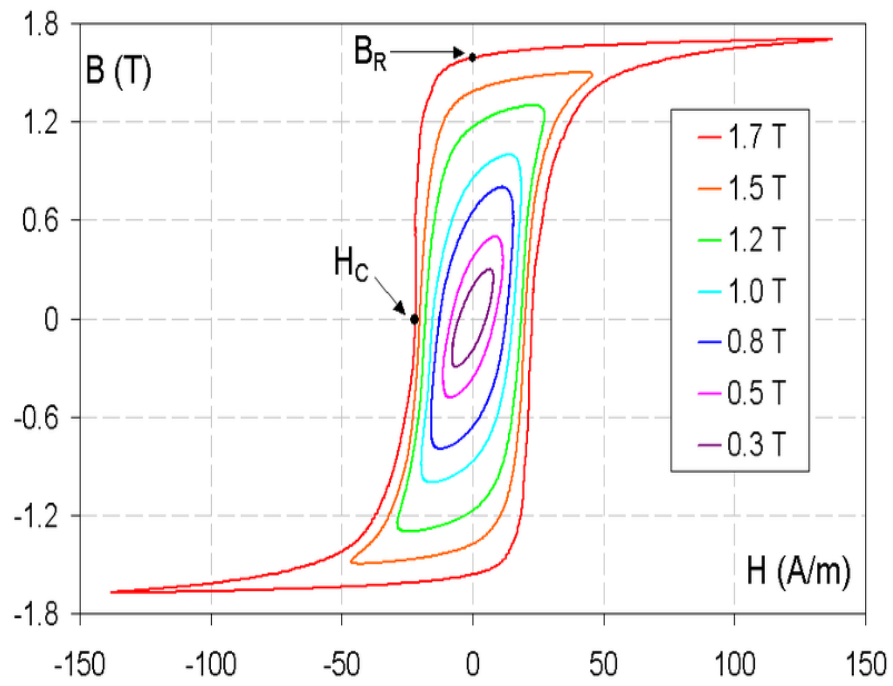


Figure 3.4. Hysteresis loops of a soft-magnetic material [25].

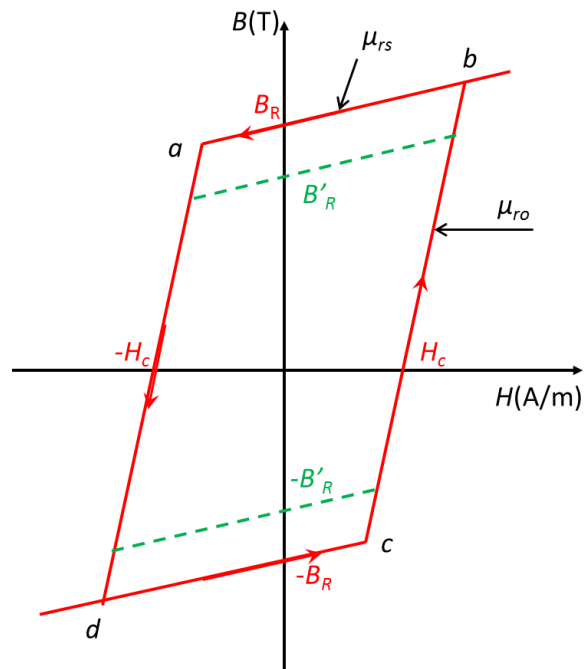


Figure 3.5. Parallelogram modeling of the hysteresis loops of a soft-magnetic material.

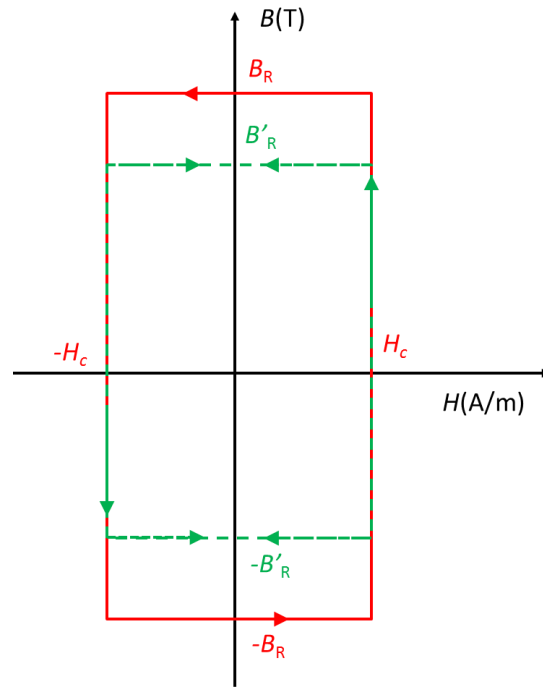


Figure 3.6. Rectangular modeling of the hysteresis loops of a soft-magnetic material

Copeland and Slemon presented analysis of both radial and circumferential flux hysteresis motors using a parallelogram approximation of the hysteresis phenomenon [16]-[17]. O'Kelly, Rahman and Osheiba presented a different set of equivalent circuit models of hysteresis motors for both synchronous and sub-synchronous operations using the parallelogram approach [18]-[21]. In a parallelogram model presented in Figure 3.5, the lag angle  $\delta$  between  $B$  and  $H$  is assumed to be in the range of  $0 < \delta < 60^\circ$ . The parallelogram modelling is a viable method for an early analysis of a hysteresis motor. This model is based on a piecewise continuous function approximation of the  $B$ - $H$  loop. It leads to non-linear equations for analytical solution of hysteresis motors. Rahman and Qin have presented equivalent circuit modeling of circumferential flux type hysteresis permanent magnet motors using rectangular

modeling of the hysteresis curves [1]. In rectangular modeling, the hysteresis lag angle is assumed to be at a constant  $90^0$  as shown in Figure 3.6. In practice, it is much less than  $90^0$  for semi-hard hysteresis materials. In the cases of semi-hard and soft magnetic materials,  $\delta$  varies over a wide range during synchronization. As a result, the equivalent hysteresis resistance and inductance go through successive oscillations before approaching steady state values. Rectangular modeling assumes constant hysteresis resistance and inductance which is not suitable for transient analysis of hysteresis motors with semi-hard isotropic/anisotropic magnetic materials [15]-[16]. As a result, rectangular modeling is applicable for modeling hysteresis loops of hard magnetic materials such as rare earth magnets where  $\delta=90^0$ .

O'Kelly, Miyairi, Kataoka and Ishikawa used an elliptical model of hysteresis loops to develop an equivalent circuit model for hysteresis motors [21]-[25]. In the elliptical model, the hysteresis loops are approximated by a set of inclined ellipses. The inclination angle of the ellipse depends on the hysteresis lag angle  $\delta$  and it is normally less than  $45^0$ . Elliptical modelling is a better approximation and computationally much simpler than other models for hysteresis motors with semi hard magnetic materials [25].

Figure 3.7 shows the manufacturer-provided major hysteresis loop of a hysteresis ring made of 36% Cobalt-Steel alloy. The initial magnetization curve is presented by the red dotted line. In elliptical modeling, the hysteresis curves of the rotor material are approximated by a group of inclined ellipses of similar shapes [20]-[25]. The elliptical approximations of the hysteresis curves are shown in Figure 3.8.  $B_r$  is called the remanence which is the residual value of flux density when the applied field becomes

zero.  $H_c$  is called the coercive force or coercivity of the material which is a negative value of the applied magnetic field intensity, required to force the flux density to zero.

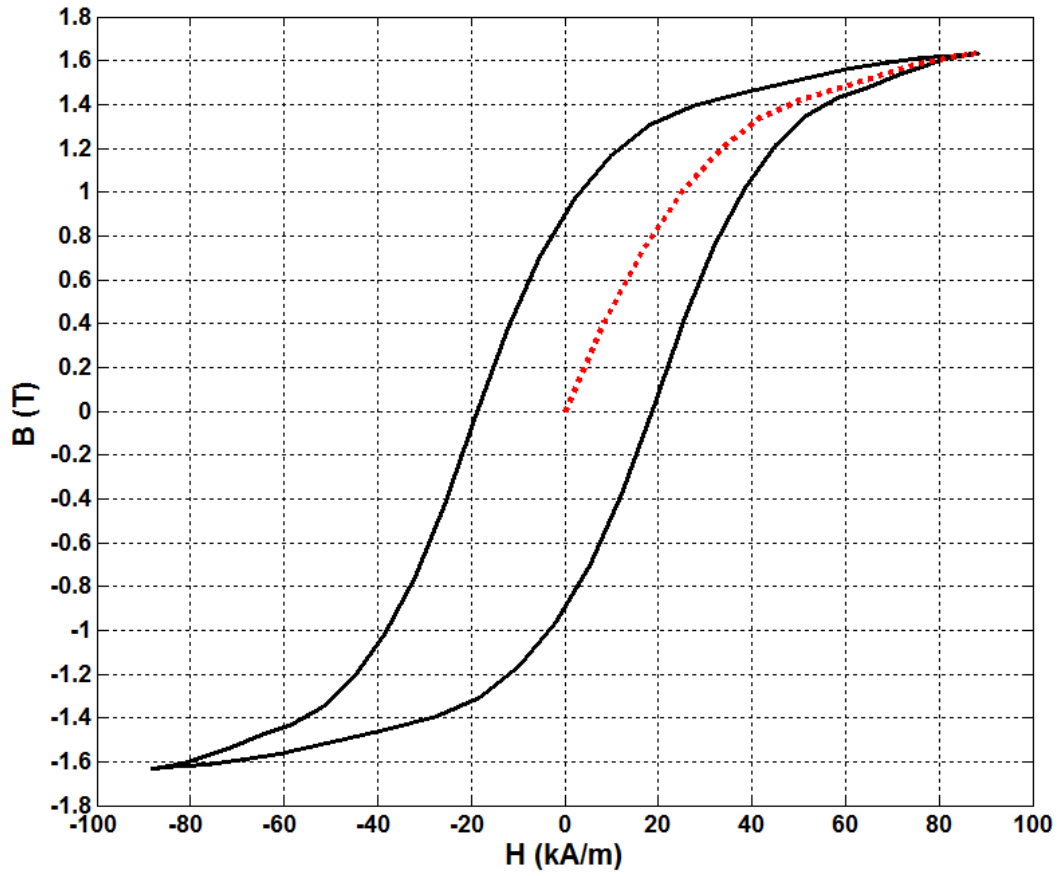


Figure 3.7. Major hysteresis loop of 36% Cobalt-Steel alloys.

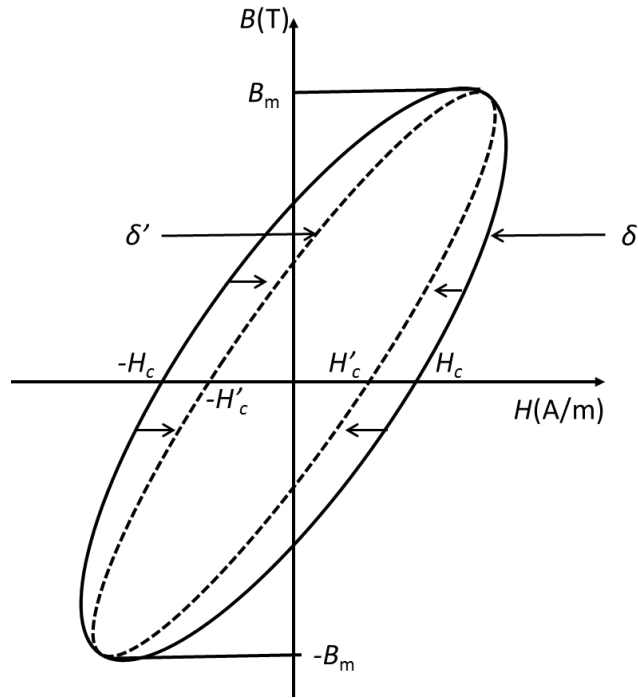


Figure 3.8. Elliptical approximation of hysteresis loops.

The trajectory of a B-H curve lies on the ellipse if the motion around the ellipse is in the counter clockwise direction. The lag angle between  $B$  and  $H$  remains constant as long as the direction of the motion remains counter clockwise. When the direction of motion changes to clockwise, it results in a movement between the inner ellipses with different lag angles along the minor loop. This phenomena is illustrated in Figure 3.8 for one inner ellipse and one outer ellipse with two different lag angles  $\delta$  and  $\delta'$ , respectively. The flux density  $B$  and the magnetic field intensity  $H$  in an elliptical model can be expressed as follows [25],

$$B = B_m \cos(\omega t - \psi - \varphi_0) \quad (3.1)$$

$$H = \left(\frac{B_m}{\mu}\right) \cos(\omega t - \psi - \varphi_0 + \delta) \quad (3.2)$$

$$\varphi_0 = \tan^{-1} \frac{\frac{r_r \sin \delta}{p\mu}}{\frac{l_g p t_r}{\mu_0 r_g} + \frac{r_r}{p\mu} \cos \delta} \quad (3.3)$$

where  $B_m$  is the maximum flux density of the rotor material,  $\mu$  is the permeability of the elliptic hysteresis loop,  $\omega$  is the synchronous angular frequency,  $\psi$  ( $\psi = p\theta_r$ ;  $\theta_r$  is the mechanical angle of the rotor and  $p$  is the number of pole pairs) is the electrical angle coordinate in the stator frame,  $\varphi_0$  is the phase shift,  $r_r$  is the average of the inner and the outer radius of the rotor,  $r_g$  is the average radius of the air-gap,  $t_r$  is the thickness of the rotor hysteresis ring,  $l_g$  is the radial length of the air-gap and  $\delta$  is the hysteresis lag angle between  $B$  and  $H$ .

Figure 3.9 illustrates the inclined elliptical approximations of the hysteresis loops of 36% Cobalt-Steel alloy using (3.1)-(3.3). A hysteresis motor follows the major hysteresis loop during starting which is represented by a rotated ellipse. During the period of synchronization, the hysteresis motor experiences a series of minor loops with progressively smaller excursion lengths which are shown by the recoil lines inside the major hysteresis loop. These minor loops result in high losses and consequently increases temperature rise in the rotor of the motor.

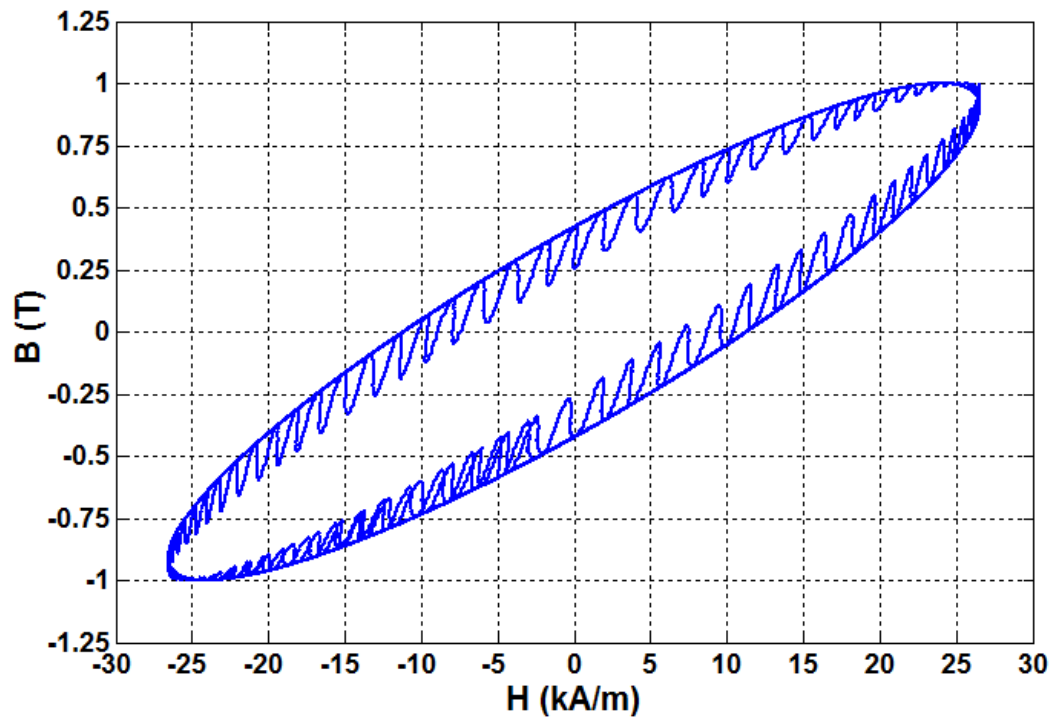


Figure 3.9. Elliptical modeling of the hysteresis loop for 36% Cobalt-Steel alloys.

### 3.3.2 Modeling of Permanent Magnet Excitation

In a permanent magnet (PM) machine, the operation of the magnet is determined by the demagnetization regions of its hysteresis curves and also by the dimensions of the magnet. The linear demagnetization curves of a Nd-B-Fe magnet are illustrated in Figure 3.10 [26]. A permanent magnet is a source of mmf, and the equivalent magnet mmf acts over the angular width of the magnet inside the rotor as depicted in Figure 3.11. The magnet mmf  $\mathcal{F}_m$  is generally in rectangular form as shown in Figure 3.12.

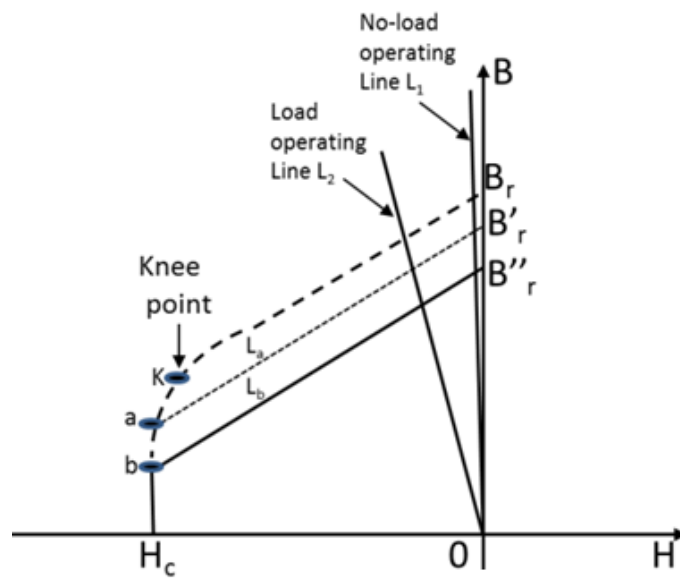


Figure 3.10. Demagnetization curves of an Nd-B-Fe magnet.

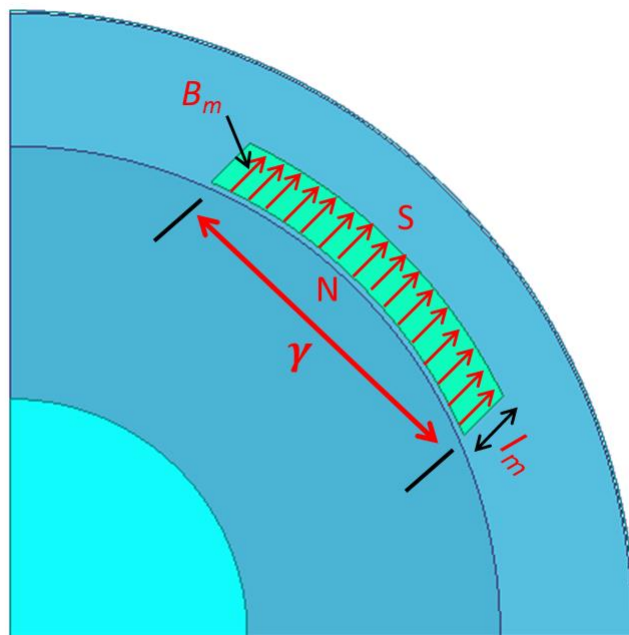


Figure 3.11. Modeling of the permanent magnet a source of mmf.

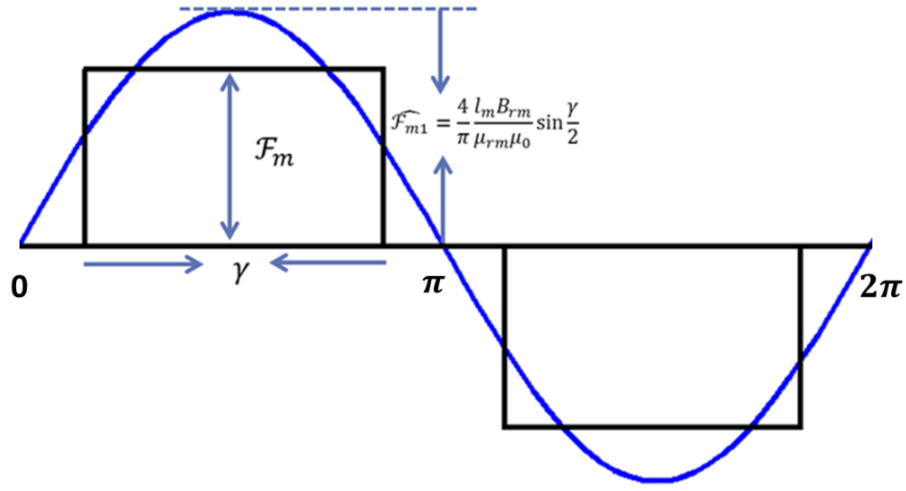


Figure 3.12. Equivalent mmf of a permanent magnet.

Using Fourier expansion of  $\mathcal{F}_m$ , the peak value of its fundamental component can be expressed by [27],

$$\widehat{\mathcal{F}}_{m1} = \frac{4 l_m B_{rm}}{\pi \mu_{rm} \mu_0} \sin \frac{\gamma}{2} \quad (3.4)$$

where  $l_m$  is the radial length of the magnet,  $B_{rm}$  is the effective residual flux density of a permanent magnet (T),  $\mu_{rm}$  is the recoil permeability of the magnet,  $\gamma$  is the angular width of the magnet in radian.

The permanent magnet can be modeled as a set of coils carrying sinusoidal currents. The fundamental mmf produced by the currents in the coils can be written as [27],

$$\widehat{\mathcal{F}}_{m1} = \frac{3}{2P} K_{sw} N_{sw} I_m \quad (3.5)$$

where  $K_{sw}$  is the winding factor of the stator,  $N_{sw}$  is the number of stator series turns per phase,  $P$  is the number of poles and  $I_m$  (A) is the amplitude of the currents source representing the magnet, as seen from the stator.

Equating (3.4) and (3.5), the expression for equivalent magnet current can be obtained, and it is given below,

$$I_m = \frac{8Pl_m B_{rm}}{3\pi\mu_{rm}\mu_0 K_{sw} N_{sw}} \sin \frac{\gamma}{2} \quad (3.6)$$

### 3.3.3 Magnetic Equivalent Circuits of a Hysteresis IPM Motor

A hysteresis IPM motor is a salient pole machine due to the variation of air-gap reluctances caused by the permanent magnets inside the rotor hysteresis ring. Consequently, the magnetic equivalent circuits for a hysteresis IPM motor consist of a  $d$ -axis equivalent circuit and a  $q$ -axis equivalent circuit. The  $d$ - $q$  axes magnetic equivalent circuits are developed based on the following assumptions:

- The stator is assumed to have a balanced  $3\phi$  sinusoidally distributed winding.
- The magnetic flux density is assumed radial in the airgap, but circumferential inside the rotor hysteresis ring.
- The rotor and stator flux leakages are modeled by equivalent leakage reluctances.
- The hysteresis phenomenon in the ring is modelled by elliptical approximations and the saturation of the hysteresis material is neglected.
- The equivalent source of mmf due to the temporarily magnetized hysteresis ring is considered to be present in the  $d$ -axis along with the permanent magnet excitation.

Figures 3.13(a) and 3.13(b) present the  $d$  and  $q$  axes magnetic equivalent circuits of a hysteresis IPM motor. The permanent magnet is modeled as a mmf source  $\mathcal{F}_{md}$  in series with a reluctance  $\mathcal{R}_{md}$ . The hysteresis effect is included in the circuit as a mmf source  $\mathcal{F}_{hd}$ . The  $d$ - $q$  axes reluctances of the hysteresis material are modelled as nonlinear

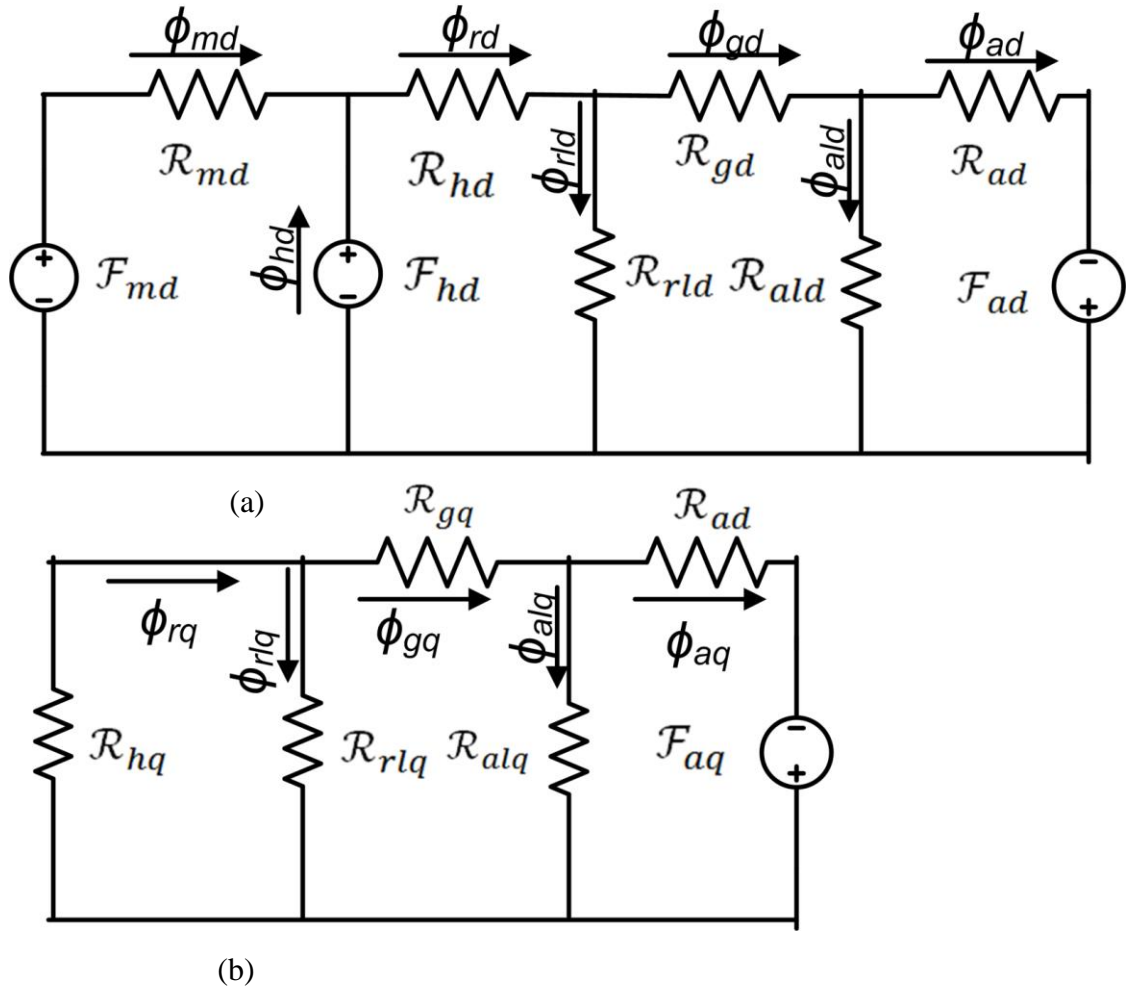


Figure 3.13. Magnetic equivalent circuits of a hysteresis IPM motor: (a)  $d$ -axis and (b)  $q$ -axis.

reluctances  $\mathcal{R}_{hd}$  and  $\mathcal{R}_{hq}$ , respectively.  $\mathcal{R}_{rld}$  and  $\mathcal{R}_{rlq}$  are the  $d$ - $q$  axes rotor leakage reluctances. The effects of hysteresis and permanent magnet mmfs are negligible in the  $q$ -

axis, and are not included in the  $q$ -axis equivalent circuit. The  $d$ - $q$  axes airgap reluctances are presented by  $\mathcal{R}_{gd}$  and  $\mathcal{R}_{gq}$ , respectively. The primary armature magnetomotive forces in the  $d$  and  $q$  axes are presented by  $\mathcal{F}_{ad}$  and  $\mathcal{F}_{aq}$ , respectively.  $\mathcal{R}_{ad}$  and  $\mathcal{R}_{aq}$  are the  $d$  and  $q$  axes reluctances of the stator back-iron. The  $d$ - $q$  axes total leakage reluctance of the stator are modelled by  $\mathcal{R}_{ald}$  and  $\mathcal{R}_{alq}$ , respectively.

### 3.3.4 Electrical Equivalent Circuits of a Hysteresis IPM Motor

A set of electrical equivalent circuits for a hysteresis IPM motor is developed based on its magnetic equivalent circuits using the duality theorem [28]. The following assumptions are considered for developing the electrical equivalent circuit of a hysteresis IPM motor,

- a. The stator is assumed to have a balanced 3 $\phi$  sinusoidally distributed winding.
- b. Only the fundamental component of the flux density  $B$  in response to the magnetizing field  $H$  is considered.
- c. The magnetic flux density is radial in the airgap, but circumferential inside the rotor hysteresis ring.
- d. The B-H curve of the hysteresis material is approximated using the elliptical modeling.
- e. The hysteresis ring is assumed to be isotropic and the permeability of the hysteresis material is assumed to be constant at its normalized saturated value.
- f. The maximum hysteresis lag angle is assumed to be between 30-70 degrees.

- g. The permanent magnet is assumed to be radially magnetized and operating within the linear limits.
- h. The excess parasitic losses due to mmf and tooth ripple harmonics are not considered.

The direct and quadrature axes ( $d$ - $q$ ) electrical equivalent circuits of a hysteresis IPM motor are depicted in Figures 3.14a and 3.14b, respectively. The permanent magnet is modeled as a constant current source  $I_m$ . Eddy current effect is included in the circuit by modeling it as an equivalent resistance  $R_e$ . Hysteresis effect is modeled as an equivalent hysteresis resistance  $R_h$ , and an equivalent hysteresis inductance  $L_{hr}$ . In the parallelogram modeling, the hysteresis resistance  $R_h$  and the hysteresis inductance  $L_{hr}$  are assumed to be constant whereas  $R_h$  and  $L_{hr}$  are sinusoidal functions of the hysteresis lag angle  $\delta$  in the elliptical modeling of the hysteresis curves [20]-[25]. The detailed derivation for finding the analytical expressions for the hysteresis resistance  $R_h$ , the hysteresis inductance  $L_{hr}$  and the  $q$ - $d$  axes airgap inductances  $L_{mq}$ ,  $L_{md}$  using the elliptical modeling are provided in the appendix. Using elliptical modeling of the hysteresis loop, these parameters can be expressed as,

$$R_h = \omega_b \frac{3K_{sw}^2 N_{sw}^2 V_h \mu}{\pi^2 r_r^2} \sin \delta \quad (3.7)$$

$$L_{hr} = \frac{3K_{sw}^2 N_{sw}^2 V_h \mu}{\pi^2 r_r^2} \cos \delta \quad (3.8)$$

$$L_m = \frac{6lr_g K_{sw}^2 N_w^2 \mu_0}{\pi p^2 l_g} \quad (3.9)$$

$$L_{mq} = k_{fq} L_m ; L_{md} = k_{fd} L_m \quad (3.10)$$

The base angular frequency is denoted by  $\omega_b$ ,  $V_h$  is the volume of the hysteresis ring,  $l$  is the axial length of the hysteresis ring,  $k_{fq}$  and  $k_{fd}$  are form factors of the armature reaction. The form factors are defined as [29],

$$k_{fq} = \frac{B_{aq1}}{B_{aq}} \quad (3.11)$$

$$k_{fd} = \frac{B_{ad1}}{B_{ad}} \quad (3.12)$$

where  $B_{aq1}$  and  $B_{ad1}$  are the fundamental components of the  $d$ - $q$  axis armature magnetic flux densities  $B_{aq}$  and  $B_{ad}$ , respectively.

The form factors for interior permanent magnet type machines can be expressed as [29],

$$k_{fq} = \frac{4}{\pi} \frac{\alpha}{1 - \alpha^2} \cos \frac{\pi}{2} \alpha \quad (3.13)$$

$$k_{fd} = \frac{1}{\pi} (\alpha\pi - \sin \alpha\pi) \quad (3.14)$$

where  $\alpha$  is equal to the ratio of the width of the pole shoe to the pole pitch. The width of the pole shoe for a permanent magnet machine is the electrical angular width of the magnet and the pole pitch is  $180^\circ$ .

Hysteresis and eddy current resistances are divided into two components. One component reflects the hysteresis loss and the eddy current loss in the rotor, modeled by  $R_e$  and  $sR_h$ , respectively. The other component contributes to the output power of the motor, combining power derived from the effective eddy current resistance and the effective hysteresis resistance. The effective eddy current and hysteresis resistances are expressed as  $((1-s)/s)R_e$  and  $(1-s)R_h$ , respectively, where  $s$  is the slip of the motor. In the

sub-synchronous mode of operation, both the loss component and the effective load component of the eddy current resistance and the hysteresis resistance exist in the rotor, and results in high  $I^2R$  losses in the rotor. At synchronous speed, the eddy current resistance and the hysteresis loss component vanish and the torque is produced by the motor due to combinations of the permanent magnet and the hysteresis effects. The total developed electromagnetic torque at synchronous speed is the summation of the magnet alignment torque, reluctance torque and the hysteresis torque. The hysteresis IPM motor can synchronize larger load torques than the conventional squirrel cage line start IPM motor because of the large hysteresis and eddy current torque.

The  $d$ - $q$  axis equations of the motor with respect to the rotor reference frame are derived from the equivalent circuits and are expressed as [19],

$$V_{qs} = R_s I_{qs} + \frac{d\lambda_{qs}}{dt} + \omega_{re} \lambda_{ds} \quad (3.15)$$

$$V_{ds} = R_s I_{ds} + \frac{d\lambda_{ds}}{dt} - \omega_{re} \lambda_{qs} \quad (3.16)$$

$$V_{qr} = 0 = R_r I_{qr} + \frac{d\lambda_{qr}}{dt} \quad (3.17)$$

$$V_{dr} = 0 = R_r I_{dr} + \frac{d\lambda_{dr}}{dt} \quad (3.18)$$

$$\lambda_{qs} = I_{qs}(L_{mq} + L_{ls}) + L_{mq}(I_{qe} + I_{qh}) \quad (3.19)$$

$$\lambda_{ds} = I_{ds}(L_{md} + L_{ls}) + L_{md}(I_{de} + I_{dh} + I_m) \quad (3.20)$$

$$\lambda'_{qr} = (I_{qe} + I_{qh})(L_{hr} + L_{mq}) + L_{mq}I_{qs} \quad (3.21)$$

$$\lambda'_{dr} = (I_{de} + I_{dh})(L_{hr} + L_{md}) + L_{md}I_{ds} + L_{md}I_m \quad (3.22)$$

$$R_r = \left( \frac{R_e}{s} \parallel R_h \right) = \frac{\frac{R_e}{s} * R_h}{\frac{R_e}{s} + R_h} = \frac{1}{\frac{1}{R_h} + \frac{s}{R_e}} \quad (3.23)$$

$$T_e = \frac{3}{2} p (\lambda_{ds} I_{qs} - \lambda_{qs} I_{ds}) \quad (3.24)$$

where  $R_s$  is the stator phase resistance,  $L_{ls}$  is the per phase stator leakage inductance,  $L_{mq}$  and  $L_{md}$  are the  $d$ - $q$  axis magnetizing inductances respectively and  $\omega_{re}$  is the electrical angular frequency of the rotor.  $V_{qs}$  and  $V_{ds}$  are the  $q$ - $d$  axes stator voltages,  $I_{qs}$  and  $I_{ds}$  are the  $q$ - $d$  axes stator currents,  $V_{qr}$  and  $V_{dr}$  are the  $q$ - $d$  axes rotor induced voltages,  $I_{qr}$  and  $I_{dr}$  are the  $q$ - $d$  axes rotor currents referred to the stator,  $\lambda_{qs}$  and  $\lambda_{ds}$  are the  $q$ - $d$  axes stator flux linkages,  $\lambda'_{qr}$  and  $\lambda'_{dr}$  are the  $q$ - $d$  axes rotor flux linkages,  $R_r$  is the total equivalent rotor resistance and  $T_e$  is the developed electromagnetic torque. The  $d$ -axis rotor current  $I_{dr}$  is the summation of the currents due to hysteresis and eddy effects which are represented by  $I_{dh}$  and  $I_{de}$ , respectively.

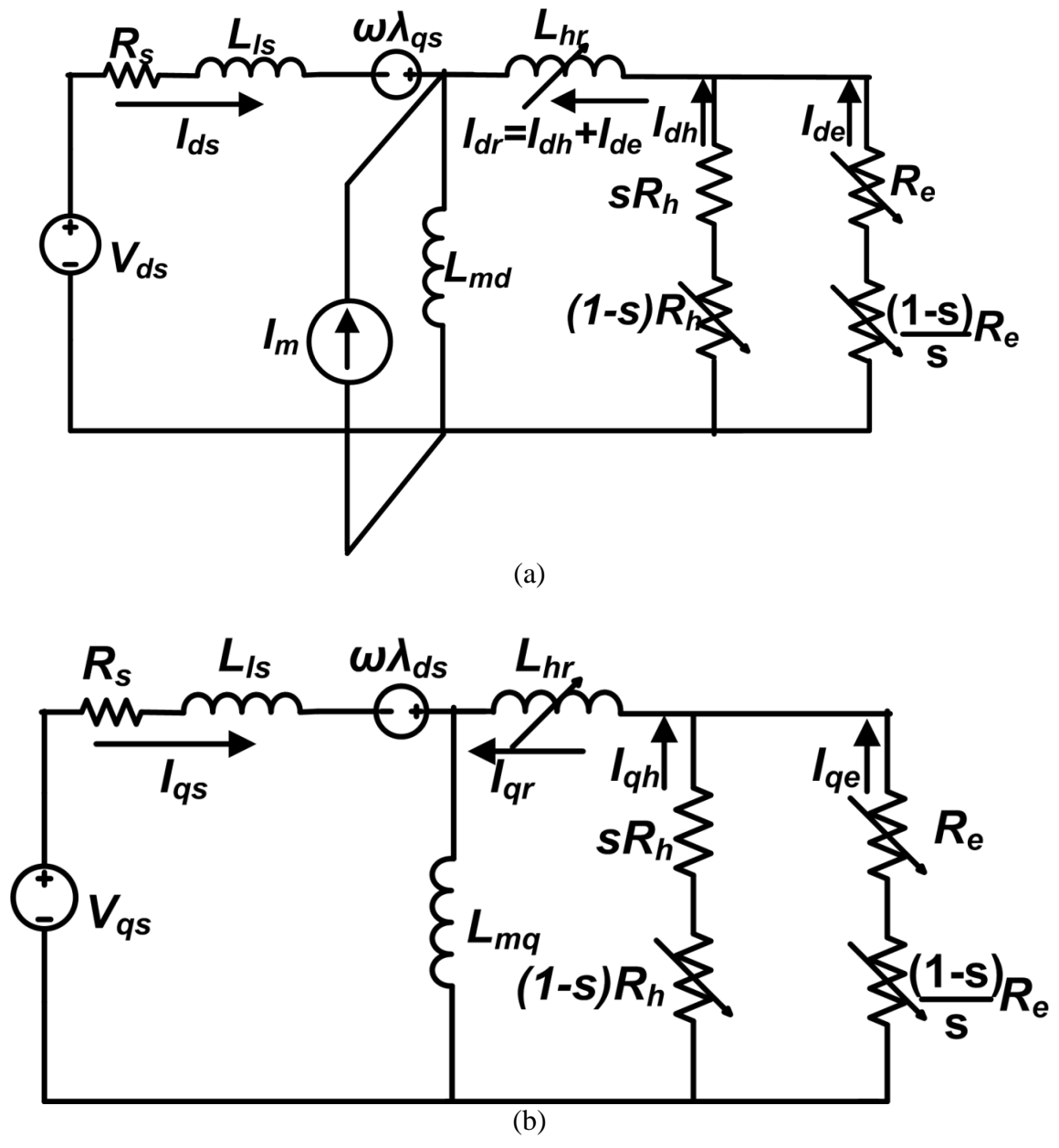


Figure 3.14. Electrical equivalent circuits: (a) *d*-axis and (b) *q*-axis.

### 3.4 Analytical Results

A 3-phase 4-pole 208V 2.50-kW hysteresis IPM motor is studied using its state space equations obtained from the electrical equivalent circuits. Matlab software is used for solving the state space equations. The run-up responses of the motor for different load torques are demonstrated in Figure 3.15. The motor is run by a 3-phase  $\Delta$ -connected 208V 60Hz balanced ac supply. The motor is able to self-start using the starting torque developed due to the presence of a hysteresis ring. The magnet brake torque is high at low speeds. This results in significant speed oscillations of the motor during start-up periods. The motor overcomes the magnet brake torque at a low speed with the help of the high hysteresis torque and eddy current torque, and runs up towards the synchronous speed. The starting time remains almost the same for different load torques, whereas the motor goes through more speed overshoots and undershoots during the synchronization process as the load torque increases.

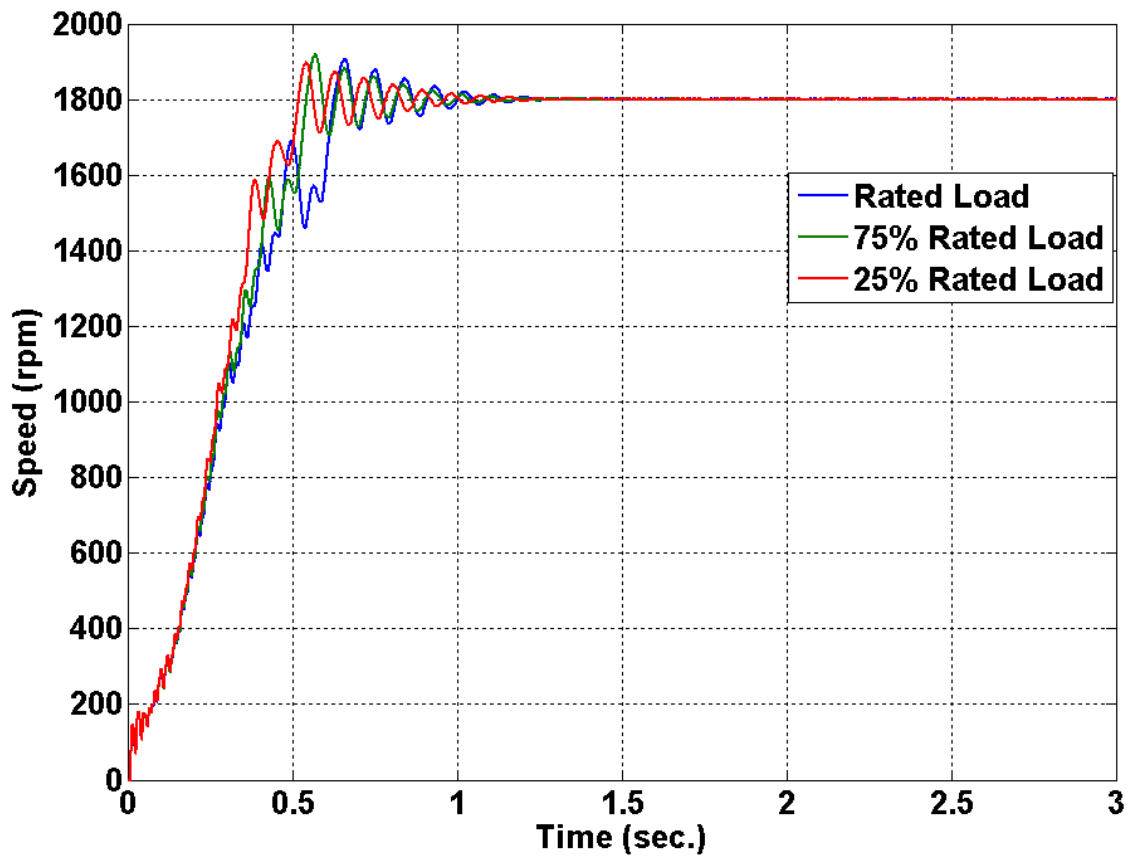


Figure 3.15. Run-up responses of a hysteresis IPM motor.

The developed instantaneous electromagnetic torque waveforms are illustrated in Figure 3.16 for different load torques. The developed torque is comprised of an average asynchronous torque and a pulsating torque. The average asynchronous torque combines the hysteresis torque, the eddy current torque and the magnet brake torque. Due to the presence of permanent magnets acting as a current source in the rotor, there is a pulsating torque superimposed on the average asynchronous torque. The pulsating torque assists the motor to a fast acceleration towards the synchronous speed. During the period of synchronization, the torque pulsation dies out and turns into a part of the synchronous torque which is a combination of the magnet alignment torque and the reluctance torque.

The eddy current torque vanishes when the slip approaches zero. The magnet brake torque reverses its role and becomes a part of the synchronous torque. The hysteresis ring behaves like a temporarily magnetized permanent magnet in the rotor and provides some additional excitation in the rotor.

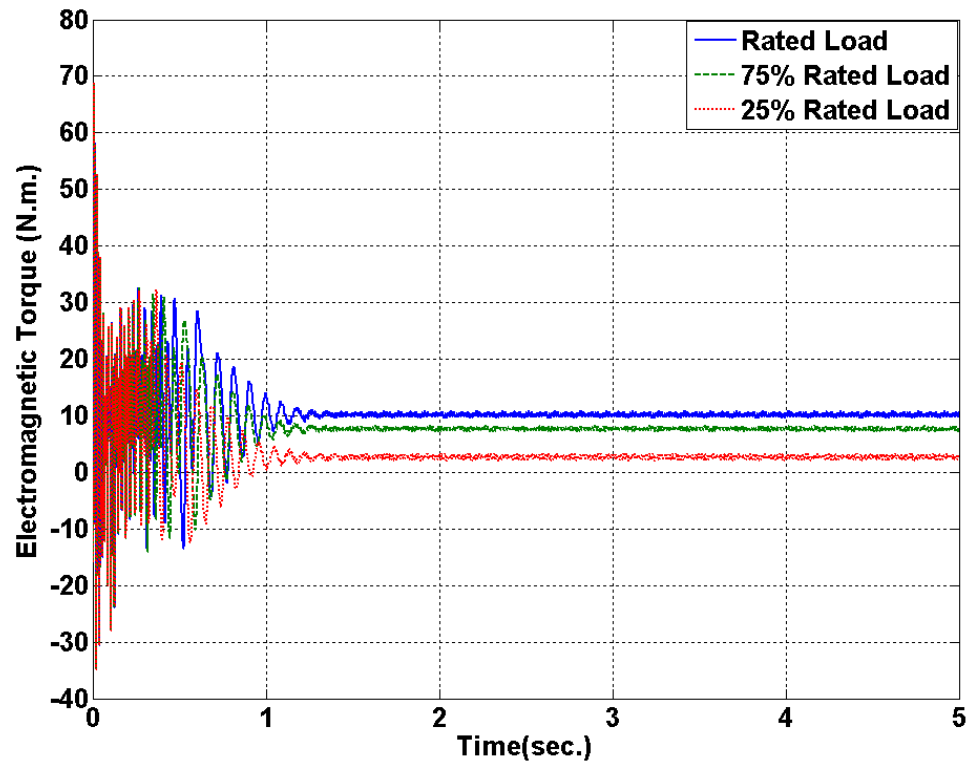


Figure 3.16. Electromagnetic torque responses of a hysteresis IPM motor.

The traces of the peak line current for different load torques are illustrated in Figure 3.17. The starting current is few times higher than the steady state current. There is significant modulation in the starting current due to speed oscillations during run-up. The magnitude of the line current goes down when the motor reaches synchronism. The motor draws more current from the line when the load torque goes up.

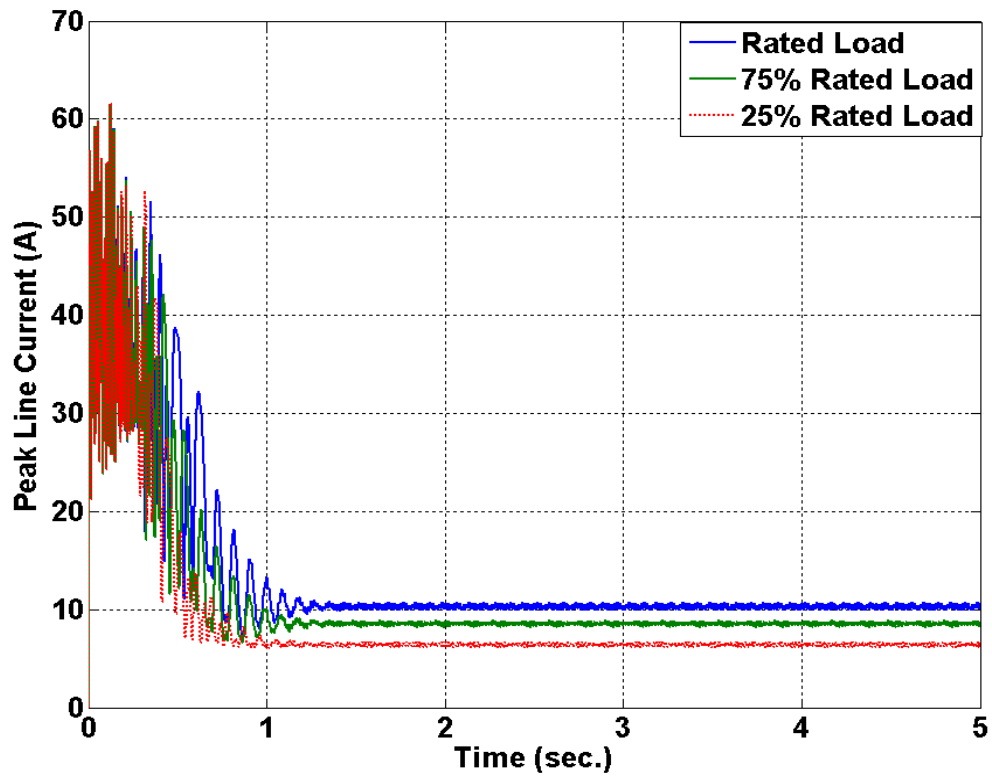


Figure 3.17. Traces of the peak line current of a hysteresis IPM motor.

The trajectories of hysteresis lag angle during the run-up process are illustrated in Figure 3.18. The motor starts with a constant hysteresis lag angle but goes through cyclic oscillations during the synchronization period before reaching a steady state value. The final value of the lag angle depends on the point of synchronization. In the case of direct on-line start, the points of synchronization sought by the motor are random. As a result, the hysteresis lag angle is randomly picked by the motor during line starting and it is limited by the maximum hysteresis lag angle of the material.

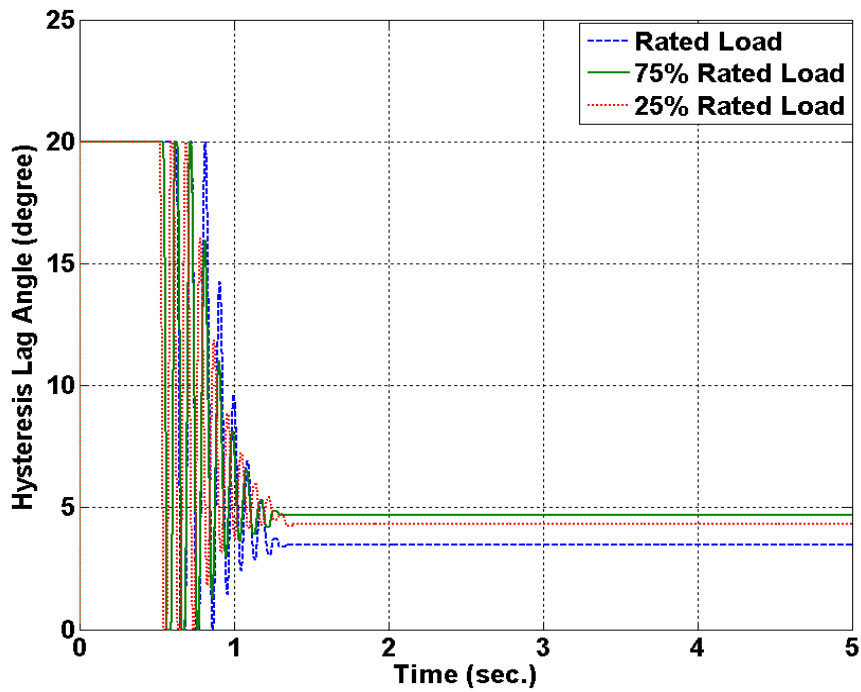


Figure 3.18. Hysteresis lag angle of a hysteresis IPM motor.

The rotor resistance for a hysteresis IPM motor is a combination of equivalent hysteresis resistance and eddy current resistance. Figure 3.19 demonstrates the oscillations in the rotor resistance during the transient period. The eddy current resistance is assumed constant in the analysis. The hysteresis resistance is a function of the hysteresis lag angle. The rotor resistance is high during start, providing a high starting torque for the rotor to accelerate. Although the rotor resistance becomes lower during the synchronization period, it provides enough torque to assist in motor stabilization.

The equivalent hysteresis inductance of the rotor is illustrated in Figure 3.20. The hysteresis inductance is high and provides enough stiffness against sudden changes in load or supply. The inductance is accountable for some additional phase shift in the line current. The inductance goes up slightly during the synchronization process.

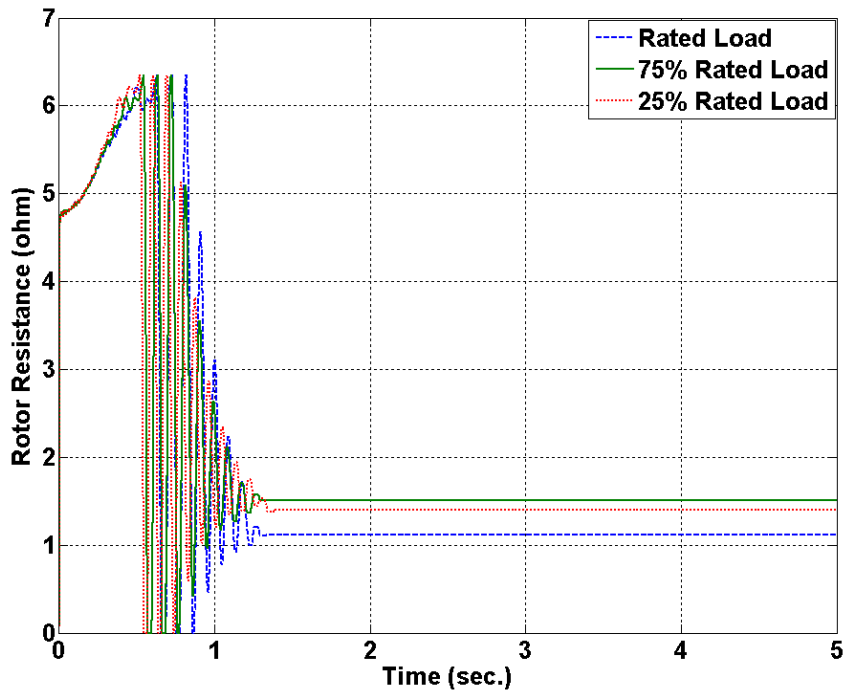


Figure 3.19. Equivalent rotor resistance of a hysteresis IPM motor.

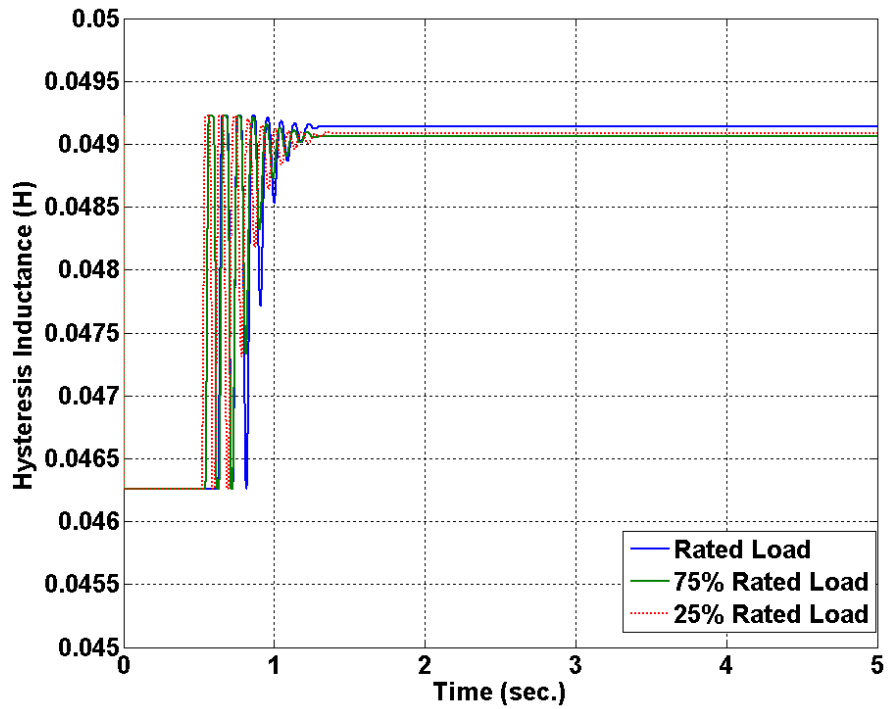


Figure 3.20. Equivalent hysteresis inductance of a hysteresis IPM motor.

### 3.5 Finite Element Analysis

Figure 3.21 depicts a 2D finite element (FE) model of the prototype hysteresis IPM motor. The FE model is developed using ANSYS Maxwell which is an electromagnetic field simulation software. The design specification of the motor is presented in table 3.2. The model is discretized into small triangular elements. All the triangles are assembled together by a mesh technique. The magnetic vector potential,  $A$  in each element is approximated using a second order quadratic polynomial. The magnetic transient solver of ANSYS Maxwell is used to analyze the magnetic fields, energy, torque, losses, speed, currents and flux of the hysteresis IPM motor model using time stepping finite element analysis. In time stepping finite element analysis, the desired vector field is computed at various time steps of a solution over a specified time period. The time dependent magnetic equation which is used by the Maxwell magnetic transient solver is given by [30],

$$\nabla \times v \nabla \times A = J_s - \sigma \nabla V + \nabla \times H_c + \sigma v \times \nabla \times A \quad (3.25)$$

where  $H_c$  is the coercivity of the permanent magnet,  $v$  is the velocity of the rotor,  $A$  is the magnetic vector potential,  $V$  is the electrical potential,  $v$  is the reluctivity,  $\sigma$  is the electrical conductivity and  $J_s$  is the source current density.

The motor excitation is set up as a balanced three phase ac voltage source and the conductors are assumed to be stranded. The 2D FE model is reduced to a quarter model based on the geometric and electrical symmetry of the motor in order to reduce the computational complexity and time. Figure 3.22 illustrates the one quarter 2D model of the hysteresis IPM motor. The boundary condition of the model is chosen as the odd

symmetry boundary which capitalizes the geometric and electrical symmetry of a model in order to reduce the computational time. In the odd symmetry boundary, the signs of the magnetic/ electric fields on one side of a symmetry plane are the opposite of those on the other side of the plane [30].

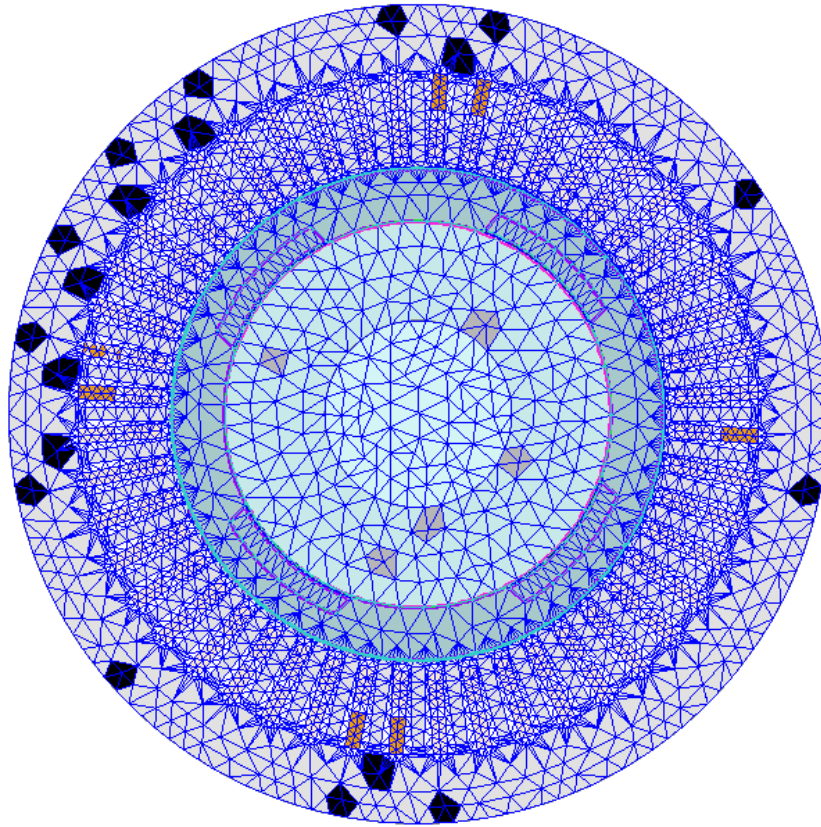


Figure 3.21. An Ansys Maxwell 2D finite element model of a hysteresis IPM motor.

In two dimensional magnetic field solutions, the vectors have only one component in the  $z$ -direction. The magnetic transient solver computes  $A_z$ : the magnetic vector potential in the  $z$ -direction. The magnetic field intensity  $H$  and the magnetic flux density  $B$  are derived from  $A_z$ .

The hysteresis loss is calculated using the advanced vector hysteresis modeling technique which calculates the magnetic field intensity in x and y directions, and also considers both rotational and alternating hysteresis losses [30].

Table 3.2. Design parameters of the hysteresis IPM motor.

Symbol	Name	Value
$m$	number of phases	3
$p$	number of pole pairs	2
$I_{rated}$	rated line current	10 A
$f_{rated}$	rated frequency	60 Hz
$P_{rated}$	rated power	2.5 kW
$T_{rated}$	rated torque	13.45 N. m
$V_{rated}$	rated voltage (L-L)	208 V
$r_{in}$	stator inner diameter	151 mm
$r_{out}$	number of stator slots	48
$N_s$	number of turns/coil	27
$N_c$	number of coils	48
$k_w$	winding factor	0.859
	winding type	double layer lap
$\tau$	stator coil pitch	1-13
$r_{out}$	rotor outer diameter	150 mm
$l$	length of the rotor ring	105 mm

$t_r$	thickness of the ring	16 mm
$g$	length of the airgap	0.5 mm
$t_m$	thickness of the PM	6.25 mm
$w$	width of the PM	40 mm
$\gamma$	angular width PM	38 deg.
$R_s$	stator resistance/phase	1.0 $\Omega$
$L_{ls}$	stator leakage inductance	0.0086 H
$\mu_r$	recoil permeability of 36% Co-Steel	18
$J$	total inertia	0.084 Kg. m <sup>2</sup>
$BH_{max}$	energy product of 36% Co-Steel	1 MGOe

---

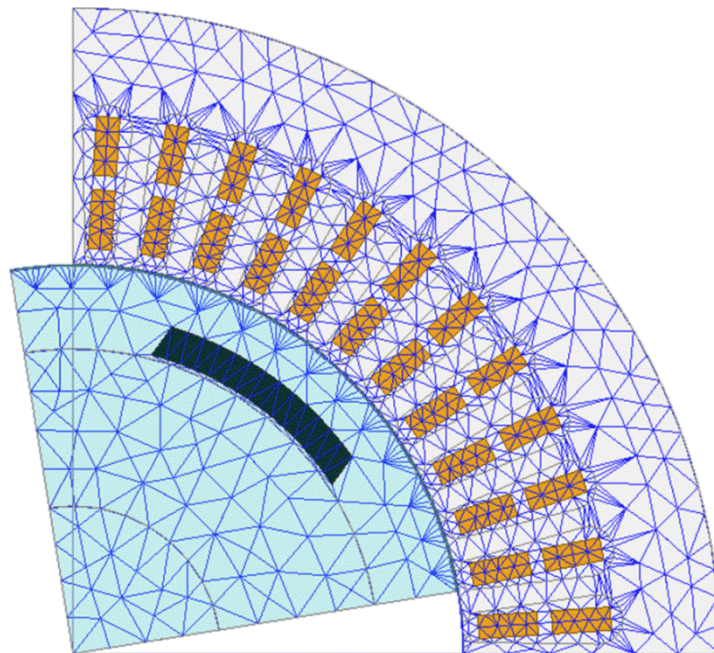


Figure 3.22. A quarter Ansys Maxwell 2D FE model.

Figure 3.23 depicts the flux density inside the motor during the transient state. The flux lines are shown in Figure 3.24. The magnetic flux lines leave the air-gap radially. Due to the presence of the hysteresis material in the ring, maximum flux lines bend inside the ring and become circumferentially distributed. Some flux lines travel through the ring radially. As a result, the flux lines are more concentrated in the region where they are circumferentially distributed. This also results in a higher magnitude of magnetic flux density in that region.

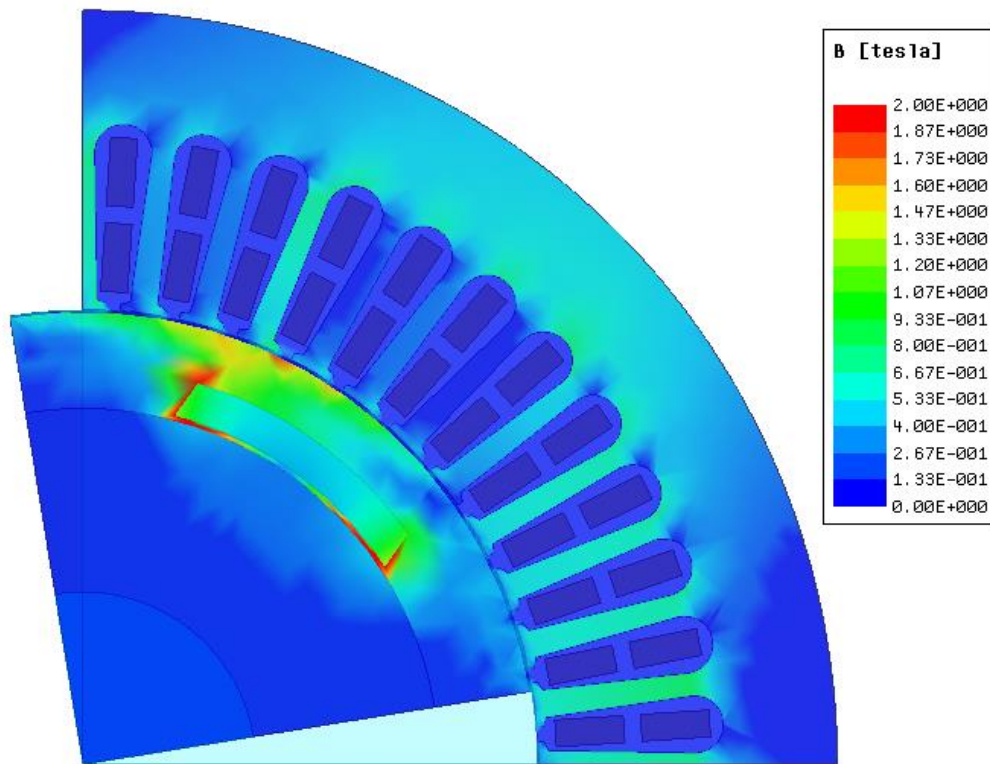


Figure 3.23. Magnetic flux density distribution in the motor.

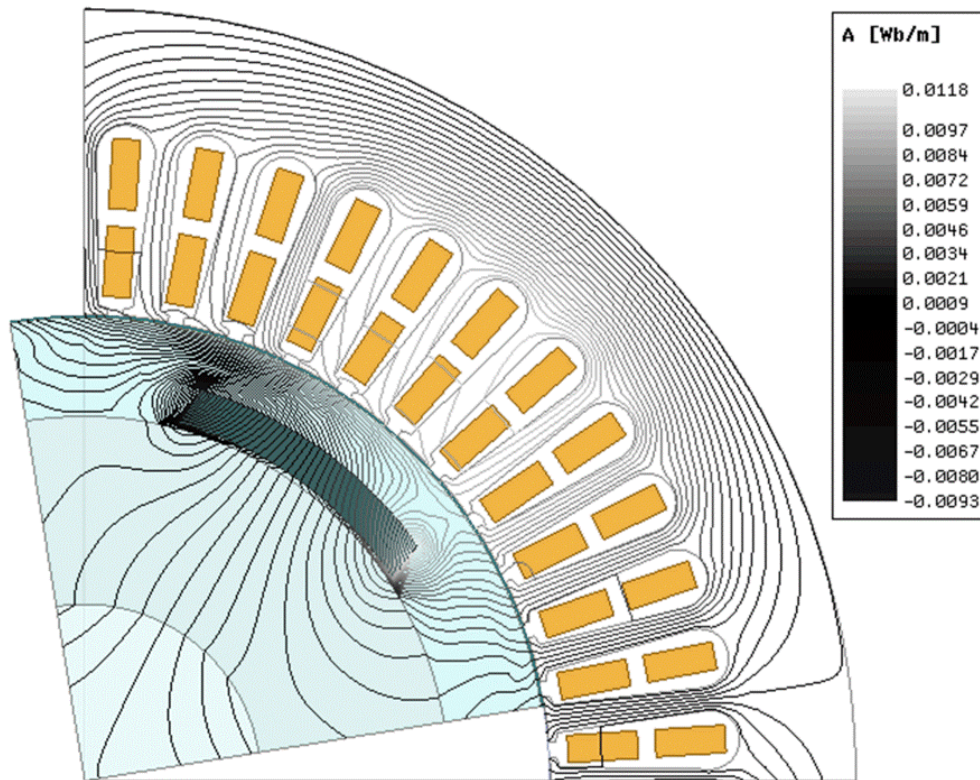
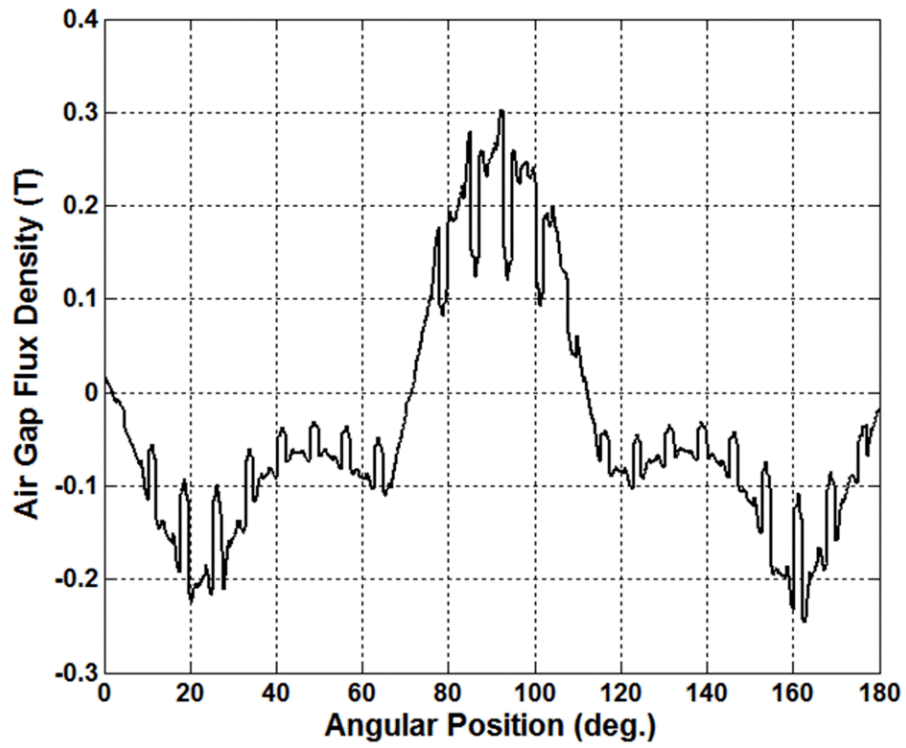
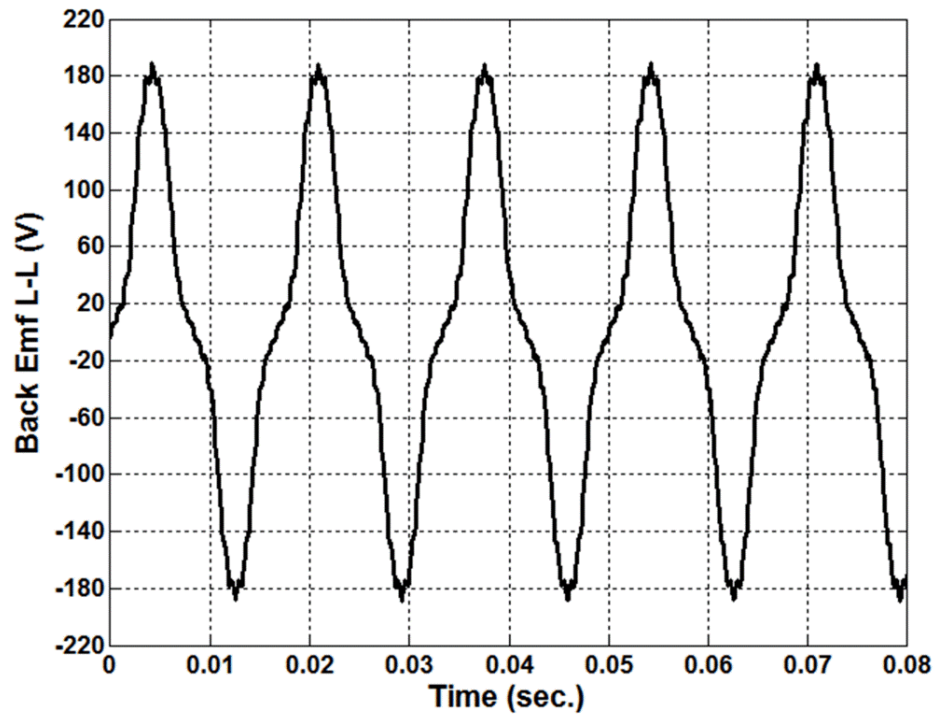


Figure 3.24. Magnetic flux lines inside the motor.

The air-gap flux density and the back-emf generated due to the magnets at rated speed are illustrated in Figures 3.25a and 3.25b, respectively. The back-emf is non-sinusoidal due to the presence of high space harmonics generated by the hysteresis ring. The high space harmonics can also be realized from the air-gap flux density.



(a)



(b)

Figure 3.25. (a) Air-gap flux density due to the magnets and (b) air-gap back-emf.

The simulated speed responses of the motor using both analytical and finite element solutions are shown in Figure 3.26. The motor is run by a 3-phase  $\Delta$ -connected 208V 60Hz balanced ac supply. The load inertia is assumed to be four times the rotor inertia. The motor is started at no-load. It starts smoothly and goes through few speed overshoots and undershoots during the synchronization process. It takes longer for the motor to synchronize than the presented analytical results in section 3.4 as the inertia is significantly higher in this case. A 5 N.m. load torque is applied at  $t = 5$  s. The response of the motor for a sudden change in the load torque is zoomed in the figure. The motor resynchronizes itself at ease with slight rotor oscillations. The hysteresis ring is providing the necessary damping torque to stabilize the rotor. It is to be noted that there is a close agreement between analytical and finite element results.

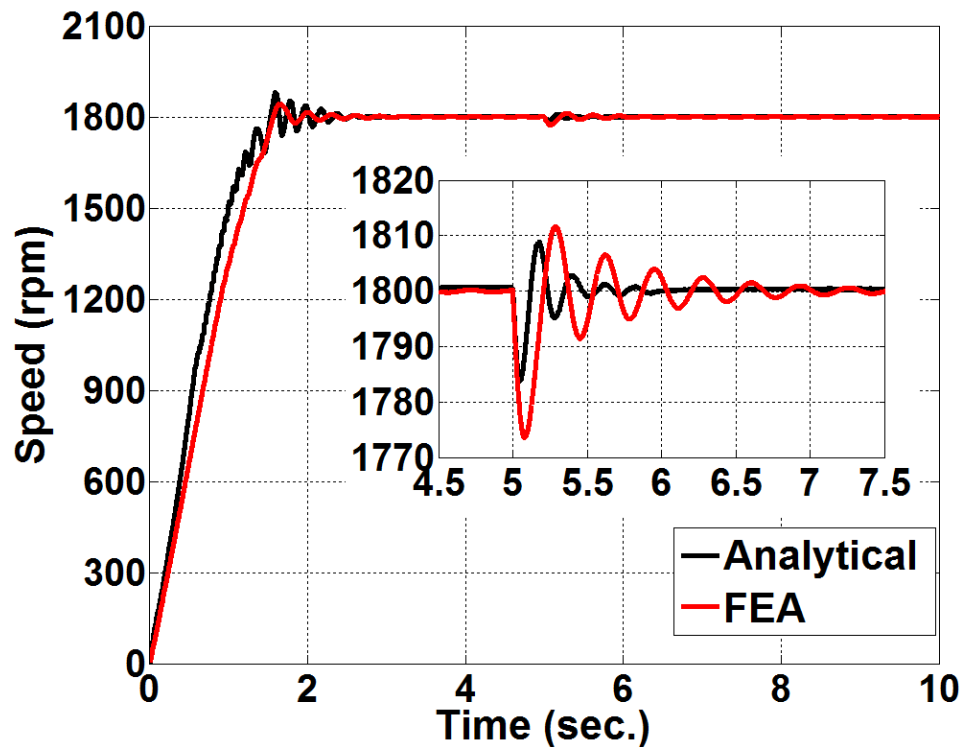


Figure 3.26. Analytical and FEA run-up responses of the motor.

The torque responses of the motor for both analytical solutions and finite element simulation are presented in Figure 3.27. The electromagnetic torque is comprised of an average asynchronous torque and a pulsating torque. The average asynchronous torque combines the hysteresis torque, the eddy current torque and the magnet brake torque. The pulsating torque assists the motor to a fast acceleration towards the synchronous speed. The torque pulsation is higher in the analytical result due to the linearized solutions of the state equations.

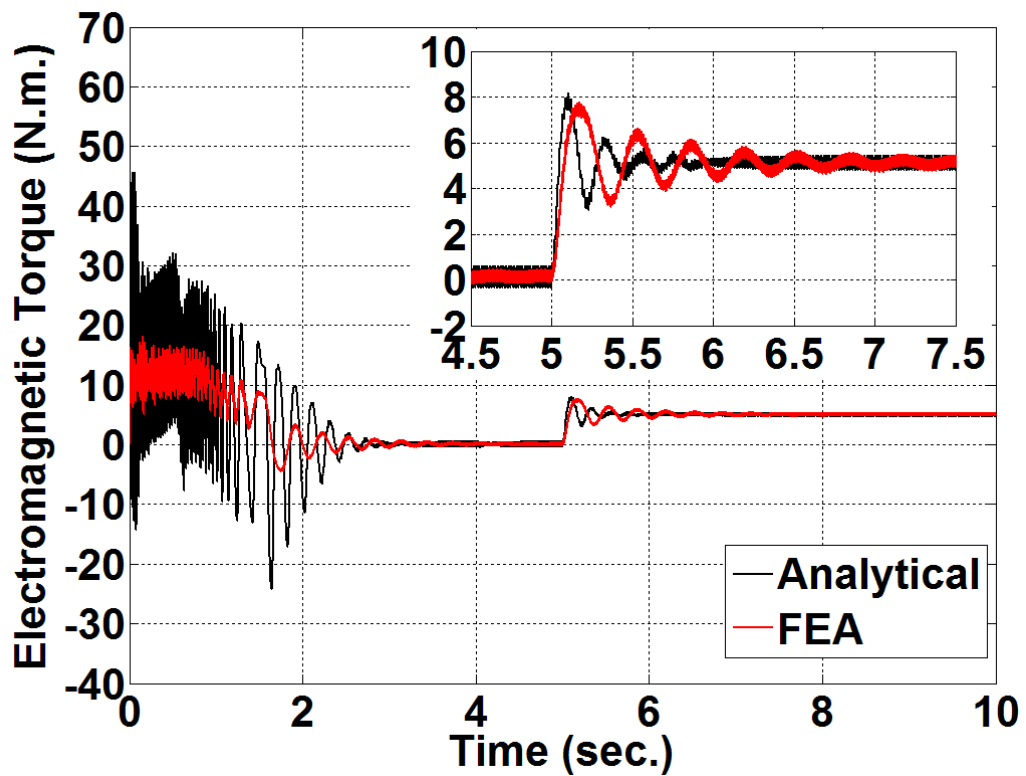


Figure 3.27. Analytical and FEA torque responses of the motor.

Figures 3.28 and 3.29 illustrate the traces of the peak line current and the core loss in the hysteresis ring, respectively. The core loss contains the hysteresis losses and the eddy current losses in the motor. The initial starting current and the initial core loss are higher in the analytical results due to the linear solver of the state equations. However, there is a close agreement between analytical and FEA results in the steady state.

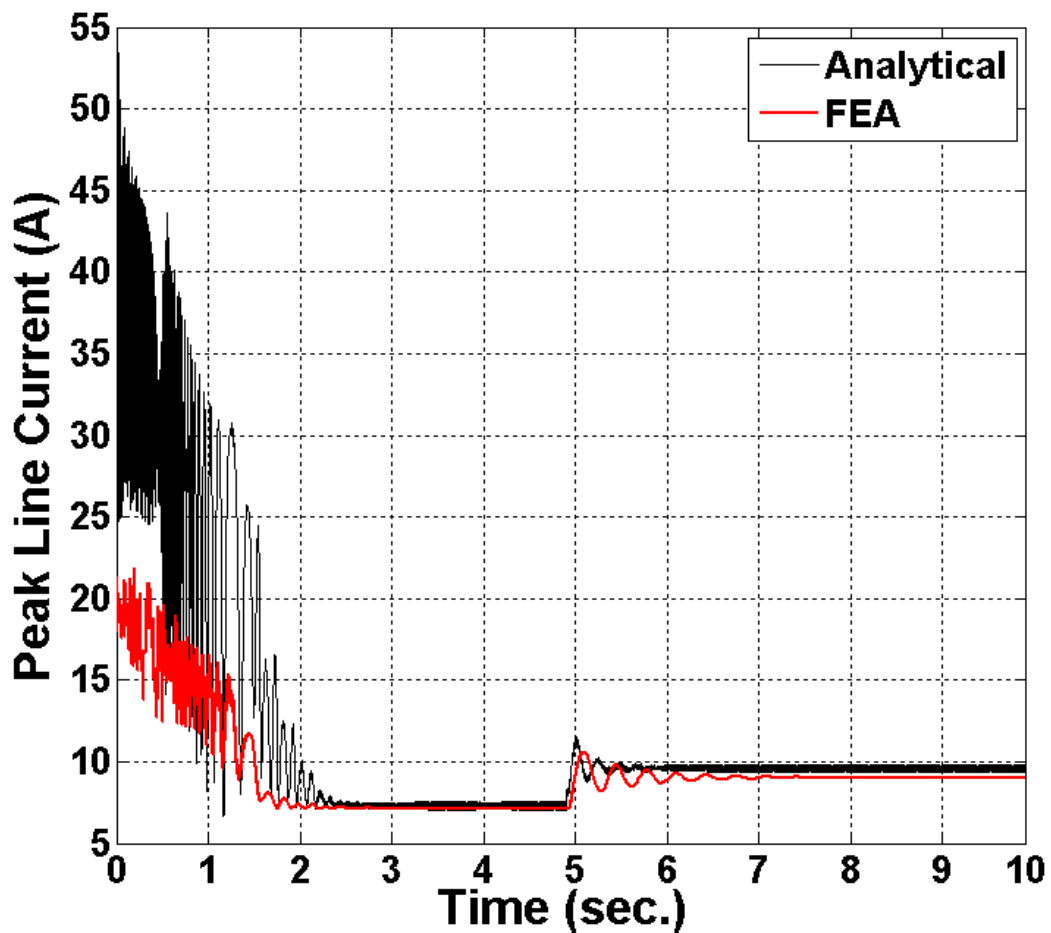


Figure 3.28. Analytical and FEA current responses of the motor.

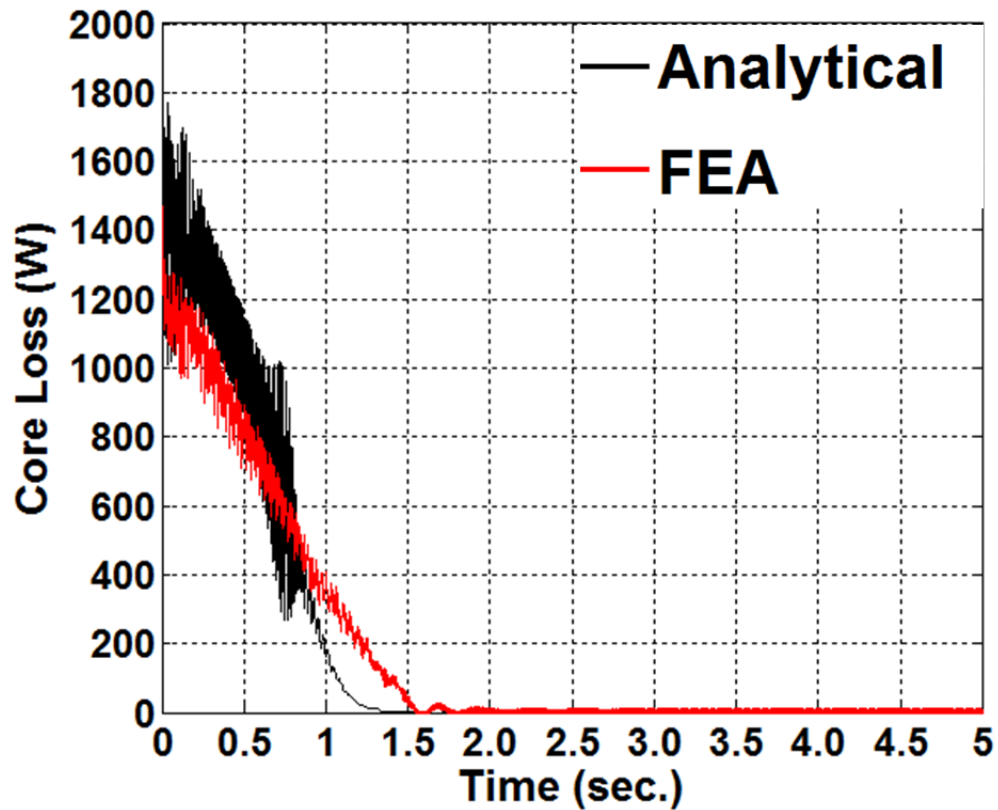


Figure 3.29. Rotor core losses of the motor.

### 3.6 Experimental Results

The 4-pole 2.5-kW laboratory prototype hysteresis IPM rotor, as illustrated in Figure 3.1, has been built and tested in a 3-phase 4-pole 208V Mawdsley generalized machine setup. The motor is started from a fixed frequency 3-phase 208V 60Hz balanced AC supply. The motor is lightly loaded by a DC generator. Figure 3.30 illustrates the analytical and experimental run-up responses of the motor. Load inertia and friction torque are included in the analytical model to match the conditions of the experimental set-up. The motor has a smooth start because of the high starting torque provided jointly by the hysteresis and eddy current torque. The motor synchronizes easily with small

overshoots and undershoots. There are few oscillations in the experimental run-up response of the motor after synchronization due to mechanical vibration.

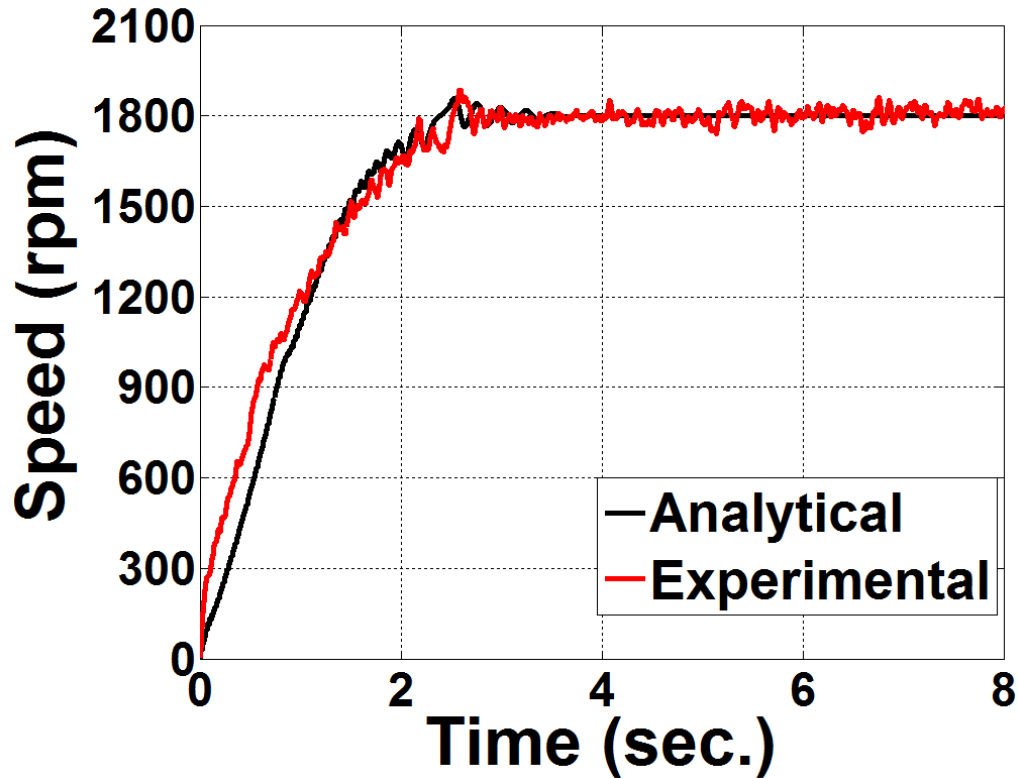


Figure 3.30. Experimental vs analytical run-up response of the motor.

Figure 3.31 shows peak values of the analytical and experimental instantaneous line currents of the motor. The steady state experimental current is slightly higher than the current obtained from the analysis because of the presence of higher harmonics. The starting current is clipped in the experimental results due to saturation effects of the current sensors. There is a reasonably close agreement between analytical, FEA and experimental results which validates the accuracy of the equivalent circuit models. The starting current is higher in simulation results due to the linearized solutions of the state

equations where the nonlinearities (such as saturation, dead zone, nonlinear friction, etc.) associated with the motor dynamics is not considered.

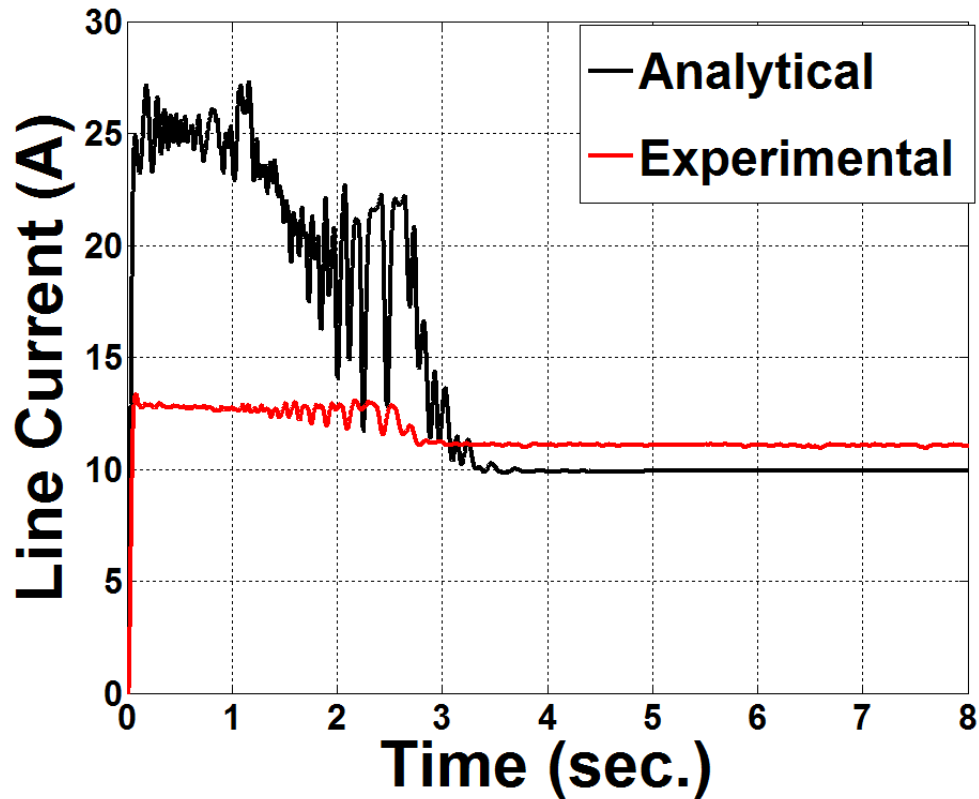


Figure 3.31. Experimental vs analytical line current of the motor.

### 3.7 Conclusions

In this chapter, basic equivalent circuit models that can be used for dynamic performance analysis of a hysteresis IPM motor drive for submersible pump loads are provided. The proposed analytical model is validated with finite element analysis and experimental investigations. The developed model can predict transients of the motor with a reasonably good accuracy. However, due to experimental limitations, the proposed

model is not fully validated for other motor states such electro-magnetic torque, space harmonics etc.

This chapter investigates circumferential flux type hysteresis IPM motors. In the following chapter, the design of a new radial flux type hysteresis IPM motor for self-starting a high inertial pump load is presented.

## Appendix

### Equivalent Circuit Derivation of a Circumferential Flux Hysteresis Motor

#### A.1 Derivation of the Apparent Currents of a Circumferential Flux Hysteresis Motor

Figure 3.32 displays the closed magnetic path inside a circumferential flux hysteresis motor. Using Ampere's law in the closed magnetic path, the following governing equation can be obtained [25]:

$$\mathcal{F}_a d\psi = -(H_g + dH_g)l_g + H_g l_g + H r_h \frac{d\psi}{p} \quad (3.25)$$

where  $\mathcal{F}_a$  is the armature mmf,  $H_g$  is the magnetic field intensity in the airgap,  $l_g$  is the length of the airgap and  $r_h$  is the mean radius of the hysteresis ring.

The armature mmf can be obtained using (3.25), and is expressed as,

$$\mathcal{F}_a = l_g \frac{\partial H_g}{\partial \psi} + H \frac{r_h}{p} \quad (3.26)$$



$$t_r((B + dB))dr - t_r B dr = -B_g r_g \left( \frac{d\psi}{p} \right) dr \quad (3.28)$$

Simplifying (3.28), the airgap flux can be expressed as,

$$B_g = -\frac{pt_r}{r_g} \frac{\partial B}{\partial \psi} \quad (3.29)$$

The airgap magnetic field intensity is given below,

$$H_g = \frac{B_g}{\mu_0} \quad (3.30)$$

Using (3.1)-(3.3), the airgap flux density can be expressed as a function of the flux density inside the hysteresis ring:

$$B_g = -\frac{pt_r}{r_g} B_m \sin(\omega t - \psi - \varphi_0) \quad (3.31)$$

$$\frac{\partial H_g}{\partial \psi} = \frac{pt_r}{r_g \mu_0} B_m \cos(\omega t - \psi - \varphi_0) \quad (3.32)$$

Using (3.31)-(3.32),  $\mathcal{F}_a$  can be expressed as,

$$\mathcal{F}_a = \frac{B_m l_g p t_r}{r_g \mu_0} \cos(\omega t - \psi - \varphi_0) + \frac{B_m r_h}{p \mu} \cos(\omega t - \psi - \varphi_0 + \delta) \quad (3.33)$$

For a balanced 3-phase ac supply, the stator current in phase  $k$  is provided below:

$$I_k = I_m \cos(\omega t - \psi_k) \quad (3.34)$$

The rotating magnetic field in the airgap produced by the 3-phase currents can be expressed as [25],

$$\mathcal{F}_a = \frac{3}{2} F_{max} \cos(\omega t - \psi) \quad (3.35)$$

where,

$$F_{max} = \frac{2}{\pi p} K_w N_w I_m \quad (3.36)$$

Substituting (3.36) into (3.35), the expression for armature mmf becomes,

$$\mathcal{F}_a = \frac{3}{\pi p} K_w N_w I_m \cos(\omega t - \psi) \quad (3.37)$$

Equating (3.33) and (3.37), one gets the following expression,

$$\begin{aligned} & \frac{3}{\pi p} K_w N_w I_m \cos(\omega t - \psi) \\ &= \frac{B_m l_g p t_r}{r_g \mu_0} \cos(\omega t - \psi - \varphi_0) + \frac{B_m r_h}{p \mu} \cos(\omega t - \psi - \varphi_0 + \delta) \end{aligned} \quad (3.38)$$

Multiplying both sides of (3.38) by  $j$  and adding  $\frac{\pi}{2}$  to  $\psi$ , one gets the following expression,

$$\begin{aligned} & j \frac{3}{\pi p} K_w N_w I_m \sin(\omega t - \psi) \\ &= j \frac{B_m l_g p t_r}{r_g \mu_0} \sin(\omega t - \psi - \varphi_0) + j \frac{B_m r_h}{p \mu} \sin(\omega t - \psi - \varphi_0 + \delta) \end{aligned} \quad (3.39)$$

Converting (3.39) from polar form into exponential form, one can get,

$$\frac{3}{\pi p} K_w N_w I_m e^{j(\omega t - \psi)} = \frac{B_m l_g p t_r}{r_g \mu_0} e^{j(\omega t - \psi - \varphi_0)} + \frac{B_m r_h}{p \mu} e^{j(\omega t - \psi - \varphi_0 + \delta)} \quad (3.40)$$

Or,

$$B_m e^{j(\omega t - \psi - \varphi_0)} \left( \frac{l_g p t_r}{r_g \mu_0} + \frac{r_h e^{j\delta}}{p \mu} \right) = \frac{3}{\pi p} K_w N_w I_m e^{j(\omega t - \psi)} \quad (3.41)$$

Or,

$$B_m = \frac{3 K_w N_w I_m}{\pi p \left( \frac{l_g p t_r}{r_g \mu_0} + \frac{r_h e^{j\delta}}{p \mu} \right)} e^{j\varphi_0} \quad (3.42)$$

Or,

$$B_m = \frac{3K_w N_w I_m}{\left(\frac{\pi p^2 l_g t_r}{r_g \mu_0} + \frac{\pi r_h e^{j\delta}}{\mu}\right)} e^{j\varphi_0} \quad (3.43)$$

Equation (3.43) can be simplified as,

$$B_m = \frac{\kappa}{\alpha + j\beta} [\cos \varphi_0 + j \sin \varphi_0] \quad (3.44)$$

Where,

$$\alpha = \mu \pi p^2 l_g t_r + \pi r_h r_g \mu_0 \cos \delta \quad (3.45)$$

$$\beta = \pi r_h r_g \mu_0 \sin \delta \quad (3.46)$$

$$\kappa = 3K_w N_w I_m r_g \mu_0 \mu \quad (3.47)$$

Simplifying (3.44), one can get,

$$B_m = \frac{\kappa(\alpha + j\beta)}{(\alpha^2 + \beta^2)} [\cos \varphi_0 + j \sin \varphi_0] \quad (3.48)$$

Or,

$$B_m = \left[ \frac{\kappa\alpha}{(\alpha^2 + \beta^2)} \cos \varphi_0 - \frac{\kappa\beta}{(\alpha^2 + \beta^2)} \sin \varphi_0 \right] \\ + j \left[ \frac{\kappa\alpha}{(\alpha^2 + \beta^2)} \sin \varphi_0 + \frac{\kappa\beta}{(\alpha^2 + \beta^2)} \cos \varphi_0 \right] \quad (3.49)$$

As  $B_m$  is a real number,  $\mathbf{Im}(B_m)$  is zero. Equating  $\mathbf{Im}(B_m) = 0$ , one can get,

$$\frac{\kappa\alpha}{(\alpha^2 + \beta^2)} \sin \varphi_0 + \frac{\kappa\beta}{(\alpha^2 + \beta^2)} \cos \varphi_0 = 0 \quad (3.50)$$

Or,

$$\tan \varphi_0 = \frac{\beta}{\alpha} \quad (3.51)$$

Substituting  $\alpha$  and  $\beta$  into (3.51), the phase shift can be calculated as,

$$\varphi_0 = \tan^{-1} \frac{\pi r_h r_g \mu_0 \sin \delta}{\mu \pi p^2 l_g t_r + \pi r_h r_g \mu_0 \cos \delta} \quad (3.52)$$

The complex stator phase- $k$  current can be expressed in the exponential form as follows,

$$\mathbf{I}_k = I_m e^{j(\omega t - \psi_k)} \quad (3.53)$$

The stator current can be divided into airgap current  $\mathbf{I}_{gk}$  and rotor current  $\mathbf{I}_{rk}$  as depicted in the equivalent circuit of the motor [25]. Thus,

$$\mathbf{I}_k = \mathbf{I}_{gk} + \mathbf{I}_{rk} \quad (3.54)$$

Or,

$$I_m e^{j(\omega t - \psi_k)} = I_{gm} e^{j(\omega t - \psi_k - \varphi_0)} + I_{rm} e^{j(\omega t - \psi_k - \varphi_0 + \delta)} \quad (3.55)$$

Equating (3.40) and (3.55), the apparent airgap and rotor currents can be formulated as,

$$\mathbf{I}_{gk} = \frac{l_g p t_r \pi p}{3 K_w N_w r_g \mu_0} B_m e^{j(\omega t - \psi_k - \varphi_0)} \quad (3.56)$$

$$\mathbf{I}_{rk} = \frac{\pi r_h p}{3 K_w N_w p \mu} B_m e^{j(\omega t - \psi_k - \varphi_0 + \delta)} \quad (3.57)$$

## A.2 Derivation of the Induced EMF

The per phase emf induced in the  $k^{\text{th}}$  stator winding can be calculated using the Lorentz force. Using Lorentz force, the induced motional emf can be obtained using the following equation [25]:

$$e_k = \oint \mathbf{F} \cdot d\mathbf{l} = \oint (\mathbf{v} \times \mathbf{B}) \cdot d\mathbf{l} \quad (3.58)$$

Assuming sinusoidally distributed stator windings, the conductor density for the  $k^{\text{th}}$  phase stator windings can be formulated as [25],

$$W_k = \frac{2K_w N_w}{p\pi} \cos(\psi - \psi_k) \quad (3.59)$$

The induced emf in the airgap of the motor can be expressed as,

$$e_k = - \int_0^{2p\pi} \frac{\omega r_g}{p} \mathbf{B}_g l W_k d\psi \quad (3.60)$$

Substituting (3.59) into (3.60), one gets,

$$e_k = - \int_0^{2p\pi} \mathbf{B}_g \frac{\omega l r_g}{p} \frac{2K_w N_w}{p\pi} \cos(\psi - \psi_k) d\psi \quad (3.61)$$

The airgap flux density in (3.31) can be expressed in the following complex form,

$$\mathbf{B}_g = j \frac{p t_r}{r_g} B_m e^{j(\omega t - \psi - \varphi_0)} \quad (3.62)$$

Using (3.61) and (3.62), the induced emf can be expressed as,

$$e_k = -j \frac{1}{2} \int_0^{2p\pi} B_m \frac{2K_w N_w \omega l t_r}{p\pi} [e^{j(\psi - \psi_k)} + e^{-j(\psi - \psi_k)}] e^{j(\omega t - \psi - \varphi_0)} d\psi \quad (3.63)$$

Or,

$$e_k = -j B_m \frac{K_w N_w \omega l t_r}{p\pi} \int_0^{2p\pi} [e^{j(\omega t - \psi_k - \varphi_0)} + e^{j(\omega t - 2\psi + \psi_k + \varphi_0)}] d\psi \quad (3.64)$$

Integrating (3.64), one can get,

$$e_k = -j B_m \frac{K_w N_w \omega l t_r}{p\pi} e^{j(\omega t - \psi_k - \varphi_0)} (2p\pi - 0) + 0 \quad (3.65)$$

Simplifying (3.65),

$$e_k = -j 2 B_m K_w N_w \omega l t_r e^{j(\omega t - \psi_k - \varphi_0)} \quad (3.66)$$

### A.3 Calculation of Circuit Parameters

The equivalent circuit parameters of a circumferential flux hysteresis motor can be calculated using the apparent currents and induced emfs [25]. The airgap impedance is calculated using (3.56) and (3.57), and is expressed below,

$$\mathbf{Z}_m = \frac{-\mathbf{e}_k}{\mathbf{I}_{gk}} \quad (3.67)$$

Or,

$$\mathbf{Z}_m = \frac{j2B_m K_w N_w \omega l t_r e^{j(\omega t - \psi_k - \varphi_0)}}{\frac{l_g p t_r \pi p}{3K_w N_w r_g \mu_0} B_m e^{j(\omega t - \psi_k - \varphi_0)}} \quad (3.68)$$

Or,

$$\mathbf{Z}_m = j\omega \frac{6l r_g K_w^2 N_w^2 \mu_0}{\pi p^2 l_g} \quad (3.69)$$

The airgap inductance is,

$$L_m = \frac{6l r_g K_w^2 N_w^2 \mu_0}{\pi p^2 l_g} \quad (3.70)$$

Using (3.57) and (3.66), the equivalent hysteresis impedance can be calculated as,

$$\mathbf{Z}_{hr} = \frac{-\mathbf{e}_k}{\mathbf{I}_{rk}} \quad (3.71)$$

Or,

$$\mathbf{Z}_{hr} = \frac{j2B_m K_w N_w \omega l t_r e^{j(\omega t - \psi_k - \varphi_0)}}{\frac{\pi r_h p}{3K_w N_w p \mu} B_m e^{j(\omega t - \psi_k - \varphi_0 + \delta)}} \quad (3.72)$$

Simplifying (3.72), one gets,

$$\mathbf{Z}_{hr} = j\omega \frac{6K_w^2 N_w^2 l t_r \mu}{\pi r_h} (\cos \delta - j \sin \delta) \quad (3.73)$$

The equivalent hysteresis impedance can be divided into equivalent hysteresis resistance and hysteresis inductance as follows,

$$\mathbf{Z}_{hr} = R_{hr} + j\omega L_{hr} \quad (3.74)$$

Equating (3.73) and (3.74),

$$R_{hr} = \frac{6\omega K_w^2 N_w^2 l_t r \mu}{\pi r_h} \sin \delta \quad (3.75)$$

$$L_{hr} = \frac{6K_w^2 N_w^2 l_t r \mu}{\pi r_h} \cos \delta \quad (3.76)$$

The volume of the hysteresis ring can be calculated from the following expression,

$$V_h = 2\pi r_h l_t r \quad (3.77)$$

Substituting (3.77) into (3.76) and (3.75), the equivalent hysteresis resistance and inductance can be expressed as,

$$R_{hr} = \omega_b \frac{3K_w^2 N_w^2 V_h \mu}{\pi^2 r_h^2} \sin \delta \quad (3.78)$$

$$L_{hr} = \frac{3K_{sw}^2 N_{sw}^2 V_h \mu}{\pi^2 r_r^2} \cos \delta \quad (3.79)$$

## References

1. M. A. Rahman and R. Qin., "Starting and synchronization of permanent magnet hysteresis motors", *IEEE Transactions on Industry Applications*, Vol. 32, No. 5, pp. 1183-1189, September 1996.
2. M. A. Rahman, "Combination Hysteresis, Reluctance and Permanent Magnet Motor", U.S. Patent No. 5, 187, 401; Date of Issue, February 16, 1993.
3. M. A. Rahman and R. Qin, "A permanent magnet hysteresis hybrid synchronous motor for electric vehicles", *IEEE Transactions on Industrial Electronics*, Vol. 44, No. 1, pp. 46–53, February 1997.

4. J. Qian and M. A. Rahman, "Analysis of field oriented control for permanent magnet hysteresis synchronous motors", *IEEE Transactions on Industry Applications*, Vol. 29, No. 6, pp. 1156-1163, November 1993.
5. A. M. Osheiba, J. Qian, and M. A. Rahman, "Performance of hysteresis permanent magnet motors", *Electric Machines and Power Systems*, vol. 16, no.4, pp. 265–280, May 1989.
6. R. Qin and M. A. Rahman, "Magnetic equivalent circuit of PM hysteresis synchronous motor", *IEEE Transactions on Magnetics*, Vol. 39, No. 5, pp. 2998 – 3000, September 2003.
7. K. Kurihara and M. A. Rahman, "Transient performance analysis for permanent-magnet hysteresis synchronous motor," *IEEE Transactions on Industry Applications*, Vol. 40, No. 1, pp. 135–142, January 2004.
8. M. Jagiela, T. Garbiec and M. Kowol, "Design of high-speed hybrid hysteresis motor rotor using finite element model and decision process", *IEEE Transactions on Magnetics*, vol. 50, no.2, pp. 861-864, February 2014.
9. R. Nasiri-Zarandi, M. Mirsalim and Alberto Tenconi, "A novel hybrid hysteresis motor with combined radial and axial flux rotors", *IEEE Transactions on Industrial Electronics*, vol. 63, no.3, pp. 1684-1693, March 2016.
10. G. Friedman, "Generalization of the vector Preisach hysteresis model", *Journal of Applied Physics*, Vol. 69, No. 8, pp. 4832-4834, April 1991.
11. D. C. Jiles and D. L. Atherton, "Theory of ferromagnetic hysteresis", *Journal of Magnetism and Magnetic Materials*, Vol. 55, No. 1-2, pp. 48-60, September 1986.
12. R. Du and P. Robertson, "Dynamic Jiles-Atherton model for determining the magnetic power loss at high frequency in permanent magnet machines", *IEEE Transactions on Magnetics*, Vol. 51, No. 6, pp. 1-10, June 2015.
13. H. Hauser, "Energetic model of ferromagnetic hysteresis: Isotropic magnetization", *Journal of Applied Physics*, Vol. 97, pp. 099901-1, 2005.
14. R. Grössinger, H. Hauser, L. Stoleriu and P. Andrei, "Hysteresis modeling of anisotropic Barium Ferrite", *IEEE Transactions on Magnetics*, Vol. 36, No. 5, pp. 3357-3359, September 2000.

15. H. Hauser, Y. Melikhov and D. C. Jiles, "Examination of the equivalence of ferromagnetic hysteresis models describing the dependence of magnetization on magnetic field and stress", *IEEE Transactions on Magnetics*, Vol. 45, No. 4, pp. 1940-1949, April 2009.
16. M. A. Copeland and G. R. Slemon, "An analysis of the hysteresis motor II-the circumferential-flux machine", *IEEE Transactions on Power Apparatus and Systems*, Vol. 83, No. 6, pp. 619-625, June 1964.
17. M. A. Rahman, M. A. Copeland and G. R. Slemon, "An Analysis of the Hysteresis Motor Part III: Parasitic Losses", *IEEE Transactions on Power Apparatus and Systems*, Vol. PAS-88, No. 6, pp. 954 - 961, June 1969.
18. M. A. Rahman and A. M. Osheiba, "Dynamic performance prediction of polyphase hysteresis motors", *IEEE Transactions on Industry Applications*, Vol. 26, No. 6, pp. 1026-10333, Nov. 1990.
19. M. A. Rahman, "Analytical models of polyphase hysteresis motors", *IEEE Transactions on Power Apparatus and Systems*, Vol. PAS-92, No. 1, pp. 237-242, January 1973.
20. L. Cao and G. Li, "Complete parallelogram hysteresis model for electric machines", *IEEE Transactions on Energy Conversion*, Vol. 25, No. 3, pp. 626-632, September 2010.
21. D. O'Kelly, "Eddy-current and hysteresis effects in rotating machines", *Proceedings of the IEE*, Vol. 116, No. 3, pp. 391-394, March 1969.
22. S. Miyairi and T. Kataoka, "A basic equivalent circuit of the hysteresis motor", *IEE Transactions of Japan*, Vol. 85, pp. 41-50, October 1965.
23. S. Miyairi and T. Kataoka, "Analysis of hysteresis motors considering eddy current effects", *IEE Transactions of Japan*, Vol. 85, pp. 67-77, June 1966.
24. T. Ishikawa and T. Kataoka, "Basic analysis of disc-type hysteresis motors," *Journal of Electrical Engineering Japan*, Vol. 101, No. 6, pp. 659-666, November 1981.

25. J. J. Nitao, E. T. Scharlemann and B. A. Kirkendall, "Equivalent circuit modeling of hysteresis motors", Lawrence Livermore National Laboratory, Livermore, CA, Tech. Rep. LLNL-TR-416493, July 2009.
26. P. Zhou, D. Lin, Y. Xiao, N. Lambert and M. A. Rahman, "Temperature dependent demagnetization model of permanent magnets for finite element Analysis", *IEEE Transactions on Magnetics*, Vol.48, No.2, pp. 1031-1034, February 2012.
27. G. R. Slemon, *Electric Machines and Drives*, Reading, MA: Addison-Wesley Publishing Company, 1992.
28. E. Colin Cherry, "The duality between interlinked electric and magnetic circuits and the formation of transformer equivalent circuits", in *Proceedings of the Physical Society of London*, ,Vol. 62, No. 2, pp. 101-111, February 1949.
29. J. F. Gieras, et. al., "Calculation of synchronous reactances of small permanent-magnet alternating-current motors: comparison of analytical approach and finite element method with measurements", *IEEE Transactions on Magnetics*, Vol. 34, No. 5, pp. 3712-3720, November 1998.
30. Maxwell Online Help: Release v15.0 (December 2013), ANSYS, Inc., [Online], Available: [http: www.ansys.com](http://www.ansys.com).

## Chapter 4

### Radial Flux Hysteresis IPM Motor

#### 4.1 Introduction

Hysteresis motors are widely used in gyroscopes, centrifuges, tape recorders, clocks and some other applications for their smooth self-starting capability and simple rotor construction. A hysteresis motor can start with any load that it can carry to the synchronous speed, irrespective of the load inertia [1]-[4]. It has almost flat torque vs. speed trajectories, constant synchronizing torque, nearly constant power factor and smooth starting with low noise [1]-[4]. Although the hysteresis motor has a good self-starting capability, it suffers from some limitations such as high magnetizing current, low power factor, high parasitic losses and low efficiency [5].

In recent years, the design of interior permanent magnet (IPM) motors capable of starting and synchronization from a fixed frequency balanced ac supply has been a topic of interest among the researchers [6]-[9]. Traditional designs of self-starting IPM motors are induction-start synchronous motors containing cage windings in the rotor. The cage windings provide the starting torque, and act as a damper during steady state. Permanent magnets are buried underneath the cage inside the rotor, providing the excitation for synchronous operation at steady-state. Although the cage torque is high during start to accelerate the rotor, it becomes lower during the synchronization process when the slip becomes small. The cage torque eventually becomes zero at the point of synchronization. Thus, existing cage-equipped IPM motors have limited starting and synchronization

capabilities, especially for high inertial loads. Some researchers have focused on the improvement of the starting characteristics by either changing the design of cage windings or the structure of the rotor [6]-[7]. Few researchers have concentrated on the enhanced steady state performances by varying the orientation of magnets inside the rotor [6]-[9]. Hysteresis and hybrid hysteresis motors have been proposed as self-start synchronous motors in the literature [10]-[14]. However, the existing literature has mainly focused on the use of circumferential flux (CF) type hysteresis motors in order to increase the effective area of the hysteresis material, maximizing the available hysteresis energy in the motor [10]-[11]. Wakui et.al. has proposed designs of radial flux (RF) isotropic and anisotropic hysteresis motors for improving the output torque and efficiency of conventional hysteresis motors [12]-[13]. Although, their RF-hysteresis motor designs provide higher starting torque and better efficiency than similar CF-hysteresis motors, they still suffer from low efficiency and power factor. Thus, there still exists a need for the development of high efficiency self-starting IPM motors with improved starting characteristics and excellent synchronization capabilities to replace standard induction motors deployed in motion control applications such as compressors, fans and pumps, where high dynamic performance is not necessary.

This chapter introduces the design of a novel 1-HP 3-phase 4-pole radial flux hysteresis IPM motor by combining the advantages of both hysteresis and permanent magnet motors. An initial design of the motor is obtained using the specifications of a standard 1-HP cage IPM motor. Parametric analysis is conducted for improving performance of the initial design. Performance results of the final design are presented and explained in this chapter. Finite element analysis results exhibit that the designed

IPM motor has better self-starting and synchronization capabilities than similar rating cage-equipped and CF-hysteresis IPM motors.

#### 4.2 Radial Flux Hysteresis IPM Motor

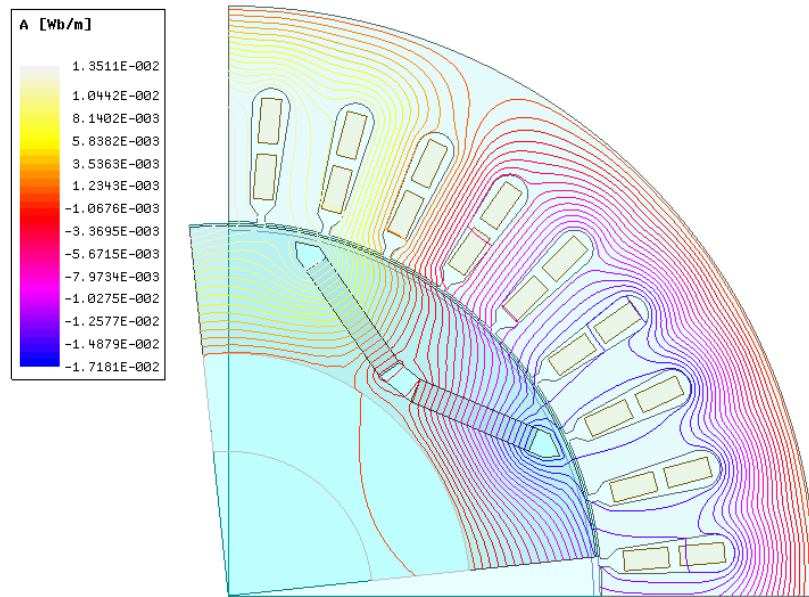
Figures 4.1a and 4.1b illustrate magnetic flux lines of a circumferential flux (CF) and radial flux (RF) hysteresis IPM motor, respectively. The stator is equipped with a 3-phase sinusoidally distributed whole-coiled Y-connected double layer winding. The hysteresis ring is made of 36% Cobalt-steel alloy. The initial magnetization curve of 36% Cobalt-steel alloy is presented by the dotted line. Based on elliptical modeling of the B-H loop, the hysteresis torque can be expressed as [11],

$$T_{hys} = \frac{pV_r B_m^2}{2\mu} \sin \delta \quad (4.1)$$

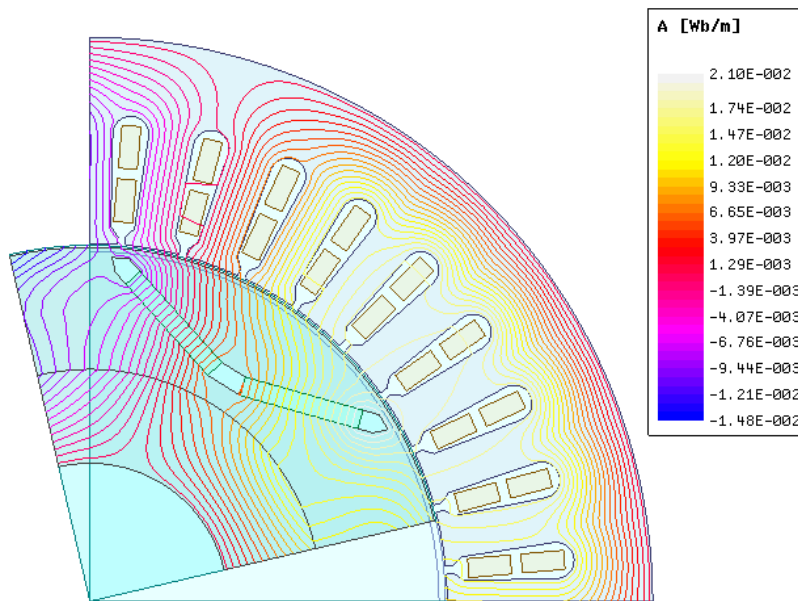
where  $B_m$  is the maximum flux density of the rotor material,  $\mu$  is the permeability,  $V_r$  is the volume of the hysteresis ring,  $p$  is the number of pole pairs and  $\delta$  is the hysteresis lag angle between  $B$  and  $H$ .

High energy density V-shaped radially magnetized Nd-B-Fe magnets are inserted into the slots inside the hysteresis ring. V-shape magnet orientation allows more flux focused into the air-gap which reduces the amount of rare-earth magnets in the motor. It also allows greater reluctance variation than that of a straight magnet orientation, and improves the total harmonic distortion (THD) of the motor back-emf. The hysteresis ring is supported by a sleeve. In a circumferential flux (CF) hysteresis motor, the sleeve is made of nonmagnetic material such as aluminum. The nonmagnetic sleeve forces the flux

to travel circumferentially inside the ring. The RF-hysteresis IPM motor has a laminated steel sleeve, allowing the flux to travel radially through the rotor.



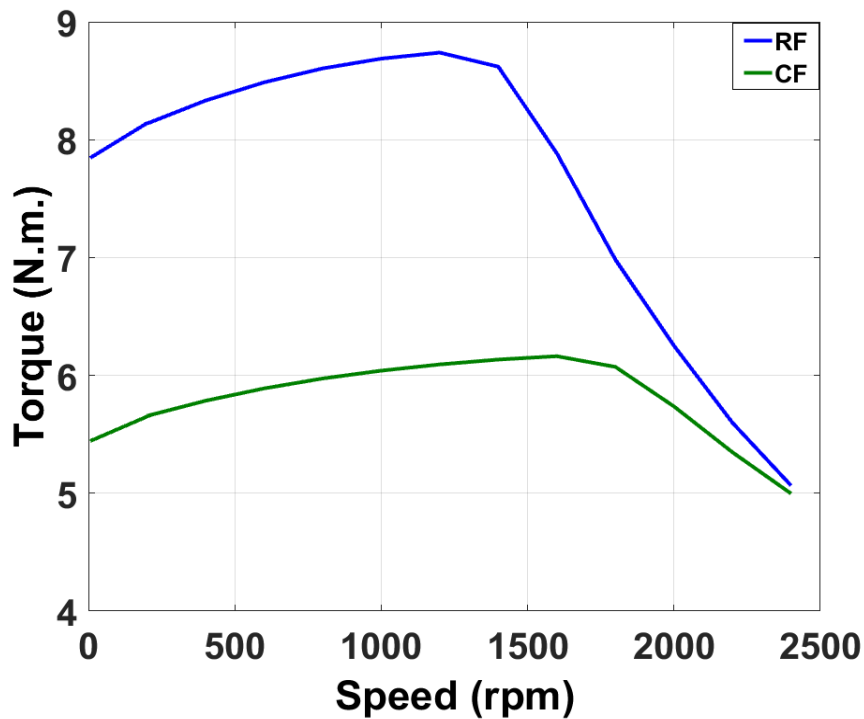
(a)



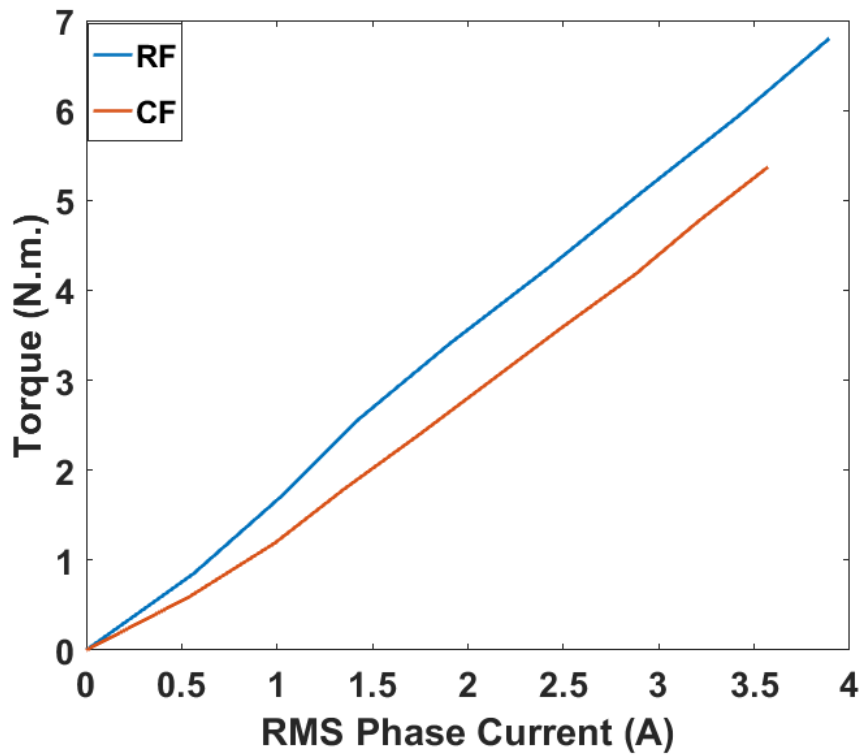
(b)

Figure 4.1. Flux distribution for: (a) CF-hysteresis and (b) RF- hysteresis IPM motors.

Figures 4.2a and 4.2b demonstrate a comparison between similar RF-hysteresis IPM and CF-hysteresis IPM motors in terms of average output torque and rms phase current, respectively. The RF-hysteresis IPM motor produces more output torque during start and delivers higher torque at synchronous speed. It also requires reduced phase current to produce the same amount of torque than the CF-hysteresis IPM motor. Thus, a RF-hysteresis IPM motor has higher starting torque and lower steady state line current at synchronous speed than that of a CF-hysteresis IPM motor. At steady state, the temporarily magnetized hysteresis ring and permanent magnets together provide the necessary excitation current in the motor. A RF-hysteresis IPM motor provides higher equivalent magnet excitation current than that of a CF-hysteresis IPM motor. As a result, a RF-hysteresis IPM motor has better synchronization capabilities than a similar CF-hysteresis IPM Motor.



(a)



(b)

Figure 4.2. Comparisons between CF and RF hysteresis IPM motors: (a) torque vs. speed and (b) torque vs. current.

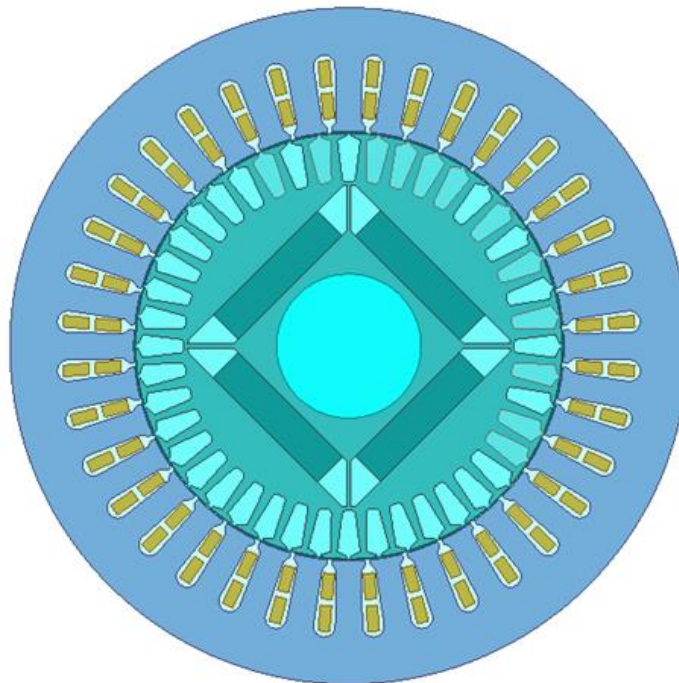
### 4.3 Design of a Radial Flux Hysteresis IPM Motor

A laboratory prototype 3-phase 4-pole 208V 1-HP squirrel-cage equipped self-starting IPM motor is considered as the base design. Figure 4.3a illustrates the cross section of the motor. A RF-hysteresis IPM motor is designed using the same frame size of the prototype motor. The detailed specifications of the cage-IPM motor are provided in table 3.1. The stator windings along with the outer and inner stator diameters of the proposed RF-hysteresis IPM motor are kept same as the prototype motor. The shaft-diameter is also kept constant. The air-gap is modified from 0.45mm to 0.65mm for reducing the space

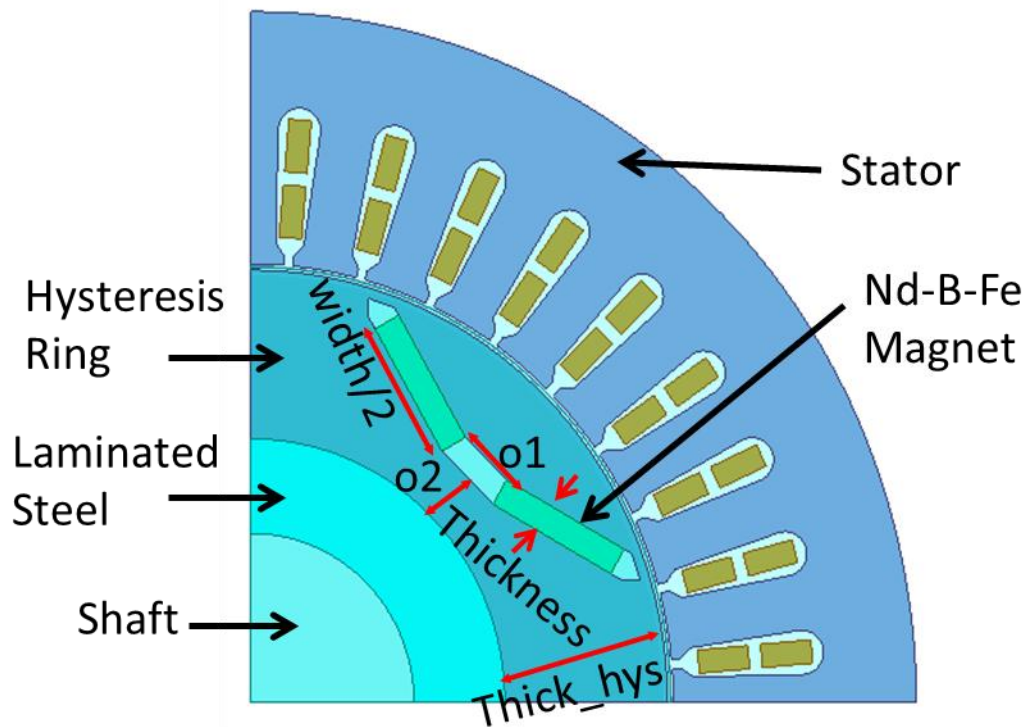
harmonics associated with hysteresis motors [14]. An initial design of the RF- hysteresis IPM motor is presented in Figure 4.3b. Parametric analysis of the initial design is conducted for the following variables,

- Thick\_hys: Thickness of the hysteresis ring,
- Thickness: Thickness of the magnet,
- Width: Total width of the magnet,
- o1: Distance between the magnets and
- o2: Distance of the magnet from the sleeve.

These variables are also depicted in Figure 4.3b. The Magnetic transient solver of ANSYS Maxwell software is used for finite element analysis of the motor. The core loss for 36% Cobalt-steel alloy is calculated using advanced vector hysteresis modeling technique by ANSYS [15]-[16].



(a)



(b)

Figure 4.3. Self-start IPM motor: (a) Cage rotor and (b) radial flux hysteresis rotor.

The thickness of the hysteresis ring is a primary concern for the design optimization of a hysteresis motor. At first, the motor is considered as a pure RF-hysteresis motor. Figure 4.4 depicts starting torque vs.  $Thick\_hys$  of the pure RF-hysteresis motor. The permeability of the hysteresis material goes down as the hysteresis ring becomes thinner, due to high inrush current. This results in more hysteresis torque based on (4.1) for a thin hysteresis ring. The starting torque becomes lower when the thickness of the hysteresis ring goes up.

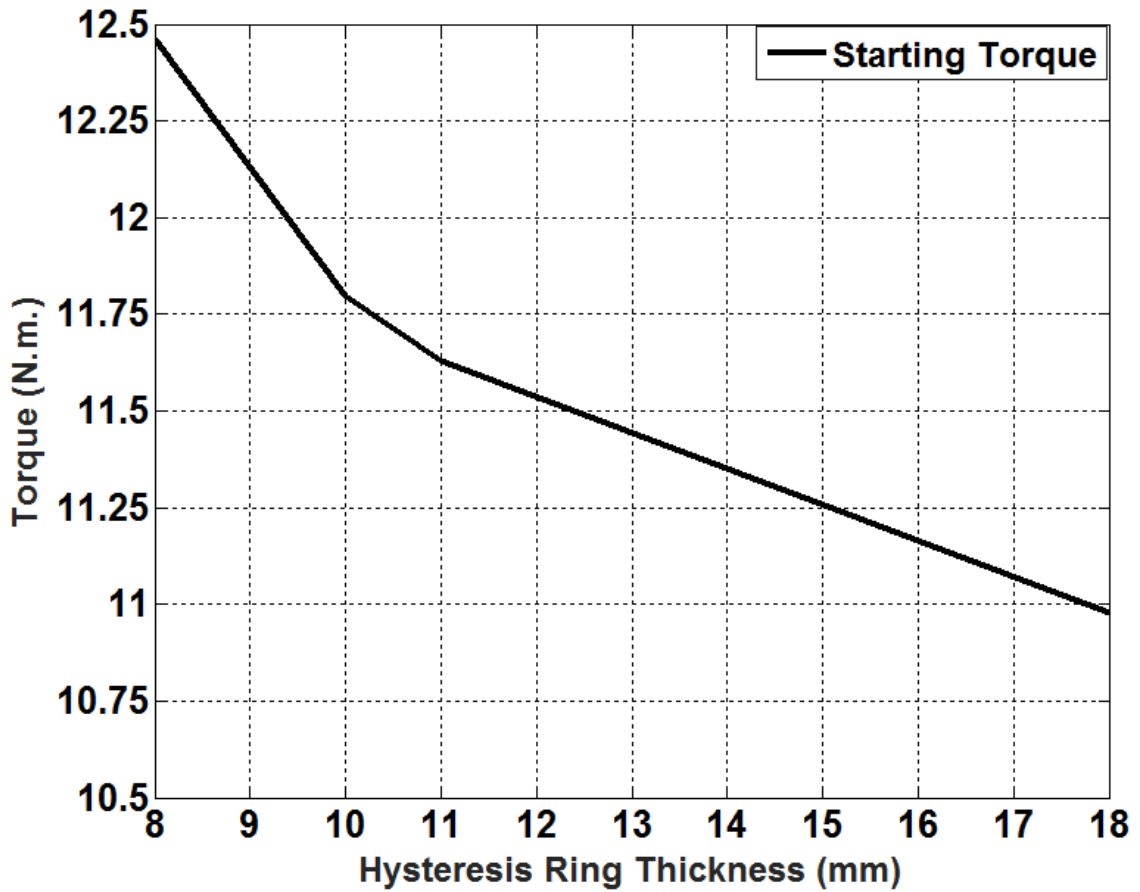


Figure 4.4. Starting torque vs. ring thickness for a radial flux hysteresis motor.

Figure 4.5 demonstrates the steady-state average torque of a RF-hysteresis IPM motor at rated current for different values of the hysteresis ring thickness. Although a lower value of the ring thickness produces more starting torque, it does not necessarily provide higher torque at steady state. At steady state, the permeability of the hysteresis ring does not vary significantly with the ring thickness. Consequently, the hysteresis torque goes up with increasing thickness of the ring. At a certain thickness such as 16mm, the permanent magnet torque starts becoming low, resulting in an overall decrease in the output torque.

Thus, in order to achieve high starting as well as steady-state torque, a hysteresis ring of 16mm thickness is considered for designing the RF-hysteresis IPM motor. This will provide the motor good starting and synchronization capabilities.

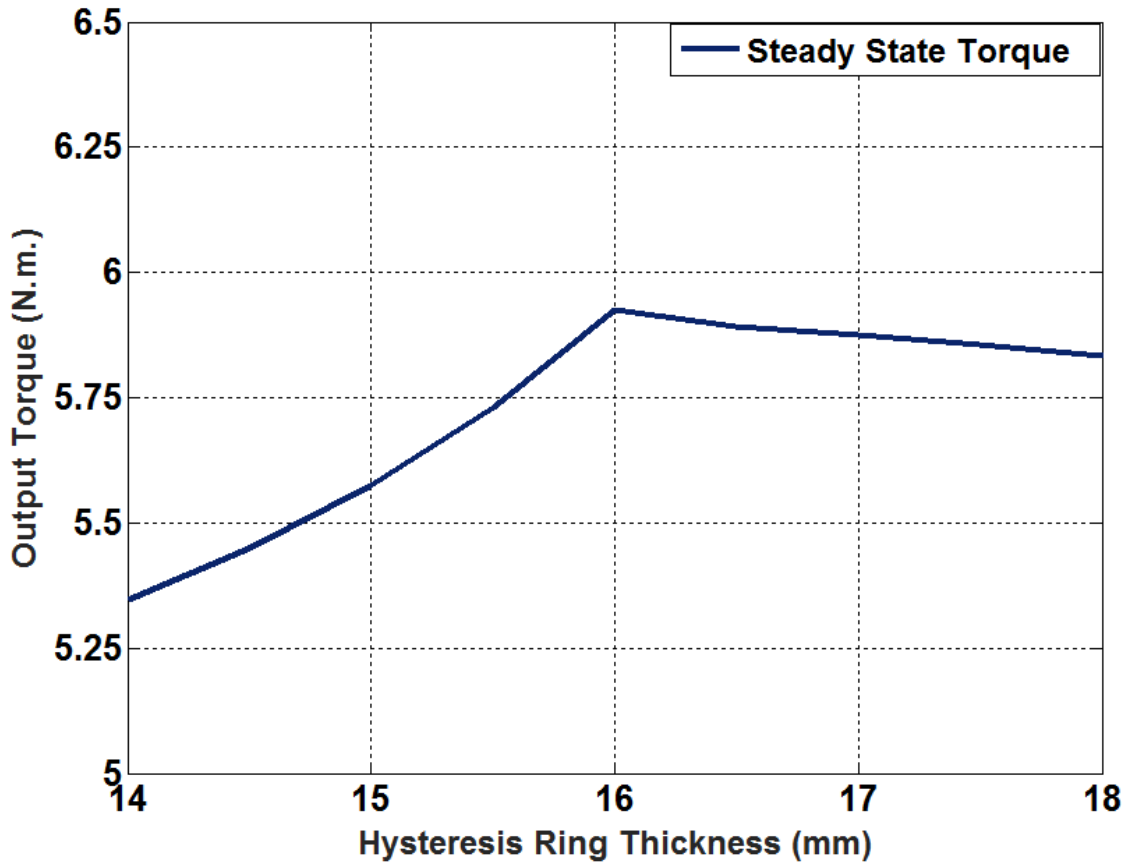


Figure 4.5. Steady-state torque vs. ring thickness for a radial flux hysteresis IPM motor.

Figures 4.6 and 4.7 demonstrate maximum output torque and efficiency of the RF-hysteresis IPM motor, respectively, for different values of magnet-width and magnet-thickness. Lower magnet thickness provides higher efficiency but reduces the maximum output torque. As the price of Nd-B-Fe magnets is high, reduction of the amount of rare-

earth magnets decreases the cost of the motor significantly. The thickness and the width of the magnet are chosen as 2.5mm and 32mm, respectively. A thickness value of 2.5mm provides the highest efficiency while a 32mm magnet width produces sufficient running torque for the motor.

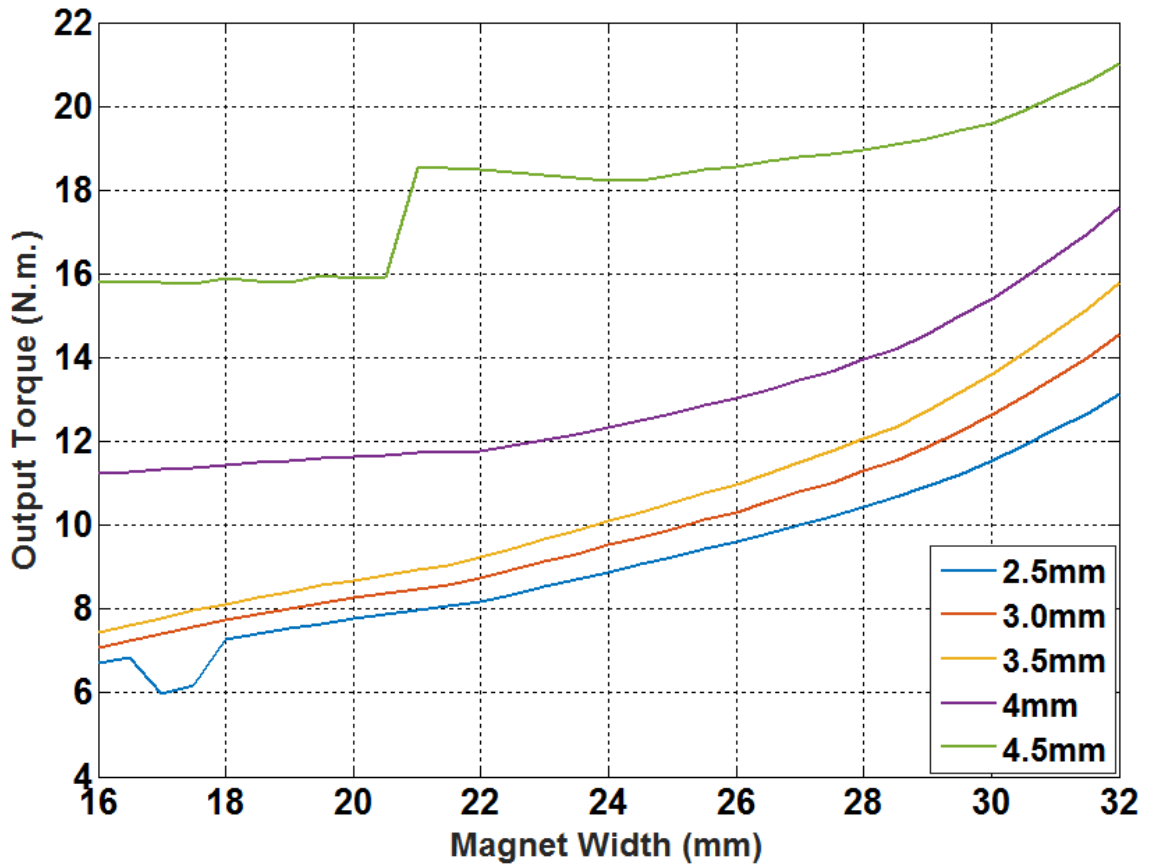


Figure 4.6. Output torque vs. magnet width.

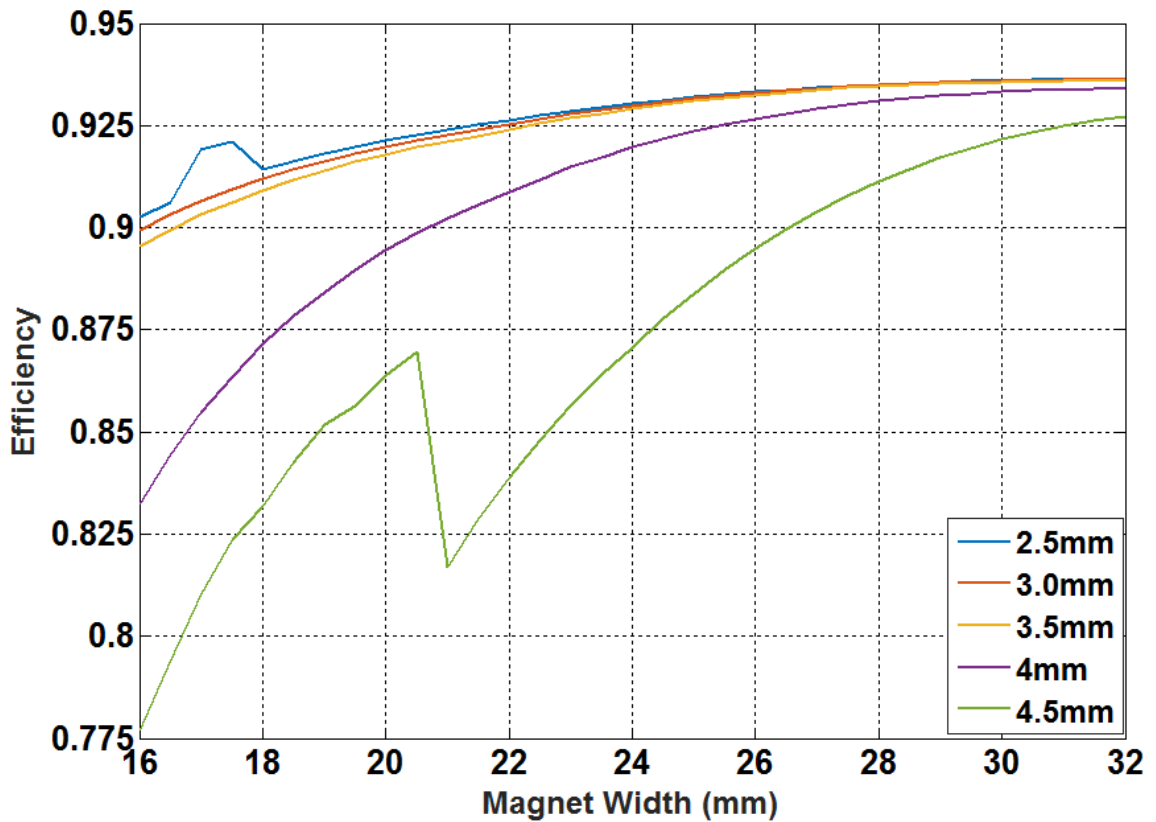


Figure 4.7. Efficiency vs. magnet width for variable magnet thickness.

The positioning of the magnet depends on the values of  $o_1$  and  $o_2$ . Figures 4.8 and 4.9 illustrate the maximum average output torque and rms phase current of the motor at rated voltage for different arrangements of the magnet. The magnitude of  $o_1$  is varied from 2mm to 5mm, and  $o_2$  is varied from 1mm to 5mm. The torque becomes maximum for  $o_1=2\text{mm}$  and  $o_2=5\text{mm}$ . The phase current does not vary significantly with  $o_1$  and  $o_2$ . Thus, the values of  $o_1$  and  $o_2$  are selected as 2mm and 5mm, respectively, to obtain the maximum torque.

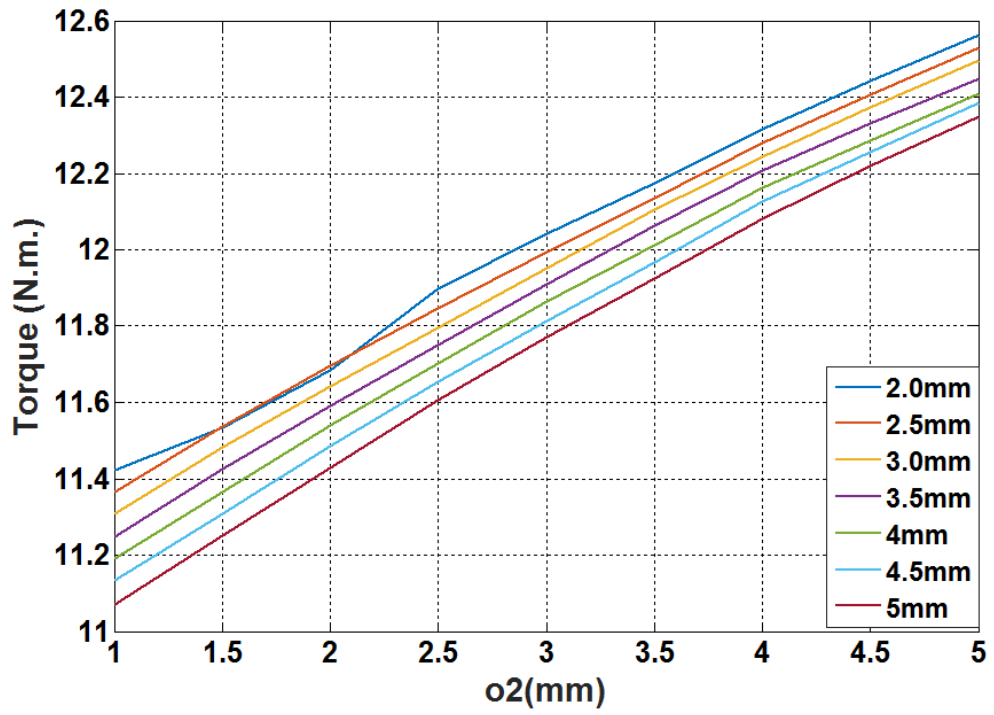


Figure 4.8. Output torque vs. o2.

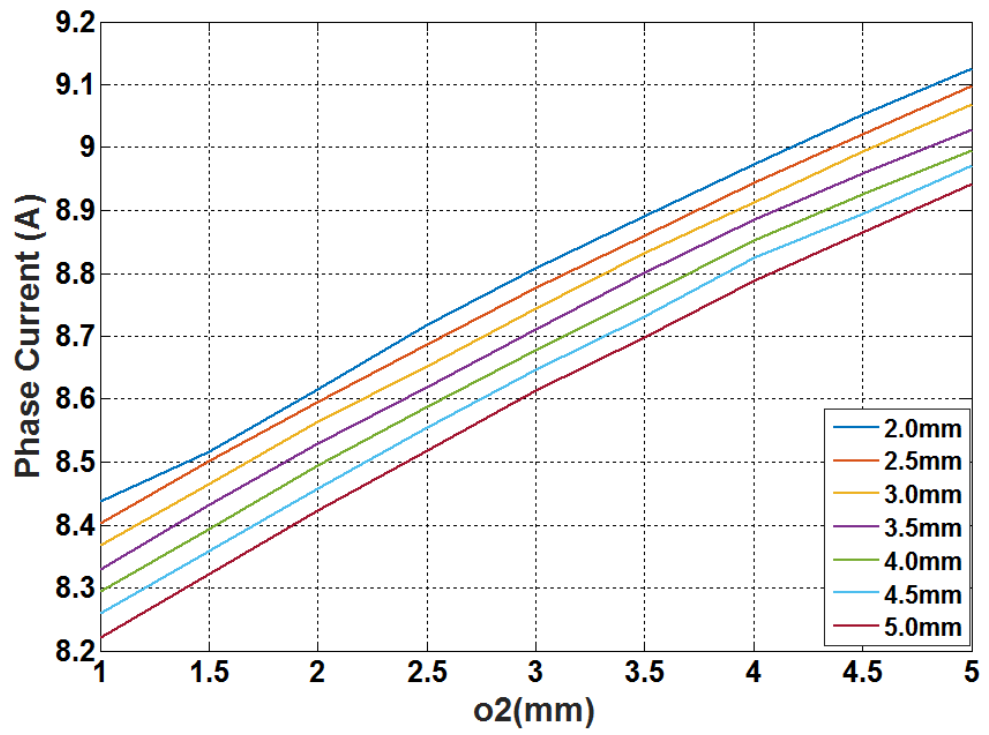
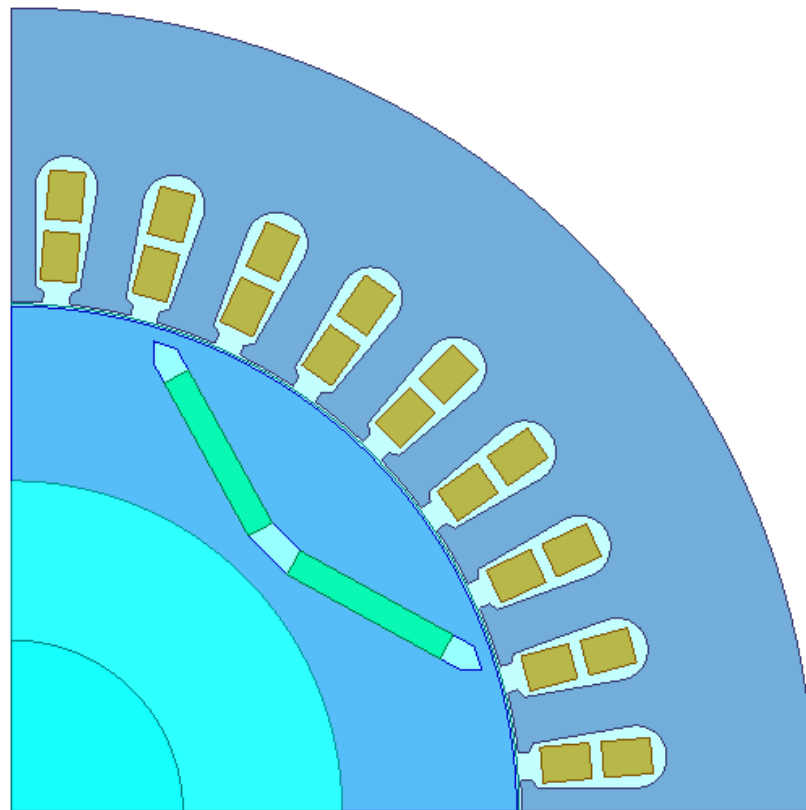
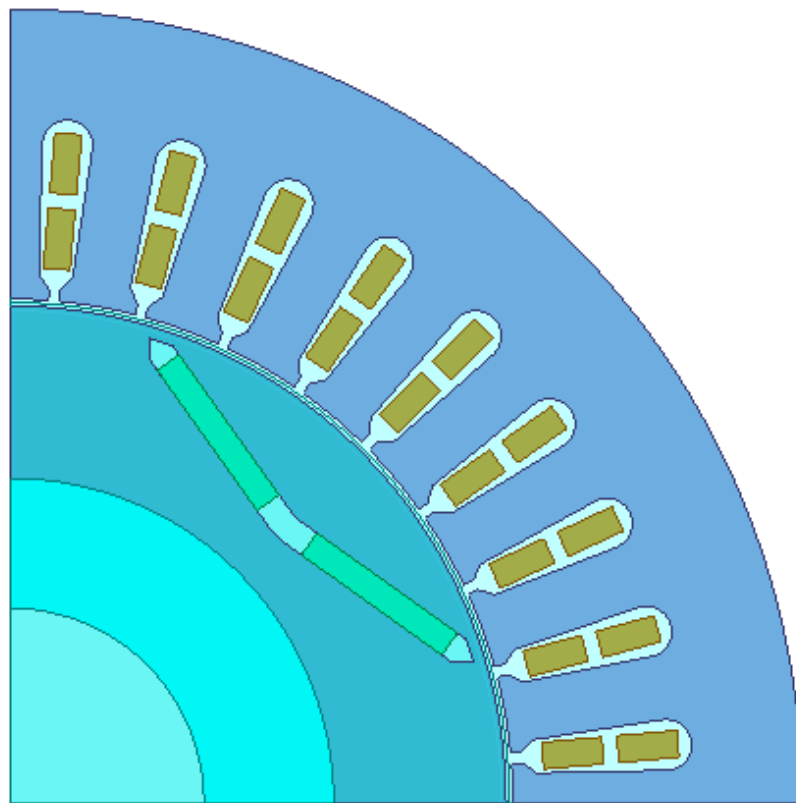


Figure 4.9. Design B of the RF-hysteresis IPM motor.

The initial Design A and final Design B of the RF-hysteresis IPM motor are depicted in Figures 4.10a and 4.10b, respectively. Detailed specifications of both designs are presented in table 4.1. Design A requires higher starting and running voltages than the design B. Design B also requires less input power than Design A, becoming more energy efficient.



(a)



(b)

Figure 4.10. (a) Design A and (b) Design B of the RF-hysteresis IPM motor.

#### 4.4 Performance Analysis

The transient run-up responses of the Design A RF-hysteresis IPM motor for different load torques are shown in Figure 4.11. The motor is run by a 3-phase Y-connected 60Hz balanced ac supply. For the Design A motor, the required minimum starting voltage is 240V which is higher than the motor rated voltage. The motor starts smoothly with some rotor oscillations at low speeds because of the magnet brake torque. The motor overcomes the maximum magnet brake torque with the help of high hysteresis torque and eddy current torque, and ramps up towards the synchronous speed. As the load torque

increases, it experiences longer rotor oscillations whereas the speed overshoots and undershoots decrease during the synchronization process. When the motor reaches the steady state, the running voltage is reduced to the motor rated voltage at  $t=0.6s$ . This improves the power factor and the efficiency of the motor.

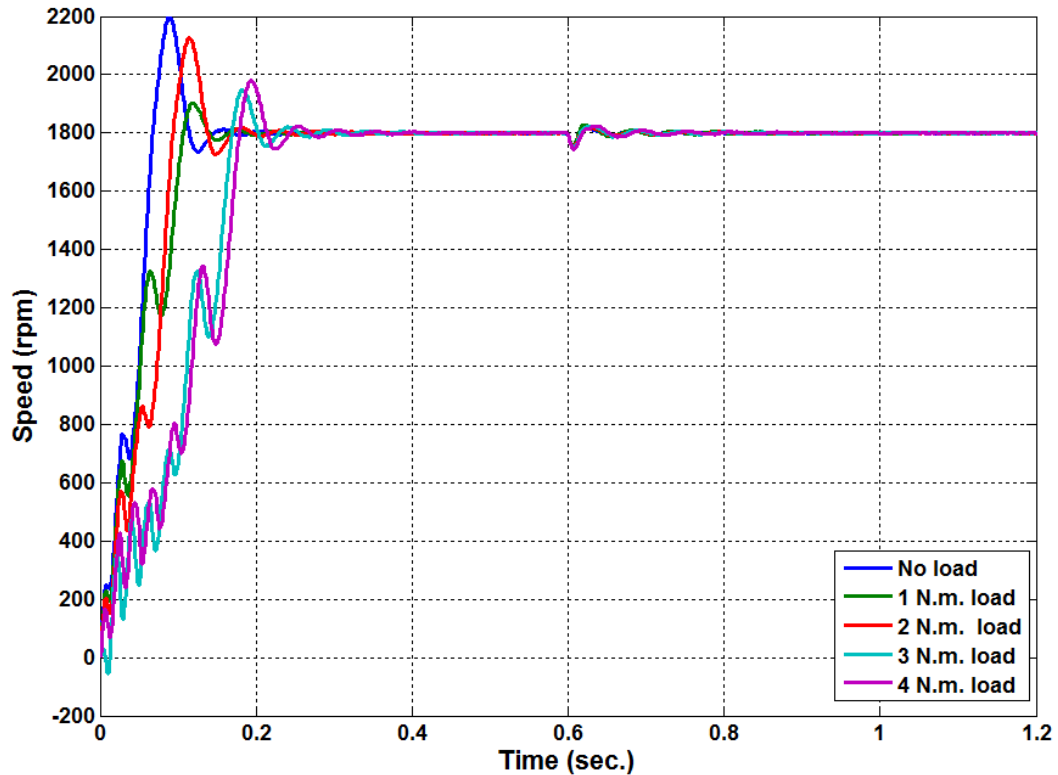


Figure 4.11. Run-up responses of the Design A radial flux hysteresis IPM motor.

The developed instantaneous electromagnetic torque for various loads is illustrated in Figure 4.12. The hysteresis IPM motor has a starting torque due to the presence of a hysteresis ring in the rotor. The developed torque is comprised of an average asynchronous torque and a pulsating torque. The average asynchronous torque combines the hysteresis torque, the eddy current torque and the magnet brake torque. Due to the presence of permanent magnets acting as a current source in the rotor, there is a pulsating

torque superimposed on the average asynchronous torque. The pulsating torque assists the motor to a fast acceleration towards the synchronous speed. During the period of synchronization, the torque pulsation dies out and turns into a part of the synchronous torque. The eddy current torque also vanishes when the slip approaches zero.

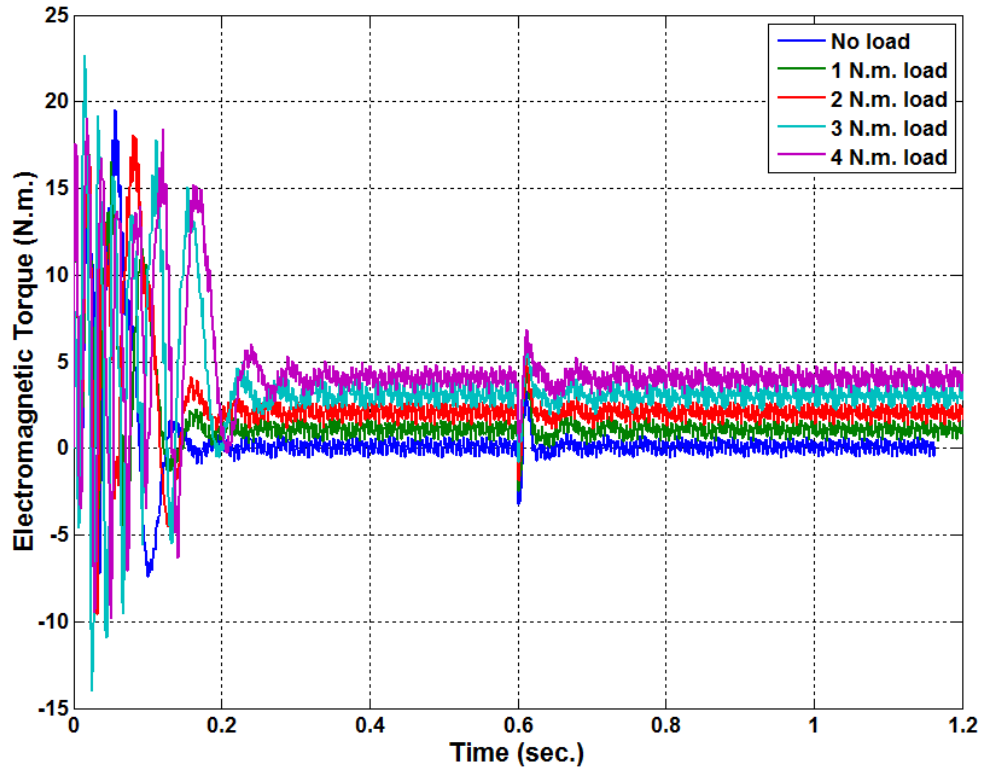


Figure 4.12. Developed torque of the Design A radial flux hysteresis IPM motor.

The stator phase currents for no load and 3 Nm. load torque are illustrated in Figure 4.13. The starting current is a few times higher than the steady state rated current because of the required high magnetizing current for the hysteresis material. The current goes down significantly at the steady state when the input voltage is reduced to the operating rated voltage. This improves the efficiency of the motor.

In Figure 4.14, the torque vs. speed trajectory for rated load is depicted. Because of the interaction between the permanent magnet flux and the currents inside the hysteresis ring, the line start hysteresis IPM motor suffers from a small number of torque reversals at low a speed. Before reaching the synchronization, there is a series of slow pole-slips which appears in Figure 4.14 as almost elliptical. The final synchronization trajectory follows a spiral that terminates at the synchronous speed.

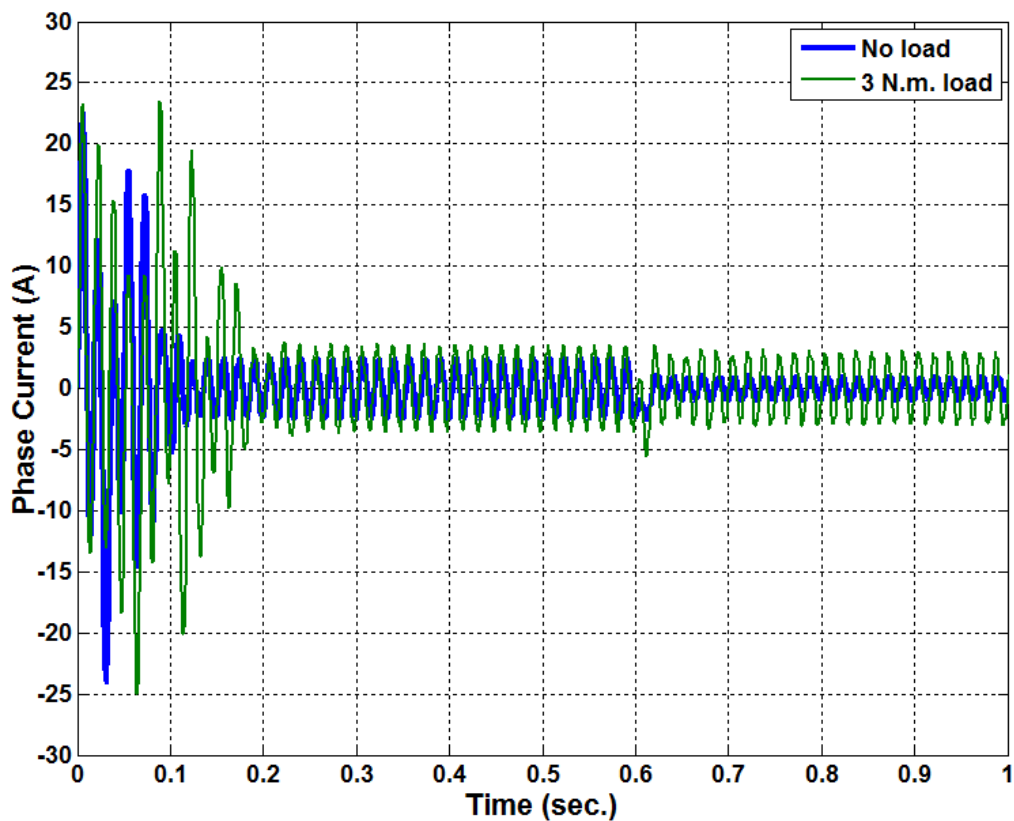


Figure 4.13. Phase current of the Design A radial flux hysteresis IPM motor.

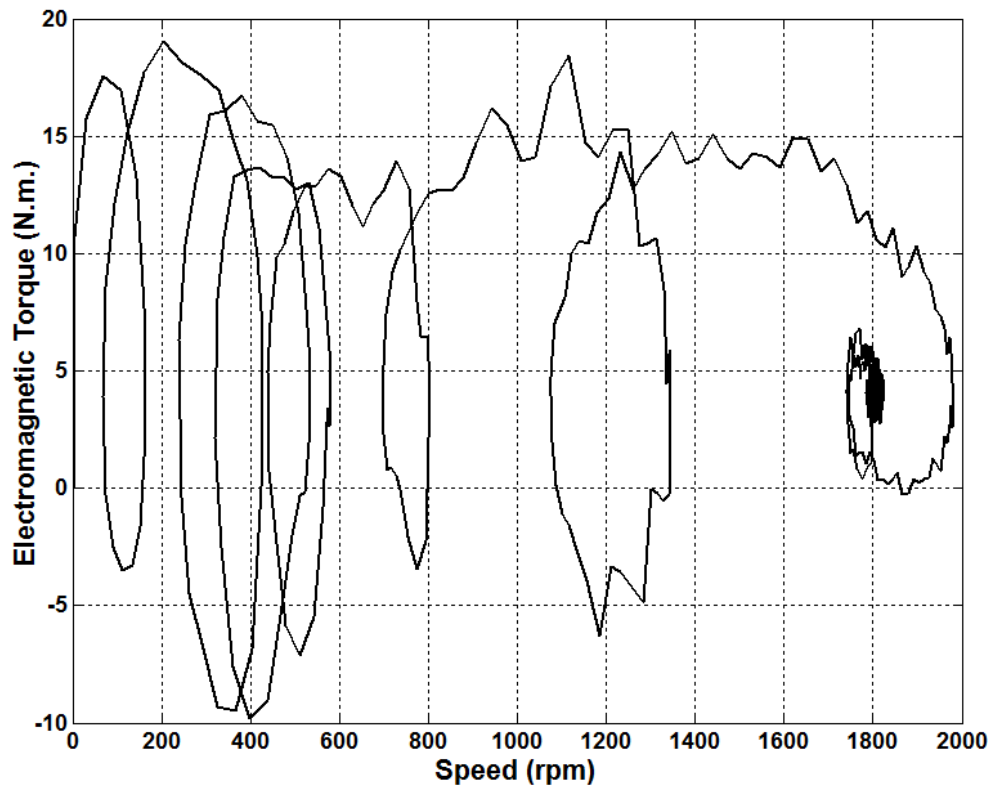
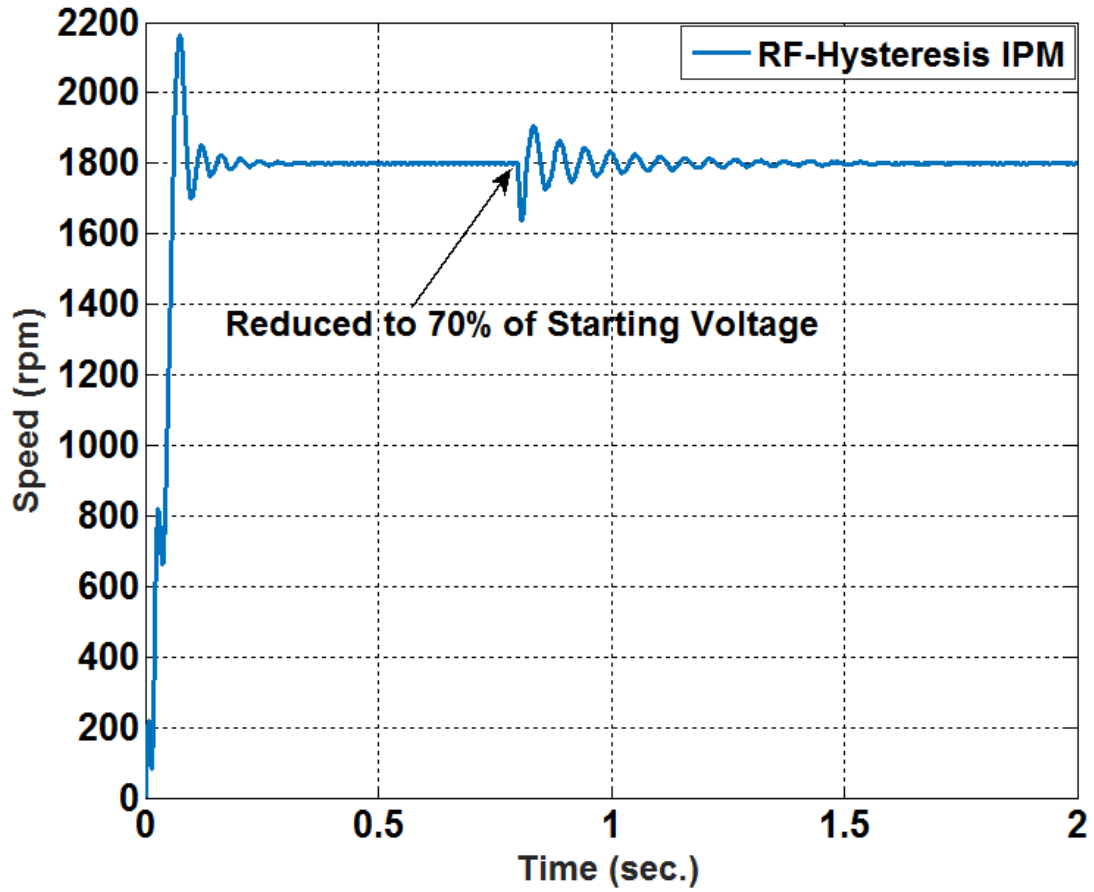


Figure 4.14. Torque vs. speed trajectory at rated load of the Design A motor.

The Design A motor requires a starting voltage that is higher than the motor rated voltage. Thus, it cannot be operated from the line directly unless there is a step-up type autotransformer available. The optimized Design B motor can start at the rated voltage and can also operate efficiently at a lower voltage. Figures 4.15-4.18 illustrate comparative responses between 1-HP Design B RF and CF hysteresis IPM motors. In the case of the CF-hysteresis IPM motor, the sleeve material in the Design B is changed to aluminum. The motor inertia is selected as equal to the rotor inertia. The starting voltage for the motor is selected as the rated voltage 208V. The load torque is considered as the rated torque of 4 N.m. The run-up responses are provided in Figures 4.15a and 4.15b.

Both the motors have a smooth start because of the high starting torque jointly provided by the hysteresis and eddy current phenomena.



(a)

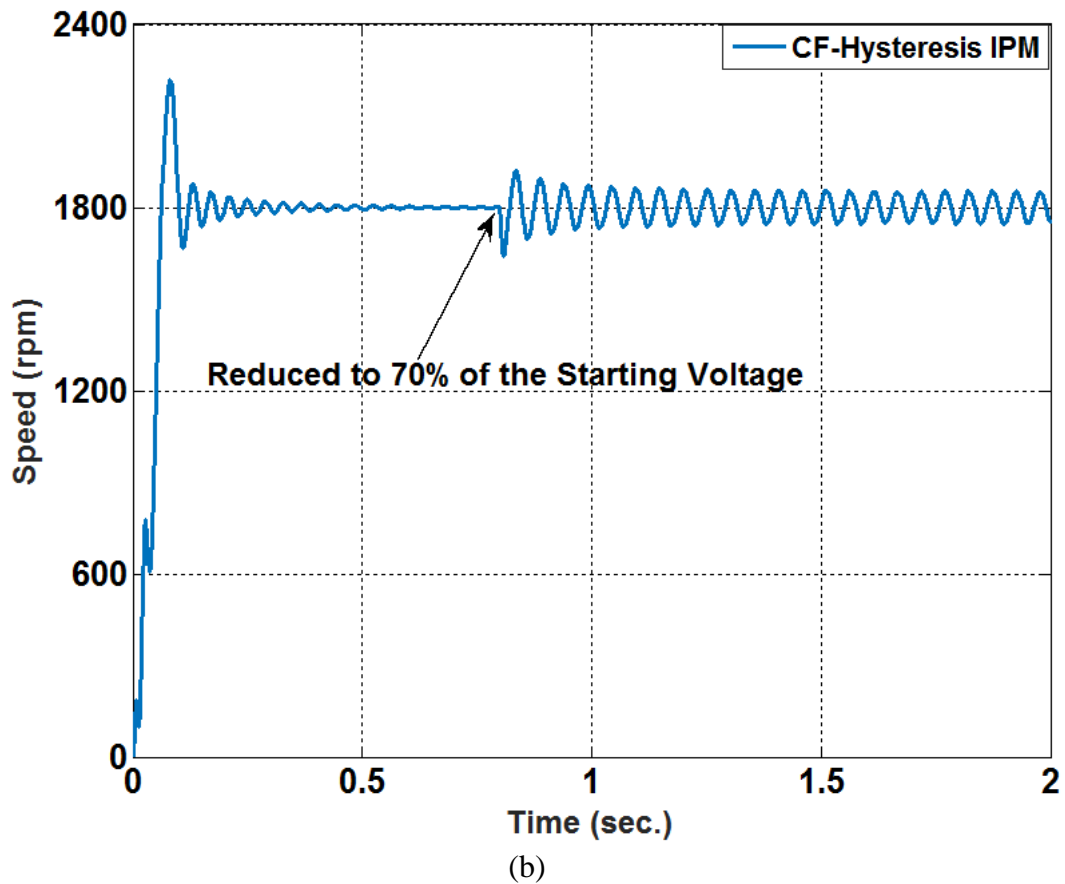
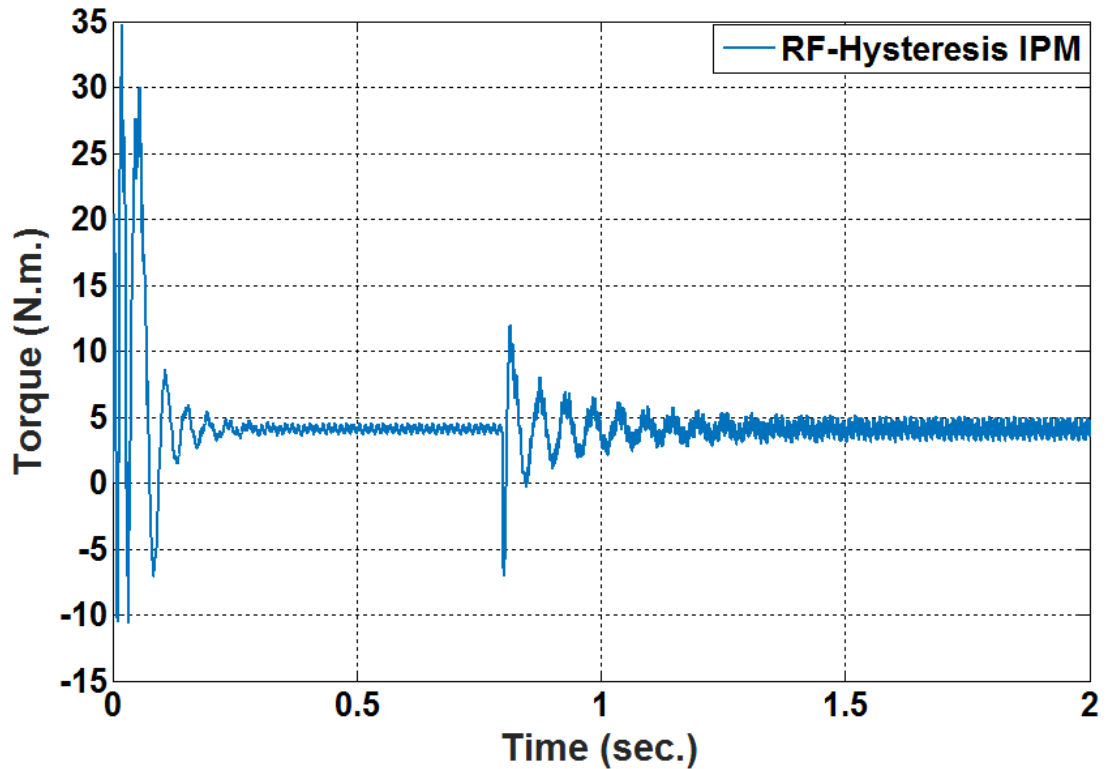


Figure 4.15. Run-up responses of the Design B type: (a) RF-hysteresis IPM and (b) CF-Hysteresis IPM motors.

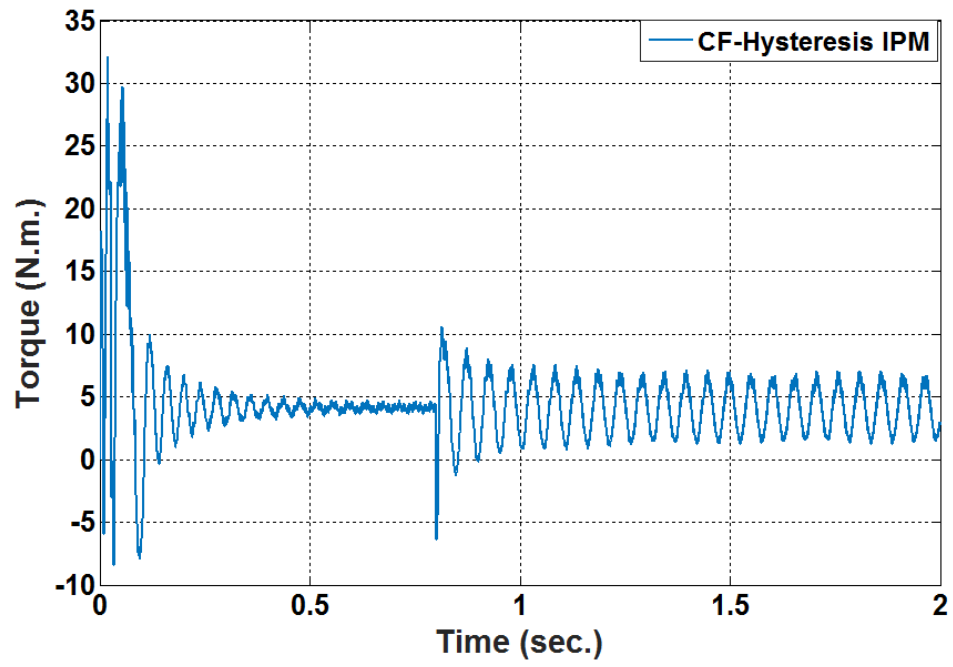
The torque responses are illustrated in Figures 4.16a and 4.16b. Both the motors synchronize easily with some speed overshoots and undershoots. The speed oscillation is more prominent in the CF motor, as shown in Figure 4.15b. The supply voltage is reduced to 70% of the rated voltage at  $t=0.8$ s. The RF-hysteresis IPM motor maintains the synchronization while the CF motor fails to synchronize and experiences hunting. Thus, the RF-hysteresis IPM motor provides more damping to the motor drive during fluctuations in the load/voltage supply. It also requires less operating voltage and less

input power. Thus, it is more energy efficient than the Design B type circumferential flux hysteresis IPM motor.

Figures 4.15b and 4.16b depict the hunting phenomenon in the CF-hysteresis IPM motor. The rms current waveforms for the two motors are illustrated in Figures 4.16a and 4.16b. The starting current is higher in the CF-hysteresis motor than the RF-hysteresis motor. Thus, a CF-hysteresis IPM motor requires more input current and voltage to maintain the synchronization than a similar RF-hysteresis IPM motor and is less efficient than a similar rating RF-hysteresis IPM motor.

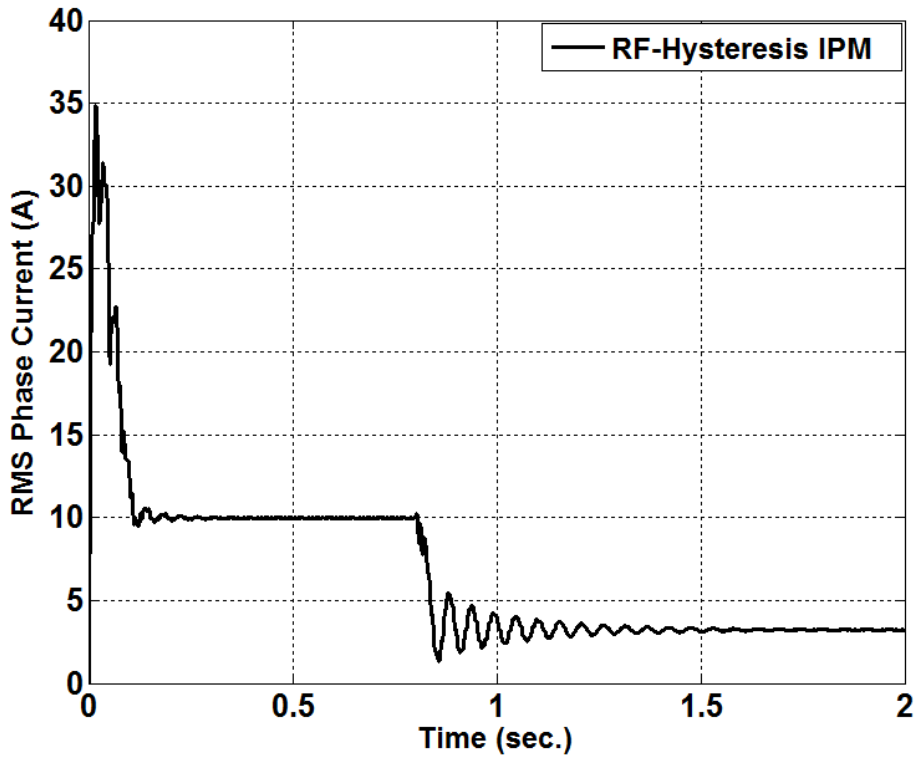


(a)

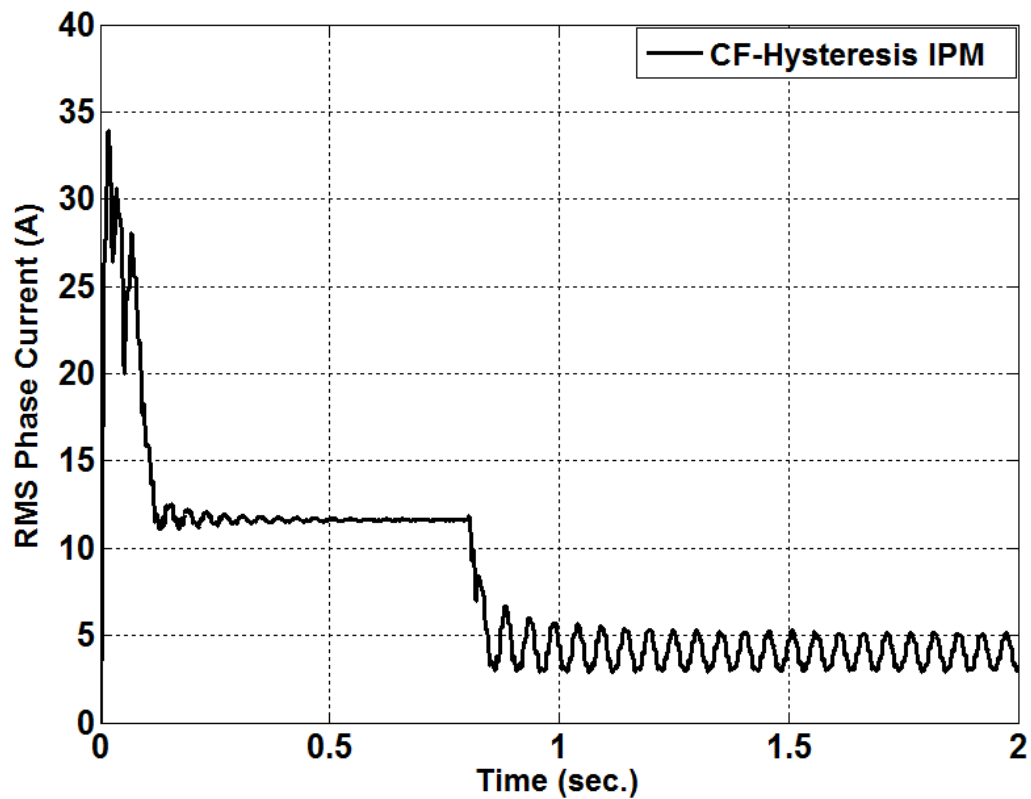


(b)

Figure 4.16. Run-up torque responses of the Design B type: (a) RF-hysteresis IPM and (b) CF-Hysteresis IPM motors.



(a)



(b)

Figure 4.17. Run-up current responses of the Design B type: (a) RF-hysteresis IPM and (b) CF-hysteresis IPM motors.

The air-gap flux densities (rms) of the two motors are shown in Figures 4.18-4.19. The RF-Hysteresis IPM motor has slightly higher air-gap flux density than the similar CF-motor. The air-gap flux density is more distorted in the CF-hysteresis IPM motor during starting. The oscillatory air-gap flux causes more torque pulsations in the CF-hysteresis motor than an equivalent RF-hysteresis motor. It also reduces the damping capability of the motor, making it more vulnerable to experience limit cycles during sudden changes in the operation condition.

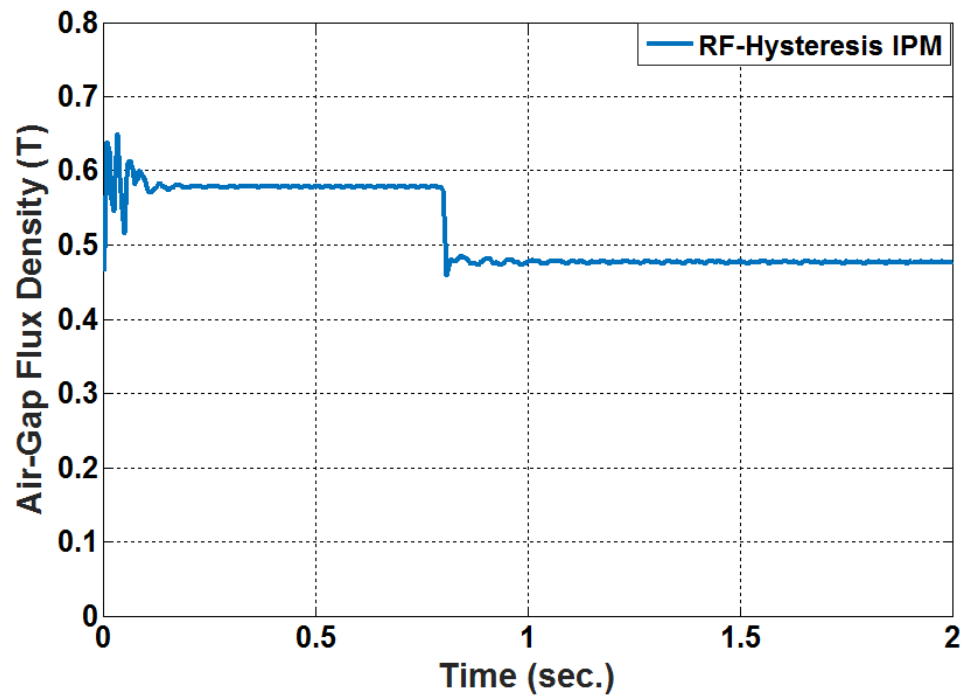


Figure 4.18. Air-gap flux density of a RF-hysteresis IPM motor.

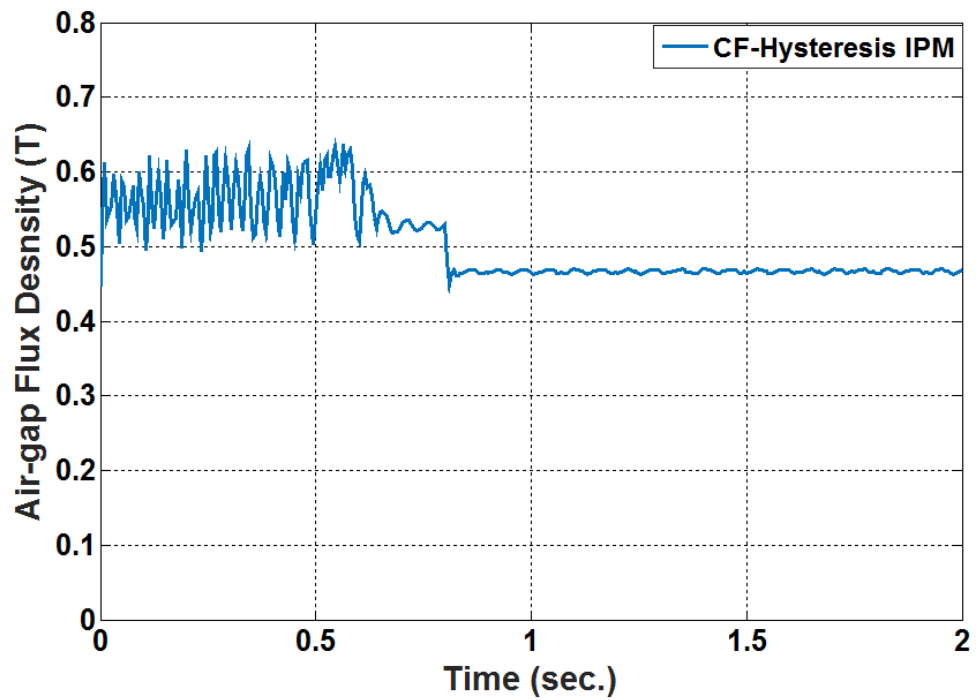
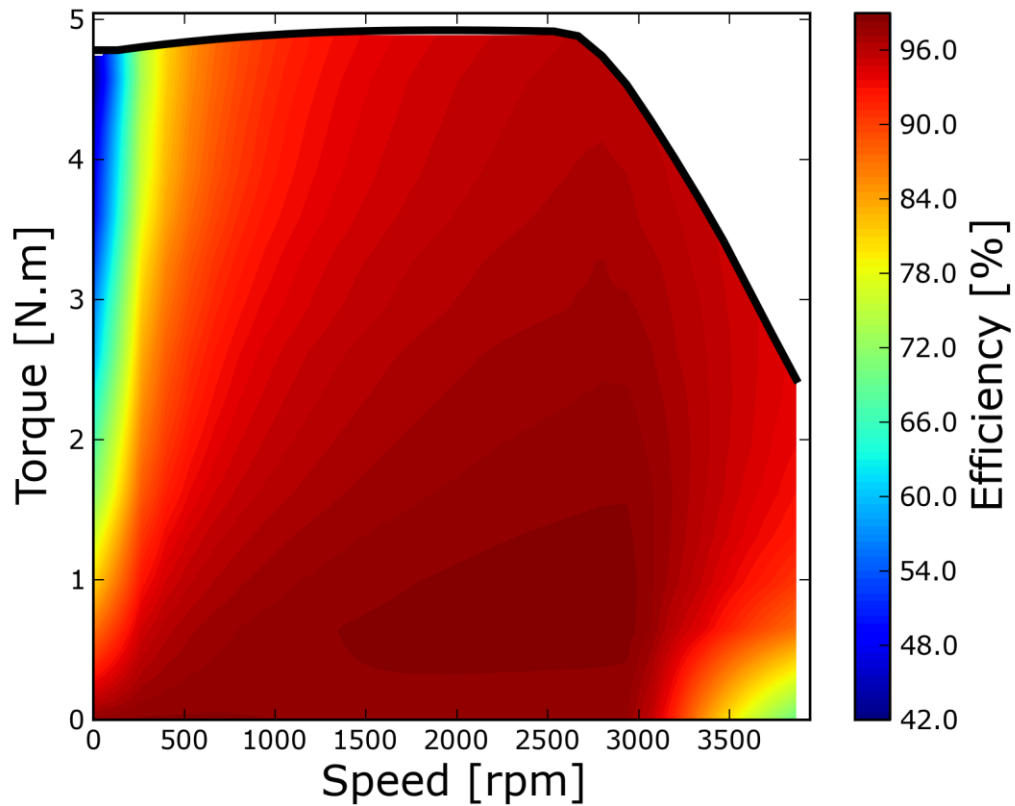


Figure 4.19. Air-gap flux density of a CF-hysteresis IPM motor.

The efficiency and power factor contours of the RF-hysteresis motor for rated current and reduced steady-state voltage are displayed in Figures 4.20a and 4.20b, respectively. The motor operates at a high efficiency at steady-state due to vanishing core losses at synchronous speed. The excess loss in the rotor hysteresis ring is not considered during calculation of the motor efficiency. The mechanical friction and windage losses are also not taken into account. The power factor is high over a wide range of operation due to the excitation provided by permanent magnets. Thus, the inclusion of permanent magnets greatly overcomes the problem of low power factor associated with conventional hysteresis motors.



(a)

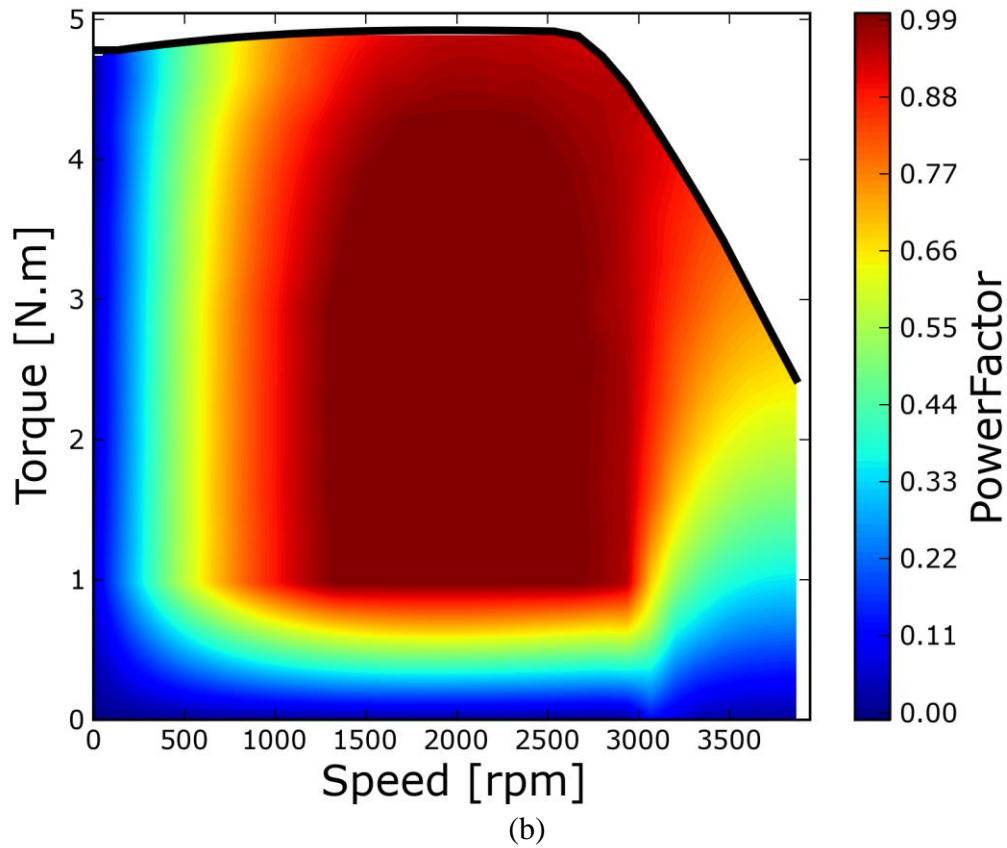


Figure 4.20. Performance analysis of the Design B RF-Hysteresis IPM motor: (a) efficiency and (b) power factor.

A comparison between the cage-IPM motor and the RF-hysteresis IPM motor in terms of starting and synchronization capacities is provided in Figure 4.21. Both the motors are started at rated load and voltage. The inertia for the cage-IPM motor is two times its rotor inertia whereas the inertia for the RF-hysteresis IPM motor is selected as four times its rotor inertia. The RF-hysteresis IPM motor can successfully start and synchronize the load. However, the cage-IPM fails to start and accelerate the rotor to the synchronous speed.

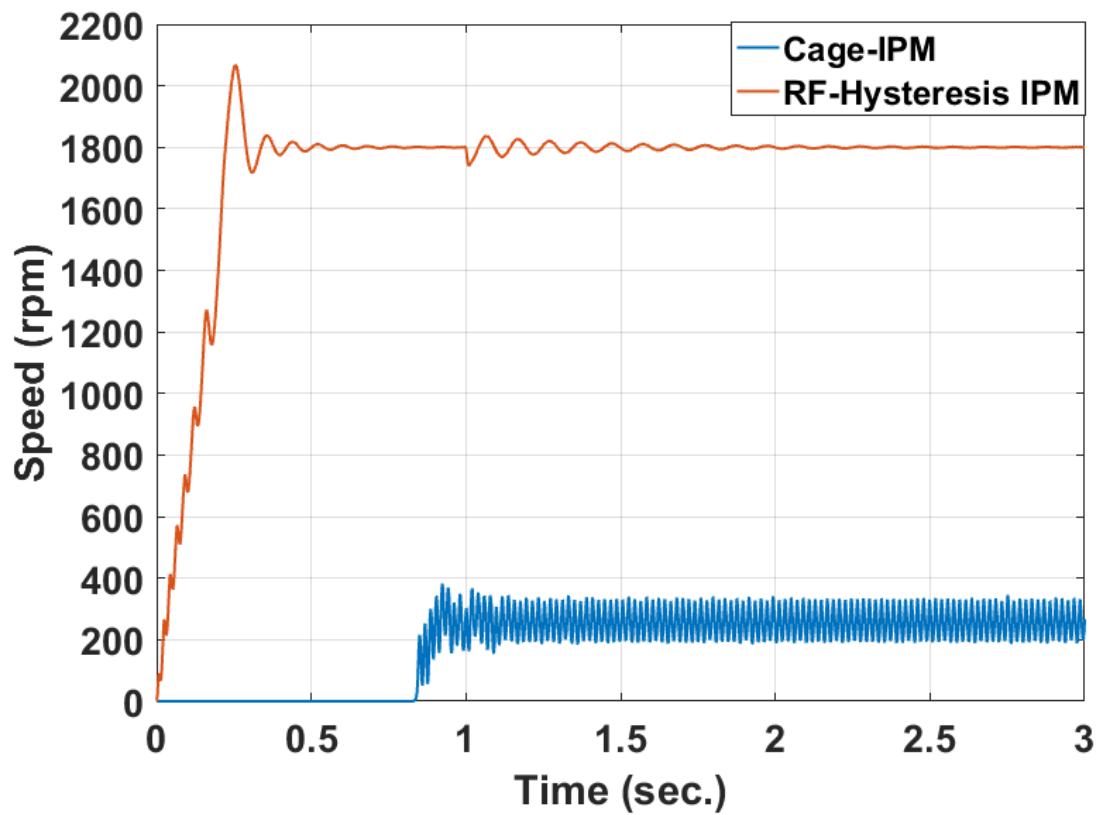


Figure 4.21. Run-up responses of a cage-IPM motor and a RF-hysteresis IPM motor for high inertial loads.

#### 4.5 Conclusions

This chapter presents design and analysis of a 3-phase, 4-pole 1-HP radial flux hysteresis IPM motor. The RF-hysteresis IPM motor is found to possess superior synchronization and stabilization capabilities compared to CF-hysteresis and cage IPM motors. The availability of self-starting and active stabilization capability make the RF-hysteresis IPM motor a suitable candidate for sensorless ESP drive applications.

In the next chapter, an analysis of the mechanical dynamics of a hysteresis IPM motor driven electric submersible pump system is presented.

Table 4.1. Design Parameters of Self-Starting IPM Motors.

<b>Parameters</b>	<b>Cage-IPM</b>	<b>CF-Hysteresis Design A</b>	<b>RF-Hysteresis Design B</b>
Rated Power (HP)	1	1	1
Rated Voltage (V)	208	240/208	208/146
Stator-Outer Dia. (mm)	147.3	147.3	147.3
Stator-Inner Dia.(mm)	93.5	93.5	93.5
Number of Stator Slots	36	36	36
No. of Conductors/slot	44	42	28
Stack Length (mm)	78.8	78.8	78.8
Air-gap Length (mm)	0.45	0.45	0.65
Rotor-Inner Dia. (mm)	31.4	31.4	31.4
Hysteresis Ring Thick. (mm)	None	16	16
Magnet Width (mm)	32	32	32
Magnet Thickness (mm)	7.7	2.5	2.5
o1 (mm)	18	5	2
o2 (mm)	0	3	5
Magnet Type	Nd-B-Fe (35)	Nd-B-Fe (35)	Nd-B-Fe (35)

## References

1. G. R. Slemon, R. D. Jackson and M. A. Rahman, "Performance predictions for large hysteresis motors", *IEEE Transactions on Power Apparatus and Systems*, vol. 96, no. 6, pp. 1915 – 1919, November 1977.
2. C.E. Gunn, "Improved starting performance of wound rotor motors using saturistors", *IEEE Transactions on Power Apparatus and Systems*, vol. 82, no. 66, pp. 298-302, June 1963.
3. D. O'Kelly, "Hysteresis motor with overexcitation and solid-state control", *Proceedings of the Institution of Electrical Engineers*, vol. 125, no. 4, pp. 288-292, April 1978.
4. K. R. Rajagopal, "Design of a compact hysteresis motor used in a gyroscope", *IEEE Transactions on Magnetics*, vol. 39, no. 5, pp. 3013-3015, September 2003.
5. M. A. Rahman, A. Osheiba, T. A. Little and G. Slemon, "Effects of samarium cobalt permanent magnet on the performance of polyphase hysteresis-reluctance motors", *IEEE Transactions on Magnetics*, vol. 20, no. 5, pp. 1765-1767, September 1984.
6. S. Saha, G. Choi and Y. Cho, "Optimal rotor shape design of LSPM with efficiency and power factor improvement using response surface methodology", *IEEE Transactions on Magnetics*, vol. 51, no. 11, pp.1-4, November 2015.
7. W. Fei, P. Luk, J. Ma, J. X. Shen, and G. Yang, "A high-performance line-start permanent magnet synchronous motor amended from a small industrial three-phase induction motor," *IEEE Transactions on Magnetics*, vol. 45, no.10, pp. 4724–4727, October 2009.
8. P. Huang and M. Tsai, "Investigation of V-Shaped lines permanent magnet motors based on reactance effect", *IEEE Transactions on Magnetics*, vol. 49, no. 5, pp. 2311–2314, May 2013.
9. E. Sanchez, A. C. Smith and J. Rodriguez-Rivas, "Steady-State Analysis of a Canned Line-Start PM Motor", *IEEE Transactions on Magnetics*, vol. 47, no. 10, pp. 4080–4083, October 2011.

10. K. Kurihara and M. A. Rahman, "Transient performance analysis for permanent-magnet hysteresis synchronous motor," *IEEE Transactions on Industry Applications*, vol. 40, no. 1, pp. 135–142, January 2004.
11. S. Miyairi and T. Kataoka, "A basic equivalent circuit of the hysteresis motor", *IEE Transactions on Japan*, vol. 85, pp. 41-50, October 1965.
12. G. Wakui, K. Kurihara and T. Kubota, "Radial flux type hysteresis motor with reaction torque-numerical analysis of hysteresis motor using finite element, *IEEE Transactions on Magnetics*, vol. 23, no. 5, pp. 3845 – 3852, September 1987.
13. G. Wakui, K. Kurihara and T. Kubota, "Radial flux type hysteresis motor with rotor ring of copper-sprayed surface layer", *Electrical Engineering in Japan*, vol. 23, no. 5, pp. 3845 – 3852, September 1987
14. T. Kubota, H. Sawa and G. Wakui, "Experimental formula for pull-out torque of hysteresis motor with space higher harmonics", *IEE Transactions on Japan*, vol. 112, no.4, pp. 132-143, 1992.
15. D. Lin, P. Zhou and A. Bergqvist, "Improved Vector Play Model and Parameter Identification for Magnetic Hysteresis Materials", *IEEE Transactions on Magnetics*, vol. 50, no. 2, pp. 1-4, February 2014.
16. Maxwell Online Help: Release v15.0 (December 2013), ANSYS, Inc., [Online], Available: <http://www.ansys.com/>

## Chapter 5

### Mechanical Dynamics of a Hysteresis IPM Motor Driven Electric Submersible Pump System

#### 5.1 Introduction

Oil and gas exploitation is a key element for the prosperity, growth and industrial development of Canada. An oil and gas reservoir is basically a formation of rock located from several hundreds to thousands of feet under the surface. The oil and gas are trapped inside the porous space of the reservoir rock. Figure 5.1 displays a typical oil and gas reservoir and the production well [1]. The recovery of oil and gas from a reservoir mainly depends on the well's ability to produce fluids. The production ability of a well is represented by a set of curves called inflow performance relationship (IPR) curves.

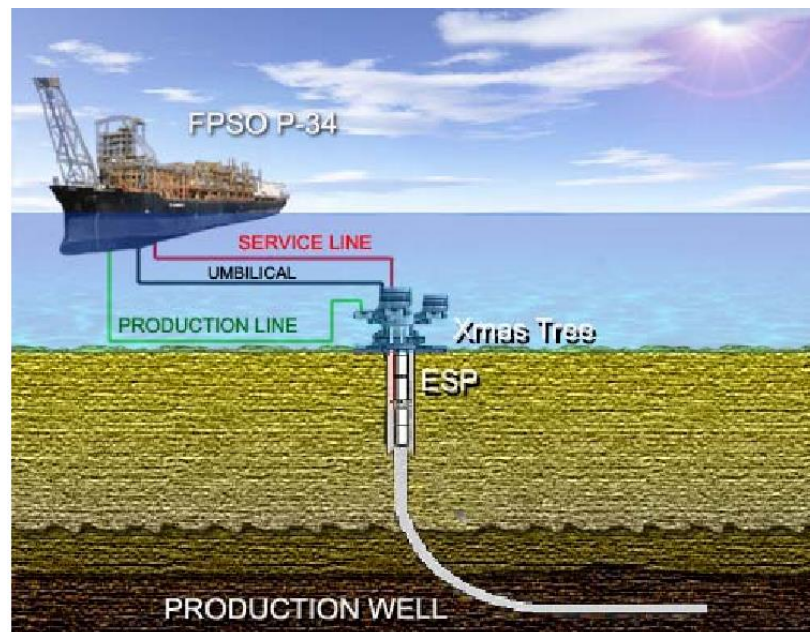


Figure 5.1. An offshore oil and gas production well using electric submersible pumps [1].

Figure 5.2 displays a set of IPR curves for different wells [2]. The production rate gradually falls with time, and after certain number of years, the well becomes economically infeasible meaning the cost of recovery exceeds the profits gained from the oil production. An oil well never attains its maximum inflow performance due to the limitations created by the piping arrangement such as separator, flowline, chokes, tubing string safety valves, etc. and the lift system. The moving fluid through the production tubing exerts backpressure on the system. The backpressure contains the following components [2],

- hydrostatic pressure due to weight of the fluid column,
- frictional pressure due to the interaction of the moving fluid with the tubing system, and
- other potential or kinetic losses associated with the tubing system.

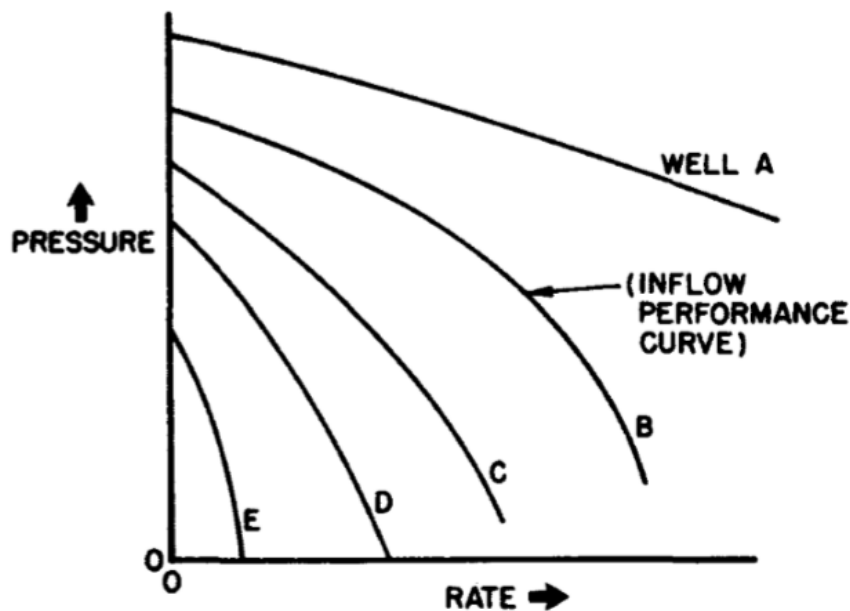
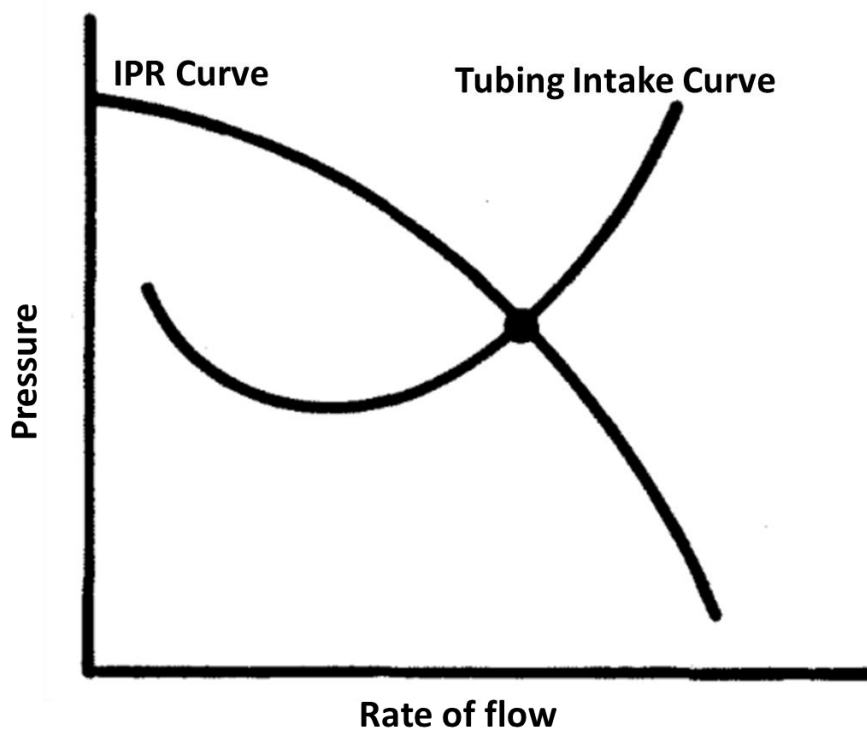
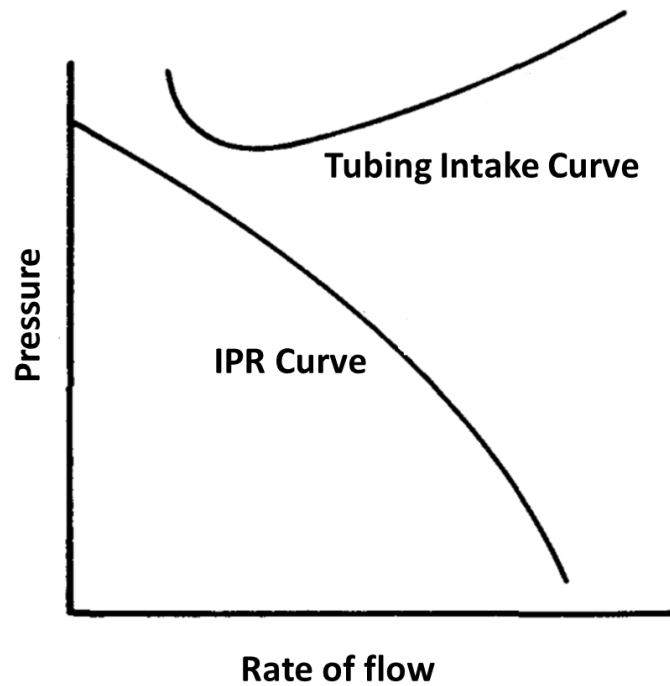


Figure 5.2. Inflow performance relationship (IPR) curves [2].

In order to recover fluid from the reservoir through the well, a certain amount of tubing intake pressure is needed to overcome the backpressure. Figure 5.3a and 5.3b illustrate IPR vs. tubing intake pressure for a stable well and a dead well, respectively. The point of intersection between the IPR curve and the tubing intake pressure curve provides the flow rate. In Figure 5.3b, the tubing intake pressure is too high compared to the IPR curve of the well. Thus, production of fluid from this well is not possible. In order to achieve a desired production rate, an artificial lift method is needed to overcome the bottom-hole pressure of the well. There are several artificial lift techniques currently available such as gas lift, plunger lift, sucker rod pump, hydraulic jet pump, electric submersible pump (ESP), electric submersible progressive cavity pump (ESPCP), hydraulic piston pump and submersible turbine pump [1]-[3] systems.



(a)



(b)

Figure 5.3. IPR vs. tubing intake pressure for a: (a) stable well and (b) dead well [2].

Figure 5.4 displays configurations of the major types of artificial lift systems. There are basically two categories of artificial lift systems. The first category is the pump assisted artificial lift system and the other one is non-pump assisted lift techniques. Among pump assisted lift systems, the rod pump is the most widely used artificial lift system in the world. Gas lift is a non-pump assisted artificial lift system that injects compressed gas inside the well either continuously or intermittently for lowering the back pressure, allowing the reservoir pressure to lift fluids through the production well.

An artificial lift system produces a predefined amount of tubing intake pressure in the well to recover a desired rate of reservoir fluid. Figure 5.5 illustrates pressure vs. flow rates of a well for different artificial lift techniques.

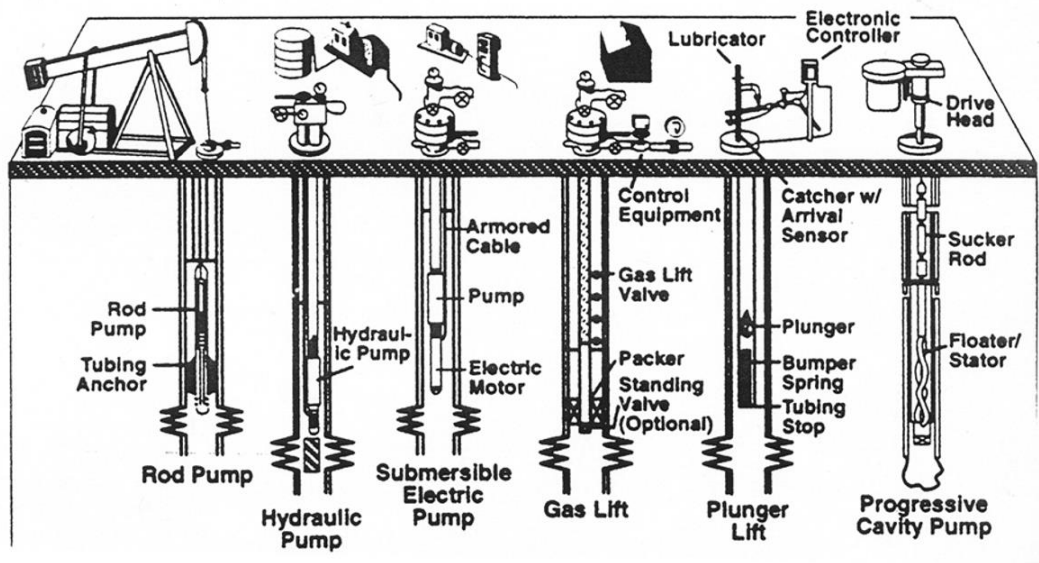


Figure 5.4. Major types of artificial lift systems [3].

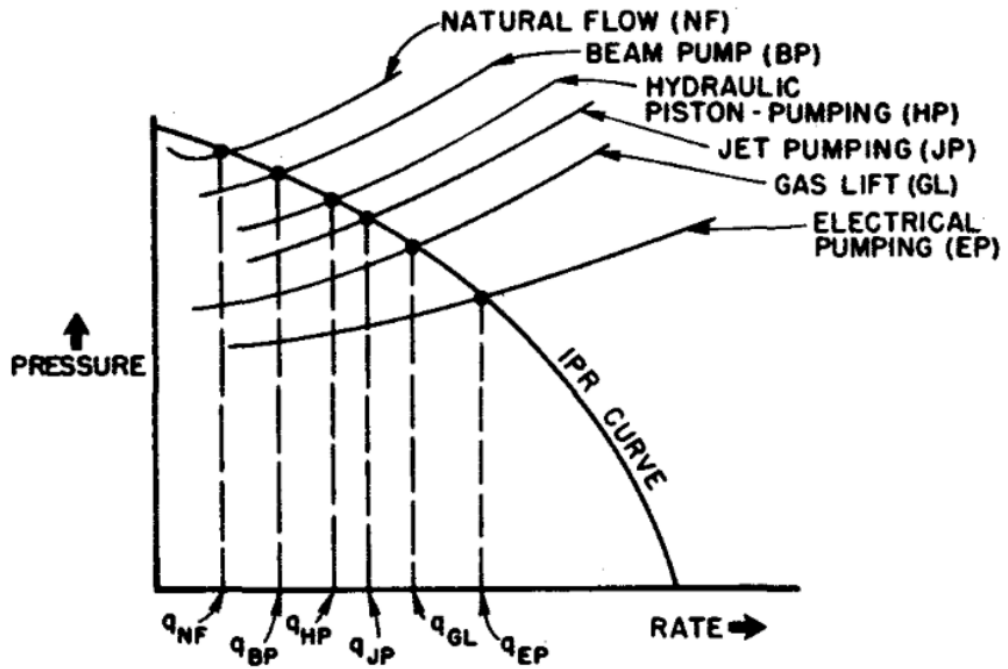


Figure 5.5. Pressure vs. flow rates of a well for different artificial lift techniques [3].

The selection of an artificial lift does not only depend on the available maximum flow rate but on many selection criteria. The list of criteria for selecting an artificial lift system is given below,

- The depth/flow rate of a lift system
- Relative merits and demerits
- Use of expert computer programs
- Net Present Value (NPV) comparison
- Run life

The depth of the well and the desired rate of fluid flow are the primary criteria for selecting an appropriate artificial lift system. Figure 5.6 illustrates a comparative analysis between the most popular lift techniques in terms of well depth and production rate in barrel per day (BPD). Gas lift provides a wide range of production rates for various well depths. Beam pumps and progressive cavity pumps (PCPs) are suitable for shallow wells. Plunger lift is suitable for ultra-deep wells but it limits the rate of production for deeper wells, because the energy storage increases in the casing annulus as the depth becomes greater. ESP provides the highest fluid production rate. ESPs are capable of working at a higher depth than the gas lift system, and also are competitive with the gas lift system over a wide range of depths. The relative advantages and disadvantages of the artificial lift systems such as system efficiency, simplicity, modularity, applicability for onshore or offshore applications and for different types of well (horizontal, vertical, deviated), etc. are also considered for the selection of an artificial lift system. The NPV and run-life are

very important criteria for the proper selection of a well as the well becomes mature and the price of oil varies over time.

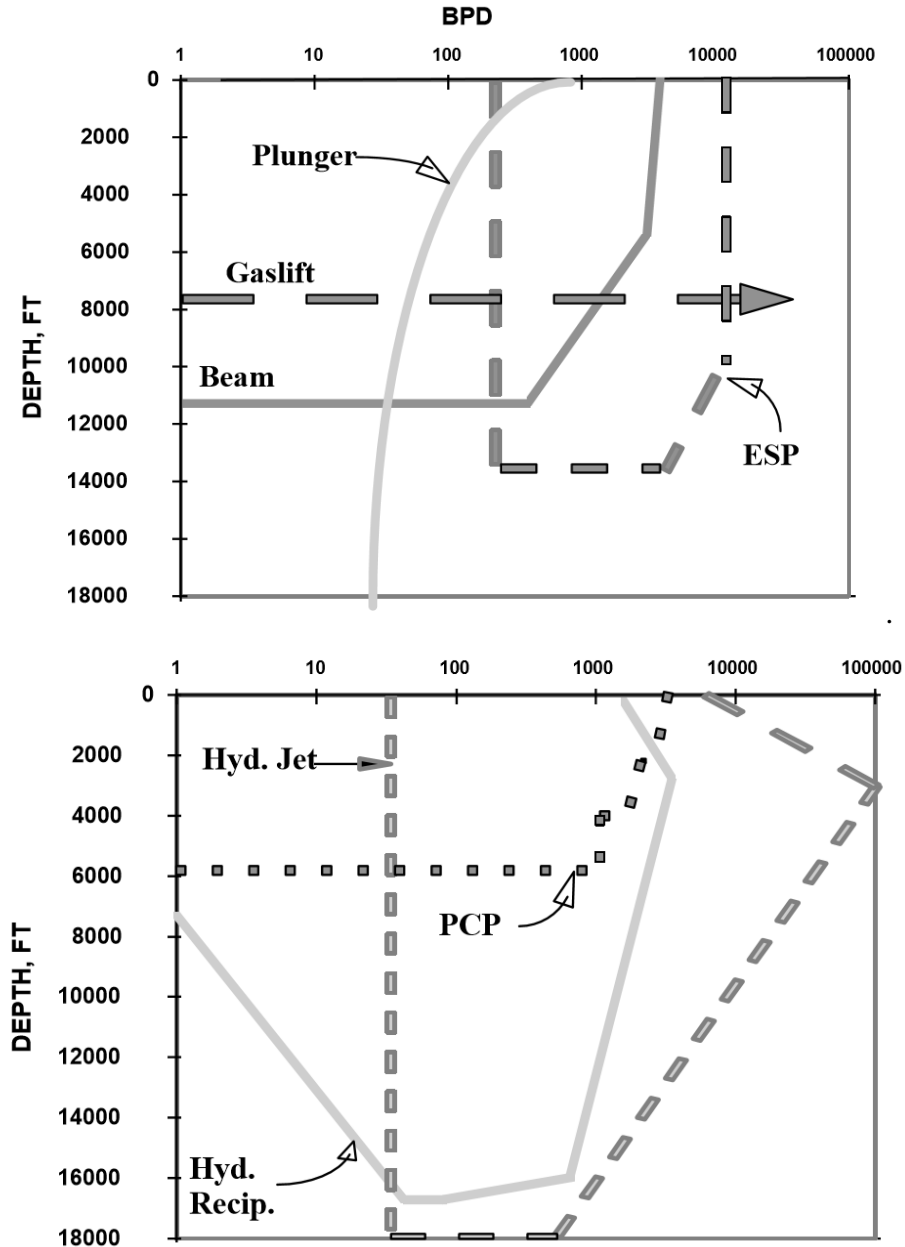


Figure 5.6. Comparative analysis between popular lift techniques in terms of well depth and production rate [3].

Gas lift is the most popular technique among the non-pump assisted artificial lift techniques. It is suitable for both onshore and offshore oil and gas production. However, it suffers from poor lift efficiency and is limited by the well depth. Among the pump assisted lift techniques, the rod pump is the most popular as well as economical artificial lift technique and is suitable for land based oil production systems. ESPs and ESP-PCPs provide high flow rate, suitable for deep wells and also are highly efficient in comparison with other lift techniques. ESPs are suitable for low viscosity fluid recovery whereas ESP-PCPs are applicable for high viscosity fluids such as heavy oil. Figure 5.7 shows the production rate vs. well life of a typical subsea well using natural flow, gas lift and ESP lift. The feasible economic limit (FELs) for each recovery method is shown by point “A”, “B” and “C”, respectively. After an economic limit is surpassed, the respective recovery method becomes infeasible. As wells age, artificial lift is essential towards extending the well life beyond point “A”. Currently in the offshore industry, gas lift is used as the standard artificial lift technique. Gas lift has poor efficiency, lower rates of production, and is economically infeasible for mature wells. Point “B” indicates the state of a mature well where gas lift becomes infeasible. A downhole ESP is a type of artificial lift that boosts the pressure inside subsea reservoirs to achieve higher lift rates than gas lift. Pump assisted recovery provides more system efficiency than any other artificial lift techniques while producing more barrels per day. It is illustrated in Figure 5.7 that the use of ESP enhances the production rate and extends the well life up to point “C”, surpassing the point “B” (Gas Lift FEL). During times of lower oil prices, exploration and production (E&P) companies retract on their offshore drilling programs, and focus on extending the life of existing wells. An ESP based lift technique with a fast and reliable control system

provide an economical alternative to traditional lift methods for the offshore E&P companies to prolong well productions for years to come.

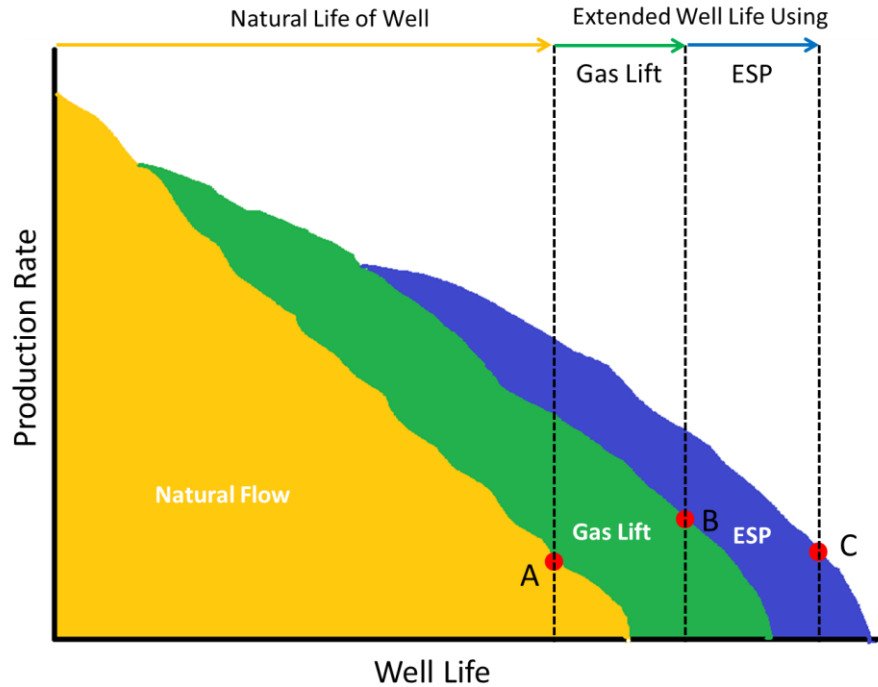


Figure 5.7. Production Rate vs. Well Life.

Direct on-line starting of an electric submersible pump (ESP) system from a fixed frequency ac supply creates significant dynamic stress on the electro-mechanical assembly [4]-[5]. The pump shaft geometry (length and diameter) is primarily accountable for the torsional vibration of the system. It is crucial to model the mechanical dynamics to observe the effects of vibration on the ESP. Severe torsional vibration may occur if the vibrational frequency of the shaft reaches its resonant value. One way to accurately model the dynamics of an ESP system is the multi-physics simulation using finite element analysis [6]. However, multi-physics simulation is computationally

overburdened and requires a high performance computer with multi-core processors. The simulation process is resource exhaustive and is also extremely time consuming.

Another way to model the mechanical dynamics of an ESP system is the approximate lumped parameter approach [4]. Thorsen and Dalva proposed a combined electrical and mechanical model of induction motor driven ESP systems [4]. They have modeled the motor, shafts and pump impellers as equivalent mass spring damper systems. The starting transient mechanical stress on the pump assembly for different starting conditions is observed in their paper. The effects of different shaft diameters as well as shaft lengths on the starting torsional vibration of the ESP are also presented by Thorsen and Dalva.

This chapter presents an analysis of the mechanical dynamics of a hysteresis IPM motor driven electric submersible pump (ESP) system. The modeling of a 5-HP 4-stage 6-inch ESP system is presented in this chapter. A bond graph model of the hysteresis IPM motor ESP drive is used to predict the dynamic behaviour of the drive system during start-up as well as running conditions. The relative twisting motion of the pump shaft is observed, and the effect of the pump shaft geometry on the torsional vibration of the system is investigated. Simulation results obtained using the bond graph model are presented and analyzed in this chapter. The torsional oscillations in a laboratory hysteresis IPM motor drive system during starting under different line frequencies are presented in this chapter.

## **5.2 Mechanical Dynamics of an Electric Submersible Pump System**

An electric submersible pump (ESP) is a motor/pump configuration made up of multi-stage centrifugal pumps connected in series in order to provide the required pump head. The interconnected centrifugal pumps are normally driven by a three phase submersible ac motor. Figure 5.8 illustrates the multi-stage centrifugal pump configuration. The exploded view of an ESP is shown in Figure 5.9. The fluid from the reservoir travels through the porous media and enters the bottom hole. The fluid enters the pump through an intake. There is a seal section between the pump intake and the motor which prohibits the fluid flowing into the motor. The pump rotates at the same speed as the motor. The fluid first passes through the rotating impeller which adds kinetic energy to the fluid. The fluid leaves through the diffuser which converts the kinetic energy into potential energy, increases the fluid pressure and guides the fluid to the next pump stage. Thus, each stage adds enough pressure to the fluid so that it can reach the well head which is attached to the tubing string. The number of pump stages depends on the required pump volumetric flow rate and the head (height) of the pump.

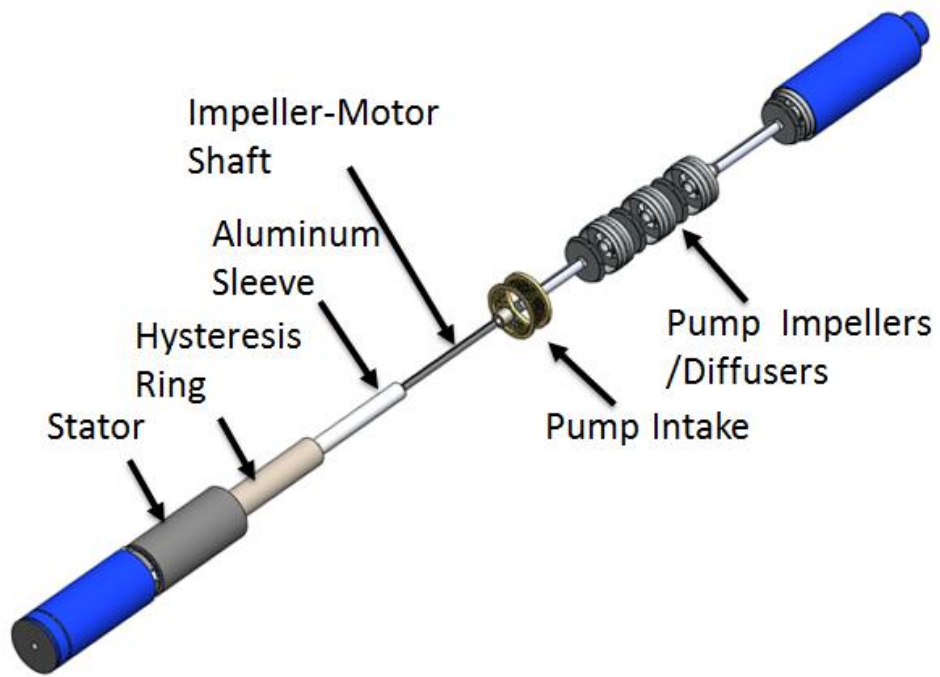


Figure 5.8. A hysteresis IPM motor equipped ESP.

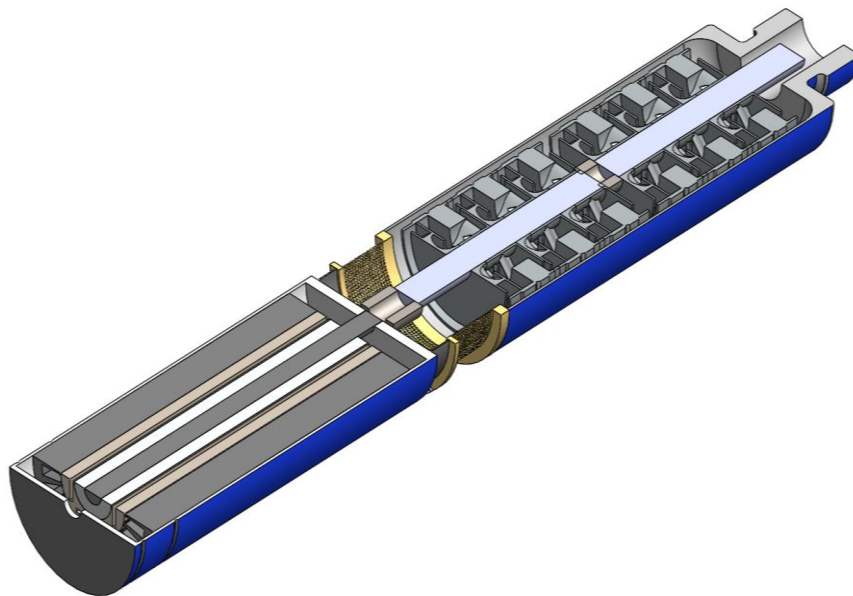


Figure 5.9. Cross sectional view of a multi-stage ESP.

The rotor of a submersible hysteresis interior permanent magnet (IPM) motor is demonstrated in Figure 5.10. The performance curves of a 5-HP 4-stage 6-inch submersible pump are depicted in Figure 5.11. The system curve is shown with the red line. The intersection between the system curve and the total dynamic head curve of the pump determines the pump operating point i.e. the pump flow rate and the pump head. The pump can be operated at its best efficiency operating point with the aid of a variable speed drive (VSD). The pump volumetric flow rate  $Q$  depends on the rotational speed of the impeller and can be expressed as,

$$Q = k_q N_s \quad (5.1)$$

where  $k_q$  is a proportional constant which depends on the impeller geometry and  $N_s$  is rotational speed of the impeller in rpm.



Figure 5.10. Rotor of a submersible hysteresis IPM motor.

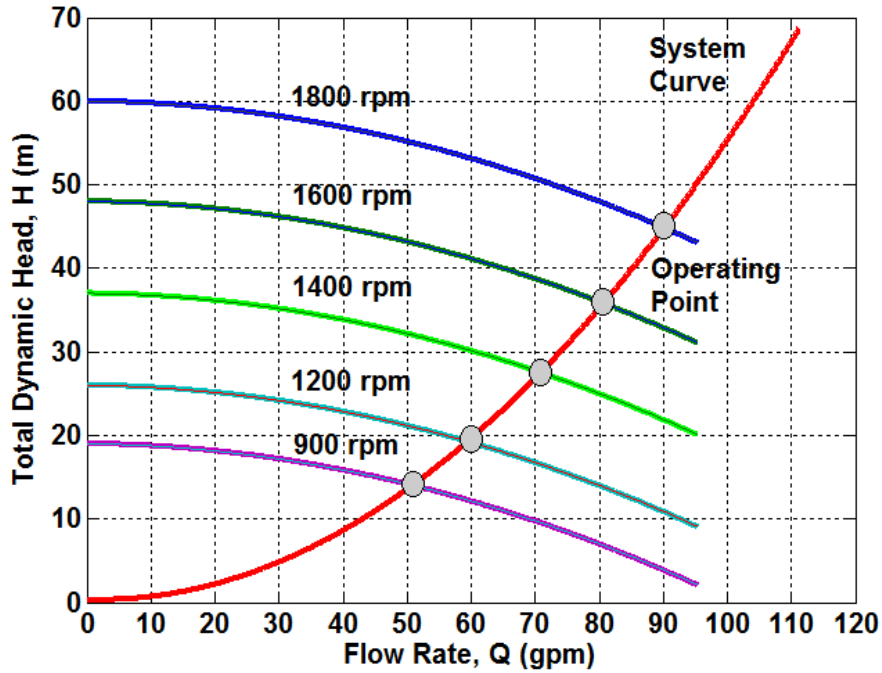


Figure 5.11. Characteristics curves of a variable speed ESP.

The operating head of the pump is calculated from the system curve and is given below,

$$H = k_{h2}Q^2 + k_{h1}Q + H_0 \quad (5.2)$$

where  $H$  is the operating head,  $k_{h2}$  and  $k_{h1}$  are proportional constants and  $H_0$  is the minimum head of the pump.

In a centrifugal pump, the volume of the fluid delivered by the pump against a constant pressure head is proportional to the power of the motor. So, the required load torque for the pump is proportional to the square of the speed of the motor. As a result, the load torque is relatively small at starting. The required mechanical input power  $P_{esp}$  to a centrifugal pump is given below [7],

$$P_{esp} = HQg \frac{1}{\eta} \quad (5.3)$$

where  $P_{esp}$  is the mechanical input power to the ESP,  $g$  is the gravitational acceleration and  $\eta$  is the pump efficiency.

Figure 5.12 illustrates a lumped element model of the 4-stage ESP system. The model is used to investigate mechanical dynamics of the ESP system. The following assumptions are considered during the lump element modeling of the ESP drive chain:

1. The motor is modelled as a lumped body with inertia and viscous damping. The electro-magnetic torque obtained from electrical equivalent circuits of the hysteresis IPM motor is considered as the driving torque for the ESP system.
2. Each of the pump impellers is modeled as a single lumped inertial body with a fluid viscous damping torque and a load torque [4].
3. The load torque of the impeller is modeled as a function of the square of the speed.
4. The shaft is considered as a massless spring system. Each of the shaft segments is modeled as a spring with a torsional stiffness factor and a viscous damping coefficient.

The mechanical dynamics of the ESP system are modelled as a torsional mass spring damper system similar to [4]. The equations for modeling ESP dynamics are provided below,

**Between Motor and Impeller 1:**

$$J_m \frac{d^2\theta_m}{dt^2} + D_m \frac{d\theta_m}{dt} + D_{m1} \left( \frac{d\theta_m}{dt} - \frac{d\theta_1}{dt} \right) + C_{m1}(\theta_m - \theta_1) = T_e \quad (5.4)$$

**Between Impeller 1 and Impeller 2:**

$$J_1 \frac{d^2\theta_1}{dt^2} + D_1 \frac{d\theta_1}{dt} + D_{m1} \left( \frac{d\theta_1}{dt} - \frac{d\theta_m}{dt} \right) + C_{m1}(\theta_1 - \theta_m) + D_{12} \left( \frac{d\theta_1}{dt} - \frac{d\theta_2}{dt} \right) + C_{12}(\theta_1 - \theta_2) = -K_{l1} \left( \frac{d\theta_1}{dt} \right)^2 \quad (5.5)$$

**Between Impeller 2 and Impeller 3:**

$$J_2 \frac{d^2\theta_2}{dt^2} + D_2 \frac{d\theta_2}{dt} + D_{12} \left( \frac{d\theta_2}{dt} - \frac{d\theta_1}{dt} \right) + C_{12}(\theta_2 - \theta_1) + D_{23} \left( \frac{d\theta_2}{dt} - \frac{d\theta_3}{dt} \right) + C_{23}(\theta_2 - \theta_3) = -K_{l2} \left( \frac{d\theta_2}{dt} \right)^2 \quad (5.6)$$

**Between Impeller 3 and Impeller 4:**

$$J_3 \frac{d^2\theta_3}{dt^2} + D_3 \frac{d\theta_3}{dt} + D_{23} \left( \frac{d\theta_3}{dt} - \frac{d\theta_2}{dt} \right) + C_{23}(\theta_3 - \theta_2) + D_{34} \left( \frac{d\theta_3}{dt} - \frac{d\theta_4}{dt} \right) + C_{34}(\theta_3 - \theta_4) = -K_{l3} \left( \frac{d\theta_3}{dt} \right)^2 \quad (5.7)$$

**Impeller 4:**

$$J_4 \frac{d^2\theta_4}{dt^2} + D_4 \frac{d\theta_4}{dt} + D_{34} \left( \frac{d\theta_4}{dt} - \frac{d\theta_3}{dt} \right) + C_{34}(\theta_4 - \theta_3) = -K_{l4} \left( \frac{d\theta_4}{dt} \right)^2 \quad (5.8)$$

$J_m$  is the inertia of the motor;

$J_1 \dots J_4$  are the inertias of impellers 1...4, respectively;

$D_m$  is the viscous damping coefficient of the motor;

$D_1 \dots D_4$  are the viscous damping coefficients of impellers 1...4, respectively;

$K_{l1} \dots K_{l4}$  are the load torque coefficients of impellers 1...4, respectively;

$C_{m1}$  is the compliance (inverse of stiffness) of the shaft between motor and impeller 1;

$C_{12}$ ,  $C_{23}$  and  $C_{34}$  are the compliances of the shafts between the impellers 1...4, respectively;

$D_{12}$ ,  $D_{23}$  and  $D_{34}$  are the viscous damping coefficients of the shafts between the impellers 1...4, respectively;

$\theta_m$  is the angular position of the motor; and

$\theta_1 \dots \theta_4$  are the angular positions of the impellers 1...4, respectively.

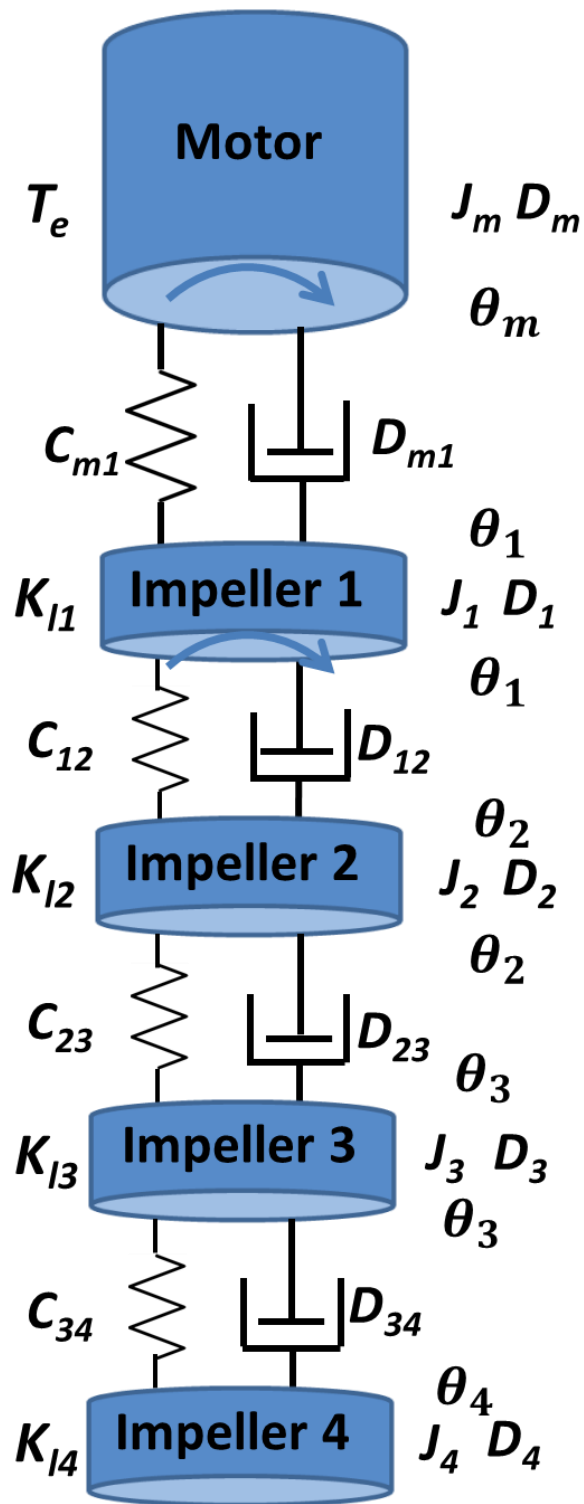


Figure 5.12. A lumped element model of the 4-stage ESP system.

### 5.3 Bond Graph Modeling of ESP-Dynamics

A bond graph is a graphical approach to model a dynamic system [8]-[11]. Bond graphs use a small set of generalized elements to model energy storage, dissipation, boundary conditions, energy transformations and gyrations in a system. It also applies the generalized Kirchoff's laws for multiple energy domains. Thus, a bond graph is a powerful tool to model the dynamics of a system involving mechanical, electrical, and electromagnetic elements such as the hysteresis interior permanent magnet (IPM) ESP drive system. The dynamics of the ESP presented in (5.4)-(5.8) can be investigated using a bond graph model of the ESP system.

The word bond graph of the 4-stage hysteresis IPM ESP drive system is illustrated in Figure 5.13. Each stage is represented by a rotating impeller driven by the hysteresis IPM motor. The input and output of each bond graph element is power, which is the product of conjugate generalized effort and flow variables. Power bonds are labelled with a half arrow. Small "causal strokes" normal to the power bonds indicate whether an effort or flow is the output of the adjacent element's constitutive law. The power variables used for the mechanical portion of the simulation are torque,  $\tau$  and angular velocity,  $\omega$ .

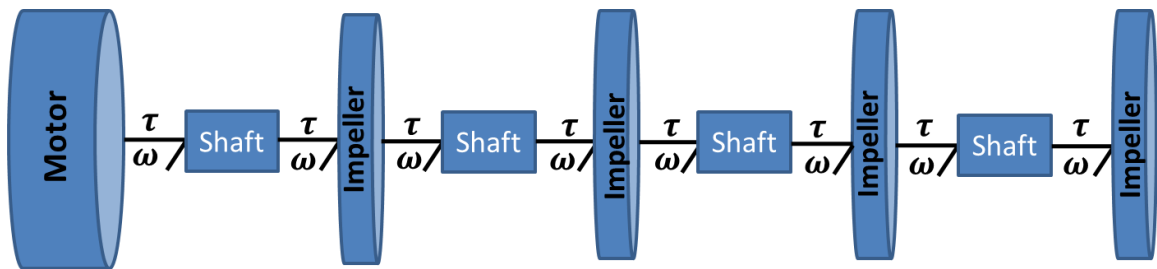


Figure 5.13. Word Bond Graph Model of an ESP System.

The bond graph model of a hysteresis IPM motor is developed using the equivalent circuits presented in chapter 3. Figure 5.14 shows the electromagnetic coupling between electrical and mechanical systems. The inductive coupling between the stator and rotor are considered in the  $d^r-q^r$  reference frame rotating with the rotor electrical angular velocity  $\omega_e$ . The conversion from electrical speed to mechanical speed is performed using a gearbox. The gear ratio is  $\frac{P}{2}:1$ , where  $P$  is the number of poles in the motor.

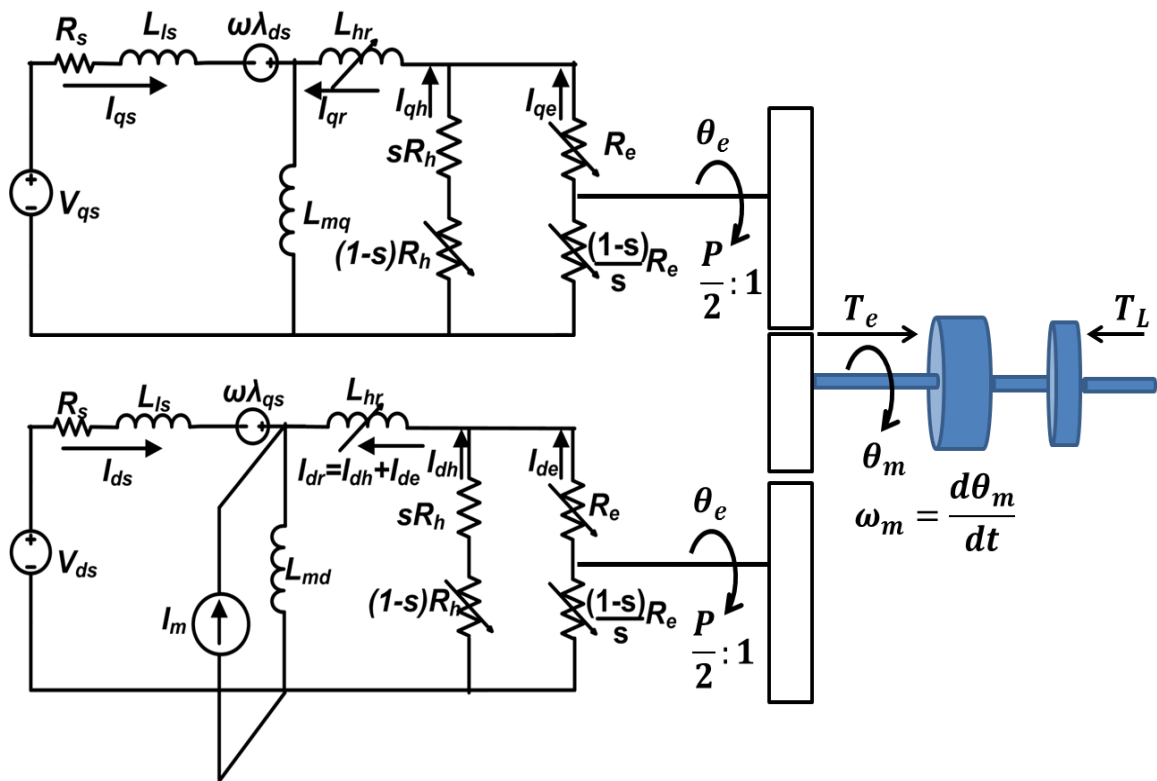


Figure 5.14. Electromagnetic Coupling between electrical and mechanical system.

Figure 5.15 illustrates a two-level interconnection between the  $\{a, b, c\}$  bond graph model and the  $\{d, q\}$  bond graph model.  $\mathbf{Se}$  is the 3-phase input voltage source,  $\mathbf{TF}$  is a transformer that converts voltages from the  $\{a, b, c\}$  reference frame to the  $\{\alpha, \beta\}$

reference frame. **MTF** is a modulated transformer that converts voltages from the  $\{\alpha, \beta\}$  reference frame to the  $\{d, q\}$  frame using the rotor electrical position  $\theta_r$ .

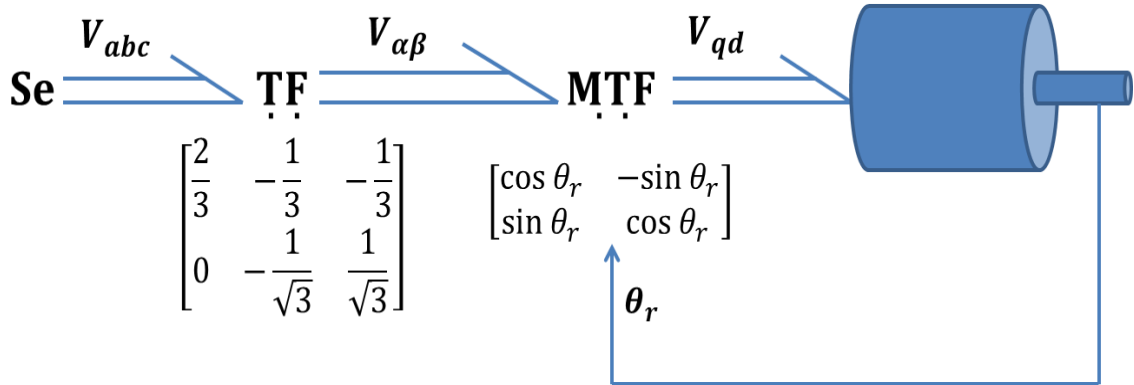
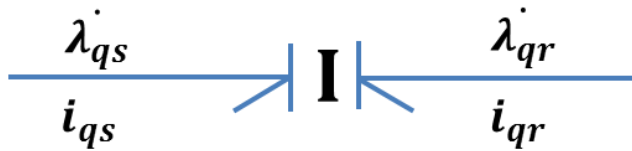


Figure 5.15. A 2-level interconnection between  $\{a, b, c\}$  and  $\{d, q\}$  bond graph models.

The linear relationships between the stator flux linkages and currents, and the rotor flux linkages and currents are represented in terms of self and mutual inductances. These relationships are provided by using the generalized inertia (**I**) fields in the bond graph [11]. Figure 5.16 shows the coupling between the stator and rotor state variables.

The electromagnetic torque and the induced voltages are calculated using the state equations of the hysteresis IPM motor. The electromagnetic torque equation contains the flux and current terms. A gyrator structure for the torque and the induced voltages is illustrated in Figure 5.17. The modulated gyrator enforces the relations between the electromagnetic torque  $\tau_e$  and the  $d$ - $q$  axis currents ( $i_{ds}$  and  $i_{qs}$ ) as well as the relation between the induced voltages ( $e_{ds}$  and  $e_{qs}$ ) and the rotor angular speed  $\omega_r$ .

$$\begin{bmatrix} \dot{i}_{ds} \\ \dot{i}_{dr} \end{bmatrix} = \frac{1}{L_{dr}L_{ds} - L_{md}^2} \begin{bmatrix} L_{dr} & -L_{md} \\ L_{md} & L_{ds} \end{bmatrix} \begin{bmatrix} \dot{\lambda}_{ds} - \dot{\lambda}_m \\ \dot{\lambda}_{dr} - \dot{\lambda}_m \end{bmatrix}$$



$$\begin{bmatrix} \dot{i}_{qs} \\ \dot{i}_{qr} \end{bmatrix} = \frac{1}{L_{qr}L_{qs} - L_{mq}^2} \begin{bmatrix} L_{qr} & -L_{mq} \\ L_{mq} & L_{qs} \end{bmatrix} \begin{bmatrix} \dot{\lambda}_{ds} \\ \dot{\lambda}_{dr} \end{bmatrix}$$

Figure 5.16. I-field relations and casualties for the rotor and the stator in the  $d$ - $q$  axis

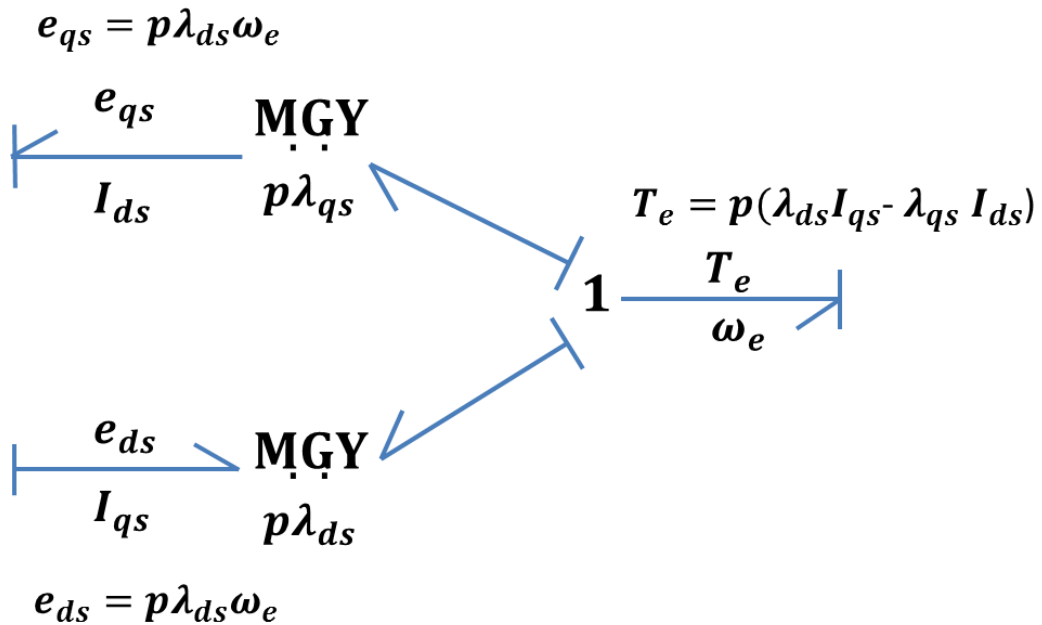


Figure 5.17. Gyrator structure for torque and induced voltages.



The lumped segment approach is used to model torsional dynamics of the shafts. In the lumped segment approach, the system is divided into a number of elements, interconnected with springs [9]. This model is a more cumbersome bond graph representation, and the accuracy of the model depends on the number of elements considered. However, analytic mode shapes and natural frequencies need not be determined. A total of 4 segments are used in the dynamic model for each shaft. Figure 5.19 depicts the torsional dynamic sub-model for a single shaft segment.

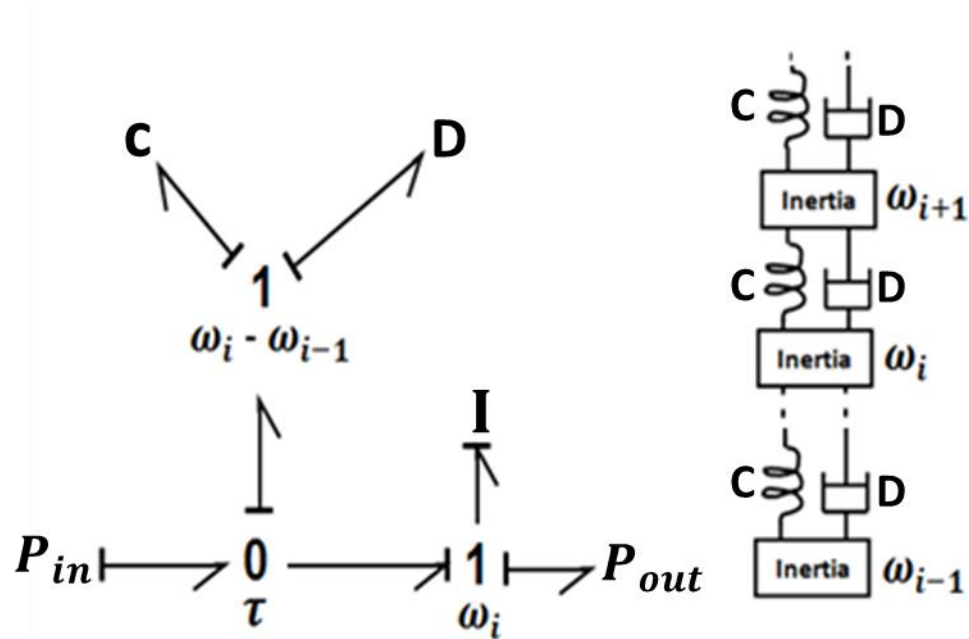


Figure 5.19. A bond graph torsional model of a shaft-segment.

The pump impeller is modeled as a single lumped inertial body with a fluid viscous damping torque and a load torque. The damping torque and the load torque for the impellers are estimated as  $D\omega$  and  $K_l\omega^2$ , respectively.  $D$  and  $K_l$  are viscous damping

factor and impeller load factor, respectively. The bond graph dynamic model of an impeller is shown in Figure 5.20.

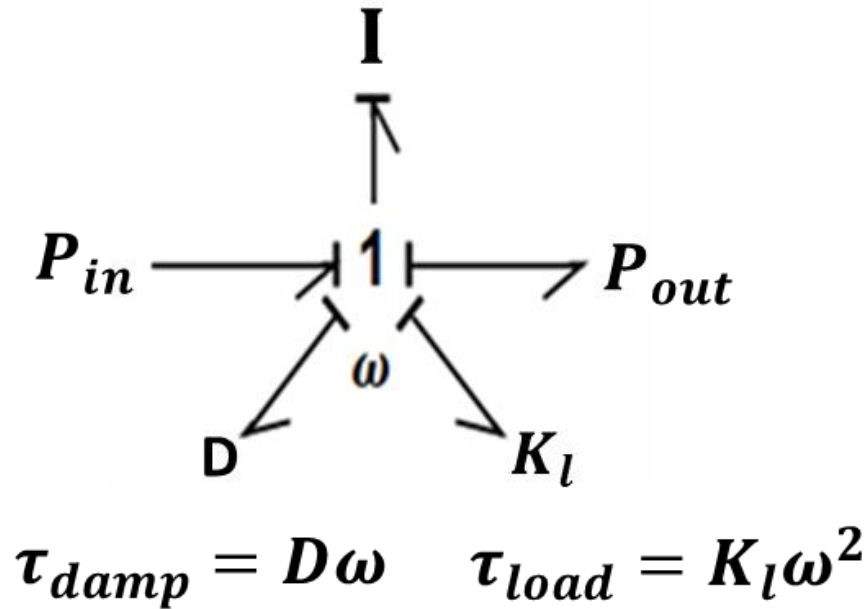


Figure 5.20. A bond graph torsional model of an impeller.

#### 5.4 Simulation Results

Simulations are carried out for a 90 GPM 4-stage electric submersible pump system driven by a 5 hp, 3-phase, 1800 rpm, 240V hysteresis IPM motor. *20sim*® software is used for modeling of bond graphs. Figure 5.21 illustrates the run-up responses of the ESP system for different motor shaft lengths. The motor is loaded at 75% of its rated load. The length of the motor shaft which is connected to the multi-stage pump is varied from 500mm to 1500mm. The hysteresis IPM motor is started directly from a fixed frequency 60 Hz line supply. Due to its hysteresis ring, the motor generates the starting torque for

self-starting and overcomes the magnet brake torque while ramping up towards the command speed. The motor synchronizes at the command frequency with some speed overshoots and undershoots. These oscillations happen due to the hysteresis phenomenon in the rotor. The hysteresis lag angle goes through some cyclic oscillations before it settles down to a steady state value. It is found that the length of the shaft has negligible impact on the speed response of the motor.

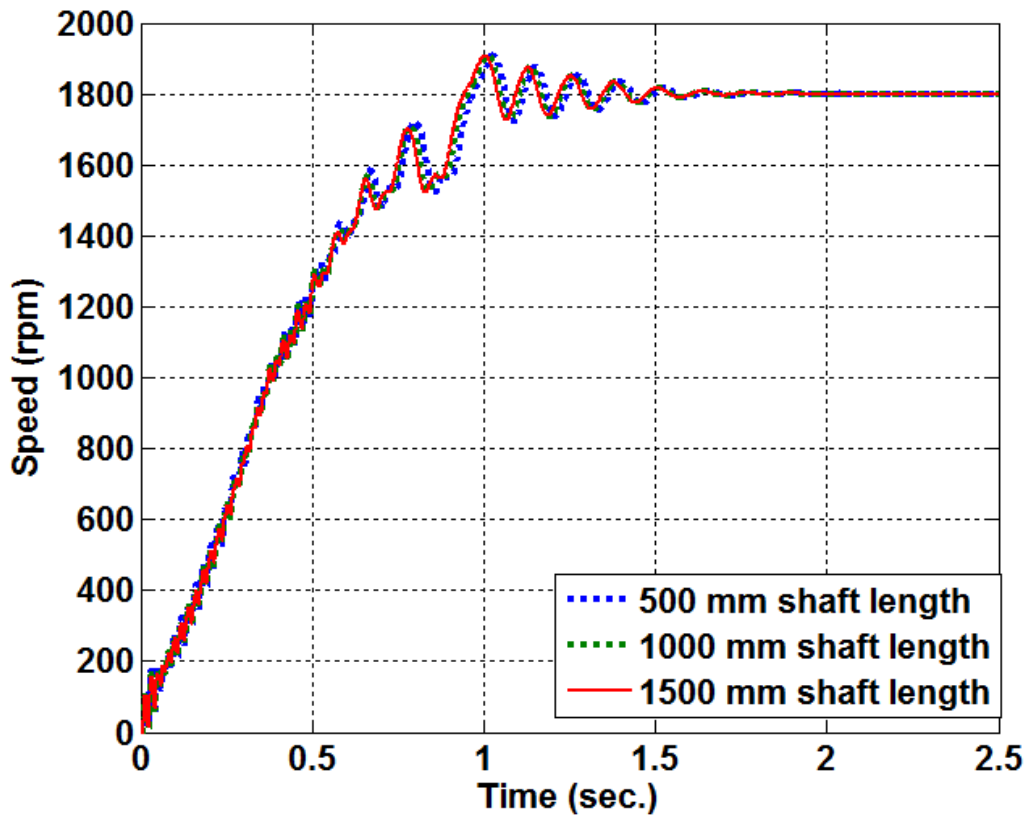


Figure 5.21. Speed responses of the motor for different shaft-lengths.

The electromagnetic torque responses of the hysteresis IPM ESP drive for different shaft lengths are illustrated in Figure 5.22. The developed torque is comprised of an average asynchronous torque and a pulsating torque. The average asynchronous torque is a combination of the hysteresis torque, the eddy current torque and the magnet brake torque. The presence of permanent magnets as a current source in the rotor, there is a pulsating torque superimposed on the average asynchronous torque. The pulsating torque assists the motor to a fast acceleration towards the synchronous speed. During the period of synchronization, the torque pulsation dies out and turns into the synchronous torque which is a combination of the magnet alignment torque and the reluctance torque. As the length of the shaft is increased, the amplitude of the pulsating torque goes down but the frequency of torque pulsations remains the same. This phenomenon is illustrated in Figure 5.22. Thus, as the shaft length increases, the system becomes more damped.

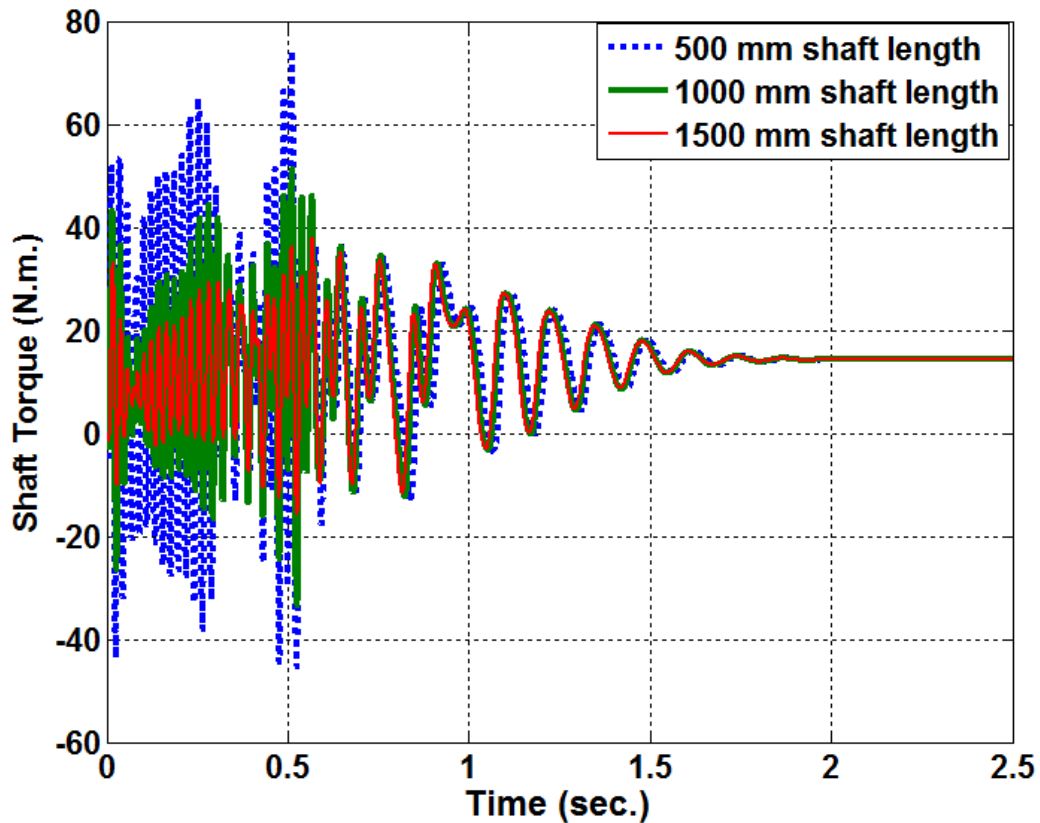


Figure 5.22. Torque responses of the motor for different shaft-lengths.

Figures 5.23 and 5.24 demonstrate the speed and the torque responses of the ESP drive, respectively, for different diameters of the shaft. The length of the shaft and the impeller loads are kept constant at 1000mm long and 75% of the rated load. The magnitude and the frequency of torque oscillations increase as the diameter of the shaft becomes larger. This also affects the motor run-up responses and reduces the motor's synchronization capability, taking a longer time to reach the steady state.

The speed responses of the impellers are depicted in Figure 5.25. The length and diameter of the shafts are considered as 1000mm and 25mm, respectively. The impeller

loads are kept constant at 75% of the rated load. The output shaft torque of the motor and shaft torques between the impellers are displayed Figure 5.26. The system is becoming more damped as the torque is being transmitted from one impeller shaft to the others. The magnitude and frequency of the torque oscillations are much lower in the case of shaft 4 in comparison to the motor output torque transmitted through the shaft 1.

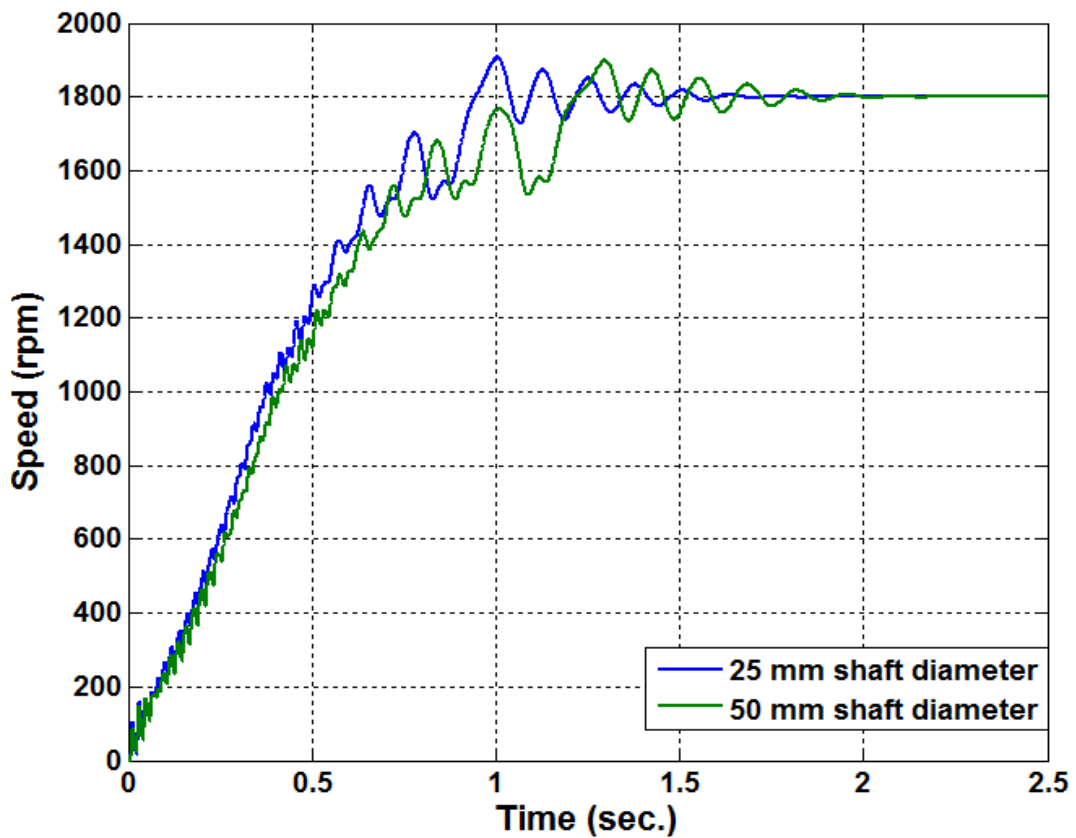


Figure 5.23. The speed response of the motor for different shaft-diameters.

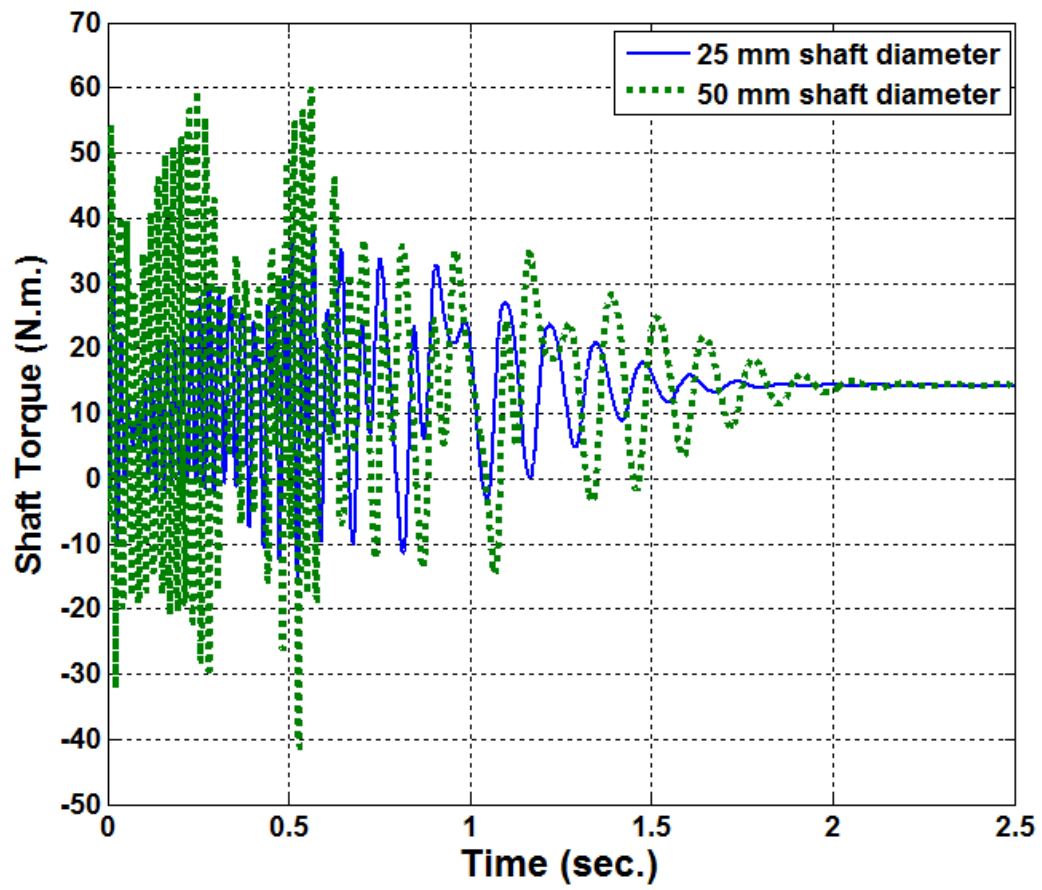


Figure 5.24. Torque responses of the motor for different shaft-diameters.

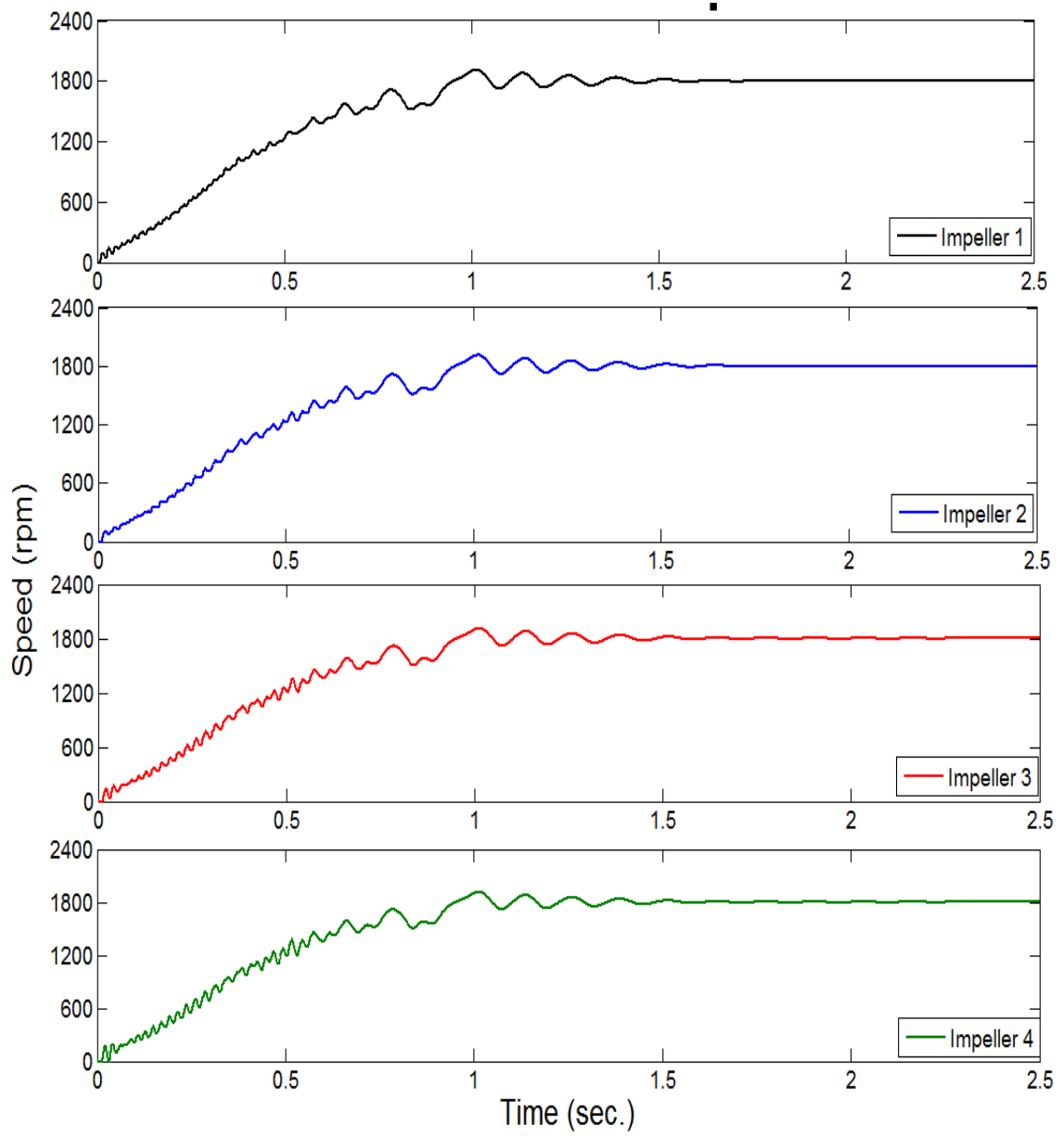


Figure 5.25. Speed responses of the ESP impellers.

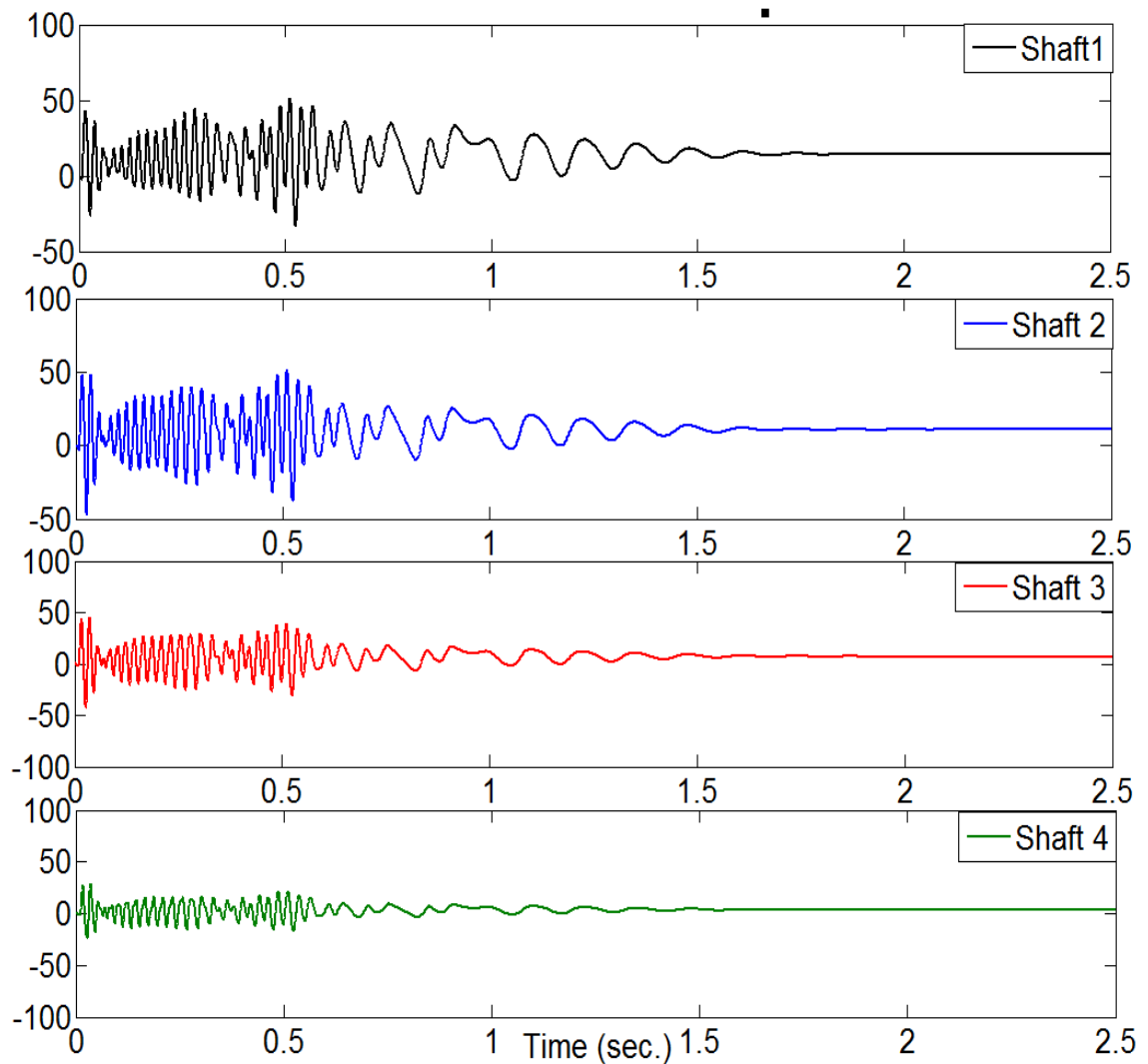
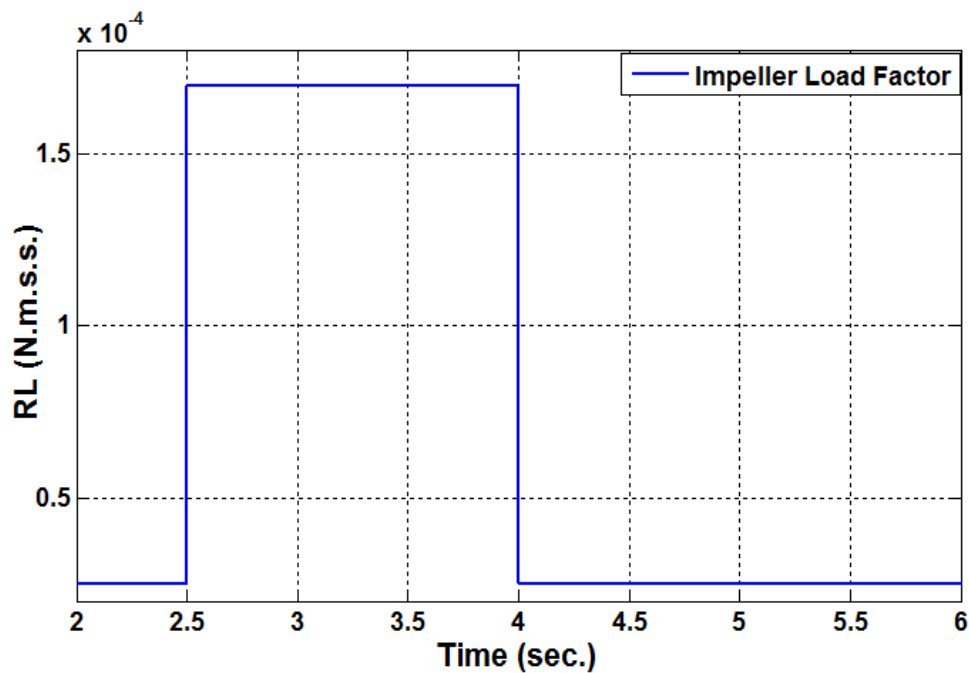


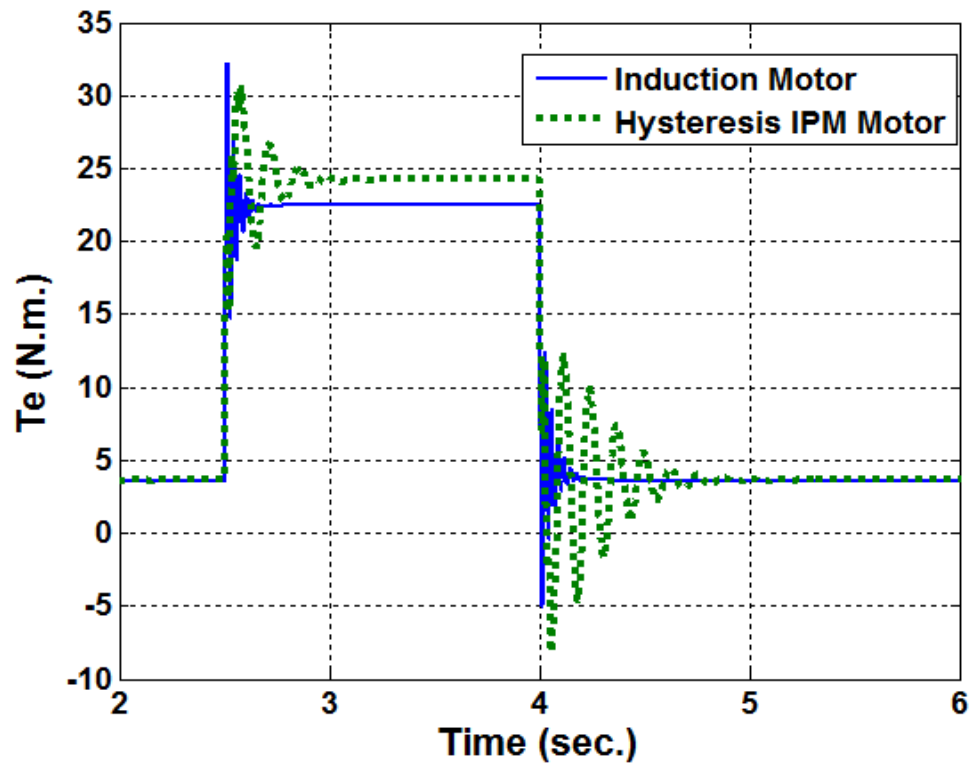
Figure 5.26. The shaft torque response of the ESP.

The comparative performances of a squirrel cage induction motor (IM) ESP drive system and a hysteresis IPM motor ESP drive system are displayed in Figures 5.27a-5.27d. Both the IM and hysteresis IPM motors are rated as 5-HP 3-phase 1800-rpm 240V, and are supplied from the same 60 Hz balanced AC supply. The impeller load factor is suddenly changed to apply the rated load to the motor as shown in Figure 5.27a. As the load torque becomes higher, the induction motor slows down and the slip becomes almost

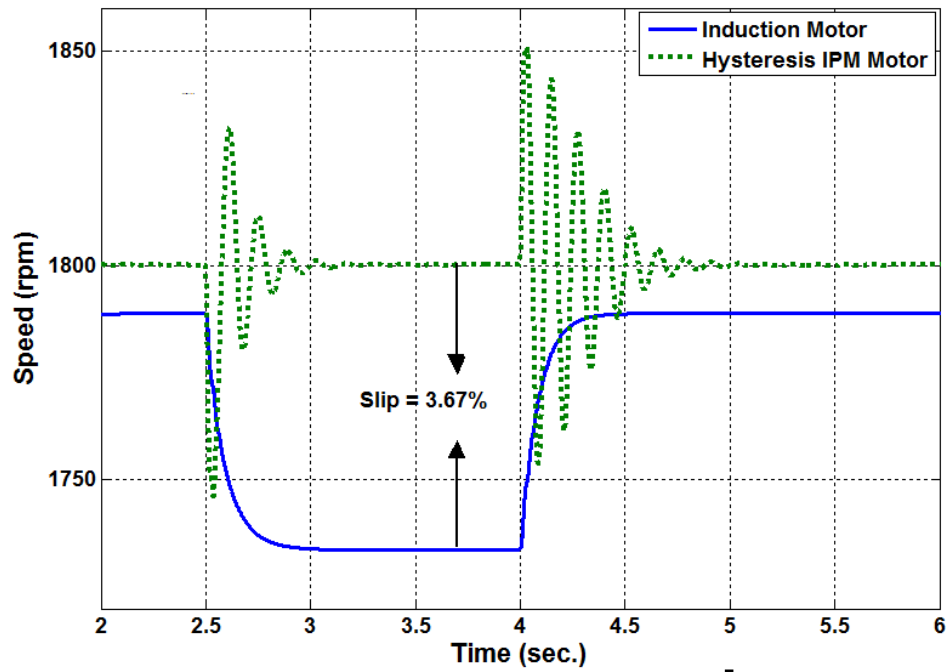
3.67%. This phenomenon results in higher slip losses which in turn increases the temperature of the IM motor and reduces the efficiency as well as the thermal reliability of the ESP. However, in the case of the hysteresis IPM motor, the speed remains the same as the magnets produce the necessary excitation to sustain the load change. At this point, the hysteresis ring works as a damper to stabilize the rotor to remain at the synchronous speed. Figures 5.27b and 5.27c demonstrate the speed and torque responses, respectively, of the IM and hysteresis IPM motor ESP drive systems for a sudden change in the load torque. The input phase current of the IM drive and hysteresis IPM motor drive are shown in Figure 5.27d. The IM draws more current from the line than the hysteresis IPM motor as the load increases. As a result, a hysteresis IPM motor ESP drive has a higher efficiency at full-load than that of an IM-ESP drive.



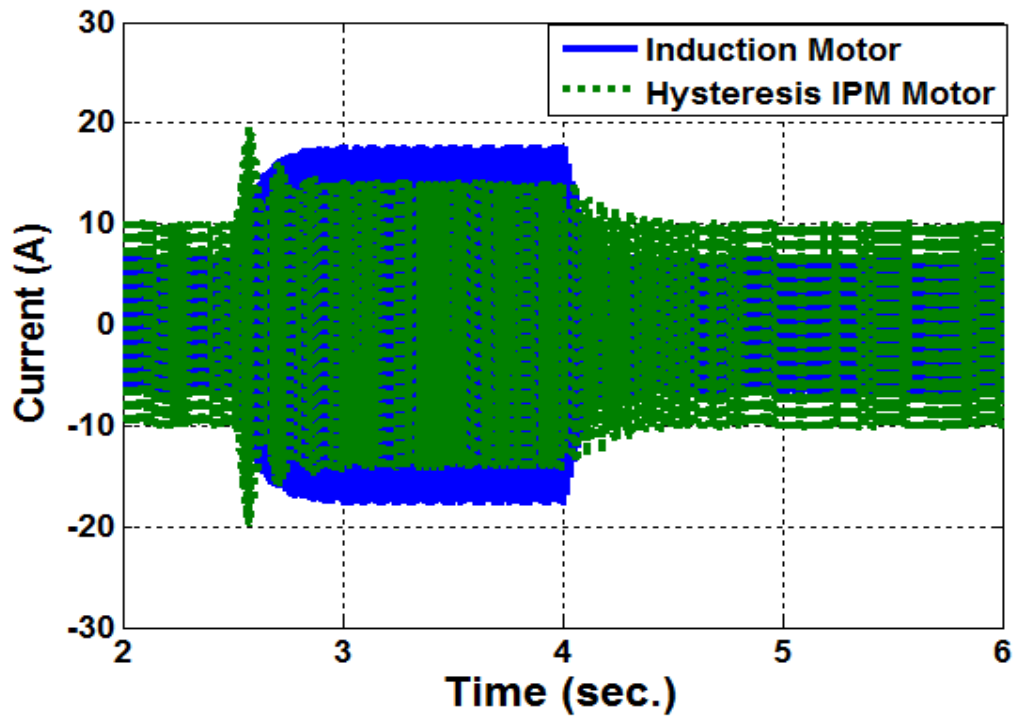
(a)



(b)



(c)



(d)

Figure 5.27. Comparative performances between IM-ESP and hysteresis IPM-ESP drives: (a) impeller load factor (b) shaft torque (c) shaft speed and (d) input line current.

### 5.5 Experimental Results

The experimental testing has been performed on a Mawdsley generalized machine. The stator of the machine is rated at 3-phase 4-pole 208V with delta connected double layer windings. The rotor of the Mawdsley machine is replaced by a 36% Cobalt-Steel hysteresis IPM rotor with Nd-B-Fe magnets. The block diagram of the overall system set-up is displayed in Figure 5.28. The motor is the laboratory prototype hysteresis IPM motor. The motor is lightly loaded by a dc generator that emulates the ESP load torque. The motor is started from a variable frequency power supply. The power supply is

configured to have a fast acceleration time for the motor. To observe the effect of the shaft geometry on the motor run-up performances, the shaft of the motor is chosen as 1000mm while the diameter of the shaft is configured as 50mm. Based on simulation results presented in section 5.4, a 1000 mm long motor shaft with an outer diameter of 50 mm provides low torsional vibration.

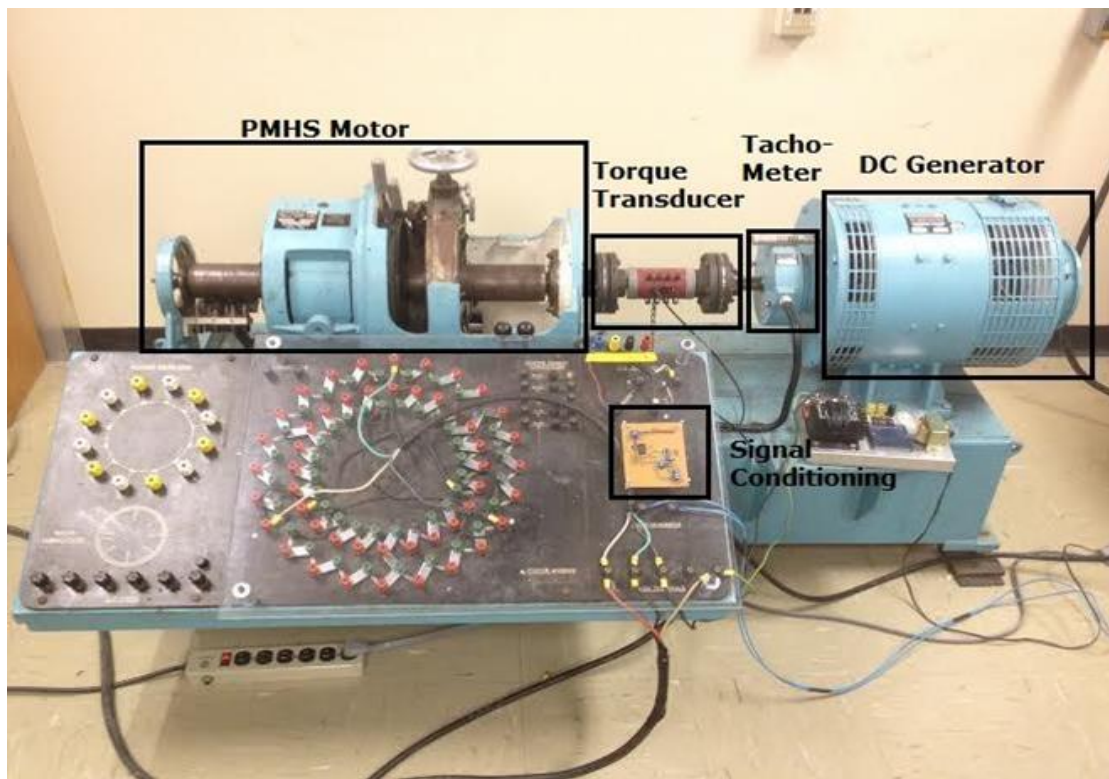
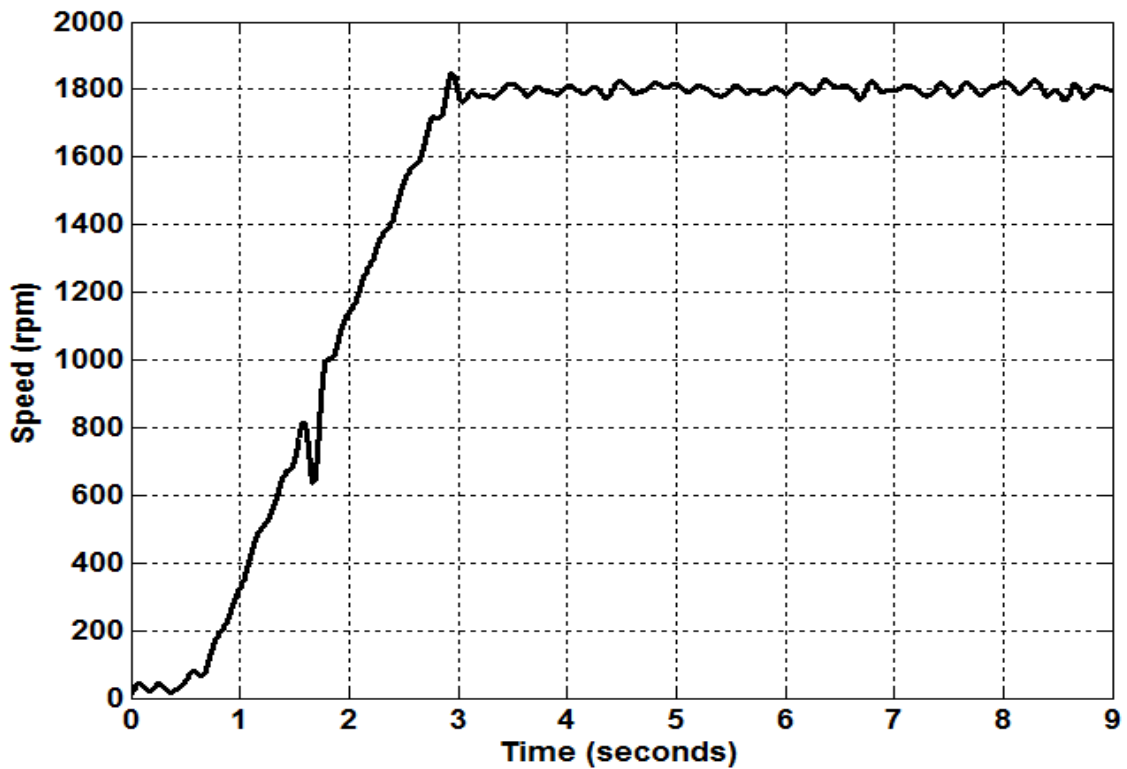


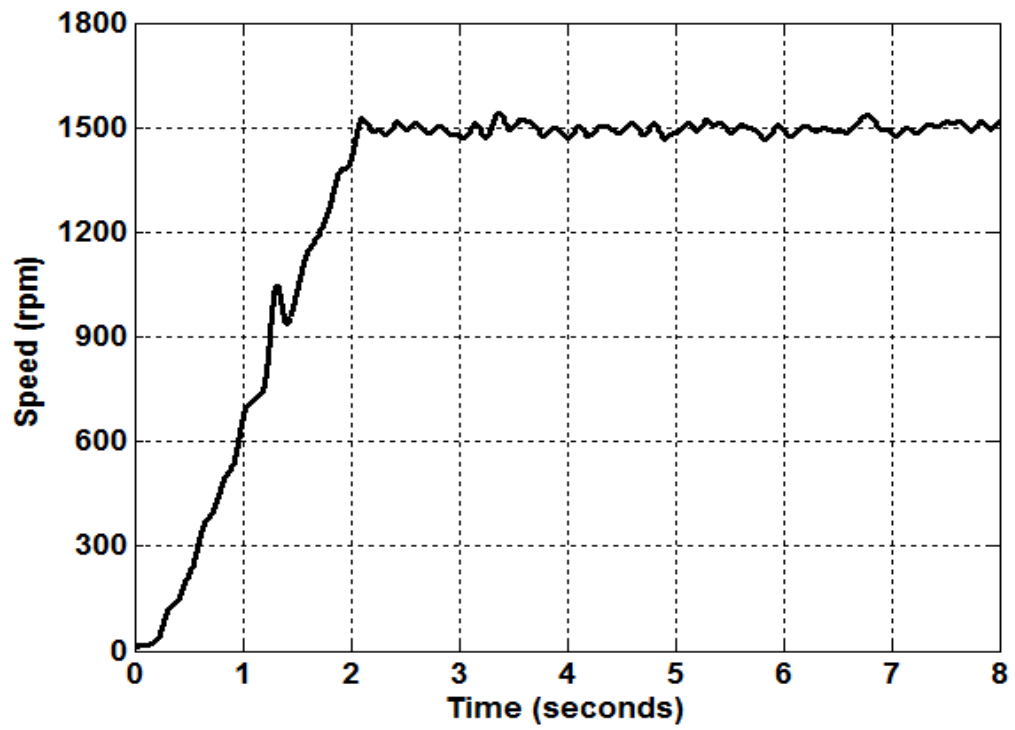
Figure 5.28. Experimental test set-up.

The run-up performance of the motor for 60 Hz and 50 Hz command frequencies are illustrated in Figures 5.29a and 5.29b, respectively. After a successful start, the motor ramps up smoothly towards the synchronous speed. Due to torque pulsations, there are few speed reversals in the run-up response of the motor. There is no significant

mechanical vibration during the start-up. The synchronization process commences at  $t=3$ s and the motor synchronizes with few speed overshoots and undershoots around the synchronous speed. The instantaneous torque waveforms for 60 Hz and 50 Hz command frequencies are presented in Figures 5.30a and 5.30b, respectively. The rising instantaneous torque helps the motor reach close to the synchronous speed. The pulsating torque superimposed on the total hysteresis and eddy current torque results in torque reversals in the instantaneous torque curve. During the synchronization process, the frequency and the magnitude of the torque pulsation die out slowly and the pulsating torque becomes a part of the total synchronous torque. The line current waveform of the inverter is shown in Figure 5.31. The motor starts with a low starting current which reduces the electrical stress on the drive.

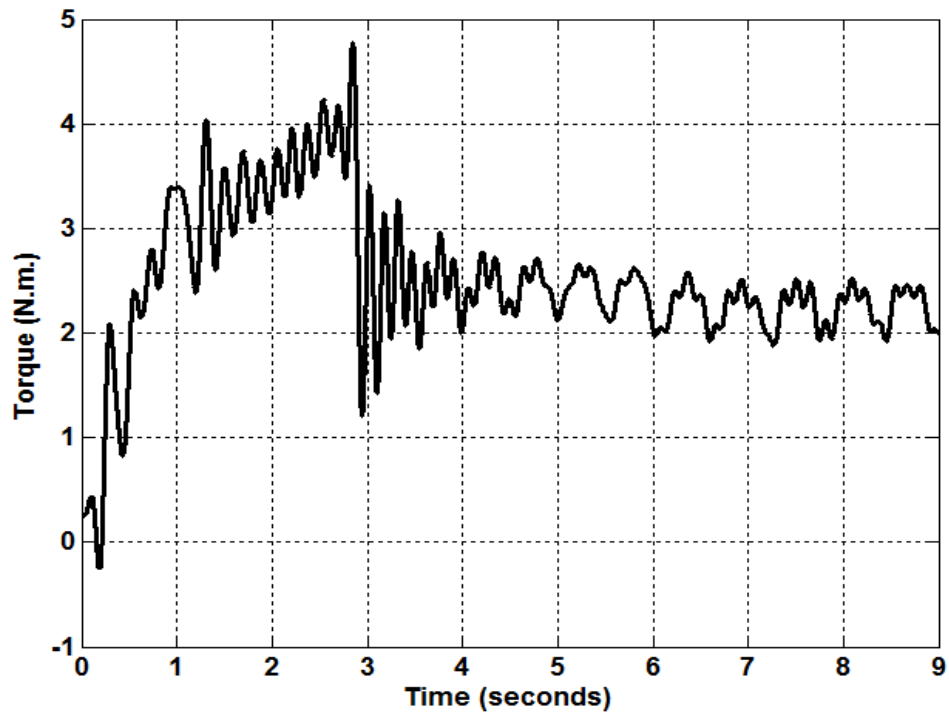


(a)

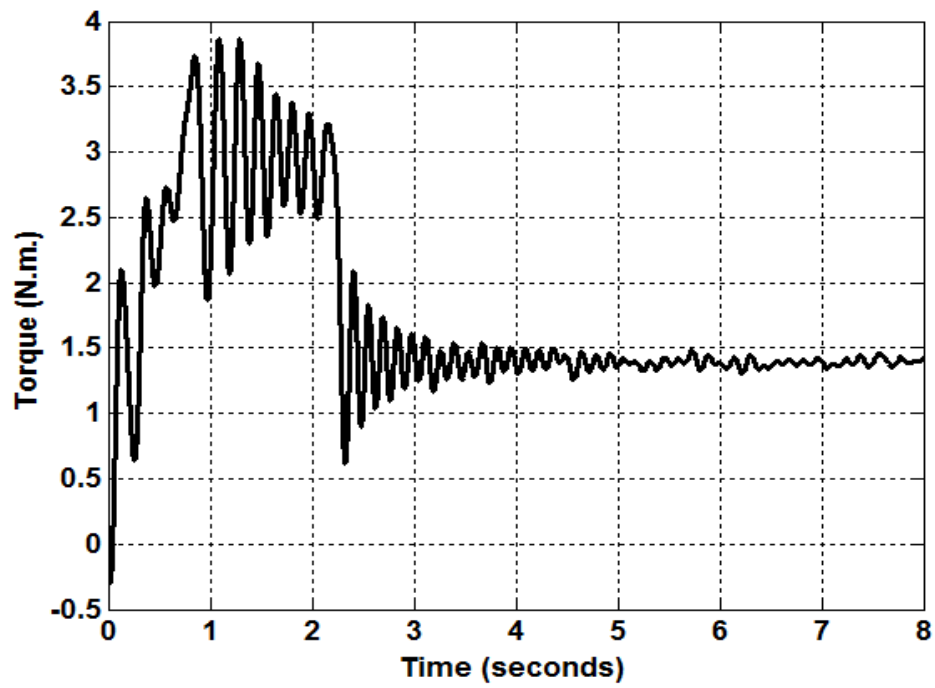


(b)

Figure 5.29. Experimental run-up responses: (a) 60 Hz and (b) 50 Hz.



(a)



(b)

Figure 5.30. Experimental torque responses: (a) 60 Hz and (b) 50 Hz.

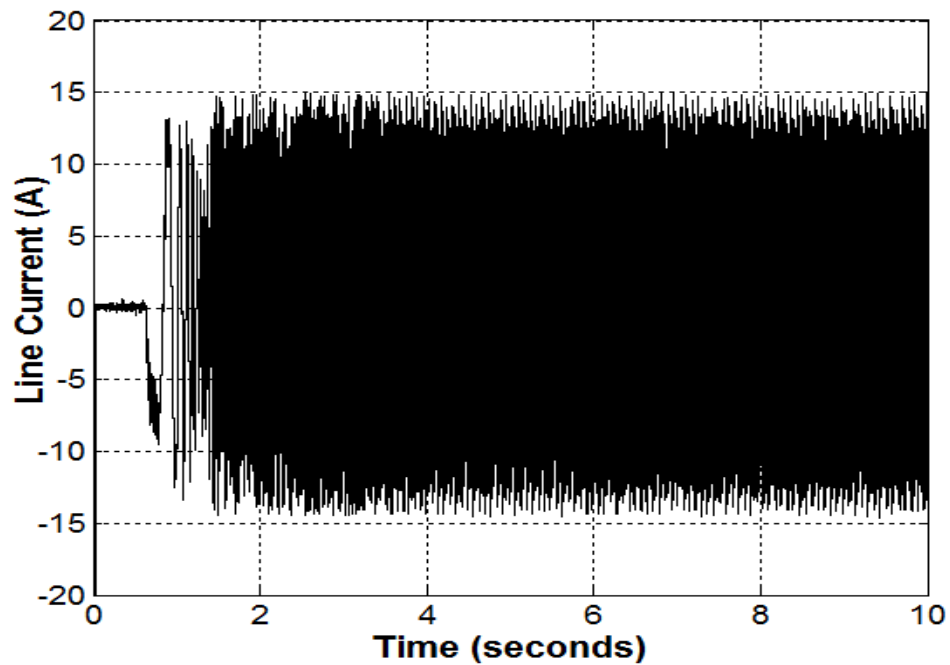


Figure 5.31. Experimental line current of the motor at 60 Hz.

## 5.6 Conclusion

In this chapter, modeling and analysis of the shaft dynamics are carried out for a hysteresis IPM motor driven ESP drive system. A bond graph modeling software is used to simulate the dynamics of the hysteresis IPM-ESP system started directly from a fixed frequency 3-phase balanced ac source. Simulation results are presented in this chapter. Experimental investigations on the torsional dynamics of a hysteresis IPM motor drive system during the run-up are carried out in this chapter. Simulation and experimental results suggest that the hysteresis IPM motor can self-start and synchronize an ESP drive system. However, the starting speed and torque oscillations during an on-line start can be detrimental to the ESP system, and may result in premature ESP failures. It is also presented in this chapter that the dimensions of the shafts, especially the shaft-diameter, have significant effects on the torsional vibration of an ESP system.

The following chapter presents the development of a power electronics based soft-starter for hysteresis IPM motor drive systems for reducing torsional vibration in the system.

## References

1. O. J. Romero and A. Hupp, "Subsea electrical submersible pump significance in petroleum offshore production," *ASME Journal of Energy Resources Technology*, vol. 136, no. 1, pp. 012902, September 2014.
2. K. E. Brown, "Overview of artificial lift systems", *Journal of Petroleum Technology*, vol. 34, no. 10, pp. 2384-2396, October 1982.

3. J. F. Lea and H. V. Nickens, "Selection of artificial lift", *Proceedings of the SPE Mid-Continent Operations Symposium, Oklahoma City, Oklahoma*, March 1999, pp. 1-30.
4. O. V. Thorsen and M. Dalva, "Combined electrical and mechanical model of electric submersible pumps," *IEEE Transactions on Industry Applications*, Vol. 37, No. 2, pp. 541-547, March 2001.
5. R. L. Hyde and T. R. Brinner, "Starting Characteristics of Electric Submersible Oil Well Pumps", *IEEE Transactions on Industry Applications*, Vol. 22, No. 1, pp. 133–144, January 1986.
6. Hong Guo, Zhenhua Lv, Zhiyong Wu and Bo Wei, "Multi-physics design of a novel turbine permanent magnet generator used for downhole high-pressure high-temperature environment", *IET Electric Power Applications*, Vol. 7, No. 3, pp. 214-222, March 2013.
7. J. F. Douglas, J. M. Gasiorek and J. A. Swaffield, *Fluid Mechanics*, Harlow: England, Pearson Education, 2001.
8. S. Junco and A. Donaire, "Bond Graph Modeling and Simulation of Electrical Machines," in *Bond Graph Modelling of Engineering Systems*, W. Borutzky, Ed. New York: Springer, 2011, pp. 269-321.
9. D. C. Karnopp, D. L. Margolis and R. C. Rosenberg, *System Dynamics: A Unified Approach*, New York: Wiley, 1990.
10. D. G. Rideout, J. L. Stein and L. S. Louca, "Systematic Assessment of Rigid Internal Combustion Engine Dynamic Coupling." *J. Eng. for Gas Turbines and Power*, Vol. **130**, pp. 022804, 2008.
11. D. C. Karnoop, "Understanding Induction Motor State Equations Using Bond Graphs", in *Proceedings of the International Conference on Bond Graph Modeling and Simulation*, Orlando, Florida, USA, 2008.

## **Chapter 6**

### **Soft-Starting of a Hysteresis IPM Motor Drive**

#### **6.1 Introduction**

Based on the discussion provided in previous chapters, it is evident that on-line starting of an interior permanent magnet motor driven electric submersible pump (ESP) creates severe torsional oscillations in the electromechanical system. The frequency of torsional oscillations may reach the mechanical resonant frequency, creating premature ESP failures. In this chapter, a novel design of a  $V/f$  controller for soft-starting of a hysteresis interior permanent magnet motor drive is presented. Simulations have been carried out using the developed equivalent circuit models presented in chapter 3 to obtain the transient run-up responses of a 3-phase 4-pole 208V, 2.5-kW laboratory Mawdsley prototype hysteresis interior permanent magnet motor drive. The  $V/f$  controller has been implemented in real time to investigate the starting and synchronization capabilities of the 2.5-kW motor. Both the simulation and experimental results are presented and discussed at the end of this chapter.

#### **6.2 Design of a Soft-Starter for a Hysteresis IPM Motor Drive**

Soft-starting is a type of starting technique for a motor drive where the torque is gradually applied on the mechanical transmission system during run-up in order to reduce the inrush current and torque [1]-[3]. Sometimes, the load torque is also relieved during starting for reducing the mechanical stress on the drive system. Soft starting of a motor

drive is particularly useful for high inertial loads. It can be performed using either mechanical soft-starters such as dry fluid drives [2], or power electronics based variable speed drives (VSDs). In recent years, due to the technological and manufacturing advancements in power electronics, VSD based soft-starters have become popular for various applications such as pumps, compressors, conveyor belts, elevators and fans where high dynamic performance is not required [3].

Figure 6.1 displays a basic open-loop  $V/f$  controller for line-start permanent magnet motor drives equipped with cage windings. In this type of controller, the applied voltage is gradually increased with a predefined rate that is proportional to the command frequency. Due to the presence of damper windings in the rotor, there is no need for frequency stabilization in the control system [4]-[5]. Although the open-loop  $V/f$  controller is easy to implement, it provides sluggish responses to load changes and cannot compensate for the voltage drop in the line resistance. Thus, it is prone to failures in certain applications where the line impedance is significantly high such as offshore power systems.

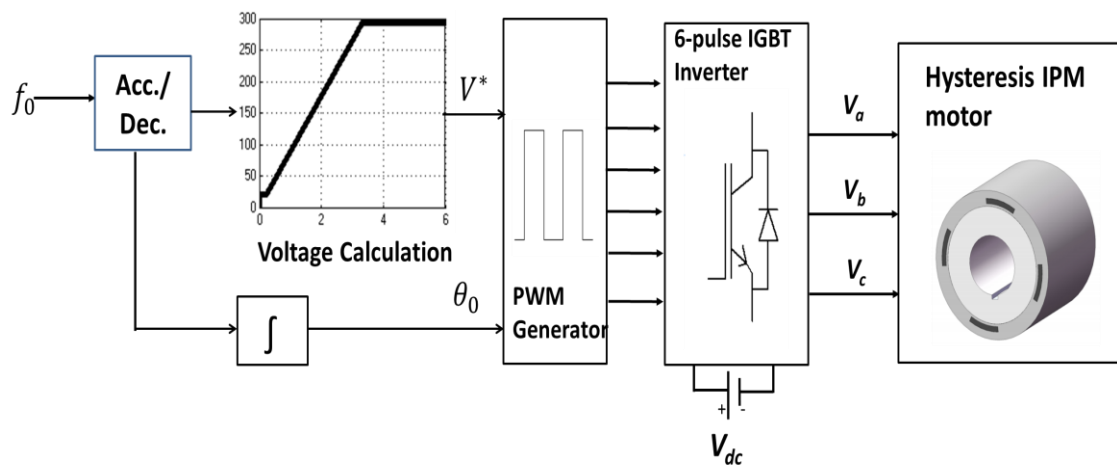


Figure 6.1. Block diagram of a typical open loop  $V/f$  controller.

Design of closed loop stable  $V/f$  controllers for variable speed permanent magnet (PM) motor drives has been a topic of interest among the researchers over the last three decades [4]-[10]. Closed loop  $V/f$  controllers typically contain stabilizing loops in their algorithms for providing active damping to PM motor drives. There are basically two types of stabilization loops: voltage stabilization and frequency stabilization loops [7]-[10]. A voltage stabilization loop reads the instantaneous dc current or 3-phase ac current signals to dynamically adjust the command voltage with changing load conditions. It improves the starting capabilities of the motor and also compensates for the voltage drop across the line resistance. It allows low speed operation of a PM motor drive.

The frequency stabilization loops modulates the command frequency to the VSD by using active power perturbations [7]-[8]. The active power is generally measured or estimated using the line voltages and currents. The frequency stabilization loop provides active damping to permanent magnet motor drives with no physical damper windings.

A stable  $V/f$  controller has been proposed by Perera et. al. for PM motors without any squirrel cage or damper windings [9]. They have proposed a stabilization technique by modulating the applied frequency to stabilize the rotor hunting at the command frequency. In a hysteresis IPM motor, the hysteresis ring behaves like damper windings. Thus, a simple  $V/f$  controller similar to [9] can be extended for the hysteresis IPM motor drive using the current feedback loops to adjust the command voltage for proper synchronization of the motor drive without any additional frequency stabilization loop. The proposed hysteresis IPM motor behaves like a predominantly IPM motor at steady state. The hysteresis ring becomes temporarily magnetized in the rotor and can be represented as a current source similar to the permanent magnet excitation in the rotor.

Therefore, the total excitation in the rotor of a hysteresis IPM motor is provided mainly by the permanent magnet and partly by the temporarily magnetized hysteresis ring.

The block diagram for the  $V/f$  control of a hysteresis IPM motor drive is illustrated in Figure 6.2. The steady state phasor diagram of the motor is illustrated in Figure 6.3. The voltage vector  $V_s$  is the summation of the voltage induced due to stator flux linkage  $E_s$  and the voltage drop in the stator winding resistance. The equations for calculating the magnitude of  $V_s$  are given below [9],

$$V_s = ON + NL \quad (6.1)$$

$$NL = I_s R_s \cos \varphi \quad (6.2)$$

$$ON^2 = OM^2 - MN^2 = E_s^2 - (I_s R_s \sin \varphi)^2 \quad (6.3)$$

where  $\varphi$  is the power factor angle.

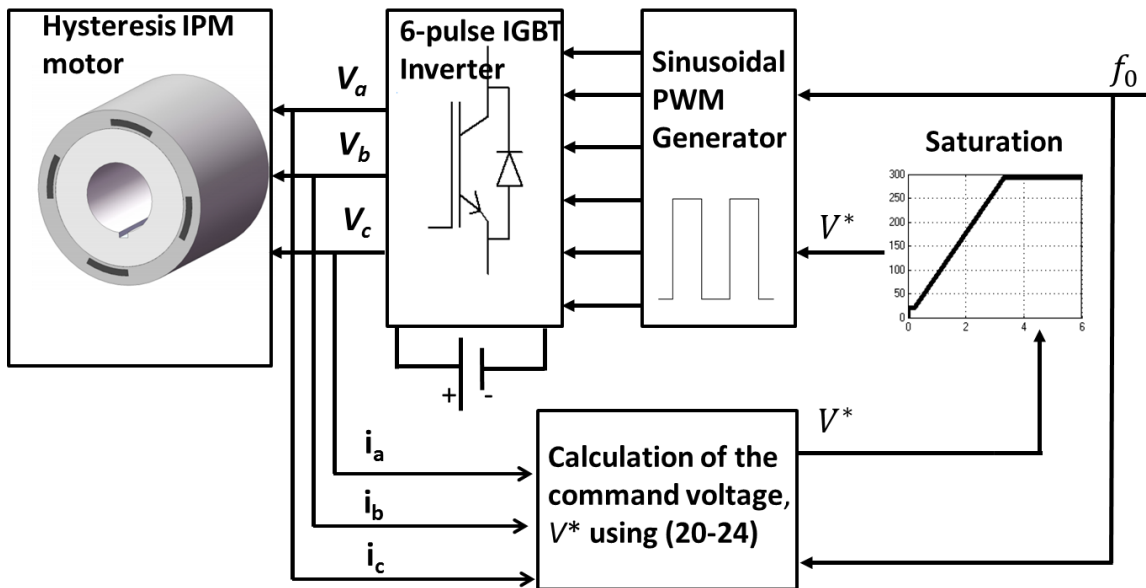


Figure 6.2. Block diagram of a  $V/f$  controller for a hysteresis IPM motor drive.



The applied command voltage  $V_s$  largely depends on the magnitude of the stator flux-linkage. In order to soft-start a hysteresis IPM motor, the magnitude of the stator flux linkage needs to be constant at steady state so that the motor can ramp-up smoothly to the desired speed. Thus, the magnitude of the stator flux induced voltage  $E_s$  is assumed to be equal to the magnitude of the motor back-emf  $E_0$ . The rms magnitude of  $E_s$  is calculated as,

$$E_s = E_0 = 4.44\pi f_0 \lambda'_{mh} \quad (6.7)$$

where  $f_0$  is the command frequency and  $\lambda'_{mh}$  is the peak flux linkage due to the permanent magnet excitation and hysteresis effect.

The magnitude of the in-phase component of the stator current vector  $I_q^s$  is calculated by  $d$ - $q$  axis transformation of the 3-phase stator currents  $i_{abc}$  with respect to the synchronously rotating reference frame  $\theta_s$ , and it can be expressed as [9],

$$I_q^s = I_s \cos \varphi = \frac{2}{3} \left\{ i_a \cos \theta_s + i_b \cos \left( \theta_s - \frac{2\pi}{3} \right) + i_c \cos \left( \theta_s + \frac{2\pi}{3} \right) \right\} \quad (6.8)$$

where,

$$\theta_s = \int (2\pi f_0) dt \quad (6.9)$$

The magnitude of the stator current vector  $I_s$  can be calculated from the  $\alpha$ - $\beta$  components of the stator 3-phase currents. The equations for calculating  $I_s$  are given below,

$$I_s = \sqrt{(i_\alpha)^2 + (i_\beta)^2} \quad (6.10)$$

$$i_\alpha = \frac{2}{3} \left( i_a - \frac{i_b}{2} - \frac{i_c}{2} \right) \quad (6.11)$$

$$i_\beta = -\frac{2}{\sqrt{3}}\left(\frac{i_b}{2} - \frac{i_c}{2}\right) \quad (6.12)$$

In order to avoid unwarranted chattering in the command voltage, the stator current vector  $I_s$  and its in-phase component  $I_q^s$  are passed through 2<sup>nd</sup> order discrete low pass filters as follows,

$$I_{sf} = \frac{\omega_c^2}{s^2 + 2\xi\omega_c s + \omega_c^2} I_s \quad (6.13)$$

$$I_{qf}^s = \frac{\omega_c^2}{s^2 + 2\xi\omega_c s + \omega_c^2} I_q^s \quad (6.14)$$

where  $I_{sf}$  and  $I_{qf}^s$  are filtered versions of  $I_s$  and  $I_q^s$ , respectively,  $\omega_c$  is the cut-off frequency for the low pass filter (2Hz~5Hz) and  $\xi$  is the damping ratio.

Using (6.7)-(6.14), the equation of the applied instantaneous command voltage to the motor drive is expressed as follows,

$$V_s^* = I_{qf}^s R_s + \sqrt{(2\pi f_0 \lambda'_{mh})^2 + (I_{qf}^s)^2 R_s^2 - I_{sf}^2 R_s^2} \quad (6.15)$$

The instantaneous command voltage  $V_s^*$  is calculated at each time step to keep the stator flux linkage constant during the acceleration/deceleration period of the rotor. The stator phase resistance is considered during the calculation of the command voltage  $V_s^*$  to compensate for the voltage drop in the line.

For a conventional IPM motor with no damper windings in the rotor, a second frequency stabilization loop is required for operating the motor at the command frequency. However, in the case of a hysteresis IPM motor, the hysteresis ring acts as a damper and provides the necessary damping torque to the motor drive. Also, the eddy current in the hysteresis ring provides additional damping torque for the motor. The

hysteresis damping torque available from the hysteresis ring at steady state can be expressed as,

$$T_{hys} = \frac{pV_r B_m^2}{2\mu} \sin \delta \quad (6.16)$$

where  $B_m$  is the maximum flux density and  $\mu$  is the permeability of the of the hysteresis material, respectively,  $V_r$  is the volume of the hysteresis ring,  $p$  is the number of pole pairs and  $\delta$  is the hysteresis lag angle/ motor load angle.

The equation of motion of a hysteresis IPM motor drive can be written as,

$$J \frac{d^2 \delta}{dt^2} = T_s(\delta) - (T_{hysD} + T_{vD}) \frac{d\delta}{dt} - T_L(\delta) \quad (6.17)$$

where  $J$  is the inertia of the motor,  $T_s$  is the synchronous torque of the motor,  $T_{vD}$  is the viscous damping torque coefficient,  $T_{hysD}$  is the hysteresis damping coefficient and  $T_L$  is the load torque for the motor.

### 6.3 Simulation Results

The simulated run-up responses of a  $V/f$  controlled 3-phase 4-pole 208V  $\Delta$ -connected 2.5-kW hysteresis IPM motor drive at light load for different operating frequencies are shown in Figure 6.4. The applied frequency to the motor is gradually increased to the command frequency in order to reduce the magnitude of inrush torque and current. Due to permanent magnets buried in the rotor, the motor experiences a high magnet brake torque during starting which causes some rotor oscillations. The motor overcomes this brake torque with the aid of the hysteresis and eddy current torque, starts smoothly and ramps up towards the command speed. The

motor synchronizes at the command frequency with some speed overshoots and undershoots due to hysteresis cycles. The permanent magnet provides the points of synchronization to overcome the hunting problems associated with conventional hysteresis motors. At steady state, the hysteresis ring provides the necessary damping torque to stabilize the rotor at the command frequency.

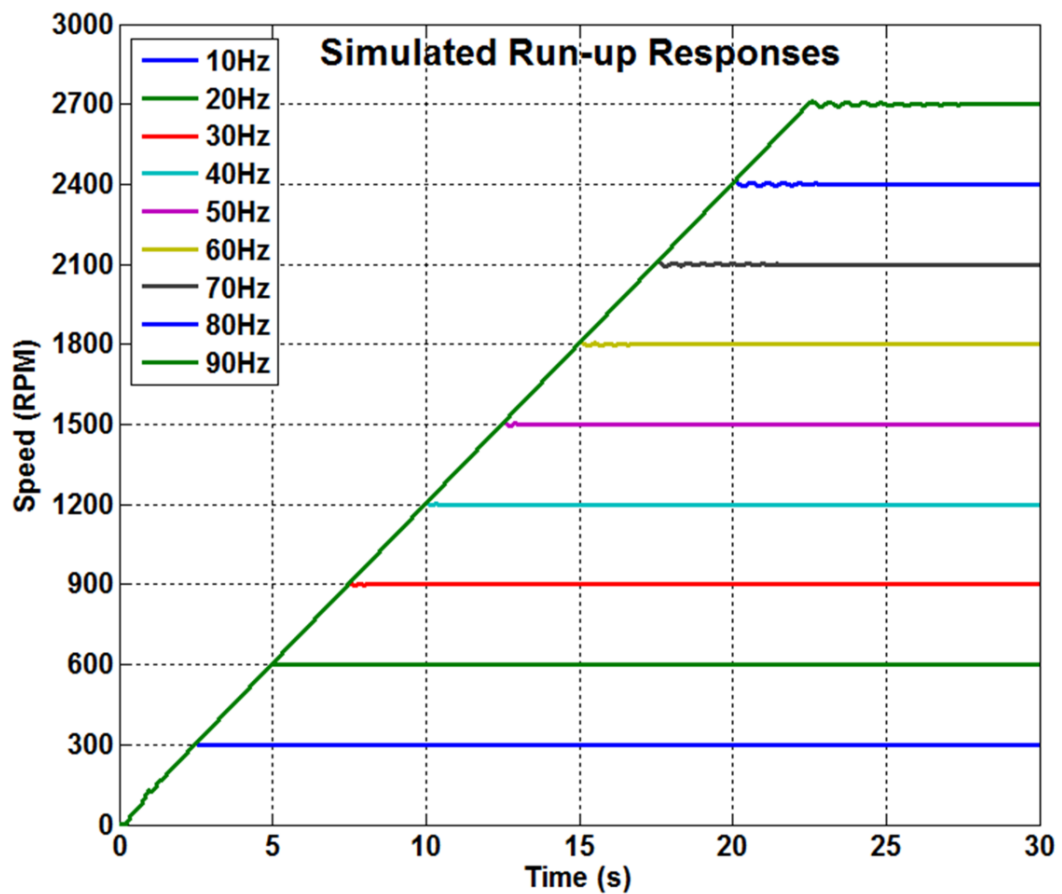


Figure 6.4. Simulated run-up responses of the motor for 10 Hz-90Hz frequencies

The developed instantaneous electromagnetic torque at rated load torque for 60Hz command frequency is illustrated in Figure 6.5. The developed torque is comprised of an

average asynchronous torque and a pulsating torque. The average asynchronous torque combines the hysteresis torque, the eddy current torque and the magnet brake torque. Due to the presence of permanent magnets acting as a current source in the rotor, there is a pulsating torque superimposed on the average asynchronous torque. The pulsating torque assists the motor to a fast acceleration of the rotor. The motor starts to synchronize at a low frequency around  $t = 2\text{s}$ . During the period of synchronization, the torque pulsation dies out. Consequently, the trajectory of the starting torque becomes almost flat after  $t = 3\text{s}$  as depicted in Figure 6.5. When the applied frequency reaches the command frequency, it becomes constant. At this point, the hysteresis ring behaves like a damper and provides a combined hysteresis and eddy current damping torque to stabilize the rotor at the synchronous speed. After successful stabilization of the rotor, the eddy current torque vanishes. The hysteresis ring becomes temporarily magnetized in the rotor and provides some additional excitation along with the permanent magnets.

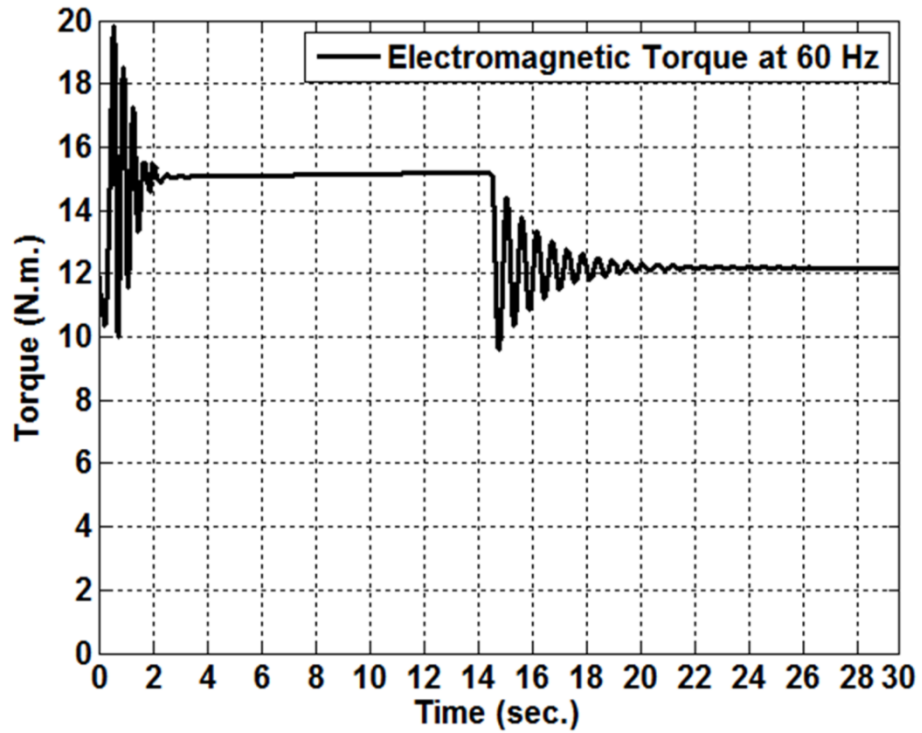


Figure 6.5. Simulated torque of the motor for 60Hz frequency.

The trace of the peak of the line current waveform for 60Hz command frequency at rated load is depicted in Figure 6.6. The starting current is limited by the  $V/f$  controller and it is slightly higher than the steady state current. The command voltage is calculated using the designed  $V/f$  controller so that the inrush current during start remains low-restricted within two times of the rated current.

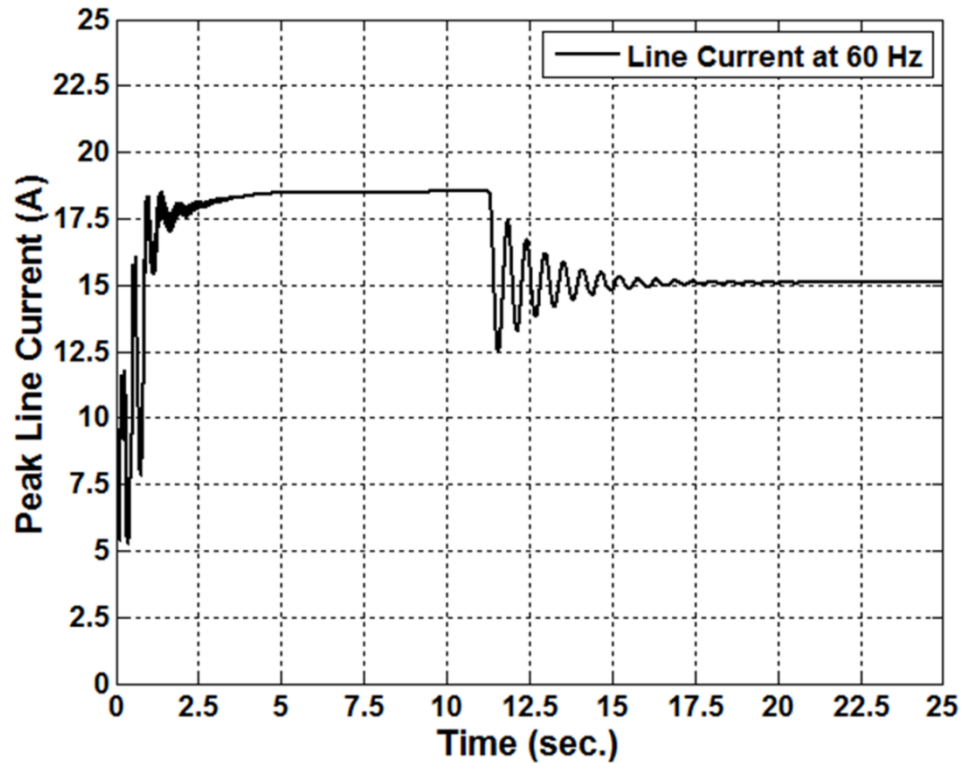


Figure 6.6. Simulated line current of the motor for 60Hz frequency.

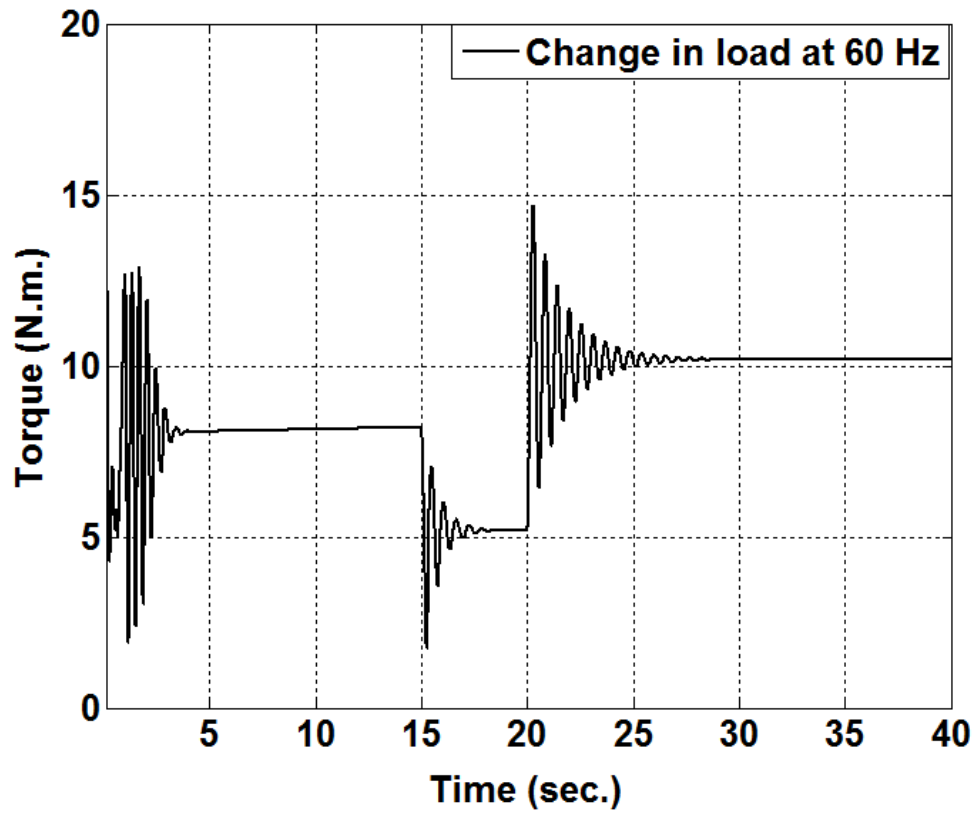
The responses of the motor for sudden changes in the load torque are depicted in Figures. 6.7a-6.7d. The motor is started with a 8 Nm. constant load torque at a 60 Hz command frequency. A step change is introduced at  $t = 15$ s by reducing the load torque from 8 Nm. to 5 Nm. Another step change is introduced in the system at  $t = 20$ s by increasing the load torque by 5 Nm. The trajectory of the motor torque during the load change is depicted in Figure 6.7a. During a sudden load change, the motor goes through some speed oscillations caused by the minor oscillations in the developed electromagnetic torque. These oscillations are damped out due to the hysteresis phenomenon in the rotor. The hysteresis lag angle goes through cyclic oscillations,

generates a damping torque for the motor drive for stabilizing the system and finally settles down to a stable steady state value.

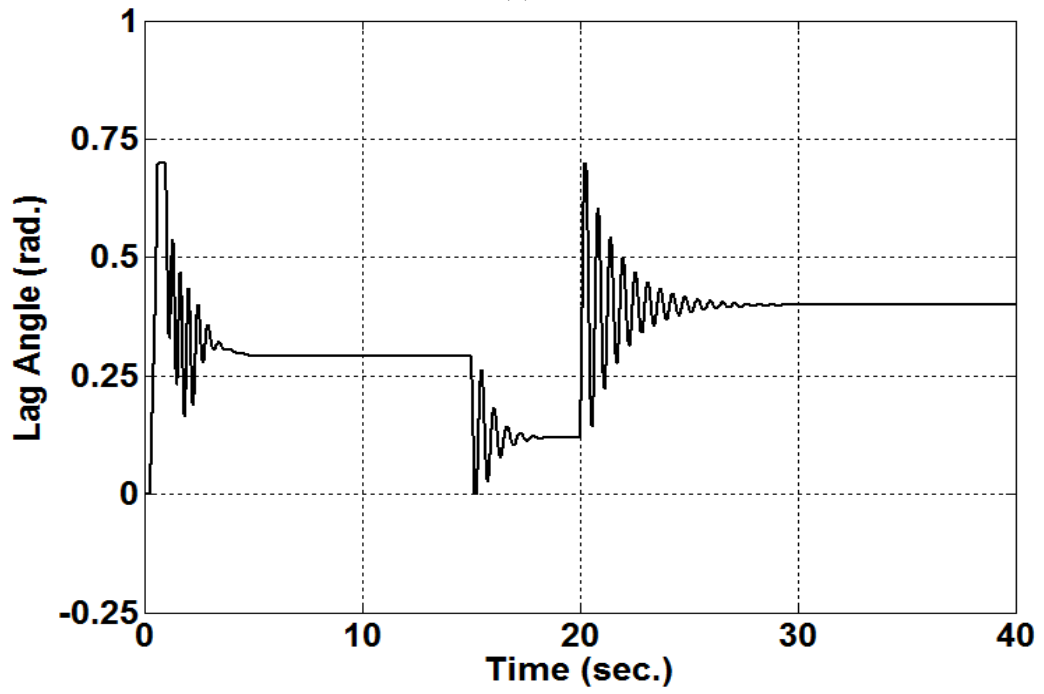
The trajectory of the hysteresis lag angle  $\delta$  is depicted in Figure 6.7b. The motor follows the outer hysteresis loop during start and settles down to an inner loop after the motor is synchronized. The rotor hysteresis loop travels from one inner loop to another inner loop when the load torque is different.

The maximum flux density  $B_m$  of the hysteresis ring is illustrated in Figure 6.7c. The flux density varies with the hysteresis lag angle. Thus, it oscillates after a step change in the load torque. The maximum flux density also varies with the load torque, becoming higher or lower in accordance with the magnitude of the hysteresis lag angle.

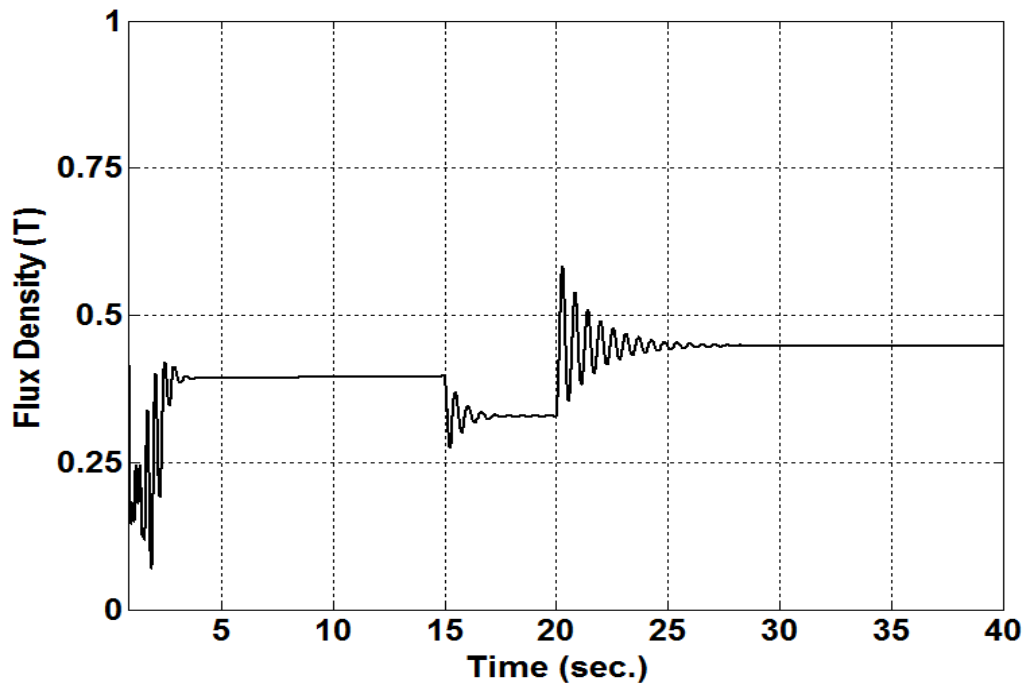
The changes in the peak of the current waveform during sudden load changes are illustrated in Figure 6.7d. The motor current oscillates slightly during load variations. However, the amplitude of the oscillation remains within the operating limit, reducing the stress on the drive system.



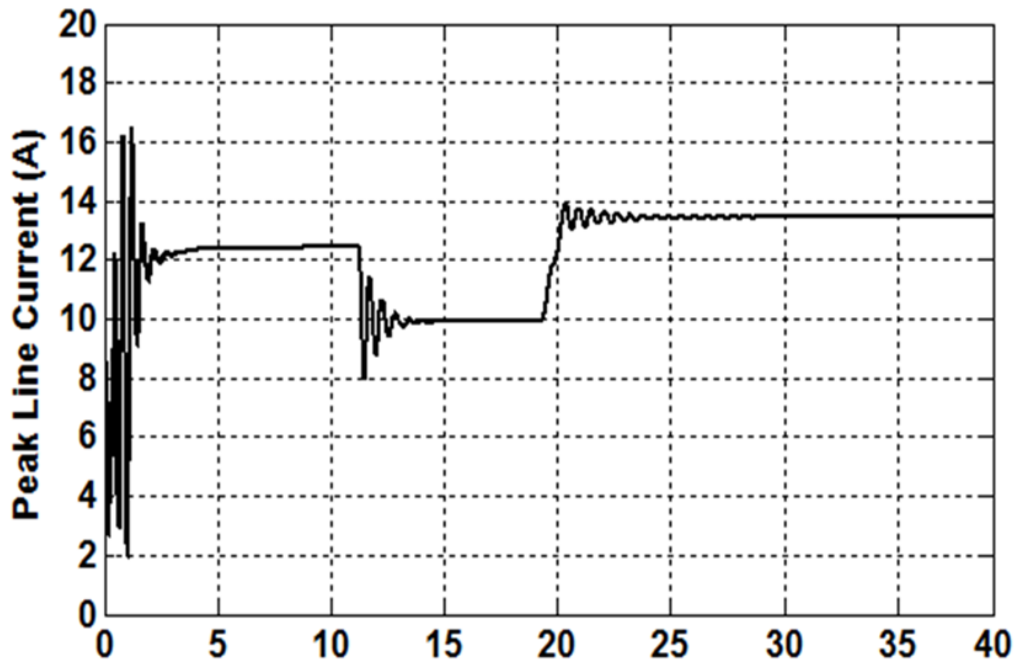
(a)



(b)



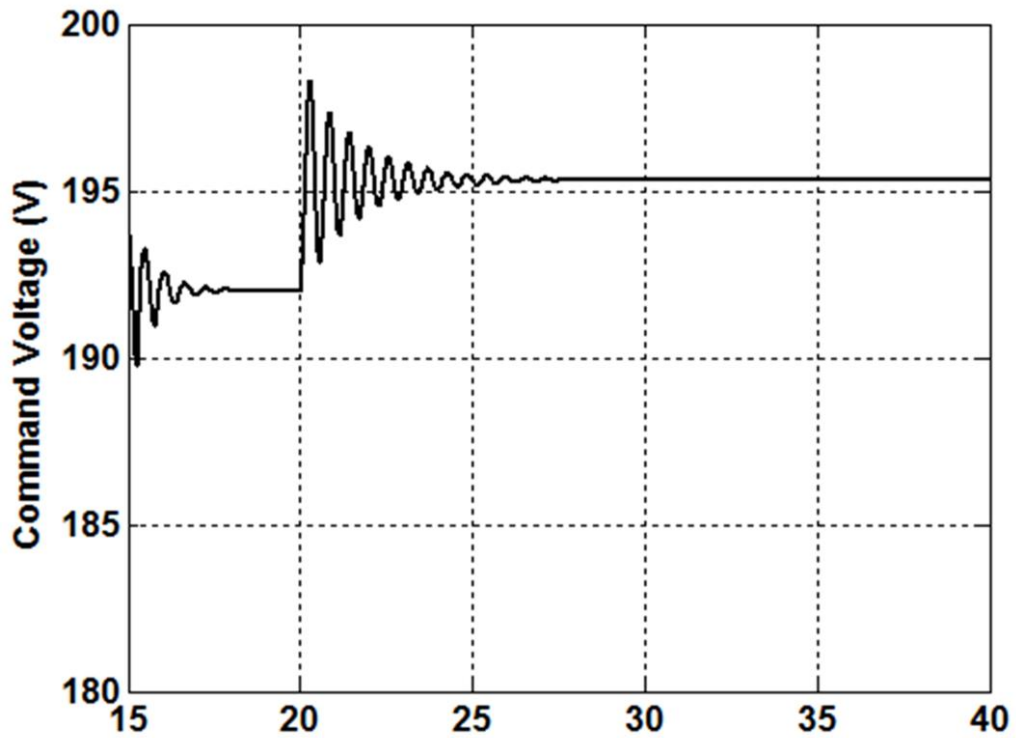
(c)



(d)

Figure 6.7. Responses of the motor for step change in load: (a) torque, (b) hysteresis lag angle, (c) flux density vector and (d) line current

The performance of the proposed  $V/f$  controller for a step change in load is presented in Figures 6.8a-6.8b. The command voltage  $V_s^*$  is calculated at each time step and compensates for the voltage drop in the stator phase resistance  $R_s$ . This phenomenon is depicted in Figure 6.8a. Thus, the proposed controller has the ability to adjust the command voltage dynamically in step with the load torque for better and quicker stabilization of the rotor. Figure 6.8b shows the magnitude of the stator current vector  $I_s$  and the magnitude of the in-phase component of  $I_s$  along with the voltage vector  $I_q^s$ .



(a)

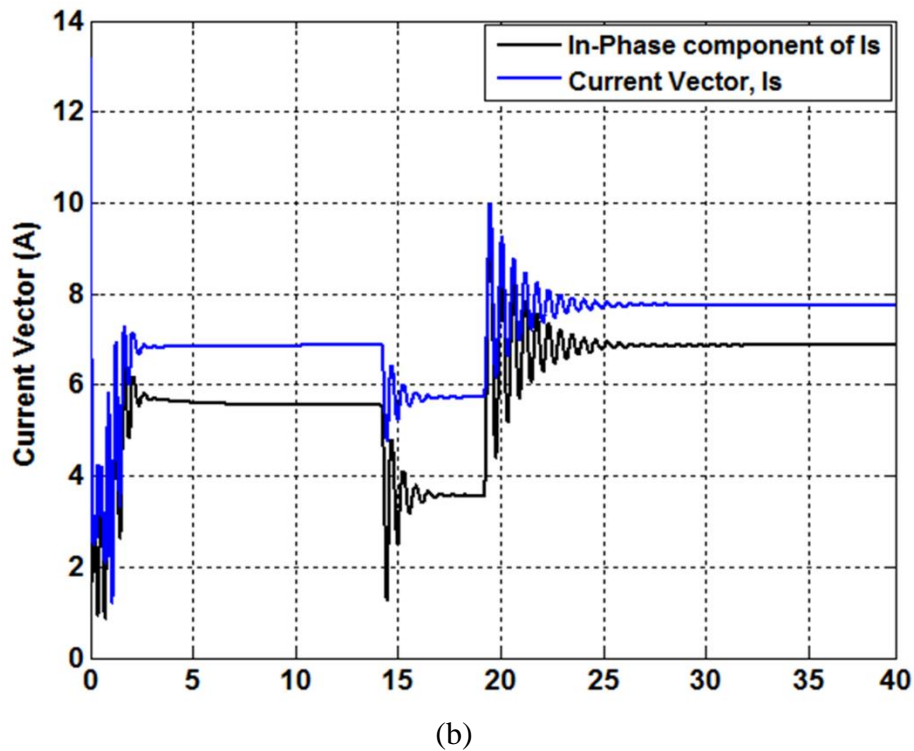


Figure 6.8. Responses of the  $V/f$  controller for a step change in load: (a) command voltage and (b) magnitude of the current vector.

#### 6.4 Experimental Results

The experimental testing has been performed on a Mawdsley generalized machine. The stator is rated at 3-phase 4-pole 208V with delta connected double layer windings. The rotor is replaced by the rotor of a 36% Cobalt Steel hysteresis IPM motor with Nd-B-Fe magnets. The motor is run by the proposed  $V/f$  controller. The block diagram of the overall system set-up is displayed in Figure 6.9. Figure 6.10 displays the experimental prototype hysteresis IPM motor. A dc motor is connected as a load for the hysteresis IPM motor. A sinusoidal pulse-width modulated 3-phase full-bridge IGBT inverter controlled

by a dSPACE DS-1104 R&D controller board is used for driving the hysteresis IPM motor. The switching frequency is selected as 3 kHz.

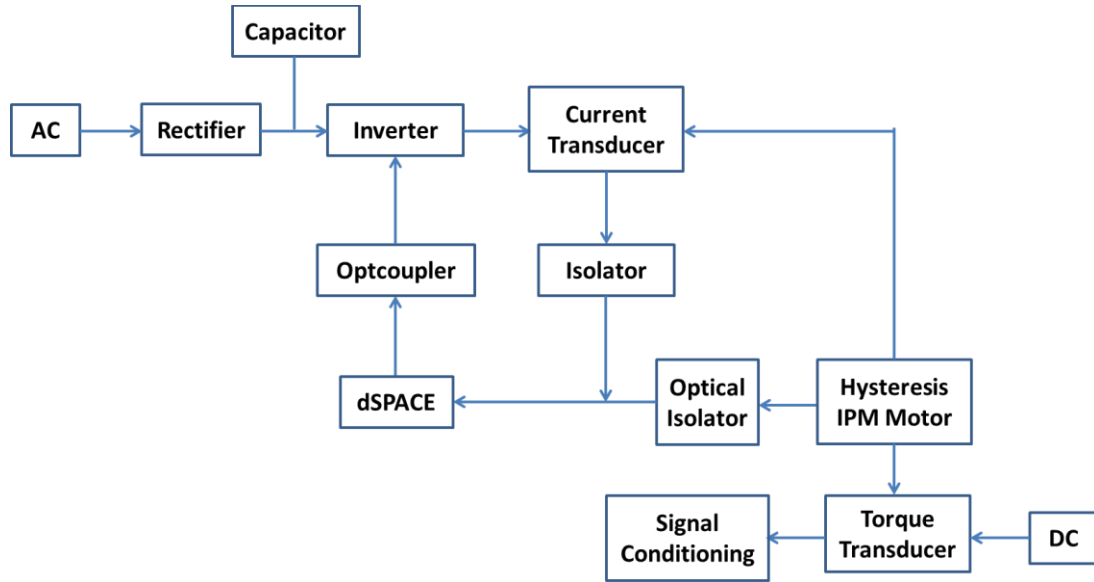


Figure 6.9. Block diagram of the experimental setup.

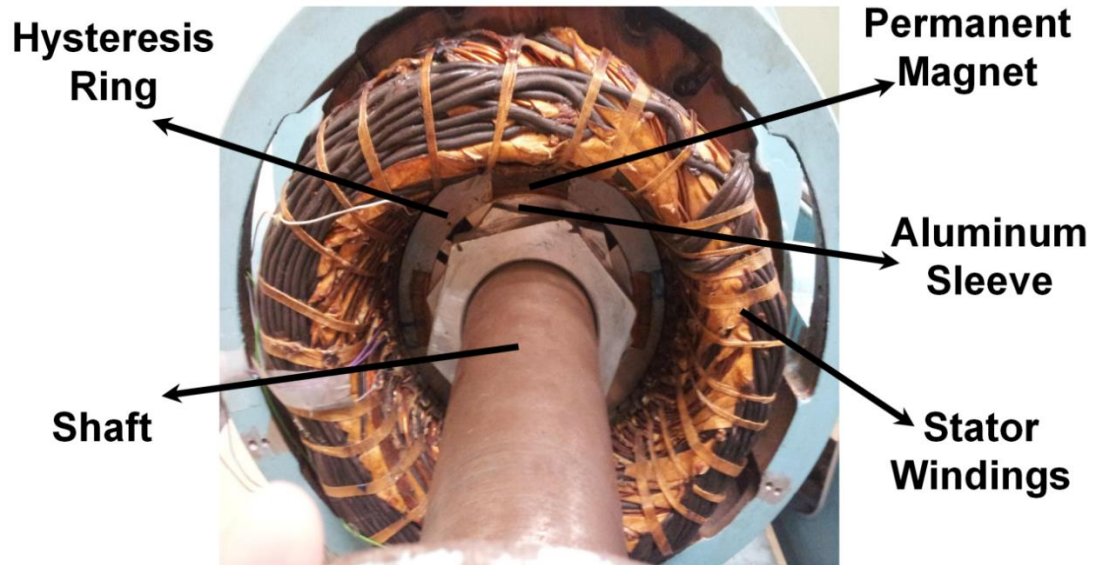


Figure 6.10. The prototype hysteresis IPM motor.

The experimental run-up responses of the motor for different command frequencies are illustrated in Figure 6.11. The motor is lightly loaded. In order to overcome the brake torque, the motor is started with some initial voltage of 30V which results in sharp responses with a high slope in the speed curves. After that, the motor ramps up smoothly towards the synchronous speed as the command voltage increases along with the command frequency. The synchronization process starts at close to the synchronous speed and the motor synchronizes at ease with small speed overshoots.

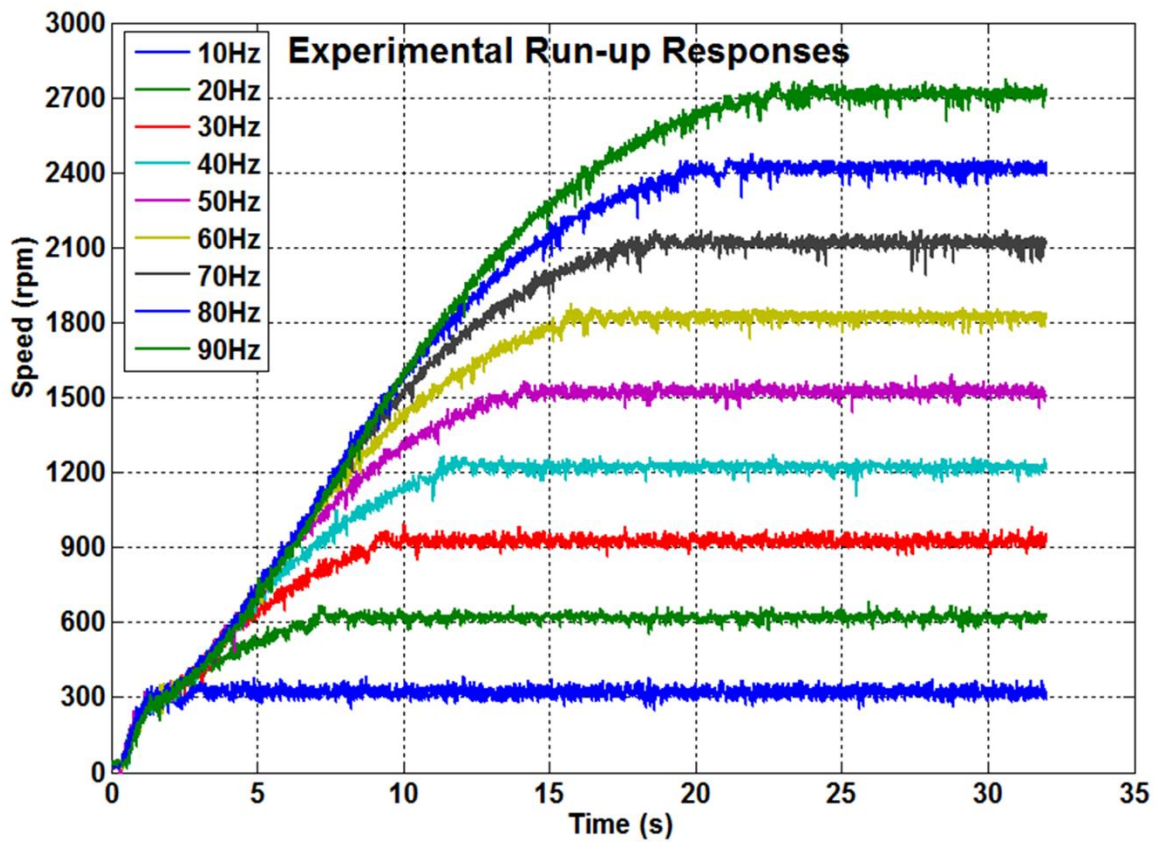


Figure 6.11. Experimental run-up responses for 10Hz-90Hz command frequencies.

The trace of the peak line current while starting the motor at 60 Hz command frequency is illustrated in Figure 6.12. The motor starts with a low starting current which reduces the electrical stress on the inverter. There is a sharp rise of the current due to the applied initial fixed voltage of 30V. After the sharp rise, the current increases gradually to a maximum value. The maximum starting current is slightly higher than the steady state current. At steady state, the rotor synchronizes itself with the applied stator field and behaves like an IPM motor. The oscillations in the trace of the peak current waveforms are due to high frequency noise coming from the inverter and also due to mechanical vibrations associated with the experimental set-up.

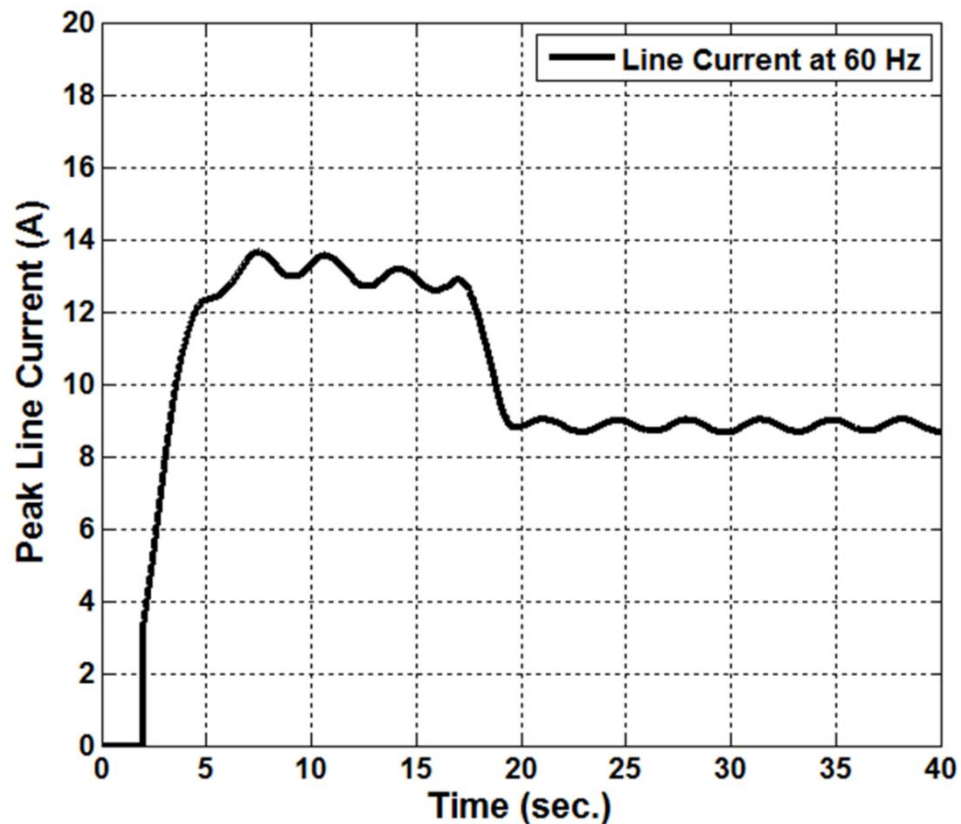
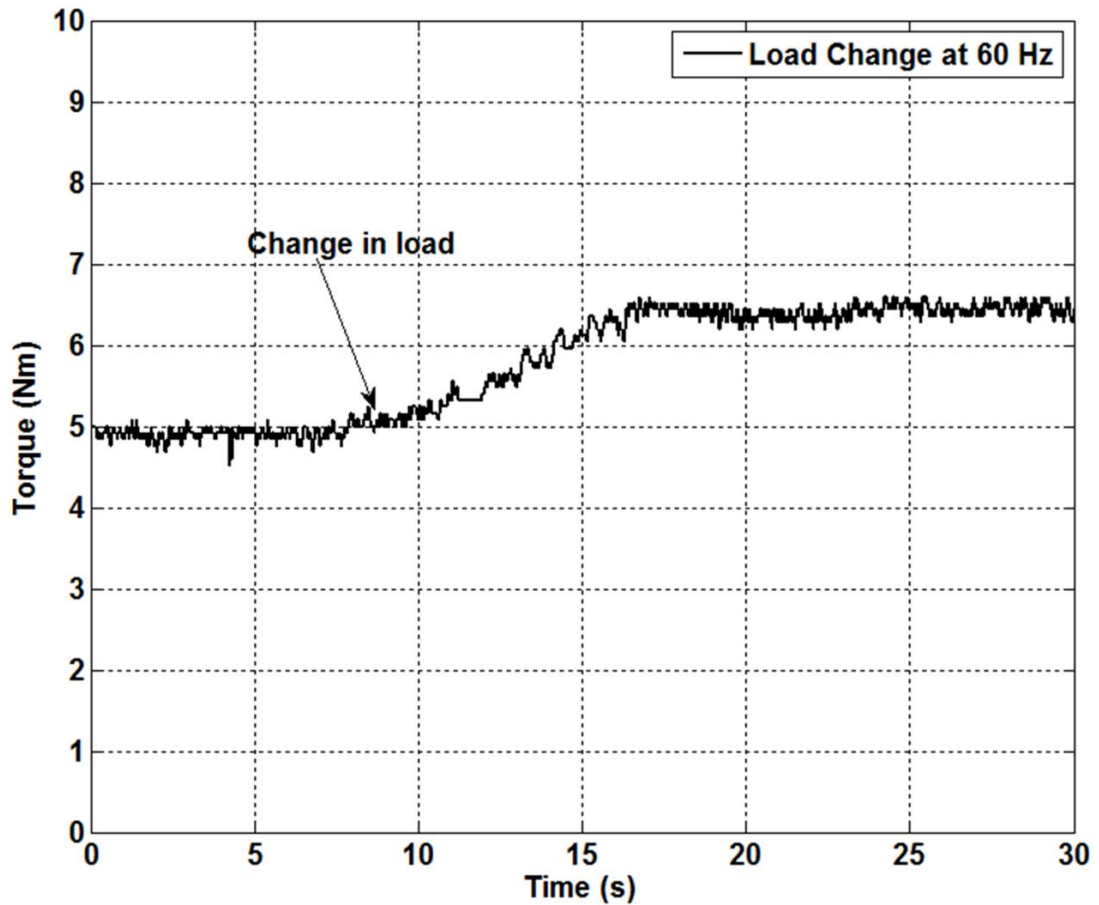
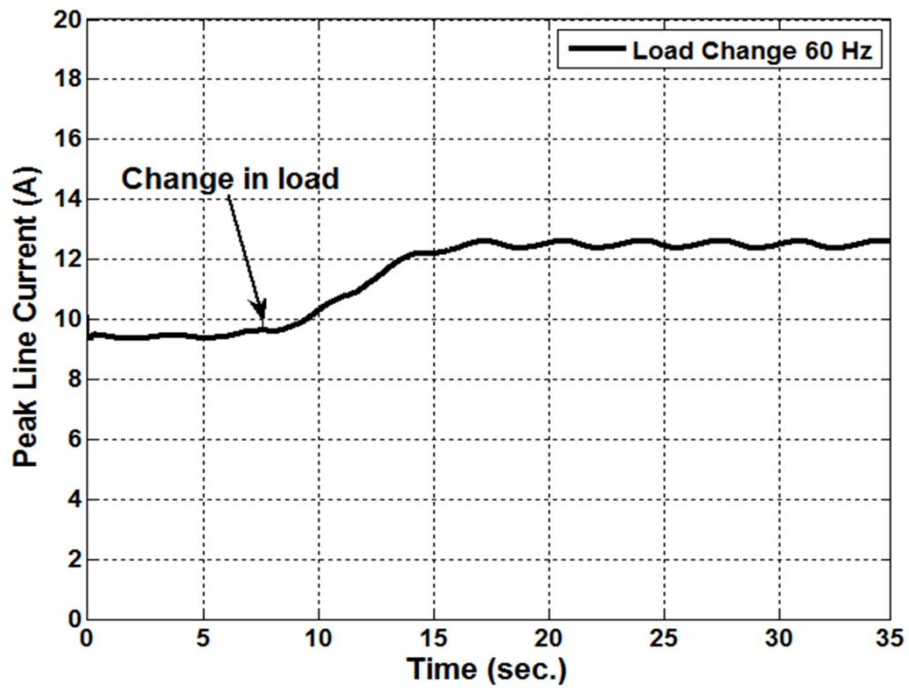


Figure 6.12. Experimental line current for 60Hz.

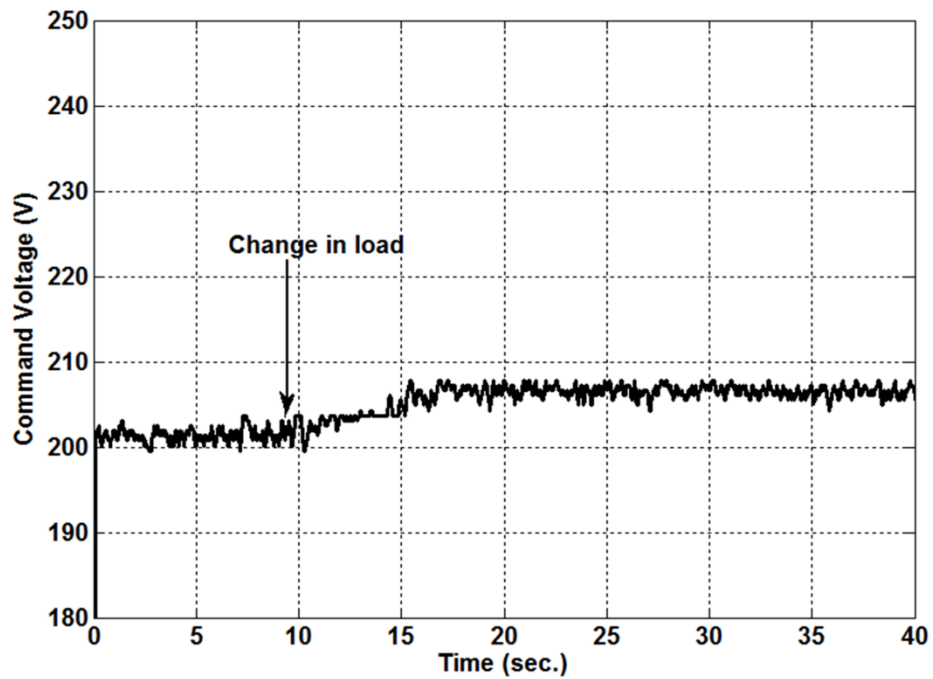
The responses of the motor for a sudden change in the load torque at 60 Hz are depicted in Figures 6.13a-6.13c. The load torque is gradually changed from 5 Nm. to 6.5 Nm. The trajectory of the motor torque during the load change is depicted in Figure 6.13a. The torque ramps up smoothly and settles down to the desired value. The current waveform during the sudden load change is illustrated in Figure 6.13b. The motor draws higher current from the line as the load increases. Figure 6.13c demonstrates the trajectory of the command voltage during the load change. The command voltage also increases to compensate for the voltage drop in the line resistance.



(a)



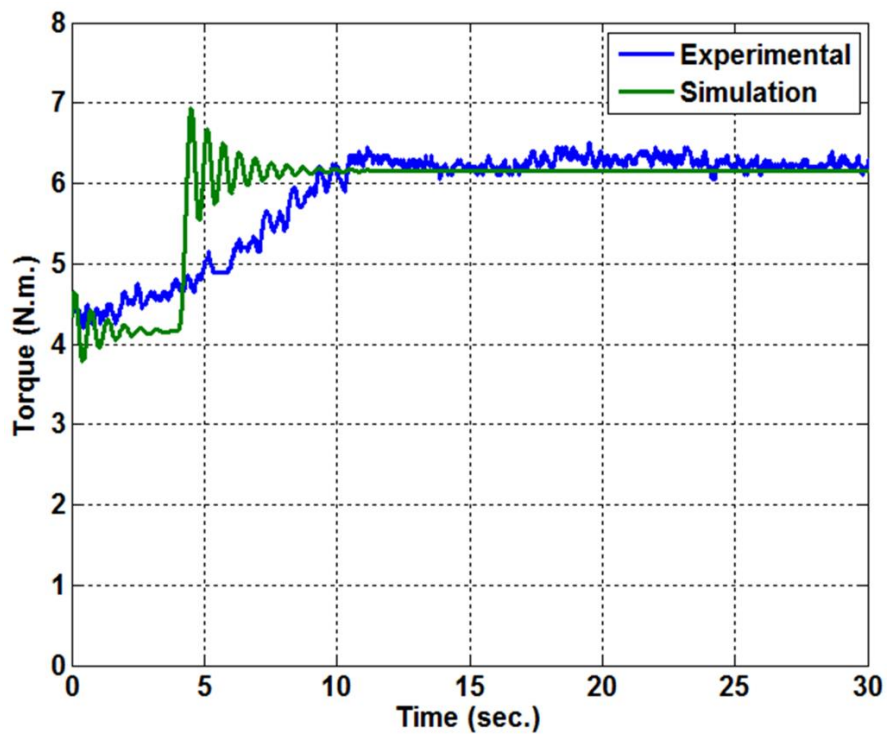
(b)



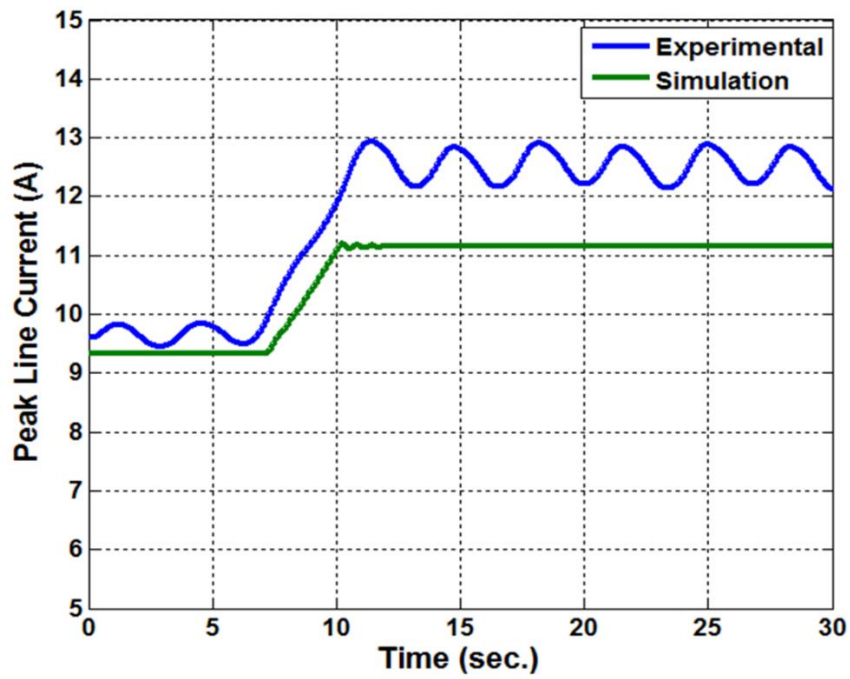
(c)

Figure 6.13. Experimental response of the motor for step load change at 60Hz: (a) torque, (b) line current and (c) command voltage.

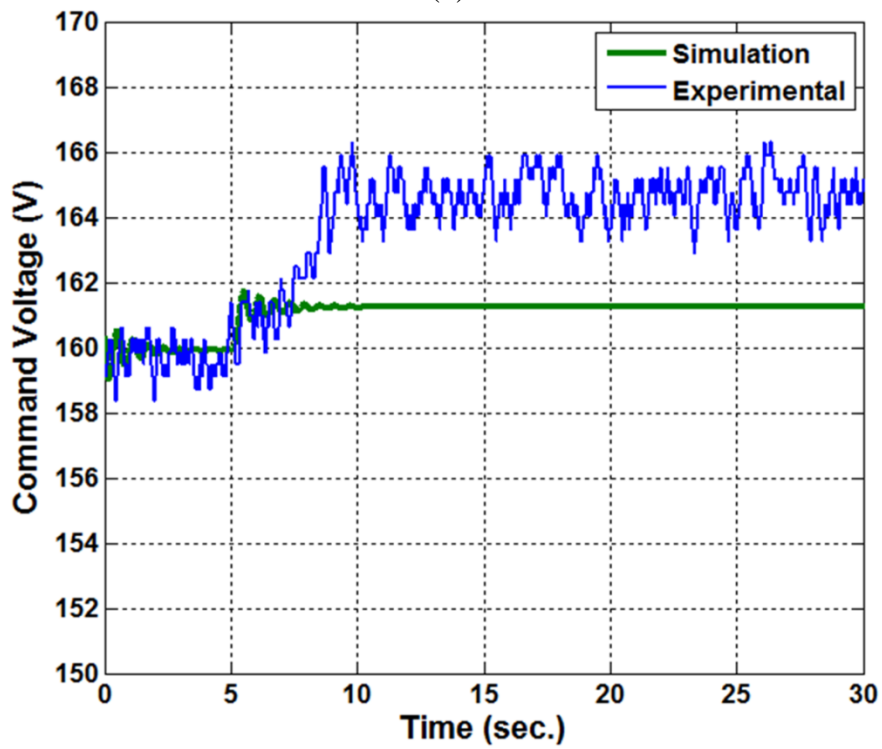
The experimental and simulated performances of the motor at 50 Hz frequency are shown in Figures 6.14-6.14c. There is a close agreement between the simulated and the experimental results. In simulations, the load torque is applied abruptly as a step input whereas the load torque is gradually applied in the case of experimental investigation. Thus, there are torque oscillations in simulation results as shown in Fig. 6.14a. The oscillations in the experimental current waveforms are mainly due to the mechanical vibrations associated with the experimental assembly. The experimental current is higher than the simulated one for the same load torque because the motor has to overcome the frictional losses associated with the mechanical set-up along with viscous damping torque. In the case of experimental results, the change in the command voltage is higher than in the simulated result as it also compensates for the voltage drop in the line resistance along with the motor phase resistance.



(a)



(b)



(c)

Figure 6.14. Experimental vs. simulated responses of the motor for a step load change at 50Hz: (a) torque, (b) line current and (c) command voltage.

## 6.5 Conclusion

This chapter presents the design of a soft-starter for a hysteresis IPM motor drive. A  $V/f$  controller based soft-starter has been designed to run the motor drive at different command speeds. Both simulations and experimental investigations have been carried out to obtain the transient run-up performances of the motor. There is a close agreement between the simulation and the experimental results. Both the results exhibit good run-up and synchronization performances of the hysteresis IPM motor. The designed  $V/f$  controller limits the starting current and compensates for the line voltage drop.

Failure to stabilize an IPM motor at the command frequency using a soft-starter will cause hunting in the system. The torsional oscillation associated with sustained hunting is detrimental to the health of electromechanical assembly of the drive. In the next chapter, analysis and detection of hunting induced torsional oscillations in IPM motor drives are investigated using motor current signature analysis.

## References

1. P. P. Acarnley and J. F. Watson, "Review of position-sensorless operation of brushless permanent-magnet machines", *IEEE Transactions on Industrial Electronics*, vol. 53, no.2, pp. 352- 362, April 2006.
2. M. J. Melfi, S. D. Umans and J. E. Atem, "Viability of Highly Efficient Multi-Horsepower Line-Start Permanent-Magnet Motors", *IEEE Transactions on Industry Applications*, vol. 51, no. 1, pp. 120–128, January 2015.
3. J. Liu, T. A. Nondahl, P. B. Schmidt, S. Royak and T. M. Rowan, "Generalized stability control for open loop operation of motor drives", *IEEE Transactions on Industry Applications*, to be published.

4. P. H. Mellor, M. A. Al-Tae and K. J. Binns, "Open loop stability characteristics of synchronous drive incorporating high field permanent magnet motor", in *Proc. IEE-Electric Power Applications*, vol. 138, no. 4, pp. 175-184, July 1991.
5. R. S. Colby and D. W. Novotny, "An efficiency-optimizing permanent magnet synchronous motor drive", *IEEE Transactions on Industry Applications*, vol. 24, no. 3, pp. 462-469, May/June 1988.
6. D. W. Shimmin, J. Wang, N. Bennett and K. J. Binns, "Modeling and stability analysis of a permanent-magnet synchronous machine taking into account the effects of cage bars", in *Proc. IEE-Electric Power Applications*, vol. 142, no. 2, pp. 137-144, March 1995.
7. R. Ancuti, I. Boldea and G. D. Andreescu, "Sensorless V/f control of high-speed surface permanent magnet synchronous motor drives with two novel stabilising loops for fast dynamics and robustness", *IET Electric Power Applications*, vol. 4, no. 3, pp. 149 – 157, March 2010.
8. S. C. Agarlita, C. E. Coman, G. D. Andreescu and I. Boldea, "Stable V/f control system with controlled power factor angle for permanent magnet synchronous motor drives", *IET Electric Power Applications*, vol. 7, no. 4, pp. 278 – 286, February 2013.
9. P. D. Chandana Perera, F. Blaabjerg, J. K. Pedersen and P. Thogersen, "A Sensorless, Stable V/f Control Method for Permanent-Magnet Synchronous Motor Drives", *IEEE Transactions on Industry Applications*, vol. 39, no. 3, pp. 783-791, May/June 2003.
10. L. I. Iepure, I. Boldea, and F. Blaabjerg, "Hybrid I-f starting and observer-based sensorless control of single-phase BLDC-PM motor drives", *IEEE Transactions on Industrial Electronics*, vol. 59, no. 9, pp. 3436- 3444, September 2012.

## Chapter 7

### Analysis and Offline Diagnosis of Hunting in IPM Motor Drives

#### 7.1 Introduction

The overwhelming advancement in rare earth permanent magnet materials, power electronics and fast microprocessor technology has popularized the use of interior permanent magnet (IPM) motors in high performance variable speed drives [1]-[7]. The starting and synchronization of self-starting IPM motors for different load torques and inertias are the biggest concerns for their successful applications [7]. The synchronization capability of an IPM motor operated from a fixed frequency balanced ac supply is limited by the load torque and load inertia, due to the fixed excitation provided by magnets. Failure to start or failure of synchronization in IPM motors causes periodic rotor oscillations called hunting [8]-[10]. A self-starting IPM motor suffers from large torque pulsations during start which creates significant temporary hunting of the rotor. Also, applications like reciprocating pumps and compressors cause periodic load torque variations, inducing hunting in the system [11].

During hunting, the rotor undergoes torsional oscillations, seeking a new point of equilibrium to remain in synchronism with the stator field. The damper windings work to suppress this oscillation. If the damper windings are not able to suppress hunting, a control action is required to stabilize the rotor. In a typical synchronous motor, the external excitation provided in the rotor windings is adjusted to suppress hunting. This method is inapplicable to IPM motors as the rotor excitation is provided by the embedded

permanent magnets, and is therefore fixed. Open loop  $V/f$  controlled and fixed frequency power supply operated IPM motors do not have a stabilization loop in their control algorithm. Consequently, hunting suppression relies solely on the damping provided by the cage windings [2], [6]-[8]. Self-starting IPM motors operated from a fixed frequency fixed voltage ac supply are vulnerable to sustained hunting due to the lack of external stabilization options. Hunting results in high power losses, increases the motor temperature and applies severe stress on the electro-mechanical assembly. Sustained hunting is potentially amplified by the resonance effect, allowing the possibility of seriously damaging the integrity of the electromechanical system.

Hunting introduces torsional vibration in the motor drive system. Detection of the level of torsional vibration is crucial in order to avoid failures in the mechanical transmission system, and is traditionally carried out using external vibration sensors such as accelerometers/encoders mounted on the shaft of the motor [12]-[14]. Vibration sensors have a short lifetime and the cost for the maintenance of the vibration monitoring system is generally high [14]. Also, they are not suitable for remote monitoring of the system, and often exhibit noisy/erratic readings. Sustained hunting introduces severe stress on the mechanical drive system. The onset of sustained hunting can be viewed as a mechanical failure, and the drive system needs to be protected against any potential occurrence of sustained hunting.

Diagnosis of faults in ac motor drives has been an issue of interest for several decades. A popular method of fault diagnosis is the motor current signature analysis (MCSA) [15]-[29]. MCSA typically involves the analysis of stator current signals to detect various internal faults such symmetrical and unsymmetrical faults, magnet

demagnetization, insulation failures, overheating, winding turn-turn faults, etc. [15]-[23]. In recent years, MCSA has become popular for detecting mechanical load failures in motor drives. Blodt et. al. have investigated detection of torque oscillations due to mechanical faults using time-frequency analysis of stator current signals [24]. In their paper, stator current spectral analysis is carried out to detect load torque oscillations in an electromechanical system. Schoem and Habetler proposed a stator current spectrum analysis based condition monitoring system for detecting time varying and oscillating loads in induction motor drives [25]. Detection of torsional vibration in induction motor drives using estimated electromagnetic torque of the motor is provided in [26]. Transient electrical and mechanical faults in permanent magnet motor drives are investigated using time frequency analysis of stator current signals in [27]-[28]. Mechanical faults due to broken rotor bar, faulty gears, rotor eccentricity and bearing damage are diagnosed using stator current signatures in the literature [29]-[42].

Recent applications of MCSA based techniques involve time-frequency analysis of the stator current signal using various signal processing techniques such as the Fourier transform (FT), the discrete and continuous Wavelet transform, Wavelet packet decomposition (WPD), Wigner-Ville Distribution, the Hilbert-Huang transform, etc. [15]-[42]. The electrical signatures of different fault conditions are established through comparison of the stator current between healthy operation and the appropriate fault condition. The majority of MCSA-based fault diagnostic techniques are focused on IM drives, switch reluctance motor drives, traditional dual excitation synchronous motor drives, and closed loop feedback controlled variable speed permanent magnet motor drives. The application of self-starting IPM motors was confined to low power usages in

the past [5]-[7], and the analysis and development of a MCSA based diagnostic and protection technique for sustained hunting in IPM motors has not been conducted in the existing literature yet. MCSA based fault diagnosis is significantly faster than the traditional mechanical sensor based monitoring systems [14].

A novel procedure for analysis and real time diagnosis of hunting in IPM motors based on stator current signatures is presented in this chapter. The hunting phenomenon is defined as the sustained oscillation of the rotor around a point of equilibrium. Hunting results in electromagnetic field variations inside the motor, and thus modulates the stator currents. Frequency-domain analysis of the current signal reveals the induced modulation, expressed as variable amplitude lower and upper sidebands superimposed on the fundamental supply frequency, making the current signal non-stationary with time varying statistical properties. In this chapter, short-time Fourier transform and wavelet packet decomposition techniques are applied for analysis of the nonstationary current signals for detection and extraction of the hunting induced sideband frequency components. Statistical properties such as mean and variance of the extracted sideband signals are calculated, and a signature for the diagnosis of the hunting phenomenon is established. The proposed current signature is validated by carrying out finite element simulation for a 1-HP line-start IPM motor. Experimental investigations have been carried out for a 3-phase 4-pole 208V, 1-HP line-start IPM motor drive in order to validate the performance of the proposed method under non-ideal operating conditions. Both simulation and experimental results are presented, and analyzed in this chapter.

## 7.2 Hunting in IPM Motor Drives

The equation of motion of an IPM motor drive can be written as,

$$J \frac{d^2\delta}{dt^2} = T_s(\delta) - T_d \frac{d\delta}{dt} - T_L(\delta) \quad (7.1)$$

where  $J$  is the inertia of the motor,  $T_s$  is the synchronous torque of the motor,  $T_d$  is the damping torque coefficient,  $T_L$  is the load torque for the motor and  $\delta$  is load angle.

The synchronous torque of an IPM motor can be represented as the summation of the magnet alignment torque and reluctance torque. The equation of the synchronous torque is given below [6]:

$$T_s(\delta) = \frac{3pE_0V}{2\omega_s X_{ds}} \sin\delta + \frac{3pV^2(X_{ds} - X_{qs})}{4\omega_s X_{qs} X_{ds}} \sin 2\delta \quad (7.2)$$

where  $V$  is the supply voltage per phase,  $E_0$  is the motor back-emf,  $p$  is the number of pole pairs,  $X_{ds}$ ,  $X_{qs}$  are  $d$ - $q$  axis inductances, respectively,  $\omega_s$  is the synchronous angular frequency and  $\delta$  is electrical load angle.

Figure 7.1 shows the synchronous torque for an IPM motor. The maximum or pull out torque occurs at the load angle  $\delta_{max}$  which is between an electrical angle of  $90^\circ$  and  $180^\circ$ . The load torque is assumed constant, represented by a straight-line in the figure. When such a fixed load is applied to the motor, the points of intersection between the load line and the synchronous torque curve define the operating electrical load angle. The load angle  $\delta'_s$  is the unstable load point where the net motoring torque and the load torque are balanced. The angle  $\delta_s$  represents the stable load point sought during motor synchronization. If successful synchronization is achieved following stabilization due to inertia and damping, the operating load angle will quickly converge to  $\delta_s$ . Successive

variations in load conditions or in the power supply results in a periodic change in the load angle. This phenomenon is depicted in Figure 7.1 where the motor is experiencing a dynamic load torque varying between  $T_{L1}$  and  $T_{L2}$  with a mean value of  $T_L$ .

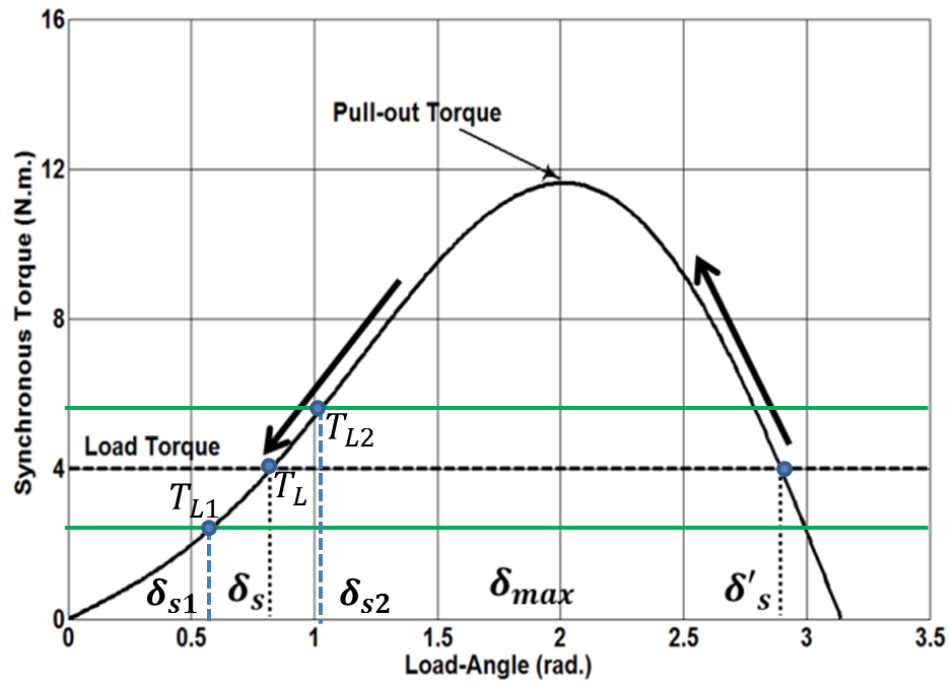


Figure 7.1. Synchronous torque vs. load angle of an IPM motor.

Due to torque variations, the operating load angle  $\delta_s$  is oscillating between  $\delta_{s1}$  and  $\delta_{s2}$  in accordance with  $T_{L1}$  and  $T_{L2}$ . Minor oscillations in the rotor speed are eventually damped out by the cage along with the shaft stiffness and viscous damping. In this event, the IPM motor operates within a practically stable limit cycle with the load angle exhibiting a low amplitude periodic variation. In the event of large oscillations in the load torque, the cage becomes unable to damp out the oscillations and the load angle  $\delta$  changes successively over a wide range. This creates large pulsations in the

developed electromagnetic torque. Thus, the whole electromechanical system starts swinging as the rotor speed periodically oscillates in order to remain synchronized with the field. At this point, the motor operates in a practically unstable limit cycle, exhibiting high amplitude torsional oscillations [43]-[45].

Figure 7.2 shows the trajectories of the load angle  $\delta$  for stable, practically stable and unstable operations of an IPM motor. Figure 7.3 illustrates the stable, practically stable and unstable limit cycles for an IPM motor. For unstable limit cycles, a sustained torsional oscillation takes place which creates significant mechanical vibrations and may lead to serious damage of the electro-mechanical assembly.

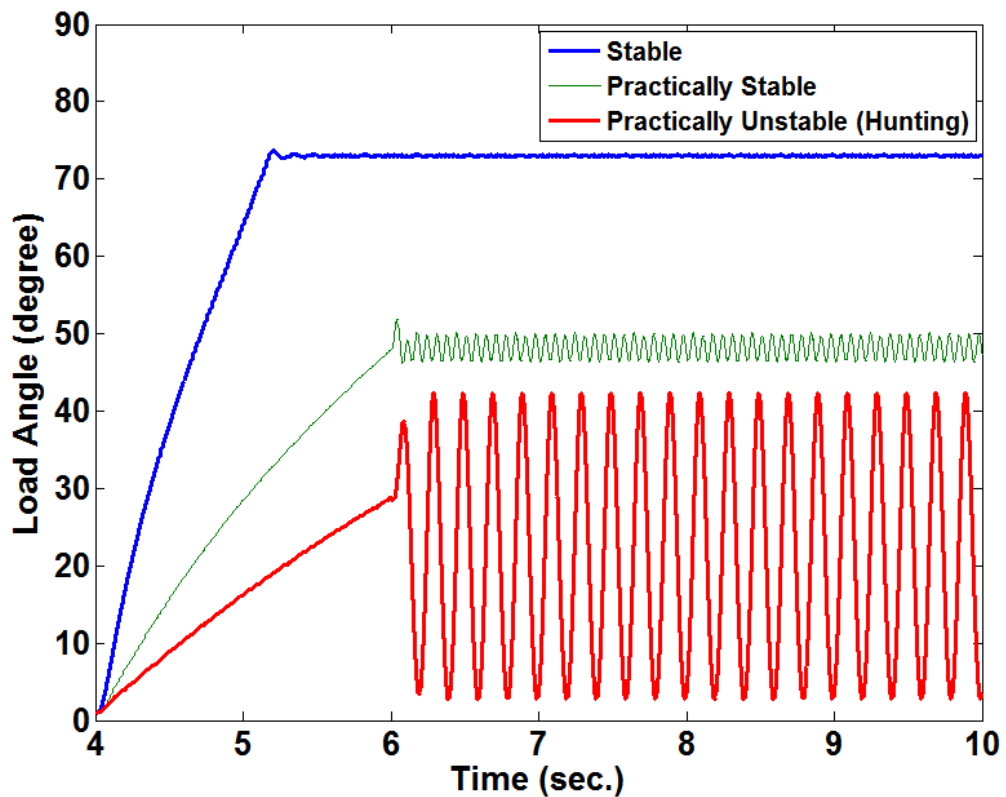


Figure 7.2. Oscillations in load angle during hunting.

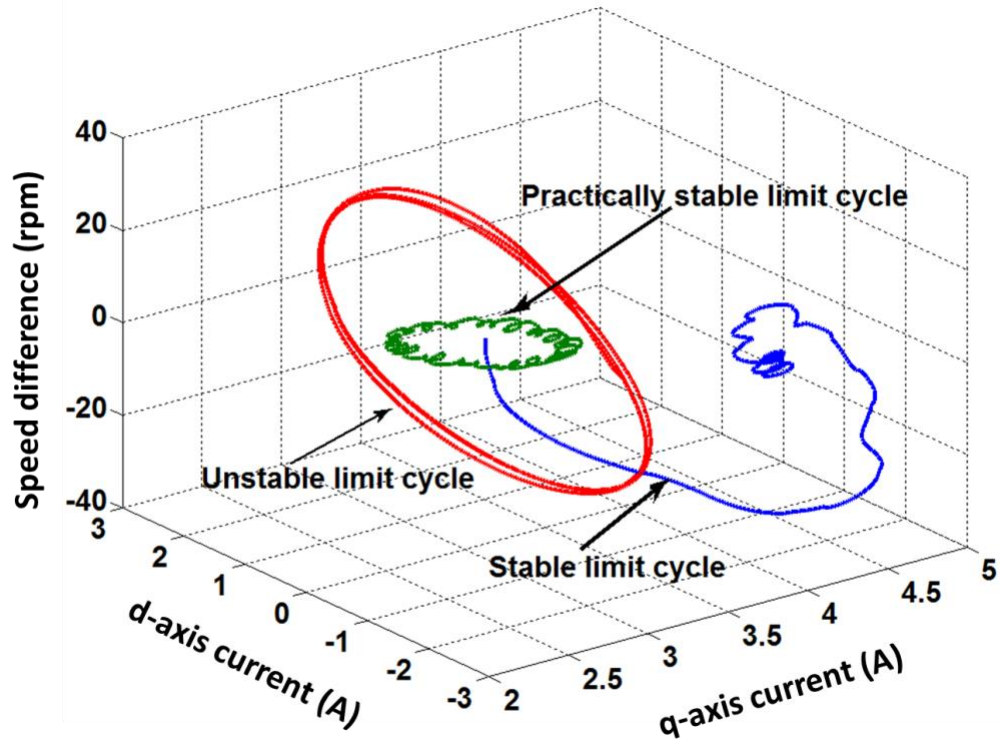


Figure 7.3. Limit cycles in an IPM motor.

### 7.3 Stator Current Signature for Detection of Hunting

Hunting in an IPM motor influences the electrical supply of the motor and creates periodic torsional oscillations [5]-[6]. The rotor speed due to torsional oscillations can be expressed as:

$$\omega_r(t) = \omega_{r0} + \sum_{j=1}^m \Delta\omega_{rj} \sin(\omega_j t + \xi_j) \quad (7.3)$$

where  $\omega_r$  is the instantaneous rotor speed,  $\omega_{r0}$  is the steady state synchronous speed,  $\Delta\omega_{rj}$  is the amplitude of the  $j^{\text{th}}$  oscillation,  $\xi_j$  is the phase shift from the torque oscillation,  $\omega_j$  is the frequency of the  $j^{\text{th}}$  oscillation and  $t$  is the time.

The rotor angle during hunting can be determined from the following equation:

$$\begin{aligned}\theta_r(t) &= p \int_0^t \omega_r(\tau) d\tau \\ &= \theta_{r0} + \sum_{j=1}^m \Delta\theta_{rj} \sin(\omega_j t + \gamma_j)\end{aligned}\quad (7.4)$$

where  $\theta_r$  is the instantaneous rotor electrical angle,  $\theta_{r0}$  is the steady state rotor angle,  $\Delta\theta_{rj}$  is the amplitude of the  $j^{\text{th}}$  oscillation,  $\gamma_j$  is the phase shift and  $p$  is the number of pole pairs. During normal behavior of the motor, the rotor lags behind the stator field and can be expressed as:

$$\theta_r(t) = \theta_{r0} = p\omega_{r0}t - \delta \quad (7.5)$$

Figure 7.4 illustrates a simplified magnetic equivalent circuit of an IPM motor. The total flux in the air-gap is a combination of the flux generated due to the magnets in the rotor and the flux generated by a rotating magnetic field due to 3-phase stator currents. The total air-gap flux can be stated by the following equation [24]:

$$\begin{aligned}\phi_g(t) &= \widetilde{\phi}_s + \widetilde{\phi}_r \\ &= \sum_{h=1}^n [\phi_{sh} \cos(\omega_{sh}t + \lambda_{sh}) + \phi_{rh} \cos(\omega_{sh}t + \psi(t))]\end{aligned}\quad (7.6)$$

where  $\phi_g$  is the air-gap flux,  $\widetilde{\phi}_s$  is the rotating magnetic flux,  $\widetilde{\phi}_r$  is the flux due to the permanent magnets,  $\lambda_{sh}$  is the phase shifts,  $\omega_{sh} = p\omega_{r0} = 2\pi f_{sh}$ ,  $h$  indicates the number of harmonics (1, 3, 5, ...) and,

$$\psi(t) = \sum_{j=1}^m \Delta\theta_{rj} \sin(\omega_j t + \gamma_j) \quad (7.7)$$

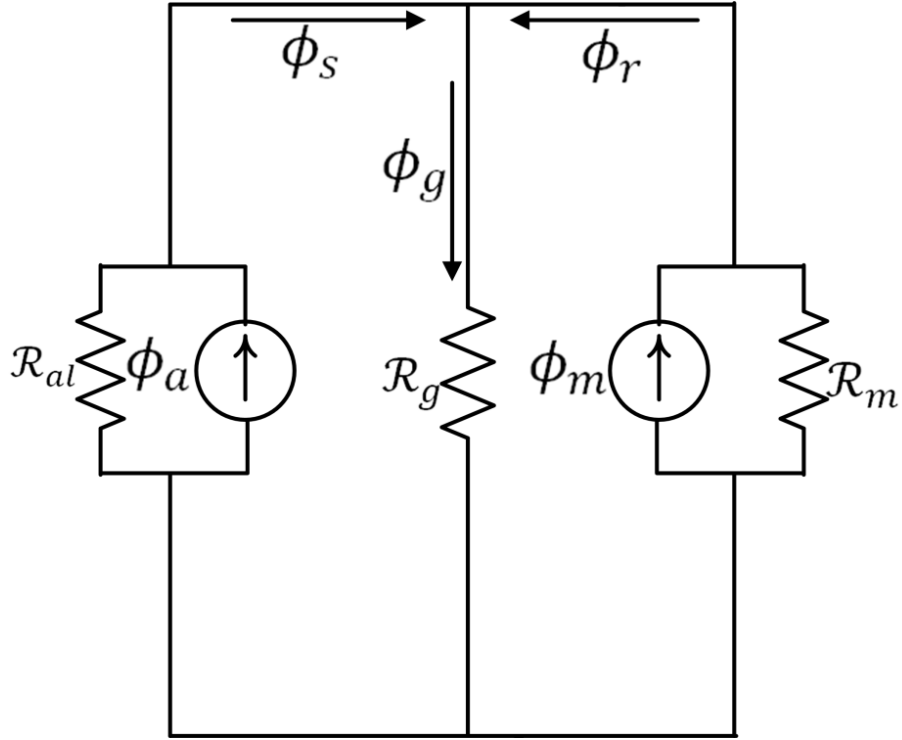


Figure 7.4. Simplified magnetic equivalent circuit of an IPM motor.

The back electromotive force (EMF) due to the air-gap flux induced in the stator coils can be calculated from the following equations:

$$\begin{aligned}
 E(t) &= \frac{d}{dt}(\phi_g(t)) \\
 &= -\sum_{h=1}^n [\omega_{sh} \phi_{sh} \sin(\omega_{sh}t + \lambda_{sh})] - \sum_{h=1}^n [\omega_{sh} \phi_{rh} \sin(\omega_{sh}t + \psi(t))] \\
 &\quad - \sum_{h=1}^n \left[ \phi_{rh} \sin(\omega_{sh}t + \psi(t)) \left\{ \sum_{j=1}^m \Delta\theta_{rj} \omega_j \cos(\omega_jt + \gamma_j) \right\} \right] \quad (7.8)
 \end{aligned}$$

Equation (7.8) can be simplified as:

$$E(t) = -\sum_{h=1}^n [V_{sh} \sin(\omega_{sh}t + \lambda_{sh})] - \sum_{h=1}^n [V_{rh} \sin(\omega_{sh}t + \psi(t))]$$

$$- \sum_{h=1}^n \frac{\phi_{rh}}{2} \left[ \sum_{j=1}^m \beta_{rj} [\sin\{(\omega_{sh} \pm \omega_j)t + \psi(t) \pm \gamma_j\}] \right] \quad (7.9)$$

where,

$$\beta_{rj} = \Delta\theta_{rj}\omega_j \quad (7.10)$$

Neglecting the stator phase resistance, the phase current is directly proportional to the induced voltage in the stator windings. The stator phase current  $I_a$  can be written as:

$$I_a(t) = \sum_{h=1}^n [I_{sh} \sin(\omega_{sh}t + \sigma_{sh})] + \sum_{h=1}^n [I_{rh} \sin(\omega_{sh}t + \psi(t))] \\ + \sum_{h=1}^n \frac{\phi_{rh}}{2} \left[ \sum_{j=1}^m \beta_{r1j} [\sin\{(\omega_{sh} \pm \omega_j)t + \psi(t) \pm \gamma_j\}] \right] \quad (7.11)$$

where  $\sigma_{sh}$  is the phase shift and  $\beta_{r1j}$  is a fraction of the amplitude of the modulation current depending on the magnitude and frequency of the rotor oscillation. It is evident from (7.11) that the stator current is both amplitude and phase modulated during hunting, becoming a non-stationary signal with time varying statistical properties.

#### 7.4 Detection of Hunting using Short-Time Fourier Transform

The Fourier transform (FT) is a standard signal processing technique for frequency domain analysis of stationary signals. However, the stator current becomes a non-stationary signal during hunting and can be realized from (7.11). In order to transform the stator current signal from time-domain to frequency domain, the third term in (7.11) is neglected because the magnitudes of  $\beta_{r1j}$  and  $\phi_{rh}$  are very small. Based on this assumption, the stator current during hunting can be expressed as,

$$I_a(t) = I_s(t) + I_r(t) \quad (7.12)$$

or,

$$I_a(t) = \sum_{h=1}^n [I_{sh} \sin(\omega_{sh}t + \sigma_{sh})] + \sum_{h=1}^n \left[ I_{rh} \sin \left( \omega_{sh}t + \sum_{j=1}^m \Delta\theta_{rj} \sin(\omega_jt + \gamma_j) \right) \right] \quad (7.13)$$

where  $I_s$  is the unmodulated current induced by the stator mmf and  $I_r$  is the modulated current induced due to the rotor mmf. Constant phase shifts such as  $\sigma_{sh}$  and  $\gamma_j$  are insignificant in the frequency domain and can be assumed to be zero. The modulated current  $I_r$  for  $j = 1$  can be expressed as,

$$I_r(t) = \sum_{h=1}^n [I_{rh} \sin(2\pi f_{sh}t + \Delta\theta_{r1} \sin(2\pi f_1t))] \quad (7.14)$$

or,

$$I_r(t) = \sum_{h=1}^n \text{Im}(I_{rh} e^{j2\pi f_{sh}t} e^{j\Delta\theta_{r1} \sin(2\pi f_1t)}); \quad (7.15)$$

The Fourier series expansion of (7.15) can be approximated as [46],

$$I_r(t) = \sum_{h=1}^n \sum_{m=-\infty}^{m=\infty} \text{Im}(I_{rh} J_m(\Delta\theta_{r1}) e^{j2\pi f_{sh}t} e^{j2\pi m f_1t}) \quad (7.16)$$

Or,

$$I_r(t) = \sum_{h=1}^n \sum_{m=-\infty}^{m=\infty} I_{rh} J_m(\Delta\theta_{r1}) \sin(2\pi(f_{sh} + m f_1)t) \quad (7.17)$$

Figure 7.5 displays the Bessel function of the first kind for different orders. For narrowband frequency modulated signals with a low modulation index, the higher order order Bessel functions ( $m \geq 2$ ) have negligible contributions to the overall signal value and can be ignored. For small values of  $\Delta\theta_{r1}$ ,  $I_r$  can be represented as,

$$I_r(t) = \sum_{h=1}^n I_{rh} J_0(\Delta\theta_{r1}) \sin(2\pi f_{sh}t) + \sum_{h=1}^n I_{rh} J_1(\Delta\theta_{r1}) \sin(2\pi(f_{sh} + f_1)t) + \sum_{h=1}^n I_{rh} J_{-1}(\Delta\theta_{r1}) \sin(2\pi(f_{sh} - f_1)t) \quad (7.18)$$

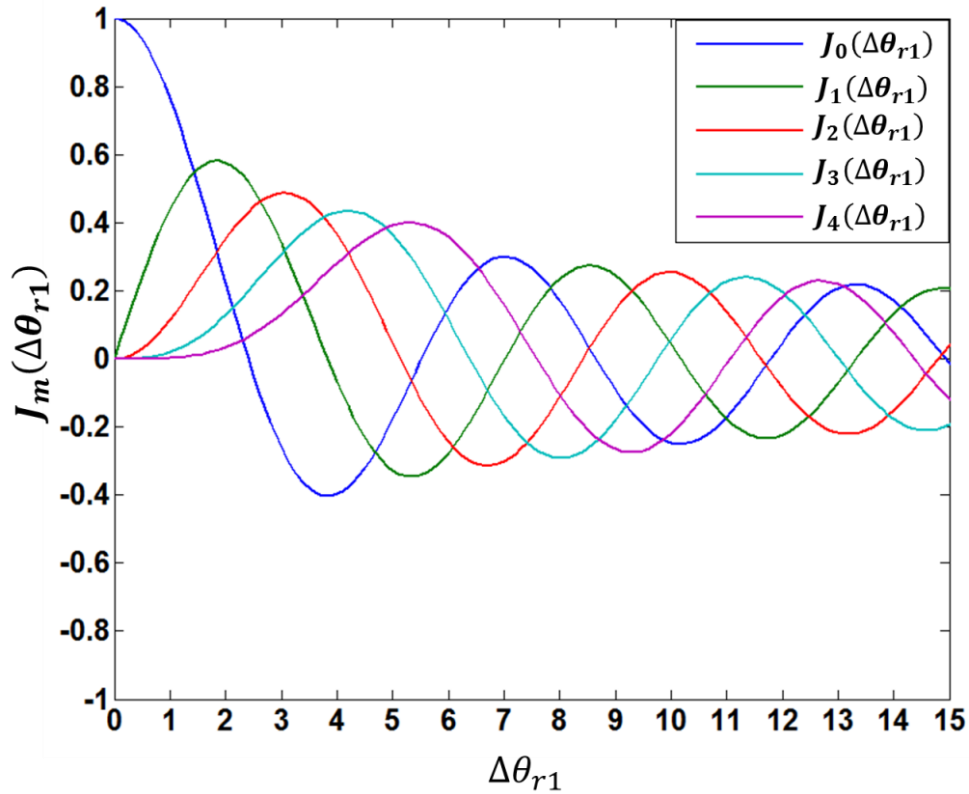


Figure 7.5. Bessel functions of the first kind for different orders.

Using FT of (7.18), the frequency domain representation of (7.18) can be expressed as follows [46],

$$\begin{aligned}
I_r(j\omega) = & \sum_{h=1}^n I_{rh} J_0(\Delta\theta_{r1}) \frac{\pi}{j} [\delta(2\pi(f - f_{sh})) - \delta(2\pi(f + f_{sh}))] \\
& + \sum_{h=1}^n I_{rh} J_1(\Delta\theta_{r1}) \frac{\pi}{j} [\delta(2\pi(f - (f_{sh} + f_1))) - \delta(2\pi(f + (f_{sh} + f_1)))] \\
& + \sum_{h=1}^n I_{rh} J_{-1}(\Delta\theta_{r1}) \frac{\pi}{j} [\delta(2\pi(f - (f_{sh} - f_1))) - \delta(2\pi(f + (f_{sh} - f_1)))] \quad (7.19)
\end{aligned}$$

It is evident from the frequency domain analysis of the stator current signal that the modulated current signal during hunting contains lower and upper sidebands around the fundamental frequency and its multiples. The frequencies of the sidebands can be expressed as:

$$[\{f_1^1, f_1^2, \dots\}, \{f_3^1, f_3^2, \dots\}, \dots] = \sum_{h=1}^n \left[ f_{sh} \pm \sum_{j=1}^m f_j \right] \quad (7.20)$$

The sideband components around the fundamental frequency will have the following frequencies,

$$[\{f_s^1\}, \{f_s^2\}] = \left[ \left\{ f_s - \sum_{j=1}^m f_j \right\}, \left\{ f_s + \sum_{j=1}^m f_j \right\} \right] \quad (7.21)$$

where  $f_s^1$  and  $f_s^2$  are the set of lower and upper sideband frequencies, respectively,  $f_j$  is the frequency of the  $j$ th oscillation and  $f_s$  is the supply frequency.

The Fourier transform is a standard signal processing tool suitable for stationary signals. In the case of hunting, the motor current becomes non-stationary due to phase

modulation as presented in (7.13). The short-time Fourier transform (STFT) is an extension of the Fourier Transform. STFT can perform time-frequency analysis of nonstationary signals. It breaks the whole data set into a series of data frames of equal length called windows. The windows are generally overlapped to avoid any loss of information near the boundaries. The FT of a discrete stator phase current  $i_a$  can be expressed as follows [46],

$$\text{STFT}\{i_a[n]\} = I_a[m, \omega] = \sum_{n=-\infty}^{\infty} i_a[m] w[n - m] e^{-j\omega n} \quad (7.22)$$

where  $i_a [m]w[n - m]$  is a short-time window of  $i_a [n]$  at time  $m$ .

The discrete version of the STFT applies a Fourier transform to each of the window segments of  $i_a [n]$ , and can be expressed as follows [46]:

$$\text{discrete STFT}\{i_a [n]\} = I_a [m, k] = I_a [m, \omega] \Big|_{\omega = \frac{2\pi k}{N}} \text{ for } 0 \leq k \leq N - 1 \quad (7.23)$$

where  $n$  is the time and  $k$  is the frequency of the discrete signal ( $k = 0, 1, 2, \dots, N-1$ ),  $N$  is the size of the window and  $m$  is the index. A Hamming type of window is used in this thesis for carrying out the discrete STFT.

The power spectral density (PSD) of a signal provides the distribution of energy in the signal over a range of frequencies. The PSD of a discrete non-stationary signal can be obtained using the STFT. The expression for calculating the PSD of the stator current can be expressed as [46],

$$PSD_{I_a}(f) = \left(\frac{1}{N}\right) \sum_{n=1}^N |\text{STFT}\{i_a [n]\}|^2 \quad (7.24)$$

Figure 7.6a illustrates the phase-A stator current waveform of a 3-phase 4-pole 1-HP line-start IPM motor during its stable operation at 60 Hz supply frequency. The current waveform is sinusoidal with minimum harmonic distortion. There exists no significant amplitude modulation in the current waveform. The existing low amplitude sidebands are due to the pole pass frequency 30Hz for the 4-pole motor. Figure 7.6b displays the PSD of stator currents using STFT. No substantial sideband components exist within the frequency spectrum.

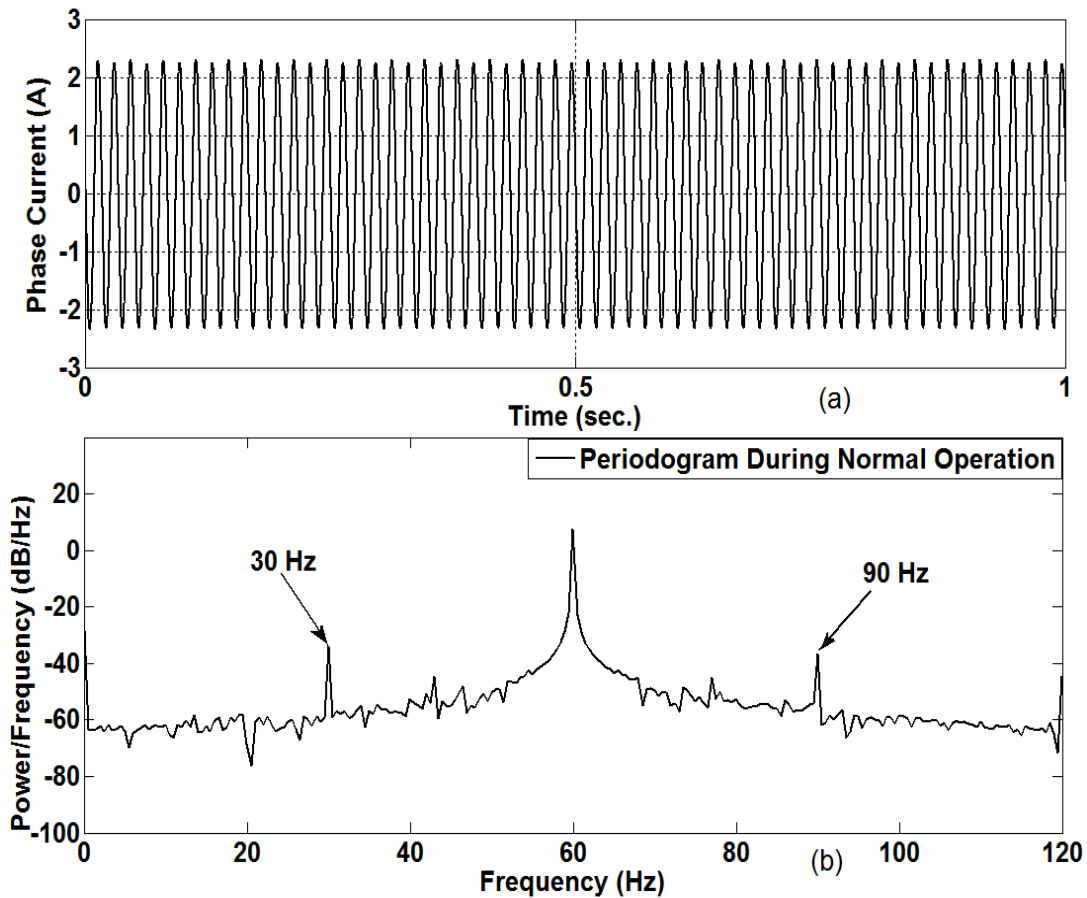
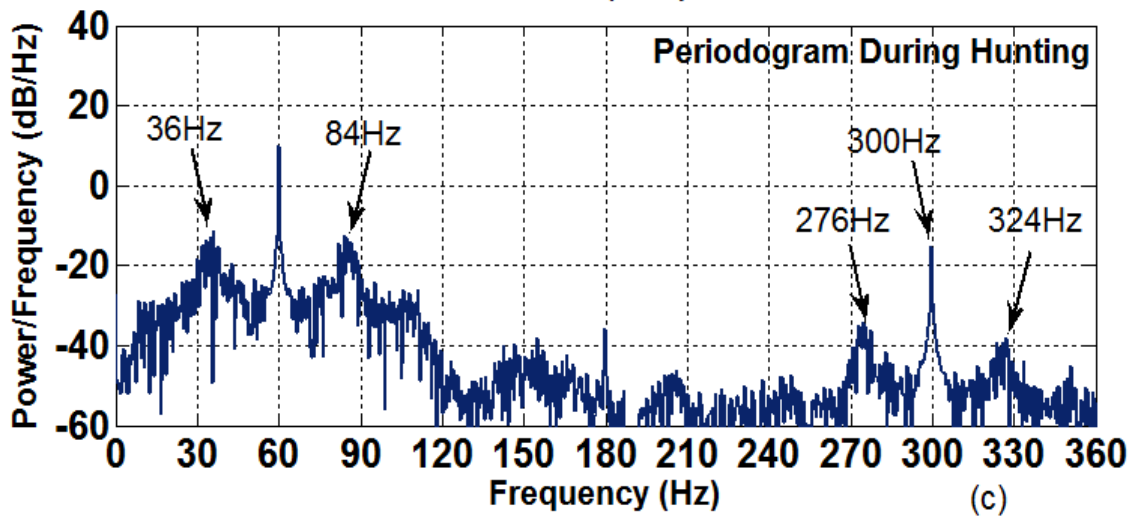
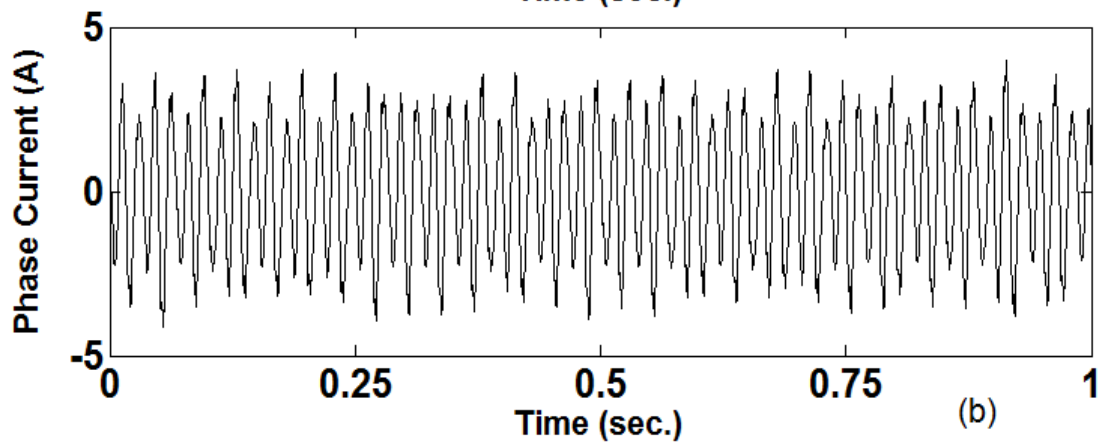
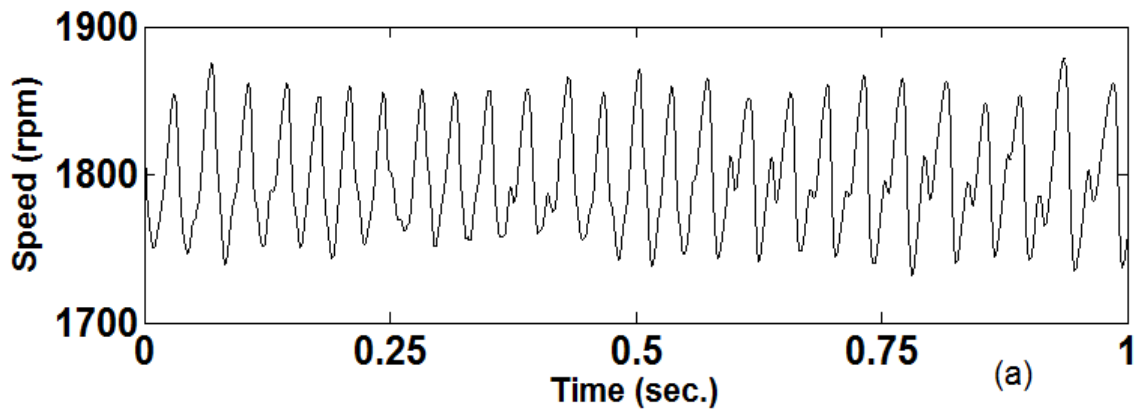


Figure 7.6. Current response at normal operation: (a) phase-A current and (b) PSD of the current signal.

The rotor speed of the motor during hunting and the distorted stator current waveform are demonstrated in Figures 7.7a and 7.7b, respectively. The rotor is experiencing a sustained oscillation around the synchronous speed resulting in an unstable operation of the motor. This sustained rotor oscillation creates torsional vibration in the electromechanical system. Figure 7.7c presents the frequency spectrum of the phase-A current of the motor during this unstable operation. The frequency spectrum contains a series of low and high frequency sidebands centered on the fundamental frequency 60Hz. The energies of the sidebands are spread over a range of frequencies, demonstrating significant phase modulation in the system. The prominent frequencies of the lower and upper sidebands are 36Hz and 84Hz, respectively.

Figure 7.7d displays the vibration spectrum which contains frequencies of the rotor oscillation. The rotor vibration due to hunting is reflected back into the stator currents, producing amplitude modulation of the current waveform. The notable vibrational frequencies with high energies are 24Hz and 48Hz. The frequencies of the major sidebands in the current spectrum are related to the vibrational frequencies based on (7.21). The presence of the sideband frequencies in the current waveform is a signature that can be used to detect hunting phenomena for a line-start IPM motor without the need of a mechanical vibration sensor or a rotor position sensor.



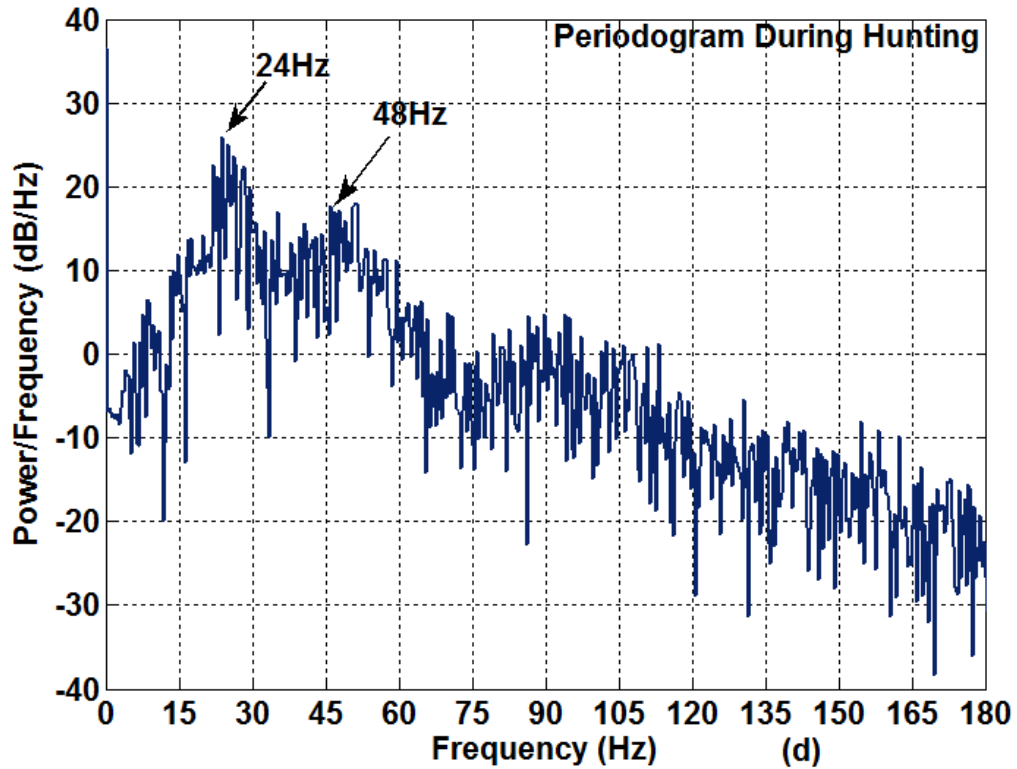


Figure 7.7. Responses during hunting condition: (a) rotor speed, (b) phase-A current (c) PSD of the current signal and (d) PSD of the rotor speed oscillations.

### 7.5 Diagnosis of Hunting Using Wavelet Packet Decomposition (WPD)

The short-time Fourier transform (STFT) suffers from the inability to perform multi-resolution analysis of a signal. It requires a longer window size for good frequency resolution. However, a shorter window for STFT provides good time resolution but limits the frequency resolution [39]. In order to identify the onset of hunting phenomenon, the stator current needs to be analyzed with good frequency resolution as well as high time resolution. Wavelet Packet Decomposition (WPD) is a signal processing tool that uses the discrete wavelet transformation (DWT) to perform multi-resolution analysis of a signal.

The WPD offers high time resolution at high frequencies and good frequency resolution at low frequencies. It also allows time localization within any given frequency band. This capability is crucial for the detection and localization of hunting phenomena using the stator current signal. The WPD has higher degree of frequency resolution than the DWT and is computationally less expensive than the continuous wavelet transform (CWT). It can decompose a given signal to create a full binary tree containing the low pass (approximate) and high pass (detail) components of the signal measured at different decomposition levels.

### 7.5.1 Wavelet Packet Decomposition (WPD)

Wavelet packet decomposition (WPD) is a signal processing tool that uses the discrete wavelet transformation (DWT) to perform multi-resolution analysis of a signal. A multiresolution analysis of the Lebesgue space  $\mathcal{L}^2(\mathbb{R})$  is a sequence of closed subspaces  $\{\dots, V_{-1}, V_0, V_1, V_2, \dots, V_j\}$  that meets the following criteria [47]:

- Containment:  $V_j \subset V_{j-1} \subset \mathcal{L}^2$  for all  $j \in \mathbb{Z}$
- Decrease:  $\lim_{j \rightarrow \infty} V_j = 0$ , i. e.  $\bigcap_{j > N} V_j = \{0\}$  for all  $N$
- Increase:  $\lim_{j \rightarrow -\infty} V_j = \mathcal{L}^2$ , i. e.  $\bigcup_{j < N} V_j = \mathcal{L}^2$  for all  $N$
- Dilation:  $v(2t) \in V_{j-1} \Leftrightarrow v(t) \in V_j$
- Generator: There is a function  $\phi \in V_0$  whose translations  $\{\phi(t - k): k \in \mathbb{Z}\}$  form a Riesz basis for  $V_0$ .

The WPD method decomposes a signal into its details (high pass) and approximations (low pass) by a multiresolution analysis of the signal using successive

applications of a wavelet filtering operation to each level of the decomposition. Wavelet filters are orthogonal quadrature mirror filter functions  $g[k]$  and  $h[k]$  that perform high and low pass filtering operations to the discrete signal, respectively. The coefficients of  $g[k]$  and  $h[k]$  are determined by solving refinement equations of a scaling function  $\Phi(t)$  and its associated mother wavelet function  $\psi(t)$ . Using the containment, dilation and generator properties of a subspace  $V_0 \subset \mathcal{L}^2(\mathbb{R})$ , a normalized scaling function  $\phi \in V_0$  satisfies a two-scale equation [47]:

$$\phi(t) = \sqrt{2} \sum_{k=0}^{2N-1} g[k] \phi(2t - k) \stackrel{\text{def}}{=} G\phi(t) \quad (7.25)$$

where  $2N$  is the length of the two filters,  $k$  is the index,  $t$  denotes the time and  $G$  is a quadrature filter.

Any Lebesgue space  $\mathcal{L}^2(\mathbb{R})$  can be divided in a set of complementary subspaces  $W_i$  where  $W_i = V_{i-1} - V_i$  so that  $V_{i-1} = V_i + W_i$ . Using the increase property of MRA, the Lebesgue space can be written as [47]:

$$\mathcal{L}^2 = \sum_{i \in \mathbb{Z}} W_i \quad (7.26)$$

Each of the subspaces  $W_i$  is called a wavelet subspace and a wavelet decomposition of  $\mathcal{L}^2$  is obtained using (7.26). Any mother wavelet function  $\psi \in W_0$  satisfies the following wavelet equation [47]:

$$\psi(t) = \sqrt{2} \sum_{k=0}^{2N-1} h[k] \phi(2t - k) \stackrel{\text{def}}{=} H\psi(t) \quad (7.27)$$

where  $H$  is a quadrature filter. The filter coefficients of  $g[k]$  and  $h[k]$  satisfy the following relationship [47],

$$h[k] = (-1)^k g[2N - 1] \quad (7.28)$$

The selection of a mother wavelet function in order to determine filter coefficients depends on selection factors such as the minimum description length (MDL) data criterion, minimum Shannon entropy criterion, maximum likelihood criterion, minimum mean squared error (MSE) between wavelet coefficients and reconstructed signals, etc. In this thesis, MDL is considered as the selection factor and “daubechies” wavelet families have low MDL index values [48]. “daubechies6 (*db6*)” is found to be the appropriate wavelet basis function for the fast detection of the hunting and is also suitable for reliable reconstruction of the wavelet coefficients in order to identify the severity of hunting [15], [48]. The magnitudes of the frequency response of ‘*db6*’ filter coefficients are illustrated in Figure 7.8. The exact values of the ‘*db6*’ decomposition and reconstruction filter coefficients are listed in table 7.1 in the appendix.

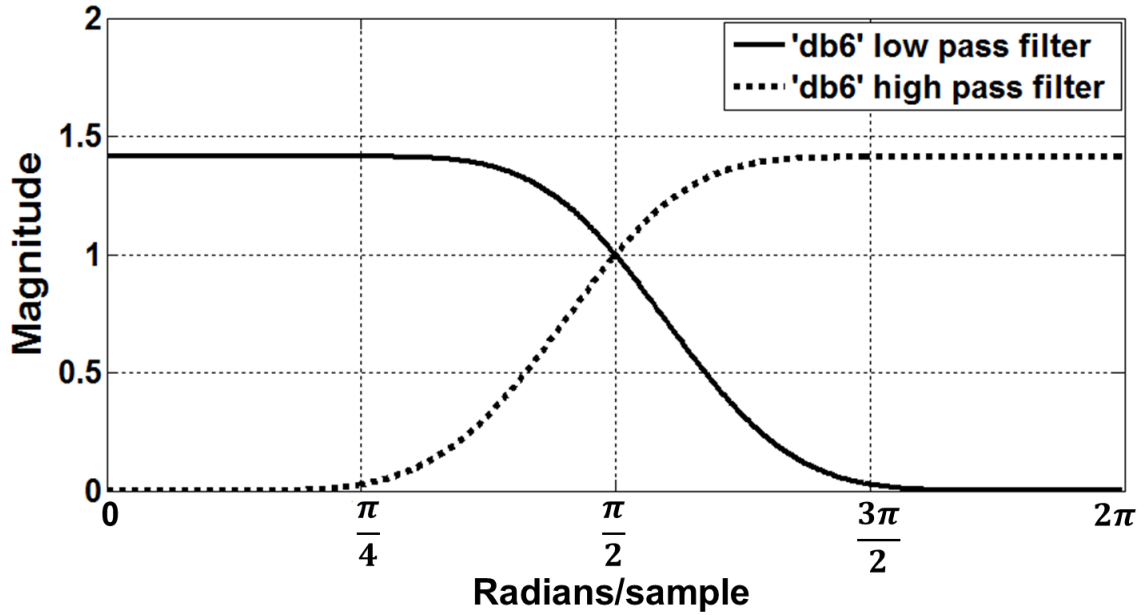


Figure 7.8. Magnitudes of the frequency responses of ‘db6’ wavelet filters.

### 7.5.2 Diagnosis of Hunting Using WPD

Figure 7.9 illustrates a wavelet packet tree (WPT) of the decomposed stator current signal obtained by successive applications of wavelet filtering operation to each level of the decomposition. The first level node coefficients of the WPT are calculated from the following equations [47],

$$I_{1,0}[n] = (g * I)[n] = \sum_{k=0}^{N-1} g[k] I(N - k) \quad (7.29)$$

$$I_{1,1}[n] = (h * I)[n] = \sum_{k=0}^{N-1} h[k] I(N - k) \quad (7.30)$$

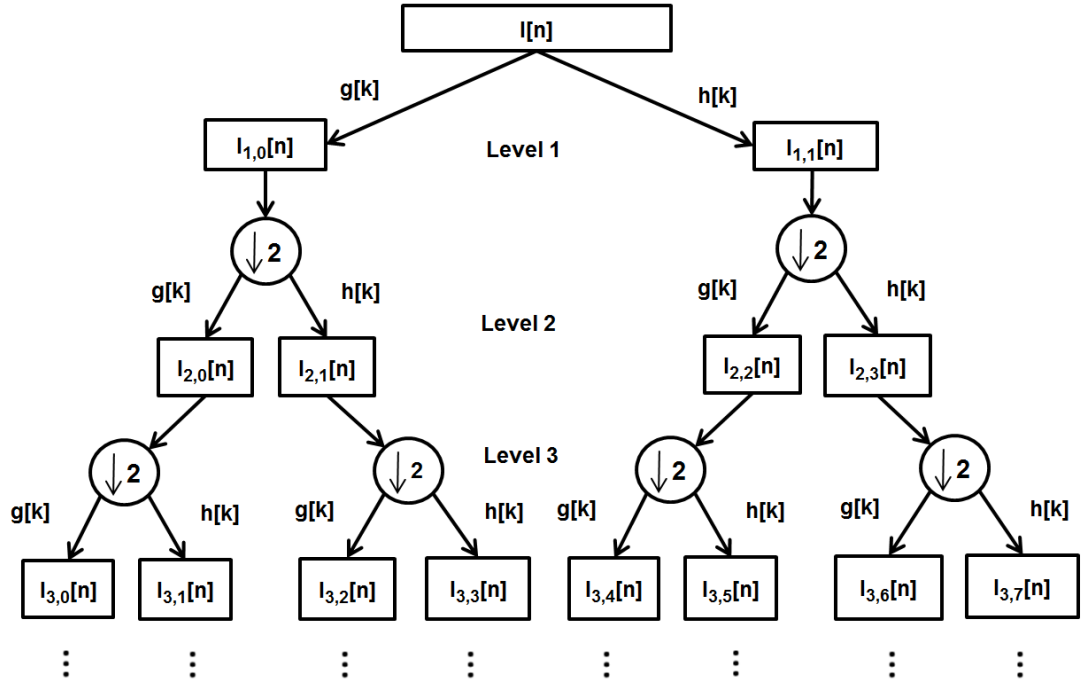


Figure 7.9. Wavelet packet decomposition tree of the current signal.

The second level node coefficients are obtained after down-sampling the first level nodes by 2 and applying wavelet filtering on the downsampled data. The equations for obtaining 2<sup>nd</sup> level coefficients are [47],

$$I_{2,0}[n] = (g * (I_{1,0} \downarrow 2))[n] = \sum_{k=0}^{\frac{N}{2}-1} g[k] I_{1,0}\left(\frac{N}{2} - k\right) \quad (7.31)$$

$$I_{2,1}[n] = (h * (I_{1,0} \downarrow 2))[n] = \sum_{k=0}^{\frac{N}{2}-1} h[k] I_{1,0}\left(\frac{N}{2} - k\right) \quad (7.32)$$

$$I_{2,2}[n] = (g * (I_{1,1} \downarrow 2))[n] = \sum_{k=0}^{\frac{N}{2}-1} g[k] I_{1,1}\left(\frac{N}{2} - k\right) \quad (7.33)$$

$$I_{2,3}[n] = (h * (I_{1,0} \downarrow 2))[n] = \sum_{k=0}^{\frac{N}{2}-1} h[k] I_{1,1} \left( \frac{N}{2} - k \right) \quad (7.34)$$

The abovementioned process is iterated up to the 5<sup>th</sup> level of decomposition in order to construct the full tree. The stator current is sampled with 16 samples per cycle for a window of 64 cycles. The level 5 WPD exhibits a balance of time-frequency resolution optimal for signature detection. At this level, several nodes contain frequencies corresponding to the signature of hunting.

### 7.5.3 Feature Extraction

Signature identification proceeds with the evaluation of the WPT feature coefficients. The feature co-efficient of each node is defined as the variance of the node's coefficient vector, and is calculated from the following equations:

$$F_{i,j} = \sigma_{i,j}^2 = \frac{1}{L-1} \sum_{k=1}^L (I_{i,j}[k] - \mu_{i,j})^2 \quad (7.35)$$

$$\mu_{i,j} = \frac{1}{L} \sum_{k=1}^L I_{i,j}[k] \quad (7.36)$$

where  $F_{i,j}$  is the feature co-efficient of the WPT node  $(i, j)$ ,  $I_{i,j}[k]$  is the magnitude of the co-efficient  $k$  at node  $(i, j)$ ,  $\sigma_{i,j}^2, \mu_{i,j}$  are the variance and the mean of the coefficients at node  $(i, j)$ , respectively and  $L$  is the total number of co-efficients inside that node.

During hunting phenomena, the side band frequencies in the WPT are widely distributed, and will spread over more than one node in the WPT. The energy of the nodes containing the sideband frequency components will be very low and insignificant during

normal operation of the motor. However, the energy contained within these nodes will be higher than the normal values during hunting, varying significantly corresponding to the frequency of the rotor speed oscillations. The energy within the other nodes will not change significantly. This relative variation of node energy is considered in this thesis as a signature for hunting detection in a line start IPM motor.

## 7.6 Simulation Results

Finite element (FE) simulations are carried out using ANSYS Maxwell to analyze hunting phenomena for a 3-phase 4-pole 208V 1-HP line-start IPM motor drive. Figure 7.10 displays a FE model of the motor. Hunting is introduced in the motor by periodic variations of the load torque. The load torque is assumed as time varying based on the following relationship,

$$T_L(t) = A + B \sin(2\pi f_L t) \quad (7.37)$$

where  $A$  is constant load torque,  $B$  is the coefficient of the time varying load torque and  $f_L$  is the frequency of load torque oscillation.

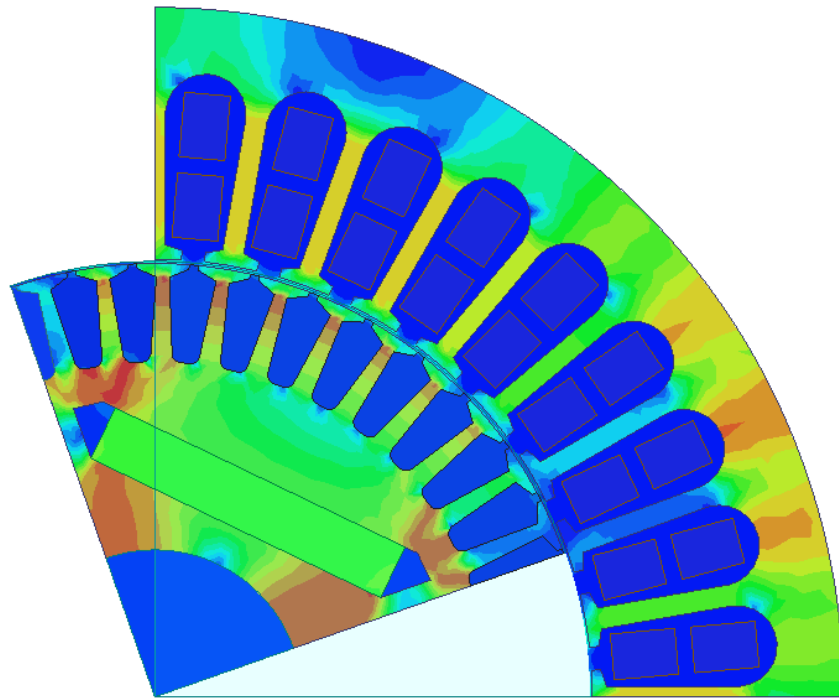
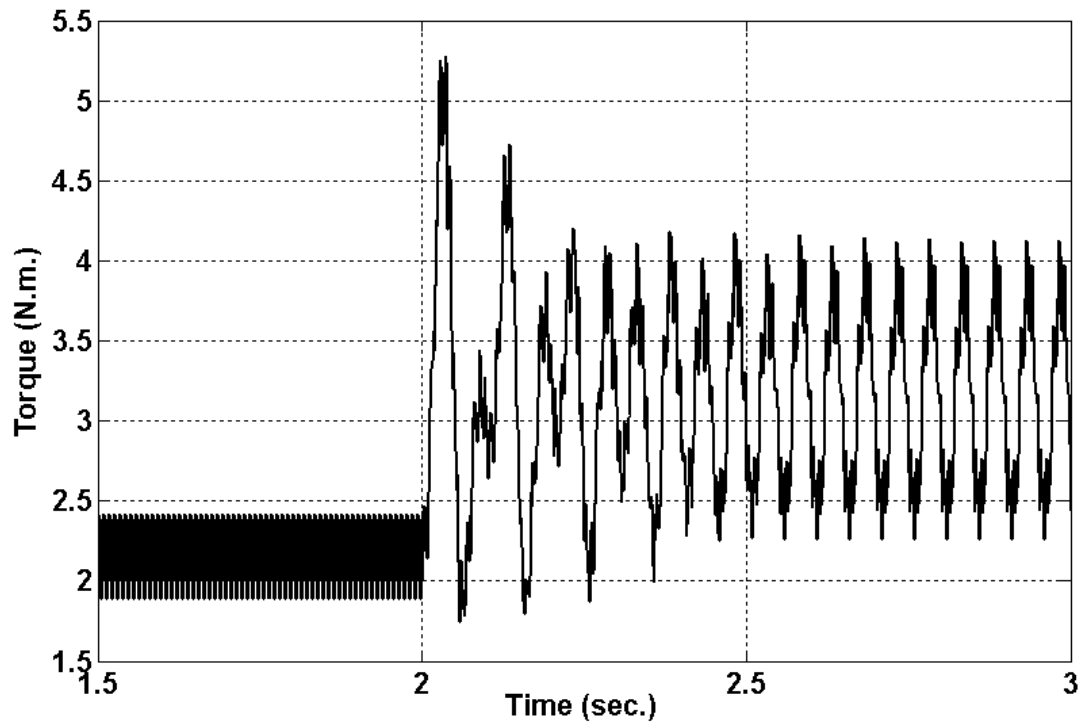
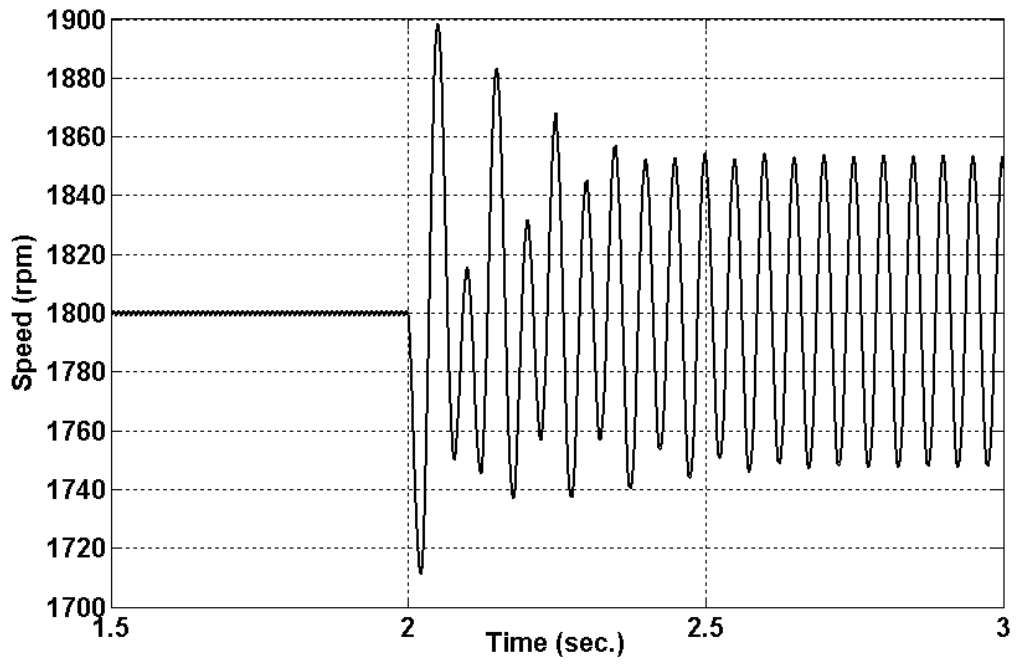


Figure 7.10. Finite element model of the 1-HP LSIPM motor.

The hunting phenomenon for the motor drive is studied for different operating frequencies. Figures 7.11a-7.11c illustrate the torque, speed and current responses of the motor, respectively, for both normal and hunting induced operations. The main supply frequency is fixed at 60Hz. Hunting is introduced after 2s by injecting load torque oscillations using (7.28).  $f_L$  is selected as 20Hz. The effect of load variations is reflected into the motor electromagnetic torque and rotor speed, introducing significant torque and speed oscillations. This phenomenon is depicted in Figures 7.11a-7.11b. The variation of the air-gap torque influences the stator current, creating noticeable amplitude and phase modulation. The modulated stator current waveform is depicted in Figure 7.11c.



(a)



(b)

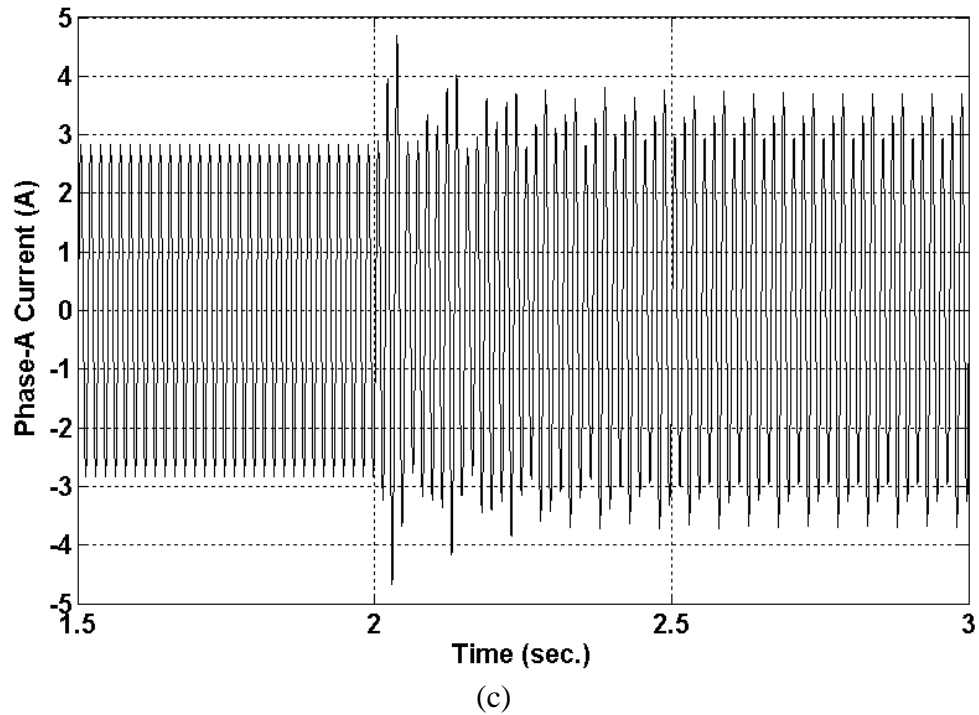
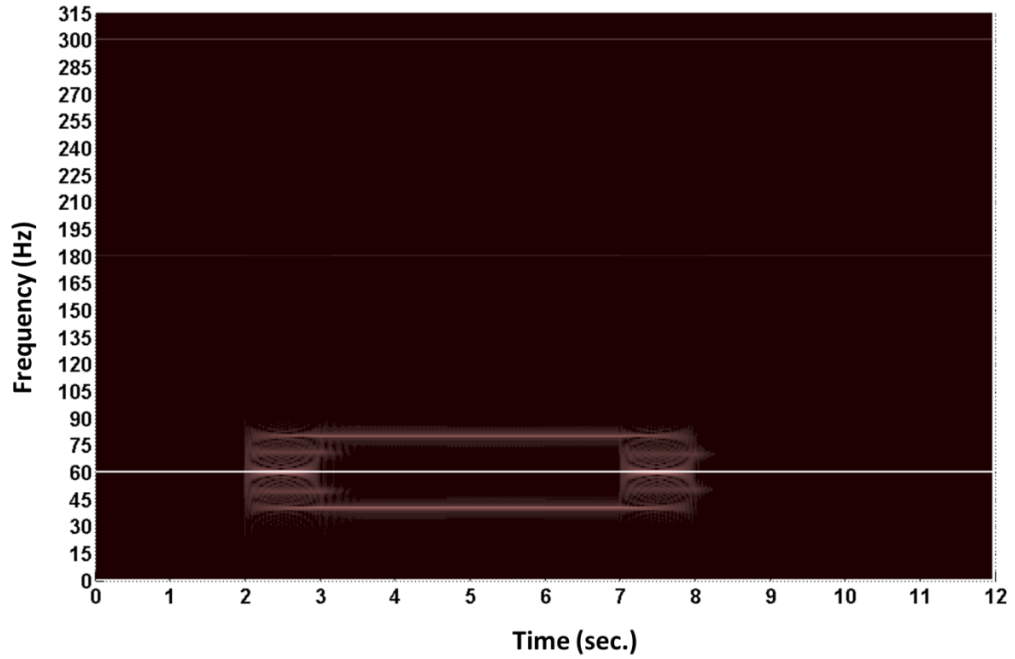


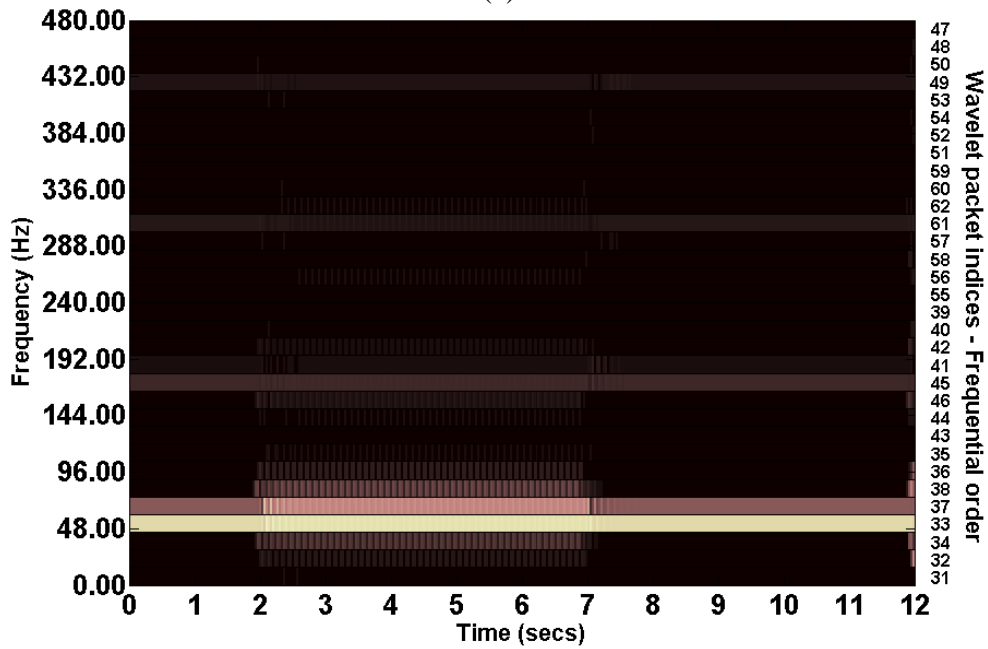
Figure 7.11. Responses of the motor during hunting at 60 Hz supply frequency: (a) torque, (b) speed and (c) current.

Frequency domain analysis of the simulated phase current signal is carried out using short-time Fourier Transform (STFT) and wavelet packet decomposition (WPD) techniques. The spectrogram of the stator current signal using STFT is illustrated in Figure 7.12a. Hunting is removed from the system after  $t=7$ s. At the onset of hunting, the rotor experiences severe torsional oscillations, resulting in significant phase and amplitude modulation of the stator current. The severity of phase modulation goes down but the stator current remains considerably amplitude modulated during the entire period of hunting. Due to the primary hunting frequency of 20Hz, the frequencies of the major lower and upper sidebands around the fundamental frequency are 40Hz and 80Hz, respectively. A large modulation also takes place in the stator current signal at the

moment when the hunting is removed. During this period, the rotor snaps itself back to synchronism.



(a)



(b)

Figure 7.12. Spectrogram for 60Hz using: (a) STFT and (b) WPD.

The frequency spectrum of the stator current using WPD is illustrated in Figure 7.12b. Only level 5 wavelet nodes are depicted in the figure. The frequency band of each node in level 5 is 15Hz for 60Hz supply frequency due to the sampling frequency of 960Hz. The level 5 nodes are numbered based on the natural ordering during the construction of the WPT. Node 31 is the first node in level 5 and corresponds to the node (5, 0) in the WPT. The fundamental component is distributed between nodes 33 and 37. The sideband components appear during the presence of hunting- appearing as hotspots around nodes 33 and 37 in the stator current spectrum. The prominent lower sidebands around the fundamental are present in nodes 32 (15Hz-30Hz) and 34 (30Hz-45Hz). The higher sidebands are contained in nodes 38 (75Hz-90Hz) and 36 (90Hz-105Hz). The feature coefficients of these nodes are displayed in Figure 7.13. Nodes 32, 34, 36, 38 correspond to nodes (5, 1), (5, 2), (5, 6) and (5, 5) in the wavelet decomposition tree, respectively. These nodes are the descendants from the first level approximation at node (1, 0) in the tree. The magnitude of the feature coefficients of these nodes is low during normal operation of the motor, indicating stable operation with no significant mechanical vibration. The hunting phenomenon starts at time  $t = 2$  and the introduction of modulation causes the feature coefficients of nodes 32, 34, 36 and 38 to become high. The feature coefficients of nodes 34 and 38 have the highest values among the wavelet nodes because they contain the prominent lower and upper sidebands. The sharp rise of the coefficient values indicates the onset of hunting.

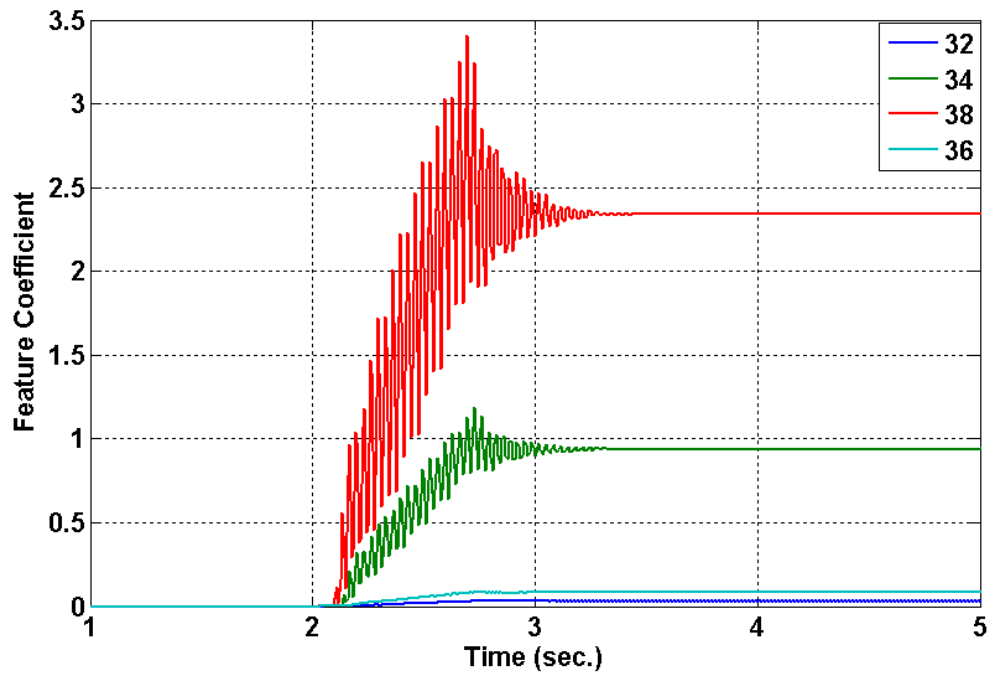
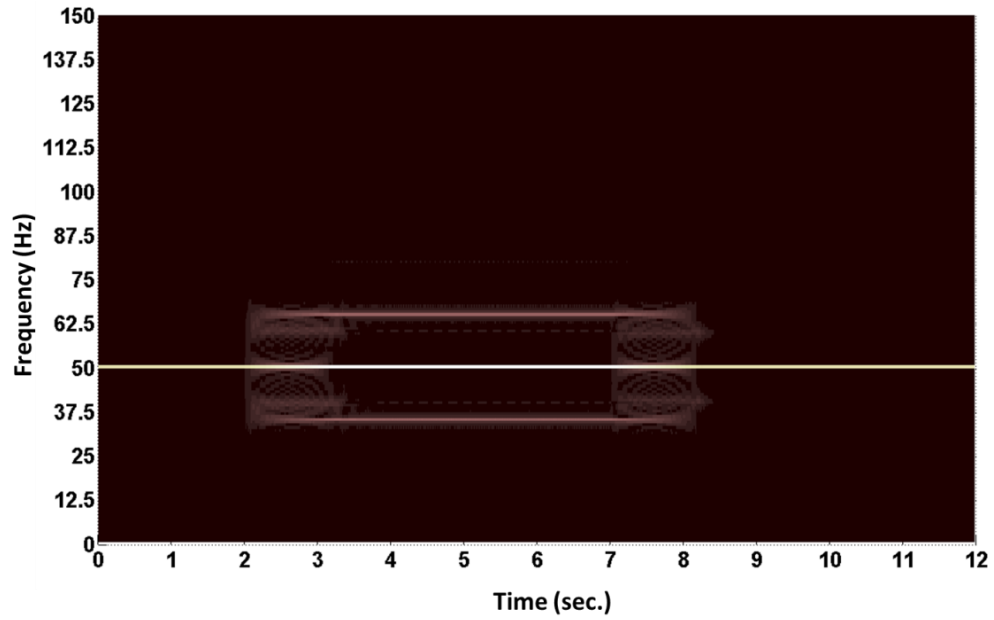


Figure 7.13. Feature coefficients at 60Hz command frequency.

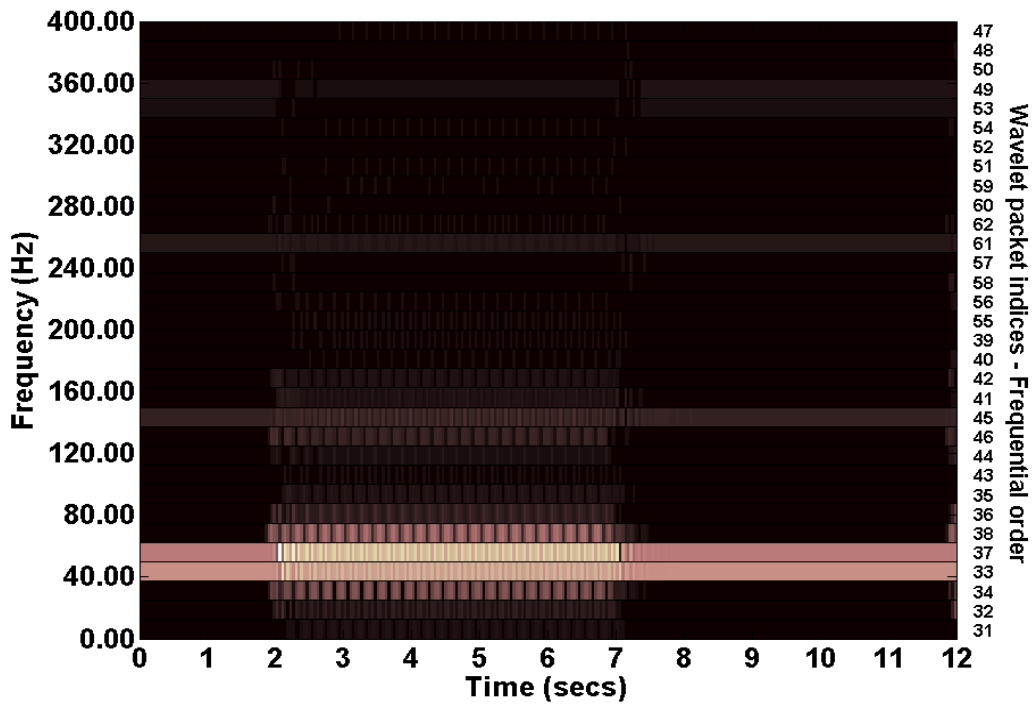
The hunting phenomenon for the 1-HP motor drive is also investigated for a 50Hz supply frequency. Hunting is created in the motor drive at  $t=2s$  by varying the load torque with  $f_L$  equal to 15Hz. Figures 7.14a-7.14b depict the spectrogram of the stator current using STFT and WPD, respectively. The frequency band of each node in level 5 is 12.5Hz for 50Hz supply frequency due to the sampling frequency of 800Hz. Frequencies of the major lower and upper sidebands are 35Hz and 65Hz, respectively.

The feature coefficients of nodes 34 and 38 pick up the hunting instantly as shown in Figure 7.15. The steady high values of feature coefficients indicate sustained hunting in the system. The slopes of the trajectories of feature coefficients can be used to determine the beginning and end of hunting phenomenon in a motor drive. A

positive slope indicates the start of hunting whereas the negative slope shows the stabilization of the motor after load torque oscillation is removed from the system.



(a)



(b)

Figure 7.14. Spectrogram for 50Hz using: (a) STFT and (b) WPD.

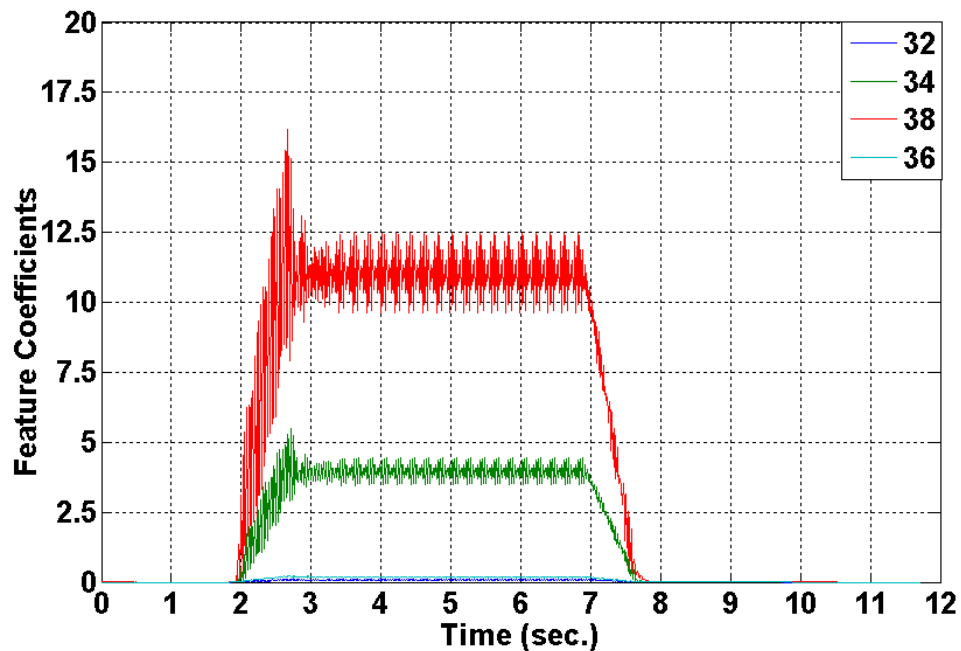


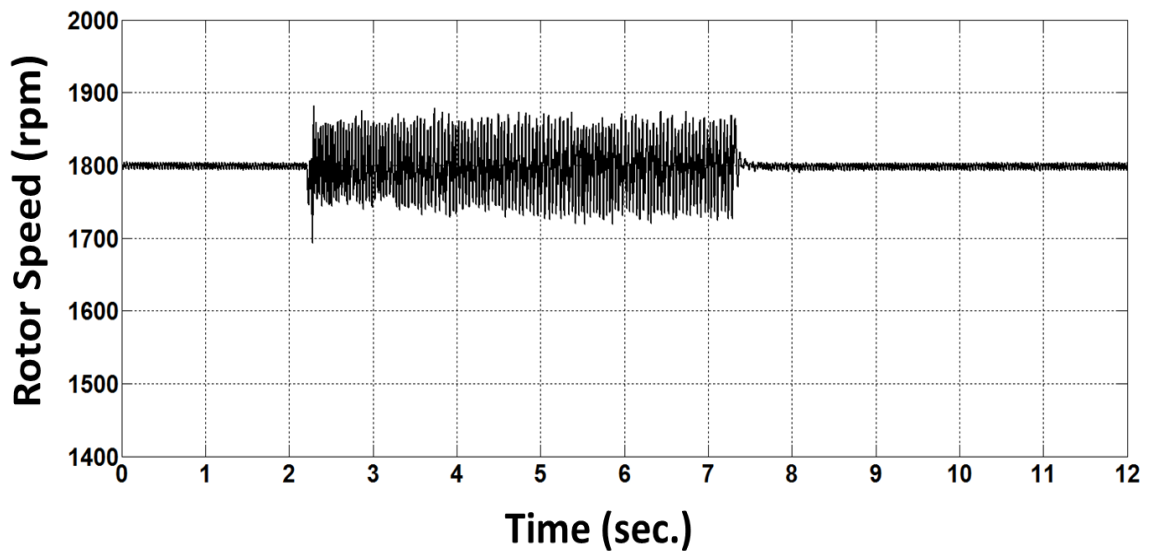
Figure 7.15. Feature coefficients at 50Hz command frequency.

## 7.7 Experimental Results

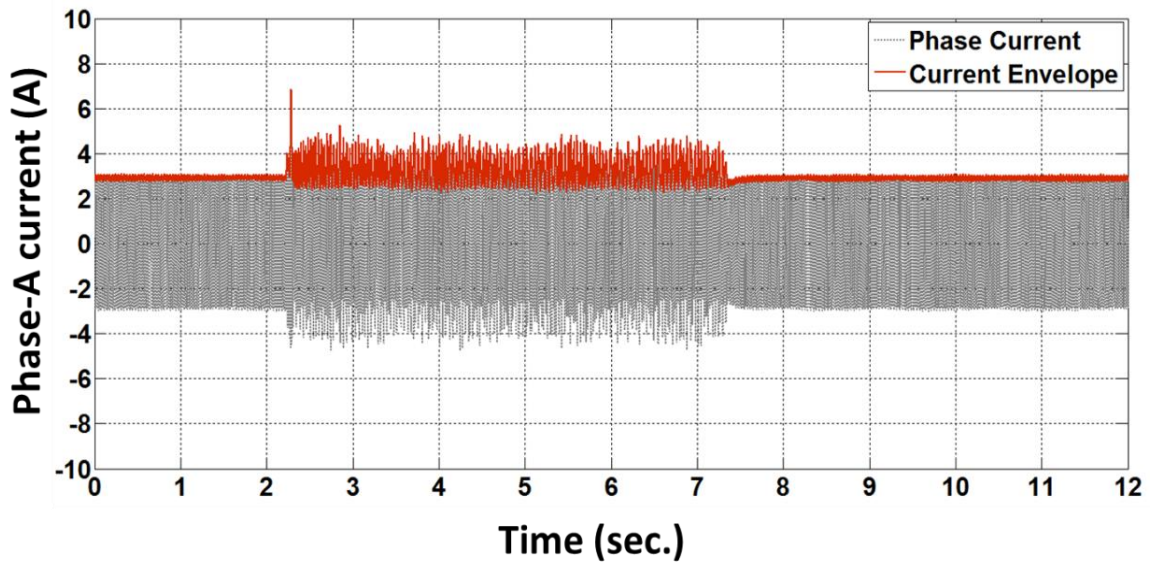
A laboratory 1-HP, 3-phase, 208V, 4-pole line-start interior permanent magnet motor has been used for experimental validation of the proposed hunting detection algorithm. The detailed specifications of the motor are provided in table 7.2 in the appendix. The motor is run directly from a Y-connected 3-phase, 208V balanced fixed frequency 60 Hz ac line supply. Additionally, experiments were conducted using a 3-phase full bridge open loop  $V/f$  controlled sinusoidal pulse-width modulated (SPWM) IGBT inverter to provide the supply voltage. An AC dynamometer is used as a loading machine. A pulley is attached to the shaft of the motor and another pulley is coupled with the dynamometer's shaft. The motor and the dynamometer are connected by a belt running over the pulleys, allowing the inducement of hunting

phenomena. A dSPACE DS-1104 R&D controller board is used for data acquisition and online implementation of the algorithm for diagnosis of hunting in the motor drive.

The speed and current responses of the motor during hunting condition for fixed 60 Hz supply are presented in Figures 7.16a and 7.16b, respectively. The hunting phenomenon occurs after  $t=2$ s due to load variations and it is removed after  $t=7$ s. The rotor suffers from sustained oscillations around the synchronous speed. This oscillatory behavior influences the stator current, with amplitude modulation depicted in the current signal envelope. The magnitude of the stator current remains below the motor rating. In addition, the phase currents remain balanced. As a result, a traditional overcurrent relay or a differential motor protection relay will not pick up the effects of hunting.



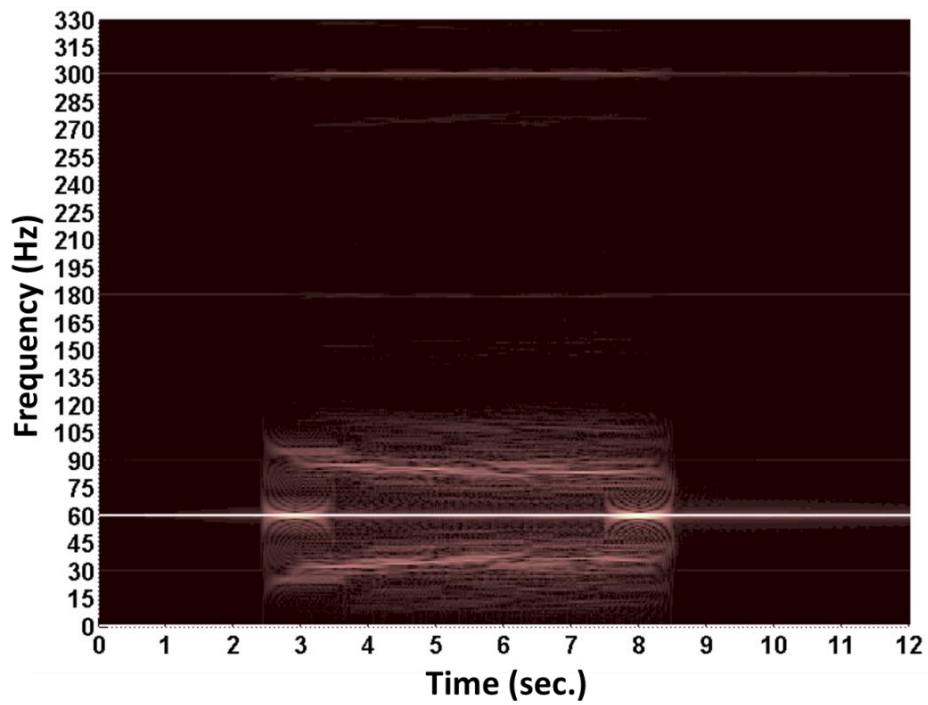
(a)



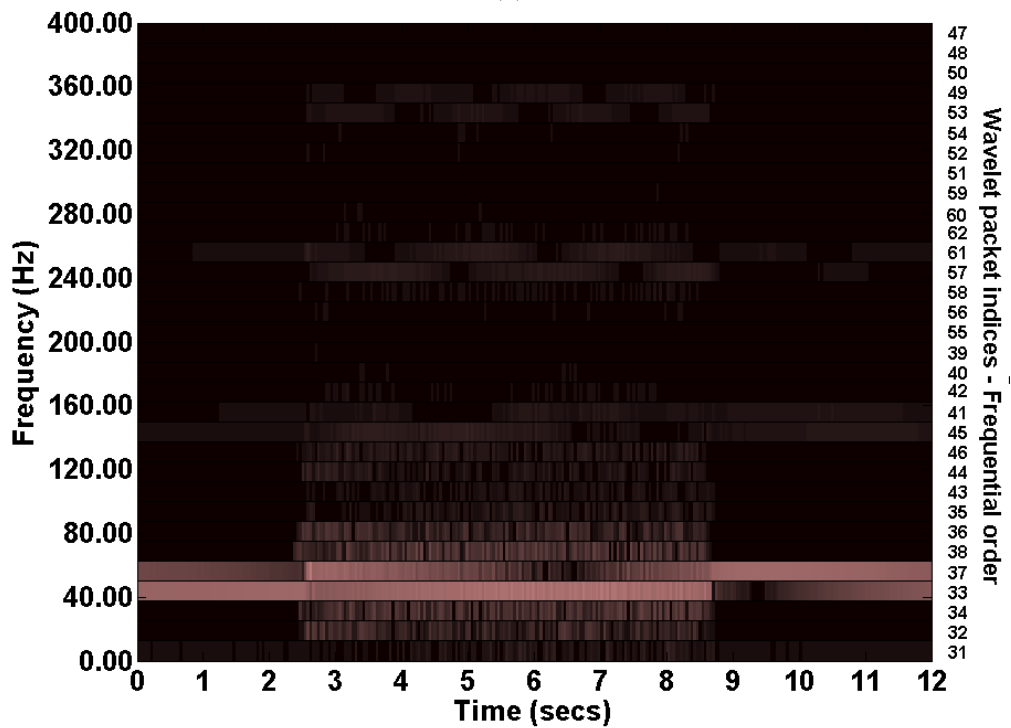
(b)

Figure 7.16. Responses of the motor during hunting at 60 Hz: (a) speed and (b) current.

A time frequency analysis of the current signal is carried out using short-time Fourier transform and wavelet packet decomposition techniques. Figures 7.17a and 7.17b demonstrate spectrograms of the stator current obtained using STFT and WPD, respectively. Hunting introduces significant wide spread lower and upper sidebands around the fundamental frequency. Sidebands also exist around higher harmonics as evident from the wavelet spectrum in Figure 7.17b. However, the sidebands around the fundamental frequency have higher energy than the rest. Higher degree of phase modulation occurs in the stator current during experimental testing than simulation due to the non-linearity associated with the electromechanical system.



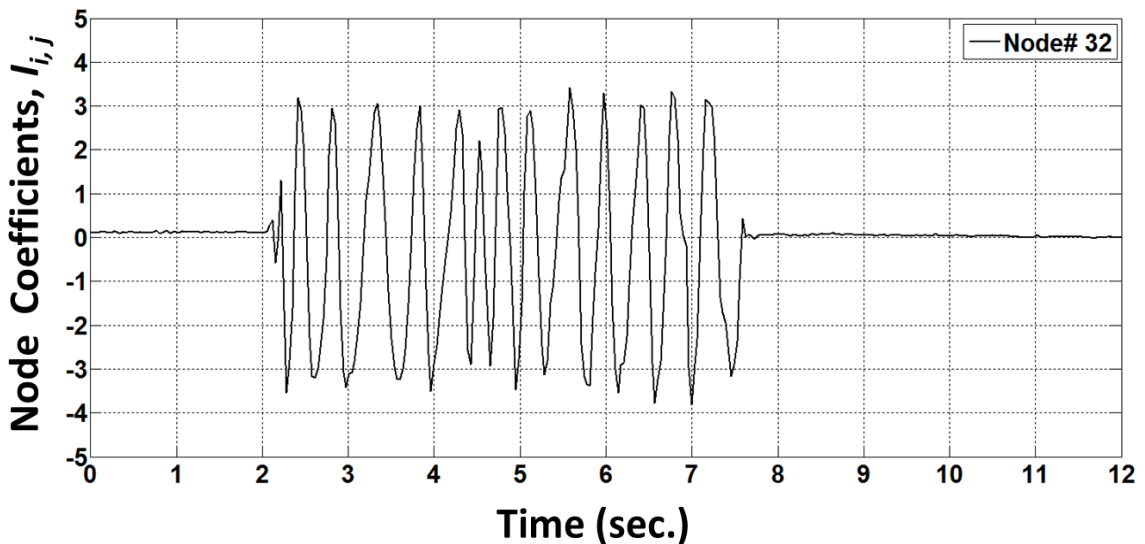
(a)



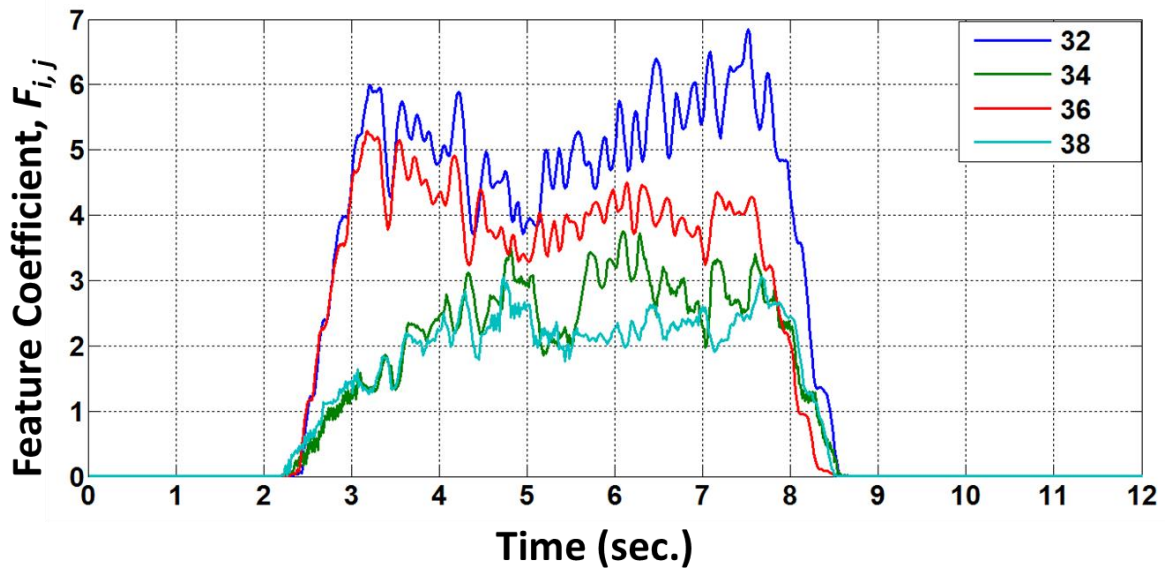
(b)

Figure 7.17. Spectrogram of the current using: (a) STFT and (b) WPD.

The coefficient vector of the node 32 using WPD of the motor phase current is plotted in Figure 7.18a. Figure 7.18b illustrates feature coefficients of nodes 32, 34, 36 and 38 extracted from their coefficient vectors. The amplitude modulation introduces signals with low (<60 Hz) and high (>60Hz) frequency sidebands around the fundamental component of the signal. The low frequency sidebands are picked up by nodes 32 and 34, and the high frequency ones are detected by nodes 36 and 38. The magnitude of the feature coefficients are close to zero during normal operation of the motor i.e. before  $t= 2s$  and after  $t=7s$ . It starts rising to a nonzero value at the beginning of the hunting and becomes significantly high during the hunting condition. The magnitude of these feature coefficients is the signature that is used to detect hunting condition of the motor almost instantaneously. This will prevent the motor and the electromechanical system from suffering mechanical failures due to excessive torsional oscillations.



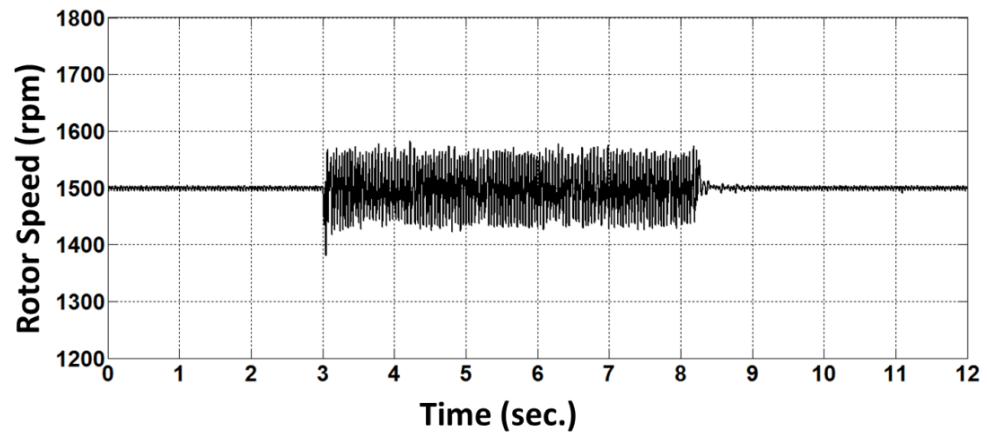
(a)



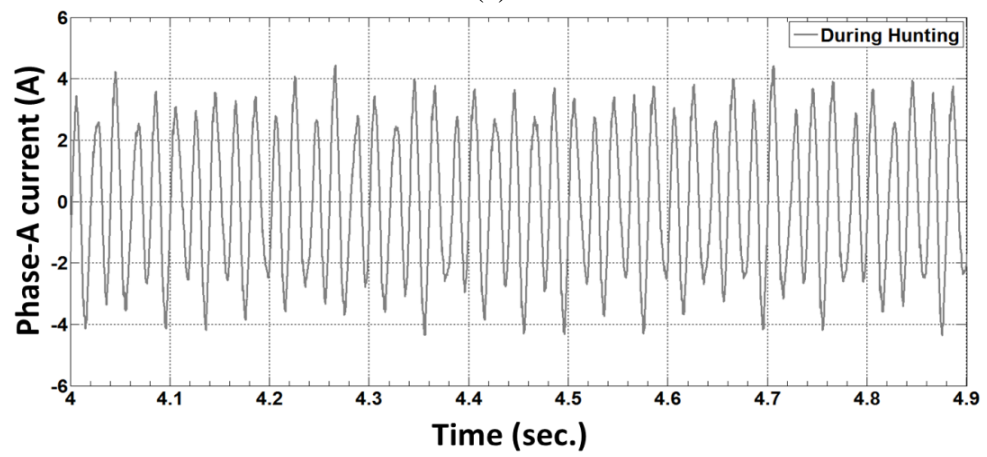
(b)

Figure 7.18. Hunting at 60Hz: (a) Coefficients of node 32 and (b) feature coefficients.

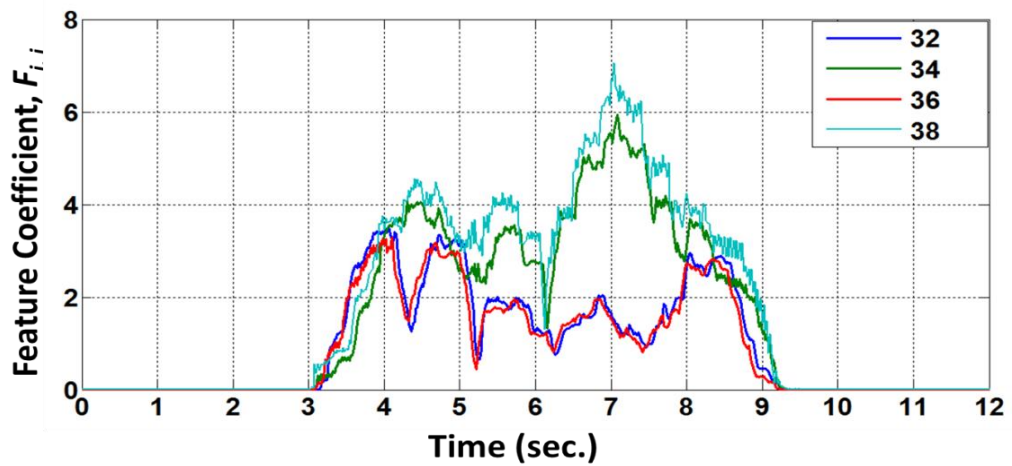
Figure 7.19a illustrates the speed response of the motor at 50 Hz command frequency. The corresponding motor phase current during hunting is depicted in Figure 7.19b. Figure 7.19c presents the feature coefficients of nodes 32-38 for the 50 Hz supply. In this case, the motor is operated by the open loop  $V/f$  controlled inverter drive. The proposed method based on WPD of the stator current can confidently detect the hunting condition, even during the presence of extra harmonics due to the PWM switching and power electronics. Further investigations are carried out to observe the performance of the proposed method for above rated speed operation of the motor.



(a)



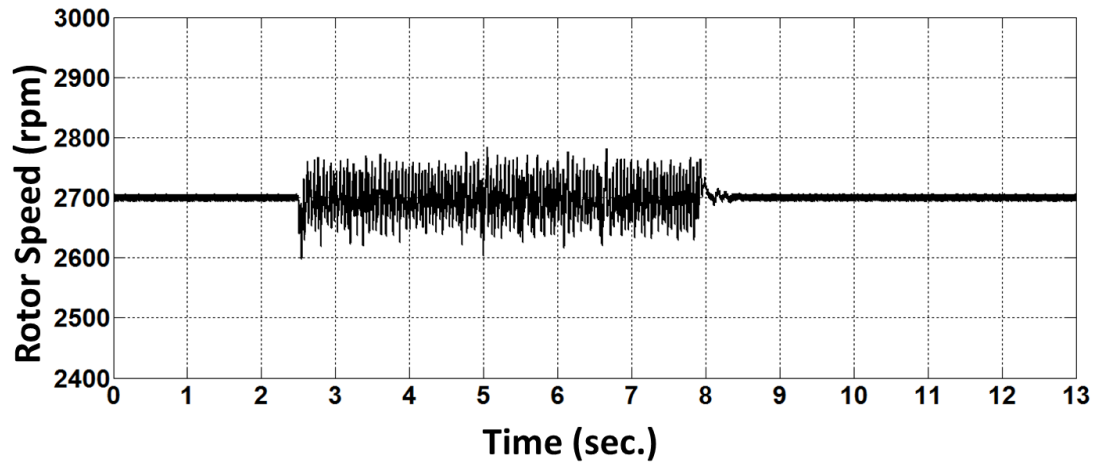
(b)



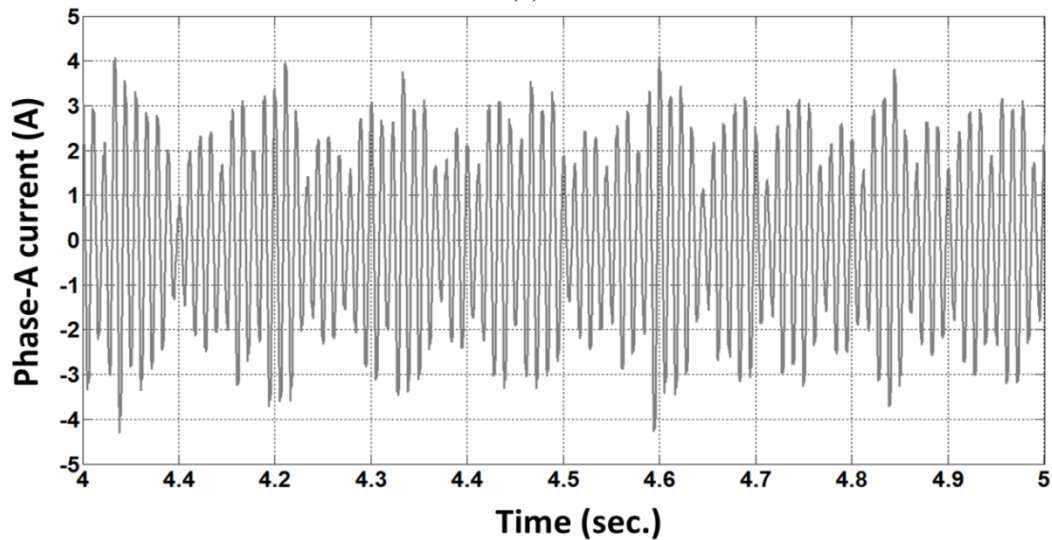
(c)

Figure 7.19. Hunting at 50 Hz: (a) speed, (b) current and (c) feature coefficients.

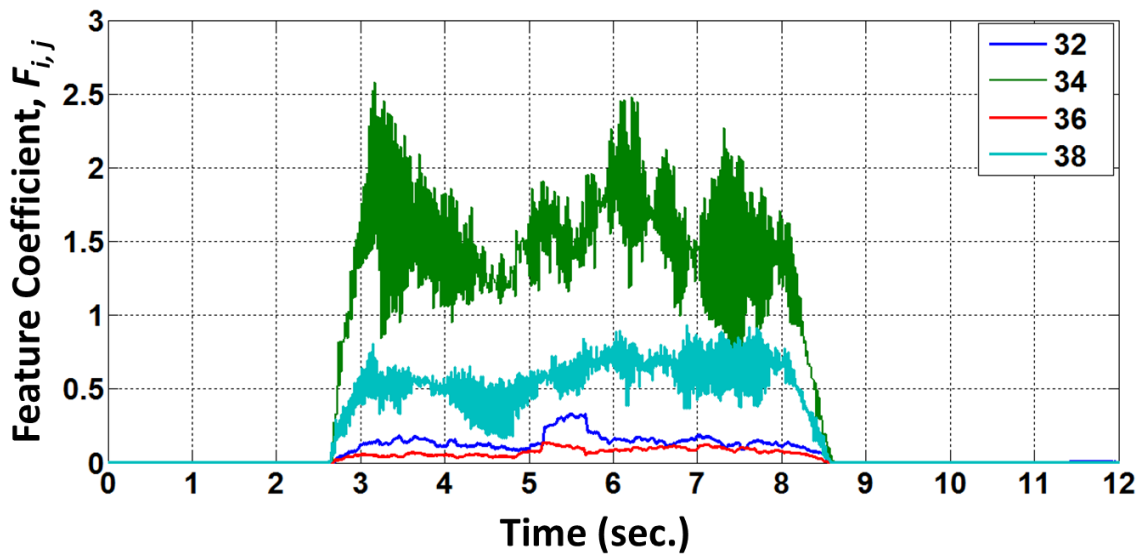
Figures 7.20a-7.20c present a case scenario where the motor is operating at 90 Hz command frequency and experiencing hunting. The proposed method is able to successfully detect the hunting at 90 Hz. The applied voltage is saturated at 60Hz command frequency and the motor is operating at constant power mode. As a result, the magnitude of the stator currents is significantly lower than in the normal operation in order to keep the output power constant. This is reflected in the feature nodes as the magnitude of the nodes is considerable smaller at 90 Hz than at frequency 60Hz or below.



(a)



(b)



(c)

Figure 7.20. Hunting at 90 Hz: (a) speed, (b) current and (c) feature coefficients.

## 7.8 Conclusions

This chapter has introduced a novel stator current signature analysis based technique for detection of hunting phenomena in IPM motor drives. An in-depth analysis of the modulation effects in non-stationary current signals during hunting is carried out using short-time Fourier transform and wavelet packet decomposition techniques. The proposed stator current signature for hunting is validated by performing simulation and experimental investigations for a prototype line-start IPM motor drive for different starting and loading conditions. Based on simulation and experimental results, the developed method can detect hunting in an IPM motor with a high degree of confidence.

The following chapter provides a diagnostic system for real time detection of hunting in IPM motor drives using the stator current signature developed in this chapter.

## Appendix

Table 7.1. 'db6' filter coefficients.

$g[k]$	$h[k]$
-0.0011	-0.1115
0.0048	0.4946
0.0006	-0.7511
-0.0316	0.3153
0.0275	0.2263
0.0975	-0.1298
-0.1298	-0.0975
-0.2263	0.0275
0.3153	0.0316
0.7511	0.0006
0.4946	-0.0048
0.1115	-0.0011
-0.0011	-0.1115

Table 7.2. Parameters of the line-start IPM motor.

Symbol	Name	Value
$N_p$	number of phases	3
$p$	number of pole pairs	2
$I_{rated}$	rated line current	3 A
$f_{rated}$	rated frequency	60 Hz
$P_{rated}$	rated power	1 hp
$T_{rated}$	rated torque	4 N. m
$V_{rated}$	rated voltage (L-L)	208 V
$L_q$	q axis inductance	0.07957 H
$L_d$	d axis inductance	0.04244 H
$r_s$	stator resistance/phase	1.93 $\Omega$
$J$	rotor inertia	0.003 Kg. m <sup>2</sup>
$B_m$	rotor damping constant	0.0008 (N. m)/rad./sec.
$\Psi_m$	magnet flux linkage	0.314 volts/rad./sec.

## References

1. M. A. Rahman, "History of interior permanent magnet motors," *IEEE Industry Applications Magazine*, vol.19, no. 1, pp. 10-15, Jan. 2013.
2. P. D. Chandana Perera, F. Blaabjerg, J. K. Pedersen and P. Thogersen, "A Sensorless, Stable  $V/f$  Control Method for Permanent-Magnet Synchronous Motor Drives", *IEEE Transactions on Industry Applications*, Vol. 39, No. 3, pp. 783-791, May/June 2003.
3. T. Marčič, B. Štumberger and G. Štumberger, "Comparison of induction motor and line-Start IPM synchronous motor performance in a variable-Speed drive ", *IEEE Transactions on Industry Applications*, Vol. 48, No. 6, pp. 2341-2352, Nov./Dec 2012.
4. Bojan Štumberger, Tine Marcič and Miralem Hadžiselimovic, "Direct Comparison of Induction Motor and Line-Start IPM Synchronous Motor Characteristics for Semi-Hermetic Compressor Drives", *IEEE Transactions on Industry Applications*, Vol. 48, No. 6, pp. 2310 - 2321, November 2012.

5. S. F. Rabbi and M. A. Rahman, "Critical criteria for successful synchronization of line start IPM motors", *IEEE Journal of Emerging and Selected Topics in Power Electronics*, Vol. 2, No.2, pp. 348-358, June 2014.
6. T. J. E. Miller, "Synchronization of line start permanent magnet ac motors," *IEEE Transaction on Power Apparatus and Systems*, Vol. PAS-103, No. 7, pp. 1822-1828, July 1984.
7. M. J. Melfi, S. D. Umans and J. E. Atem, "Viability of Highly Efficient Multi-Horsepower Line-Start Permanent-Magnet Motors", *IEEE Transactions on Industry Applications*, Vol. 51, No. 1, pp. 120–128, January 2015.
8. Wei-Hann Yao, Pi-Cheng Tung, Chyun-Chau Fuh and Fu-Chu Chou, "Suppression of hunting in an ILPMSM driver system using hunting compensator", *IEEE Transactions on Industrial Electronics*, Vol. 60, No. 7, pp. 2586–2594, July 2013.
9. Z. Li, J. B. Park, Y. H. Joo, B. Zhang, and G. Chen, "Bifurcations and chaos in a permanent-magnet synchronous motor", *IEEE Transactions on Circuits and Systems-I: Fundamental and Applications*, Vol. 49, No. 3, pp. 383-387, March 2002.
10. J. Liu, T. A. Nondahl, P. B. Schmidt, S. Royak, T. M. Rowan, "Generalized stability control for open loop operation of motor drives", *Proc. 2015 IEEE Industry Applications Society Annual Meeting*, Addison, TX, USA, pp. 1-8, 18-22 Oct. 2015.
11. K. Lee, D. Kim, B. Kim and B. Kwon, "A novel starting method of the surface permanent-magnet BLDC motors without position sensor for reciprocating compressor", *IEEE Transactions on Industry Applications*, Vol. 44, No.1, pp. 85-92, January 2008.
12. G. G. Yen and K. Lin, "Wavelet Packet Feature Extraction for Vibration Monitoring", *IEEE Transactions on Industrial Electronics*, Vol. 47, No. 3, pp. 650-667, June 2000.

13. W. Wang and O. A. Jianu, "A smart sensing unit for vibration measurement and monitoring", *IEEE/ASME Transactions on Mechatronics*, Vol. 15, No. 1, pp. 70-78, February 2010.
14. K. N. Castleberry, "High-vibration detection using motor current signature analysis", Oak Ridge National Laboratory, Oak Ridge, Tennessee, 37831-6285, Tech. Rep. ORNUTM-I3266, August 1996.
15. S. A. Saleh, R. Ahshan and M. A. Rahman, "Performance evaluation of an embedded  $d-q$  WPT-based Digital protection for IPMSM Drives", *IEEE Transactions on Industry Applications*, Vol. 50, No.3, pp. 2277 -2291, May 2014.
16. J. Vico and R. Hunt, "Principles in motor protection", *IEEE Industry Applications Magazine*, Vol. 17, No. 6, pp. 52-61, Nov.-Dec. 2011.
17. M. A. S. K. Khan and M. A. Rahman, "Development and implementation of a novel fault diagnostic and protection technique for IPM motor drives", *IEEE Transactions on Industrial Electronics*, Vol. 56, No. 1, pp. 85-92, September 2008.
18. P. Ostojic, A. Banerjee, D. C. Patel, W. Basu and S. Ali, "Advanced Motor monitoring and diagnostics", *IEEE Transactions on Industry Applications*, Vol. 50, No.5, pp. 3120 -3127, September 2014.
19. G. Choi and T. M. Jahns, "PM synchronous machine drive response to asymmetrical short-circuit faults", *IEEE Transactions on Industry Applications*, Vol. 52, No. 3, pp. 2176 - 2185, May 2016.
20. J. R. Ruiz, J. A. Rosero, A. G. Espinosa, and L. Romeral, "Detection of demagnetization faults in permanent-magnet synchronous motors under nonstationary conditions", *IEEE Transactions on Magnetics*, Vol. 45, No. 7, pp. 2961-2969, July 2009.
21. W. G. Zanardelli, E. G. Strangas and S. Aviyente, "Identification of intermittent electrical and mechanical faults in permanent-magnet AC drives based on time-frequency analysis", *IEEE Transactions on Industry Applications*, Vol. 43, No. 4, pp. 971-980, July/August 2007.

22. N. Obeid, T. Boileau, and B. Nahid-Mobarakeh, "Modeling and diagnostic of incipient inter-turn faults for a three phase permanent magnet synchronous motor", *IEEE Transactions on Industry Applications*, Vol. PP, No. PP, pp., June 2016.
23. M. Zafarani, T. Goktas and B. Akin, "A comprehensive magnet defect fault analysis of permanent-magnet synchronous motors", *IEEE Transactions on Industry Applications*, Vol. 52, No. 2, pp. 1331-1339, March/April 2016.
24. M. Blodt, M. Chabert, J. Regnier and J. Faucher, "Mechanical load fault detection in induction motors by stator current time-frequency analysis", *IEEE Transactions on Industry Applications*, vol. 42, no. 6, pp. 1454-1463, November 2006.
25. R. R. Schoen and T. G. Habetler, "Effects of time-varying loads on rotor faults detection in induction machines", *IEEE Transactions on Industry Applications*, vol. 31, no. 4, pp. 900-906, July 2006.
26. S. H. Kia, H. Henaou and G. A. Capolino, "Torsional vibration assessment using induction machine electromagnetic torque estimation", *IEEE Transactions on Industrial Electronics*, vol. 57, no. 1, pp. 209–219, January 2010.
27. W. G. Zanardelli, E. G. Strangas and S. Aviyente, "Identification of Intermittent Electrical and Mechanical Faults in Permanent-Magnet AC Drives Based on Time–Frequency Analysis", *IEEE Transactions on Industry Applications*, vol. 43, no. 4, pp. 971-980, July/August 2007.
28. Z. Ye, B. Wu, and A. Sadeghian, "Current signature analysis of induction motor mechanical faults by wavelet packet decomposition", *IEEE Transactions on Industrial Electronics*, vol. 50, no. 6, pp. 1217-1228, December 2003.
29. J. Seshadrinath, B. Singh and B. K. Panigrahi, "Investigation of vibration signatures for multiple fault diagnosis in variable frequency drives using Complex wavelets", *IEEE Transactions on Power Electronics*, vol. 29, no. 2, pp. 936-945, February 2014.
30. K. Teotrakool, M. J. Devaney, and L. Eren, "Adjustable-speed drive bearing-fault detection via wavelet packet decomposition", *IEEE Transactions on Instrumentation and Measurement*, vol. 58, no. 8, pp. 2747-2754, August 2009.

31. P. Karvelis, G. Georgoulas, I. P. Tsoumas, J. A. Antonino-Daviu, V. Climente-Alarcón and C. D. Stylios, “A symbolic representation approach for the diagnosis of broken rotor bars in induction motors”, *IEEE Transactions on Industrial Informatics*, vol. 11, no. 5, pp. 1028-1037, October 2015.
32. B. M. Ebrahimi, M. J. Roshtkhari, J. Faiz and S. V. Khatami, “Advanced eccentricity fault recognition in permanent magnet synchronous motors using stator current signature analysis”, *IEEE Transactions on Industrial Electronics*, vol. 61, no. 4, pp. 2041-2052, April 2014.
33. R. R. Obaid, T. G. Habetler and D. J. Gritter, “A simplified technique for detecting mechanical faults using stator current in small induction motors”, in *Proc. Industry Applications Conference*, Rome, Italy, October 2000.
34. S.M. Yang and S. C. Wang, “The detection of resonance frequency in motion control systems”, *IEEE Transactions on Industry Applications*, vol. 50, no. 5, pp. 3423-3427, September 2014.
35. D. Grignon, X. Chen, N. Kar and H. Qian, “Estimation of load disturbance torque for dc motor drive systems under robustness and sensitivity consideration”, *IEEE Transactions on Industrial Electronics*, vol. 61, no. 2, pp. 930-942, February 2014.
36. H. Henao, S. H. Kia and G. A. Capolino, “Torsional-vibration assessment and gear-fault diagnosis in railway traction system”, *IEEE Transactions on Industrial Electronics*, vol. 58, no. 5, pp. 1707-1717, May 2011.
37. S. H. Kia, H. Henao and G. A. Capolino, “Analytical and experimental study of gearbox mechanical effect on the induction machine stator current signature”, *IEEE Transactions on Industry Applications*, Vol. 45, No. 4, pp. 1405 - 1415, July 2009.
38. H. Kim, S. B. Lee, S. Park, S. H. Kia and G. A. Capolino, “Reliable detection of rotor faults under the influence of low-frequency load torque oscillations for applications with speed reduction couplings”, *IEEE Transactions on Industry Applications*, Vol. 52, No.1, pp. 1460 -1468, March 2016.

39. M. Sahraoui, A. J. M. Cardoso and A. Ghoggal, "The use of a modified prony method to track the broken rotor bar characteristic frequencies and amplitudes in three-phase induction motors", *IEEE Transactions on Industry Applications*, Vol. 51, No. 3, pp. 2136-2147, May/June 2015.
40. Sang Bin Lee, et. al., "Identification of False Rotor Fault Indications Produced by Online MCSA for Medium-Voltage Induction Machines", *IEEE Transactions on Industry Applications*, Vol. 52, No. 1, pp. 729- 739, January 2016.
41. J. R. Cameron, W.T. Thomson and A. B. Dow, "Vibration and current monitoring for detecting airgap eccentricity in large induction motors", *IEE Proceedings B - Electric Power Applications*, Vol. 133, No. 3, pp. 155 – 163, May 1986.
42. T. Ilamparithi, S. Nandi and J. Subramanian, "A disassembly-free offline detection and condition monitoring technique for eccentricity faults in salient-pole synchronous machines", *IEEE Transactions on Industry Applications*, Vol. 51, No.2, pp. 1505-1515, March 2015.
43. A. Gelb and W. E. Vander Velde, *Multiple-input describing functions and nonlinear system design*, New York, NY: McGraw-Hill, 1968.
44. A. Gelb, "The analysis and design of limit cycling adaptive automatic control systems", Sc. D. thesis, MIT, Cambridge, MA, August, 1961.
45. A. Gelb and W. E. Vander Velde, "On limit cycling control systems", *IEEE Transactions on Automatic Control*, Vol. AC-8, No. 2, pp. 142-157, April 1963.
46. A. V. Oppenheim, A. S. Willsky and S. H. Nawab, *Signals and Systems*. Upper Saddle River, NJ, USA: Prentice Hall, 1997.
47. M. V. Wickerhauser, *Adapted wavelet analysis from theory to software*, Wellesley, MA: IEEE Press, 1994.
48. S. A. Saleh and M. A. Rahman, "Modeling and protection of a three-phase power transformer using wavelet packet transform", *IEEE Transactions on Industry Applications*, Vol. 20, No. 2, pp. 1273 -1282, April 2005.

## Chapter 8

### Real Time Diagnosis of Hunting in IPM Motor Drives

#### 8.1 Introduction

Online diagnosis of motor faults has traditionally been achieved using different types of protection relays. These relays are equipped with various algorithms designed to detect and classify faults in drive systems. Some of the algorithms are based on frequency domain analysis while the others perform time domain analysis of different types of measured signals such as current, vibration, speed, etc. to determine signatures of both internal and external motor faults. Online fault diagnostic algorithms are run in real time in embedded microprocessors such as digital signal processors/FPGA systems. Due to real time operation of the protection relay, online fault diagnostic algorithms are designed to provide speedy responses to faults while working like a silent sentinel during normal operation. The performance of these types of algorithms is limited by the available computational power and memory. Thus, simplicity, reliability, quick responsiveness and selectivity are the major requirements for designing a real time fault diagnostic system for motor drive systems.

Design of a digital protection system for motor fault diagnosis in real time has been a topic of interest among the researchers over the last four decades [1]-[13]. Faults in motor drives can be classified into two groups: electrical faults and mechanical faults. Online detection of mechanical faults such as broken rotor bars,

bearing damage, rotor eccentricity, mechanical vibration, etc. have been investigated in the existing literature [1]-[6].

A simplified embedded real time rotor faults diagnostic system using  $d-q$  axes current spectra is proposed by Akin et. al. [1]. They have analyzed the stator current of an induction motor drive in a rotating reference frame to find the induced higher harmonics in the stator current due to various rotor faults, such as broken rotor bars and rotor eccentricity.

Liu et. al. have presented an online fault diagnostic system for detecting various rotor faults in induction motor drives [2]. The frequency spectrum of the calculated motor instantaneous power is used to detect faults in the motor drive in real time.

An open loop torque observer based mechanical unbalanced detection algorithm for high speed permanent magnet motors is proposed by Kim [3]. The mathematical models of permanent magnet motors are used along with instantaneous current readings to estimate the mechanical unbalance of a permanent magnet motor drive in real time.

A FPGA based online rotor fault diagnostic system for induction motor drives is presented by Jose de Jesus Rangel-Magdaleno et. al. [4]. They have used frequency spectra of both vibration and current data to detect various types of rotor bar failures during online operation of the motor drive.

A sensorless faults diagnostic system for induction motor drives is presented in [5]. The proposed technique does not require mechanical position/speed sensors and vibration sensors. It only uses electrical voltage and current signals to detect various electrical and mechanical faults in induction motor drives. The classification of faults using neural networks is also presented in this paper.

A motor current signature analysis based algorithm for online detection of broken rotor bars in induction motors is presented in [6]. A wavelet packet decomposition technique is used to extract the features of broken rotor bars from the stator current signal. An artificial neural network is used to detect the fault signature and distinguish between healthy and unhealthy induction motors.

Online diagnosis of motor electrical faults has been carried out in the existing literature [7]-[13]. Electrical faults such as asymmetrical short-circuits, turn-turn faults and drive faults are detected using analysis of stator current signals or injected voltage/current signals. Various signal processing algorithms have been used to determine the appropriate signature related to a particular fault.

In the previous chapter, analysis and offline diagnosis of the hunting phenomenon in IPM motor drives are presented. A stator current signature of hunting is also established in that chapter. Based on the analysis, hunting in IPM motor drives can be detected using the stator phase current. This chapter presents an algorithm for real time diagnosis of hunting in IPM motor drives. A multi-resolution analysis of the stator current signal is carried out in real time using wavelet packet decomposition for detection and extraction of the hunting induced sideband frequency components. Statistical properties such as mean and variance of the extracted sideband signals are calculated in real time. The severity of hunting in real time is determined using the relative magnitude of sideband signals. The developed algorithm is validated using simulation and experimental investigations for two line-start IPM motor drives of different power ratings. Both simulation and experimental results are presented in this chapter.

## 8.2 Real Time Diagnosis of Hunting

The majority of MCSA-based fault diagnostic techniques are focused on induction motor drives, switch reluctance motor drives, traditional dual excitation synchronous motor drives, and closed loop feedback controlled variable speed permanent magnet motor drives. The application of line-start IPM motors was confined to low power usages in the past, and the analysis and development of a real time MCSA based diagnostic and protection technique for sustained hunting in IPM motors has not been conducted in the existing literature yet. MCSA based fault diagnosis is significantly faster than the traditional mechanical sensor based monitoring systems [13]. As the self-starting IPM motor is a special type of motor that suffers from hunting for various conditions, there exists a need to develop a MCSA-based fault diagnostic technique for the fast and reliable detection of hunting phenomenon in self-starting IPM motor drives in order to ensure its application in electric submersible pump systems.

Figure 8.1 illustrates an overview of the algorithm for diagnosis of hunting in IPM motors using stator current signature analysis. The diagnostic process can be divided into four major parts: acquisition of sampled current signal, application of signal conditioning to filter out the noises as well as getting rid of the fundamental component of the current signal, application of the WPD to extract the sideband components of the current signal and finally checking the existence of hunting in the system along with its severity. The complete diagnostic process is described in the following sections.

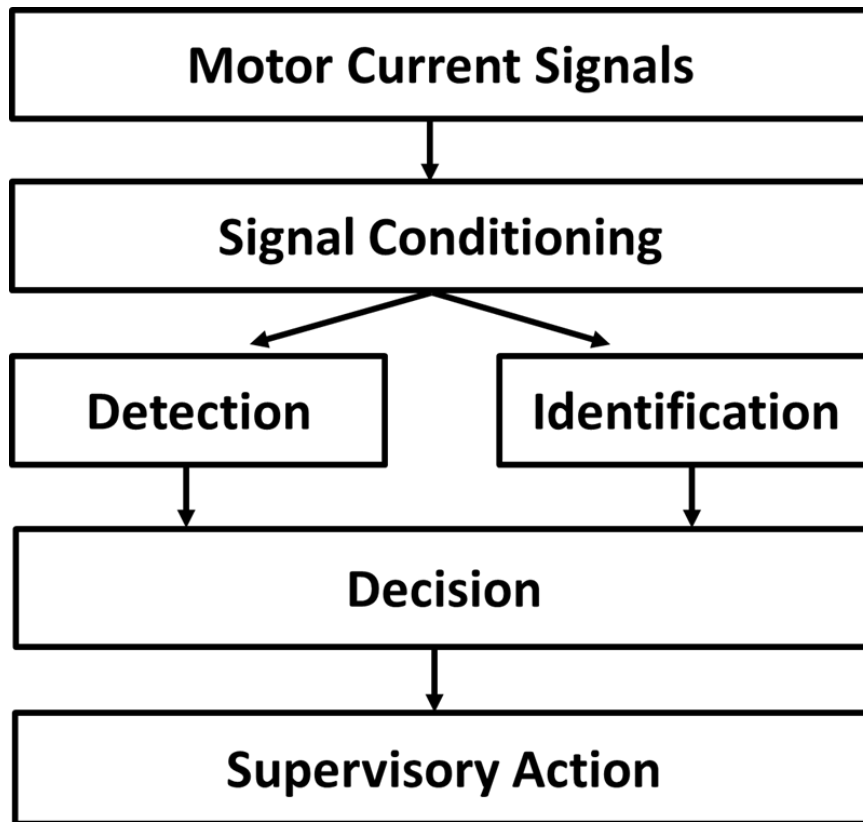


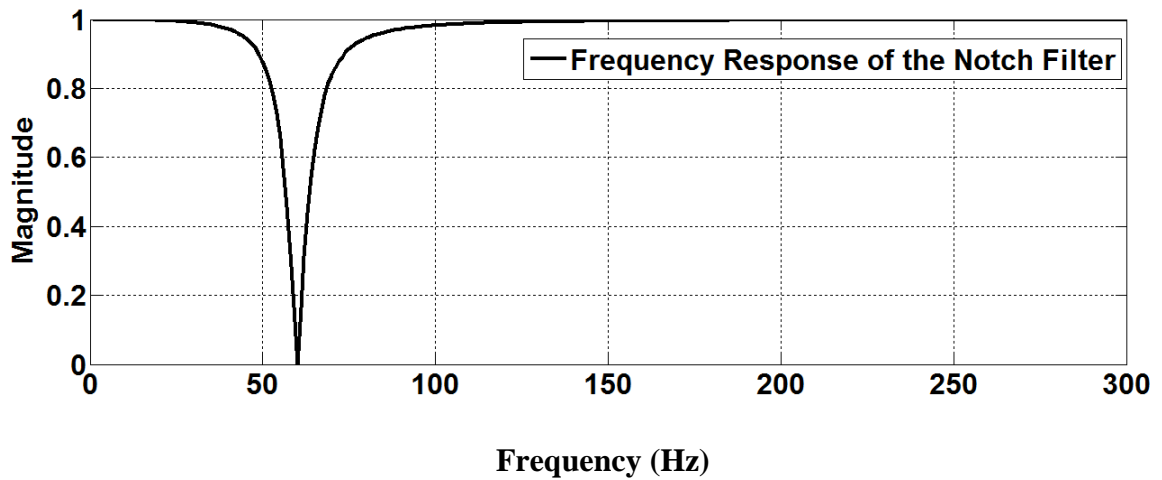
Figure 8.1. Block diagram of the hunting diagnostic process.

### 8.2.1 Signal Conditioning

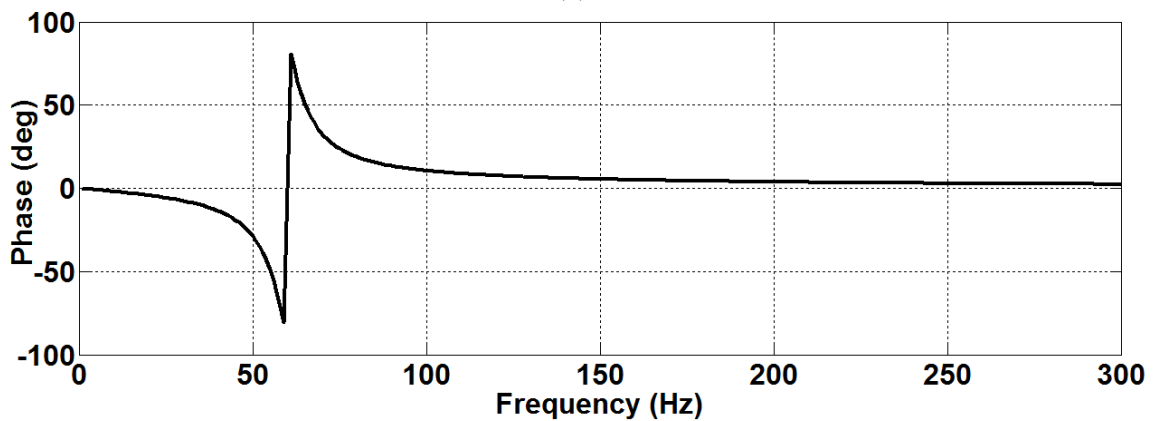
The diagnostic process for hunting begins with the acquisition of instantaneous current signals from the motor. The stator current signal can be divided into a fundamental current signal with the supply frequencies, and a modulating current signal containing the sideband components. The magnitude of the fundamental component does not change significantly during hunting and it is separated from the instantaneous signal using a 2<sup>nd</sup> order notch filter. The transfer function for a 2<sup>nd</sup> order notch filter is given below [14]:

$$\frac{I_F(s)}{I_a(s)} = \frac{s^2 + \omega_n^2}{s^2 + \frac{\omega_n}{Q}s + \omega_n^2} \quad (8.1)$$

where  $I_F(s)$  is the filtered current response,  $I_a(s)$  is the input phase current,  $Q$  is the quality factor,  $f_n$  is the natural frequency and  $\omega_n = 2\pi f_n$ .  $f_n$  is selected as the fundamental supply frequency  $f_s$ . The magnitude and phase responses of the applied notch filter with a  $Q=5$  for 60Hz cut-off frequency are presented in Figures 8.2a and 8.2b, respectively.



(a)



(b)

Figure 8.2. Frequency responses of the applied notch filter: (a) magnitude and (b) phase.

During normal operation of the motor at a steady synchronous speed, the filtered current signal will only contain the higher harmonics induced by the power supply along with some external noise. If the rotor goes through speed oscillations, the filtered signal will contain the sidebands along with the higher harmonics and noise.

### 8.2.2 Detection of Hunting Phenomenon

The algorithm for detection of hunting using wavelet packet decomposition of the current signal is described in the following steps:

- I. The filtered current  $I_F$  is sampled with a frequency  $f_d$ . The sampling frequency  $f_d$  is selected using the following equation:

$$f_d = 2^l f_s \quad (8.2)$$

where  $l$  is the number of wavelet level and  $f_s$  is the fundamental supply frequency.

- II. The input current samples are buffered into a sequence of frames. The window size  $N$  for the framing is selected as 1024 with an overlap by 1016 samples. A window size of 1024 samples provides high frequency resolution for the wavelet packet decomposition which is critical for reliable detection of the hunting phenomenon. Overlap by 1016 samples is considered to attain high time resolution for the detection of a fast transient abnormality in the current spectrum.
- III. Figure 8.3 illustrates a 3-level wavelet packet tree (WPT) of the decomposed stator current signal. The first level approximate and detail coefficients of the current samples using WPD are calculated from the following equations [15]:

$$a_1^l[n] = \sum_{k=0}^{N-1} g[k] I_F[N-k] \quad (8.3)$$

$$d_1^l[n] = \sum_{k=0}^{N-1} h[k] I_F[N-k] \quad (8.4)$$

IV. The second level approximate and detail coefficients of  $a_1^l[N]$  are obtained from the following equations [15]:

$$a_{2,1}^l[n] = \sum_{k=0}^{\frac{N}{2}-1} g[k] a_1^l\left(\frac{N}{2}-k\right) \quad (8.5)$$

$$d_{2,1}^l[n] = \sum_{k=0}^{\frac{N}{2}-1} h[k] a_1^l\left(\frac{N}{2}-k\right) \quad (8.6)$$

V. The third level approximate and detail coefficients of  $a_2^l[n]$  and  $d_2^l[n]$  are calculated from the following equations [15]:

$$a_{3,1}^l[n] = \sum_{k=0}^{\frac{N}{4}-1} g[k] a_{2,1}^l\left(\frac{N}{4}-k\right) \quad (8.7)$$

$$d_{3,1}^l[n] = \sum_{k=0}^{\frac{N}{4}-1} h[k] a_{2,1}^l\left(\frac{N}{4}-k\right) \quad (8.8)$$

$$a_{3,2}^l[n] = \sum_{k=0}^{\frac{N}{4}-1} g[k] d_{2,1}^l\left(\frac{N}{4}-k\right) \quad (8.9)$$

$$d_{3,2}^l[n] = \sum_{k=0}^{\frac{N}{4}-1} h[k] d_{2,1}^l \left( \frac{N}{4} - k \right) \quad (8.10)$$

Coefficients of  $a_{3,1}^l$ ,  $d_{3,1}^l$ ,  $a_{3,2}^l$  and  $d_{3,2}^l$  represent the current signals in the frequency range of  $[0 \dots \frac{f_s}{2}]$ ,  $[0 \dots f_s]$ ,  $[f_s \dots \frac{3f_s}{2}]$  and  $[\frac{3f_s}{2} \dots 2f_s]$ , respectively. Consequently, the lower sidebands will be present in  $a_{3,1}^l$  and  $d_{3,1}^l$ .  $a_{3,2}^l$  and  $d_{3,2}^l$  will contain the upper sidebands.

VI. The level 3 node coefficients  $a_{3,1}^l, d_{3,1}^l, a_{3,2}^l, d_{3,2}^l$  are used to develop feature coefficients. The coefficients are used as a signature for the detection of hunting. The feature co-efficient of each node is defined as the variance of the node's coefficient vector. The feature coefficient for nodes  $a_{i,j}^l$  and  $d_{i,j}^l$  are calculated from the following equations:

$$F_{a_{i,j}} = \sigma_{a_{i,j}}^2 = \frac{1}{L-1} \sum_{k=1}^L \left( a_{i,j}^l[k] - \mu_{a_{i,j}} \right)^2 \quad (8.11)$$

$$\mu_{a_{i,j}} = \frac{1}{L} \sum_{k=1}^L a_{i,j}^l[k] \quad (8.12)$$

$$F_{d_{i,j}} = \sigma_{d_{i,j}}^2 = \frac{1}{L-1} \sum_{k=1}^L \left( d_{i,j}^l[k] - \mu_{d_{i,j}} \right)^2 \quad (8.13)$$

$$\mu_{d_{i,j}} = \frac{1}{L} \sum_{k=1}^L d_{i,j}^l[k] \quad (8.14)$$

where  $\sigma^2_{i,j}$  is the variance of the node energy,  $F_{a_{i,j}}$  and  $F_{d_{i,j}}$  are the feature coefficients,  $\mu_{a_{i,j}}$  and  $\mu_{d_{i,j}}$  are the mean for  $a^l_{i,j}$  and  $d^l_{i,j}$ , respectively and  $L$  is the number of coefficient in nodes  $a^l_{i,j}$  and  $d^l_{i,j}$ .

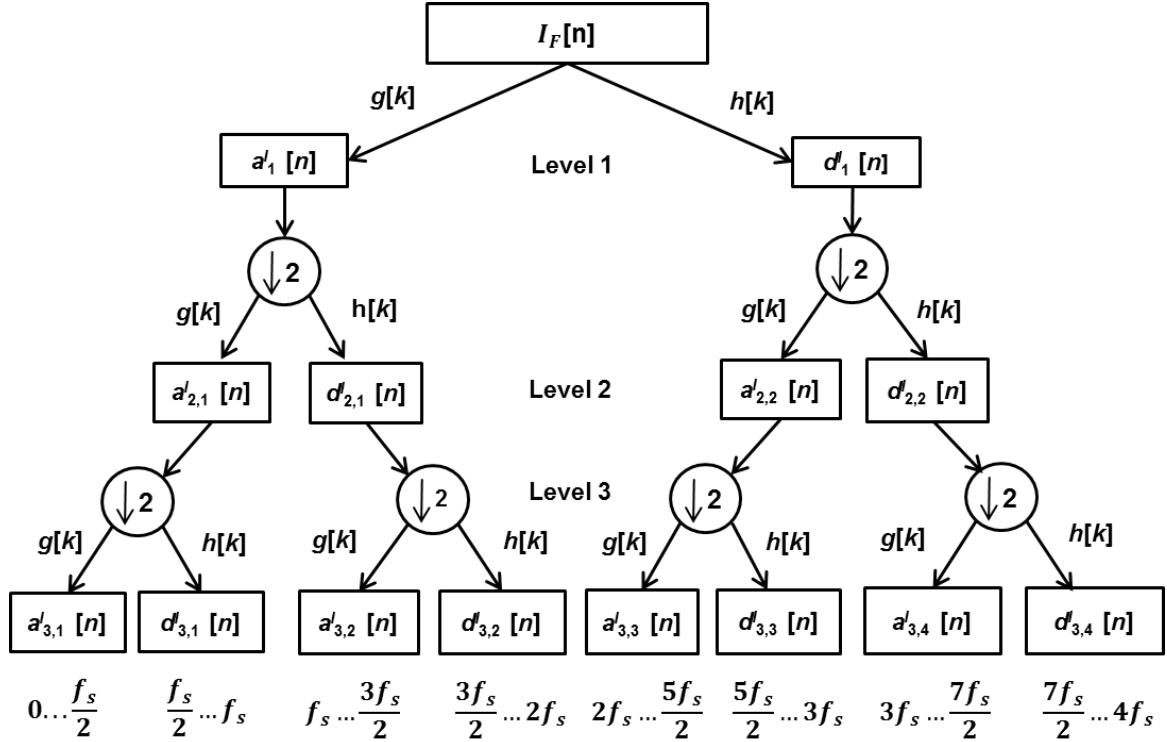


Figure 8.3. A 3-level wavelet packet tree of the current signal.

### 8.2.3 Identification of the Severity of Hunting

The stator phase current modulation depends on the magnitude and frequency of the rotor oscillation based on (7.11) in the previous chapter. The amplitude of the modulating current  $\beta_{r1j}$  is directly proportional to the amplitude and the frequency of rotor oscillation  $\theta_{rj}$  based on equation (7.10) in the previous chapter. Consequently, large rotor oscillations with a high value of  $\theta_{rj}$  introduce greater modulation in the stator current

signals. The degree of stator current modulation can be used as a relative indication of the severity of hunting, and is obtained using the following equation:

$$\chi = \frac{(I_m)_{rms}}{(I_a - I_F)_{rms}} \quad (8.15)$$

where  $I_m$  is the modulating current,  $\chi$  is the degree of modulation ( $0 \leq \chi \leq 1$ ) and  $I_a - I_F$  is the magnitude of the fundamental current signal.

Figure 8.4 presents the block diagram showing the process for obtaining the modulating current using wavelet reconstruction of the level 3 nodes  $a'_{3,1}$ ,  $d'_{3,1}$ ,  $a'_{3,2}$  and  $d'_{3,2}$  of the wavelet packet tree. The coefficients of the 'db6' wavelet reconstruction filters are provided in table 8.3 in the appendix. The reconstructed signal only contains the modulating signal due to hunting and gets rid of the external noise and higher harmonics present in the original filtered stator current signal  $I_F$ .

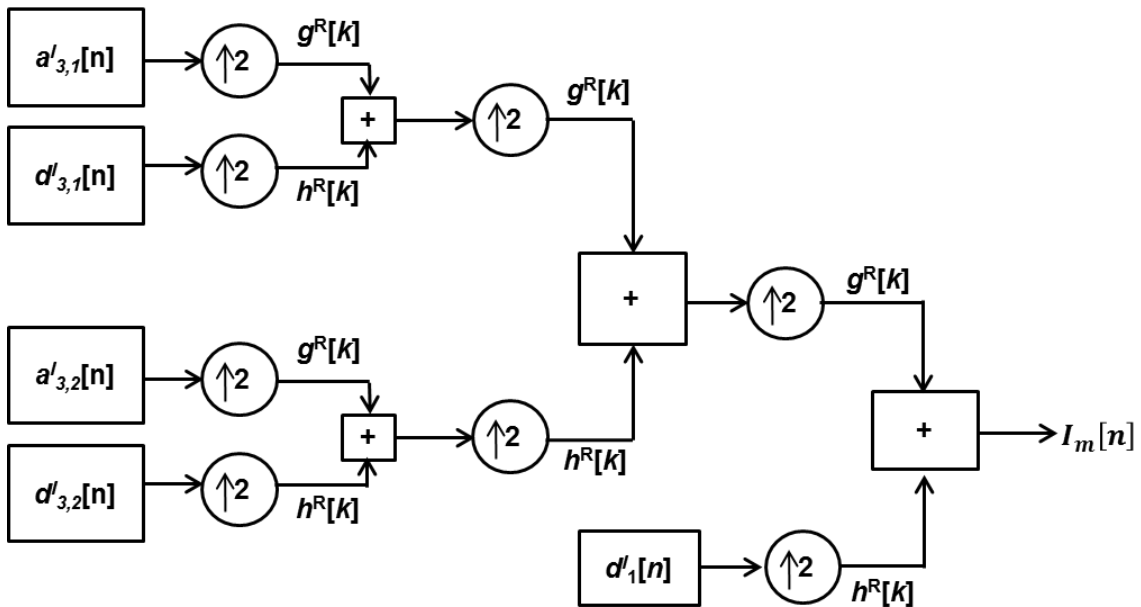


Figure 8.4. Wavelet reconstruction of the level 3 nodes.

### 8.2.4 Decision

A threshold value  $\epsilon_F$  for feature coefficients is set to distinguish between hunting and normal operation of the motor. As hunting induces symmetrical sidebands around the fundamental, the feature coefficient for both approximates and corresponding details must be higher than the threshold during hunting i.e.  $(F_{a_{3,1}} \& F_{d_{3,2}}) \geq \epsilon_F$  or  $(F_{d_{3,1}} \& F_{a_{3,2}}) \geq \epsilon_F$ . Otherwise, it is not a hunting phenomenon and the presence of a single sideband may be a result of noise or disturbances.

Another threshold value  $\epsilon_a$  for the degree of stator current modulation is set to distinguish between practically stable operation of the motor with little oscillations in the speed and unstable operation of the motor with significant torsional oscillations. The decision of hunting is made based on the following conditions:

$$\begin{cases} \text{Hunting} = \text{True}, & \text{if } (F_{low} \& F_{up} \geq \epsilon_F) \text{ and } \chi \geq \epsilon_a \\ \text{Hunting} = \text{False}, & \text{otherwise} \end{cases} \quad (8.16)$$

Figure 8.5 illustrates a flow chart for the proposed hunting detection algorithm. A supervisory action is needed when the conditions for detecting hunting are met by the algorithm.

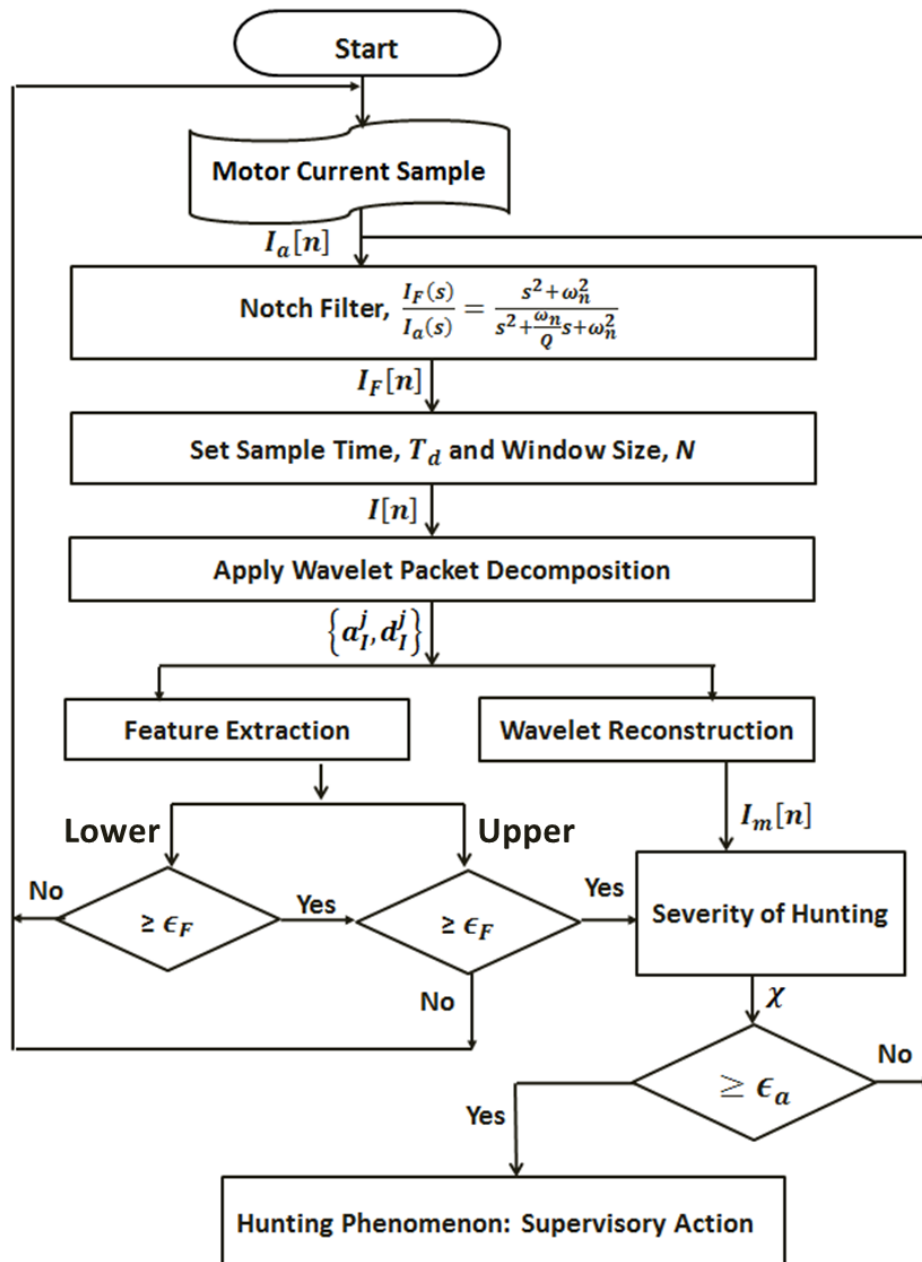


Figure 8.5. Flowchart of the hunting diagnosis algorithm.

### 8.3 Simulation Results

The hunting phenomenon is studied using finite element simulations of two 3-phase 4-pole line-start IPM motor models of different power ratings in order to observe the effects of motor parameters such as inductances, magnet flux linkage, inertia, viscous damping, cage resistances, etc. on the performance of the proposed diagnostic technique. ANSYS Maxwell software is used for time stepping finite element (FE) analysis of the motors. The first motor is rated as 5-kW and has  $\Delta$ -connected stator windings. The second motor is rated as 1-HP with Y-connected windings. The FE models of the motors are displayed in Figures 8.6a and 8.6b, respectively. The motors are run directly from a 3-phase, 208V balanced fixed frequency 60Hz ac supply. The detailed specifications of the motors are presented in table 8.4 in the appendix.

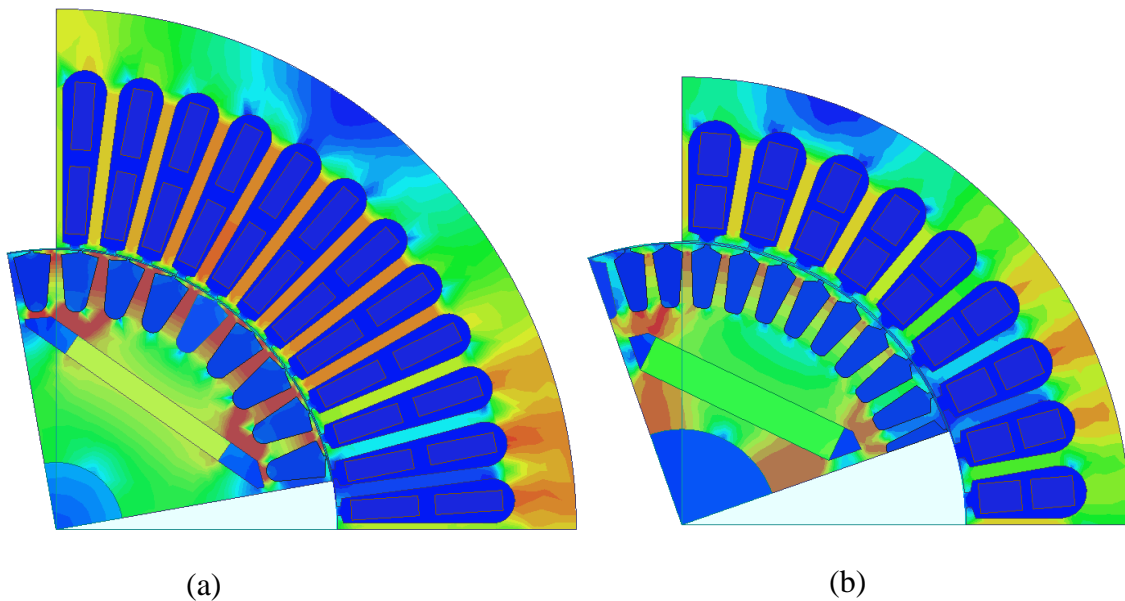
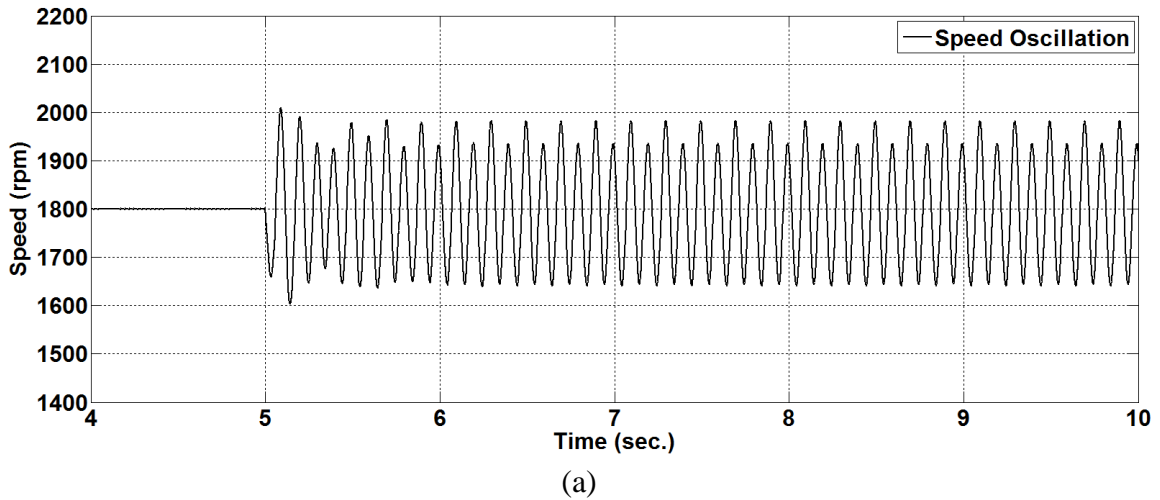
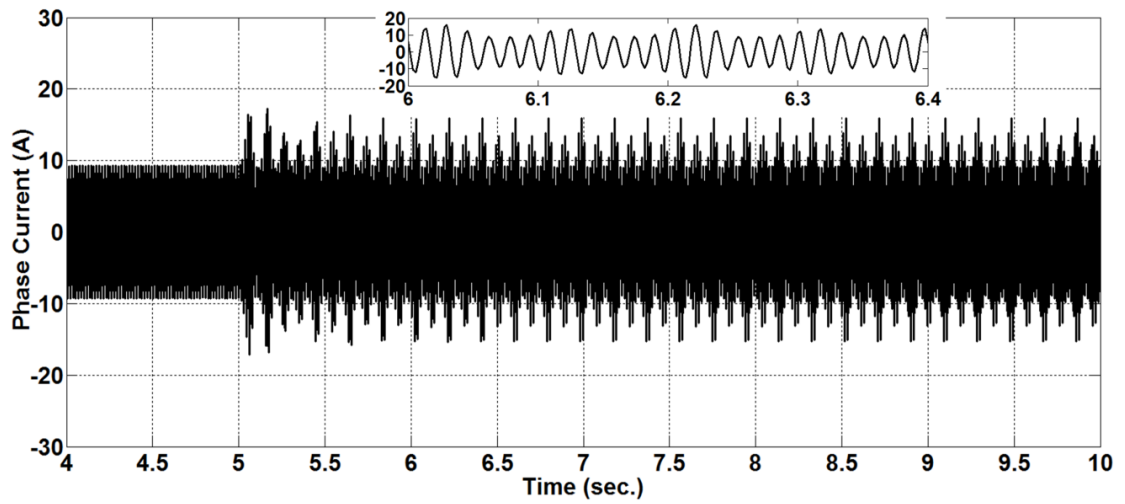


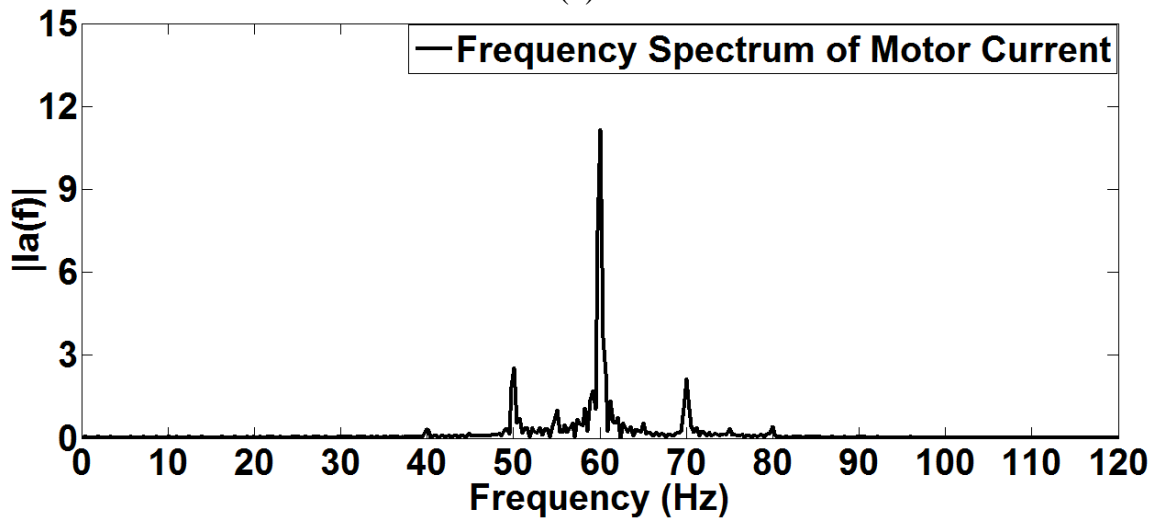
Figure 8.6. Finite element models of line-start IPM motors: (a) 5-kW and (b) 1-HP.

A hunting phenomenon is introduced in the 5kW motor at  $t = 5$ s by periodic variations of the load torque. The speed and current responses of the motor before and during hunting are presented in Figures 8.7a and 8.7b, respectively. The phase current waveform during hunting is zoomed in Figure 8.7b for better illustration of the modulation effects. The modulation in the current signal starts instantaneously when the rotor oscillates. The level of modulation depends on the frequency and amplitude of the oscillations. The Fourier spectrum of the current signal during hunting is illustrated in Figure 8.7c. The frequency of the rotor oscillation is 10Hz. Thus, symmetric sidebands with frequencies of 50Hz and 70Hz are present in the spectrum along with the fundamental. The magnitude of the stator current remains below the motor rating during hunting. In addition, the phase currents remain balanced. As a result, a traditional overcurrent relay or a differential motor protection relay will not pick up the effects of hunting.





(b)



(c)

Figure 8.7. Responses of the motor: (a) rotor speed, (b) stator phase current and (c) Fourier spectrum of the motor current during hunting.

The hunting diagnosis algorithm presented in section 8.2 is applied on the phase current data as shown in Figure 8.7b. Figures 8.8a-8.8c illustrate the responses of the algorithm for the given dataset. The feature coefficients of level three nodes  $a_{3,1}^l$ ,  $d_{3,1}^l$ ,  $a_{3,2}^l$  and  $d_{3,2}^l$  are presented in Figure 8.8a. These nodes are descendants from

the first level approximations  $a_1^l$  in the wavelet packet tree in Figure 8.3, and are constructed based on the frequency ordering of (0-30)Hz, (30-60)Hz, (60-90)Hz, and (90-120)Hz, respectively, for  $f_s = 60$  Hz. The magnitude of the feature coefficients is close to zero before hunting is introduced, indicating stable operation with no modulation in the current signals. The hunting phenomenon starts at time  $t = 5$ s. Consequently, the modulation causes the feature coefficients of  $d_{3,1}^l$ ,  $a_{3,2}^l$  to become greater than zero immediately. This implies that the frequencies of the lower sidebands are in between (30-60) Hz and the upper sidebands have frequencies in the range of (60-90)Hz. The magnitude of these feature coefficients keeps rising with a constant slope, and becomes constant after few seconds. A steady large value of the feature coefficient denotes the presence of sustained hunting in the drive system. A sample threshold  $\epsilon_F = 0.2$  is selected for fast detection of the hunting, and the zoomed-in response of the algorithm is depicted at the topmost portion of Figure 8.8a.

Wavelet reconstruction is applied to the decomposed stator current in order to extract the modulating current signal superimposed on the fundamental. Figure 8.7b presents the modulating current signal extracted by the wavelet reconstruction procedures. The degree of stator current modulation  $\chi$  obtained using the proposed algorithm is shown in Figure 8.8c. The value of  $\chi$  is zero when the current is not modulated and becomes almost 25% during sustained hunting.  $\chi$  reaches a steady value a lot faster than the feature coefficients. A sample threshold  $\epsilon_a = 0.15$  is selected for the 5-kW motor as the acceptable limit of modulation due to hunting. The response of the algorithm for  $\epsilon_a = 0.15$  is zoomed in Figure 8.8c.

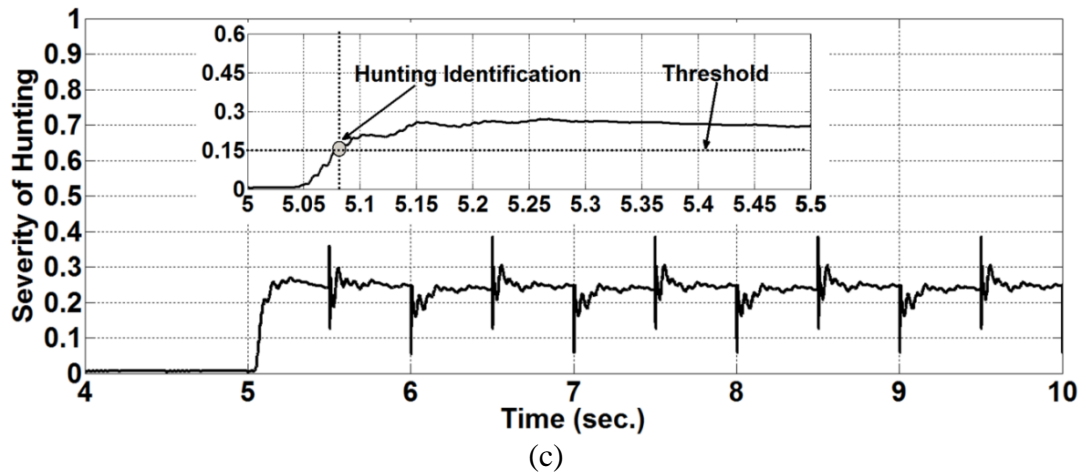
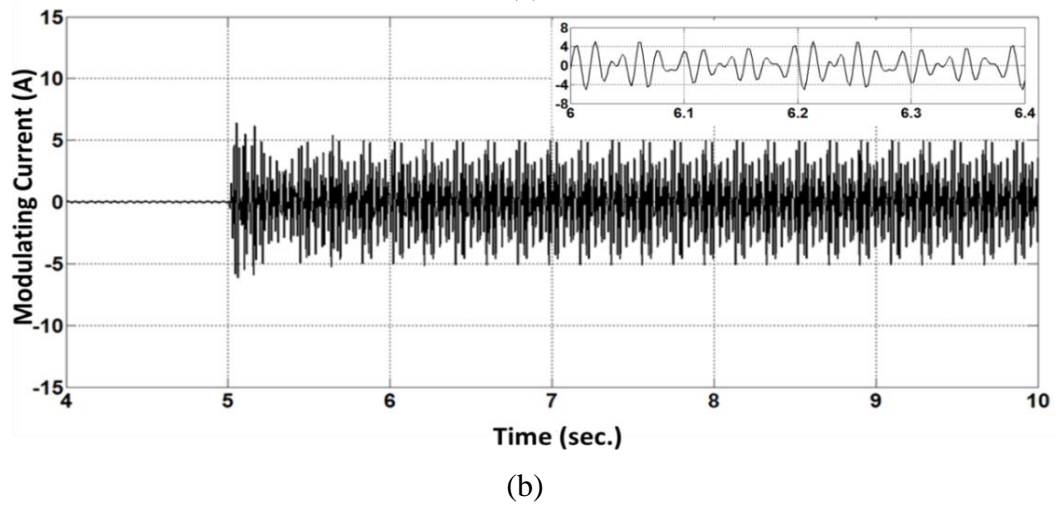
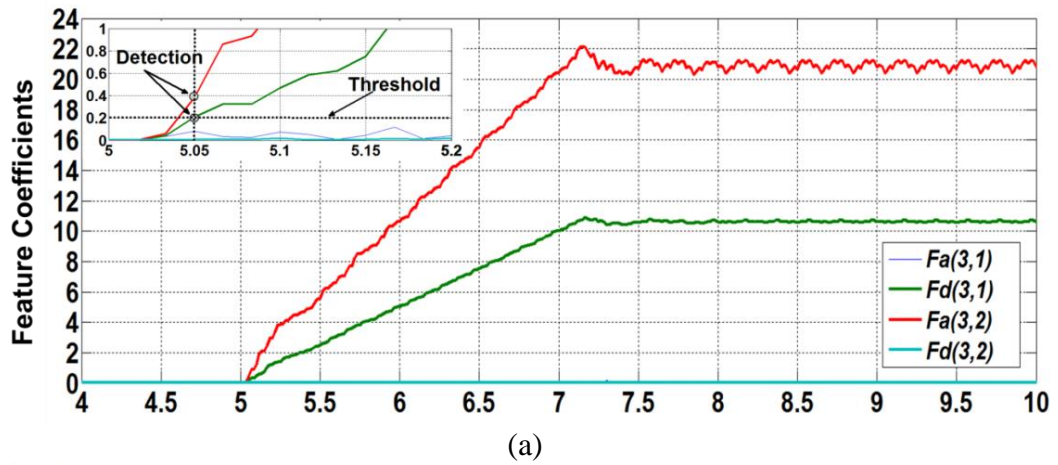


Figure 8.8. Response of the hunting diagnostic algorithm: (a) magnitude of the feature coefficient, (b) modulating current signal and (c) degree of stator current modulation.

The results indicate that the developed diagnostic technique can be used to detect and identify the hunting phenomenon in a line-start IPM motor in fraction of a second. The robustness of the hunting detection algorithm is investigated by additional testing using the 1-HP motor model. Figures 8.9-8.10 present the responses of the algorithm for hunting and normal behavior of the motor. The motor is operated from a fixed frequency balanced 60Hz ac supply. The hunting phenomenon is introduced in the motor at  $t = 2\text{s}$  and removed at  $t = 7\text{s}$ . The rotor oscillation due to hunting is depicted in Figure 8.9a. The stator phase current becomes modulated as shown in Figure 8.9b. Figure 8.9c illustrates the modulating current superimposed on the fundamental current signal. The developed detection algorithm responds to the onset of hunting instantaneously. Feature coefficients of the level 3 nodes  $a_{3,1}^l, d_{3,1}^l, a_{3,2}^l$  and  $d_{3,2}^l$  are presented in Figures 8.9d, 8.10a, 8.10b and 8.10c, respectively. These feature coefficients become nonzero with a sharp rise in their magnitude during the onset of hunting, indicating the presence of sidebands with frequencies in the range of (0-30)Hz, (30-60)Hz, (60-90)Hz and (90-120)Hz. The values of feature coefficients are smaller in the 1-HP motor than the 5-kW motor because the magnitude of the motor phase current is lower in a 1-HP motor drive in comparison to a 5kW motor drive. The severity of hunting  $\chi$  is illustrated in Figure 8.10d, corresponding with the level of modulation in the stator phase currents.

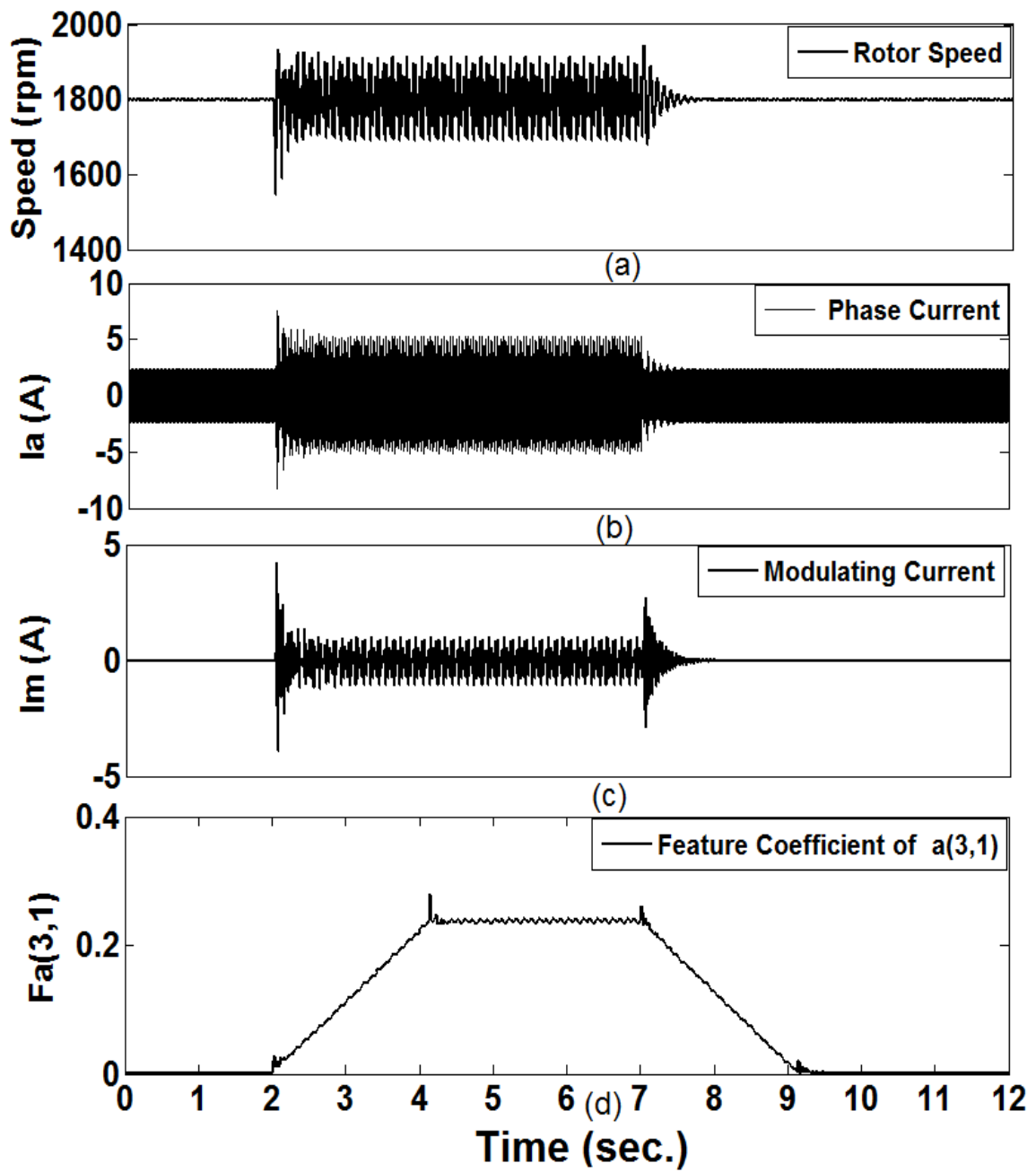


Figure 8.9. Responses for the 1HP motor drive: (a) rotor speed, (b) phase current, (c) modulating current signal and (d) magnitude of the feature coefficient  $F_{a_{3,1}}$ .

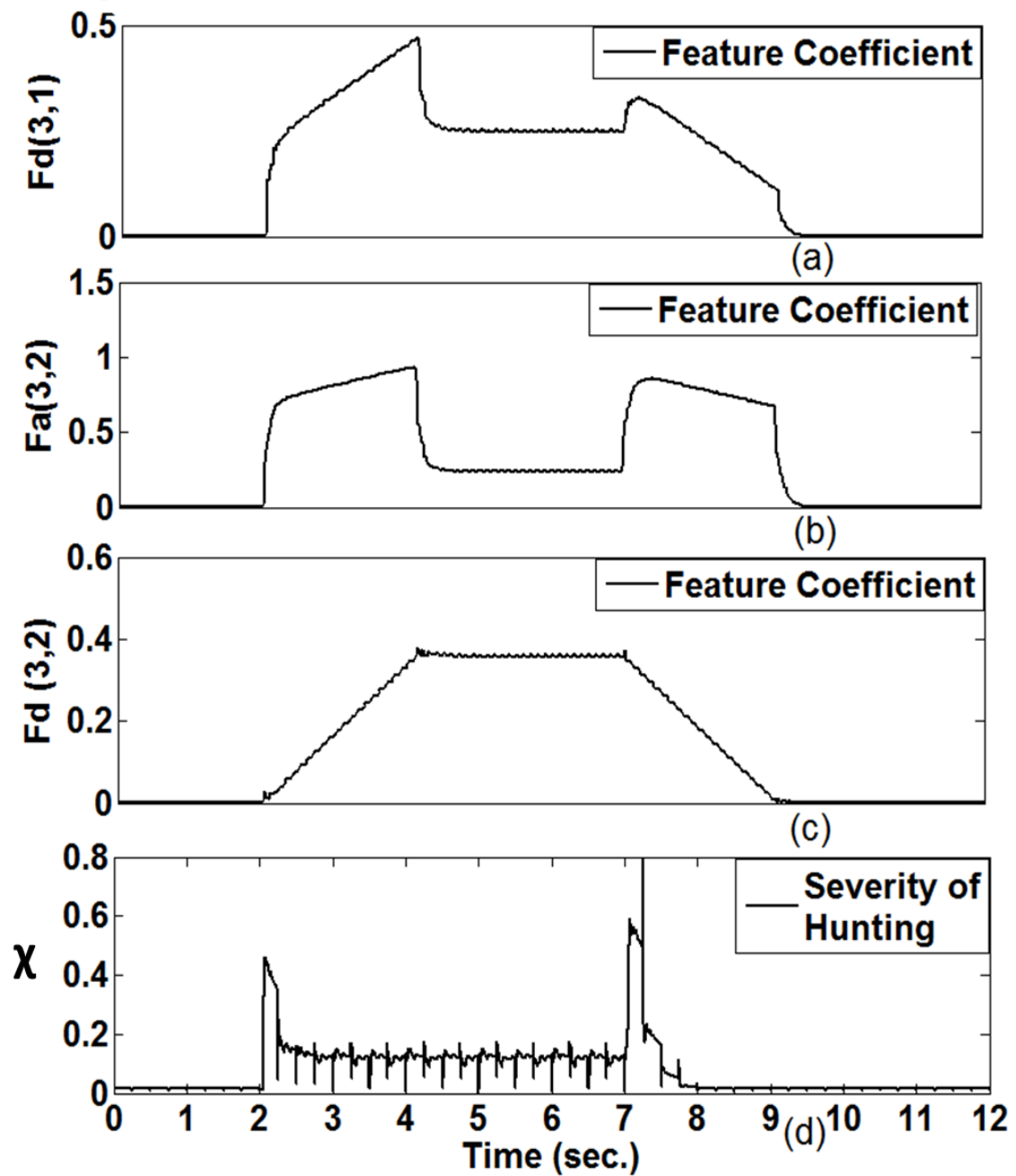
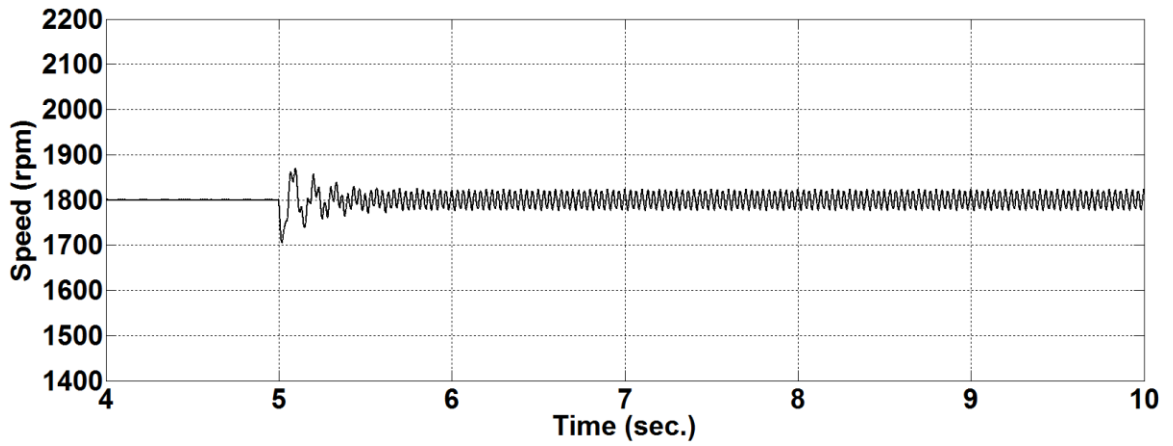


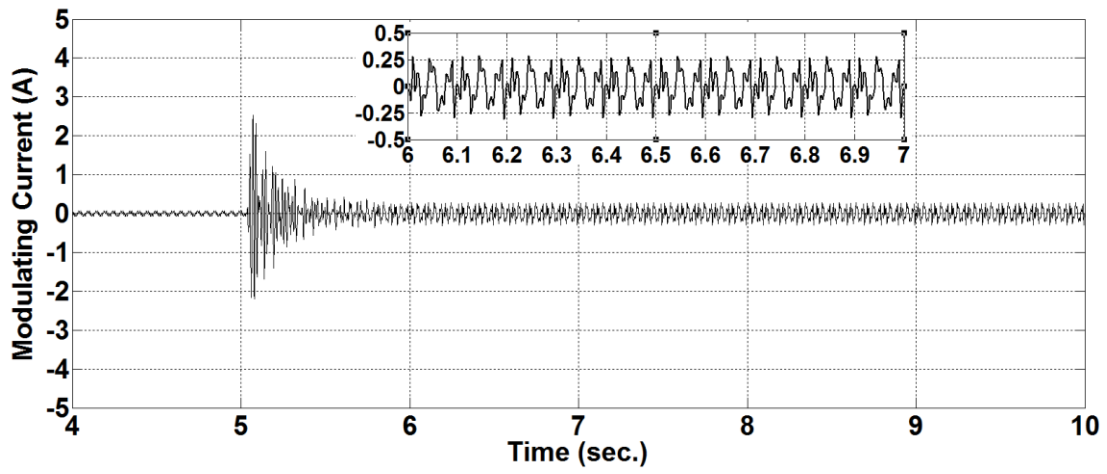
Figure 8.10. Responses for the 1HP motor drive: (a) magnitude of the feature coefficient  $F_{d_{3,1}}$  (b) magnitude of the feature coefficient  $F_{a_{3,2}}$ , (c) magnitude of the feature coefficient  $F_{d_{3,2}}$  and (d) degree of stator current modulation.

A line-start IPM motor operates in a practically stable mode if the magnitude of torsional oscillation is not severe and stays within the allowable limit. In such cases, the rotor goes into sustained hunting around the synchronous speed with slight speed overshoots and undershoots. Figures 8.11a-8.11d present a case scenario where the 5-kW IPM motor is experiencing hunting with low torsional oscillations. The rotor is oscillating around 1800rpm with a peak-peak magnitude of only 40rpm. The speed of the motor is depicted in Figure 8.11a. The rotor oscillation creates an insignificant level of amplitude modulation in the stator current signals. The modulating current signal is illustrated in Figure 8.11b. However, the modulation in the stator current is still picked up by the feature coefficients. Figure 8.11c illustrates trajectories of the feature coefficients. The degree of modulation in the current signal is presented in Figure 8.11d. As the value of  $\chi$  is less than the selected threshold, the response of the algorithm indicates that the severity of hunting is low.

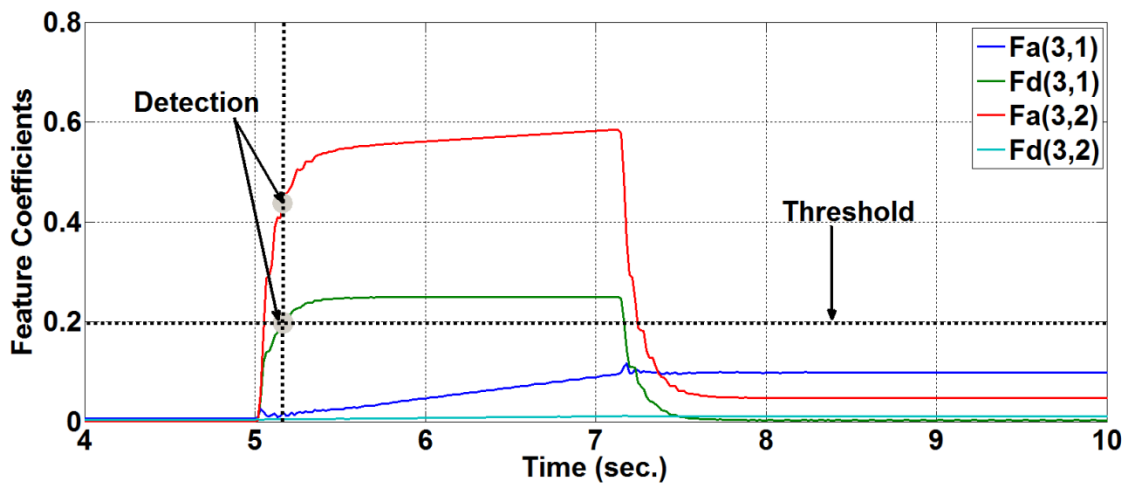
The performance of the proposed hunting diagnostic algorithm for different levels of rotor oscillations in the 5-kW motor drive due to hunting is presented in table 8.1. The value of  $\chi$  is related with the degree of rotor oscillations and becomes higher as the hunting becomes more severe.



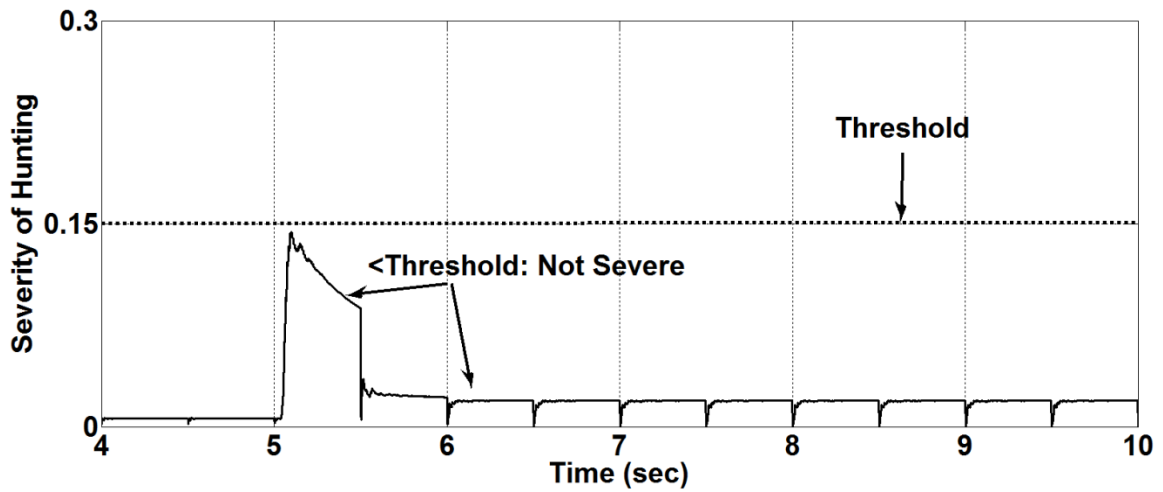
(a)



(b)



(c)



(d)

Figure 8.11. Responses during practically stable hunting: (a) rotor speed (b) modulating current signal, (c) magnitude of the feature coefficients and (d) degree of stator current modulation.

## 8.4 Experimental Results

Figure 8.12 illustrates the block diagram for real time experimental validation of the proposed wavelet packet decomposition based hunting diagnostic algorithm. A 1-HP, 3-phase, 208V, 4-pole line-start interior permanent magnet motor is used for the experiments. The detailed specifications of the motor are provided in table 8.4 in the appendix. The motor is run directly from a Y-connected 3-phase, 208V balanced fixed frequency 60 Hz ac line supply. Additionally, experiments are conducted using a 3-phase full bridge open loop  $V/f$  controlled sinusoidal pulse-width modulated IGBT inverter to provide the supply voltage. An AC dynamometer is used as a loading machine. A pulley is attached to the shaft of the motor and another pulley is connected with the

dynamometer's shaft. The motor and the dynamometer are connected by a belt running over the pulleys, allowing the inducement of hunting phenomena. A dSPACE DS-1104 R&D controller board is used for data acquisition and online implementation of the algorithm for diagnosis of hunting in the motor drive.

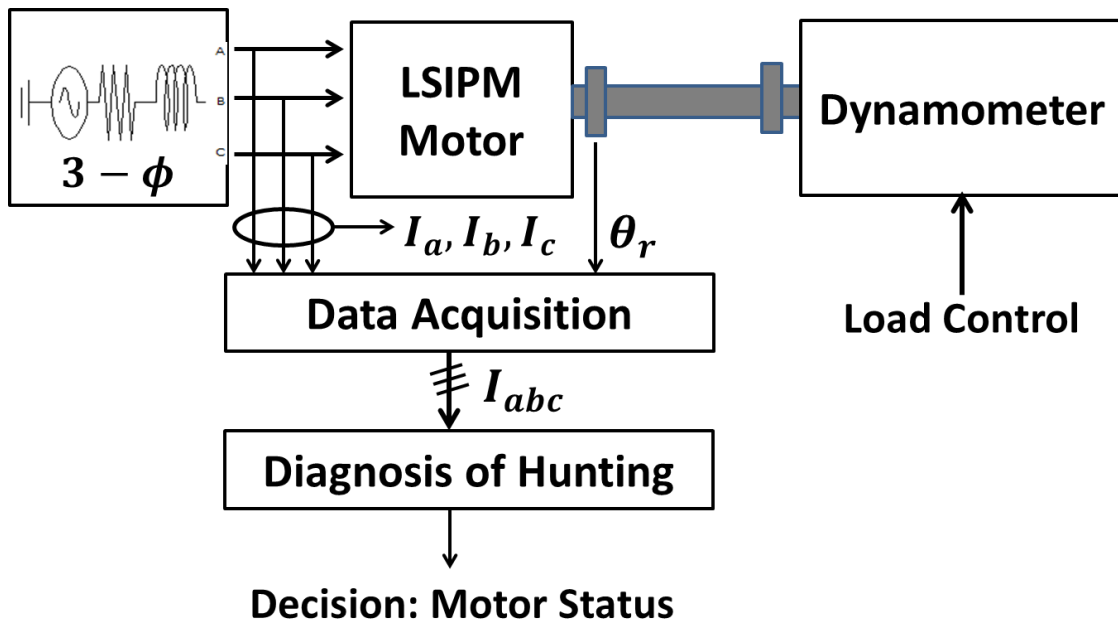


Figure 8.12. Block diagram for the real time diagnosis of hunting.

#### 8.4.1 Operated from the Line Supply

The speed and current response of the motor during a hunting condition for a fixed 60 Hz supply are presented in Figures 8.13a and 8.13b, respectively. The hunting phenomenon is introduced after  $t=3.5s$  by load variations and it is removed after  $t=8s$ . The responses of the developed hunting detection algorithm are provided in Figure 8.13c-8.13d and Figures 8.14a-8.14d. The motor operates at a steady synchronous

speed of 1800 rpm before hunting, and goes through successive torsional oscillations around the synchronous speed as depicted in Figure 8.13a. The peak to peak speed oscillation is around 135 rpm. Figure 8.13b depicts the modulation in the current signal due to torsional oscillations. The level 3 nodes in the WPT pick up the amplitude modulation in real time. The extracted modulating current from the instantaneous current signals using the wavelet reconstruction is illustrated in Figure 8.13c. The magnitude of the feature coefficients for nodes  $a_{3,1}^l, d_{3,1}^l, a_{3,2}^l, d_{3,2}^l$  starts rising towards a steady state value as soon as the modulation takes place in the current signal. The feature coefficients of  $a_{3,1}^l, d_{3,1}^l, a_{3,2}^l, d_{3,2}^l$  are presented in Figure 8.13d and Figures 8.14a-8.14c, respectively. The severity of hunting is related to the amount of modulation happening in the current waveform, and is picked up in real time by  $\chi$ . Figure 8.14d illustrates the trajectory of  $\chi$ . The magnitude of  $\chi$  is close to zero during normal operation, and becomes more than 40% indicating the existence of severe torsional vibration in the system. Thus, the hunting diagnosis algorithm is able to detect hunting and identify the severity of hunting in real time.

There is a close relationship between experimental results and simulation results that further validates the performance of the hunting diagnostic algorithm. However, the severity of hunting and the magnitude of feature coefficients are slightly lower in the experimental investigation in comparison to their values during the simulated hunting of the motor. This is due to the availability of higher stiffness and viscous damping in the experimental setup than in the finite element simulation model.

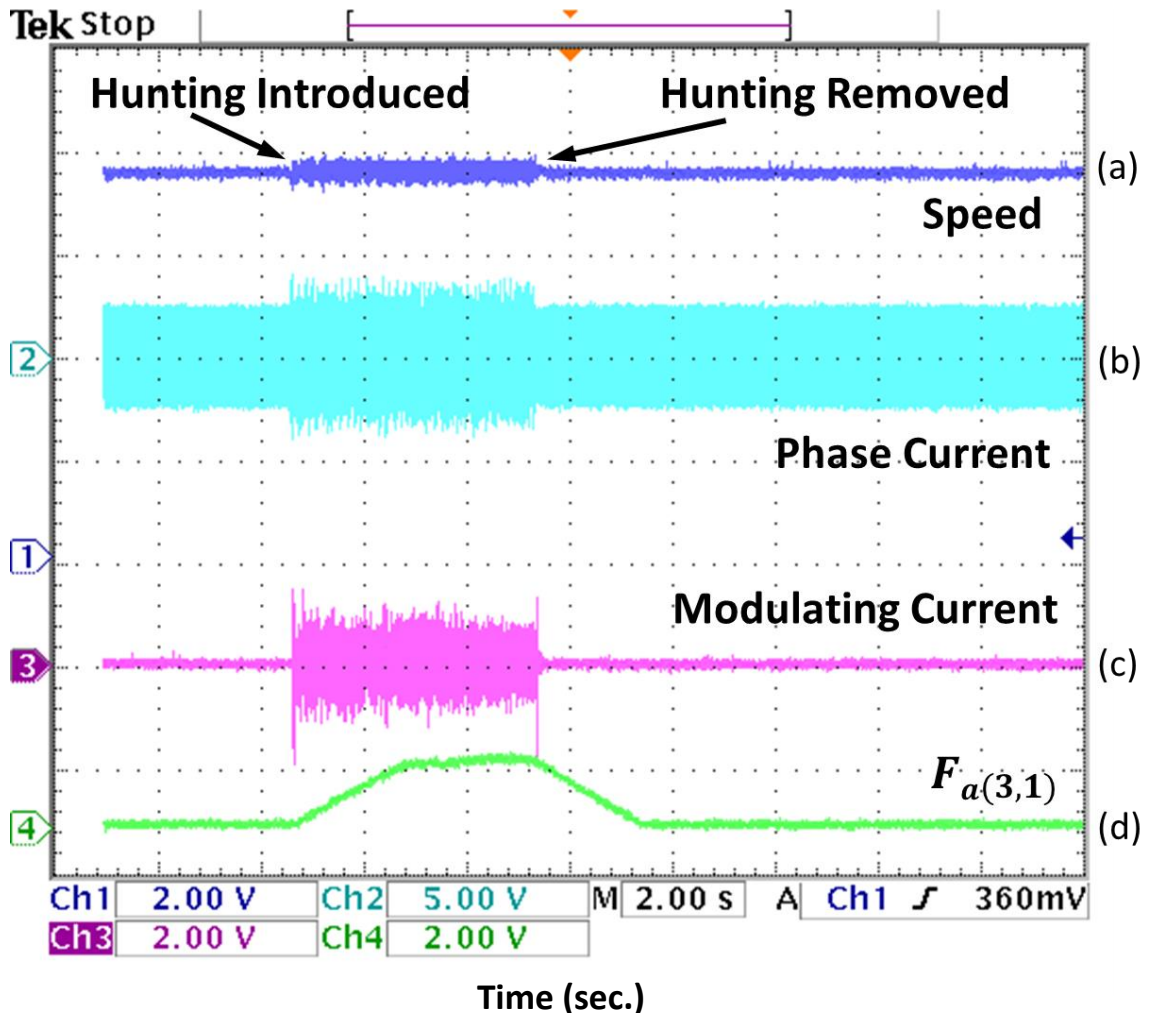


Figure 8.13. Responses of the diagnostic technique for detecting hunting at 60Hz: (a) rotor speed, (b) motor phase current, (c) modulating current signal and (d) magnitude of the feature coefficient of node  $a_{(3,1)}$ .

**Scales:** Speed, 240rpm/V, phase current, 1A/V, modulating current, 1A/V and  $F_{a(3,1)}$ , 0.5unit/V.

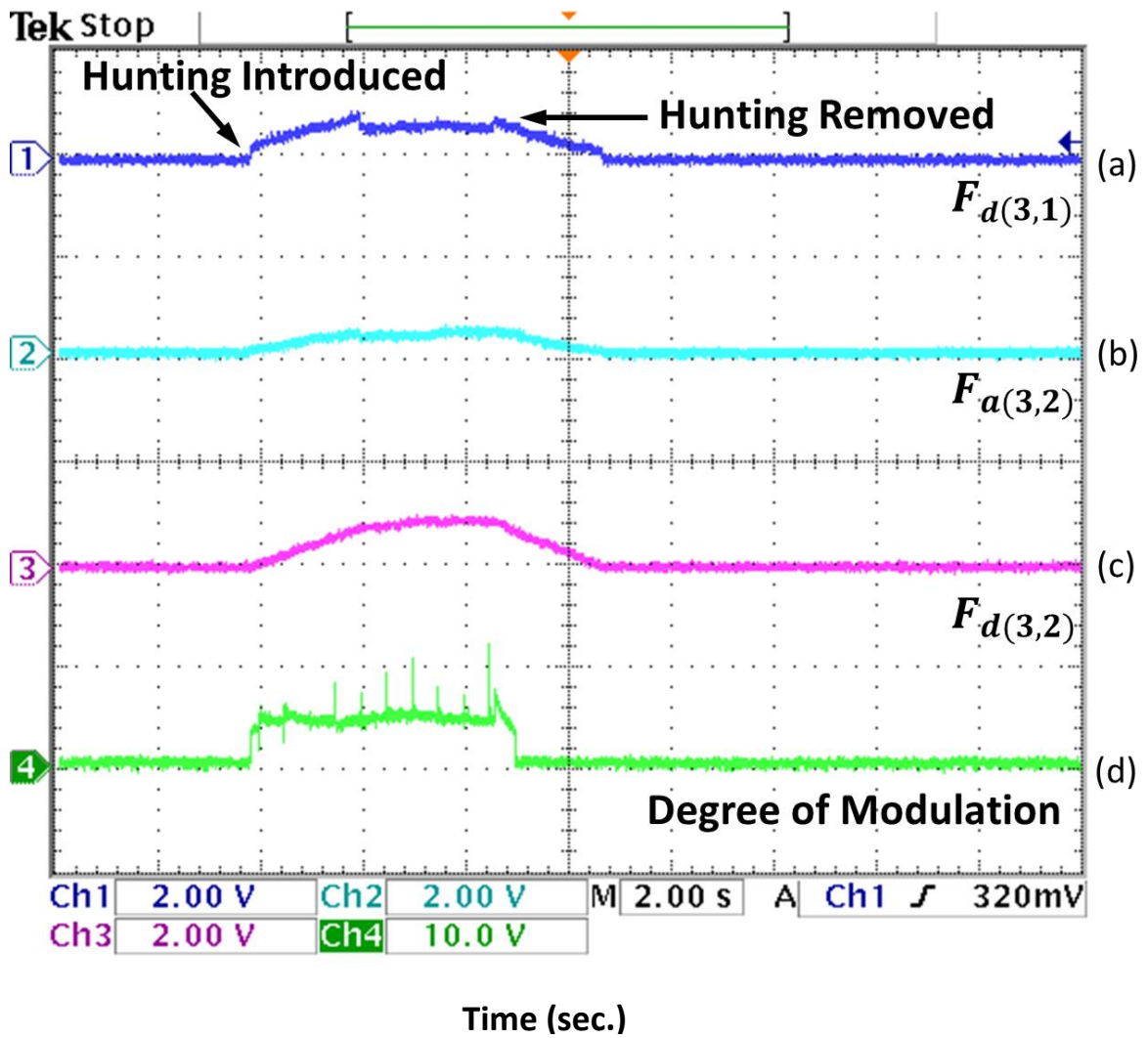


Figure 8.14. Responses of the diagnostic technique for detecting hunting at 60Hz:

(a)  $F_{d(3,1)}$ , (b)  $F_{a(3,2)}$ , (c)  $F_{d(3,2)}$  and (d) relative degree of modulation.

Scales:  $F_{a(3,1)}$  to  $F_{d(3,2)}$ , 0.5unit/V and degree of modulation, 10%/V.

### 8.4.2 Operation from a $V/f$ Controlled Inverter

A power electronics based  $V/f$  controlled inverter introduces extra harmonics in the motor line current due to PWM switching. In order to observe the robustness of the hunting detection algorithm, the motor is run from a  $V/f$  controlled inverter drive. The switching frequency of the inverter is selected to be 5 kHz. Figure 8.15a illustrates the speed response of the motor at 50 Hz command frequency. The corresponding motor phase current during hunting is depicted in Figure 8.15b. The extracted modulating current is illustrated in Figure 8.15c. The feature coefficients of nodes  $a_{3,1}^l, d_{3,1}^l, a_{3,2}^l, d_{3,2}^l$  are presented in Figure 8.15d and Figures 8.16a-8.16c, respectively. The severity of hunting is presented in Figure 8.16d. In table 8.2, test results for different cases of hunting induced oscillations using the proposed technique are depicted. Extreme levels of hunting are not induced in the system, in order to maintain the integrity of the mechanical set-up. Based on the experimental results, the proposed method based on WPD of the stator current can confidently detect the hunting condition, even during the presence of extra harmonics due to power electronics and PWM switching.

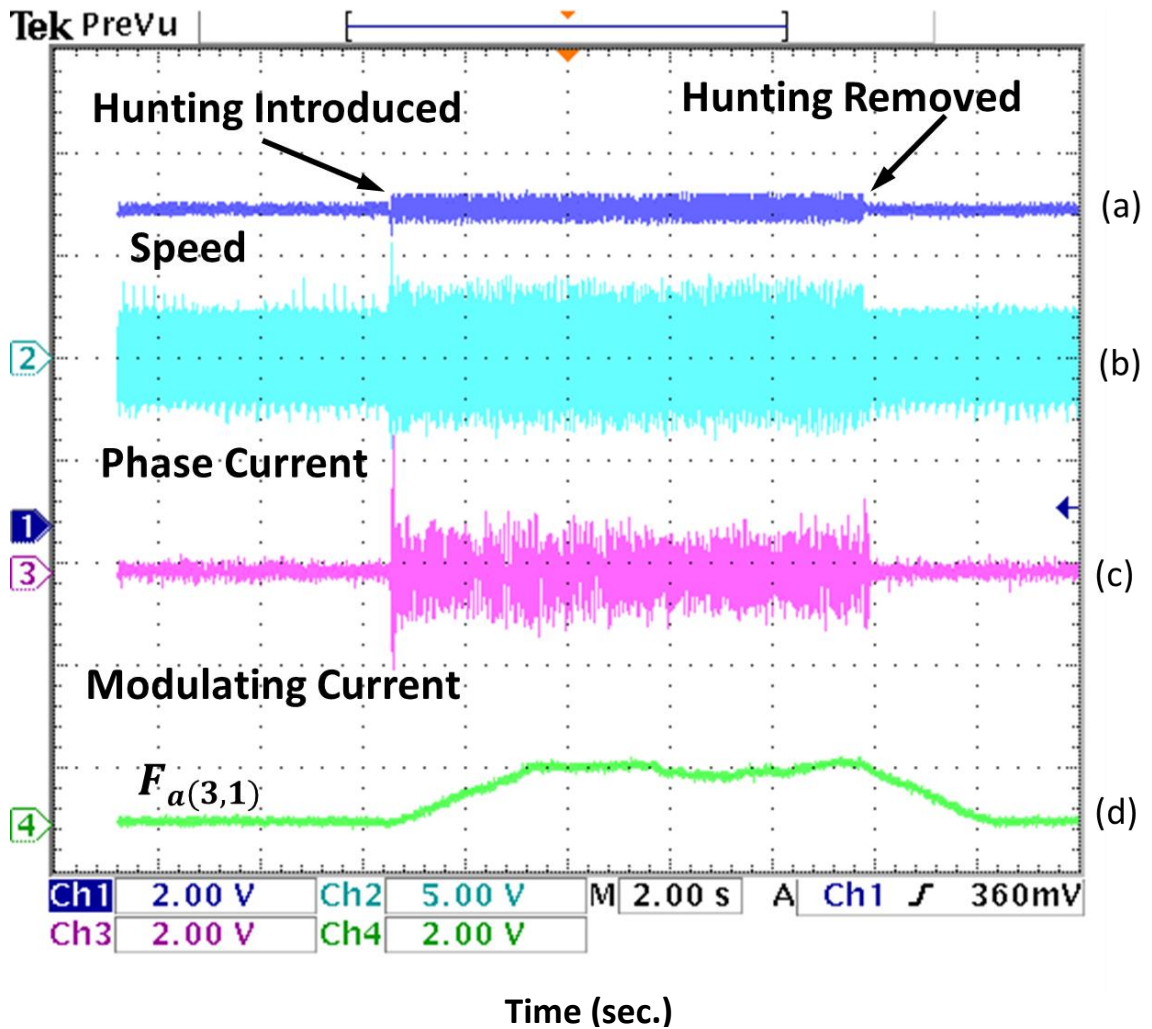


Figure 8.15. Responses of the diagnostic technique for detecting hunting at 50Hz: (a) rotor speed, (b) motor phase current, (c) modulating current signal and (d) magnitude of the feature coefficient of node  $a_{(3,1)}$ .

**Scales:** speed, 240rpm/V, phase current, 1A/V, modulating current, 1A/V and  $F_{a(3,1)}$ , 0.5unit/V.

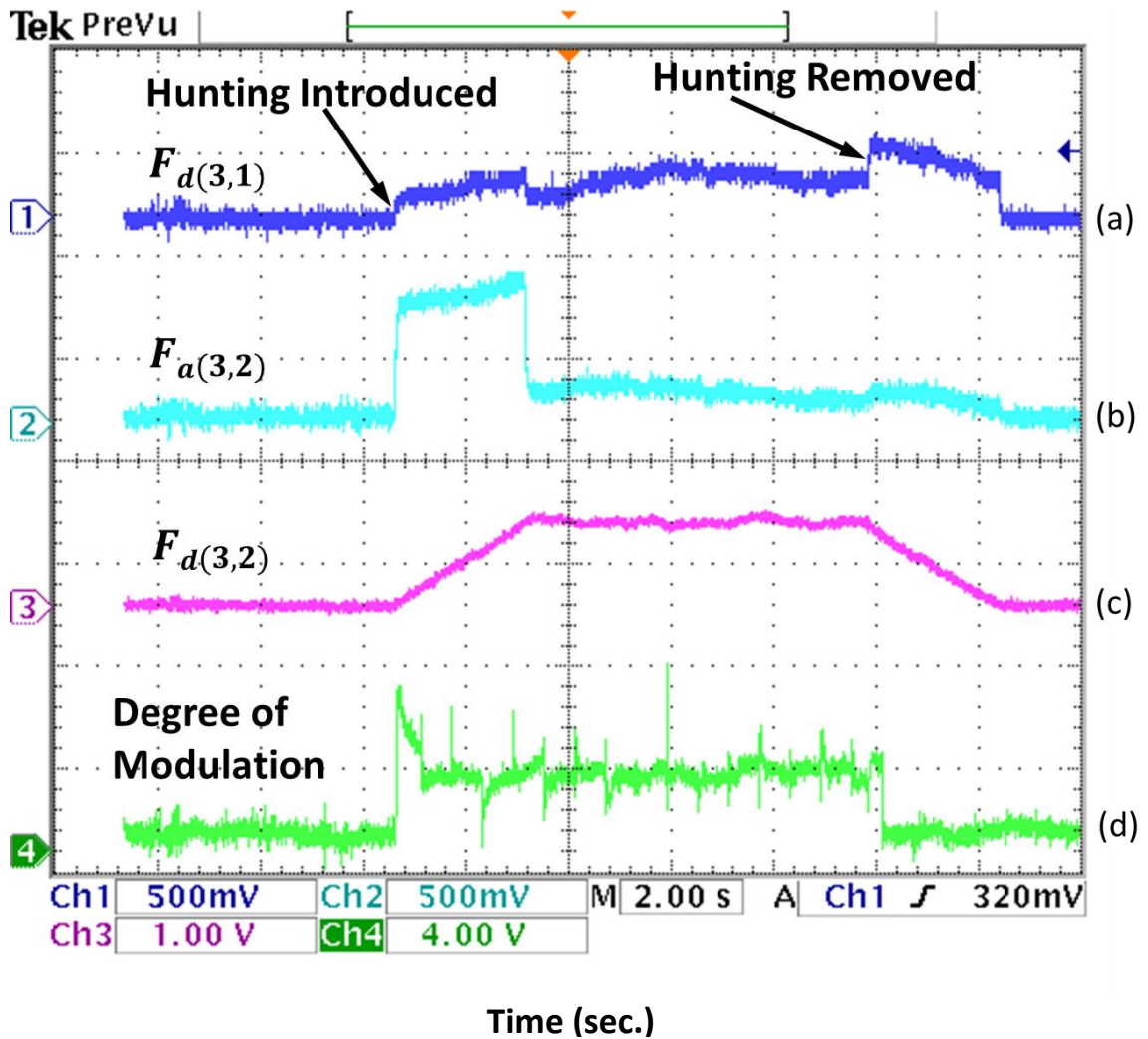


Figure 8.16. Responses of the diagnostic technique for detecting hunting at 50Hz: (a)  $F_{d(3,1)}$ , (b)  $F_{a(3,2)}$ , (c)  $F_{d(3,2)}$  and (d) relative degree of modulation.

**Scales:**  $F_{a(3,1)}$  to  $F_{d(3,2)}$ , 0.5unit/V and degree of modulation, 10%/V.

### 8.4.3 Effects of Source Impedance

The effects of source impedance on the starting and synchronization of line-start IPM (LSIPM) motors are demonstrated in Figures 8.17a-8.17c. An inductor bank is connected in series with the 3-phase AC supply to increase the source impedance. Initially, the inductance value is set to 5mH. The high source impedance induces a start-up failure by decreasing the effective stator voltage. The motor assembly exhibits hunting around a steady sub-synchronous speed of 200rpm as shown in Figure 8.17a. The phase-A voltage waveform is illustrated in Figure 8.17b. The phase-A current remains high as the magnitude of the motor's back-emf is small at the sub-synchronous speed as depicted in Figure 8.17c. The inductance is reduced to a small value of 0.8mH after  $t = 4.65$ s. The increased effective stator voltage induces rotor acceleration with hunting continuing during the ramp-up process. The LSIPM motor successfully synchronizes within 1 second of the impedance change, with the phase current magnitude and modulation decreasing to their small, steady-state values.

The hunting diagnostic algorithm successfully detects the rotor oscillations around the sub-synchronous speed. The performance of the algorithm is illustrated in Figures 8.18a-8.18f. During sub-synchronous hunting, the main frequency of rotor oscillations is the product of the slip and the supply frequency. In this case, the slip of the rotor is 0.89 and the supply frequency is 60Hz. As a result, the rotor is hunting with a frequency of 53.4Hz around the sub-synchronous speed of 200 rpm. The modulating current caused by the hunting is shown in Figure 8.18a. The most prominent lower sidebands in the current signal have low frequencies in between (0-30) Hz. The upper sidebands contain

frequencies in between (90-120) Hz. This phenomenon can be recognized from the feature coefficients depicted in Figures 8.18b-8.18e. Nodes  $a_{3,1}^I$  and  $d_{3,2}^I$  correspond to the frequency bands of (0-30) Hz and (90-120) Hz, respectively. Accordingly, the feature coefficients of these nodes are higher in comparison to the rest of the nodes. The magnitudes of all the feature coefficients remain high while the motor ramps up to the synchronous speed. This implies the presence of significant hunting during the acceleration period. After the successful synchronization, there exist no hunting induced torsional oscillations in the motor. Consequently, the magnitude of the feature coefficients of nodes  $a_{3,1}^I, d_{3,1}^I, a_{3,2}^I$  and  $d_{3,2}^I$  falls to zero, indicating stable operation of the motor. The severity of hunting indicated by the degree of modulation in the stator current signal is illustrated in Figure 8.18f.

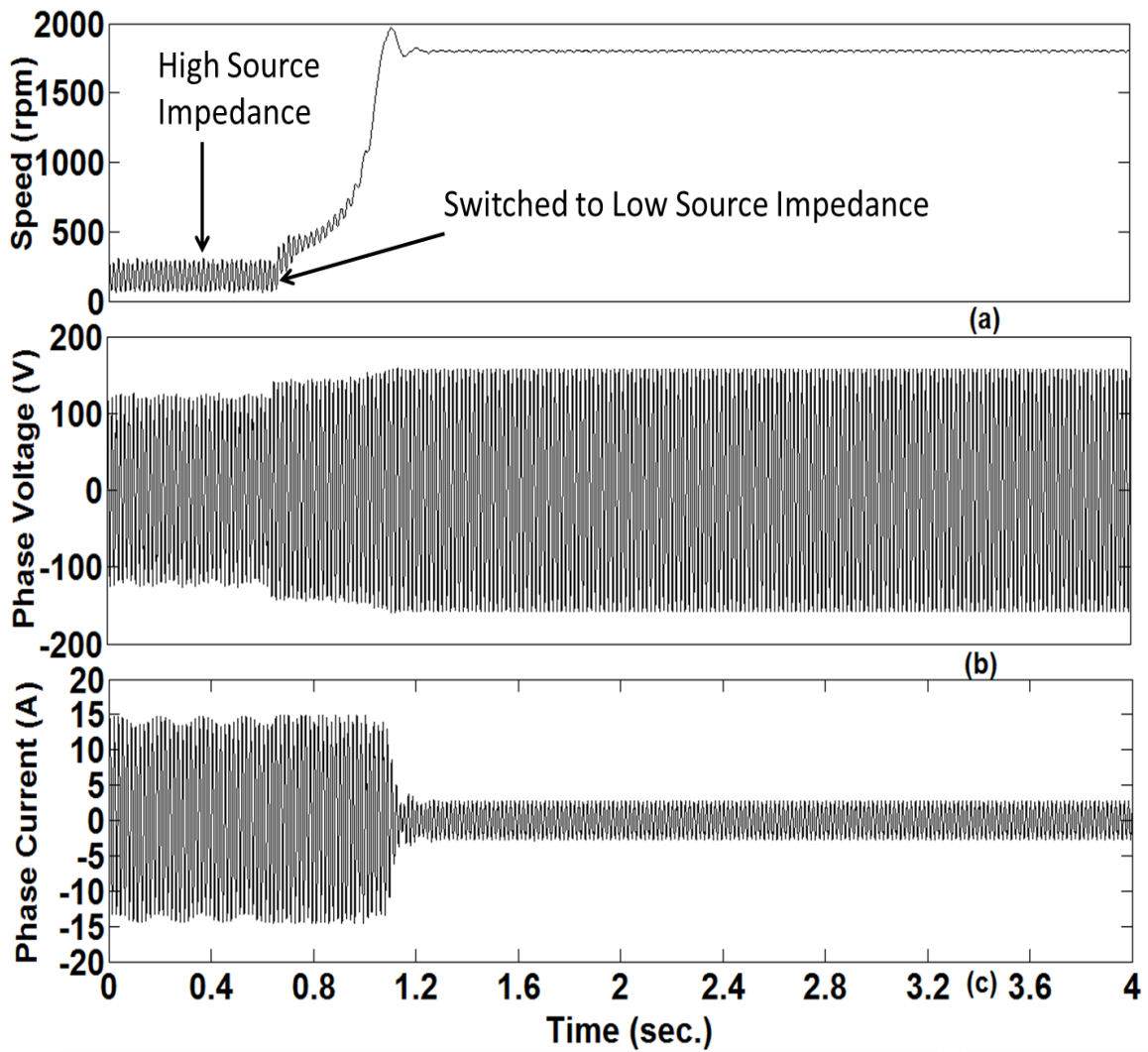


Figure 8.17. Effects of source impedance on the: (a) rotor speed, (b) phase voltage and (c) phase current.

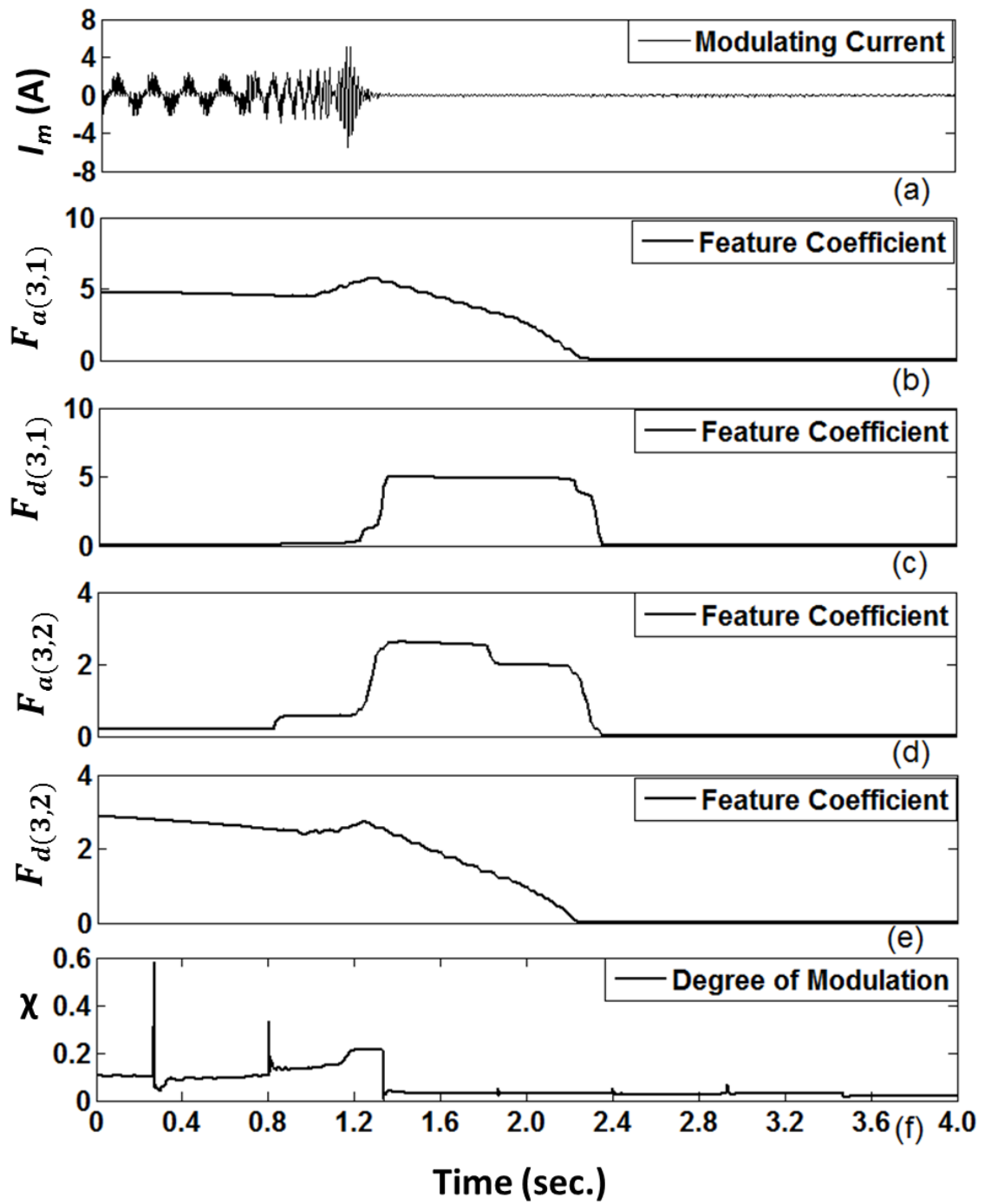


Figure 8.18. Performance of the sub-synchronous hunting detection algorithm: (a) modulating current (b)  $F_{a(3,1)}$ , (c)  $F_{d(3,1)}$ , (d)  $F_{a(3,2)}$ , (e)  $F_{d(3,2)}$  and (f)  $\chi$ .

## 8.5 Conclusion

This chapter presents a novel wavelet packet decomposition (WPD) based current signature analysis technique for real time diagnosis of hunting phenomena in IPM motors operated by the fixed frequency line supply. The efficacy of the proposed method is validated by performing finite element simulation and experimental investigations on different line-start IPM motor drives for various starting and loading conditions. Based on the simulation and experimental results, the developed method can detect hunting in a line-start IPM motor instantaneously and can identify the severity of it with a high degree of confidence. It is fast, remote, non-intrusive, and invisibly works as a silent sentinel for the motor drive system. It is highly suitable to be a part of protection relays for any type of IPM motor drive system.

However, the processing time to recognize severe hunting by the proposed algorithm depends on the relative thresholds defined by the user. In this work, absolute values for the thresholds are not set and left for the users because the experimental investigation has been performed on a laboratory prototype system and an AC dynamometer has been used to emulate real life loads for the motor drive. In practical case scenarios, the loads will more likely be pumps, compressors, conveyor belts, fans, etc. The allowable limits of torsional vibration for such loads are defined by the IEEE/NEMA standards. This chapter presents a generalized algorithm that can be easily customized for any type of application. An experimental basis for a hunting diagnosis algorithm for IPM motors is presented in this thesis. In the following chapter, a sensorless control technique for IPM motor driven ESP drive systems is developed using the online hunting detection algorithm.

## Appendix

Table 8.1. Performance of the proposed technique for different levels of hunting in the 5-kW line-start IPM motor drive.

<b>Properties</b>	<b>Severity: Low</b>	<b>Severity: Moderate</b>	<b>Severity: High</b>	<b>Severity: Extreme</b>
<b>% Slip</b>	1	3.5	10	36
<b><math>F_{a(3,1)}</math></b>	0	0.02	0.1	8
<b><math>F_{d(3,1)}</math></b>	0.24	1.26	10.6	350
<b><math>F_{a(3,2)}</math></b>	0.155	1.16	2.1	9
<b><math>F_{d(3,2)}</math></b>	0.002	0.012	0.04	0.25
<b><math>\chi</math></b>	0.034	0.085	0.3	0.6

Table 8.2. Performance of the proposed technique for different levels of hunting in the 1-HP line-start IPM motor drive.

<b>Properties</b>	<b>Severity: Low</b>	<b>Severity: Moderate</b>	<b>Severity: High</b>
<b>% Slip</b>	1.2	4	10
<b><math>F_{a(3,1)}</math></b>	0.0015	0.35	0.8
<b><math>F_{d(3,1)}</math></b>	0.0012	1.1	1.65
<b><math>F_{a(3,2)}</math></b>	0.0025	1.0	2.2
<b><math>F_{d(3,2)}</math></b>	0.0012	0.3	0.44
<b><math>\chi</math></b>	0.03	0.3	0.41

Table 8.3. 'db6' wavelet decomposition and reconstruction filter coefficients.

$g[k]$	$g^R[k]$	$h[k]$	$h^R[k]$
-0.0011	-0.0011	-0.1115	0.1115
0.0048	-0.0048	0.4946	0.4946
0.0006	0.0006	-0.7511	0.7511
-0.0316	0.0316	0.3153	0.3153
0.0275	0.0275	0.2263	-0.2263
0.0975	-0.0975	-0.1298	-0.1298
-0.1298	-0.1298	-0.0975	0.0975
-0.2263	0.2263	0.0275	0.0275
0.3153	0.3153	0.0316	-0.0316
0.7511	-0.7511	0.0006	0.0006
0.4946	0.4946	-0.0048	0.0048
0.1115	-0.1115	-0.0011	-0.0011

Table 8.4. Parameters of the 5kW and 1-HP line-start IPM (LSIPM) motors.

<b>Symbol</b>	<b>Name</b>	<b>5 kW LSIPM Motor</b>	<b>1 HP LSIPM Motor</b>
$N_p$	number of phases	3	3
$p$	number of pole pairs	2	2
$I_{rated}$	rated line current	15.0219 A	3 A
$f_{rated}$	rated frequency	60 Hz	60 Hz
$P_{rated}$	rated power	5 kW	1 HP
$T_{rated}$	rated torque	26.5 N. m	4 N. m
$V_{rated}$	rated voltage (L-L)	208 V	208 V
$L_{qs}$	$q$ -axis inductance	0.0805 H	0.07957 H
$L_{ds}$	$d$ -axis inductance	0.01254 H	0.04244 H
$R_s$	stator resistance/phase	0.1 $\Omega$	1.93 $\Omega$
$J$	rotor inertia	0.0807 Kg. m <sup>2</sup>	0.003 Kg. m <sup>2</sup>
$D_m$	rotor damping constant	0.0069 (N. m.)/rad./sec.	0.0008 (N.m.)/rad./sec.
$\lambda_m$	magnet flux linkage	0.3265 volts/rad./sec.	0.314 volts/rad./sec.

## References

1. B. Akin, S. Choi, U. Orguner and and A. Toliyat, "A simple real-time fault signature monitoring tool for motor-drive-embedded fault diagnosis systems", *IEEE Transactions on Industrial Electronics*, Vol. 58, No. 5, pp. 1990-2001, 2011, November 2013.
2. Z. Liu, X. Yin, Z. Zhang, D. Chen and Wei Chen, "Online rotor mixed fault diagnosis way based on spectrum analysis of instantaneous power in squirrel cage induction motors", *IEEE Transactions on Energy Conversion*, Vol. 19, No. 3, pp. 485-490, September 2004.
3. H. Kim, "On-line mechanical unbalance estimation for permanent magnet synchronous machine drives", *IET Electric Power Applications*, Vol. 3, No. 3, pp. 178–186, May 2009.
4. Jose de Jesus Rangel-Magdaleno et. al., "Novel Methodology for online half-broken-bar detection on induction motors", *IEEE Transactions on Instrumentation and Measurement*, Vol. 58, No. 5, pp. 1690- 1698, May 2009.
5. Kyusung Kim, A.G. Parlos and R. Mohan Bharadwaj, "Sensorless fault diagnosis of induction motors", *IEEE Transactions on Industrial Electronics*, Vol. 50, No. 5, pp. 1038-1051, November 2009.
6. A. Sadeghian, Z. Ye and Bin Wu, "Online Detection of Broken Rotor Bars in Induction Motors by Wavelet Packet Decomposition and Artificial Neural Networks", *IEEE Transactions on Instrumentation and Measurement*, Vol. 58, No. 7, pp. 2253 – 2263, July 2009.
7. S. C. Yang, "Online turn fault detection of interior permanent-magnet machines using the pulsating-type voltage injection", *IEEE Transactions on Industry Applications*, Vol. 52, No. 3, pp. 2340- 2349, May 2016.
8. M. Eftekhari, M. Moallem, S. Sadri and Min-Fu Hsieh, "Online Detection of Induction Motor's Stator Winding Short-Circuit Faults", *IEEE Systems Journal*, Vol. 8, No. 4, pp. 1272-1282, December 2014.

9. K.-H. Kim, B.-G. Gu and I.-S. Jung, "Online fault-detecting scheme of an inverter-fed permanent magnet synchronous motor under stator winding shorted turn and inverter switch open", *IET Electric Power Applications*, Vol. 5, No. 6, pp. 529-539, July 2011.
10. A. Gandhi, T. Corrigan and L. Parsa, "Recent Advances in Modeling and Online Detection of Stator Interturn Faults in Electrical Motors", *IEEE Transactions on Industrial Electronics*, Vol. 58, No. 5, pp. 1564-1575, May 2011.
11. Cristian H. De Angelo, et. al., "Online Model-Based Stator-Fault Detection and Identification in Induction Motors", *IEEE Transactions on Industrial Electronics*, Vol. 56, No. 11, pp. 4671-4680, November 2009.
12. M. Arkan, D. K. Perovic and P. Unsworth, "Online stator fault diagnosis in induction motors", *IEE Proceedings - Electric Power Applications*, Vol. 148, No. 6, pp. 537-547, November 2001.
13. Jee-Hoon Jung, Jong-Jae Lee and Bong-Hwan Kwon, "Online Diagnosis of Induction Motors Using MCSA", *IEEE Transactions on Industrial Electronics*, Vol. 53, No. 6, pp. 1842 - 1852, December 2006.
14. R. Schaumann and M. E. V. Valkenburg, *Design of analog filters*, New York, NY: Oxford University Press, 2001.
15. M. V. Wickerhauser, *Adapted wavelet analysis from theory to software*, Wellesley, MA: IEEE Press, 1994.

## Chapter 9

### Sensorless Control of a Submersible IPM Motor Drive

#### 9.1 Introduction

The squirrel cage submersible induction motor has been the industrial standard for electric submersible pump (ESP) drives [1]. In recent years, permanent magnet submersible motor (PMSM) driven ESPs have been introduced in the market which indicates better efficiency, smaller dimensions, wide operating range, lower heat generation and superior performance than similar IM driven ESPs [2]-[5]. However, PMSM-ESPs have not gained popularity due to control problems associated with the nonlinearity in PM motors [4]-[5]. The control system for a PM motor drive is complicated, and requires information on the instantaneous rotor position. For downhole ESPs operated in oil and gas production units, it is not feasible to have position sensors under thousands of feet from the surface. It requires the design of a position sensorless control technique for a PMSM-ESP system. Sensorless control techniques can be summarized into two broad categories including equivalent circuit model based sensorless control and magnetic saliency based sensorless control methods. In model based techniques, the equivalent circuits of an IPM motor in a stationary/rotating reference frame coupled with a linear/non-linear observer are used to estimate the back-emfs of the motor [7]-[16]. The rotor position and speed are obtained either directly from the back-emfs or through the use of a PLL. Different types of observers have been used for the back-emf estimation such as linear Luenberger observer, Kalman filter, extended Kalman

filter, model reference adaptive controller and non-linear sliding mode observer. The non-linear sliding mode observers are the most popular for back-emf estimation, and widely used in the industry for sensorless control of permanent magnet motors [7]-[10], [12] and [16]. However, sliding mode based controllers/observers suffer from an inherent chattering phenomenon due to high frequency oscillations of the control signal around the sliding surface, created by discontinuous switching actions. In order to reduce the chattering associated with sliding mode observers, many researchers have proposed different solutions such as low pass filtering, use of sigmoid functions, application of a secondary observer and higher order sliding mode observers. Although the back-emf estimation based sensorless control techniques can confidently estimate the rotor position, these are suitable for medium and high speed operation of the motor. At a low speed, the magnitude of the motor back-emf is too low to be used for position estimation, making the back-emf estimation based sensorless controller infeasible at stand-still and low speed [17]-[18].

IPM motors have inherent magnetic saliency due to the positioning and orientation of permanent magnets inside the rotor. The saliency of IPM motors can be used to determine the rotor position by injecting high frequency voltage/current signals into the motor [17]-[21]. At stand-still, high frequency signals with various injection angles are superimposed over the torque producing command currents to calculate the spatial distribution of  $d$ - $q$  axis inductances which vary with the injection angle. The  $d$ - $q$  axis inductances are functions of the rotor position. Thus, the position of the rotor can be obtained from the inductance variation. However, the presence of a load-side power transformer and long power cables in ESP drives prohibits the injection of high

frequency ac signals. Thus, existing high-frequency signal injection based sensorless control techniques are inapplicable for ESP systems.

Sensorless  $V/f$  or  $I/f$  control techniques are suitable for IPM motor drives where high dynamic performances are not required. Some researchers have proposed sensorless  $V/f$  controllers for permanent magnet motor drives without shaft sensors [21]-[23]. A stable  $V/f$  controller has been proposed by Perera et. al. for permanent magnet motors without any squirrel cage or damper windings [22]. Their proposed sensorless  $V/f$  can start an IPM motor from standstill by modulating the applied frequency to stabilize the rotor hunting at the command frequency.

Stellas et. al. have proposed a sensorless control technique for submersible permanent magnet motor drives fed over a long subsea cable and a load side transformer [23]. They have used a close loop  $V/f$  controller similar to [22] to start the submersible drive from arbitrary starting positions. In their paper, the control technique for the submersible motor drive has been switched to a sensorless vector control technique at a certain speed. Although their proposed  $V/f$  algorithm can start a submersible IPM motor drive from stand-still, it does not use any information from the position estimator. Thus, it is vulnerable to instability due to any dynamic change in the motor drive during the transition to a vector control technique. Also, their sensorless vector control technique uses a linear observer that does not account for the effects of magnetic saliency and cross couplings. Thus, it is inapplicable for IPM motors.

This chapter introduces a novel sensorless control strategy for submersible interior permanent magnet (IPM) motor drives. The design of a prototype submersible IPM motor is presented in this chapter. The performance of the designed motor is investigated using

finite element simulations. A non-linear sliding mode observer (SMO) based equivalent back-emf estimation algorithm is developed to determine the rotor position. An adaptive low pass filter is designed to reduce the chattering caused by the SMO. A novel sensorless  $V/f$  controller coupled with the back-emf estimation algorithm is designed for starting the motor drive. The proposed controller applies both voltage and frequency stabilization loops to run the ESP at a low speed. A sensorless vector controller is developed to run the ESP at the command frequency. A transition algorithm is used to switch from the sensorless  $V/f$  controller to the sensorless vector controller without any significant mechanical vibration. The proposed method is validated using extensive simulations for various case scenarios. Pertinent simulation results are presented in this chapter.

## **9.2 Submersible IPM Motor Drive**

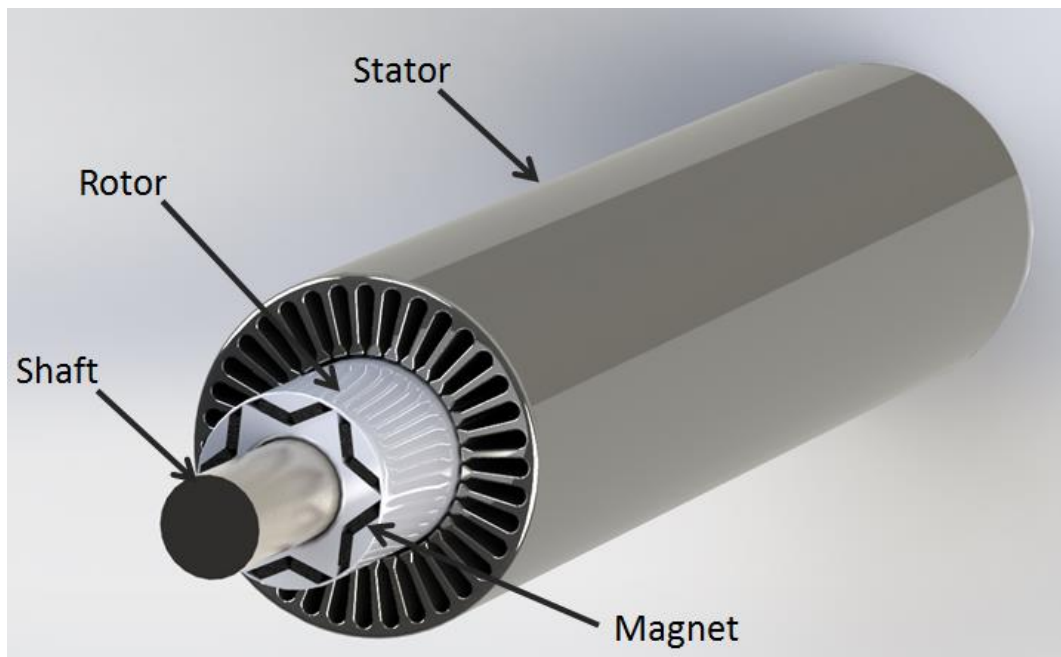
Submersible motors operate in a hostile environment and experience severe temperature, high pressure and the presence of debris. The diameter of an ESP motor is restricted by the outside diameter of the casing which is between 4 and 10 inches [3]. Submersible motors in ESPs are modular in nature and comprised of multiple rotors. The multi-rotor assembly is supported by intermediate bearings between consecutive rotors. Submersible induction motors have been the de-facto standard for ESPs. There are two types of most widely used submersible induction motors: IM5 and IM10 [3]-[4]. Brushless permanent magnet motors (PMMs) have been recently introduced in the market [2]-[3]. The relative comparison between these three types of motors is provided in table 3.1. Each of the rotors in IM5, IM10 and PMM are rated

as 5-HP, 10-HP and 22-HP, respectively. During field tests, the PMM indicates better efficiency, higher reliability, wider operating range, lower heat generation and superior performance than IM5 and IM10 [3]. However, the PMM is not a self-starting type of motor. It has trapezoidal windings in the stator and operates as a sensorless brushless dc motor using electronic commutation of the excitation to the stator windings [3]-[4]. Due to a fixed set of commutation steps with a constant interval angle, it suffers from significant torque ripples and total harmonics distortion. Also, the control system for a brushless dc motor is slow and does not provide high dynamic responses [26]. Thus, it reduces the reliability of an ESP system against any dynamic changes in the operating condition. Furthermore, the IM5, IM10 and PMM are designed to fit inside a 6-inch casing and are expensive when used for offshore oil and gas recovery.

Table 9.1. Relative comparison between different types of submersible motors.

<b>Properties</b>	<b>IM5</b>	<b>IM10</b>	<b>PMM</b>
Power/rotor (HP)	5	100	22
Input Voltage (kV)	2.4	2.4	2.4
Number of Poles	2	2	4
Stator Outside Diameter (inches)	4.56	4.56	4.62
Rotor Outside Diameter (inches)	2.27	2.21	2.64
Rotor Length (inches)	13	13.9	13.5

Figure 9.1a illustrates a prototype low voltage submersible IPM motor. The cross section of its rotor is depicted in Figure 9.1b. The motor is designed using the same frame size of a 5-HP Franklin submersible oil stripper induction motor that fits inside a 4-inch casing. The outer diameter of the motor is 3.75 inches and the stack length is 25.68 inches. The motor is rated at 3-phase, 6-pole, 460V, 3600 rpm. Each rotor of the motor is rated at 10-HP.



(a)

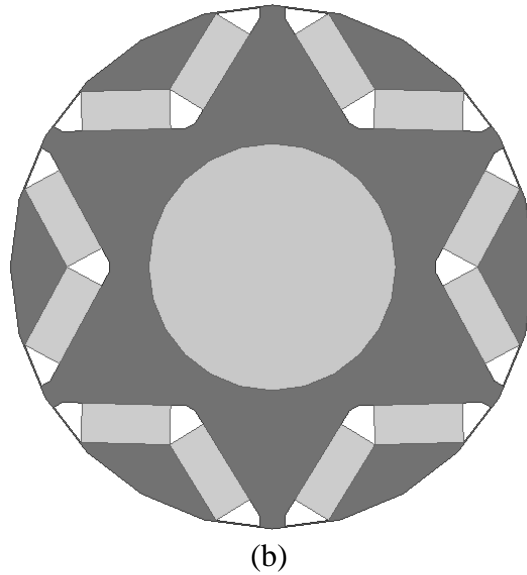


Figure 9.1. Submersible IPM motor: (a) assembly and (b) rotor cross section.

Figure 9.2 shows the performance of the IPM-ESP motor. The maximum efficiency and power factor maps of the motor with one IPM rotor are displayed in Figures 9.2a and 9.2b, respectively. The motor is capable to operate with a high efficiency ( $>90\%$ ) over the entire operating speed range. The efficiency reaches to its peak when the motor is operated at a speed over 2400rpm with a load torque between 50% of the rated torque and rated torque. The motor can operate at the constant torque mode with a rotor speed up to 3600 rpm. It operates in the constant power mode when the rotor speed becomes higher than 3600 rpm. These operating zones are defined in Figure 9.2b with black border lines. The power factor becomes high ( $>0.95$ ) when the motor is operated at a command frequency higher than 60 Hz. The power factor remains high over a wide range of the load torque. Thus, the designed IPM submersible motor can be driven efficiently with a high power factor for ESP systems if it is controlled precisely to operate within the preferred operating zones.

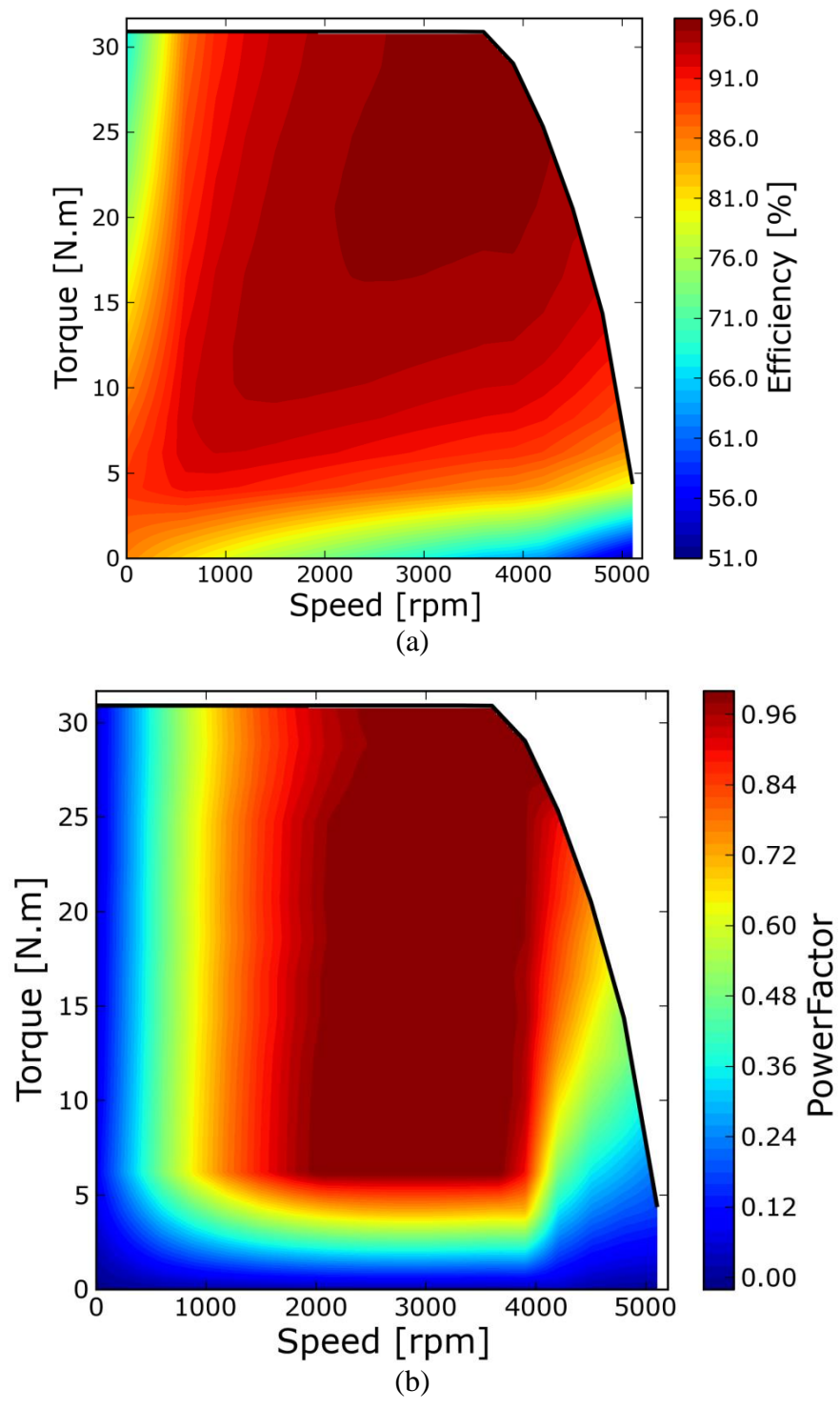


Figure 9.2. Performance of the submersible IPM motor: (a) efficiency and (b) power factor.

The detailed specifications of this motor are provided in table 9.2. A comparison between the Franklin motor and the designed IPM submersible motor is provided in table 9.3. The IPM motor has higher power and torque density than the Franklin motor. Thus, replacing the Franklin induction submersible motor by the proposed submersible IPM motor will reduce the overall length of the ESP by half, making it viable for wells where the length is a restricting factor such as deviated or horizontal wells.

Table 9.2. Specification of the 10-HP submersible IPM motor.

<b>Symbol</b>	<b>Name</b>	<b>Value</b>
$N_p$	number of phases	3
$p$	number of pole pairs	3
$I_{rated}$	rated line current	15 A
$f_{rated}$	rated frequency	180 Hz
$P_{rated}$	rated power	10 HP
$T_{rated}$	rated torque	20 N. m.
$V_{rated}$	rated voltage (L-L)	460 V
$L_{qs}$	$q$ -axis inductance	0.008H
$L_{ds}$	$d$ -axis inductance	0.0048 H
$r_s$	stator resistance/phase	0.417 $\Omega$
$J$	Total inertia	0.02 Kg. m <sup>2</sup>
$D_m$	rotor damping constant	0.001 (N.m.)/rad./sec.
$\lambda_m$	magnet flux linkage	0.2706 volts/rad./sec.

Table 9.3. Comparison between a Franklin submersible motor and the IPM motor.

Motor Specifications	Franklin Submersible Oil Stripper Induction Motor	Submersible IPM Motor
Phase Type	3-phase	3-phase
Outside Diameter	3.75 inches	3.75 inches
Overall Length	25.68 inches	25.68 inches
Number of Poles	2-poles	6-poles
Rated Voltage	460 V	460 V
Rated Speed	3600 rpm	3600 rpm
Rated Power	5 HP (3.7 kW)	10 HP (7.5 kW)

### 9.3 Sensorless Control of IPM-ESP Drives

Electric submersible pump (ESP) motors are subjected to severe mechanical vibrations due to their unique construction. Also, the presence of gas and solids creates time varying transients in the downhole system. The price of an ESP system is only a small fraction of the total operating cost. ESP failures may result in a long downtime for the plant. The cost to replace and/or repair an ESP unit can run into millions of dollars, especially for offshore installations. Thus, the design of the control system for IPM motor driven ESPs must exhibit a high level of dynamic response, and should be extremely reliable. In order to meet these demands, the sensorless control strategy for submersible IPM drives is divided into the following sections:

- Develop a rotor position sensing algorithm using the motor back-emf,

- implement a sensorless start-up  $V/f$  controller to run the IPM-ESP system at a low speed,
- design a transition algorithm to switch the controller smoothly from the  $V/f$  to vector control technique, and
- create a ramp-up procedure for the ESP drive towards a command speed using a sensorless vector controller.

Figure 9.3 displays the flowchart of the sensorless control technique for IPM-ESP drives. The IPM-ESP drive is started using a sensorless  $V/f$  controller that uses the estimated position of the motor. The  $V/f$  uses estimated  $d-q$  axes currents of the motor and the estimated active power to provide active damping to the system for avoiding any significant torsional vibration. The rotor stabilization is checked with the on-line hunting diagnostic algorithm presented in chapter 8. The hunting diagnostic algorithm monitors the degree of rotor stabilization using the stator current signal. After successful stabilization of the rotor, the diagnostic algorithm provides a command signal to switch the controller from a sensorless  $V/f$  technique to a sensorless vector control technique for improving the dynamic performance and efficiency of the IPM-ESP drive system. The vector controller can be operated at either unity power factor mode or maximum torque per ampere (MTPA) mode. The MTPA mode of operation improves the efficiency of the IPM motor, maximizes its capability to produce high output torque and makes it viable for wide-speed operations.

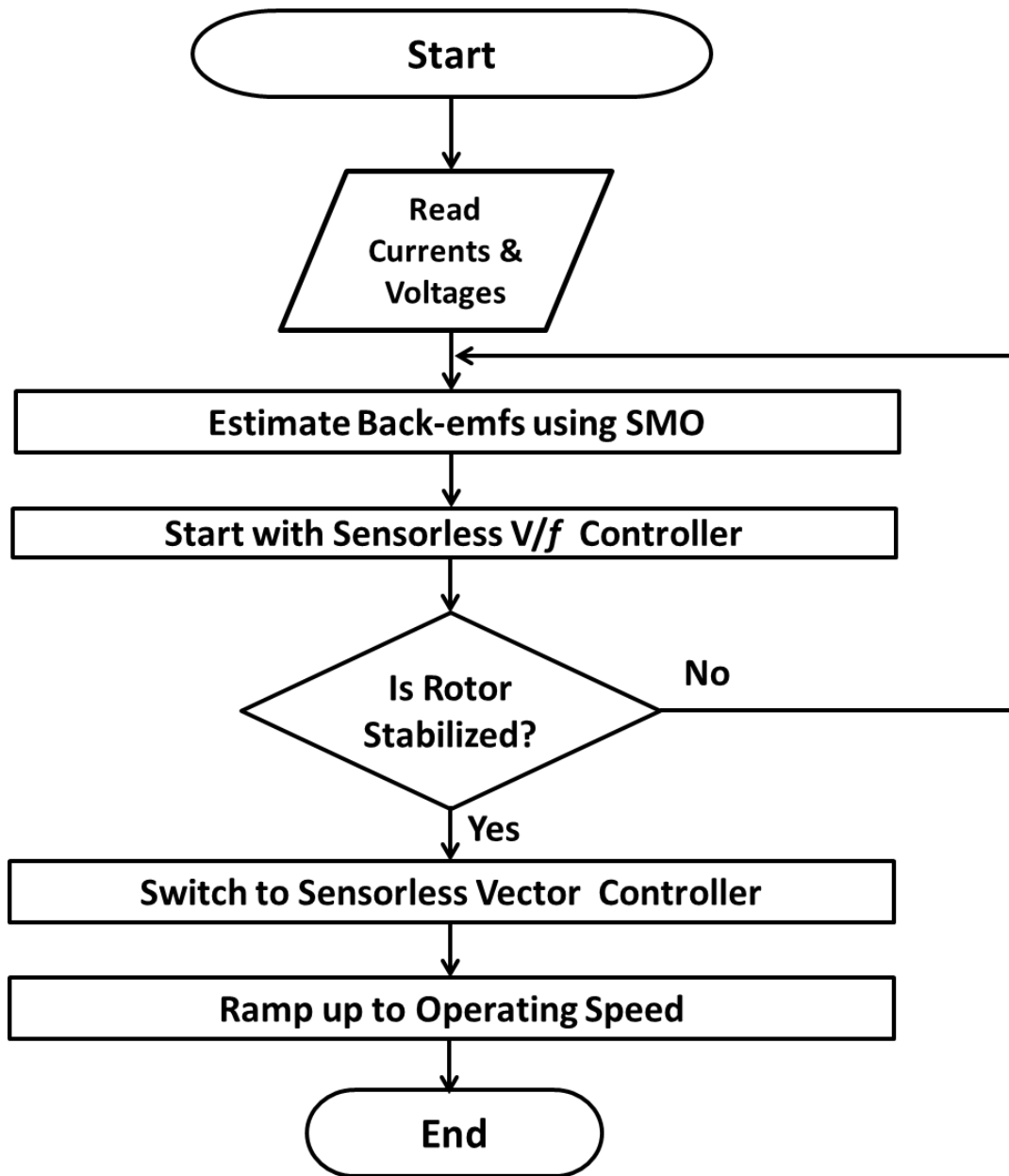


Figure 9.3. Flowchart of the sensorless controller for IPM-ESP drives.

### 9.3.1 Estimation of the Rotor Position Using Motor Back-Emfs

The  $d$ - $q$  axis model of an interior permanent magnet motor can be expressed as [26],

$$\frac{di_{dq}}{dt} = Ai_{dq} + B(v_{dq} - e_{dq}) \quad (9.1)$$

where,

$$i_{dq} = \begin{bmatrix} i_{ds} \\ i_{qs} \end{bmatrix}, v_{dq} = \begin{bmatrix} v_{ds} \\ v_{qs} \end{bmatrix}, e_{dq} = \begin{bmatrix} e_{ds} \\ e_{qs} \end{bmatrix} \quad (9.2)$$

$$A = \begin{bmatrix} -\frac{R_s}{L_{ds}} & \frac{\omega_{re}L_{qs}}{L_{ds}} \\ -\frac{\omega_{re}L_{ds}}{L_{qs}} & -\frac{R_s}{L_{qs}} \end{bmatrix}, B = \begin{bmatrix} \frac{1}{L_{ds}} & 0 \\ 0 & \frac{1}{L_{qs}} \end{bmatrix} \quad (9.3)$$

$i_{dq}$  are the currents in ( $d - q$ ) axes with respect to rotor reference frame,  $v_{dq}$  are the input voltages in the ( $d - q$ ) reference frame,  $e_{dq}$  are the back-emfs,  $R_s$  is the stator phase resistance,  $L_{ds}$  and  $L_{qs}$  are the motor inductances in the ( $d - q$ ) reference frame, and  $\omega_{re}$  is the rotor electrical angular frequency.

An IPM motor has high magnetic saliency which results in significant cross-coupling effects. Thus, the back-emfs in an IPM motor can be expressed as a function of motor saliency and the permanent magnet excitation. Expressing back-emfs as a function of saliency, (9.1)-(9.3) can be represented in the following forms [14]-[15],

$$\frac{di_{dq}}{dt} = \begin{bmatrix} -\frac{R_s}{L_{ds}} & \frac{\omega_{re}L_{qs}}{L_{ds}} \\ -\frac{\omega_{re}L_{ds}}{L_{qs}} & -\frac{R_s}{L_{qs}} \end{bmatrix} \begin{bmatrix} i_{ds} \\ i_{qs} \end{bmatrix} + \begin{bmatrix} \frac{1}{L_{ds}} & 0 \\ 0 & \frac{1}{L_{qs}} \end{bmatrix} \begin{bmatrix} v_{ds} - e_{ds} \\ v_{qs} - e_{qs} \end{bmatrix} \quad (9.4)$$

$$e_{dq} = \begin{bmatrix} e_{ds} \\ e_{qs} \end{bmatrix} = \begin{bmatrix} 0 \\ \omega_{re} [(L_{ds} - L_{qs})i_{ds} + \lambda_m] - (L_{ds} - L_{qs}) \frac{di_{qs}}{dt} \end{bmatrix} \quad (9.5)$$

where  $\lambda_m$  is the flux linkage due to permanent magnet excitation and  $e_{dq}$  are the extended back-emfs.

The proposed sensorless control technique estimates back-emfs of the IPM motor in the alpha-beta ( $\alpha - \beta$ ) reference frame. The model of an IPM motor in (9.5) is converted into the ( $\alpha - \beta$ ) frame using the following equation [14],

$$\frac{di_{\alpha\beta}}{dt} = A_{ext}i_{\alpha\beta} + B_{ext}(v_{\alpha\beta} - e_{\alpha\beta}^{ext}) \quad (9.6)$$

where,

$$i_{\alpha\beta} = \begin{bmatrix} i_{\alpha} \\ i_{\beta} \end{bmatrix}, v_{\alpha\beta} = \begin{bmatrix} v_{\alpha} \\ v_{\beta} \end{bmatrix}, e_{\alpha\beta}^{ext} = \begin{bmatrix} e_{\alpha}^{ext} \\ e_{\beta}^{ext} \end{bmatrix} \quad (9.7)$$

$$A_{ext} = \begin{bmatrix} -\frac{R_s}{L_{ds}} & -(1 - \zeta)\omega_{re} \\ (1 - \zeta)\omega_{re} & -\frac{R_s}{L_{ds}} \end{bmatrix}, \quad B_{ext} = \begin{bmatrix} \frac{1}{L_{ds}} & 0 \\ 0 & \frac{1}{L_{ds}} \end{bmatrix} \quad (9.8)$$

where  $i_{\alpha\beta}$  are the currents in the ( $\alpha - \beta$ ) reference frame,  $v_{\alpha\beta}$  are the input voltages in the ( $\alpha - \beta$ ) reference frame,  $e_{\alpha\beta}^{ext}$  are the extended back-emfs and  $\zeta = \frac{L_{qs}}{L_{ds}}$  is the saliency ratio.

Sensorless control of an IPM motor using its extended back-emfs requires the knowledge of the instantaneous rotor angular speed. Thus, it is sensitive to speed transients. In order to remove the speed dependency from the back-emf estimation

algorithm, the equivalent emf can be used instead of the extended emf to model the dynamics of an IPM motor [24]. The equivalent emf based model of an IPM motor in the  $(\alpha - \beta)$  reference frame is given below [24],

$$\frac{di_{\alpha\beta}}{dt} = A'i_{\alpha\beta} + B'(v_{\alpha\beta} - e'_{\alpha\beta}) \quad (9.9)$$

where

$$A' = \begin{bmatrix} -\frac{R_s}{L_{qs}} & 0 \\ 0 & -\frac{R_s}{L_{qs}} \end{bmatrix}, B' = \begin{bmatrix} \frac{1}{L_{qs}} & 0 \\ 0 & \frac{1}{L_{qs}} \end{bmatrix}, e'_{\alpha\beta} = \begin{bmatrix} e_{\alpha'} \\ e_{\beta'} \end{bmatrix} \quad (9.10)$$

Equivalent back-emfs in the  $(\alpha - \beta)$  reference frame are related with the motor actual emf based on the following relationship [24],

$$e_{\alpha'} = -[(2L_1)i_{ds}\omega_{re} + E] \sin \theta_{re} \quad (9.11)$$

$$e_{\beta'} = [(2L_1)i_{ds}\omega_{re} + E] \cos \theta_{re} \quad (9.12)$$

where  $\omega_{re} = \omega_{re} \lambda_m$ ,  $\theta_{re}$  is the rotor electrical angular position and,

$$L_1 = \frac{L_{ds} - L_{qs}}{2} \quad (9.13)$$

A non-linear sliding mode observer is designed to estimate the motor back-emfs of an IPM motor from its equivalent model presented in (9.9)-(9.13). These estimated back-emfs are used to calculate the rotor position  $\theta_{re}$ .

Figure 9.4 presents the overall block diagram of the back-emf estimation algorithm. The non-linear sliding mode observer for estimating the rotor position can be expressed as [28]-[29],

$$\frac{d\widehat{i}_{\alpha\beta}}{dx} = A\widehat{i}_{\alpha\beta} + Bv_{\alpha\beta} - e_{\alpha\beta}^{con} \quad (9.14)$$

$$e_{\alpha\beta}^{con} = \begin{bmatrix} e_{\alpha}^{con} \\ e_{\beta}^{con} \end{bmatrix} = \begin{bmatrix} k * \text{sgn}(\widehat{i}_{\alpha} - i_{\alpha}) \\ k * \text{sgn}(\widehat{i}_{\beta} - i_{\beta}) \end{bmatrix} \quad (9.15)$$

where  $\widehat{i}_{\alpha\beta}$  are estimated currents in the  $(\alpha - \beta)$  reference frame,  $e_{\alpha\beta}^{con}$  are the control signals obtained using the sliding mode controller,  $k$  is switching gain which is chosen as sufficiently high for the observer stability. The detailed proof of the SMO stability is provided in the appendix.

The equivalent emfs  $e_{\alpha\beta}'$  are obtained by performing low pass filtering operations on the discontinuous control signals  $e_{\alpha\beta}^{con}$ .  $e_{\alpha\beta}'$  can be obtained using the following expression,

$$e_{\alpha\beta}' = \frac{\omega_c^2}{s^2 + 2\xi\omega_c s + \omega_c^2} e_{\alpha\beta}^{con} \quad (9.16)$$

where  $\omega_c$  is the cut-off frequency and  $\xi$  is the damping ratio.  $\omega_c$  is varied adaptively with the command frequency and  $\xi$  is chosen judiciously for minimizing the phase lag in the system.

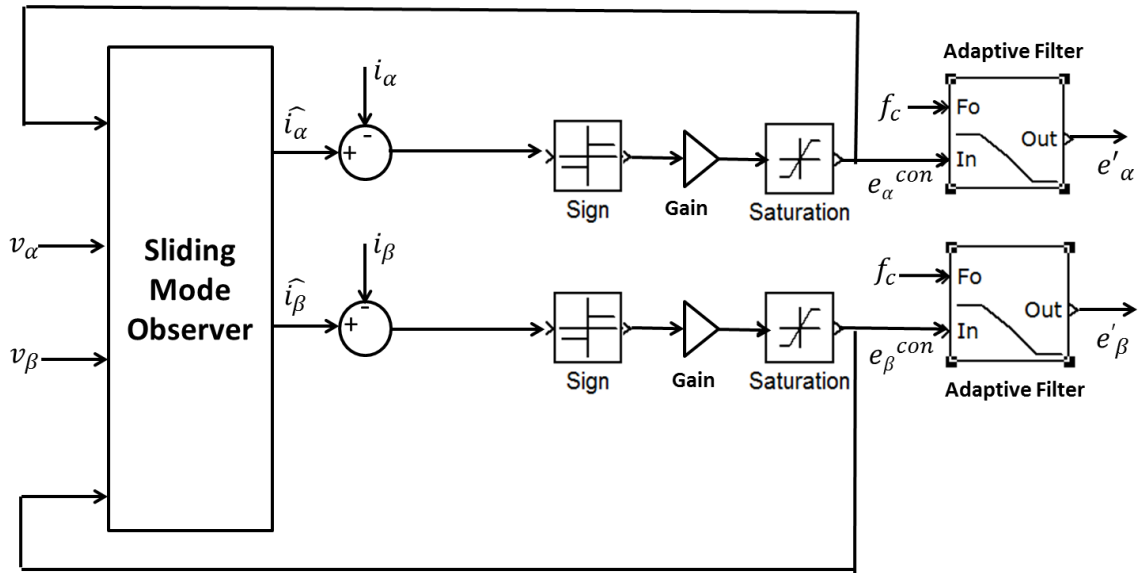


Figure 9.4. Block diagram of the back-emf estimation algorithm.

The rotor position and speed can be calculated using the following equation:

$$\theta_{re}^{est} = -\arctan\left(\frac{e_{\alpha}'}{e_{\beta}'}\right) + \theta_{com} \quad (9.17)$$

$$\omega_{re}^{est} = \frac{d\theta_{re}^{est}}{dt} \quad (9.18)$$

where  $\theta_{re}^{est}$  is the estimated rotor electrical angular position and  $\theta_{com}$  is the phase compensation due to the phase delay incurred by the low pass filter.

Although the arctan calculation has no intrinsic phase lag, it is sensitive to signal to noise ratio. It can provide a significant rotor position estimation error when there is noise in the system. SMO suffers from an inherent chattering phenomenon and introduces noise in the system. Thus, applying the arctan operation on the extended back-emfs obtained from the SMO for estimating the dynamic rotor position can create significant chattering

in the estimated rotor position. Also, the differentiation operation for obtaining the motor speed can cause singularity phenomena during implementation.

In order to avoid the chattering and singularity phenomena, an observer is applied to calculate the rotor electrical speed and position using  $e'_{\alpha\beta}$ . The equivalent emfs can be expressed as,

$$e_{\alpha}' = -E_{sal} \sin \theta_{re} - \omega_{re} \lambda_m \sin \theta_{re} \quad (9.19)$$

$$e_{\beta}' = E_{sal} \cos \theta_{re} + \omega_{re} \lambda_m \cos \theta_{re} \quad (9.20)$$

where  $E_{sal} = (2L_1)i_d\omega_{re}$ .

Assuming  $E_{sal} \ll \omega_{re}\lambda_m$ , the extended back-emfs can be expressed as,

$$e_{\alpha}' = -\omega_{re}\lambda_m \sin \theta_{re} \quad (9.21)$$

$$e_{\beta}' = \omega_{re}\lambda_m \cos \theta_{re} \quad (9.22)$$

Using (9.20) and (9.21), an observer similar to [8] can be used to calculate the rotor electrical position and speed. The observer also avoids the differentiation operation of the rotor position for obtaining the motor speed as it creates singularity phenomena during implementation. It can be formulated as [8],

$$\frac{d\widehat{e}_{\alpha}}{dx} = -\widehat{\omega}_{re}\widehat{e}_{\beta} - l(\widehat{e}_{\alpha} - e_{\alpha}') \quad (9.23)$$

$$\frac{d\widehat{e}_{\beta}}{dx} = \widehat{\omega}_{re}\widehat{e}_{\alpha} - l(\widehat{e}_{\beta} - e_{\beta}') \quad (9.24)$$

$$\frac{d\widehat{\omega}_{re}}{dx} = (\widehat{e}_{\alpha} - e_{\alpha}')\widehat{e}_{\beta} - \widehat{e}_{\alpha}(\widehat{e}_{\beta} - e_{\beta}') \quad (9.25)$$

$$\theta_{re}^{est} = -\arctan\left(\frac{\widehat{e}_{\alpha}}{\widehat{e}_{\beta}}\right) \quad (9.26)$$

where  $\widehat{e}_\alpha$ ,  $\widehat{e}_\beta$  and  $\widehat{\omega}_{re}$  are the estimated back-emfs in the  $\alpha$ - $\beta$  reference frame and rotor electrical speed, respectively and  $l$  is the observer gain. The magnitude of  $l$  is less than  $k$  but sufficiently high to gain fast convergence.

### 9.3.2 Sensorless $V/f$ Controller for Starting an IPM-ESP Drive

Figure 9.5 presents a block-diagram of the designed sensorless  $V/f$  controller. The controller consists of double stabilization loops. The first loop calculates the command voltage for the motor drive using the line current feedbacks from the current sensors and the estimated back-emfs from the observer. It also performs the voltage stabilization using the current feedbacks and compensates for voltage drops in the line resistance [22]. As the load torque for ESPs varies with the speed, the stabilizing loop changes the command voltage dynamically. The equations for the voltage stabilizing loop are expressed as,

$$V_s^* = i_q^e R_s + \sqrt{(E_0)^2 + (i_q^e)^2 R_s^2 - I_s^2 R_s^2} \quad (9.27)$$

$$i_q^e = \frac{2}{3} \left\{ i_a \cos \theta_{re}^{est} + i_b \cos \left( \theta_{re}^{est} - \frac{2\pi}{3} \right) + i_c \cos \left( \theta_{re}^{est} + \frac{2\pi}{3} \right) \right\} \quad (9.28)$$

$$I_s = \sqrt{(i_\alpha)^2 + (i_\beta)^2} \quad (9.29)$$

$$E_0 = \widehat{\omega}_{re} \lambda_m \quad (9.30)$$

where  $V_s^*$  is the command voltage,  $E_0$  is the estimated back-emf and  $i_q^e$  is the estimated  $q$ -axis current.

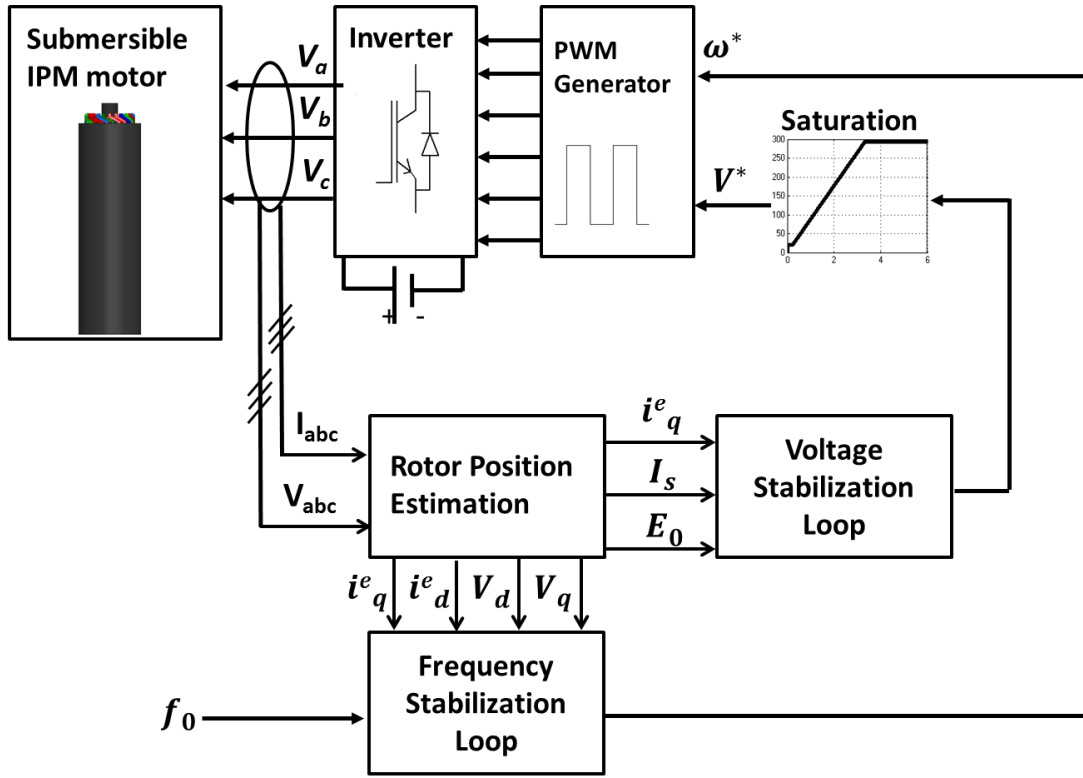


Figure 9.5. Sensorless  $V/f$  control algorithm for starting the IPM-ESP drive.

The second stabilizing loop is needed for variable speed IPM motors incapable of self-starting. This loop works to modulate the applied frequency to the motor drive in order to prohibit the rotor from losing the synchronism with the stator field. The frequency stabilizing loop provides the necessary damping to the motor by active power perturbation [22]. The equations for the frequency stabilizing loops are given below:

$$P = \frac{3}{2} (V_d i_d^e + V_q i_q^e) = P_0 + \Delta P \quad (9.31)$$

$$\Delta P = \frac{3}{2} \Delta V_d i_d^0 + \frac{3}{2} V_d^0 \Delta i_d + \frac{3}{2} \Delta V_q i_q^0 + \frac{3}{2} V_q^0 \Delta i_q \quad (9.32)$$

$$\Delta\omega_e = -k_\omega\Delta P; k_\omega = \frac{k_p}{\omega_0}; \omega_0 = 2\pi f_0 \quad (9.33)$$

$$\omega^* = \omega_0 + \Delta\omega_e \quad (9.34)$$

where  $P$  is the active power,  $i_d^e$  and  $i_q^e$  are the estimated  $d$ - $q$  axes currents, respectively,  $V_d$  and  $V_q$  are  $d$ - $q$  axes command voltages, respectively,  $\Delta P$  is the perturbed active power obtained using a high-pass filter,  $\Delta\omega_e$  is the frequency damping coefficient and  $\omega^*$  is the command angular frequency.

### 9.3.3 Sensorless Vector Controller for IPM-ESP Drives

Figure 9.6 illustrates a block diagram of the developed sensorless vector control technique for a submersible IPM-ESP drive system. Decoupled PI-controllers are used to generate the reference  $d$ - $q$  axes voltages to the 6-pulse PWM generator. The simplified  $d$ -axis current loop is presented in Figure 9.7. The  $i_{d,ref}$  is considered zero for unity power factor operation of the IPM motor.  $K_{id}$  and  $T_{id}$  are the proportional gain and integral time constant of the  $d$ -axis current PI controller, respectively.  $L_d$  is the  $d$ -axis motor inductance and, motor  $d$ -axis times constants can be expressed as [26],

$$K_{md} = \frac{1}{R_s}, T_{md} = \frac{L_d}{R_s} \quad (9.35)$$

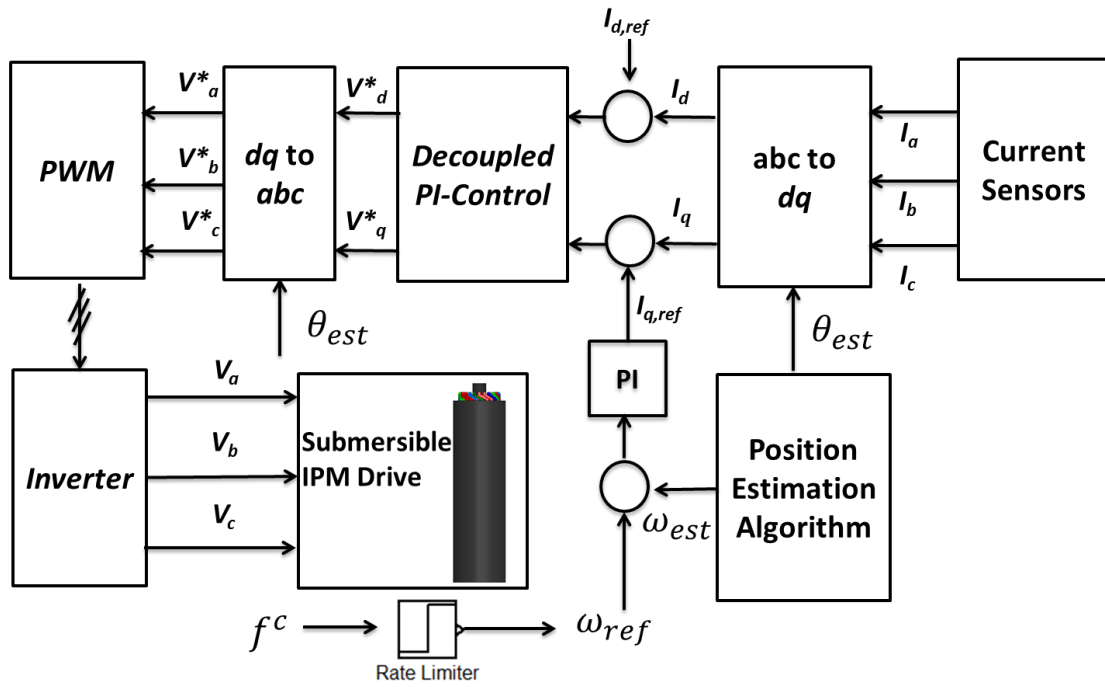


Figure 9.6. Sensorless vector control technique for the IPM-ESP drive.

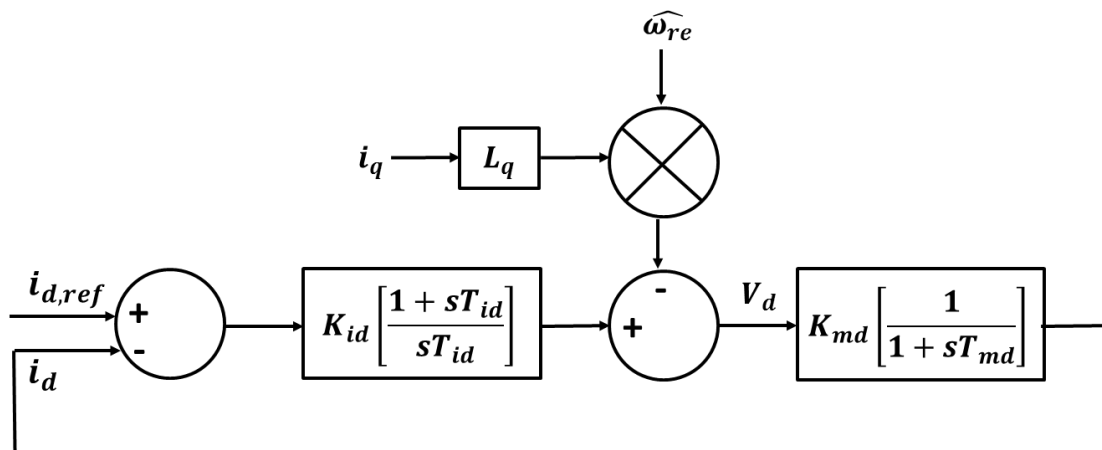


Figure 9.7. The simplified  $d$ -axis current controller.

Figure 9.8 illustrates the simplified speed and  $q$ -axis current loops. The reference  $q$ -axis current  $i_{q,ref}$  is calculated from the speed controller.  $K_{i\omega}, K_{iq}$  and  $T_{i\omega}, T_{iq}$  are the proportional gains and integral time constants of the speed PI controller and  $q$ -axis current PI controller, respectively.  $L_d$  is the  $d$ -axis motor inductance and motor  $q$ -axis times constants are given by [26],

$$K_{mq} = \frac{1}{R_s}, T_{mq} = \frac{L_q}{R_s} \quad (9.36)$$

The  $q$ -axis reference current is obtained from the PI speed controller. The  $d$ -axis current is calculated from the maximum torque per amp (MTPA)-trajectory of an IPM motor, as shown in Figure 9.9.

The  $d$ -axis reference current for the MTPA control can be expressed as [27],

$$i_{d,ref} = \frac{\lambda_m}{2(L_{ds} - L_{qs})} - \sqrt{\frac{\lambda_m^2}{4(L_{qs} - L_{ds})^2} + i_{q,ref}^2} \quad (9.37)$$

$$I_{ref} = \sqrt{i_{d,ref}^2 + i_{q,ref}^2} \quad (9.38)$$

where  $I_{ref}$  is the reference stator phase current to follow the MTPA trajectory of the motor. The  $d$ - $q$  axis inductances and  $\lambda_m$  are obtained from the finite element simulation results using ANSYS Maxwell.

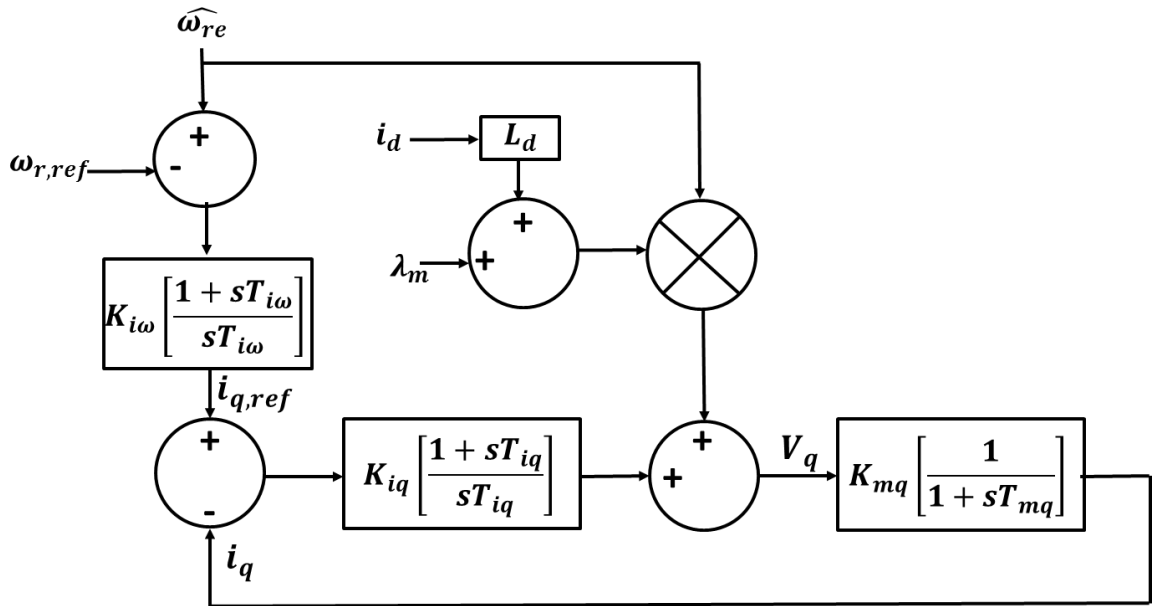


Figure 9.8. The simplified speed and  $q$ -axis current controllers.

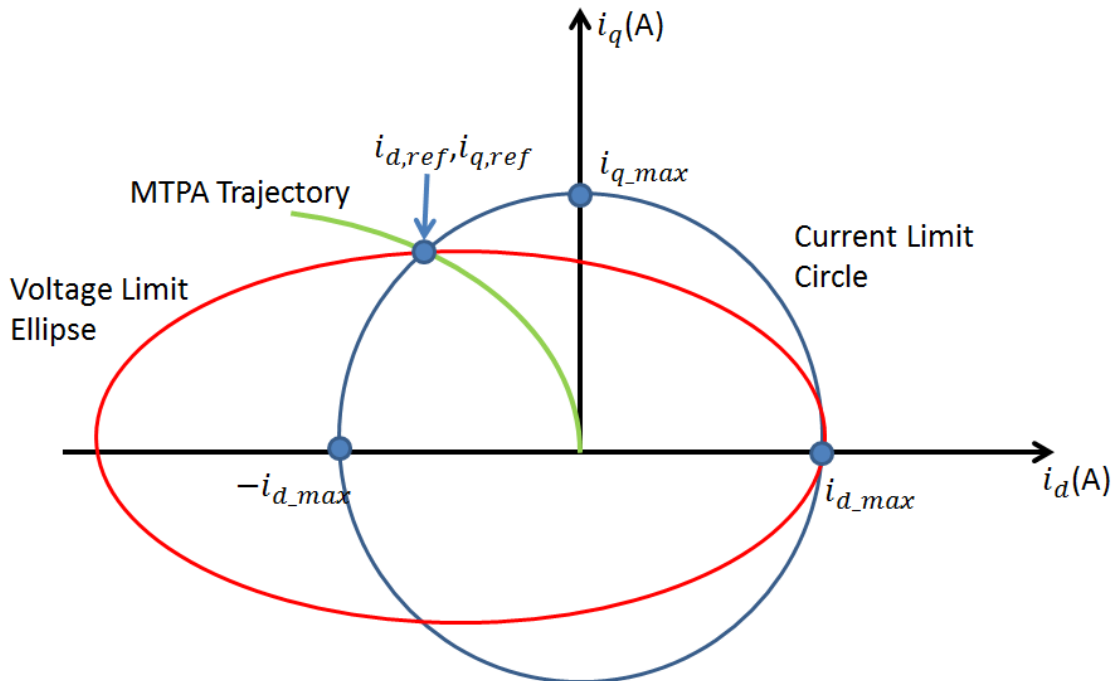


Figure 9.9. The MTPA trajectory for an IPM motor.

## 9.4 Simulation Results

The proposed sensorless control technique is simulated for a 3-phase, 6-pole, 460V, 10-HP IPM-ESP drive system. The parameters of the submersible IPM motor are obtained from finite element simulations using Ansys Maxwell. The ESP load is modelled using the characteristics curves of a standard 3-stage centrifugal pump as shown in chapter 5. The control system is implemented in the Matlab/Simulink environment. The dc-link voltage of the inverter is selected as 800V. The performance of the control system is tested for different command frequencies. The load torque for the motor induced by the ESP varies with the rotor speed. Figures 9.10a-9.10c illustrate the load torque behavior of the ESP system for different command frequencies. The command frequency is applied on the motor drive system gradually using a rate limiter in order to reduce torsional vibration in the system. The load torque for a ESP motor drive is low during start, making the  $V/f$  controller a feasible control strategy for starting of the motor. It becomes gradually higher with the rising speed of the motor drive, becoming steady when the applied frequency matches the command frequency.

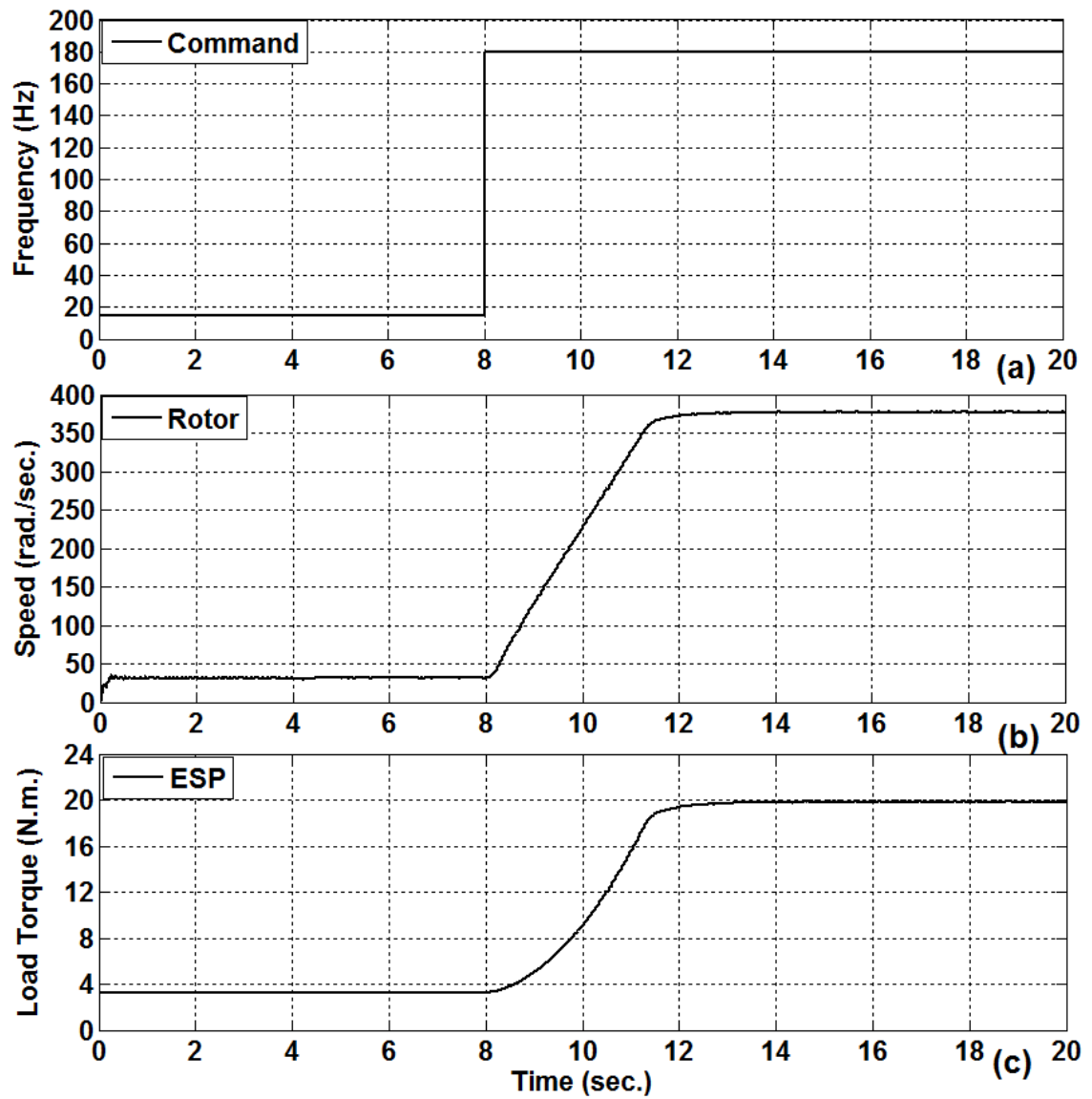


Figure 9.10. Variation of the ESP load torque with command frequency: (a) supply frequency, (b) speed and (c) ESP load torque.

The actual vs. estimated run-up responses of the IPM-ESP drive system using the sensorless control algorithm is presented in Figure 9.11. The ESP drive system is started at a command frequency of 15Hz using the sensorless  $V/f$  controller. The

control action is switched to sensorless vector control after the motor is stabilized at  $t = 4$ s. The operating frequency is changed to a command frequency of 180Hz at  $t = 8$ s. The motor ramps up smoothly; reaching the synchronous speed with no significant speed overshoot. The command frequency is changed to 90Hz at  $t = 15$ s in order to observe the performance of the control system for the speed reversal phenomenon. The control system is able to track the command frequency without any significant rotor vibration. The speed observer converges quickly and precisely estimates the rotor speed. There is a strict agreement between actual and estimated rotor speeds. The slight oscillations in the estimated speed are created by chattering because of the sliding mode observer (SMO).

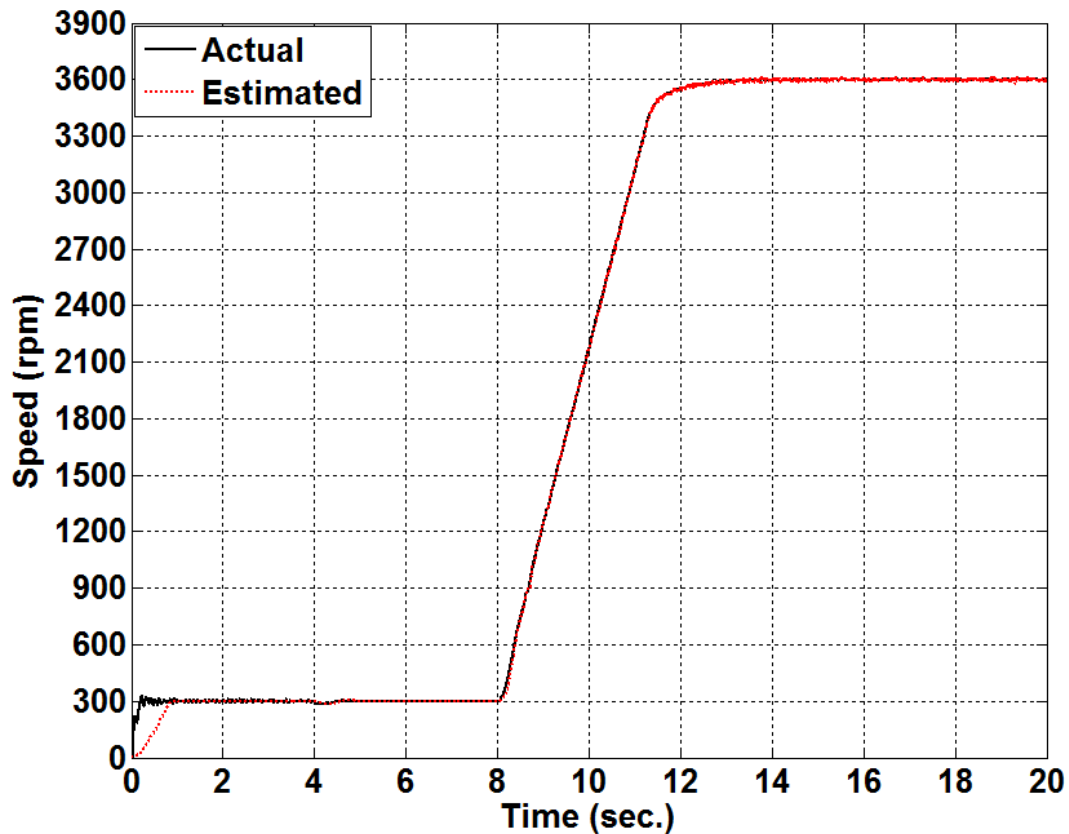


Figure 9.11. Actual vs estimated run-up responses of the IPM motor.

The actual and estimated rotor positions during low and high speed operations are depicted in Figures 9.12 and 9.13, respectively. The developed sensorless controller can accurately track the rotor position without any noticeable phase delay.

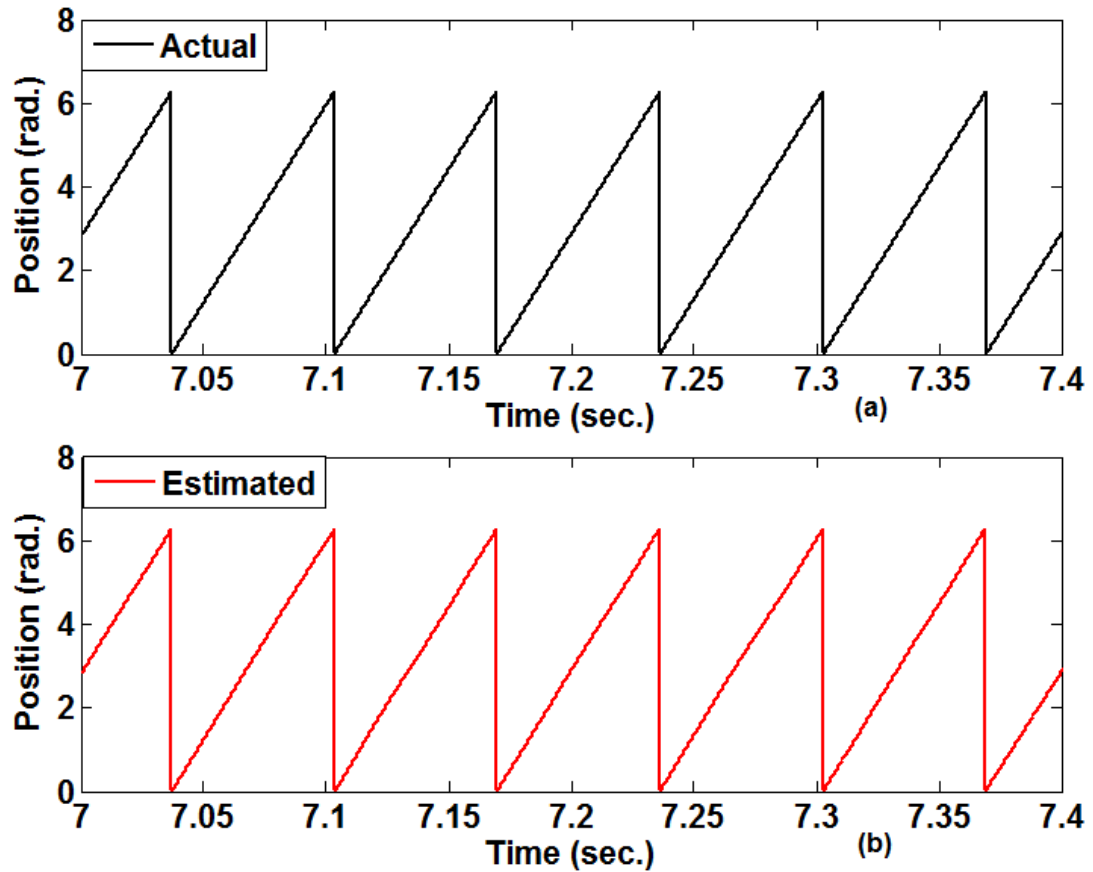


Figure 9.12. Actual vs estimated rotor position of the motor at low speed.

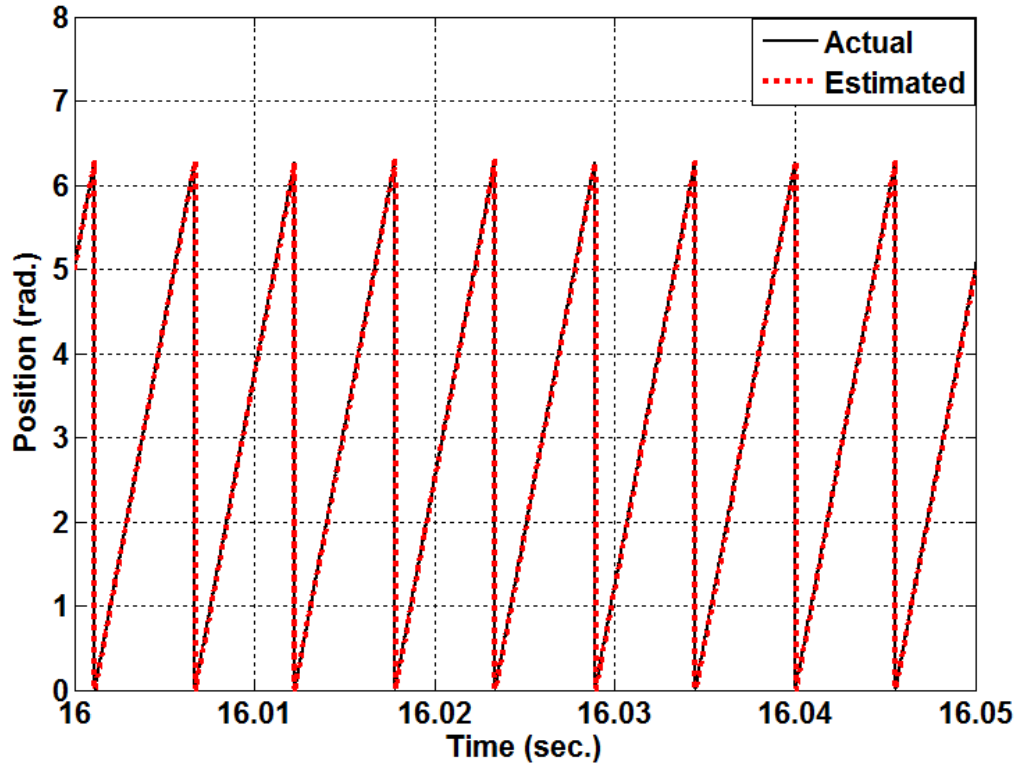
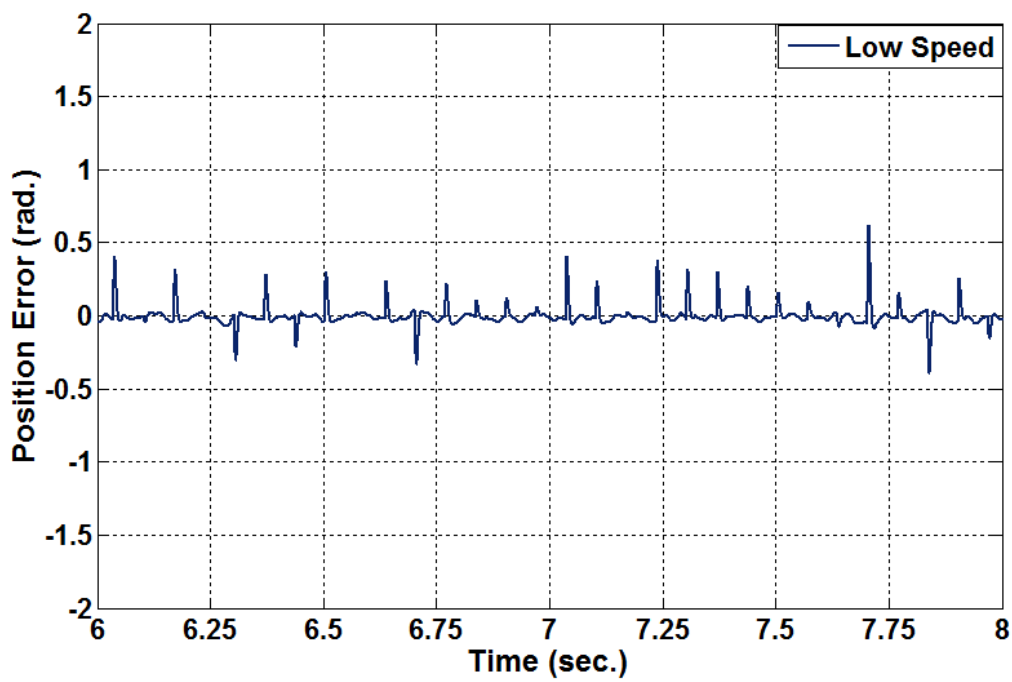
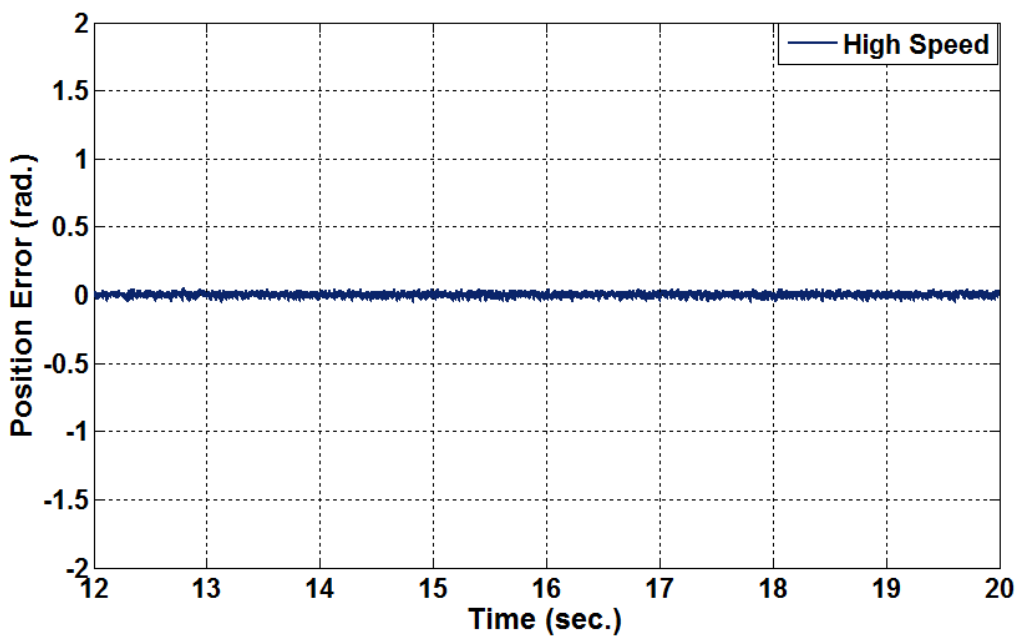


Figure 9.13. Actual vs estimated position of the rotor at a high speed.

The trajectories of the position error between actual and estimated values for low speed as well as high speed operations are illustrated in Figure 9.14a and 9.14b, respectively. There exist some oscillations in the error trajectory due to the chattering phenomenon caused by the discontinuous switching of the SMO. However, this has negligible effects on the overall performance of the system as the developed PI controllers can reject the disturbances.



(a)



(b)

Figure 9.14. Trajectory of the position error for: (a) low speed operation and (b) high speed operation.

The  $d$ - $q$  axis currents are illustrated in Figures 9.15a and 9.15b, respectively. The  $d$ - $q$  axis currents are regulated to generate the necessary torque for the motor in order to keep it synchronized with the ESP. These currents also provide active stabilization to the system for maintaining a smooth operation with low torsional vibration. The  $d$ -axis current is regulated dynamically for operating the ESP drive at its best efficiency point. There is a close agreement between actual and estimated  $d$ - $q$  axis currents that further validates the position sensing capability of the proposed control system.

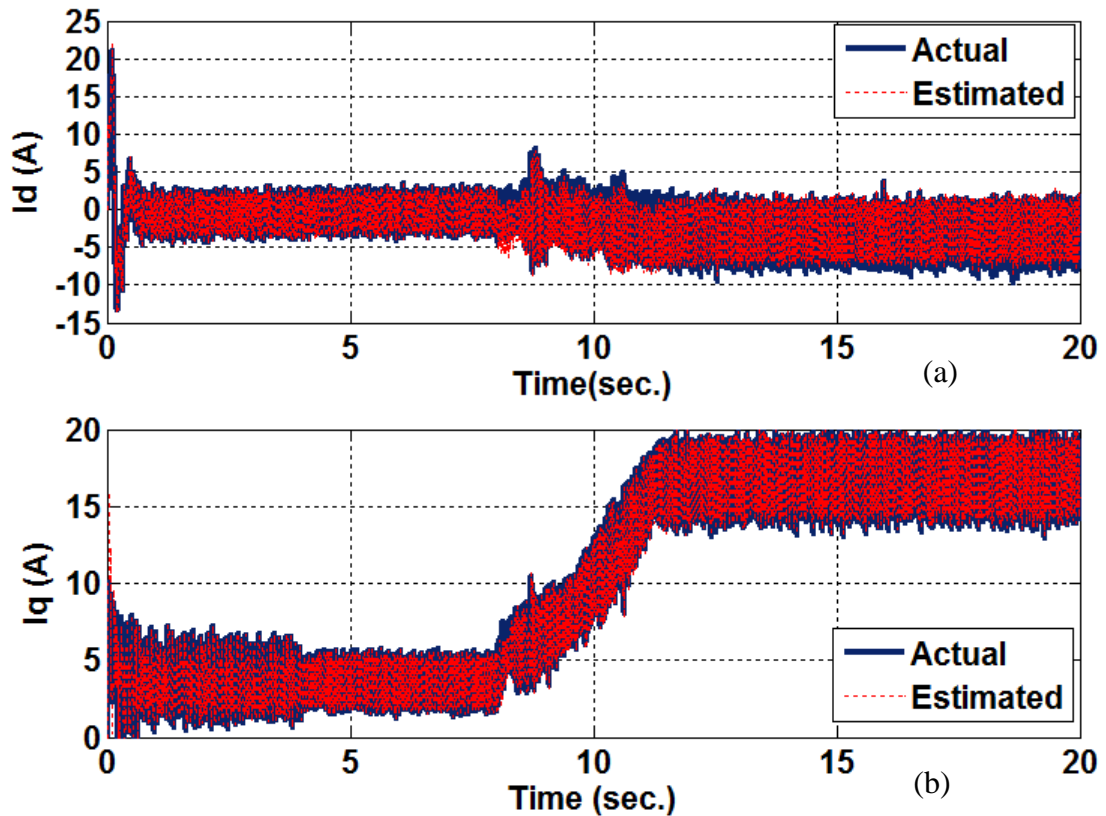


Figure 9.15. Actual vs. estimated currents: (a) d-axis and (b) q-axis.

The electromagnetic torque and the rms line current are depicted in Figures 9.16a and 9.16b, respectively. The electromagnetic torque increases as the rotor speed goes up and settles down to a steady state value when the motor attains synchronism. The torque and current oscillations are reduced when the control strategy is switched from the sensorless  $V/f$  controller to the sensorless vector controller.

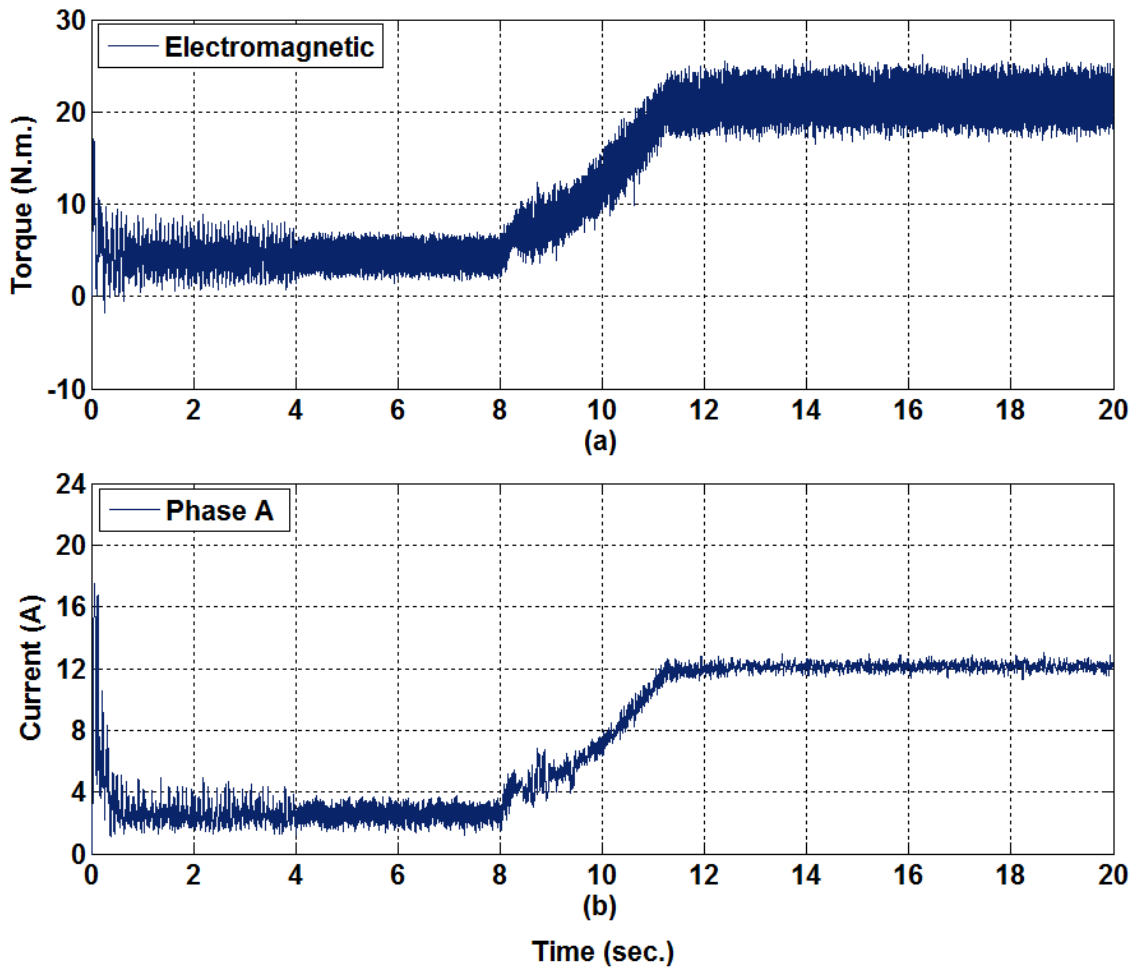


Figure 9.16. Responses of the motor: (a) torque and (b) line current.

The performance of the developed sensorless controller for a step change in the command frequency is demonstrated in Figure 9.17. The motor was operating at a command frequency of 180Hz using the standard sensorless vector controller. The command frequency is changed to 120Hz at  $t = 12$ s. The sensorless controller is able to smoothly track the command frequency, and is able to stabilize the rotor at the operating frequency.

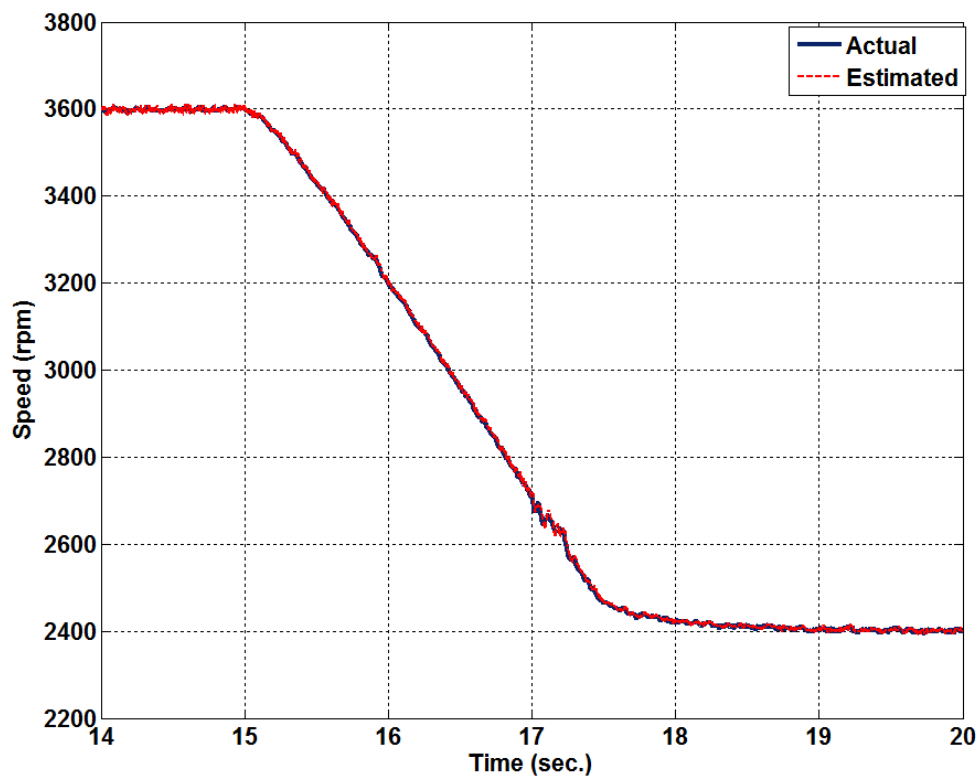


Figure 9.17. Performance of the controller for a step change in the command frequency.

In order to investigate the robustness of the controller, a sudden step change in the load torque is introduced in the system at  $t = 14$ s which is depicted in Figure 9.18a. The speed and torque responses are presented in Figures 9.18b and 9.18c, respectively. The controller exhibits high dynamic performance by fast stabilization of the rotor speed for

maintaining the motor synchronization. The rotor experiences slight speed undershoots but overcomes it very quickly by the control action. This phenomenon is shown in Figure 9.18b.

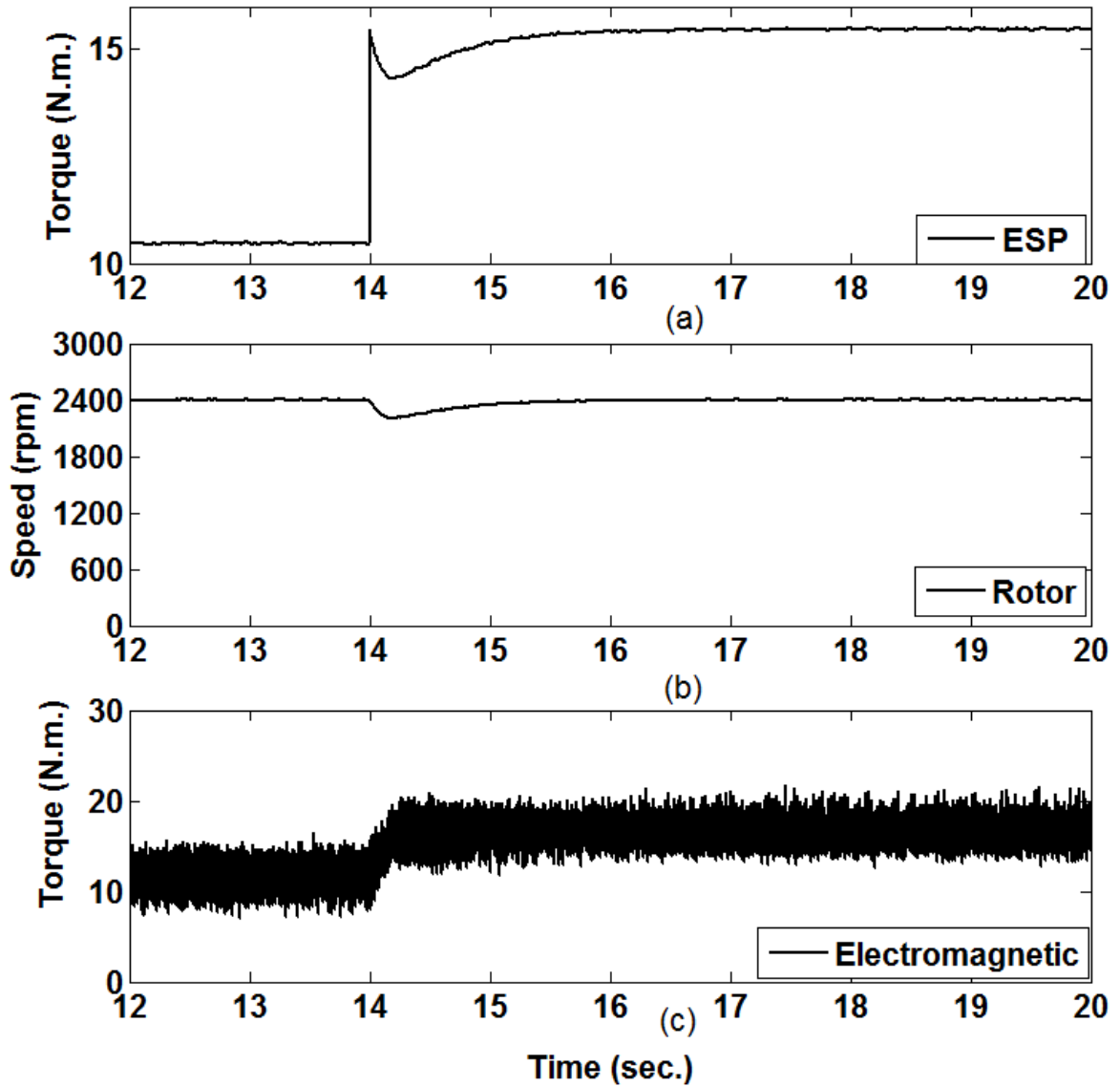


Figure 9.18. Performance of the sensorless controller for a step change in the load: (a) load torque, (b) speed and (c) electromagnetic torque.

Figures 9.19a and 9.19b illustrate the performance of the SMO for a step change in the load torque. The SMO can track the dynamic changes in the motor position and speed confidently during sudden speed/torque variations. There are no phase lags and speed estimation errors during a sudden change in the speed of the motor.

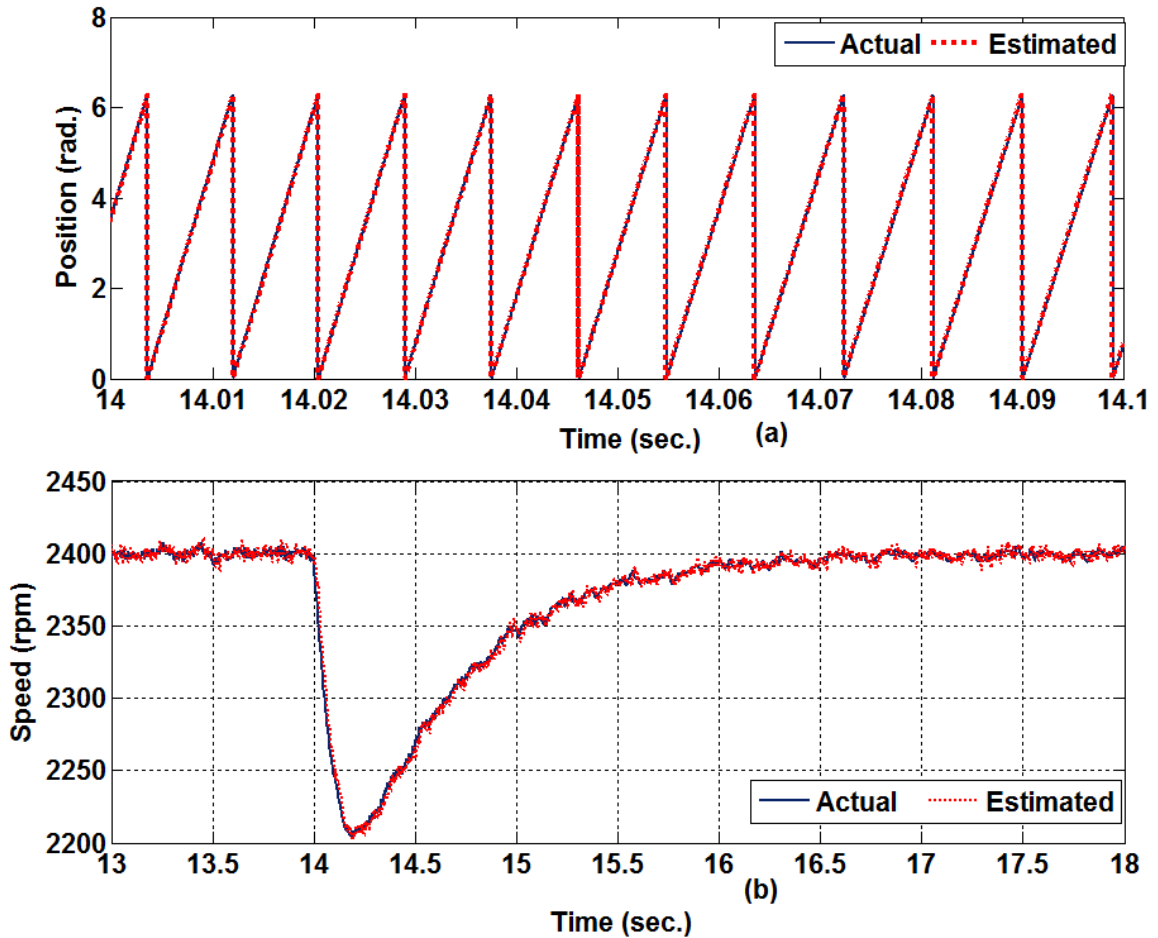


Figure 9.19. Performance of the sensorless controller for a step change in the load: (a) actual vs. estimated rotor position and (b) actual vs. estimated speed of the rotor.

## 9.5 Conclusion

This chapter presents a novel sensorless control strategy for submersible IPM motor drives. The proposed technique does not require any high frequency signal injections for starting an IPM motor unlike existing sensorless control techniques for IPM motor drives. The effectiveness of the algorithm is investigated on a 10-HP submersible IPM motor drive using Matlab/Simulink. Simulation results confirm the proposed control technique can start an IPM motor from stand-still without the need for position sensors. The developed sensorless vector controller can reliably operate the IPM-ESP drive at high speeds. It is robust against any sudden change in the operating condition for the motor drive.

## Appendix

The sliding surface for a sliding mode observer (SMO) is selected based on the variable structure theory, and follows the trajectory of the error. The surfaces of the SMO for back-emf estimation are given by,

$$S_{\alpha} = \hat{t}_{\alpha} - i_{\alpha} \quad (9.39)$$

$$S_{\beta} = \hat{t}_{\beta} - i_{\beta} \quad (9.40)$$

The following Lyapunov function can be selected to prove the stability of the SMO [23],

$$V = \frac{1}{2} (S_{\alpha}^2 + S_{\beta}^2) \quad (9.41)$$

where  $V$  is a positive definite function.

The sliding mode observer is stable if the following condition is met [27]-[28],

$$V\dot{V} \leq 0 \quad (9.42)$$

As  $V$  is a positive definite function, the following condition must be satisfied in order to meet the condition in (9.40),

$$\dot{V} \leq 0 \quad (9.43)$$

Differentiating (9.41), one gets,

$$\dot{V} = S_\alpha \dot{S}_\alpha + S_\beta \dot{S}_\beta \quad (9.44)$$

or,

$$\dot{V} = (\hat{i}_\alpha - i_\alpha)(\dot{\hat{i}}_\alpha - \dot{i}_\alpha) + (\hat{i}_\beta - i_\beta)(\dot{\hat{i}}_\beta - \dot{i}_\beta) \quad (9.45)$$

Using (9.14) and (9.15),

$$\dot{S}_\alpha = (\dot{\hat{i}}_\alpha - \dot{i}_\alpha) = -\frac{R}{L_q}(\hat{i}_\alpha - i_\alpha) - \frac{k}{L_q} \operatorname{sgn}(\hat{i}_\alpha - i_\alpha) + \frac{1}{L_q} e'_\alpha \quad (9.46)$$

$$\dot{S}_\beta = (\dot{\hat{i}}_\beta - \dot{i}_\beta) = -\frac{R}{L_q}(\hat{i}_\beta - i_\beta) - \frac{k}{L_q} \operatorname{sgn}(\hat{i}_\beta - i_\beta) + \frac{1}{L_q} e'_\beta \quad (9.47)$$

Replacing (9.46) and (9.47) into (9.44), the following expression is obtained,

$$\begin{aligned} \dot{V} = & -\frac{R}{L_q} S_\alpha^2 - \frac{R}{L_q} S_\beta^2 - \frac{k}{L_q} (\hat{i}_\alpha - i_\alpha) \operatorname{sgn}(\hat{i}_\alpha - i_\alpha) + \frac{1}{L_q} e'_\alpha (\hat{i}_\alpha - i_\alpha) \\ & - \frac{k}{L_q} (\hat{i}_\beta - i_\beta) \operatorname{sgn}(\hat{i}_\beta - i_\beta) + \frac{1}{L_q} e'_\beta (\hat{i}_\beta - i_\beta) \end{aligned} \quad (9.48)$$

Simplifying (9.48),

$$\dot{V} = -\frac{R}{L_q} S_\alpha^2 - \frac{R}{L_q} S_\beta^2 + \frac{1}{L_q} (e'_\alpha S_\alpha - k|S_\alpha|) + \frac{1}{L_q} (e'_\beta S_\beta - k|S_\beta|) \quad (9.49)$$

The condition in (9.43) will be satisfied for Lyapunov stability if the gain  $k$  is larger than both  $e'_\alpha$  and  $e'_\beta$ . The gain  $k$  is selected to meet the following criterion,

$$k \geq \max \{e'_\alpha, e'_\beta\} \quad (9.50)$$

Selection of a sufficiently large gain  $k$  will meet the condition in (9.42) and will guarantee the stability of the sliding mode observe based on Lyapunov's second method of stability [27].

## References

1. M. A. Choudhury, "An analysis of delta modulated inverters with applications to submersible motors", Doctoral Thesis, Memorial University of Newfoundland, St. John's, NL, Canada, 1988.
2. V. Pavlenko, "Permanent magnet synchronous motor (PMSM)-new type of drives for submersible oil pumps", in *proceeding of the 2008 SPE Russian Oil & Gas Technical Conference and Exhibition*, Moscow, Russia, October 28-30, 2008.
3. T. R. Brinner, R. H. McCoy and T. Kopecky, "Induction versus permanent-magnet motors for electric submersible pump field and laboratory comparisons," *IEEE Transactions on Industry Applications*, vol. 50, no.1, pp. 174-181, January 2014.
4. H. Kirby, R. Paes and J. Flores, "Speed control of electric submersible pumps - the "current" approach", *Proceedings of the Industry Applications Society Annual Meeting*, Kowloon, Hong Kong, China, 2-5 October 2005, pp. 1908-1918.
5. P. Head and H. Mansir, "Method and apparatus for control of a synchronous permanent magnet motor, particularly over a long cable in a well," U.S. Patent 20130147410A1, June13, 2013.
6. M. A. Rahman, D. M. Vilathgamuwa, M. N. Uddin and K. J. Tseng, "Nonlinear control of interior permanent-magnet synchronous motor", *IEEE Transactions on Industry Applications*, vol. 39, no.2, pp. 408-416, March 2003.
7. G. Foo and M. F. Rahman, "Sensorless Sliding-Mode MTPA Control of an IPM Synchronous Motor Drive Using a Sliding-Mode Observer and HF Signal Injection", *IEEE Transactions on Industrial Electronics*, Vol. 57, No. 4, pp. 1270-1278, April 2010.

8. Z. Qiao, T. Shi, et. al., "New Sliding-Mode Observer for Position Sensorless Control of Permanent-Magnet Synchronous Motor", *IEEE Transactions on Industrial Electronics*, Vol. 60, No. 2, pp. 710-719, February 2013.
9. S. Chi, Z. Zhang and L. Xu, "Sliding-Mode Sensorless Control of Direct-Drive PM Synchronous Motors for Washing Machine Applications", *IEEE Transactions on Industry Applications*, vol. 45, no.2, pp. 582 - 590, March 2009.
10. H. Kim, J. Son and J. Lee, "A High-Speed Sliding-Mode Observer for the Sensorless Speed Control of a PMSM", *IEEE Transactions on Industrial Electronics*, vol. 58, no.9, pp. 4069 - 4077, September 2011.
11. S. Bolognani, R. Oboe and M. Zigliotto, "Sensorless full-digital PMSM drive with EKF estimation of speed and rotor position", *IEEE Transactions on Industrial Electronics*, vol. 46, no.1, pp. 184-191, February 1999.
12. Y. Fang, L. Zhang, M. Cheng and K. T. Chau, "Sensorless SVPWM-FADTC of a new flux-modulated permanent-magnet wheel motor based on wide-speed sliding mode observer", *IEEE Transactions on Industrial Electronics*, vol. 62, no.5, pp. 3143- 3151, May 2015.
13. Y. Zhao, Z. Zhang, W. Qiao and L. Wu, "An extended flux model-based rotor position estimator for sensorless control of salient-pole permanent-magnet synchronous machines", *IEEE Transactions on Power Electronics*, vol. 30, no. 8, pp. 4412-4422, August 2015.
14. H. Kim, M. C. Harke and R. D. Lorenz, "Sensorless control of interior permanent-magnet machine drives with zero-phase lag position estimation", *IEEE Transactions on Industry Applications*, vol. 39, no. 6, pp. 1726-1733, November 2003.
15. S. Morimoto, K. Kawamoto, M. Sanada, Y. Takeda, "Sensorless control strategy for salient-pole PMSM based on extended EMF in rotating reference frame", *IEEE Transactions on Industry Applications*, vol. 38, no. 4, pp. 1054-1061, Jul./Aug. 2002.

16. J. Liu, T. A. Nondahl, P. B. Schmidt, S. Royak and M. Harbaugh, "Rotor position estimation for synchronous machines based on equivalent emf", *IEEE Transactions on Industry Applications*, vol. 47, no. 3, pp. 1310-1318, May 2011.
17. S. Kim, J. Ha and S. K. Sul, "PWM switching frequency signal injection sensorless method in IPMSM", *IEEE Transactions on Industry Applications*, vol. 48, no.5, pp. 1576-1587, September 2012.
18. M. J. Corley and R. D. Lorenz, "Rotor position and velocity estimation for a salient-pole permanent magnet synchronous machine at standstill and high speeds", *IEEE Transactions on Industry Applications*, vol. 34, no.4, pp. 784-789, July 1998.
19. J. Holtz, "Acquisition of position error and magnet polarity for sensorless control of PM synchronous machines", *IEEE Transactions on Industry Applications*, vol. 44, no.4, pp. 1172 - 1180, July 2008.
20. J. Jang, J. Ha, M. Ohto, K. Ide and S. K. Sul, "Analysis of permanent-magnet machine for sensorless control based on high-frequency signal injection", *IEEE Transactions on Industry Applications*, vol. 40, no.6, pp. 1595-1604, Nov. 2004.
21. P. P. Acarnley and J. F. Watson, "Review of position-sensorless operation of brushless permanent-magnet machines", *IEEE Transactions on Industrial Electronics*, vol. 53, no.2, pp. 352- 362, April 2006.
22. P. D. Chandana Perera, F. Blaabjerg, J. K. Pedersen and P. Thogersen, "A Sensorless, Stable V/f Control Method for Permanent-Magnet Synchronous Motor Drives", *IEEE Transactions on Industry Applications*, vol. 39, no. 3, pp. 783-791, May/June 2003.
23. D. Stellas, M. T. Hansen, T. Thiringer, T. Strømsvik, H. B. Ulvestad, "Position-sensorless control of a submersible PMSM fed over a long cable and two transformers", *Power Electronics and Applications (EPE'14-ECCE Europe) 2014 16th European Conference on*, pp. 1-10, 2014.
24. Jingbo Liu, Thomas A. Nondahl, Peter B. Schmidt, Semyon Royak, Timothy M. Rowan, "Generalized stability control for open loop operation of motor

- drives", *Proc. Industry Applications Society Annual Meeting 2015 IEEE*, pp. 1-8, 2015.
25. S. J. Merhej and W. H. Nichols, "Harmonic filtering for the offshore industry", *IEEE Transactions on Industry Applications*, vol. 30, No. 3, pp. 533-541, May/June 1994.
  26. R. Krishnan, *Electric Motor Drives: Modeling, Analysis, and Control*, Upper Saddle River, NJ, USA: Pearson, 2001.
  27. S. Morimoto, M. Sanada and Y. Takeda, "Wide-Speed Operation of Interior Permanent Magnet Synchronous Motors with High-Performance Current Regulator", *IEEE Transactions on Industry Applications*, vol. 30, no.4, pp. 920-926, August 1994.
  28. K. D. Young, V. I. Utkin and U. Ozguner, "A control engineer's guide to sliding mode control", *IEEE Transactions on Control Systems Technology*, vol. 7, no. 3, pp. 328-342, May 1999.
  29. S. Drakunov and V. Utkin, "Sliding mode observers. Tutorial", in Proceedings of the 34<sup>th</sup> conference on decision and control, New Orleans, LA, USA, pp. 3376-3378, December 1995.

## Chapter 10

### Conclusions and Future Works

#### 10.1 Research Conclusions

A detailed analysis of the synchronization process for determining the critical slip and the critical inertia of a cage-equipped interior permanent magnet (IPM) motor for both constant loads and dynamic fluid pumping loads is carried out for the first time in chapter 2 of this thesis. Chapter 2 has established that although a cage-equipped IPM motor is a favorable alternative to an induction motor in the case of both constant and variable loads, its synchronization capability becomes limited if the load inertia goes up. This chapter also provides a new simplified algorithm to evaluate the critical criteria of an IPM motor's synchronization capability for high inertial fluid pumping loads.

Chapter 3 of this thesis has dealt with the equivalent circuit modeling of self-starting hysteresis IPM motors. The magnetic and electrical equivalent circuits of hybrid hysteresis IPM motors using a new elliptical approximation of the hysteresis loops are presented in this thesis. The developed equivalent circuit models consider the dynamic variation of the rotor hysteresis impedances during line starting from a balanced ac supply. The results obtained from the equivalent circuit models are compared with finite element simulation results and experimental test results. The developed equivalent circuits can confidently predict the run-up responses of hysteresis IPM motors when fed directly from the line.

Chapter 4 introduces a new type of self-starting IPM motor named radial flux hysteresis IPM motor. A comparison between circumferential flux and radial flux type hysteresis motors is provided in this chapter. The design of a 1-HP radial flux hysteresis IPM motor is provided in chapter 4. Parametric analysis of the motor is conducted for variations of different design parameters. The proposed radial flux hysteresis IPM motor has higher starting and synchronization capabilities than similar circumferential flux hysteresis and cage-equipped IPM motors. It also reduces the amount of rare earth magnets in the rotor. The proposed motor is highly efficient and has high power factor.

Chapter 5 provides a short description of the artificial lift technology. A detailed modeling of the mechanical dynamics of an ESP drive system is provided in this chapter. It presents an original analysis of a hysteresis IPM motor driven ESP system for different shaft geometries using bond graph simulations. The effects of shaft diameter and shaft length on the pump torsional vibration are also presented in this chapter.

In chapter 6, a soft-starter using a voltage source inverter drive is designed for operating a hysteresis IPM motor driven ESP system. The soft-starter limits the amount of inrush torque on the ESP system, reducing the mechanical stress on pump impellers. This chapter does an original investigation on the damping capability of a hysteresis ring for IPM motors. Chapter 6 establishes the fact that a hysteresis IPM motor has inherent damping capability and does not require any active damping using an external controller.

Chapter 7 presents an original investigation of the hunting phenomenon in self-start IPM motors. An IPM motor suffers from inherent hunting during starting and synchronization periods. Sustained hunting also takes place in an IPM motor if it fails to synchronize with the stator field. Chapter 7 analyzes the effects of hunting induced rotor

oscillations on the stator current signal of the motor. It presents a motor current signature for detection of hunting in IPM motor drives. An offline diagnosis of hunting in a cage-equipped self-starting IPM motor drive using short-time Fourier transform and wavelet packet decomposition techniques are presented in this chapter.

Chapter 8 presents a new algorithm for on-line diagnosis of hunting in IPM motor drives. A multi-resolution analysis of the stator current signal using wavelet packet decomposition is carried out in real time for identifying the presence of hunting in the drive system. In this chapter, a novel technique for determining the severity of hunting is also provided in order to avoid false alarms. The developed algorithm is first verified by finite element simulations for 1-HP and 5-kW IPM motor drives. Real time experimental investigation is performed for the 1-HP motor drive.

Chapter 9 proposes a novel sensorless control strategy for submersible IPM motor drives. The design of a new 3-phase 6-pole 10-HP submersible IPM motor is presented in this chapter. An equivalent emf based position estimation algorithm is used to track the rotor position instantaneously. A sensorless  $V/f$  controller using the estimated rotor position is developed to start the IPM motor drive from standstill. A sensorless vector controller is designed to operate the motor drive at the command speed. The control action is switched from the sensorless  $V/f$  control to sensorless vector control when the rotor is stabilized after a successful start-up. Performances of the sensorless  $V/f$  and sensorless vector controller are investigated for the 10-HP IPM motor drive under various operating conditions.

## 10.2 Major Contributions

The major contributions of this thesis are listed below:

- A novel technique for determining the critical criteria for successful synchronization of interior permanent magnet motors with cage windings in the rotor is presented in chapter 2 of this thesis. The critical inertia vs. load torque for fluid pumping type of loads is provided in this thesis. The technique can be useful for designing a self-starting IPM motor drive for high inertial loads.
- A new simplified way of modeling equivalent circuits of hybrid hysteresis interior permanent magnet motors using elliptical approximation of the hysteresis loop is provided in chapter 3 of this thesis. The developed equivalent circuits provided a close approximation of the dynamic behavior of a hysteresis IPM motor. This model is computationally less intensive than other modeling techniques for hysteresis and hybrid hysteresis motors.
- A key contribution of this thesis is the introduction of a new hybrid self-starting IPM motor in chapter 4. This motor is named radial flux hysteresis IPM motor. It indicates higher torque density than the previously developed circumferential flux type hysteresis IPM motor. It also demonstrates higher starting and synchronization capabilities than conventional squirrel cage IPM motors. This motor can be a potential replacement of the cage IPM motor.
- An analysis of the mechanical dynamics of an ESP drive system is carried out in chapter 5 of this thesis. The torsional dynamics of intermediate shafts between

pump impellers is modelled in this thesis. Bond graph modeling of a hysteresis IPM motor driven ESP system is provided for the first time in this thesis.

- An analysis of hunting phenomenon for self-starting IPM motor drives is presented for the first time in chapter 7 of this thesis. The effect of hunting on the stator current signal of an IPM motor is mathematically modelled. Frequency domain analysis of the stator current is carried out using various signal processing techniques to detect hunting in the motor drive system.
- A new algorithm for real time diagnosis of hunting in IPM motor drives is presented in chapter 8 of this thesis. The proposed algorithm is simulated and experimentally validated. It is non-intrusive and highly suitable to be a part of the protection relay for remote condition monitoring of ESP systems.
- The final contribution of this thesis is a novel sensorless control technique for submersible IPM motor drives powered by long downhole cables. The developed sensorless controller can accurately estimate the rotor position of an IPM motor, considering the motor magnetic saliency. It is also robust and can start an IPM motor drive from the stand still position without any significant rotor vibration. It is applicable to both self-starting and variable speed IPM motor drives.

### 10.3 Future Works

Each chapter of this thesis explores areas of research that can be further investigated in future. This study has focused on different aspects of self-starting interior permanent magnet motor drives. The starting and synchronization of self-starting IPM motors have been the major area of research in this thesis. Future works for this thesis may include the following:

- Further experimental studies will be carried out in future to perform more detailed investigation on the synchronization capability of cage-equipped IPM motors for high inertial loads.
- Analytical and experimental studies will be carried out in future for exact modeling of a hysteresis IPM motor including higher harmonics and nonlinearities.
- Further research will be carried out to minimize torque ripples and total harmonic distortions in hysteresis IPM motors.
- Future works will be carried out to integrate the online hunting detection technique in a protection relay system for remote monitoring of practical applications such as ESP and compressor drive systems.
- A prototype submersible self-starting hysteresis IPM motor will be designed and fabricated in future.
- The start-up and synchronization capability of the motor for various operating conditions will be investigated.

- The sensorless controller for the prototype submersible IPM motor will be implemented to operate a multi-stage centrifugal pump drive system for lifting viscous fluids.
- Analysis of the robustness of the sensorless controller for noise and disturbance scenarios will be a subject matter for future works.
- The effects of electromagnetic transients in an offshore power system including long power cables and a load side transformer will be investigated in future.
- Further works will be carried to develop a hunting suppression control technique for submersible IPM-ESP motor drives.